Multistimuli-Responsive Cyclometalated and Noncyclometalated Ru(II) and Os(II) Complexes Based on Stilbene-Appended Terpyridine Ligands Towards the Development of Molecular Switches

A Thesis
Submitted for the Degree of
Doctor of Philosophy (Science)
of
Jadavpur University
by

Soumi Das

DEPARTMENT OF CHEMISTRY
JADAVPUR UNIVERSITY
JADAVPUR, KOLKATA 700032
INDIA

2025

যাদবপুর বিশ্ববিদ্যালয়
কলকাতা-৭০০০৩২, ভারত

*JADAVPUR UNIVERSITY
KOLKATA-700 032, INDIA

FACULTY OF SCIENCE: DEPARTMENT OF CHEMISTRY : INORGANIC CHEMISTRY SECTION

CERTIFICATE FROM THE SUPERVISOR

This is to certify that the thesis entitled "**Multistimuli-Responsive Cyclometalated and Noncyclometalated Ru(II) and Os(II) Complexes Based on Stilbene-Appended Terpyridine Ligands Towards the Development of Molecular Switches**" submitted by **Smt. Soumi Das** who got her name registered on 14.09.2020 for the award of Ph.D. (Science) Degree of Jadavpur University, is absolutely based upon her own work under the supervision of Prof. Sujoy Baitalik and that neither this thesis nor any part of it has been submitted for either any degree/diploma or any other academic award anywhere before.

Sujoy Baitalik 11/09/2025

(SUJOY BAITALIK)

Signature of the Supervisor

& Date with official seal

Professor Sujoy Baitalik
Department of Chemistry
Jadavpur University
Kolkata- 700 032, India

দূরভাষ: ২৪১৪-৬৬৬৬/৬১৯৪/৬৬৪৩/৬৪৯৫/৬৪৪৩ প্রসারণ: ২৪৬৯ Website:www.jadavpur.edu Phone:2414-6666/6194/6643/6495/6443 Extn.2469
দূরবার্তা: (৯১)-০৩৩-২৪১৪-৬৪১৪/৬২১০/২৪১৩-৭১২১ E-mail : hod@chemistry.jdvu.ac.in Fax: (91)-033-2414-6414/6210/2413-7121

Dedicated

to

My Family

"The power of concentration is the only key to the treasure-house of knowledge"

- Swami Vivekananda

PREFACE

The research documented in the thesis titled "Multistimuli-Responsive Cyclometalated and Noncyclometalated Ru(II) and Os(II) Complexes Based on Stilbene-Appended Terpyridine Ligands Towards the Development of Molecular Switches" was conducted at the Department of Chemistry of Jadavpur University from 2020 to 2025. The thesis comprises six chapters.

Chapter 1 provides a comprehensive review of the photophysical and electrochemical properties of cyclometalated and noncyclometalated Ru(II) and Os(II) polypyridine complexes, along with the stimuli-responsive photoisomerization behavior of stilbene- and azo-functionalized metal complexes. The chapter concludes by outlining the key research objectives and scope of this dissertation.

Chapter 2 deals with the synthesis, structural characterization, photo-redox properties and the acid-base behavior of a series of luminescent cyclometalated Ru(II)-terpyridine complexes of the type [(py-bpy-Ph-X)Ru(tpy-PhCH$_3$)]ClO$_4$ (X= -CH$_3$, -CH$_2$Br, and -CHO). The non-coordinated nitrogen atom in the outer coordination sphere allows fine modulation of the spectral properties by acid-base equilibria. Excess acid induces de-coordination of the Ru-C bond which again restores upon treatment with base at elevated temperature. Thus, "on-off" and "off-on" emission switching is feasible upon treatment with acid, base and temperature in appropriate sequence. Computational investigations involving density functional theory (DFT) of the compounds were performed to gain insights on their electronic structures and for appropriate assignment of the spectral bands.

Chapter 3 describes the synthesis and characterization of two NIR-emissive bimetallic cyclometalated Ru(II)-terpyridine complexes with compositions, [(ttpy)Ru(tpvpt')Ru (ttpy)](ClO$_4$)$_3$ and [(ttpy)Ru(t'pvpvpt')Ru(ttpy)](ClO$_4$)$_2$. Non-coordinated nitrogen atoms enable reversible modulation of photoredox properties via acid-base treatment, inducing de-coordination and re-coordination of Ru–C bonds. The complexes exhibit *trans-cis* photoisomerization under alternating visible and UV light irradiation. Interestingly, the isomerization process gets significantly accelerated in presence of acid. Thus, "on-off" and "off-on" emission switching in NIR region is attained via appropriate choice of stimuli.

DFT and TD-DFT studies further elucidate the electronic structures and support spectral assignments, providing comprehensive insight into their photophysical behavior.

Chapter 4 deals with the synthesis and characterization of a new series of bimetallic Ru(II)-terpyridine complexes of general composition $[XRu(tpvpvpt)RuX]^{4+}$ (X = ttpy, H_2bip, Me_2bip), followed by an in-depth examination of their photoredox behavior. The stilbene units undergo *trans-trans* to *cis-cis* isomerization upon visible-light irradiation, enabling substantial modulation of the photoredox properties. Notably, the rate of photoisomerization is significantly enhanced in the presence of chemical oxidants (CAN) and reductants (metallic Na). These complexes thus exhibit multistate switching via redox and light-induced reversible isomerization. The mode of isomerization was further elucidated by DFT calculations.

Chapter 5 explores the design of multiply configurable molecular logic devices utilizing the multistep switching characteristics of a Ru(II) complex $[(Me_2bip)Ru(tpvpvpt)Ru(Me_2bip)]^{4+}$. Distinct emission responses generated under different external stimuli are employed as optical outputs to realize diverse Boolean logic operations, including IMPLICATION, as well as more sophisticated systems such as 2-input/2-output and 3-input/2-output combinational logic gates. Additionally, a Python-based logic circuit model is devised to precisely predict the output responses under the influence of diverse inputs.

Chapter 6 presents the synthesis and comprehensive characterization of two symmetric, luminescent bimetallic Ru(II) and Os(II) complexes with composition $[(tpy\text{-}PhCH_2PPh_3Br)_2M_2(tpvpvpt)]^{4+}$. The complexes incorporate a bis-terpyridine bridging ligand with two consecutive stilbene units, together with a tridentate capping ligand containing acidic methylene groups and phosphonium functionalities. The presence of acidic methylene protons imparts selective recognition of F^- and OH^- anions. Furthermore, the complexes undergo reversible *trans-trans* ⇌ *trans-cis* isomerization upon visible or UV light irradiation. These systems exhibit efficient and reversible "on-off" emission switching across the visible to NIR region in response to multiple external stimuli, including anions, oxidants, reductants, and light of specific wavelengths. Notably, such stimuli induce a significant enhancement in the rate of photoisomerization.

ACKNOWLEDGEMENTS

As I write these words, I find myself reflecting on the remarkable journey that has led me to this point, a journey marked by moments of discovery, challenges, perseverance, and growth. This thesis represents not only the culmination of years of research but also a tribute to the steadfast support, encouragement, and kindness of many individuals who have influenced my path.

First and foremost, I extend my deepest gratitude to my supervisor, Professor Sujoy Baitalik. His wisdom, patience, and unwavering support have formed the bedrock of this research. Beyond being an advisor, he has been a true mentor, instilling in me the values of perseverance, curiosity, and academic integrity. His encouragement during moments of doubt and meticulous attention to detail have shaped not just this thesis but the scientist I have become. Every discussion, suggestion, and challenge he presented has served as a stepping stone for growth. I consider myself truly fortunate to have benefited from his mentorship, and this work stands as a testament to his invaluable influence.

I am sincerely thankful to the Department of Chemistry at Jadavpur University for providing an enriching environment that facilitated a smooth research journey. My heartfelt appreciation also goes to Prof. Mahammad Ali, Dean of the Faculty Council of Science; Prof. Kajal Krishna Rajak, Head of the Department; and Prof. Partha Roy, the Section-in-Charge, whose guidance and support have been instrumental throughout this academic journey. I am indebted to my research advisory committee member, Prof. Sasankasekhar Mohanta, for his invaluable feedback, stimulating discussions, and for challenging me in ways that strengthened my work. Their expertise and encouragement have been vital in shaping this research.

I am also obliged to Prof. Samaresh Bhattacharya, Prof. Nitin Chattopadhyay, Prof. Chittaranjan Sinha, Prof. Subrata Mukhopadhayay, Prof. Jnan Prakash Naskar, Prof. Mahammad Ali, Prof. Saurabh Das, Dr. Tapan Kumar Mondal, Dr. Bibhuti Bhushan Show, Dr. Partha Mahata, and

Dr. Ananya Bakshi for their kind cooperation and continual encouragement throughout my research journey.

I acknowledge the financial support from the Department of Science & Technology (DST) under the INSPIRE Fellowship Scheme, which has been crucial to my research. I also appreciate DST for its provision of key instruments, including the single crystal X-ray diffractometer through the FIST program and the Time-Resolved Nanosecond Spectrofluorimeter via the PURSE program, to the Department of Chemistry at Jadavpur University.

A special thanks goes to my former lab mates, Dr. Amit Chakraborty, Dr. Papri Mondal, Dr. Dinesh Maity, Dr. Manoranjan Bar, Dr. Poulami Pal, Dr. Animesh Paul, Dr. Shruti Mukherjee, Dr. Sourav Deb, Dr. Anik Sahoo, and Dr. Tanusree Ganguly—who have completed their doctoral degrees from our lab. I am also fortunate to work alongside esteemed colleagues like Toushique Ahmed, Sohini Bhattacharya, Raju Biswas and Tuhin Abedin who have turned long days in the lab into a journey filled with shared achievements, laughter, and growth. I truly appreciate the precious contribution from Dr. Subrata Ghosh for his cooperation in HRMS analysis of my samples at CSIR-North East Institute of Science & Technology (NEIST), Assam. Science is never a solitary endeavor, and I am thankful for the brainstorming sessions, troubleshooting marathons, and countless cups of coffee that sustained us through late nights. This journey would have been incomplete without their companionship, and for that, I am deeply grateful.

Words cannot fully express my profound gratitude to my family and friends, whose love and unwavering support have been my greatest source of strength. To my wonderful parents, Mr. Basudeb Das and Mrs. Krishna Das, your sacrifices, boundless encouragement, and steadfast faith in me have shaped every step of this journey. I would like to extend my sincere gratitude to my lovely elder brother, Dr. Sinjan Das, for his mental support and inspiration. I am glad to receive so much affection from my sister-in-law, Joita Joarddar, and especially her little one, Sourish, who has manifested additional happiness to my mind during this journey. I am eternally thankful

to my in-laws, Mr. Santosh Kumar Ghosh and Mrs. Babi Ghosh, for their inspiration and constant support throughout this research path.

To my beloved husband, Dr. Santanu Ghosh, your endless love, constant support, and unshakable belief in me have been my greatest blessing. Through every challenge and triumph, you have stood by my side, lifting me with your encouragement, confidence, and faith. I consider myself truly fortunate to have you.

Finally, to every person who has contributed in some way to this journey, whether through advice, encouragement, or simply being there when I needed it most—thank you. This achievement is not mine alone; it reflects the collective support, inspiration, and kindness I have been fortunate to receive. I carry this gratitude with me always.

With deepest reverence, I offer my heartfelt thanks to the Almighty, whose divine benevolence, wisdom, and boundless grace have unfailingly sustained my journey.

Soumi Das 11/09/2025

(Soumi Das)
Department of Chemistry,
Inorganic Chemistry Section,
Jadavpur University,
Kolkata-700032, India

CONTENTS

Chapter 1

General Introduction and Brief Review on Stimuli-Responsive Photoisomerization Behavior of Ru(II) and Os(II) Complexes Based on Terpyridine Ligands

and

Research Objective and Scope of the Present Work

1.1. General Introduction

Over recent decades, research efforts have significantly intensified in pivotal areas such as dye-sensitized solar cells (DSSCs), artificial photosynthesis, photocatalysis, optoelectronics, molecular-level machines, photoinduced DNA cleavage, sensors and photoswitching.[1-15] A major objective in this field is the development of molecular systems capable of exhibiting distinct functionalities in response to external triggers, including light, acid, base, cations, anions, oxidants, reductants etc.[16-25] Since light is one of the most sustainable and eco-friendly energy sources, there is a growing impetus to exploit its potential. This has fuelled the advancement of light-harvesting materials.[22-25] Among these, polypyridine complexes of low-spin d^6 transition metals, particularly Ru(II) and Os(II), have garnered significant attention owing to their exceptional thermal and photochemical stability, along with their versatile photo-redox behavior.[26-34] Notably, the electronic and photophysical properties of these complexes can be fine-tuned through targeted ligand modifications or by applying external stimuli. The rational design of such molecular building blocks, incorporating tailored ligand frameworks, has enabled progress in diverse applications, including sensors, molecular photoswitches, solar cells, and pharmaceuticals.[35-47] Ru(II) and Os(II) complexes are frequently designed using bidentate ligands, such as 2,2'-bipyridine (bpy) and 1,10-phenanthroline (phen) or tridentate ligands, notably 2,2':6',2''-terpyridine (tpy).[26-34,48-53] Although tpy-based complexes often exhibit superior enantiomeric purity, their photophysical properties are generally less favorable compared to bpy analogs due to suboptimal energy level alignments. Therefore, precise ligand design strategies are essential to optimize the excited-state energies of tpy complexes and enhance their luminescence efficiency. [48-53]

One of the most effective approaches for designing luminescent Ru(II)-tpy type complexes is to incorporate carbanionic centers in the ligand moiety (cyclometalating ligands).[54-59] Cyclometalated complexes, formed by replacing one nitrogen donor in tpy ligands with anionic carbon centers, offer a powerful strategy for tuning frontier orbital energies.[60-62] This substitution significantly modifies the electronic properties of the ligand, thereby enhancing the photoredox characteristics of the resulting bis-tridentate assemblies. While these complexes have gathered significant attention as sensitizers in DSSCs, their enhanced lipophilicity and improved cellular uptake, resulting from their reduced overall charge, make them promising candidates for photochemotherapeutic applications.[63-64]

Molecules capable of transitioning between their ground and excited states play a pivotal role in the development of functional materials.[18-24,64-69] The integration of a photo-responsive moiety into the complex framework markedly enhances its light-driven properties, enabling the development of artificial photochemical molecular systems such as photoswitches, optical materials, and memory storage devices.[64-69,70-75] The deliberate integration of azo, stilbene, diarylethene, and spiropyran moieties into ligand scaffolds effectively augments the electronic delocalization and photoreactivity of the resulting metal complexes.[76-87] Despite the extensive exploration of photoswitching behavior in purely organic systems,[88-99] their metal complex counterparts have received relatively less attention.[78-80,100-103] Furthermore, the majority of these photoswitches exhibit only two-step switching, primarily governed by either *trans-cis* isomerization or electrocyclization, thereby limiting their application to binary encoding (0/1) in circuit-based systems.[100-105] However, the development of advanced functional materials demands multi-step photoswitching processes driven by multiple external stimuli, enabling greater control over molecular states and expanding their potential for complex data storage and multifunctional device applications.[106-108]

Molecular-level information processing has rapidly progressed since de Silva's groundbreaking demonstration of storing logical states at the molecular scale.[109-112] In the past two decades, extensive research has led to the development of various molecular and supramolecular systems,[113-120] enabling the realization of basic and complex logic gates, including AND, OR, XOR, and NOR, within molecular frameworks.[121-127] Such molecular-based computation holds promise for creating smaller, faster, and more efficient alternatives to traditional silicon-based devices. However, despite notable advancements, the field still lacks intelligent molecular systems capable of performing intricate logic operations in response to multiple stimuli, offering new opportunities for next-generation advanced molecular circuits. To this end, Ru(II) complexes incorporating polyheterocyclic ligands have demonstrated remarkable potential due to their fascinating photophysical and electrochemical characteristics, which can be finely tuned by interacting with a diverse range of external stimuli.[25,28,128,129]

In this dissertation, our target is to design luminescent homo- and heteroleptic Ru(II) and Os(II) terpyridine complexes incorporating cyclometalating and/or stilbene-functionalized ligands. The inclusion of cyclometalating units is expected to significantly escalate the emission efficiency by increasing the ligand field strength and suppressing non-radiative decay pathways. Simultaneously, the stilbene units, known for their propensity to

undergo *trans-cis* photoisomerization upon light irradiation, introduce photoresponsive characteristics to the complexes, rendering them promising candidates for molecular photoswitching applications. Beyond light-induced transformations, we will also explore the complexes' responsiveness to multiple external stimuli, enabling multi-step switching processes. This versatile switching behavior is highly desirable for the development of advanced functional materials with tuneable optical and electronic properties. Finally, leveraging the multi-step switching capability, we will investigate the potential of these complexes to perform intricate molecular decision-making operations, facilitating the construction of sequential and complex logic functions.

1.2. Ru(II) and Os(II) Complexes with Polypyridine Ligands: Insights into Their Photophysical and Electrochemical Properties

Ru(II) and Os(II) polypyridine complexes have garnered considerable attention owing to their widespread applications in advanced functional materials and molecular technologies.[20-24] Polypyridine ligands, particularly bidentate systems such as 2,2′-bipyridine (bpy) and 1,10-phenanthroline (phen), as well as tridentate chelating frameworks like terpyridine (tpy), are widely utilized in transition metal coordination chemistry. Among these, $[Ru(bpy)_3]^{2+}$ and its derivatives have demonstrated exceptional photophysical properties, making them highly valuable for various applications. These complexes typically exhibit strong absorption across the UV-vis spectrum, which can be fine-tuned through strategic ligand modifications. Their photophysical behavior is characterized by prominent spin-allowed metal-to-ligand charge transfer (^{1}MLCT) transitions in the visible region, arising from $d\pi(Ru) \rightarrow \pi^*$(ligand) electronic transitions.[28-30] Os(II) complexes, on the other hand, feature an additional weak and broad absorption band at longer wavelengths, attributed to the spin-forbidden $^1GS \rightarrow {}^3$MLCT transition.[130-135] Additionally, high-energy absorption bands corresponding to intraligand charge transfer (ILCT) and π-π^* transitions are observed, primarily originating from the polypyridine ligand framework.[31,33,42,130-135]

Upon excitation at their lowest-energy absorption band, these complexes are promoted to the ^{1}MLCT excited state. This state undergoes ultrafast intersystem crossing (ISC), populating either the triplet metal-centered (^{3}MC) or triplet metal-to-ligand charge transfer (^{3}MLCT) states, or both. The subsequent relaxation to the ground state occurs via

two competing pathways: radiative decay from the ^{3}MLCT state or non-radiative deactivation through the ^{3}MC state. Each deactivation pathway is characterized by distinct parameters, including the radiative rate constant (k_r), excited-state lifetime (τ), and quantum yield (Φ). The relative positioning of the ^{3}MLCT and ^{3}MC states plays a pivotal role in determining the luminescence efficiency of these metal complexes. A small energy gap between these states, typically observed with weak-field ligands, facilitates population of the non-emissive ^{3}MC state, resulting in diminished luminescence.

Ru(II) complexes incorporating bidentate ligands exhibit enhanced luminescence arising from the lowest-lying ^{3}MLCT state, which remains well-separated from the non-radiative ^{3}MC state. For instance, $Ru(bpy)_3^{2+}$ in acetonitrile demonstrates an excited-state lifetime of 860 ns and a quantum yield of 0.062.[25,28,136] However, tris(bpy) complexes naturally exist as a mixture of Δ and Λ diastereomers, complicating their separation. In contrast, bis-terpyridine complexes, particularly those substituted at the 4'-position, adopt achiral rod-like structures. Despite this structural advantage, their luminescence is significantly weaker, and they exhibit extremely short excited-state lifetimes [τ=0.25 ns, for $Ru(tpy)_2^{2+}$], primarily due to the acute bite angle of terpyridine ligands. These limitations have driven the development of Ru(II) complexes featuring bis-tridentate ligand frameworks designed to achieve extended excited-state lifetimes.[50,137] Various synthetic strategies have been explored to enhance the energy gap between the emissive ^{3}MLCT and non-emissive ^{3}MC states. These approaches include incorporating electron-donating/withdrawing substituents,[57,138-142] introducing coplanar heteroaromatic systems,[143-147] and integrating organic chromophores[148] to stabilize the ^{3}MLCT state and improve photophysical performance. The energy gap between the ^{3}MLCT and ^{3}MC states can also be widened by raising the energy of the ^{3}MC state. This can be achieved through two primary approaches: (i) reducing the structural strain of the tridentate ligand, which enhances its ligand field strength, and (ii) increasing the ligand's electron-donating capacity by incorporating strongly donating functional groups, such as (hetero)aromatic N^-, C^-, or S.[58,148,153] These modifications contribute to stabilizing the metal-centered state while simultaneously influencing the metal-ligand electronic interactions. Cyclometalated complexes are typically generated by substituting one nitrogen atom in the tpy framework with a carbanionic center, leading to significant alterations in the electronic properties of the ligand.[54-59] The strong electron-donating nature of cyclometalating ligands elevates the energy of the non-radiative ^{3}MC state, thereby widening the ^{3}MLCT-^{3}MC energy gap.

Consequently, bis-tridentate Ru(II) complexes incorporating these ligands exhibit enhanced photo-redox activity compared to $Ru(tpy)_2^{2+}$. Furthermore, the introduction of spacer groups such as phenyl or stilbene units into the cyclometalating framework enhances the luminescence properties of these complexes by modulating their electronic properties.

Osmium(II) polypyridyl complexes exhibit photophysical properties comparable to those of their ruthenium(II) analogues. However, the larger 5d orbitals of osmium lead to a red-shift in both absorption and emission spectra due to stronger spin-orbit coupling (SOC) effects. Despite these similarities, Os(II)-bpy type complexes typically display shorter luminescence lifetimes than their Ru(II) counterparts, as dictated by the energy gap law.[30] In contrast, Os(II)-tpy derivatives exhibit significantly longer luminescence lifetimes (~50-500 ns) compared to Ru(II)-tpy complexes, even though their emissive ^{3}MLCT state remains at a lower energy. Both Ru(II) and Os(II) polypyridyl complexes emit in the red to near-infrared (NIR) spectral region, with excited-state lifetimes ranging from nanoseconds to microseconds. A schematic state diagram (Figure 1.1) provides an overview of the photophysical behavior of Ru(II)- and Os(II)-bpy and tpy complexes, while Table 1.1 summarizes key photophysical parameters of representative examples.

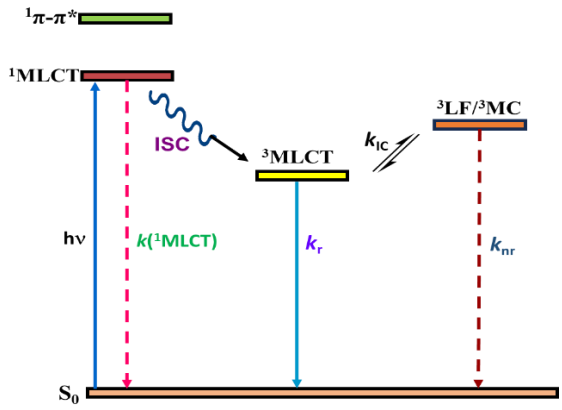

Figure 1.1

Table 1.1. Photophysical Properties of Ru(II) and Os(II) Complexes with bpy and tpy Motifs in MeCN at 298 K.

Complex	λ_{max}^{abs}/nm (MLCT)	λ_{max}^{em}/nm (MLCT)	τ/ns	Ref.
$[Ru(bpy)_3]^{2+}$	454	620	800	25, 31
$[Ru(tpy)_2]^{2+}$	475	628	< 5	25, 31
$[Os(bpy)_3]^{2+}$	480	715	19	29, 31
$[Os(tpy)_2]^{2+}$	477, 657	718	269	31, 33

Ru(II) and Os(II) polypyridyl complexes have demonstrated significant potential due to their well-defined electrochemical properties and exceptional redox stability in both ground and excited states. These complexes typically exhibit reversible oxidation peak(s) at positive potentials, while reversible and/or quasi-reversible peaks appear in the negative potential region due to reduction. Theoretical calculations reveal that the highest occupied molecular orbitals (HOMOs) are primarily localized on the metal centers, indicating oxidation from Ru(II)/Os(II)→Ru(III)/Os(III). In contrast, the lowest unoccupied molecular orbitals (LUMOs) are predominantly associated with the pyridine-based ligands, signifying ligand-centered reduction. Notably, Os(II) complexes undergo oxidation at lower potentials than their Ru(II) counterparts, a trend attributed to the greater stability of third-row transition metal ions in higher oxidation states. The electrochemical parameters of representative complexes are tabulated in Table 1.2.

Table 1.2. Electrochemical Properties of Respresentative Ru(II) and Os(II) Complexes Based on bpy and tpy Ligands in MeCN at 298 K.

Compounds	Oxidation $E_{1/2}$(ox)/V	Reduction $E_{1/2}$(red)/V	Ref.
$[Ru(bpy)_3]^{2+}$	1.27	-1.31, -1.50, -1.77	154
$[Ru(tpy)_2]^{2+}$	1.30	-1.29, -1.54	156
$[Os(bpy)_3]^{2+}$	0.78	-1.30, -1.48, -1.78	155
$[Os(tpy)_2]^{2+}$	0.97	-1.25, -1.57	156

1.3. Development of Logic Operations

Electronic devices have become indispensable in modern life, revolutionizing communication, data storage, and information processing. The operational framework of digital electronics is fundamentally based on Boolean algebra, which employs binary logic states-"On" (1) and "Off" (0), to process data. Logical operations involve one or more inputs and produce a single output, following predefined Boolean rules. The eight primary logic functions- OR, AND, XOR, NOR, NAND, XNOR, INHIBIT (INH), and IMPLICATION (IMP), serve as the foundation for more complex combinational circuits. These fundamental logic systems enable arithmetic operations and facilitate the design of advanced circuits, including half-adders and subtractors, keypad-lock mechanisms, set-reset flip-flops, memory devices, multiplexers, demultiplexers, and encoder/decoder units.[157-162]

While silicon-based technology remains the cornerstone of modern integrated circuits due to its efficiency, its miniaturization faces inherent physical limitations. In contrast, molecular computing offers an advantage by processing information at the nanometer scale, presenting a promising alternative. The concept of molecular logic gates, first proposed by A. P. de Silva in 1993, mimics traditional logic operations using molecular-level interactions.[109] The development of stimuli-responsive molecules is crucial for advancing molecular computation. These molecules generate distinct output signals in response to external stimuli such as temperature, pH, light, ionic species, oxidants and reductants enabling the construction of binary logic functions at the molecular level.

1.4. An Overview of Ruthenium(II) and Osmium(II) Complexes Featuring Polypyridine Ligands

Numerous review and research articles have already been published globally by various research groups on Ru(II) and Os(II) complexes based on polypyridine ligands featuring their synthesis, structural aspects and physicochemical properties. This dissertation mainly focuses on the synthesis and photo-redox properties of some Ru(II) and Os(II) complexes incorporating tridentate ligands.

1.4.1. A Concise Review of Photophysical and Electrochemical Properties

Terpyridine-based Ru(II) and Os(II) complexes have garnered significant attention due to their structurally rigid, achiral linear frameworks, despite their relatively weak excited-state properties.[22-24,31,33,35,143,146,147] To improve their photophysical and electrochemical performance, researchers have explored the incorporation of electron-donating or withdrawing substituents to enhance charge delocalization within the ligand framework. [53-58,146-148] These modifications can lead to improved photo-redox behavior, making such complexes valuable for applications in light-harvesting systems and supramolecular assemblies.[132-135] Furthermore, terpyridine-coordinated Ru(II) and Os(II) complexes have been investigated for their potential use in molecular devices, dye-sensitized solar cells, optical sensing platforms, and biomedical applications.[9-11,16-24,42,43] This dissertation provides a comprehensive analysis of the physicochemical properties of various monomeric and dimeric ruthenium and osmium complexes, with a focus on their structure-property relationships.

Abrahamsson *et al.* explored the impact of expanding the bite angle in tridentate metal ion coordination by incorporating 2,6-di(quinolin-8-yl)pyridine ligands, leading to

the synthesis of a series of bis-tridentate Ru(II) complexes (Figure 1.2).[163] These complexes adopt a nearly ideal octahedral geometry and exhibit excited-state lifetimes on the microsecond timescale for the ^{3}MLCT state at room temperature. Their study demonstrated that a wider bite angle results in a higher activation energy for non-radiative deactivation through the metal-centered (MC) state, distinguishing these complexes from other, less long-lived bis-tridentate Ru(II) systems, such as $[Ru(tpy)_2]^{2+}$, which has a significantly shorter excited-state lifetime (τ = 0.25 ns at room temperature). Moreover, the suppression of direct non-radiative decay from the ^{3}MLCT state was observed. Emission spectral analysis at 77 K reveals that the improved excited-state performance of these Ru(II) complexes cannot be mainly attributed to reduced geometric distortion in the excited state. Instead, the data indicate that diminished singlet-triplet mixing within the ^{3}MLCT state leads to slower radiative and non-radiative decay processes. Consequently, the complexes display markedly prolonged excited-state lifetimes and higher emission quantum yields.

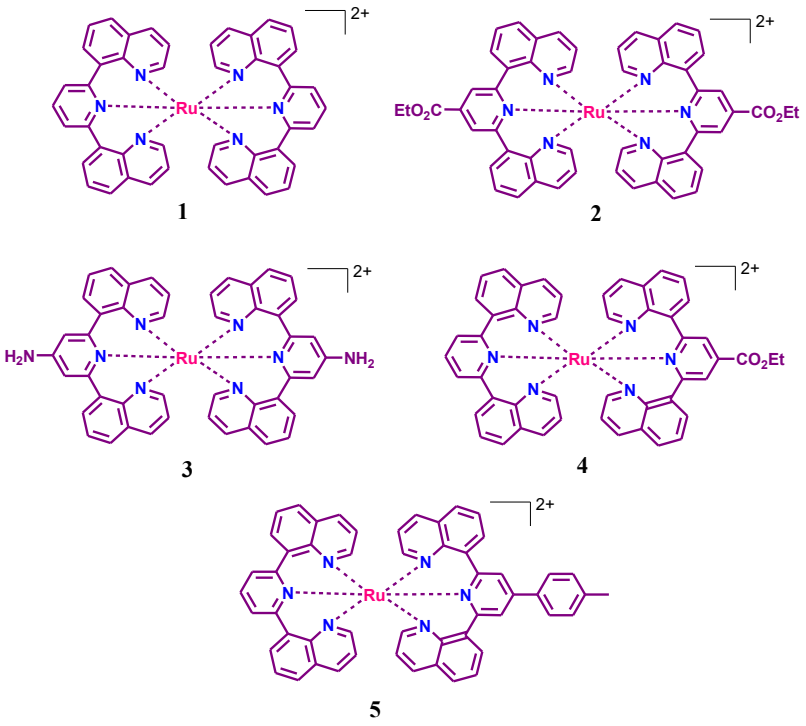

Figure 1.2

Indelli and coworkers designed two Ru(II)-terpyridine complexes incorporating cyanide ligands as ancillary groups and conducted an in-depth investigation on their solvent-dependent photophysical properties (Figure 1.3).[57] The introduction of cyanide ligands imparts pronounced solvatochromic behavior to these complexes, with their

luminescence characteristics being strongly influenced by the second-sphere donor-acceptor (SSDA) interactions between the cyanide moiety and the surrounding solvent. A significant enhancement in excited-state lifetime, spanning two orders of magnitude, was observed for the tricyano complexes [$Ru(tpy)(CN)_3^-$: τ = 48 ns in DMSO and $Ru(ttpy)(CN)_3^-$: τ = 40 ns in CH_3CN] compared to their bis-terpyridine counterparts [$Ru(tpy)_2^{2+}$: τ = 250 ps in CH_3CN; $Ru(ttpy)_2^{2+}$: τ = 860 ps in CH_3CN]. This substantial increase in excited-state lifetime is primarily attributed to the destabilization of the non-radiative MC states, resulting from the substitution of weak-field terpyridine ligands with strong-field cyanide ligands, which effectively raises the energy of the MC state and suppresses non-radiative decay pathways.

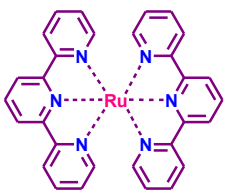

$Ru(tpy)_2^{2+}$, τ=250 ps in MeCN

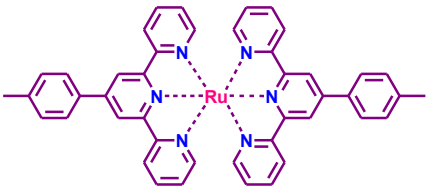

$Ru(ttpy)_2^{2+}$, τ=860 ps in MeCN

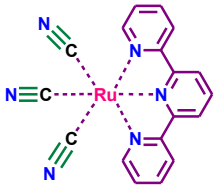

$Ru(tpy)(CN)_3^-$, τ=48 ns in DMSO

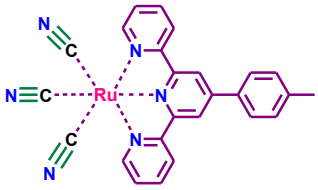

$Ru(ttpy)(CN)_3^-$, τ=40 ns in MeCN

Figure 1.3

Duati and colleagues explored an alternative approach to destabilizing the ^{3}MC states by modulating the metal-based dσ antibonding orbital. Their study involved the synthesis of a series of Ru(II)-terpyridine complexes featuring triazole and tetrazole ligands (Figure 1.4).[148] The photophysical and electrochemical properties of these complexes were systematically investigated, revealing a notable influence of ligand deprotonation on their excited-state dynamics. Upon deprotonation, the strong σ-donor characteristics of the negatively charged triazole and tetrazole ligands significantly increase the energy gap between the ^{3}MLCT and ^{3}MC states. This leads to an extended excited-state lifetime of up to 20-80 ns at RT. In contrast, protonation of the ligand framework diminishes its σ-donor ability, thereby reducing the ^{3}MLCT-^{3}MC energy separation. This facilitates non-radiative deactivation via ^{3}MC state, resulting in a substantial decrease in both quantum yield and

excited-state lifetime. Furthermore, the electrochemical behavior of these complexes differs markedly from that of the parent $[Ru(tpy)_2]^{2+}$ complex. Deprotonation induces a significant decrease in oxidation potential, aligning with spectroscopic observations and reflecting the enhanced electron-donating ability of the triazole and tetrazole ligands. Conversely, protonation of the azole ring leads to an increase in oxidation potential, further reinforcing the relationship between ligand electronic properties and redox behavior.

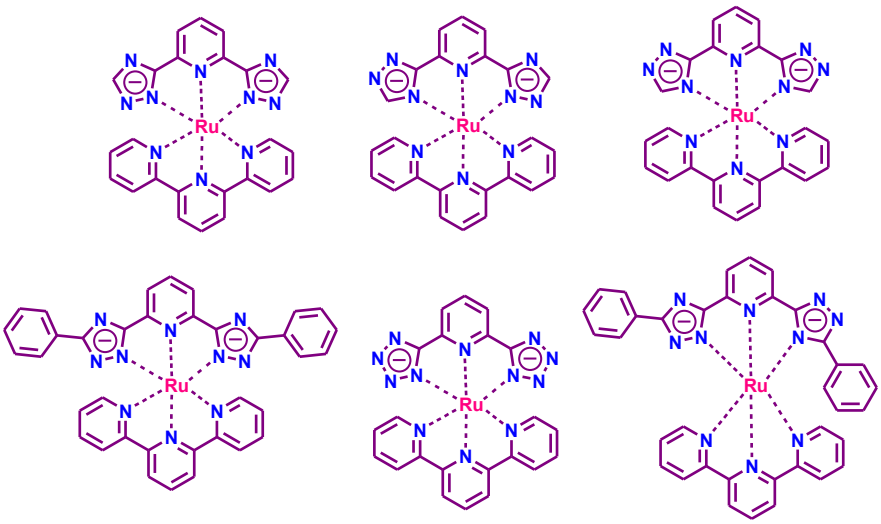

Figure 1.4

Yu *et al.* reported the synthesis of two ruthenium-terpyridine complexes (**Ru-1** and **Ru-2**) functionalized with visible light-absorbing BODIPY chromophores (Figure 1.5).[164] These complexes exhibit intense absorption in the visible region and exceptionally prolonged excited-state lifetimes. **Ru-2** demonstrates a lifetime of 37.9 µs, whereas **Ru-1** exhibits an even longer lifetime of 356 µs which is nearly hundreds of times greater than typical Ru(II)-terpyridine complexes. The pronounced enhancement in excited-state properties is attributed to the efficient population of the BODIPY-localized ^{3}IL (intraligand) state, which substantially increases the energy gap between the emissive state and the non-emissive ^{3}MC state. This energy separation effectively suppresses non-radiative deactivation, thereby extending the triplet-state lifetimes. These complexes were subsequently employed as triplet sensitizers for triplet-triplet annihilation upconversion (TTA-UC), leveraging their ultra-long-lived triplet states and strong absorption in the visible spectrum. Notably, **Ru-1** exhibited an UC quantum yield approximately seven times higher than that of **Ru-2**, whereas **Ru-3** did not display any detectable upconversion emission.

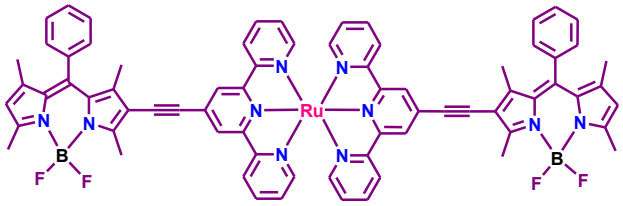

Ru-1

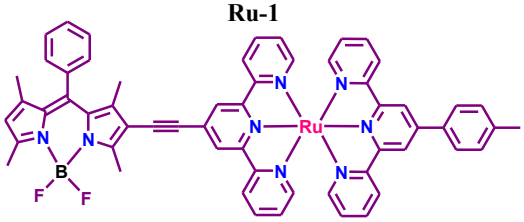

Ru-2

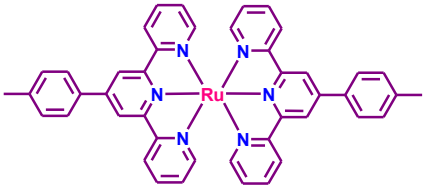

Ru-3

Figure 1.5

Aiming to expand the ligand bite angle and enhance the excited-state lifetime of ^{3}MLCT state in Ru(II) complexes coordinated with tridentate ligands, C. Turro and her research team recently synthesized two new Ru(II)-terpyridine complexes incorporating the qdppz ligand (qdppz= 2-(quinolin-8-yl)dipyrido[3,2-a:2′,3′-c]phenazine) (Figure 1.6).[165] Both complexes exhibit strong absorption in the visible region, with λ_{max} ~490 nm. Complex **1** displays a relatively short luminescence lifetime (~9 ns), primarily due to the presence of the tpy unit, which facilitates rapid deactivation of the ^{3}MLCT state by lowering the energy of the metal-centered ^{3}LF state. In contrast, the incorporation of the qdppz ligand on both sides of the Ru(II) center in complex **2** significantly increases the ligand bite angle, resulting in a much longer excited-state lifetime of ~310 ns in MeOH at room temperature. Arrhenius analysis of the temperature-dependent emission data indicates that the observed difference in excited-state properties between the two complexes is not directly related to the energy gap between the ^{3}MLCT and ^{3}LF states. Instead, Franck-Condon analysis of the 77 K emission spectra reveals that the extended lifetime of **2** is primarily due to greater distortion of the ^{3}MLCT state relative to the ground state compared to **1**. Although both complexes intercalate between DNA base pairs, only complex **2** exhibits photocleavage activity. This behavior is attributed to its ability to generate $^1O_2$ upon irradiation, with a singlet oxygen quantum yield $\Phi_\Delta = 0.69$.

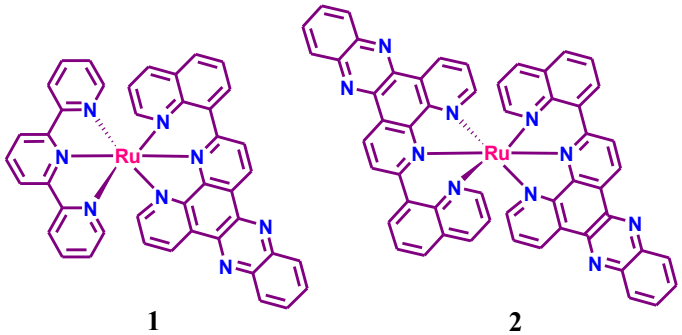

1 2

Figure 1.6

Heinze and colleagues synthesized and comprehensively characterized two redox-asymmetric, amide-bridged bis(terpyridine)ruthenium(II) complexes (**3a** and **3b**) through the amide coupling of a carboxyl-functionalized ruthenium complex with an amine-substituted counterpart (Figure 1.7).[166] These dinuclear complexes exhibit significantly higher molar extinction coefficients than their mononuclear analogs. In case of **3b**, the λ_{max} of the ^{1}MLCT band undergoes a bathochromic shift to ~522 nm, and the complex exhibits near-infrared (NIR) emission with an emission maximum at 750 nm. Both complexes display comparable emission quantum yields and excited-state lifetimes of ~20 ns. Electrochemical studies using cyclic voltammetry reveal two distinct oxidation potentials corresponding to the differently substituted ruthenium centers, with potential splitting of 0.10 V and 0.23 V for **3a** and **3b**, respectively. Furthermore, oxidation of **3b** with Ce(IV) ions results in the formation of a mixed-valence Ru(II)-Ru(III) system, which remains valence-localized, as confirmed by NIR spectroscopic measurements and theoretical analyses.

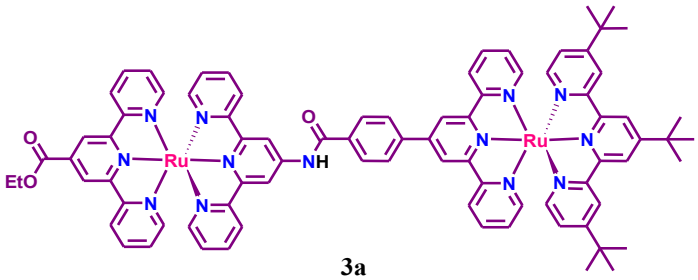

3a

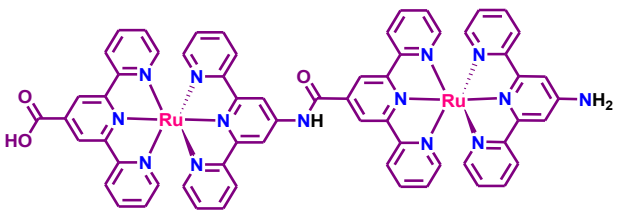

3b

Figure 1.7

In another work, Kreitner *et al.* synthesized and thoroughly characterized a dinuclear dipeptide complex, $[(EtOOC\text{-}tpy)Ru(tpy\text{-}NHCO\text{-}tpy)Ru(tpy\text{-}NHCOCH_3)]^{4+}$ ($\mathbf{3}^{4+}$), designed to achieve a high degree of electronic similarity between the two Ru(II) centers, despite the inherent structural asymmetry introduced by the amide-bridged linker (Figure 1.8).[167] Spectroscopic (UV-vis absorption and NMR) as well as electrochemical (cyclic voltammetry) studies confirmed the electronic equivalence of the metal sites. Photophysical investigations revealed that the complex exhibits dual emission at room temperature, originating from two distinct triplet excited states with differing energies and lifetimes. However, at 77 K, only a single emission band is observed. This temperature-dependent behavior is attributed to the establishment of a dynamic thermal equilibrium between two resonance forms, $[Ru^{II}(tpy\text{-}NHCO\text{-}tpy^{\bullet-})Ru^{III}]$ and $[Ru^{III}(tpy\text{-}NHCO\text{-}tpy^{\bullet-})Ru^{II}]$. These resonance structures represent a unique excited-state mixed-valent Ru^{II}/Ru^{III} system, in which the radical anion bridge ($tpy\text{-}NHCO\text{-}tpy^{\bullet-}$) facilitates electronic delocalization and mediates intramolecular charge transfer.

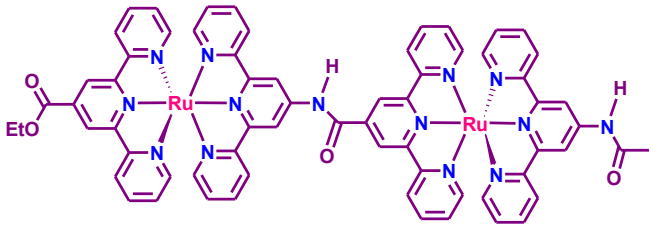

$[(EtOOC\text{-}tpy)Ru(tpy\text{-}NHCO\text{-}tpy)Ru(tpy\text{-}NHCOCH_3)]^{4+}$ ($\mathbf{3}^{4+}$)

Figure 1.8

Harriman and the group reported two alkyne-bridged binuclear ruthenium(II)-terpyridine complexes that exhibit significantly enhanced triplet excited-state lifetimes compared to the mononuclear parent complex, $[Ru(tpy)_2]^{2+}$ (Figure 1.9).[168] Specifically, the excited-state lifetimes of complexes **3a** and **3b** were measured to be 565 ns and 720 ns which are nearly 3000 times longer than that of $[Ru(tpy)_2]^{2+}$, which exhibits a lifetime of only 0.56 ns. These extended lifetimes are accompanied by substantial red-shifts in emission maxima, observed at 722 nm for complex **3a** and 735 nm for complex **3b**, indicating a substantial lowering of the ^{3}MLCT energy relative to the parent complex. This stabilization of the ^{3}MLCT state also results in a shift of the reduction potential toward more positive values. The lowering of the ^{3}MLCT energy disrupts the thermal equilibrium that typically exists between the emissive ^{3}MLCT state and non-emissive metal-centered

(MC) or ligand-centered (LC) states in $[Ru(tpy)_2]^{2+}$. As a consequence, non-radiative deactivation pathways are suppressed, and the complexes exhibit improved luminescent properties along with prolonged excited-state lifetimes.

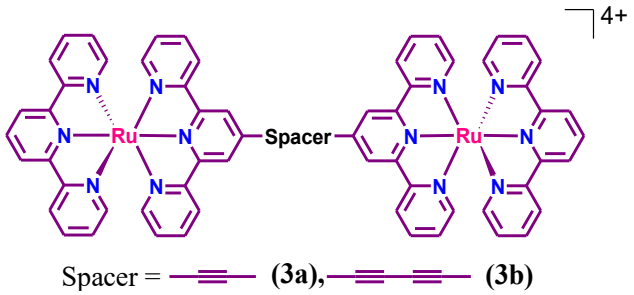

Figure 1.9

In a separate study, Ziessel and co-workers synthesized two heterobinuclear Ru(II)/Os(II) complexes incorporating identical alkyne-based bridging ligands (Figure 1.10).[169] Upon photoexcitation at 600 nm, both complexes display emission maxima at 746 nm and 760 nm, closely resembling the emission profile of $[Os(tpy)_2]^{2+}$, whereas the Ru(II)-terpyridine moiety remains non-emissive even when excited directly at 440 nm. This observation strongly indicates efficient intramolecular triplet energy transfer from the Ru(II) center to the Os(II) center within these systems. The dynamics of this energy transfer process were further investigated using transient absorption spectroscopy and time-resolved luminescence measurements conducted at both 295 K and 77 K. The results revealed that the rate constant for triplet energy transfer is higher in complex **5** compared to complex **6**. The mechanistic pathway for this transfer is attributed to a through-bond electron exchange mechanism, wherein an electron and a positive hole are simultaneously exchanged. This electron-hole pair movement facilitates efficient triplet energy migration from the Ru(II) to the Os(II) site, underscoring the role of the conjugated spacer in mediating electronic communication between the metal centers.

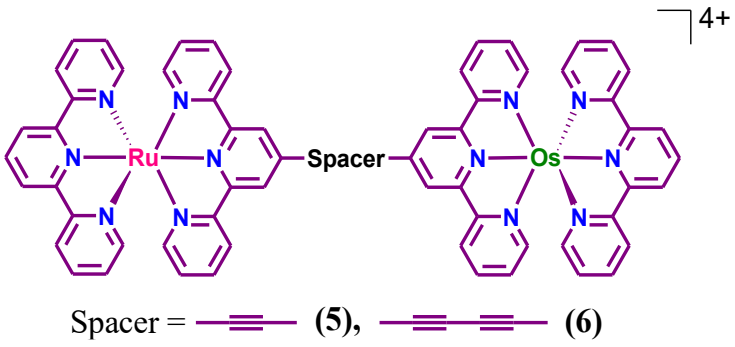

Figure 1.10

In a 2002 study, Housecroft and colleagues systematically explored the photophysical and electrochemical characteristics of multinuclear homo- and heterometallic Ru(II) and Os(II) terpyridine complexes, in which the metal centers are interconnected through bis(2,2':6',2''-terpyridin-4-yl)thiophene bridging ligands (Figure 1.11).[146] The UV-vis absorption spectra of the homometallic complexes revealed a progressive red shift of the MLCT bands accompanied by an increase in molar extinction coefficients as the nuclearity increased from mono- to bi- and trinuclear species. In contrast, the MLCT absorption profiles of the heterometallic complexes did not correspond to a simple combination of the individual monometallic components, indicating electronic interaction between the different metal centers. Photoluminescence studies further supported these observations that homometallic multinuclear complexes exhibited red-shifted emission relative to their monometallic counterparts, while heterometallic Ru-Os systems showed emission features characteristic of Os(II) centers, with negligible contribution from Ru(II)-based luminescence. These findings suggest an efficient intramolecular energy transfer from the Ru(II) center(s) to the Os(II) center, a process likely mediated by the conjugated and electron-rich thiophenediyl spacer, which facilitates delocalization and electronic communication between the metal centers.

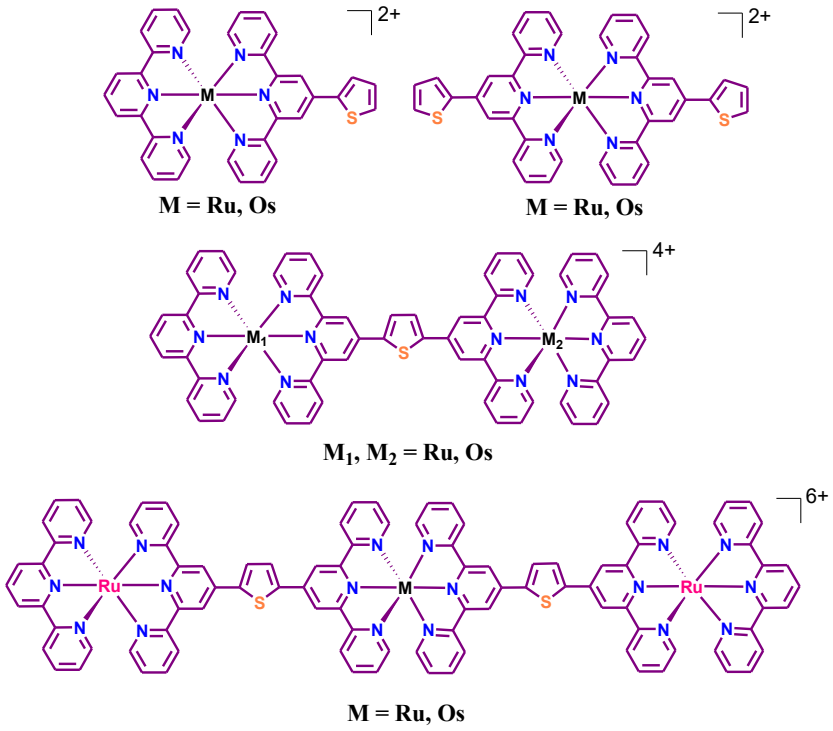

Figure 1.11

Vogler and Brewer developed two distinct classes of bimetallic complexes with the compositions $[(tpy)M(tpp)RuCl_3](PF_6)$ and $[(tpy)M(tpp)Ru(tpp)](PF_6)_4$ [M= Ru^{II}/Os^{II}], and systematically examined their photoredox properties. In both series, the LUMO is predominantly localized on the tpp ligand (Figure 1.12).[170] However, the HOMO distribution varies depending on the complex architecture. For $[(tpy)M(tpp)RuCl_3](PF_6)$ series, the HOMO is primarily associated with the $RuCl_3$ fragment, whereas in $[(tpy)M(tpp)Ru(tpp)](PF_6)_4$ complexes, it is localized on the metal center coordinated to both tpy and tpp ligands. Complexes of the type $[(tpy)M(tpp)Ru(tpp)](PF_6)_4$ are luminescent in solution and exhibit significantly red-shifted emission maxima relative to their monometallic counterparts. For example, the bimetallic complex $[(tpy)Ru(tpp)Ru(tpp)](PF_6)_4$ demonstrates an excited-state lifetime of ~100 ns, which is markedly longer than that of the mononuclear complex $[Ru(tpy)(tpp)]^{2+}$. In contrast, the heterometallic complex $[(tpy)Os(tpp)Ru(tpp)](PF_6)_4$ exhibits exclusive Os-centered ^{3}MLCT emission at 820 nm, with no detectable emission attributable to the Ru center.

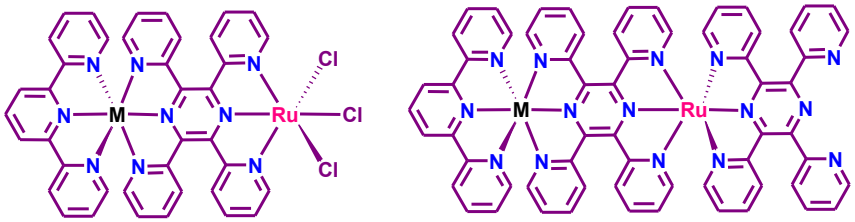

M = Ru, Os

Figure 1.12

Harriman and his research group synthesized two Ru(tpy) complexes featuring ethynyl-substituted aromatic linkers, as reported in their study (Figure 1.13).[171] The complex RTPTR, incorporating a phenylene bridge, displays a red-shifted emission at 685 nm and an extended excited-state lifetime (τ=110 ns) relative to the parent compound $[Ru(tpy)_2]^{2+}$. Another complex RTNTR, in which the phenylene unit is replaced by a naphthalene moiety, exhibits a further red-shift in the emission maximum (λ_{max}=702 nm) and a significantly prolonged excited-state lifetime (τ=475 ns). This enhancement in the excited state properties is attributed to increased π-electron delocalization in the triplet excited state, facilitated by the extended conjugation provided by the naphthalene bridge.

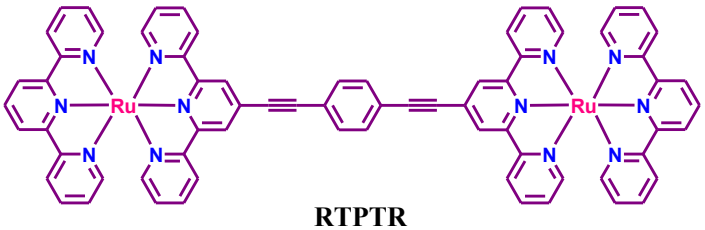

RTPTR

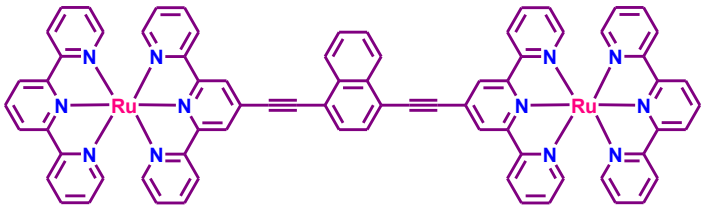

RTNTR

Figure 1.13

Baitalik and group designed three bimetallic Ru(II) complexes with a bis-terpyridine based phenyl-bisbenzimidazole bridge (Figure 1.14) and also thoroughly investigated their photoredox properties.[172] They exhibit moderately intense luminescence with emission maxima spanning between 653 and 687 nm and possess significantly prolonged excited-state lifetimes (6.3-55.2 ns) when compared to the reference complex $[Ru(tpy)_2]^{2+}$. The enhanced excited-state characteristics are attributed to efficient electronic coupling between the Ru(tpy) moieties and the conjugated phenyl-bis-benzimidazole bridge. This interaction results in a larger energy gap between the emissive ^{3}MLCT state and the thermally accessible non-emissive ^{3}MC state. Electrochemical studies revealed a single reversible oxidation wave for each complex without any detectable splitting, suggesting a concerted one-electron oxidation process involving both spatially separated Ru centers. Furthermore, the presence of acidic NH protons on the benzimidazole units imparts anion-responsive properties to the complexes. Notably, they exhibit high selectivity and sensitivity toward CN^- ions in predominantly aqueous environments, with a low detection limit of ~1×10^8 M.

In a separate study, Baitalik and coworkers reported the synthesis of three bimetallic Ru(II)-tpy complexes featuring a bis-terpyridine ligand incorporating a pyrenyl-bis-phenylimidazole bridging unit (Figure 1.15).[173] This extended π-conjugated bridge facilitates efficient electron delocalization across the molecular framework, resulting in markedly enhanced photoluminescence properties when compared to the non-emissive $[Ru(tpy)_2]^{2+}$ complex. The complexes exhibit strong room-temperature emission with maxima ranging from 657 to 703 nm, and excited-state lifetimes spanning 5.8 to 67.0 ns.

Electrochemical data reveals a single reversible oxidation wave for all complexes, consistent with a simultaneous two-electron Ru(II)/Ru(III) oxidation process at the two metal centers. Notably, the electrochemical generation of mixed-valence $Ru^{II}Ru^{II}/Ru^{II}Ru^{III}$ species is accompanied by the appearance of intervalence charge transfer (IVCT) bands in the near-infrared (NIR) region. This observation signifies effective electronic coupling between the two ruthenium centers, despite the considerable spatial separation imposed by the extended bridging ligand.

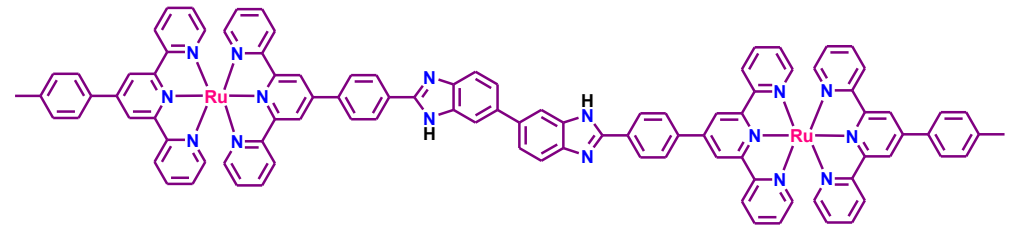

[(tpy-C_6H_4-CH_3)Ru(tpy-BPhBzimH_2-tpy)Ru(tpy-C_6H_4-CH_3)]$^{4+}$

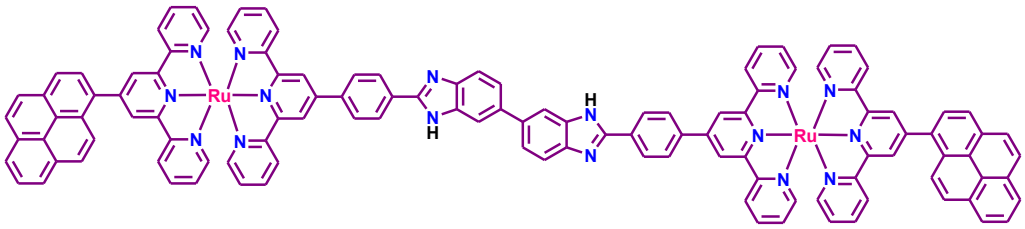

[(tpy-Py)Ru(tpy-BPhBzimH_2-tpy)Ru(tpy-Py)]$^{4+}$

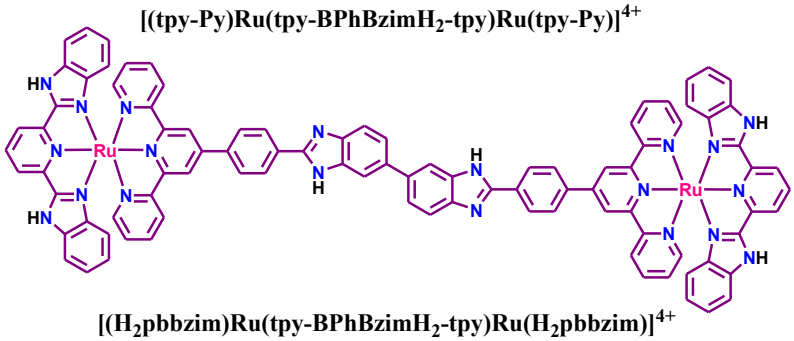

[(H_2pbbzim)Ru(tpy-BPhBzimH_2-tpy)Ru(H_2pbbzim)]$^{4+}$

Figure 1.14

These bimetallic Ru(II) complexes were further explored for their anion sensing capabilities across various environments, including aqueous, organic, and solid-state media, due to their strong room-temperature luminescence and the presence of acidic NH groups (Figure 1.15).[174] These protons enable selective anion recognition through hydrogen bonding or, in some cases, full proton transfer mechanisms. In DMSO, complexes **1** and **2** exhibit a pronounced response toward fluoride ions (F^-), with additional but weaker sensitivity to AcO^-CN^- and $H_2PO_4^-$. In contrast, complex **3** demonstrates higher selectivity, effectively detecting F^-, AcO^-, CN^-, and to a lesser extent, $H_2PO_4^-$. Remarkably, in aqueous

solutions, all three complexes show exceptional selectivity toward CN^-, with detection limits reaching the nanomolar range (~10^{-8} M). Furthermore, in the solid state, the complexes, particularly complex **3**, exhibit rapid and highly sensitive CN^- detection, making them promising candidates for practical anion sensing applications.

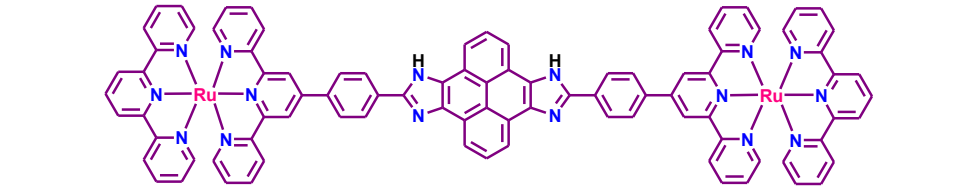

[(tpy)Ru(tpy-H_2PhImzPy-tpy)Ru(tpy)]$^{4+}$ (1)

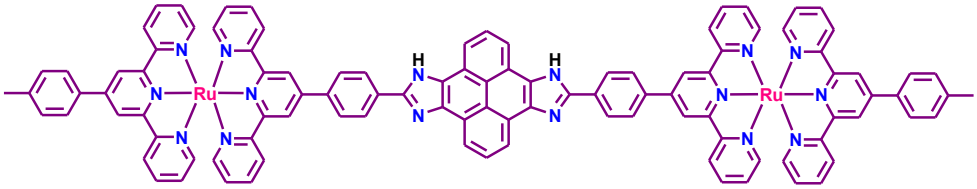

[(tpy-$PhCH_3$)Ru(tpy-H_2PhImzPy-tpy)Ru(tpy-$PhCH_3$)]$^{4+}$ (2)

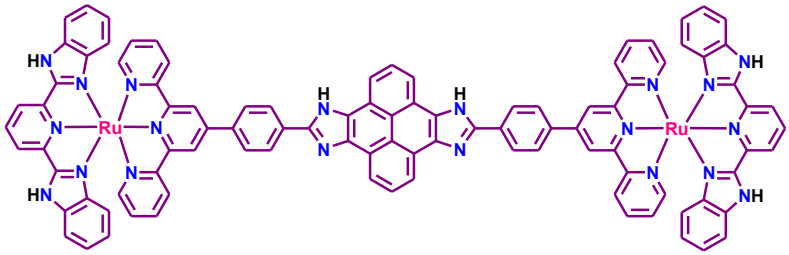

[(H_2pbbzim)Ru(tpy-H_2PhImzPy-tpy)Ru(H_2pbbzim)]$^{4+}$ (3)

Figure 1.15

Bar and co-workers designed a series of luminescent, redox-active bimetallic Ru(II) complexes featuring an asymmetric bridging architecture composed of both bipyridine and terpyridine coordination environments connected through a phenyl-imidazole linker (Figure 1.16).[175] These asymmetric dyads were specifically engineered to facilitate efficient intramolecular energy transfer between the two distinct Ru(II) centers. Photophysical investigations, including steady-state and excited-state luminescence experiments, revealed that energy transfer proceeds from the excited ^{3}MLCT state of the [(bpy/phen)$_2$Ru^{II}(dipy-Hbzim-tpy or phen-Hbzim-tpy)] unit to the [(dipy-Hbzim-tpy)Ru^{II}(tpy-$PhCH_3$ or H_2pbbzim)] moiety across all four complexes at room temperature. Kinetic analyses further confirmed the efficiency of this process, with intramolecular energy transfer rate constants estimated to be in the range of 10^6 to 10^7 s^{-1}.

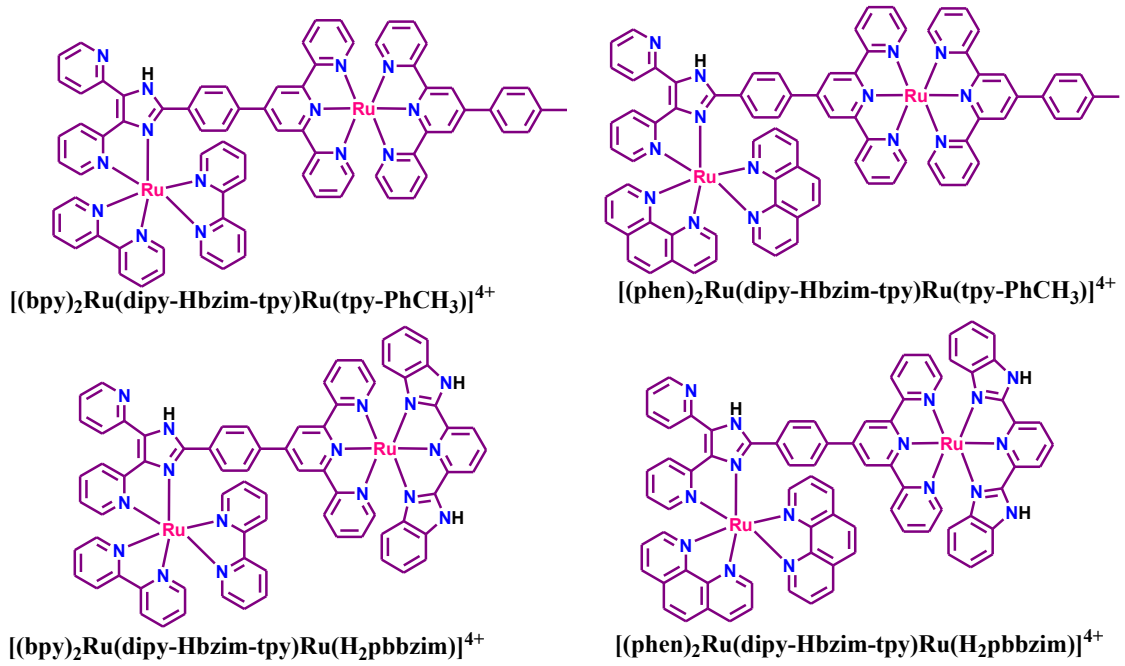

Figure 1.16

1.5. Literature Review on Cyclometalated Ruthenium Terpyridine Complexes

Ruthenium polypyridyl complexes, renowned for their rich photophysical and redox properties in both ground and excited states, have attracted significant attention owing to their wide applicability as light-harvesting materials in dye-sensitized solar cells (DSSCs), optoelectronic devices, molecular machines, chemical sensors, and molecular switches.[1,2,13-15,48] Extensive research efforts have been devoted by utilizing $[Ru(bpy)_3]^{2+}$ and its derivatives, primarily due to their broad, tunable MLCT absorption and emission profiles within the visible region, combined with high quantum yields and long excited-state lifetimes at ambient temperature.[25,136] In comparison, the terpyridine type complexes like $[Ru(tpy)_2]^{2+}$, exhibit a key advantage over $[Ru(bpy)_3]^{2+}$, namely, higher isomeric purity during synthesis. However, their application is often constrained by intrinsically weak luminescence and short excited-state lifetimes.[50,137] These limitations arise from a small energy gap between the emissive ^{3}MLCT state and the thermally accessible non-emissive ^{3}MC state. To address these challenges, several strategies have been developed to increase the ^{3}MLCT-^{3}MC energy separation, thereby enhancing the luminescent properties and excited-state stability of the complexes.

One of the most effective approaches involves destabilizing the ^{3}MC state through the introduction of strong σ-donor ligands such as N^-, C^-, or S based donors.[58,148,153] Among these, cyclometalating ligands are especially advantageous, offering fine control over frontier orbital energies.[59-61] In particular, substitution of a nitrogen atom within the tpy framework by a carbon atom significantly alters the electronic structure of the ligand without disturbing the overall coordination geometry of the complex, while simultaneously lowering the complex's overall charge. This design strategy has enabled the development of ruthenium(II) complexes featuring N,C,N′- or C,N,N′-coordinating cyclometalated ligands that display efficient luminescence at room temperature.[55,176,177] Notably, complexes bearing cyclometalating ligands that facilitate intraligand and π-π interactions show markedly enhanced emission.[178] A substantial bathochromic shift in the MLCT absorption bands relative to the parent $[Ru(tpy)_2]^{2+}$ complex (λ_{max}= 474 nm) is observed, which can be attributed to the increased electron density at the metal center induced by the carbanionic ligands. Furthermore, these cyclometalated complexes often emit in the NIR region, due to the reduced energy gap between the ^{3}MLCT state and the ground state.[30] The introduction of cyclometalating ligands also dramatically influences the redox behavior of the complexes. A significant cathodic shift (~700 mV) of the Ru^{II}/Ru^{III} oxidation potential is typically observed compared to $[Ru(tpy)_2]_{2+}$ [$E_{1/2}$(ox)= 1.30 V], highlighting the strong σ-donating nature of the cyclometalated ligands.[53] In addition, ligand-centered reductions are shifted to more negative potentials. Substantial progress has been accomplished in the design and study of cyclometalated ruthenium terpyridine complexes, with notable contributions from the research groups of Grätzel,[179-182] van Koten,[15,53,183] Berlinguette,[137,184,185] and others.[54,167,186-189] Herein, we provide a concise overview of the photo-redox properties of these cyclometalated terpyridine type complexes of Ru(II).

Sauvage and coworkers reported the synthesis of a cyclometalated ruthenium complex $[Ru(tt)(phbp)]^+$, (tt= 4'-tolyl-2,2':6'2"-terpyridine, phbp= 6-phenyl-2,2'-bi-pyridine) (Figure 1.17).[153] The complex exhibits a (N,N,N)(C,N,N) coordination environment and was thoroughly characterized by ^{1}H NMR spectroscopy, UV-vis absorption, FAB-MS and elemental analysis. Its photo-redox properties were systematically compared with those of non-cyclometalated analogs, $Ru(tt)_2^{2+}$ and $Ru(terpy)_2^{2+}$ (terpy= 2,2':6',2"-terpyridine). Electrochemical measurements revealed a significantly reduced $Ru^{III/II}$ redox potential (E^0 = 0.54 V vs. SCE in CH_3CN) for $[Ru(tt)(phbp)]^+$ compared to $Ru(tt)_2^{2+}$ (E^0 = 1.24 V vs. SCE in DMSO). This substantial cathodic shift is attributed to the strong σ-donating character of the cyclometalated $phbp^-$

ligand, which enhances electron density around the metal center relative to terpyridine-based ligands. The increased electron density also induces a pronounced bathochromic shift in the metal-to-ligand charge transfer (MLCT) absorption band, observed at λ_{max}= 523 nm for $[Ru(tt)(phbp)]^{+}$, compared to its non-cyclometalated counterparts. Furthermore, the complex exhibits an emission maximum in the NIR region (λ_{max}= 808 nm). This red shift in luminescence is a consequence of stabilization of the ^{3}MLCT state and destabilization of the ^{3}MC state due to the strong σ-donating nature of the $phbp^{-}$ ligand. Additionally, the excited-state lifetime of $[Ru(tt)(phbp)]^{+}$ was found to be 60 ns in acetonitrile at room temperature, which is significantly longer than those measured for $Ru(tt)_2^{2+}$ and $Ru(terpy)_2^{2+}$, indicating improved photostability and slower non-radiative decay pathways in the cyclometalated system.

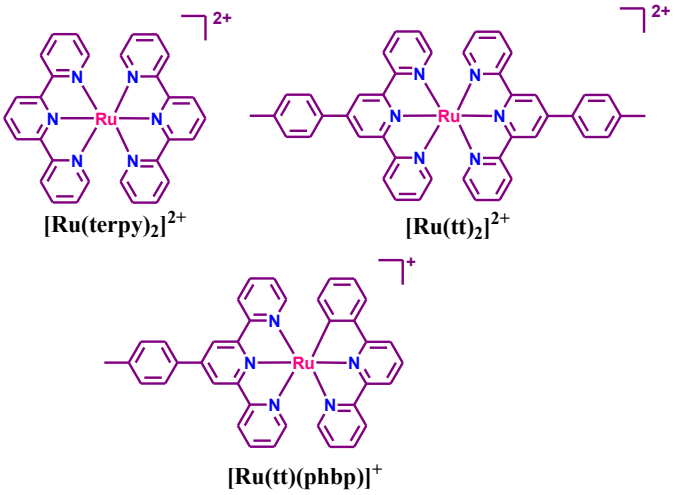

Figure 1.17

The absorption and emission spectral properties of a series of mononuclear and binuclear Ru(II) and Os(II) complexes (**Ru**, **Os**, **RuRu**, **OsOs** and **RuOs**) featuring the terpyridine-type ligand ttp and cyclometalating ligands dpb^{-} and $tpbp^{2-}$ were investigated by Barigelletti and co-workers (Figure 1.18).[190] In the absorption spectra, all the complexes exhibit two bands in the longer wavelength region (503-513 nm and 537-550 nm), which are attributed to ^{1}MLCT transitions involving the LUMO of either the ttp ligand or the cyclometalated moieties. Photoluminescence studies reveal that these complexes emit from their ^{3}MLCT excited states, with emission maxima ranging from 784 to 824 nm. The mononuclear and dinuclear Ru(II) complexes (**Ru** and **RuRu**) display significantly higher emission quantum yields compared to $Ru(ttp)_2^{2+}$ complex. In contrast, the Os(II)-based species, including **Os**, **OsOs**, and **RuOs** complexes, exhibit very weak emission relative to

$Os(ttp)_2^{2+}$. For **Ru** and **RuRu** systems, the strong σ-donating character of the cyclometalated ligands destabilizes the non-emissive ^{3}MC states, effectively raising their energy and thereby promoting stronger emissive behavior. However, this effect is not observed for Os(II)-containing complexes, as the inherent large energy separation between their ^{3}MLCT and ^{3}MC states already suppresses non-radiative deactivation, even in non-cyclometalated systems. Electrochemical analyses show that all the studied complexes possess significantly lower oxidation and reduction potentials compared to $Ru(ttp)_2^{2+}$ and $Os(ttp)_2^{2+}$, a consequence of increased electron density across the metal-ligand framework due to the presence of cyclometalating ligands. Notably, in the heterodinuclear **RuOs** complex, an efficient energy transfer from the Ru→Os center is observed, characterized by a high value rate constant (k_{en}= 2×10^9 s^{-1}), demonstrating effective intramolecular communication between the two metal centers.

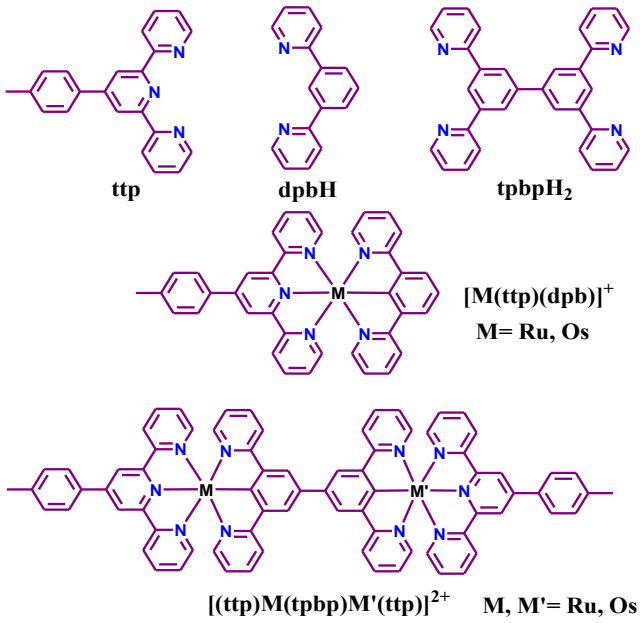

Figure 1.18

In a separate study, Barigelletti and co-workers synthesized a series of three dinuclear Ru(II)/Os(II) cyclometalated complexes, in which the two metal centers are connected by bridging ligands comprising two cyclometalating (dpb^-) units linked through varying numbers of phenylene spacers (Figure 1.19).[176] By altering the number of phenylene groups, the Ru(II)-Os(II) separation was systematically tuned over a range of ~11 to 20 Å. Luminescence spectroscopy revealed that all complexes undergo efficient

photoinduced intramolecular energy transfer from the Ru→Os center. Interestingly, the rate constants associated with the energy transfer process were found to be largely insensitive to temperature variations but showed a strong dependence on the metal-metal separation within the molecular frameworks (k_{en}= 2.6×10^{9} and $<2.2\times10^{7}$ s^{-1} for r_{MM}= 11 and 20 Å, respectively). In systems employing non-cyclometalating bridging ligands, the energy transfer occurs very fast ($k > 5\times 10^{10}$ s^{-1}), attributed to the involvement of MLCT excited states localized on the bridging ligand itself, which facilitates efficient electronic communication between the two metal centers. Conversely, in the cyclometalated complexes, the energy transfer rates were significantly slower. This reduced efficiency arises because the MLCT excited states are predominantly directed toward the terminal ligands, thus limiting direct electronic coupling through the bridge.

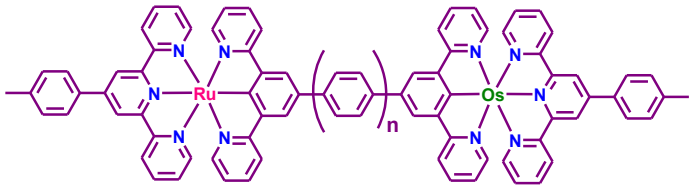

$[(ttp)Ru\{(dpb)\text{-}(Ph)_n\text{-}dpb\}Os(ttp)]^{2+}$

n= 0, 1, 2

Figure 1.19

Sauvage and his research group reported the synthesis and characterization of two cyclometalated Ru(II) complexes featuring mono- (complex **2**) and di-substituted (complex **1**) phenanthroline ligands (Figure 1.20).[191] Single-crystal X-ray diffraction studies revealed that the Ru-N bond adjacent to the tolyl group in the phenanthroline unit is longer in the disubstituted **1** than in the monosubstituted **2**, indicating increased steric hindrance in complex **1**. This steric congestion in **1** causes one of the tolyl groups to orient toward the central pyridine ring of the ttpy ligand, bringing the two into close proximity. This geometry facilitates an intramolecular donor-acceptor interaction between the electron-rich tolyl group (donor) and the electron-deficient central pyridine ring (acceptor). Such an interaction is absent in **2** due to reduced steric crowding. As a consequence of these structural differences, the two complexes exhibit distinct photophysical behavior. Complex **1** exhibits luminescence quantum yield of 0.02 along with a relatively long excited-state lifetime of 95 ns compared to the standard $Ru(tpy)_2^{2+}$ complex. In contrast, complex **2** is

practically non-luminescent, emphasizing the role of steric and electronic interactions in modulating excited-state properties.

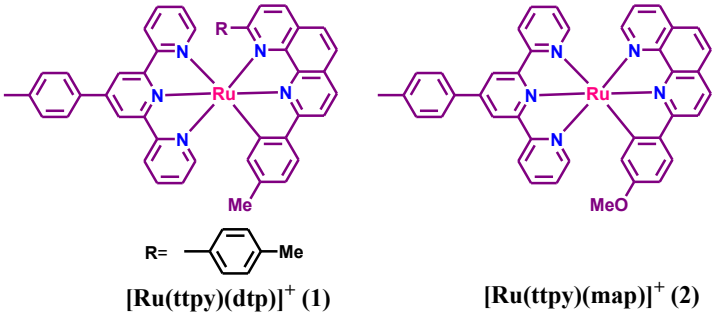

[Ru(ttpy)(dtp)]$^{+}$ (1) **[Ru(ttpy)(map)]$^{+}$ (2)**

Figure 1.20

Constable *et al.* reported an example of pH-responsive, reversible cyclometalation at a Ru(II) center involving the ligand Htbp [Htbp= 6-(2-thienyl)-2,2'-bipyridine] (Figure 1.21).[58] The cyclometalated complex [Ru(tbp)(tpy)][PF_6], in which the ligand is coordinated via a Ru-C bond, undergoes protonation at the carbanionic center when treated with dilute HCl or refluxed in glacial acetic acid. This protonation induces cleavage of the Ru-C bond, leading to the formation of the corresponding non-cyclometalated species [Ru(Htbp)(tpy)][PF_6], which exhibits an orange coloration. In the resulting complex, the thienyl moiety binds to Ru(II) through S atom, rather than through a direct Ru-C bond. Interestingly, a similar transformation is observed upon photoirradiation of the cyclometalated complex, wherein complete conversion to the non-cyclometalated species [Ru(Htbp)(tpy)][PF_6] occurs. Conversely, treatment of the protonated complex with aqueous NaOH regenerates the cyclometalated complex [Ru(tbp)(tpy)][PF_6] in quantitative yield, with the solution turning purple upon deprotonation and reformation of the Ru-C bond. This system thus represents the first documented case of a fully reversible cyclometalation process, modulated by acid-base chemistry and light.

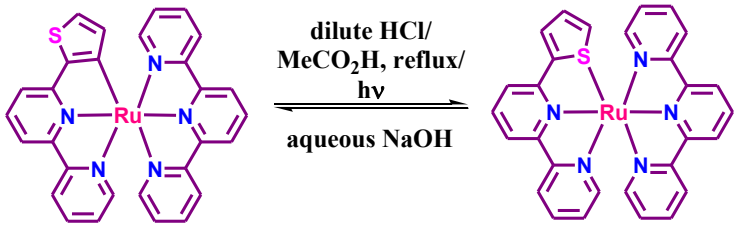

[Ru(tbp)(tpy)][PF_6] **[Ru(Htbp)(tpy)][PF_6]**

Figure 1.21

Koten and co-workers reported the development of two novel cyclometalated Ru(II) complexes of composition [Ru(C^N^N)(N^N^N)] (complexes **3** and **4**), marking their first application as sensitizers in dye-sensitized solar cells (DSSCs) (Figure 1.22).[183] Their performance was evaluated in comparison with a non-cyclometalated analogue (complex **2**) and a standard reference dye (complex **1**). All three sensitizers (**2-4**) were functionalized with carboxylic acid groups to facilitate covalent anchoring onto nanocrystalline TiO_2 solar cells. Among the cyclometalated derivatives, complex **4** exhibited superior photovoltaic performance relative to complex **3**, attributed to the presence of an additional -COOH anchoring group that enhances surface binding and electronic communication with the TiO_2 nanoparticles. UV-vis absorption spectroscopy revealed a significant red shift in MLCT bands of the cyclometalated complexes **3** and **4** (λ_{max}= 523 and 552 nm, respectively), compared to complex **2** (λ_{max}= 487 nm). This red-shift, along with broader absorption profiles in the visible region, renders the cyclometalated complexes more effective in harvesting solar energy. Photocurrent action spectra obtained through Incident Photon-to-Current Efficiency (IPCE) measurements further confirmed the enhanced sensitizing ability of the cyclometalated complexes. Complex **4** showed the highest IPCE response among the series, consistent with its dual anchoring groups and extended absorption range. These findings demonstrate that cyclometalated Ru(II) complexes, particularly complex **4**, hold significant promise as efficient sensitizers in DSSC applications due to their favorable photophysical and anchoring properties.

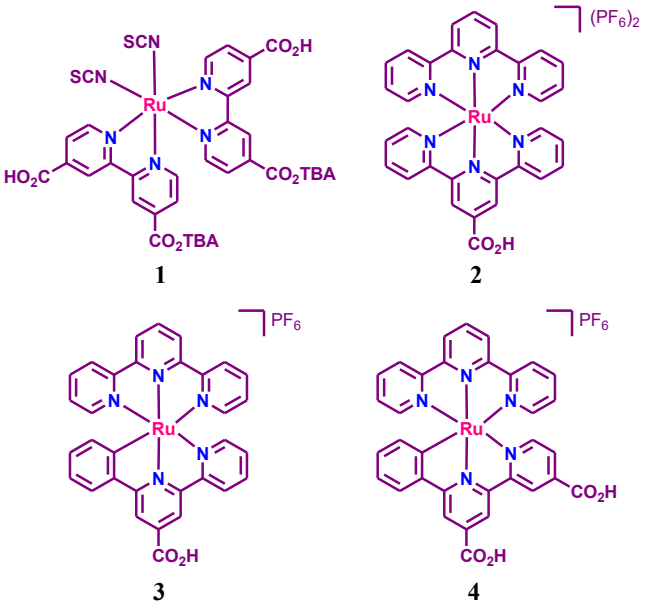

Figure 1.22

Wadman *et al.* synthesized a series of Ru(II) complexes comprising either two tpy ligands or a combination of one tpy and one cyclometalating ligand with either an N,C,N′ or C,N,N′ coordination motif (Figure 1.23).[53] The electronic and photophysical properties of these complexes were systematically investigated. Single-crystal X-ray diffraction analysis revealed that cyclometallation does not significantly disrupt the overall octahedral geometry of the Ru(II) center. However, notable changes in bond lengths were observed, particularly, elongation of the Ru-N bond trans to the carbanionic donor site, indicating increased trans influence due to cyclometalation. Electronic absorption spectroscopy

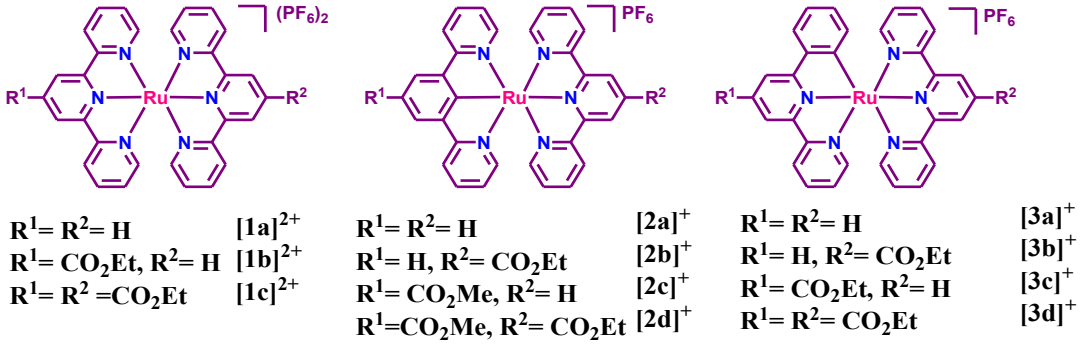

Figure 1.23

showed that the MLCT bands in the visible region are red-shifted in the cyclometalated complexes compared to their non-cyclometalated counterparts. In the N,C,N′-cyclometalated systems, the lowest-energy MLCT transition is primarily from the metal center to the tpy ligand. Conversely, in C,N,N′-cyclometalated complexes, the red-shifted MLCT transitions involve both the tpy and cyclometalating ligands, suggesting a more delocalized excited state. Photoluminescence studies at room temperature demonstrated that the emission characteristics are largely unaffected by the coordination mode of the cyclometalating ligand. In all cases, the emission arises from the ^{3}MLCT state primarily associated with the tpy ligand. An exception was noted for the C,N,N′-cyclometalated complex bearing an ester-substituted ligand, where the emission is predominantly localized on the cyclometalating unit. Electrochemical characterization via cyclic voltammetry revealed that cyclometalation induces a significant cathodic shift in both the metal-centered oxidation and ligand-centered reduction potentials. This shift is attributed to the strong σ-donating nature of the carbanionic ligand, which increases electron density around the Ru(II) center and stabilizes the reduced forms of the ligands.

Berlinguette and his research group reported the synthesis and characterization of a series of Ru(II) complexes incorporating substituted terpyridine ligands in conjunction with a tridentate C,N,C-coordinating mesoionic carbene ligand (Figure 1.24).[137] These complexes exhibit exceptionally long-lived excited states, with lifetimes reaching up to 7.9 μs. The extended excited-state lifetime is attributed to the unique electronic properties of the C,N,C- ligand, which acts as a strong σ-donor and a weak π-acceptor. This electronic configuration effectively increases the energy gap between the ^{3}MLCT state and ^{3}MC state while maintaining a high ^{3}MLCT energy. Moreover, the introduction of EWGs or EDGs on the ligand framework further modulates the energy separation between the ^{3}MLCT and ^{3}MC states, enabling fine-tuning of the excited-state dynamics. Notably, the excited-state lifetimes of these mesoionic carbene-based complexes are almost four orders of magnitude greater than that of $Ru(terpy)_2^{2+}$ complex.

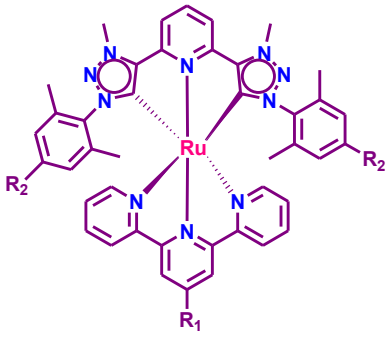

R_1	R_2	Compound
-H	-Me	1
$-CO_2Me$	-Me	2
	-Me	3
	-Br	4

Figure 1.24

Berlinguette and coworkers also systematically designed a series of substituted tridentate polypyridyl and cyclometalated Ru(II) complexes of composition [Ru-(tpy-R^1)(tpy-R^2)]$(PF_6)_2$ and [Ru(tpy-R^2)(dpb-R^1)]PF_6 respectively, for their probable application as light-harvesting materials (Figure 1.25).[184] For [Ru-(tpy-R^1)(tpy-R^2)]$(PF_6)_2$ series, the introduction of the substituents at the 4'-position of one or both tpy ligands influences the MLCT absorption band. In the cyclometalated analogs, the reduced symmetry around the metal center leads to the broadening of the lowest energy MLCT band, while an additional set of transitions in the higher energy domain arises from the excited state involving the cyclometalated ligands. Thus, a substantially broad MLCT absorption band appears for the cyclometalated complexes, which is more red-shifted compared to that for the non-cyclometalated series. Further structural modifications through various groups at the 4'-position of both tpy and dpb ligands enabled fine-tuning

of both the photophysical and redox properties of the complexes. TD-DFT calculations were also conducted to support the spectroscopic data.

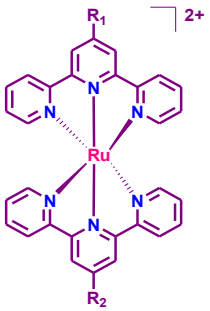

$R^1 = R^2 = H$	1
$R^1 = H$, $R^2 = CO_2H$	2
$R^1 = OMe$, $R^2 = CO_2H$	3
$R^1 = H$, $R^2 = 2$-furyl	4
$R^1 = OMe$, $R^2 = 2$-furyl	5
$R^1 = R^2 = 2$-furyl	6

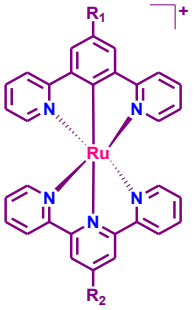

$R^1 = R^2 = H$	7
$R^1 = OMe$, $R^2 = H$	8
$R^1 = H$, $R^2 = 2$-furyl	9
$R^1 = OMe$, $R^2 = 2$-furyl	10

Figure 1.25

Wang *et al.* synthesized three cyclometalated diruthenium(II) complexes featuring a central tbibp bridging ligand and varied terminal ligands (Figure 1.26).[192] These complexes were systematically investigated to measure the extent of electronic communication between the two Ru centers. Electrochemical measurements and IVCT spectroscopy revealed that the complexes with identical or similar capping ligands exhibit stronger Ru-Ru coupling through the tbibp scaffold, compared to previously studied systems incorporating the 3,3′,5,5′-tetrakis(N-methylbenzimidazol-2-yl)biphenyl (Me-tbibp) bridge. However, this coupling remains weaker than that observed in analogs incorporating the classical 3,3′,5,5′-tetrakis(pyrid-2-yl)biphenyl (tpbp) ligand. The CNS analyses introduced by Creutz, Newton, and Sutin, based on a hole superexchange mechanism, align with the experimentally observed coupling trends. DFT calculations provided insight into the spin density distribution in the singly oxidized diruthenium complexes bearing the H-tbibp bridge. TDDFT simulations were also employed to reproduce the observed IVCT bands, offering theoretical validation of the electronic transitions involved.

Kreitner and Heinze synthesized and characterized a series of weakly emissive mononuclear cyclometalated Ru(II) complexes of the type $[Ru(dpb\text{-}R)(tpy)]^+$ ($\mathbf{1}^+$–$\mathbf{4}^+$), where electron-donating substituents were introduced on the dpb ligand (Figure 1.27).[193] Temperature-dependent luminescence studies indicated that excited-state quenching occurs via a low-lying triplet ligand-to-ligand charge transfer (^{3}LL′CT) state in addition to the ^{3}MC state. This deactivation pathway was experimentally confirmed for complexes $\mathbf{1}^+$ and $\mathbf{3}^+$, and further supported by DFT calculations. Variation in the substituents modulated the

energy gap between the ^{3}MLCT and ^{3}LL′CT states, while the ^{3}MLCT-^{3}MC energy barrier remained largely unaffected. A dinuclear complex, [(tpy)Ru(dpb-NHCO-dpb)Ru(tpy)]$^{2+}$ (**6**$^{2+}$), incorporating a bis-cyclometalating bridge, was also synthesized. Its mixed-valent cation (**6**$^{3+}$) exhibits a strong IVCT band at 1165 nm, and in solution, **6**$^{2+}$ displays dual emission from two distinct ^{3}MLCT states localized on the two remote Ru(tpy) centers.

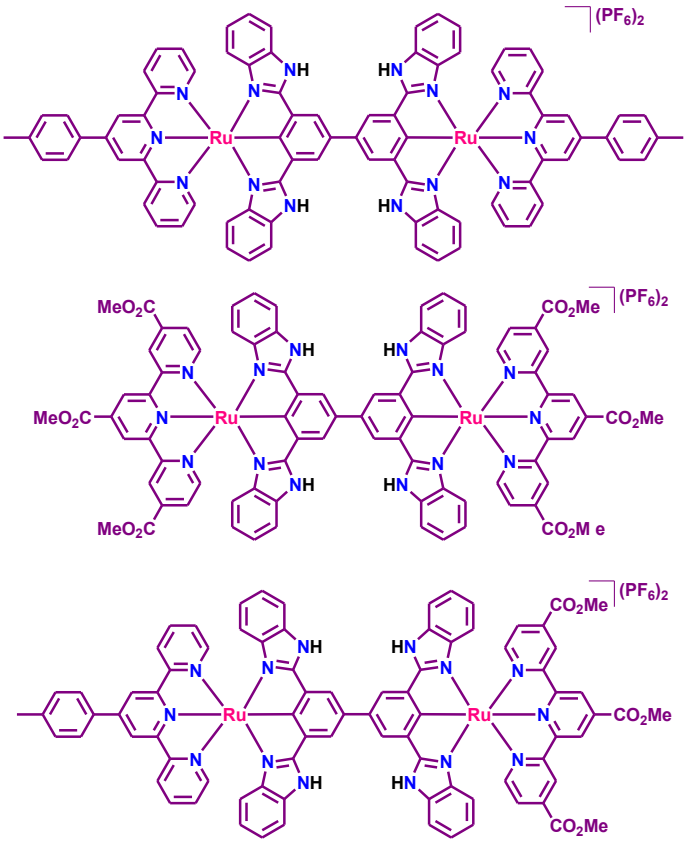

Figure 1.26

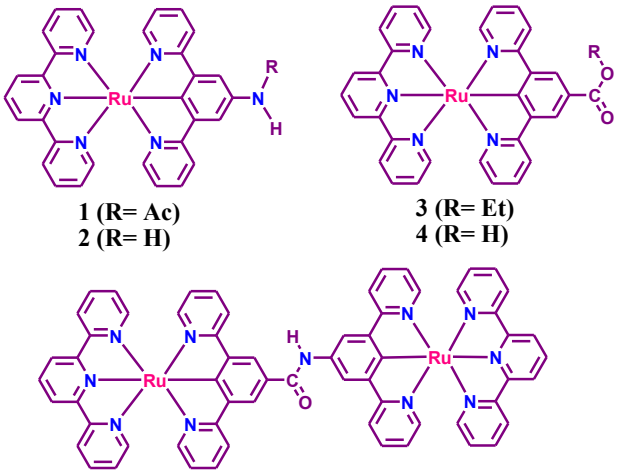

Figure 1.27

1.6. A Concise Overview on Photoisomerization Behavior of Platinum Metal Complexes

Molecular systems capable of reversibly modulating their physicochemical properties in response to external stimuli are of considerable interest for applications in optical switches, molecular memory, and data storage technologies.[194-199] Recent research in high-density molecular data storage has focused on devices that incorporate not only simple bistable switches but also molecular units capable of performing logic operations.[34-46] Among various stimuli, light stands out as an environmentally benign and spatially controllable energy source, making photoresponsive molecular units particularly promising for optical data storage materials.[1-14]

While organic molecules have been extensively utilized in the design of molecular photoswitches,[88-99] the investigation of photoisomerization processes in metal complexes remains comparatively underexplored. Several research groups like Iha, Yam, Lees, Nishihara, Gray and others have studied the photoresponsive behavior of transition metal complexes (such as those of Re, Co, Rh, Ir, Fe, and Zn) incorporating photoactive moieties like azobenzene, stilbene, spirooxazine, and diarylethene.[100-103,78-81,200-206] Although azo-functionalized bipyridine and terpyridine metal complexes have been widely examined for their photoisomerization properties, investigations involving stilbene-conjugated metal complexes are limited and remain relatively undocumented.[100-103,78-81,200-206] The present dissertation seeks to address this knowledge gap by systematically exploring the photoisomerization behavior of Ru(II) and Os(II) terpyridine complexes bearing stilbene-derived units. To the best of our knowledge, no other groups have specifically focused on the isomerization dynamics of terpyridine systems conjugated with stilbene functionalities. In this context, we provide an overview of the relevant photophysical and photoisomerization characteristics observed in platinum metal complexes that incorporate either azo or stilbene groups within their coordination frameworks.

Yam and colleagues developed and characterized a series of rhenium(I) tricarbonyl diimine surfactant complexes incorporating azo and stilbene photoactive units, highlighting their reversible photoisomerization behavior. These Re(I) complexes, featuring low-energy MLCT states, were employed as effective sensitizers for light-induced isomerization (Figure 1.28).[201] The azo-functionalized complexes demonstrated reversible trans-cis photoisomerization upon alternate irradiation with 365 nm and 450 nm light. However, the presence of an alkoxy group on the phenylazopyridine moiety inhibited isomerization,

likely due to steric hindrance. The stilbene-containing analogs also exhibited wavelength-dependent reversible isomerization, typically induced by 365 nm and either 254 or 480 nm light, though with notably reduced quantum yields relative to their corresponding free ligands.

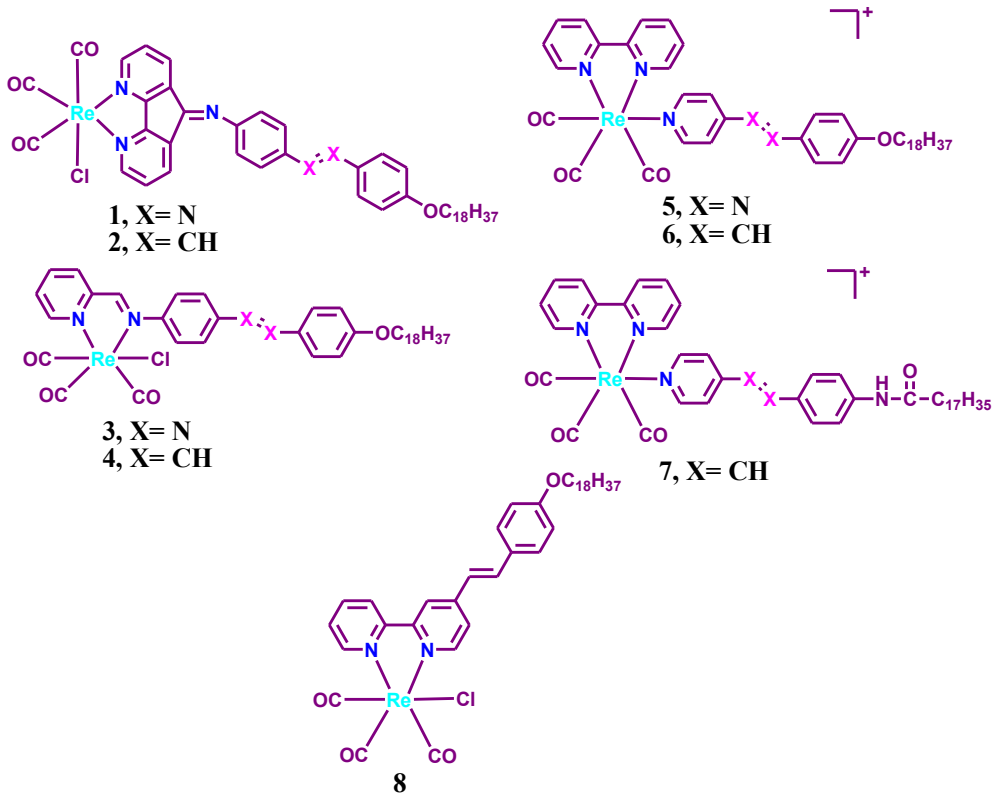

Figure 1.28

Nishihara and co-workers conducted comprehensive studies on the trans–cis photoisomerization behavior of azobenzene-functionalized mono- and dinuclear Ru(II) and Rh(III) complexes derived from terpyridine ligands (Figure 1.29).[80] While both the mono- (tpy-AB) and bis-terpyridine (tpy-AB-tpy) ligands exhibited reversible isomerization under UV (366 nm) and visible (450 nm) light, the dinuclear Ru(II) complex showed no photoresponse, and the mononuclear analog demonstrated 20% isomerization. This limited efficiency was attributed to energy transfer from the azo group to the Ru(II) center. Rh(III) complexes, although non-emissive, underwent slow thermal cis-to-trans isomerization and exhibited enhanced switching behavior in the presence of photosensitizers like benzophenone. Solvent and counter-ion effects were also noted, with bulkier ions facilitating isomerization by reducing ion-pairing and increasing rotational freedom. The findings underscore the importance of metal center identity and ligand environment in tuning photoisomerization efficiency.

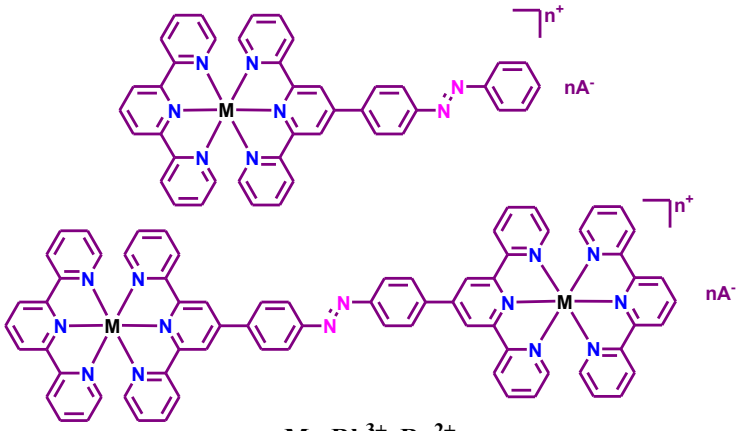

M= Rh^{3+}, Ru^{2+}
A= BF_4, PF_6, BPh_4

Figure 1.29

Nishihara and the group also investigated azo-functionalized Pt(II)-terpyridine complexes, which exhibited superior emissive properties compared to their Ru and Rh analogs (Figure 1.30).[78] These complexes showed reversible trans-cis photoisomerization and emission switching, as characterized by IR, ^{1}H NMR, absorption and emission spectroscopy. Time-resolved emission and transient absorption studies revealed that the quantum yield of isomerization decreased with increasing solvent polarity (MeCN > DMF > DMSO > PC). Under visible light (λ > 430 nm) or thermal stimulus, the complexes reverted from cis to trans. Notably, only the cis isomers were emissive (~480 nm and ~600 nm), due to reduced π-conjugation that suppresses non-radiative decay and photoinduced electron transfer. The emission lifetimes spanned from 2 ns to 40 μs, enabling efficient off-on emission switching driven by photoisomerization.

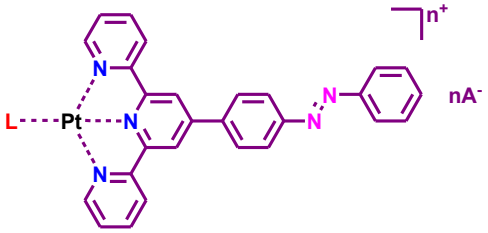

L= pyridine, Cl
A^-= PF_6^-, BPh_4^-

Figure 1.30

Sakamoto *et al.* developed a Pt(II) complex containing two azobenzene units, one appended to a dithiolato ligand and the other to a bipyridine moiety, which demonstrated light-driven, reversible tristable switching behavior (Figure 1.31).[207] The complex

exhibited a prominent visible-region absorption attributed to a mixed metal/ligand-to-ligand charge transfer (MMLL′CT) transition. Selective photoisomerization was achieved by varying the irradiation wavelength. Exposure to 405 nm light induced 44% isomerization of the azobenzene unit on the dithiolato ligand and only 9% isomerization on the bipyridine-bound azobenzene, yielding a cis-trans isomer. Conversely, 365 nm irradiation resulted in 22% isomerization at the dithiolato site and 45% at the bipyridine site, producing the trans-cis isomer. Notably, upon excitation at the MMLL′CT band with 578 nm light, both mixed isomers efficiently reverted back to the original trans-trans configuration. This tunable, wavelength-dependent isomerization demonstrates the complex's potential for multistate optical switching.

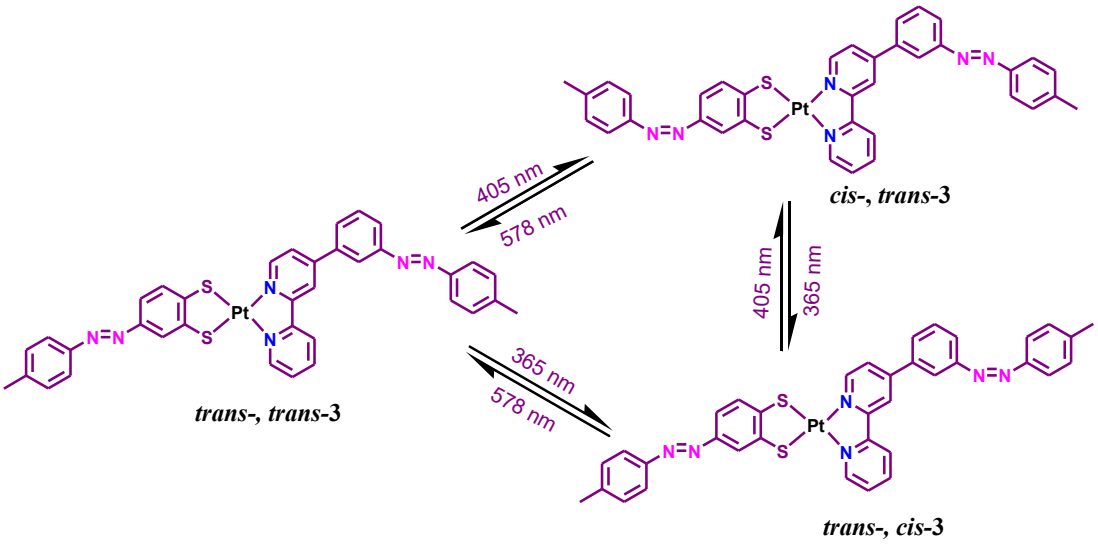

Figure 1.31

Yam and collaborators developed a diverse array of Re(I)-diimine complexes incorporating photoresponsive motifs such as azo, ethenyl, and ethyl groups (Figure 1.32).[200] Their work involved a comprehensive investigation of the photophysical behavior and photoisomerization dynamics of these systems. Upon UV irradiation (λ> 350 nm) in DCM solution, the complexes underwent trans-to-cis isomerization across the double bond. This structural transformation was accompanied by a substantial enhancement in emission properties, including a red shift of ~50 nm in the emission maximum and an increase in emission quantum yield by nearly 40-fold. The observed photoluminescence enhancement in the cis isomer is attributed to the suppression of nonradiative deactivation pathways, specifically the inhibition of energy transfer from the photoexcited ^{3}MLCT state to the azo or ethyl moiety.

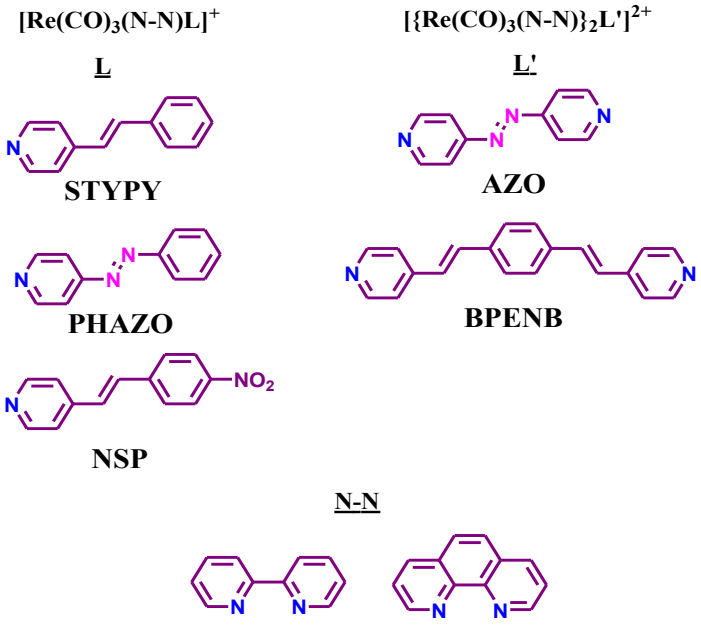

Figure 1.32

Lees and co-workers explored the photophysical characteristics and photoisomerization behavior of tetranuclear rhenium(I) tricarbonyl diimine complexes incorporating stilbene-based tetrapyridyl linkers (Figure 1.33).[208] The tetranuclear complexes exhibited efficient photoisomerization upon 405 nm irradiation, attributed to direct excitation of the ligand-centered excited state. The process resulted in a photostationary mixture of trans-trans-trans-trans, trans-trans-trans-cis, and trans-trans-cis-cis isomers, with photoisomerization quantum yields ranging from 0.19 to 0.65. Due to significant steric hindrance, complete conversion to the all-cis configuration was not achieved. Reverse isomerization could be induced thermally in the dark or photochemically under 254 nm light, though both pathways proceeded with relatively slow kinetics.

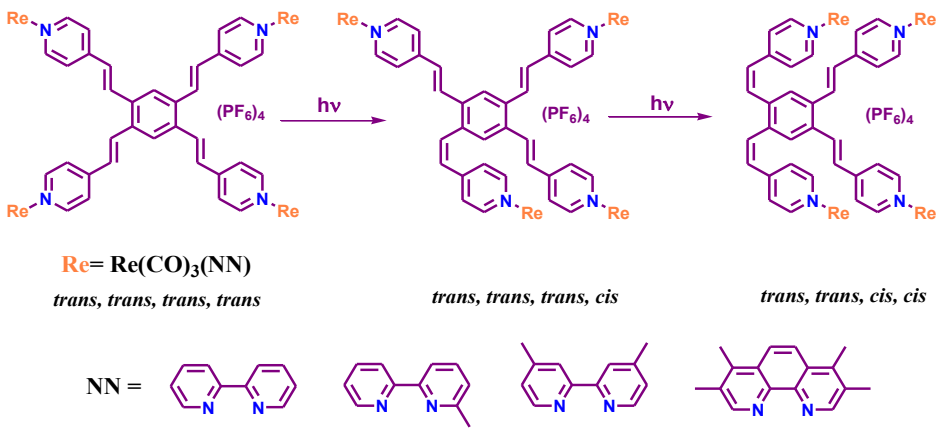

Figure 1.33

Wenger *et al.* conducted a detailed study on the photoinduced trans-to-cis isomerization of Re(diimine)$(CO)_3$(dpe) complexes, where dpe denotes 1,2-di(4-pyridyl)ethylene (Figure 1.34).[203] Upon irradiation at 350 nm in DCM, efficient photoisomerization was observed with a quantum yield of 0.2, yielding a photostationary state composed of ~70% cis and 30% trans isomers. The cis→trans reverse process was achieved by exposure to 250 nm light. Notably, the trans isomers were non-emissive, whereas the cis isomers displayed distinct yellow luminescence, enabling their potential application in photo-switchable luminescent systems.

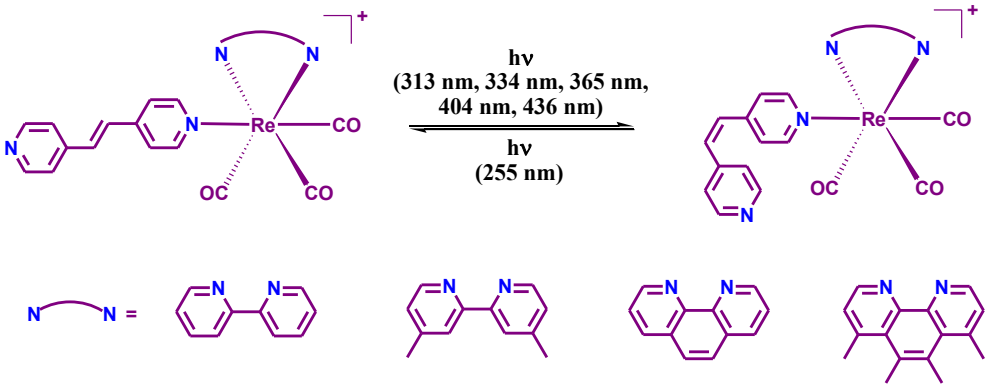

Figure 1.34

Moore and co-workers synthesized a series of rhenium(I) polypyridyl complexes in which *fac*-[Re(bpy)$(CO)_3$] fragments were connected to amine or azacrown ether moieties via a styrylpyridine linker (Figure 1.35).[209] Photoisomerization of the stilbene-like unit was only observed upon protonation of the amine or azacrown groups, with effective isomerization occurring under irradiation at 400-430 nm. The process was proposed to proceed predominantly via a stilbene-centered ^{3}LLCT state. Intramolecular energy transfer from the MLCT state to the stilbene triplet state was found to significantly influence the isomerization rate. In their free forms, the complexes exhibited very weak emission, while their acidified forms showed moderately enhanced luminescence, suggesting the presence of non-radiative deactivation pathways accessible through ^{3}MLCT-to-stilbene energy transfer. Notably, photoisomerization led to a pronounced increase in emission intensity, highlighting the potential of these systems for dual-mode emission switching controlled by both protonation and light stimuli.

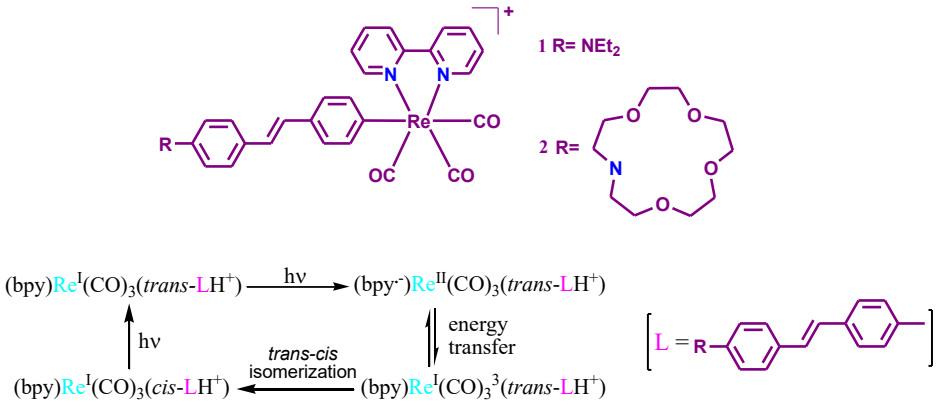

Figure 1.35

Iha and colleagues conducted a comprehensive investigation into the photoisomerization behavior of a series of stilbene-functionalized Re(I) carbonyl complexes. These included compounds of the general formula *fac*-[Re(CO)$_3$(dmcb)(*trans*-stpyR)]$^+$, where dmcb=4,4'-dimethoxycarbonyl-2,2'-bipyridine and *trans*-stpyR= *trans*-4-styrylpyridine or *trans*-4-(4-cyano)styrylpyridine, as well as related systems of the form *fac*-[Re(CO)$_3$(NN)(*trans*-stpyCN)]$^+$, with NN representing either 2,2′-bipyridine or 4,4′-dimethyl-2,2′-bipyridine (Figure 1.36).[204,205] The photophysical and photoisomerization properties of these complexes were systematically studied using a combination of spectroscopic techniques, including UV-vis absorption, steady-state emission, and ^{1}H NMR spectroscopy. These complexes demonstrated efficient *trans-cis* photoisomerization with high quantum yields ranging from 0.37 to 0.64 under irradiation at various wavelengths across the UV and visible spectrum (313, 334, 365, 404, and 436 nm). The reverse *cis*→*trans* isomerization was also effectively achieved under 255 nm light irradiation. Mechanistic analysis suggested a significant role for the ^{3}IL$_{stpyCN}$ excited state in governing the observed photochemical behavior.

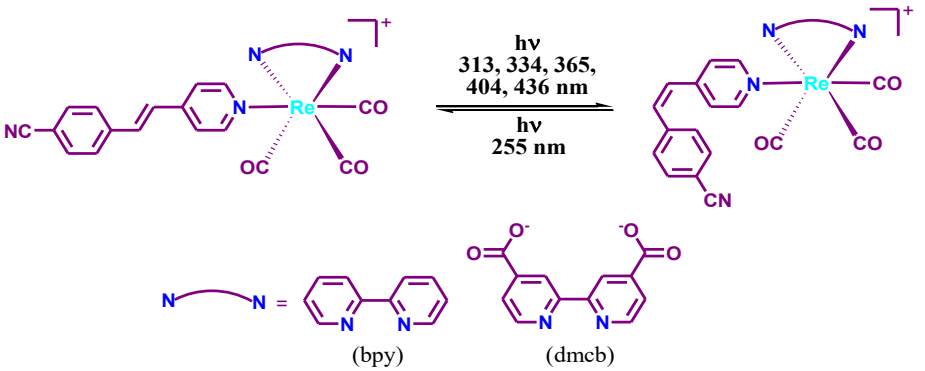

Figure 1.36

Freixa and co-workers synthesized a series of tris-cyclometalated iridium(III) complexes including up to three azobenzene moieties integrated into the coordination framework via 2-phenylpyridyl-type ligands (Figure 1.37).[210] They conducted an in-depth investigation of the photochromic and photoisomerization properties of these systems, systematically evaluating how structural parameters such as the number of azobenzene units, their substitution patterns, coordination geometries, and spatial proximity to the Ir(III) center influence the photoresponsive behavior.

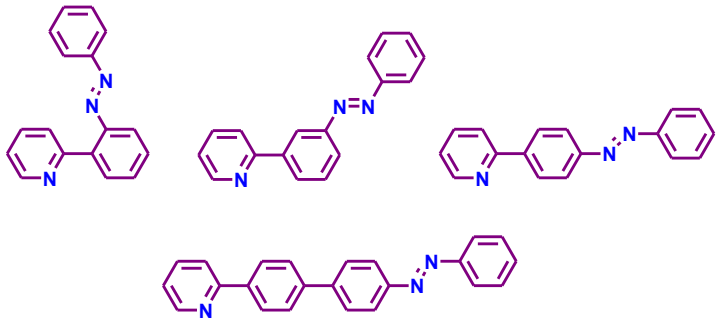

Figure 1.37

Baitalik and co-workers investigated the photoisomerization behavior of a series of terpyridine-based ligands functionalized with stilbene units and various covalently linked aliphatic electron-donating or -withdrawing substituents as well as polyaromatic moieties. Their study extended to a range of metal complexes incorporating these ligands, including Ru(II), Os(II), Fe(II), and Zn(II) centers, in both homoleptic and heteroleptic coordination environments (Figure 1.38).[124,138,139,144,211-215] The ligand frameworks, as well as their corresponding metal complexes, exhibited reversible *trans-cis* photoisomerization upon alternating exposure to UV and visible light. In some cases, thermal reversion from the *cis* to *trans* configuration was also observed. Notably, heteroleptic complexes containing benzimidazole functionalities were shown to undergo deprotonation under basic conditions or elevated pH, leading to significant modulation of their ground- and excited-state electronic properties. Deprotonation not only enhanced the photoisomerization rate but also introduced proton-coupled redox behavior, highlighting the potential of these systems for multifunctional photo- and pH-responsive applications. Introduction of polyaromatic moieties also affect the overall electronic nature and photophysics of the complexes. The effect of the polyaromatic groups on the photoisomerization kinetics and quantum yield was also thoroughly investigated.

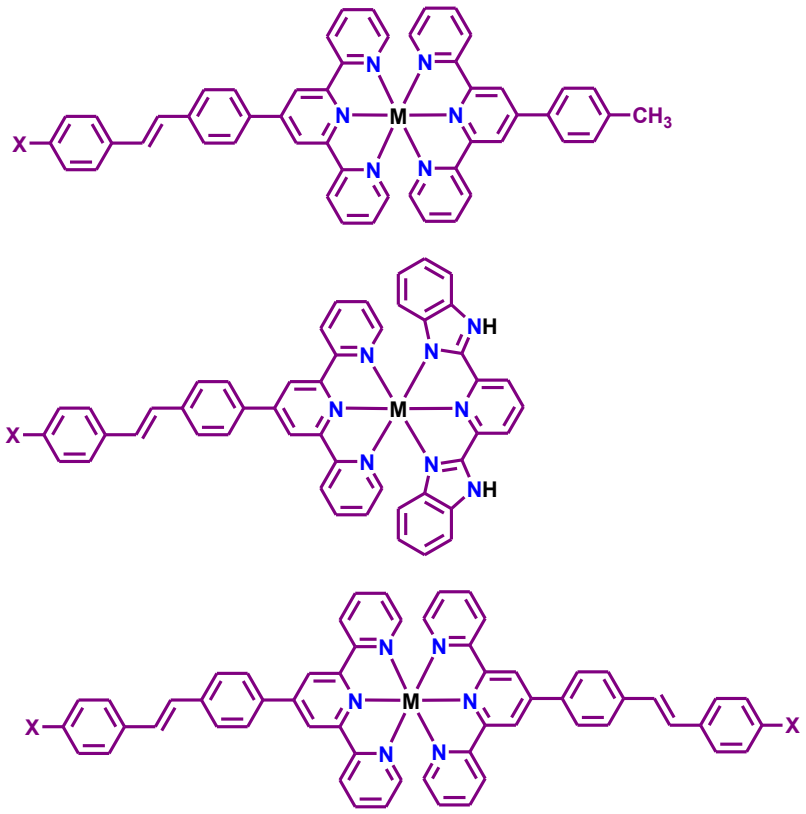

M= Ru^{II}, Os^{II}, Fe^{II}, Zn^{II}

X= H, Me, Cl, NO_2, Ph, Naphthalene, Anthracene, Pyrene

Figure 1.38

1.7. A Concise Review on Logic Gates

Over the past few decades, computers have become indispensable tools across diverse fields, enabling advanced calculations, data processing, and seamless communication.[108-120] The concept of performing computation and information processing at the molecular level was first introduced by De Silva in 1993, marking a significant shift toward the development of ultra-miniaturized computing systems beyond the limitations of conventional silicon-based technologies. At the core of digital computation lie logic gates which are fundamental units that execute binary arithmetic and logical operations. Translating this principle to the molecular scale has led to the emergence of molecular logic gates, which mimic the behavior of traditional logic gates but function within nanoscale environments. These molecular systems can be integrated into more complex architectures, enabling computational operations on a scale that traditional semiconductor technologies cannot achieve. Binary logic, which operates on two discrete states (typically denoted as

"0" and "1"), supports these systems. The following section presents a concise overview of selected molecular logic gate systems reported in the literature.

Li and coworkers reported an Ir(III)-based chemosensor capable of mimicking molecular logic gate functions, specifically AND and INHIBIT operations, in the presence of Hg^{2+} and histidine (Figure 1.39).[216] In its free form, the complex exhibits negligible luminescence. Upon addition of histidine, a slight enhancement in emission is observed, while the simultaneous presence of both Hg^{2+} and histidine induces a pronounced luminescent response. This selective behavior allows the system to function as a two-input logic device, demonstrating AND gate and INHIBIT gate characteristics under specific input conditions.

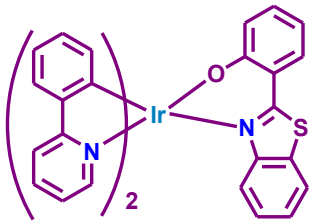

$Ir(ppy)_2(PBT)$

Figure 1.39

Biancardo *et al.* demonstrated a Ru(II)-based molecular system capable of performing two-input NOR logic gate operations (Figure 1.40).[217] In this design, an applied electric field and Cu^{2+} ions serve as the two independent inputs. The emission intensity at 668 nm is significantly quenched upon the application of either input, resulting in an "OFF" luminescent state. Only in the absence of both stimuli the system retains its luminescence, representing the "ON" state. This binary output behavior effectively replicates the logical function of a NOR gate.

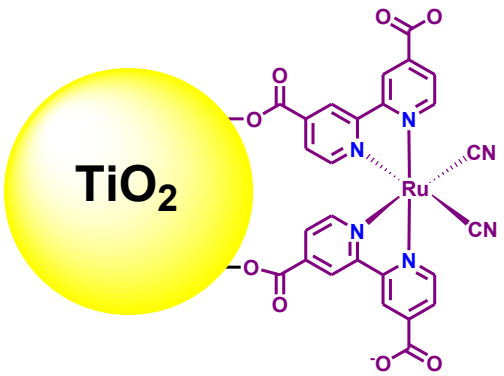

Figure 1.40

Awasthi and his group developed an Os(II)-bipyridine complex incorporating an imidazole-carboxylate ligand capable of performing combinational logic functions (Figure 1.41).[218] The complex exhibits a distinct brown color under ambient conditions, which fades upon exposure to Cu^{2+} ions. Interestingly, the original coloration is restored upon subsequent addition of water. Using Cu^{2+} and H_2O as the two chemical inputs, absorption changes at 509 nm and 293 nm were monitored as optical outputs. The response at 509 nm was consistent with the logic behavior of an INHIBIT gate, while the spectral change at 293 nm enabled the construction of an IMPLICATION gate. This system thus exemplifies a multi-output molecular logic device based on optical signaling.

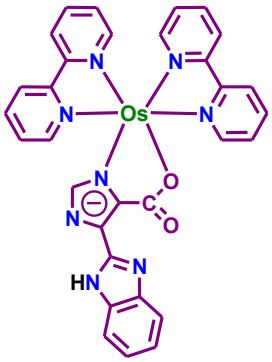

Figure 1.41

Zhong and co-workers synthesized a diruthenium complex featuring a redox-active amine-bridge and elucidated its structure using single-crystal X-ray diffraction (Figure 1.42).[219] The complex exhibits distinct NIR absorption signatures corresponding to three discrete redox states. These well-defined optical responses, along with high output contrast and prolonged state retention, render the system a promising candidate for molecular memory applications, including flip-flop, flip-flap-flop, and ternary memory devices. In the flip-flop memory model, two electrical inputs and two NIR outputs were employed to simulate binary data storage. Furthermore, the multi-level logic capabilities of the complex were demonstrated through the implementation of flip-flap-flop and ternary memory functions, utilizing three electrochemical stimuli as inputs and three NIR absorption signals as optical outputs, each representing a distinct redox state.

Schmittel *et al.* developed two linear phenanthroline-based ligands, one containing two binding sites (**2**) and the other three (**3**), designed to function as molecular logic gates through protonation-dependent luminescence responses (Figure 1.43).[220] Using protons (H^+) as input signals and emission intensity as the output, ligand **2** demonstrated behavior

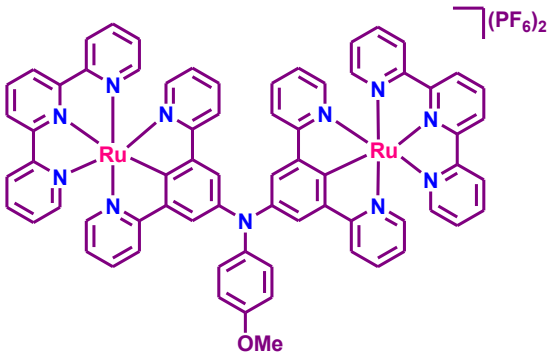

Figure 1.42

consistent with an XNOR logic gate. Specifically, the free and doubly protonated forms of **2** exhibited strong fluorescence, while the singly protonated form was non-emissive, fulfilling the criteria for XNOR logic. In contrast, ligand **3** exhibited more complex emission behavior: its strong fluorescence at 414 nm diminished for singly and doubly protonated forms, while a new emission peak at 526 nm appeared for the fully protonated form. These distinct emission profiles enabled ligand **3** to perform integrated logic functions resembling a multiport AND-NOR-OR logic gate.

Baitalik and the group recently introduced a multifunctional molecular system incorporating a terpyridine-stilbene conjugate, designed to perform diverse logic operations based on its tunable optical properties (Figure 1.44).[124] The terpyridine moiety serves as a coordination site for various cations, while the stilbene unit exhibits photoresponsive behavior under irradiation with specific wavelengths of light. This responsiveness enables modulation of the system's optical outputs upon exposure to different cationic or photonic stimuli. By treating metal ions and light wavelengths as discrete input signals and monitoring the corresponding optical responses as outputs, the system successfully

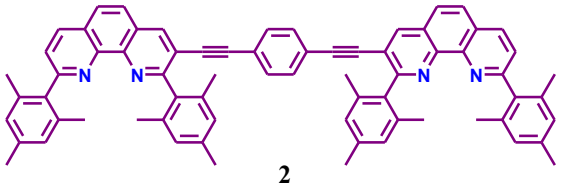

2

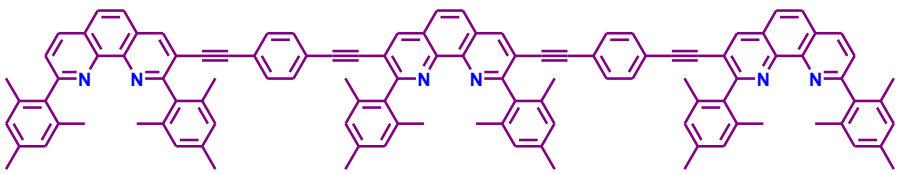

3

Figure 1.43

simulates multiple Boolean logic operations, including INHIBIT, IMPLICATION, OR, NOR, NAND, and their combinational variants. Furthermore, the platform was extended to demonstrate sequential logic applications, such as molecular keypad locks and memory functions, wherein the correct order of inputs governs the output signal, allowing for secure data encoding and logic-controlled optical switching.

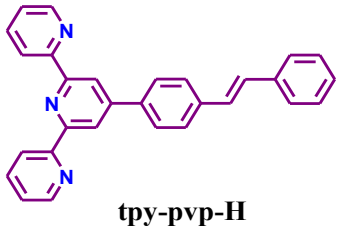

tpy-pvp-H

Figure 1.44

The group further developed multifunctional molecular logic devices using a terpyridine-based receptor featuring anthraquinone and imidazole units (Figure 1.45).[221] In this system, the terpyridine moiety functions as a recognition site for metal cations, while the imidazole unit selectively interacts with anionic species. The distinct absorption and emission responses caused by specific combinations of ionic inputs enabled the system to emulate advanced logic operations, including half-subtractor circuits, molecular keypad locks, and memory devices. Moreover, to transcend traditional binary logic, a fuzzy logic framework was employed to interpret the receptor's luminescence responses in a continuous manner, thereby facilitating the realization of an infinite-valued logic system with enhanced computational versatility.

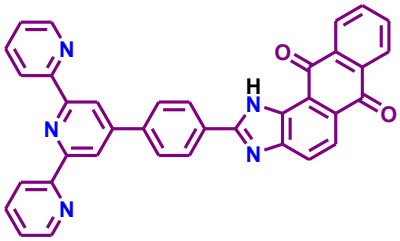

tpy-HPhImz-Anq

Figure 1.45

Mardanya *et al.* reported the synthesis and structural characterization of a bifunctional molecular receptor comprising a pyridyl-imidazole framework tethered to the 1,6-positions of a pyrene core (Figure 1.46).[68] Single-crystal X-ray diffraction confirmed its molecular structure. The receptor exhibits dual recognition capabilities: the imidazole NH group serves as a selective binding site for anions, while the bipyridyl core coordinates

with transition metal cations. Spectroscopic investigations revealed distinct optical responses upon interaction with F^- ions and divalent metal ions such as Zn^{2+} and Cd^{2+}. By analyzing these responses, the system was shown to emulate Boolean logic gate functions, including INHIBIT, OR, and XOR, when specific combinations of Zn^{2+} and F^- or Cd^{2+} and F^- were applied as input signals.

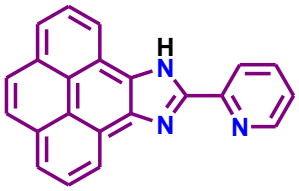

HImzPPy

Figure 1.46

1.8. Research Objectives and Scope of the Present Study

Extensive research in the field of molecular devices highlights the strategic design of functional molecular assemblies capable of responding to external stimuli such as light, temperature, pH, and specific chemical agents. Both organic chromophores and transition metal complexes have been widely explored for such applications. Among them, Ru(II) and Os(II) polypyridine complexes have attracted significant interest due to their well-defined photophysical, photochemical, and electrochemical properties, making them promising candidates for the development of stimuli-responsive molecular systems.

The coordination chemistry of Ru(II) and Os(II) complexes is predominantly centered around bidentate ligands such as 2,2'-bipyridine and 1,10-phenanthroline, owing to their favorable electronic properties in both ground and excited states. However, the use of bidentate chelators in octahedral complexes often leads to the formation of multiple geometric isomers, complicating purification and characterization. To overcome this limitation, tridentate ligands, particularly those based on the terpyridine scaffold, have been employed, as they promote the formation of structurally well-defined, achiral linear complexes. Despite these advantages, the major constraint of Ru(II) terpyridine complexes lies in their usually poor excited-state properties at ambient temperature, typically exhibiting weak or non-existent luminescence and very short excited-state lifetimes. As a result, the rational design of Ru(II) terpyridine systems with improved photophysical properties remains a significant and ongoing challenge in the field of coordination chemistry.

To this end, the prime objective of this dissertation is to design and synthesize Ru(II) terpyridine-based complexes exhibiting enhanced ground- and excited-state properties, with a view toward their application as functional components in photochemical molecular devices. Particular emphasis is placed on improving their luminescence efficiency and excited-state lifetimes at room temperature. One promising strategy to enhance RT luminescence in Ru(II)-terpyridine complexes involves the incorporation of strong σ-donating cyclometalating ligands. These ligands establish a more rigid and geometrically idealized octahedral coordination sphere around the Ru(II) center. This structural reinforcement minimizes non-radiative decay pathways and contributes to improved excited-state properties, including increased luminescence efficiency and prolonged excited-state lifetimes. Additionally, Os(II) analogues of these terpyridine ligands will also be explored, with the goal of extending their absorption and emission profiles into the near-infrared region. This spectral tuning is especially relevant for applications in biological environments, where deeper tissue penetration and minimal photodamage are critical.

Another major objective of this work is to develop coordination complexes capable of reversible modulation of their physicochemical properties in response to external stimuli, enhancing their utility in designing molecular devices. Stimuli-responsive systems are increasingly important in applications such as sensing, switching, and information storage. Compared to purely organic molecules, coordination complexes offer superior tunability in structure, photophysics, and electrochemistry. Among various stimuli, light is particularly attractive for enabling precise, non-invasive control of molecular transformations. Most of the reported photoswitches operate through a single reaction pathway such as *trans-cis* isomerization or electrocyclization and show bistable behavior suitable for binary logic functions. However, moving beyond binary switching requires systems capable of multiple independently addressable transformations. Such multi-state switches offer expanded functionality, including multi-site addressing, higher information density, and complex logic operations. This versatility is further enhanced by materials that respond to multiple stimuli e.g., light, pH, redox, temperature, or chemical species providing greater control, flexibility, and reversibility. Although the photoisomerization of stilbene- and azo-functionalized metal complexes is well documented, multi-stimuli responsive multi-state photoswitching in platinum metal complexes including stilbene-appended terpyridine ligands are relatively sparse in the literature.

To achieve our goals, we have first synthesized a series of cyclometalating ligands, py-bpy-Ph-X (X= -CH_3, -CH_2Br, -CHO) to increase the ^{3}MLCT-^{3}MC energy gap and enhance the photophysical properties of Ru(II)-terpyridine type complexes (Scheme 1.1). The cyclometalating ligand py-bpy-Ph-CH_3 is obtained as a minor product during the synthesis of tpy-PhCH_3 ligand from the reaction of 2-acetyl-pyridine, p-tolualdehyde, acetamide and ammonium acetate. The other two ligands are also synthesized upon appropriate derivatization of py-bpy-Ph-CH_3 (Scheme 1.2). The detailed synthetic procedure will be discussed in Chapter 2.

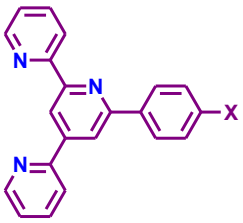

X= -CH_3, -CH_2Br, -CHO

Scheme 1.1

We have also designed a bis-terpyridine bridging ligand, tpvpvpt, incorporating two consecutive stilbene units between two terpyridine motifs to modulate the ^{3}MLCT-^{3}MC energy gap (Scheme 1.3). The ligand is prepared by mixing tpyPhCH_2PPh_3Br and terephthalaldehyde in 2:1 molar ratio in DCM at 0-5 ^{o}C under inert atmosphere (Scheme 1.4).

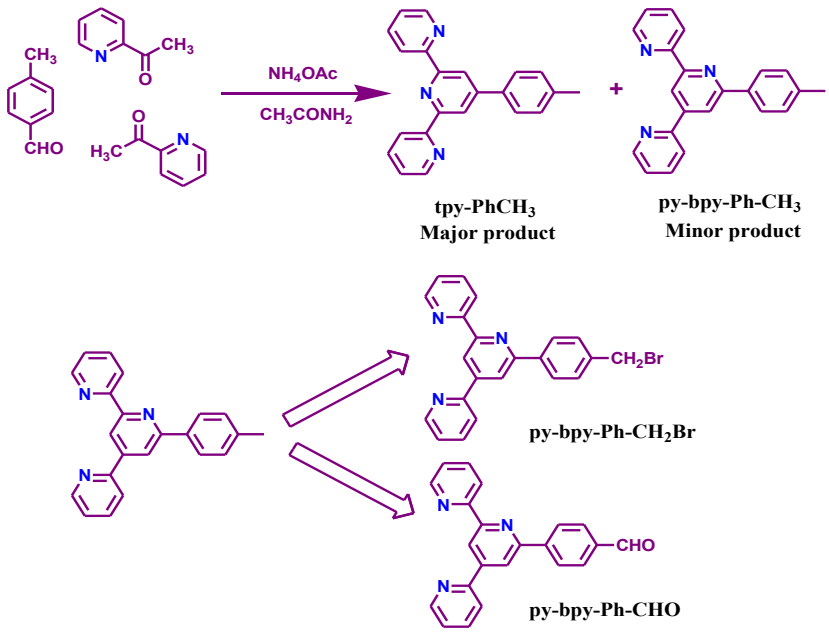

Scheme 1.2

tpvpvpt

Scheme 1.3

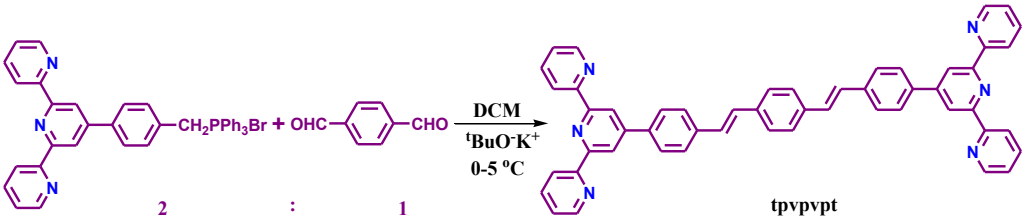

Scheme 1.4

We have also adopted a synthetic strategy to design Ru(II)-terpyridine complexes with enriched ground and excited state properties by preparing an asymmetric (tpvpt') and a symmetric bridging ligand (t'pvpvpt') by integrating stilbene moieties with cyclometalating and/or non-cyclometalating terpyridine units (Scheme 1.5). The synthetic scheme for the ligands is delineated in Scheme 1.6.

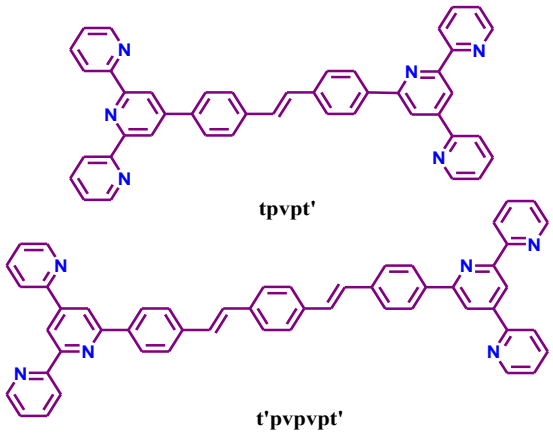

tpvpt'

t'pvpvpt'

Scheme 1.5

The formation of structurally diverse monomeric and dimeric Ru(II) and Os(II) complexes employing these ligands in conjunction with various tridentate co-ligands is depicted in Schemes 1.7-1.10. The incorporation of cyclometalating ligands with strong σ-donating ability, along with stilbene-based units featuring extended π-conjugation, significantly influences the electronic configuration of the complexes, particularly in their excited states. These electronic modifications are associated with enhanced

photoluminescence at room temperature. Furthermore, systematic variation of the capping ligands enables precise modulation of the photophysical and electrochemical properties of the resulting complexes.

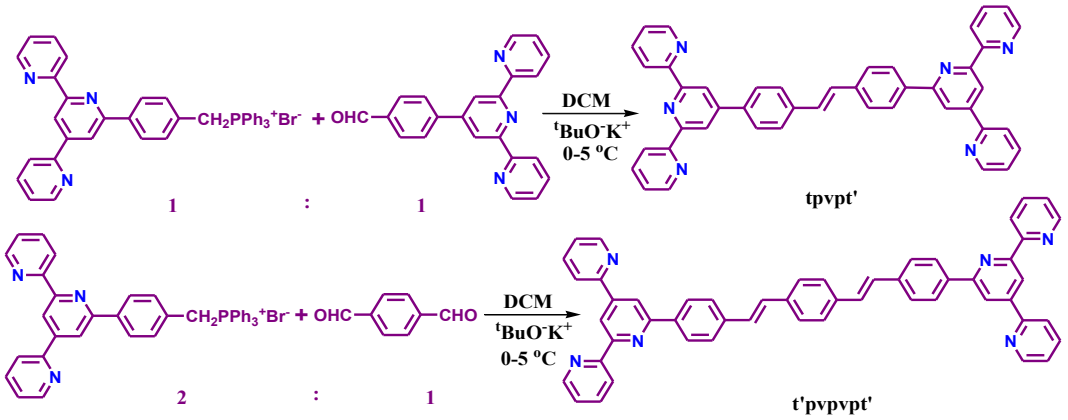

Scheme 1.6

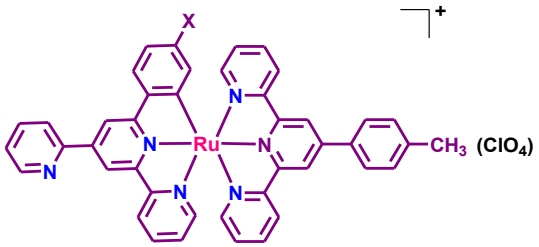

X= -CH_3, -CH_2Br, -CHO

Scheme 1.7

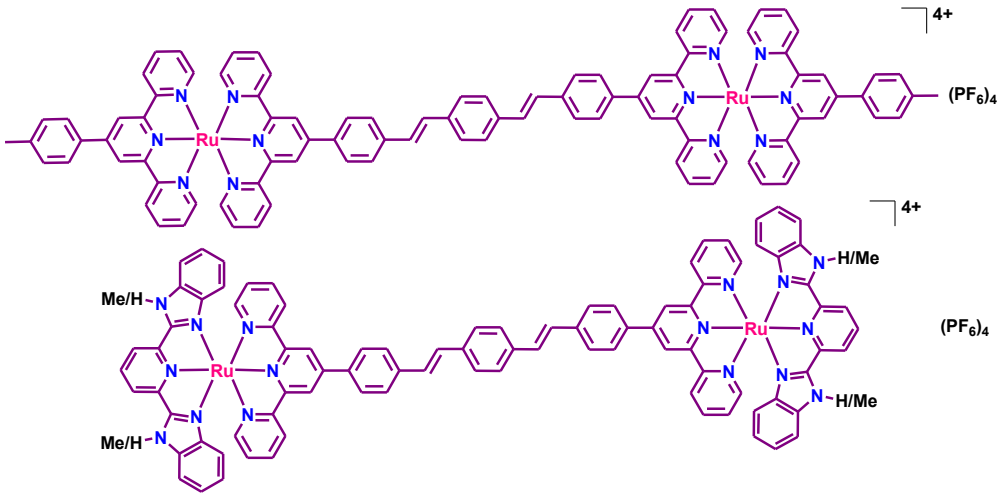

Scheme 1.8

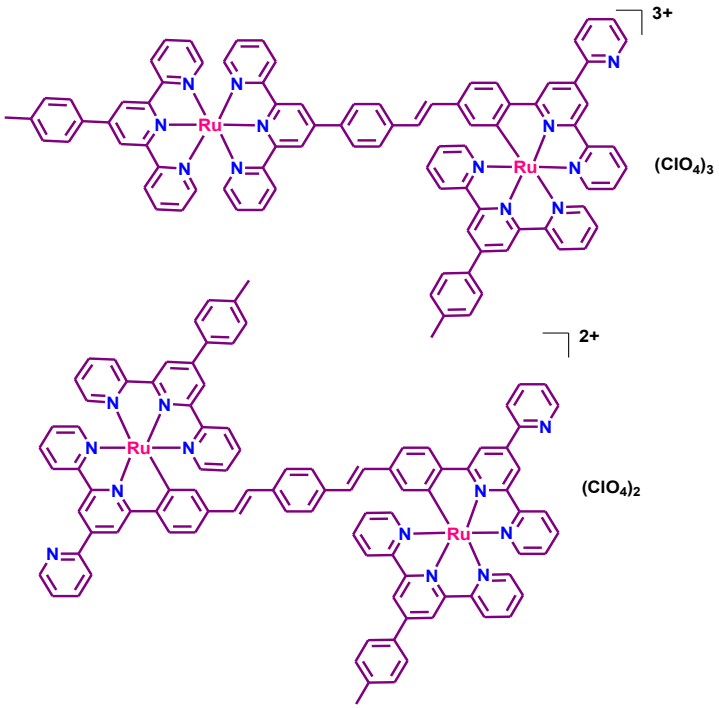

Scheme 1.9

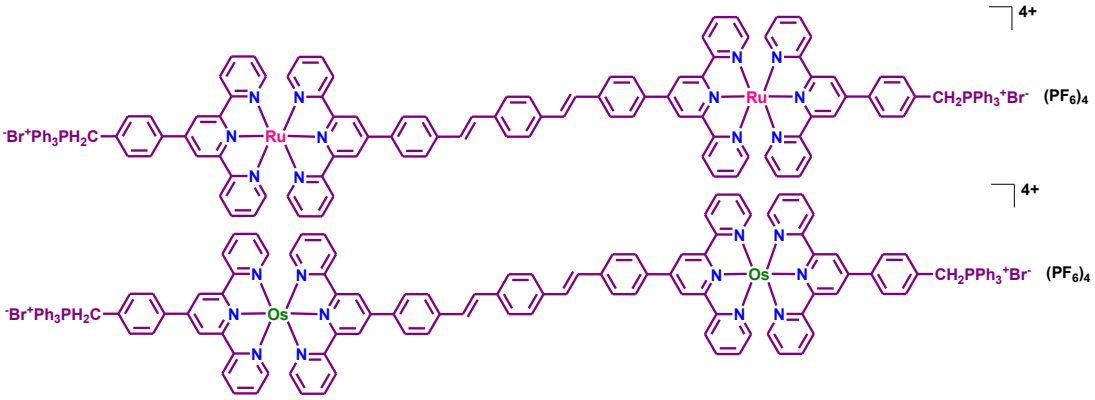

Scheme 1.10

Following the synthesis of the ligands and their corresponding metal complexes, complete characterization will be carried out using standard analytical techniques such as elemental analysis, ESI-MS or HRMS, and NMR spectroscopy. The optical properties of these complexes, including their absorption and emission spectral behavior, will be systematically investigated. Excited-state lifetimes will be determined using time-correlated single-photon counting (TCSPC), while redox characteristics will be examined through cyclic voltammetry. To gain deeper insight into their electronic structures and to rationalize the experimentally observed optical transitions, density functional theory (DFT) and time-dependent DFT (TD-DFT) calculations will be employed. In addition, the stimuli-responsive behavior of these systems will be explored, with particular attention to

photoinduced *trans-cis* isomerization about the C=C double bond. Complexes with one phenylene-vinylene unit are expected to undergo reversible *trans-cis* isomerization upon irradiation with light. In contrast, complexes bearing two phenylene-vinylene units may exhibit more complex switching behavior, transitioning between *trans-trans*, *trans-cis*, and *cis-cis* geometries under light exposure (Schemes 1.11-1.13). The reverse isomerization processes will be triggered using light of a different wavelength. Importantly, the rate and efficiency of photoisomerization can be modulated by introducing oxidants, reductants, cations, anions, acid, base and light of different wavelengths, thereby enabling precise control over photoswitching behavior and facilitating the design of efficient multi-state and multi-stimuli responsive molecular switches. This multi-state photoswitching behavior exhibited by these complexes offers significant potential for implementation in advanced molecular logic operations. By monitoring distinct spectral changes generated in response to sequential external stimuli, the feasibility of simulating complex Boolean logic functions will be systematically investigated (Scheme 1.14). Furthermore, leveraging the computational power and versatility of Python, a novel logic circuit model will be developed. This model will be designed to process a range of input combinations and reliably execute decision-making protocols, effectively emulating the behavior of conventional digital logic circuits at the molecular level.

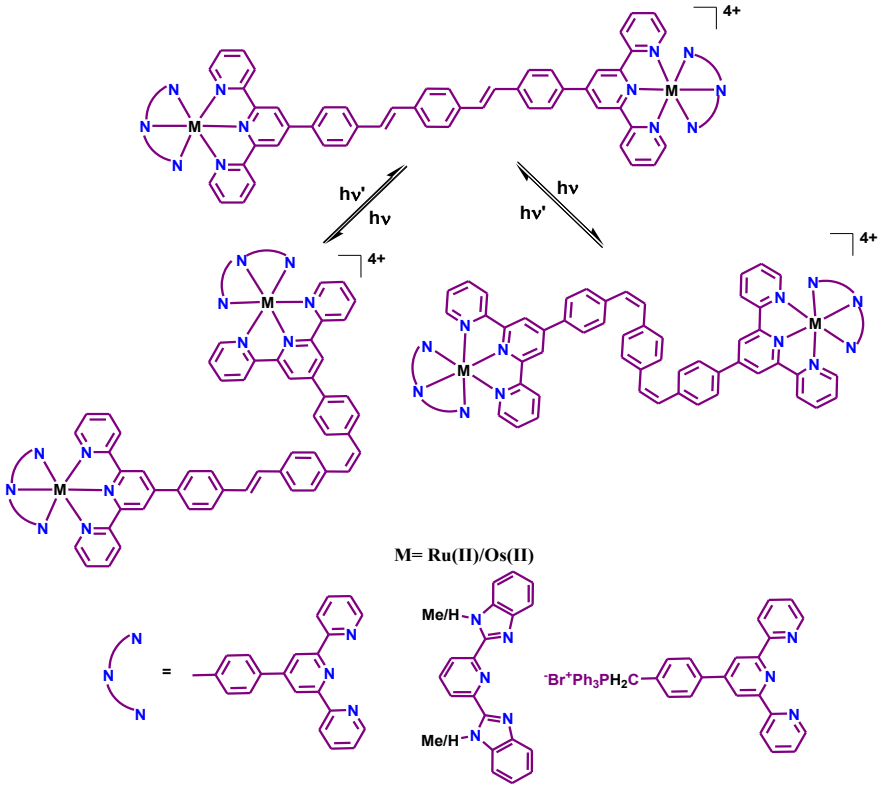

Scheme 1.11

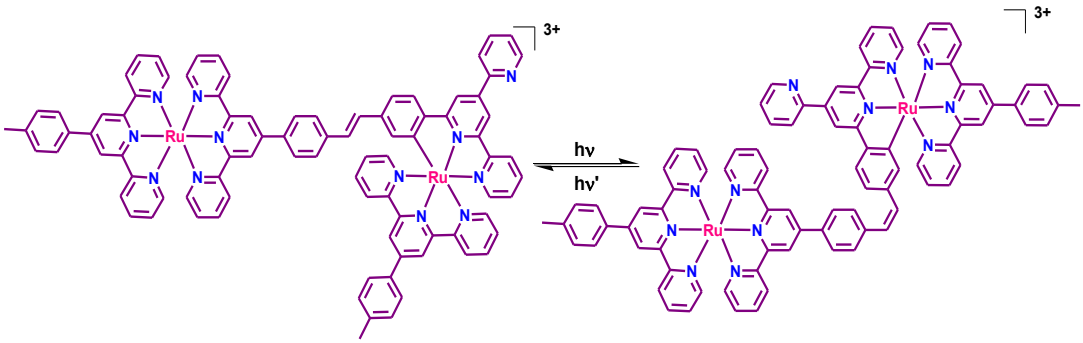

Scheme 1.12

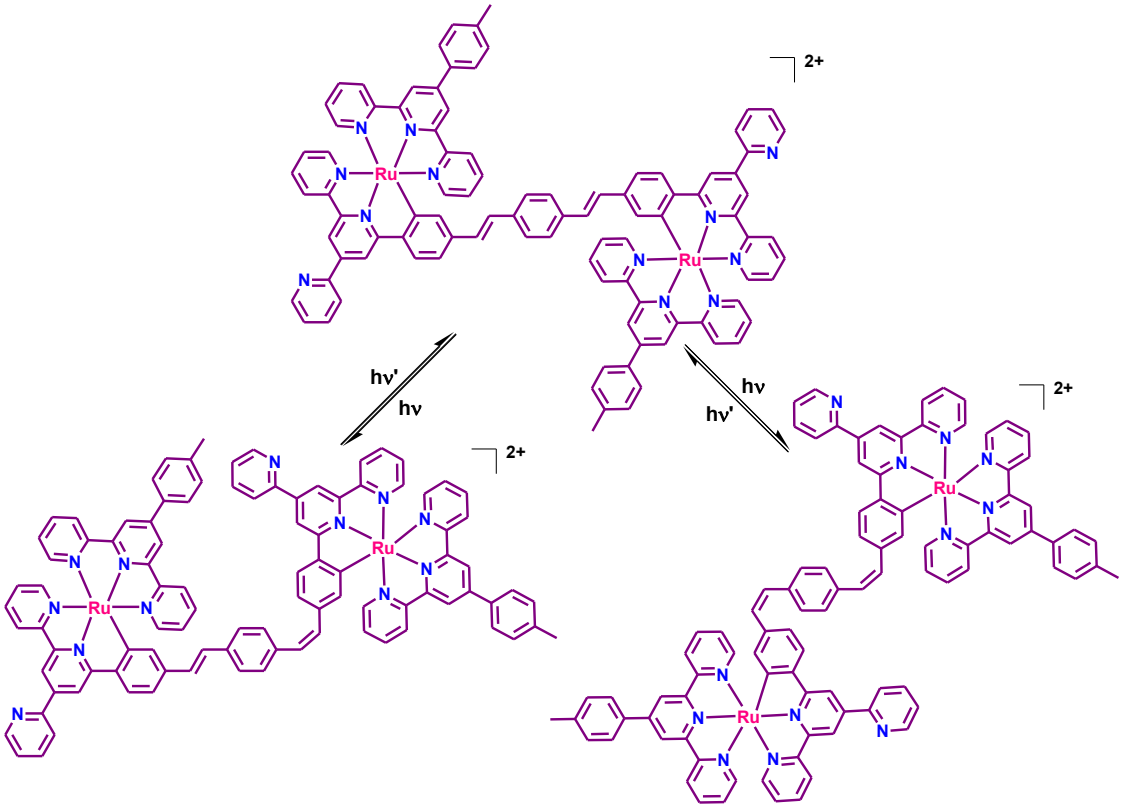

Scheme 1.13

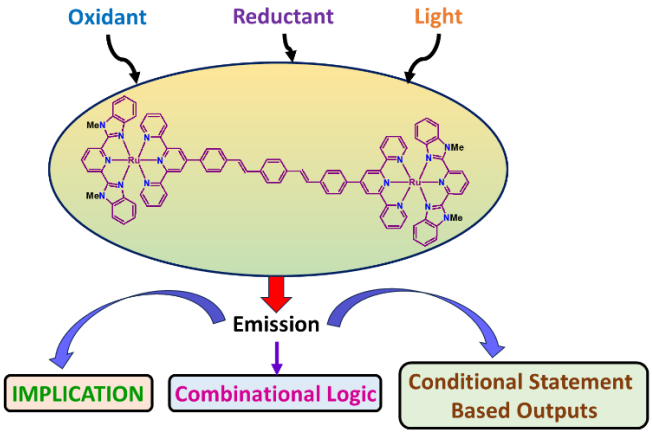

Scheme 1.14

The detailed implementation of the various research objectives, along with corresponding experimental and computational investigations, is presented in Chapters 2-6.

Chapter 2 details the synthesis and characterization of a series of luminescent Ru(II)-terpyridine complexes incorporating both cyclometalating and non-cyclometalating motifs derived from two isomeric forms of methylphenyl-substituted terpyridine (tpy-$PhCH_3$). These complexes exhibit NIR emission at RT, along with prolonged excited-state lifetimes. The presence of a non-coordinated nitrogen atom in the outer coordination sphere enables fine-tuning of the photophysical properties through acid-base interactions. Excess acid induces cleavage of the Ru-C bond, while subsequent treatment with base at elevated temperatures reinstates coordination. This reversible transformation facilitates switchable "on-off-on" emission, governed by the sequential application of acid, base and temperature. DFT and TD-DFT calculations are also employed to assign key spectral transitions and to elucidate structural changes underlying the observed switching phenomena.

Chapter 3 deals with the synthesis and characterization of two NIR emissive bimetallic cyclometalated Ru(II)-terpyridine complexes featuring phenylene-vinylene linkers within the bridging framework. Non-coordinated nitrogen atoms in the outer coordination sphere enable reversible modulation of photoredox properties through acid-base treatment, with de-coordination and re-coordination of Ru-C bonds triggered by sequential exposure to acid, base, and heat. Upon alternating exposure to visible and UV light, the complexes undergo *trans to cis* or *trans-trans* to *trans-cis* isomerization. Furthermore, the impact of acidic conditions on isomerization kinetics is systematically investigated. Quantitative analysis reveals a significant enhancement in the rate of photoisomerization in the presence of acid compared to neutral conditions. DFT and TD-DFT calculations are also carried out to get deeper insights into the electronic structure and the spectral band assignments.

In chapter 4, the synthesis, characterization and detailed investigation on the photo-redox properties of a new array of dimeric Ru(II) complexes derived from phenylene-vinylene-substituted terpyridyl ligand are presented. Owing to the presence of olefinic double bonds in the bridge, the photoisomerization behavior of these complexes is also explored. The complexes exhibit reversible *trans-trans* to *cis-cis* isomerization in presence of visible or UV light. Notably, the rate of photoisomerization can be significantly accelerated through the introduction of chemical oxidants or reductants, demonstrating the ability of the complexes to operate as multi-state molecular switches.

Chapter 5 focuses on the development of multiply-configurable molecular logic devices based on the multi-step stimuli-responsive switching behavior of a selected Ru(II) complex from the previously described series. By harnessing the distinct emission responses elicited under various external stimuli as optical outputs, a range of advanced Boolean logic operations are demonstrated. These include IMPLICATION logic, as well as more complex architectures such as 2-input 2-output and 3-input 2-output combinational logic gates. Furthermore, a logic circuit model is implemented using Python, enabling automated interpretation of input conditions and accurate output generation.

The detailed synthetic procedure and characterization of two symmetric, luminescent bimetallic Ru(II) and Os(II) complexes with a bis-terpyridine bridging ligand containing two consecutive phenylene-vinylene units, along with a tridentate capping ligand bearing acidic methylene groups and phosphonium functionalities are presented in Chapter 6. Owing to the presence of acidic methylene protons, the complexes exhibit selective responses to F^- and OH^- anions. Additionally, they undergo light-induced reversible *trans-trans* to *trans-cis* isomerization upon exposure to visible or UV light. The systems display efficient, reversible "on-off" emission switching across the visible to NIR range in response to multiple external stimuli, including specific anions, oxidants, reductants and light of distinct wavelengths. Interestingly, such stimuli induce a significant enhancement in the rate of photoisomerization.

1.9. References

(1) Grätzel, M. Photoelectrochemical Cells. *Nature* **2001**, *414*, 338-344.

(2) Badjic, J. D.; Balzani, V.; Credi, A.; Silvi, S.; Stoddart, J. F. A Molecular Elevator. *Science* **2004**, *303*, 1845-1849.

(3) Meyer, T. J. Chemical Approaches to Artificial Photosynthesis. *Acc. Chem. Res.* **1989**, *22*, 163-170.

(4) Scandola, F.; Chiorboli, C.; Indelli, M. T.; Rampi, M. A. In *Electron Transfer in Chemistry*; Balzani, V., Ed.; VCH-Wiley: 2001; Vol. 3, p 337.

(5) Natali, M.; Campagna, S.; Scandola, F. Photoinduced Electron Transfer across Molecular Bridges: Electron- and Hole-Transfer Superexchange Pathways. *Chem. Soc. Rev.* **2014**, *43*, 4005- 4018.

(6) Zhang, T.; Lin, W. Metal-Organic Frameworks for Artificial Photosynthesis and Photocatalysis. *Chem. Soc. Rev.* **2014**, *43*, 5982-5993.

(7) Glaser, F.; Wenger, O. S. Recent Progress in the Development of Transition-Metal Based Photoredox Catalysts. *Coord. Chem. Rev*. **2020**, 213139.

(8) Gütlich, P.; Garcia, Y.; Woike, T. Photoswitchable Coordination Compounds. *Coord. Chem. Rev.* **2001**, *219-221*, 839-879.

(9) Rice, A. M.; Martin, C. R.; Galitskiy, V. A.; Berseneva, A. A.; Leith, G. A.; Shustova, N. B. Photophysics Modulation in Photoswitchable Metal-Organic Frameworks. *Chem. Rev.* **2020**, *120*, 8790-8813.

(10) Zhao, W.-W.; Xu, J.-J.; Chen, H.-H. Photoelectrochemical DNA Biosensors. *Chem. Rev.* **2014**, *114*, 7421-7441.

(11) Sun, Y.; Joyce, L. E.; Dickson, N. M.; Turro, C. Efficient DNA Photocleavage by $[Ru(bpy)_2(dppn)]^{2+}$ With Visible Light. *Chem. Commun.* **2010**, *46*, 2426-2428.

(12) Song, W.; Chen, Z.; Brennaman, M.; Concepcion, J.; Patrocinio, A.; Murakami Iha, N.; Meyer, T. Making Solar Fuels by Artificial Photosynthesis. *Pure Appl. Chem.* **2011**, *83*, 749-768.

(13) Shum, J.; Leung, P. K.-K.; Lo, K. K.-W. Luminescent Ruthenium(II) Polypyridine Complexes for a Wide Variety of Biomolecular and Cellular Applications. *Inorg. Chem.* **2019**, *58*, 2231-2247.

(14) Kalyanasundaram, K.; Grätzel, M. Applications of Functionalized Transition Metal Complexes in Photonic and Optoelectronic Devices. *Coord. Chem. Rev.* **1998**, *177*, 347-414.

(15) Wadman, S. H.; Kroon, J. M.; Bakker, K.; Havenith, R. W. A.; van Klink, G. P. M.; van Koten, G. Cyclometalated Organoruthenium Complexes for Application in Dye-Sensitized Solar Cells. *Organometallics* **2010**, *29*, 1569-1579.

(16) Balzani, V.; Credi, A.; Venturi, M. Molecular Devices and Machines; Wiley-VCH: Weinheim, 2003.

(17) Intelligent Stimuli-Responsive Materials; Li, Q., Ed.; John Wiley & Sons, Inc.: Hoboken, Nj, 2013.

(18) McConnel, A.J.; Wood, C. S.; Neelakandan P. P.; Nitschke, J. R. Stimuli-Responsive Metal-Ligand Assemblies. *Chem. Rev.* **2015**, *115*, 7729-7793.

(19) Martinez-Manez, R.; Sancenon, F. Fluorogenic and Chromogenic Chemosenspors and Reagents for Anions. *Chem. Rev.* **2003**, *103*, 4419-4476.

(20) Grusenmeyer, T. A.; Chen, J.; Jin, Y.; Nguyen, J.; Rack, J. J.; Schmehl, R. H. pH Control of Intramolecular Energy Transfer and Oxygen Quenching in Ru(II) Complexes Having Coupled Electronic Excited States. *J. Am. Chem. Soc.* **2012**, *134*, 7497-7506.

(21) Amendola, V.; Fabbrizzi, L.; Licchelli, M.; Mangano, C.; Pallavicini, P.; Parodi, L. Poggi, A. Molecular Events Switched by Transition Metals. *Coord. Chem. Rev.* **1999**, *190-192*, 649-669.

(22) Haga, M.; Takasugi, T.; Tomie, A.; Ishizuya, M.; Yamada, T.; Hossain, M. D.; Inoue, M. Molecular Design of a Proton-Induced Molecular Switch Based on Rod-Shaped Ru Dinuclear Complexes with Bis-Tridentate 2,6-Bis(Benzimidazol-2-Yl)Pyridine Derivatives. *Dalton Trans.* **2003**, 2069-2079.

(23) Kume, S.; Nishihara, H. Photochrome-Coupled Metal Complexes: Molecular Processing of Photon Stimuli. *Dalton Trans.* **2008**, 3260-3271.

(24) Balzani, V.; Credi, A.; Venturi, M. Light Powered Molecular Machines. *Chem. Soc. Rev.* **2009**, *38*, 1542-1550.

(25) Juris, A.; Balzani, V.; Barigelletti, F.; Campagna, S.; Belser, P.; von Zelewsky, A. Ru(II) Polypyridine Complexes: Photophysics, Photochemistry, Eletrochemistry, and Chemiluminescence. *Coord. Chem. Rev.* **1988**, *84*, 85-277.

(26) Caspar, J. V.; Meyer, T. J. Photochemistry of Tris(2,2'-bipyridine)Ruthenium(2+) Ion ($Ru(bpy)_3^{2+}$): Solvent Effects. *J. Am. Chem. Soc.* **1983**, *105*, 5583-5590.

(27) Van Houten, J.; Watts, R. J. Temperature Dependence of the Photophysical and Photochemical Properties of the Tris(2,2'-Bipyridyl)Ruthenium(II) Ion in Aqueous Solution. *J. Am. Chem. Soc.* **1976**, *98,* 4853-4858.

(28) Balzani, V.; Juris, A.; Venturi, M.; Campagna, S.; Serroni, S. Luminescent and Redox-Active Polynuclear Transition Metal Complexes. *Chem. Rev.* **1996,** *96*, 759-834.

(29) Creutz, C.; Chou, M.; Netzel, T.; L. Okumura, M.; Sutin, N. Lifetimes, Spectra, and Quenching of the Excited States of Polypyridine Complexes of Iron (II), Ruthenium (II), and Osmium (II). *J. Am. Chem. Soc.* **1980**, *102*, 1309-1319.

(30) Meyer, T. J. Photochemistry of Metal Coordination Complexes: Metal to Ligand Charge Transfer Excited States. *Pure Appl. Chem.* **1986**, *58*, 1193.

(31) Wang, X.; Guerzo, A.; Baitalik, S.; Simon, G.; Shaw, G. B.; Chen, L.; Schmehl, R. H. The Influence of Bridging Ligand Electronic Structure on the Photophysical Properties of Noble Metal Diimine and Triimine Light Harvesting Systems**.** *Photosynth. Res.* **2006**, *87*, 83-103.

(32) Ali, C.; Banaszak, M.; Astumian, R. D.; Stoddart, J. F.; Grzybowski, B. A. Great Expectations: Can Artificial Molecular Machines Deliver on Their Promise? *Chem. Soc. Rev*. **2012**, *41*, 19-30.

(33) Sauvage, J.-P.; Collin, J. P.; Chambron, J. C.; Guillerez, S.; Coudret, C.; Balzani, V.; Barigelletti, F.; De Cola, L.; Flamigni, L. Ruthenium(II) and Osmium(II) Bis(terpyridine) Complexes in Covalently-Linked Multicomponent Systems: Synthesis, Electrochemical Behavior, Absorption Spectra, and Photochemical and Photophysical Properties. *Chem. Rev.* **1994**, *94*, 993-1019.

(34) Khaled, R. M.; Abo-Elfadl, M. T.; Radacki, K.; Zeid, M. A. A.; Shehab, O. R.; Abdel-Kader, N. S.; Mostafa, G. A.; Ali, E. A.; Al Neyadi, S. S.; Mansour, A. M. Visible-Light-Induced CO-Releasing Properties and Cytotoxicity of a Ru(II) Carbonyl Complex Containing 2-(pyridin-2-yl)-quinoxaline. *Dalton Trans.* **2025**.

(35) Momeni, B. Z.; Davarzani, N.; Janczak, J.; Ma, N.; Abd-El-Aziz, A. S. Progress in Design and Applications of Supramolecular Assembly of 2,2′:6′,2 ″-Terpyridine-Based First Row d-Block Elements. *Coord.Chem. Rev.* **2024***, 506*, 215619.

(36) Bera, M. K.; Sarmah, S.; Santra, D. C.; Higuchi, M., Heterometallic Supramolecular Polymers: From Synthesis to Properties and Applications. *Coord. Chem.Rev.* **2024**, *501*, 215573.

(37) Mandal, A. A.; Upadhyay, A.; Mandal, A.; Nayak, M.; Mohammad, S. K.; Mukherjee, S.; Banerjee, S. Visible-Light-Responsive Novel Ru(II)-Metallo-Antibiotics with Potential Antibiofilm and Antibacterial Activity. *ACS Appl. Mater. Interfaces* **2024**, *16*, 28118-28133.

(38) Juwita, R.; Liao, J. M.; Chen, C. Y.; Tsai, H. H. G. Enhancing Near-Infrared Absorption in Terpyridyl Ru/Os Complexes with Ancillary Ligands to Activate Spin-Forbidden Transitions in Dye-Sensitized Solar Cells: A TDDFT Investigation. *J. Phys. Chem. A* **2024**, *128,* 880-894.

(39) Balzani, V.; Bergamini, G.; Marchioni, F.; Ceroni, P. Ru(II)-bipyridine Complexes in Supramolecular Systems, Devices and Machines. *Coord. Chem. Rev.* **2006**, *250*, 1254-1266.

(40) Yersin, H.; Rausch, A. F.; Czerwieniec, R.; Hofbeck, T.; Fischer, T. The Triplet State of Organo-Transition Metal Compounds. Triplet Harvesting and Singlet Harvesting for Efficient OLEDs. *Coord. Chem. Rev.* **2011**, *255*, 2622-2652.

(41) Liu, P.; Wu, B-Y.; Liu, Jin.; Dai, Y.-C.; Wang, Y.-J.; Wang, K.-Z. DNA Binding and Photocleavage Properties, Cellular Uptake and Localization, and In-Vitro Cytotoxicity of Dinuclear Ruthenium(II) Complexes with Varying Lengths in Bridging Alkyl Linkers. *Inorg. Chem.* **2016**, *55*, 1412-1422.

(42) Mardanya, S.; Karmakar, S.; Mondal, D.; Baitalik, S. Homo- and Heterobimetallic Ruthenium(II) and Osmium(II) Complexes Based on a Pyrene-Biimidazolate Spacer as Efficient DNA-Binding Probes in the Near-Infrared Domain. *Inorg. Chem.* **2016**, *55*, 3475-3489.

(43) Maity, D.; Bhaumik, C.; Mardanya, S.; Karmakar, S.; Baitalik, S. Light Harvesting and Directional Energy Transfer in Long-Lived Homo- and Heterotrimetallic Complexes of Fe^{II}, Ru^{II}, and Os^{II}. *Chem. -Eur. J.* **2014**, *20*, 13242-13252.

(44) Arrigo, A.; Santoro, A.; Puntoriero, F.; Lainé, P. P. Campagna, S. Photoinduced Electron Transfer in Donor-Bridge-Acceptor Assemblies: The Case of Os(II)-Bis(Terpyridine)-(Bi)Pyridinium Dyads. *Coord. Chem. Rev.* **2015**, *304-305*, 109-116.

(45) Manner, V. W.; Mayer, J. M. Concerted Proton-Electron Transfer in a Ruthenium Terpyridyl-Benzoate System with a Large Separation between the Redox and Basic Sites. *J. Am. Chem. Soc.* **2009**, *131*, 9874-9875.

(46) Chang, K.-C.; Sun, S.-S.; Odago, M. O.; Lees, A. J. Anion Recognition and Sensing by Transition-Metal Complexes with Polarized N-H Recognition Motifs. *Coord. Chem. Rev*. **2015**, *284*, 111-123.

(47) Constable, E. C. 2,2′:6′,2′′-Terpyridines: From Chemical Obscurity to Common Supramolecular Motifs. *Chem. Soc. Rev.* **2007**, *33*, 246-253.

(48) Harriman, A.; Ziessel, R. Making Photoactive, Molecular-Scale Wires. *Chem. Commun*. **1996**, 1707-1716.

(49) Pal, A. K.; Hanan, G. S. Design, Synthesis and Excited-State Properties of Mononuclear Ru(II) Complexes of Tridentate Heterocyclic Ligands. *Chem. Soc. Rev.* **2014**, *43*, 6184-6197.

(50) Hofmeier, H.; Schubert, U. S. Recent Developments in the Supramolecular Chemistry of Terpyridine-Metal Complexes. *Chem. Soc. Rev.* **2004**, *33*, 373-399.

(51) Winkler, J. R.; Netzel, T.; Creutz, C.; Sutin, N. Direct Observation of Metal-To-Ligand Charge-Transfer (MLCT) Excited States of Pentaammineruthenium(II) Complex. *J. Am. Chem. Soc*. **1987**, *109*, 2381-2392.

(52) Medlycott, E. A.; Hanan, G. S. Synthesis and Properties of Mono- and Oligo-Nuclear Ru(II) Complexes of Tridentate Ligands: The Quest for Long-Lived Excited States at Room Temperature. *Coord. Chem. Rev.* **2006**, *250*, 1763-1782.

(53) Wadman, S. H.; Lutz, M.; Tooke, D. M.; Spek, A. L.; Hartl, F.; Havenith, R. W. A.; van Klink, G. P. M.; van Koten, G. Consequences of N,C,N- and C,N,N-Coordination Modes on Electronic and Photophysical Properties of Cyclometalated Aryl Ruthenium(II) Complexes. *Inorg. Chem.* **2009**, *48*, 1887-1900.

(54) Kreitner, C.; Erdmann, E.; Seidel, W. W.; Heinze, K. Understanding the Excited State Behavior of Cyclometalated Bis(tridentate)ruthenium(II) Complexes: A Combined Experimental and Theoretical Study. *Inorg. Chem.* **2015**, *54*, 11088-11104.

(55) Beley, M.; Collin, J.-P.; Louis, R.; Metz, B.; Sauvage, J.-P. 3,3',5,5'-Tetrapyridylbiphenyl: A Biscyclometalating Bridging Ligand with a High Coupling Ability in Ru^{III}, Ru^{II} Mixed Valence Systems. *J. Am. Chem. Soc.* **1991**, *113*, 8522-8524.

(56) Duati, M.; Fanni, S.; Vos, J. G. A New Luminescent Ru(terpy) Complex Incorporating a 1,2,4-Triazole Based σ-Donor Ligand. *Inorg. Chem. Commun.* **2000**, *3*, 68-70.

(57) Indelli, M. T.; Bignozzi, C. A.; Scandola, F.; Collin, J.-P. Design of Long-Lived Ru(II) Terpyridine MLCT States. Tricyano Terpyridine Complexes. *Inorg. Chem.* **1998**, *37*, 6084-6089.

(58) Constable, E. C.; Dunne, S. J.; Rees, D. G. F.; Schmitt, C. X. Reversible Cyclometallation at a Ruthenium(II) Centre. *Chem. Commun.* **1996**, 1169.

(59) Collin, J. P.; Gavina, P.; Heitz, V.; Sauvage, J.-P. Construction of One-Dimensional Multicomponent Molecular Arrays: Control of Electronic and Molecular Motions. *Eur. J. Inorg. Chem.* **1998**, 1-14.

(60) Wilkinson, A. J.; Puschmann, H.; Howard, J. A. K.; Foster, C. E.; Williams, J. A. G. Luminescent Complexes of Iridium(III) Containing N^C^N-Coordinating Terdentate Ligands. *Inorg. Chem.* **2006**, *45*, 8685-8699.

(61) Cocchi, M.; Virgili, D.; Fattori, V.; Rochester, D. L.; Williams, J. A. G. N^C^N-Coordinated Platinum(II) Complexes as Phosphorescent Emitters in High-Performance Organic Light-Emitting Devices. *Adv. Funct. Mater.* **2007**, *17*, 285-289.

(62) Zeng, L.; Gupta, P.; Chen, Y.; Wang, E.; Ji, L.; Chao, H.; Chen, Z.-S. The Development of Anticancer Ruthenium(II) Complexes: From Single Molecule Compounds to Nanomaterials. *Chem. Soc. Rev.* **2017**, *46*, 5771-5804.

(63) Cutillas, N.; Yellol, G. S.; de Haro, C.; Vicente, C.; Rodríguez, V.; Ruiz, J. Anticancer Cyclometalated Complexes of Platinum Group Metals and Gold. *Coord. Chem. Rev*. **2013**, *257*, 2784-2797.

(64) Benniston, A. C.; Chapman, G. M.; Harriman, A.; Rostron, S. A.; Reversible Luminescence Switching in a Ruthenium(II)Bis(2,2′:6′,2′′-Terpyridine)-Benzoquinone Dyad. *Inorg. Chem.* **2005**, *44*, 4029-4036.

(65) Meng, T.-T., Wang, H. Zheng, Z. Wang, K.-Z. pH-Switchable "Off-On-Off" Near-Infrared Luminescence Based on a Dinuclear Ruthenium(II) Complex. *Inorg. Chem.* **2017**, *56*, 4775-4779.

(66) Akasaka, T.; Otsuki, J.; Araki, K. Redox-Responsive Molecular Switches Based on Azoterpyridine-Bridged Ru/Os Complexes. *Chem. -Eur. J.* **2001**, *8*, 130-136.

(67) Bar, M.; Deb, S.; Paul, A.; Baitalik, S.; Stimuli-Responsive Luminescent Bis-Tridentate Ru(II) Complexes Toward the Design of Functional Materials. *Inorg. Chem.* **2018**, *57*, 12010-12024.

(68) Mardanya, S.; Karmakar, S.; Das, S.; Baitalik, S. Anion and Cation Triggered Modulation of Optical Properties of a Pyridyl-Imidazole Receptor Rigidly Linked to Pyrene and Construction of INHIBIT, OR and XOR Molecular Logic Gates: A Combined Experimental and DFT/TD-DFT Investigation. *Sens. Actuators B* **2015,** *206*, 701-713.

(69) Harvey, E. C.; Feringa, B. L.; Vos, J. G.; Browne, W. R.; Pryce, M. T. Transition Metal Functionalized Photo- and Redox-Switchable Diarylethene Based Molecular Switches. *Coord. Chem. Rev.* **2015**, *282-283*, 77-86.

(70) Ko, C. C.; Yam, V. W. W. Transition Metal Complexes with Photochromic Ligands Photosensitization and Photoswitchable Properties. *J. Mater. Chem*. **2010**, *20*, 2063-2070.

(71) Unjaroen, D.; Kasper, J. B.; Browne, W. R. Reversible Photochromic Switching in Ru(II) Polypyridyl Complex. *Dalton Trans.* **2014**, *43*, 16974-16976.

(72) Jacquet, M.; Lafolet, F.; Cobo, S.; Loiseau, F.; Bakkar, A.; Boggio-Pasqua, M.; Saint-Aman, E.; Royal, G. Effcient Photoswitch System Combining a Dimethyldihydropyrene Pyridinium Core and Ruthenium(II) Bis-Terpyridine Entities. *Inorg. Chem.* **2017**, *56*, 4357-4368.

(73) Bianchi, A.; Delgado-Pinar, E.; García-España, E.; Giorgi, C.; Pina, F. Highlights of Metal Ion-Based Photochemical Switches. *Coord. Chem. Rev.* **2014**, *260*, 156-215.

(74) Guerchais, V.; Ordronneau, L.; Bozec, H. Recent Developments in the Field of Metal Complexes Containing Photochromic Ligands: Modulation of Linear and Nonlinear Optical Properties. *Coord. Chem. Rev.* **2010**, *254*, 2533-2545.

(75) Colasson, B.; Credi, A.; Ragazzon, G. Light-Driven Molecular Machines Based on Ruthenium(II) Polypyridine Complexes: Strategies and Recent Advances. *Coord. Chem. Rev.* **2016**, *325*, 125-134.

(76) Bandara, H. M. D.; Burdette, S. C. Photoisomerization in Different Classes of Azobenzene. *Chem. Soc. Rev.* **2012**, *41* (5), 1809-1825.

(77) Kurihara, M.; Nishihara, H. Azo- and Quinone-Conjugated Redox Complexes-Photo- and Proton-Coupled Intramolecular Reactions Based on d-π Interaction. *Coord. Chem. Rev.* **2002**, *226*, 125-135.

(78) Yutaka, T.; Mori, I.; Kurihara, M.; Mizutani, J.; Tamai, N.; Kawai, T.; Irie, M.; Nishihara, H. Photoluminescence Switching of Azobenzene-Conjugated Pt(II) Terpyridine Complexes by Trans-Cis Photoisomerization. *Inorg. Chem.* **2002**, *41*, 7143-7150.

(79) Yutaka, T.; Kurihara, M.; Kubo, K.; Nishihara, H. Novel Photoisomerization Behavior of Rh Binuclear Complexes Involving an Azobenzene-Bridged Bis(Terpyridine) Ligand. Strong Effects of Counter-Ion and Solvent and the Induction of Redox Potential Shift. *Inorg. Chem.* **2000**, *39*, 3438-3439.

(80) Yutaka, T.; Mori, I.; Kurihara, M.; Mizutani, J.; Kubo, K.; Furusho, S.; Matsumura, K.; Tamai, N.; Nishihara, H. Synthesis, Characterization, and Photochemical Properties of Azobenzene-Conjugated Ru(II) and Rh(III) Bis(Terpyridine) Complexes. *Inorg. Chem.* **2001**, *40*, 4986-4995.

(81) Irie, M.; Yokoyama, Y. Diarylethenes for Memories and Switches. *Chem. Rev.* **2000**, *100* (5), 1685-1716.

(82) Irie, M.; Fukaminato, T.; Matsuda, K.; Kobatake, S. Photochromism of Diarylethene Molecules and Crystals: Memories, Switches, and Actuators. *Chem. Rev.* **2014**, *114*, 12174-12277.

(83) Matsuda, K.; Irie, M. Diarylethene as a Photoswitching Unit. *J. Photochem. Photobiol. C* **2004**, *5* (2), 169-182.

(84) Irie, M.; Sakemura, K.; Okinaka, M.; Uchida, K. Photochromism of Dithienylethenes with Electron-Donating Substituents. *J. Org. Chem.* **1995**, *60*, 8305-8309.

(85) Waldeck, G. H. Photoisomerization Dynamics of Stilbenes. *Chem. Rev.* **1991**, *91*, 415-436.

(86) Villarón, D.; Wezenberg, S. J. Stiff-Stilbene Photoswitches: From Fundamental Studies to Emergent Applications. *Angew. Chem.* **2020**, *132*, 13292-13302.

(87) Klajn, R. Spiropyran-Based Dynamic Materials. *Chem. Soc. Rev.* **2014**, *43*, 148-184.

(88) Rau, H.; Photoisomerization of Azobenzenes. *Photoreact. Org. Thin Films*, **2002**, *3*, 47.

(89) Feringa, B. L.; van Delden, R. A.; Koumura, N.; Geertsema, E. M. Chiroptical Molecular Switches. *Chem. Rev.* **2000**, *100*, 1789-1816.

(90) Ikeda, T.; Tsutsumi, O. Optical Switching and Image Storage by Means of Azobenzene Liquid-Crystal Films. *Science* **1995**, *268*, 1873-1875.

(91) Anggia, I. S.; Hayati, D.; Hong, J. Synthesis and Photophysical Characterization of Push-Pull Azobenzene Derivatives Featuring Different π-Bridges for Photoresponsive Applications. *Dyes Pigm.* **2025**, *234*, 112550.

(92) Ichimura, K.; Oh, S. K.; Nakagawa, M. Light-Driven Motion of Liquids on a Photoresponsive Surface. *Science* **2000**, *288*, 1624-1626.

(93) Staniak, N. T.; Staniak, M.; Dudek, M.; Grzelczak, M.; Matczyszyn, K. Thermoplasmonic Effect Enables Indirect ON-OFF Control over the *Z-E* Isomerization of Azobenzene-Based Photoswitch. *Small* **2024**, *20,* 2404755.

(94) Tian, H.; Zhang, J. *Photochromic Materials: Preparation, Properties and Applications*; Wiley-VCH: Weinheim, Germany, 2016.

(95) Dürr, H.; Bouas-Laurent, T. H. In *Photochromism: Molecules and Systems*; Elsevier, Amsterdam, 1990.

(96) Oelgemöller, M.; Frank, R.; Lemmen, P.; Lenoir, D.; Lex, J.; Inoue, Y. Synthesis, Structural Characterization and Photoisomerization of Cyclic Stilbenes. *Tetrahedron* **2012**, *68*, 4048-4056.

(97) Saltiel, J.; Papadimitriou, D.; Krishna, T. S. R.; Huang, Z.-N.; Krishnamoorthy, G.; Laohhasurayotin, S.; Clark, R. J. Photoisomerization of All-cis-1,6-diphenyl-1,3,5 Hexatriene in the Solid State and in Solution: A Simultaneous Three-Bond Twist Process. *Angew. Chem. Int. Ed*. **2009**, *48*, 8082-8085.

(98) Fan, Y.; Chen, J.; Yu, L.; Li, A.; Zhai, G.; Lei, Y.; Zhu, C. Methyl Substitution Enhanced Photoisomerization of Trans, Trans-1,4-Diphenyl-1,3-Butadiene: Direct ab Initio Trajectory Surface Hopping Dynamic Simulations. *Phys. Chem. Chem. Phys.* **2018**, *20*, 2260-2273.

(99) Jędrzejewska, B.; Ośmiałowskia, B.; Zaleśny, R. Application of Spectroscopic and Theoretical Methods in the Studies of Photoisomerization and Photophysical Properties of the Push-Pull Styryl-Benzimidazole Dyes. *Photochem. Photobiol. Sci.* **2016**, *15*, 117-128.

(100) Matos, L. S.; Amaral, R. C.; Iha N. Y. M. Visible Photosensitization of *Trans*-Styrylpyridine Coordinated to fac-$[Re(CO)_3(dcbH_2)]^+$: New Insights. *Inorg. Chem.* **2018**, *57*, 9316-9326.

(101) Polo, A. S.; Itokazu, M. K.; Frin, K. M.; Patrocınio, A. O. T.; Iha, N. Y. M. Light Driven *Trans*-To-*Cis* Isomerization of Stilbene-Like Ligands in *fac*-$[Re(CO)_3(NN)(trans\text{-}L)]^+$ and Luminescence of their Photoproducts. *Coord. Chem. Rev.* **2006**, *250*, 1669-1680.

(102) Bardaj, M.; Barrio, M.; Espinet, P. Photosensitive Azobispyridine Gold(I) and Silver(I) Complexes. *Dalton Trans.* **2011**, *40*, 2570-2577.

(103) Vlcek A. J.; Busby, M. Ultrafast Ligand-to-ligand Electron and Energy Transfer in the Complexes *fac*-$[Re^I(L)(CO)_3(bpy)]^{n+}$. *Coord. Chem. Rev.* **2006**, *250*, 1755-1762.

(104) Zanoni, K. P. S.; Iha, N. Y. M. Reversible Trans ⇌ Cis Photoisomerizations of $[Re(CO)_3(Ph_2phen)(StpyCN)]^+$ Towards Molecular Machines. *Dalton Trans.* **2017,** *46* (30), 9951-9958.

(105) Ko, C.-C.; Kwok, W.-M.; Yam, V. W.-W.; Phillips, D. L. Triplet MLCT Photosensitization of the Ring-Closing Reaction of Diarylethenes by Design and Synthesis of a Photochromic Rhenium(I) Complex of a Diarylethene-Containing 1,10-Phenanthroline Ligand. *Chem.-Eur. J.* **2006**, *12*, 5840-5848.

(106) Fihey, A.; Perrier, A.; Browne, W. R.; Jacquemin, D. Multiphotochromic Molecular Systems. *Chem. Soc. Rev.* **2015**, *44*, 3719-3759**.**

(107) Perrier, A.; Maurel, F.; Jacquemin, D. Single Molecule Multiphotochromism with Diarylethenes. *Acc. Chem. Res.* **2012**, *45*, 1173-1182.

(108) Andréasson, J.; Pischel, U. Light-Stimulated Molecular and Supramolecular Systems for Information Processing and Beyond. *Coord. Chem. Rev.* **2021**, *429*, 213695.

(109) de Silva, A. P.; Gunaratne, H. Q. N.; McCoy, C. P. A Molecular Photoionic AND Gate Based on Fluorescent Signaling. *Nature* **1993**, *364*, 42-44.

(110) de Silva, A. P.; McClenaghan, N. D. Molecular-Scale Logic Gates. *Chem. Eur. J.* **2004**, *10*, 574-586.

(111) Ling, J.; Daly, B.; Silverson, V. A. D.; de Silva, A. P. Taking Baby Steps in Molecular Logic-Based Computation. *Chem. Commun.* **2015**, *51*, 8403-8409.

(112) de Silva, A. P. Molecular Logic Gate Arrays. *Chem. Asian J.* **2011**, *6*, 750-766.

(113) Conrad, M. Molecular Computing. *Adv. Comput.* **1990**, *31*, 235-324.

(114) Gentili, P. L. A Strategy to Face Complexity: The Development of Chemical Artificial Intelligence. In Advances in Artificial Life, Evolutionary Computation, and Systems Chemistry; Rossi, F., Piotto, S., Concilio, S. *Eds.; Springer: Cham, Switzerland; New York, NY, USA.* **2017**, *708*, 151-160.

(115) Szaciłowski, K. Digital Information Processing in Molecular Systems. *Chem. Rev.* **2008**, *108*, 3481-3548.

(116) Szaciłowski, K.; Wojciech, M.; Grażyna, S. Light-Driven OR and XOR Programmable Chemical Logic Gates. *J. Am. Chem. Soc.* **2006**, *128*, 4550-4551.

(117) Adamatzky, A.; Tegelaar, M.; Wosten, H. A.; Powell, A. L.; Beasley, A. E.; Mayne, R. On Boolean Gates in Fungal Colony. *Biosystems* **2020**, *193*, 104138.

(118) Adamatzky, A.; Jones, J.; Mayne, R.; Tsuda, S.; Whiting, J. Logical Gates and Circuits Implemented in Slime Mould. *Advances in Physarum Machines.* **2016**, 37-74.

(119) Shu, Q.; Birlenbach, L.; Schmittel, M. A Bis (Ferrocenyl) Phenanthroline Iridium(III) Complex as a Lab-on-a-Molecule For Cyanide and Fluoride in Aqueous Solution. *Inorg. Chem.* **2012**, *51*, 13123-13127.

(120) Schmittel, M.; Qinghai, S. A Lab-on-a-Molecule for Anions in Aqueous Solution: Using Kolbe Electrolysis and Radical Methylation at Iridium for Sensing. *Chem. Commun*. **2012**, *48*, 2707-2709.

(121) Gentili, P. L. Boolean and Fuzzy Logic Gates Based on the Interaction of Flindersine with Bovine Serum Albumin and Tryptophan. *J. Phys. Chem. A*. **2008**, *112,* 11992-11997.

(122) Gentili, P. L. The Fundamental Fuzzy Logic Operators and Some Complex Boolean Logic Circuits Implemented by the Chromogenism of a Spirooxazine. *Phys. Chem. Chem. Phys.* **2011**, *13*, 20335-20344.

(123) Gentili, P. L.; Giubila, M. S.; Heron, B. M. Processing Binary and Fuzzy Logic by Chaotic Time Series Generated by a Hydrodynamic Photochemical Oscillator. *Chem. Phys. Chem.* **2017**, *18*, 1831-1841.

(124) Mukherjee, S.; Sahoo, A.; Deb, S.; Baitalik, S. Light and Cation-Driven Optical Switch Based on a Stilbene-Appended Terpyridine System for the Design of Molecular-Scale Logic Devices. *J. Phys. Chem. A*. **2021**, *125*, 8261-8273.

(125) Mardanya, S.; Mondal, D.; Karmakar, S.; Baitalik, S. Smart Ruthenium and Osmium Complexes Mimic the Complicated Functions of Traffic Signal and Memory Device. *Sens. Actuators B: Chem.* **2017**, *239*, 635-641.

(126) Pyne, A.; Layek, S.; Patra, A.; Sarkar, N. An Easy and Smart Way to Explore the Light-Emitting Responses of Carbon Dot and Doxorubicin Hydrochloride Assembly: White Light Generation and pH-Dependent Reversible Photoswitching. *J. Mater. Chem. C* **2019**, *7*, 6414-6425.

(127) Strack, G.; Ornatska, M.; Pita, M.; Katz, E. Biocomputing Security System: Concatenated Enzyme-Based Logic Gates Operating as a Biomolecular Keypad Lock. *J. Am. Chem. Soc.* **2008**, *130*, 4234-4235.

(128) Sauvage, J.-P.; Collin, J. P. J.; Chambron, C.; Guillerez, S.; Coudret, C.; Balzani, V.; Barigelletti, F.; de Cola, L.; Flamigni, L. Ruthenium(II) and Osmium(II) Bis(Terpyridine) Complexes in Covalently-Linked Multicomponent Systems: Synthesis, Electrochemical Behavior, Absorption Spectra, and Photochemical and Photophysical Properties. *Chem. Rev*. **1994**, *94*, 993-1019.

(129) Steinke, S. J.; Gupta, S.; Piechota, E. J.; Moore, C. E.; Kodanko, J. J.; Turro, C. Photocytotoxicity and Photoinduced Phosphine Ligand Exchange in a Ru(II) Polypyridyl Complex. *Chem. Sci.* **2022**, *13*, 7, 1933-1945.

(130) Schanze, K. S.; Neyhart, G. A. *et al.* Excited-State Electron Transfer in Ligand-Bridged Dimeric Complexes of Osmium. *J. Phys. Chem.* **1986**, *90*, 2182-2193.

(131) Kober, E. M.; Caspar, J. V.; Lumpkin, R. S.; Meyer, T. J. Application of the Energy Gap Law o Excited-State Decay of Osmium (II)-Polypyridine Complexes: Calculation of Relative Nonradiative Decay Rates from Emission Spectral Profiles. *J. Phys. Chem*. **1986**, *90*, 3722-3734.

(132) Belser, P.; Dux, R. *et al.* Electronic Energy Transfer in a Supramolecular Species Containing the $[Ru(Bpy)_3]^{2+}$, $[Os(Bpy)_3]^{2+}$, and Anthracene Chromophoric Units. *Angew. Chem. Int. Ed. Engl.* **1995**, *34*, 595-598.

(133) Kober, E. M.; Sullivan, B. P. *et al.* Solvent Dependence of Metal-To-Ligand Charge-Transfer Transitions. Evidence for Initial Electron Localization in MLCT Excited States of 2,2'-Bipyridine Complexes of Ruthenium(II) and Osmium(II). *Inorg. Chem.* **1984**, *23*, 2098-2104.

(134) Wang, X.-Y.; Guerzo, A. D.; Tunuguntla, H.; Schmehl, R. H. Photophysical Behavior of Ru(II) and Os(II) Terpyridyl Phenylene Vinylene Complexes: Perturbation of MLCT State by Intra-Ligand Charge-Transfer State. *Res. Chem. Intermed.* **2007**, *33*, 63-77.

(135) Bhaumik, C.; Das, S.; Maity, D.; Baitalik, S. Luminescent Bis-Tridentate Ruthenium(II) and Osmium(II) Complexes Based on Terpyridyl-Imidazole Ligand: Synthesis, Structural Characterization, Photophysical, Electrochemical, and Solvent Dependence Studies. *Dalton Trans.* **2012**, *41*, 2427-2438.

(136) Campagna, S.; Puntoriero, F.; Nastasi, F.; Bergamini, G.; Balzani, V. Photochemistry and Photophysics of Coordination Compounds: Ruthenium. *Top. Curr. Chem.* **2007**, *280*, 117-214.

(137) Brown, D. G.; Sanguantrakun, N.; Schulze, B.; Schubert, U. S.; Berlinguette, C. P. Bis(tridentate) Ruthenium-Terpyridine Complexes Featuring Microsecond Excited-State Lifetimes. *J. Am. Chem. Soc.* **2012**, *134*, 12354-12357.

(138) Pal, P.; Mukherjee, S.; Maity, D.; Baitalik, S. Synthesis, Structural Characterization, and Luminescence Switching of Diarylethene-Conjugated Ru(II)-Terpyridine Complexes by Trans-Cis Photoisomerization: Experimental and DFT/TD-DFT Investigation. *Inorg. Chem.* **2018**, *57*, 5743-5753.

(139) Pal, P.; Ganguly, T.; Maity, D.; Baitalik, S. Experimental and Theoretical Exploration of Photophysics and Trans-Cis Photoisomerization of Styrylbenzene Conjugated Terpyridine Complexes of Ru(II): Strong Effect of Deprotonation from Second Coordination Sphere. *J. Photochem. Photobiol. A* **2020**, *392*, 112409.

(140) Wang, J.; Fang, Y. Q.; Hanan, G. S.; Loiseau, F.; Campagna, S. Synthesis and Properties of the Elusive Ruthenium(II) Complexes of 4′- cyano-2,2′:6′,2″-terpyridine. *Inorg. Chem.* **2005**, *44*, 5-7.

(141) Kübel, J.; Schroot, R.; Wachtler, M.; Schubert, U. S.; Dietzek, B.; Jager, M. Photoredox-Active Dyads Based on a Ru(II) Photosensitizer Equipped with Electron Donor or Acceptor Polymer Chains: A Spectroscopic Study of Light-Induced Processes Toward Efficient Charge Separation. *J. Phys. Chem. C* **2015**, *119*, 4742-4751.

(142) Maestri, M.; Armaroli, N.; Balzani, V.; Constable, E. C.; Thompson, A. M. W. C. Complexes of the Ruthenium(II)-2,2′:6′,2″- Terpyridine Family. Effect of Electron-Accepting and -Donating Substituents on the Photophysical and Electrochemical Properties. *Inorg. Chem.* **1995**, *34*, 2759-2767.

(143) Maity, D.; Bhaumik, C.; Mondal, D.; Baitalik, S. Ru(II) and Os(II) Complexes Based on Terpyridyl-Imidazole Ligand Rigidly Linked to Pyrene: Synthesis, Structure, Photophysics, Electrochemistry, and Anion-Sensing Studies. *Inorg. Chem.* **2013**, *52*, 13941-13955.

(144) Ganguly, T.; Pal, P.; Maity, D.; Baitalik, S. Synthesis, Characterization and Emission Switching Behaviors of Styrylphenyl-Conjugated Ru(II)-Terpyridine Complexes via Aggregation and Trans-Cis Photoisomerization. *J. Photochem. Photobiol. A* **2023**, *440*, 114662.

(145) Maity, D.; Das, S.; Mardanya, S.; Baitalik, S. Synthesis, Structural Characterization, and Photophysical, Spectroelectrochemical, and Anion-Sensing Studies of Heteroleptic Ruthenium(II) Complexes Derived from 4′-Polyaromatic-Substituted Terpyridine Derivatives and 2,6-Bis(benzimidazol-2-yl)pyridine. *Inorg. Chem.* **2013**, *52*, 6820-6838.

(146) Encinas, S.; Flamigni, L.; Barigelletti, F.; Constable, E. C.; Housecroft, C. E.; Schofield, E. R.; Figgemeier, E.; Fenske, D.; Neuburger, M. *et al.* Electronic Energy Transfer and Collection in Luminescent Molecular Rods Containing Ruthenium(II) and Osmium(II) 2,2′:6′,2″-Terpyridine Complexes Linked by Thiophene-2,5-diyl Spacers. *Chem. - Eur. J.* **2002**, *8*, 137-150.

(147) Dietrich, J.; Thorenz, U.; Förster, C.; Heinze, K. Effects of Sequence, Connectivity, and Counter Ions in New Amide-Linked Ru(tpy)$_2$-Re(bpy) Chromophores on Redox Chemistry and Photophysics. *Inorg. Chem.* **2013**, *52*, 1248-1264.

(148) Duati, M.; Tasca, S.; Lynch, F. C.; Bohlen, H.; Vos, J. G.; Stagni, S.; Ward, M. D. Enhancement of Luminescence Lifetimes of Mononuclear Ruthenium(II)-Terpyridine Complexes by Manipulation of the Sigma-Donor Strength of Ligands. *Inorg. Chem.* **2003**, *42*, 8377-8384.

(149) Abrahamsson, M.; Lundqvist, M. J.; Wolpher, H.; Johansson, O.; Eriksson, L.; Bergquist, J.; Rasmussen, T.; Becker, H.-C.; Hammarstro¨m, L.; Norrby, P.-O.; Åkermark, B.; Persson, P. Steric Influence on the Excited-State Lifetimes of Ruthenium Complexes with Bipyridyl-Alkanylene-Pyridyl Ligands. *Inorg. Chem.* **2008**, *47*, 3540-3548.

(150) Abrahamsson, M.; Jager, M.; Osterman, T.; Eriksson, L.; Persson, P.; Becker, H. C.; Johansson, O.; Hammarstro¨m, L. A 3.0 μs Room Temperature Excited State Lifetime of a Bistridentate RuII-Polypyridine Complex for Rod-like Molecular Arrays. *J. Am. Chem. Soc.* **2006**, *128*, 12616-12617.

(151) Abrahamsson, M.; Wolpher, H.; Johansson, O.; Larsson, J.; Kritikos, M.; Eriksson, L.; Norrby, P. O.; Bergquist, J.; Sun, L. C.; Åkermark, B.; Hammarstro¨m, L. A New Strategy for the Improvement of Photophysical Properties in Ruthenium(II) Polypyridyl Complexes. Synthesis and Photophysical and Electrochemical Characterization of Six Mononuclear Ruthenium(II) Bisterpyridine-Type Complexes. *Inorg. Chem.* **2005**, *44*, 3215-3225.

(152) Wolpher, H.; Johansson, O.; Abrahamsson, M.; Kritikos, M.; Sun, L. C.; Åkermark, B. A Tridentate Ligand for Preparation of Bisterpyridine-Like Ruthenium(II) Complexes with an Increased Excited State Lifetime. *Inorg. Chem. Commun.* **2004**, *7*, 337-340.

(153) Collin, J. P.; Beley, M.; Sauvage, J.-P.; Barigelletti, F. A Room Temperature Luminescent Cyclometallated Ruthenium(I1) Complex of 6-Phenyl-2,2'-Bipyridine. *Inorg. Chim. Acta* **1991**, *186*, 91-93.

(154) Rillema, D. P.; Allen, G.; Meyer, T. J.; Conrad, D. Redox Properties of Ruthenium(II) Trischelate Complexes Containing the Ligands 2,2'-Bipyrazine, 2,2'-Bipyridine, and 2,2'-Bipyrimidine. *Inorg. Chem.* **1983**, *22*, 1617-1622.

(155) Richter, M. M.; Brewer, K. J. Synthesis and Characterization of Osmium(II) Complexes Incorporating Polypyridyl Bridging Ligands. *Inorg. Chim. Acta* **1991**, *180*, 125-131.

(156) C. Bhaumik, D. Saha, S. Das, S. Baitalik, Synthesis, Structural Characterization, Photophysical, Electrochemical, and Anion-Sensing Studies of Luminescent Homo and Heteroleptic Ruthenium(II) and Osmium(II) Complexes Based on Terpyridylimidazole Ligand. *Inorg. Chem.* **2011**, *50*, 12586-12600.

(157) Langford, S. J.; Yann, T. Molecular Logic: A Half-Subtractor Based on Tetraphenylporphyrin. *J. Am. Chem. Soc*. **2003**, *125*, 11198-11199.

(158) Margulies, D.; Melman G.; Shanzer, A. A Molecular Full-Adder and Full-Subtractor, an Additional Step Toward a Moleculator. *J. Am. Chem. Soc.* **2006**, *128*, 4865-4871.

(159) Kaur, N.; Kumar, S. Aminoanthraquinone-Based Chemosensors: Colorimetric Molecular Logic Mimicking Molecular Trafficking and a Set-Reset Memorized Device. *Dalton Trans*. **2012**, *41*, 5217-5224.

(160) MacVittie, K.; Halamek, J.; Katz, E. Enzyme-Based D-Flip-Flop Memory System. *Chem. Commun*. **2012**, *48*, 11742-11744.

(161) Erbas-Cakmak, S.; Bozdemir, O. A.; Cakmak Y.; Akkaya, E. U. Proof of Principle for a Molecular 1 : 2 Demultiplexer to Function as an Autonomously Switching Theranostic Device. *Chem. Sci.* **2013**, *4*, 858-862.

(162) Xu, S.; Hao, Y.-X.; Sun, W.; Fang, C.-J.; Lu, X.; Li, M.-N.; Zhao, M.; Peng, S. Q.; Yan, C.-H. 2:1 Multiplexing Function in a Simple Molecular System. *Sensors* **2012**, *12*, 4421-4430.

(163) Abrahamsson, M.; Becker, H. C.; Hammarström, L. Microsecond ^{3}MLCT Excited State Lifetimes in Bis-Tridentate Ru(ii)-Complexes: Significant Reductions of Non-Radiative Rate Constants. *Dalton Trans.* **2017**, *46*, 13314.

(164) Yu, X.; Gao, F.; Zhao, W.; Lai, H.; Wei, L.; Yang, C.; Wu, W. BODIPY-Conjugated Bis-Terpyridine Ru(II) Complexes Showing Ultra-Long Luminescence Lifetimes and Applications to Triplet-Triplet Annihilation Upconversion. *Dalton Trans.* **2022**, *51*, 9314-9322.

(165) Lanquist, A. P.; Piechota, E. J.; Wickramasinghe, L. D.; Silva, A. M.; Thummel, R. P. Turro, C. New Tridentate Ligand Affords a Long-Lived ^{3}MLCT Excited State in a Ru(II) Complex: DNA Photocleavage and $^{1}O_2$ Production. *Inorg. Chem.* **2023**, *62*, 15927-15935.

(166) Breivogel, A.; Hempel, K.; Heinze, K. Dinuclear Bis(Terpyridine)Ruthenium(II) Complexes by Amide Coupling of Ruthenium Amino Acids: Synthesis and Properties. *Inorg. Chim. Acta* **2011**, *374*, 152-162.

(167) Kreitner, C.; Grabolle, M.; Resch-Genger, U.; Heinze K. Dual Emission and Excited-State Mixed-Valence in a Quasi-Symmetric Dinuclear Ru-Ru Complex. *Inorg. Chem.* **2014**, *53*, 12947-12961.

(168) Benniston, A. C.; Grosshenny, V.; Harriman, A.; Ziessel, R. Electron Delocalization in Ethynyl-Bridged Binuclear Ruthenium(II) Polypyridine Complexes. *Angew. Chem. Int. Ed. Engl.* **1994**, *33* (18), 1884-1885.

(169) Grosshenny, V.; Harriman, A.; Ziessel, R. Electronic Energy Transfer across Ethynyl-Bridged Ru^{II}/Os^{II} Terpyridyl Complexes. *Angew. Chem. Int. Ed. Engl.* **1995**, *34* (10), 1100-1102.

(170) Vogler, L. M.; Brewer, K. J. Building Block Approach to the Construction of Long-Lived Osmium(II) and Ruthenium(II) Multimetallic Complexes Incorporating the Tridentate Bridging Ligand 2,3,5,6-Tetrakis(2-pyridyl)pyrazine. *Inorg. Chem.* **1996**, *35*, 818-824.

(171) El-ghayoury, A.; Harriman, A.; Khatyr, A.; Ziessel, R. Intramolecular Triplet Energy Transfer in Metal Polypyridine Complexes Bearing Ethynylated Aromatic Groups. *J. Phys. Chem. A* **2000**, *104*, 1512-1523.

(172) Mondal, D.; Biswas, S.; Paul, A.; Baitalik, S. Luminescent Dinuclear Ruthenium Terpyridine Complexes with a Bis-Phenylbenzimidazole Spacer. *Inorg. Chem.* **2017**, *56*, 7624-7641.

(173) Karmakar, S.; Maity, D.; Mardanya, S.; Baitalik S. Multichromophoric Bimetallic Ru(II) Terpyridine Complexes Based on Pyrenyl-bis-phenylimidazole Spacer: Synthesis, Photophysics, Spectroelectrochemistry, and TD-DFT Calculations. *Inorg. Chem.* **2014**, *53*, 12036-12049.

(174) Karmakar, S.; Maity, D.; Mardanya S.; Baitalik, S. Pyrene and Imidazole Functionalized Luminescent Bimetallic Ru(II) Terpyridine Complexes as Efficient Optical Chemosensors for Cyanide in Aqueous, Organic and Solid Media. *Dalton Trans.* **2015**, *44*, 18607-18623.

(175) Bar, M.; Maity, D.; Das S.; Baitalik, S. Demonstration of Intramolecular Energy Transfer in Asymmetric Bimetallic Ruthenium(II) Complexes. *Dalton Trans.* **2016**, *45*, 17241-17253.

(176) Barigelletti, F.; Flamigni, L.; Guardigli, M.; Juris, A.; Beley, M.; Chodorowski-Kimmes, S.; Collin, J.-P.; Sauvage, J.-P. Energy Transfer in Rigid Ru(II)/Os(II) Dinuclear Complexes with Biscyclometalating Bridging Ligands Containing a Variable Number of Phenylene Units. *Inorg. Chem.* **1996**, *35*, 136-142.

(177) Beley, M.; Collin, J.-P.; Sauvege, J.-P. Highly Coupled Mixed-Valence Dinuclear Ruthenium and Osmium Complexes with a Bis-Cyclometalating Terpyridine Analogue as Bridging Ligand. *Inorg. Chem.* **1993**, *32*, 4539-4543.

(178) Barigelletti, F.; Ventura, B.; Collin, J.-P.; Kayhanian, R.; Gavin˜a, P.; Sauvage, J.-P. Electrochemical and Spectroscopic Properties of Cyclometallated and Non-Cyclometallated Ruthenium(II) Complexes Containing Sterically Hindering Ligands of the Phenanthroline and Terpyridine Families. *Eur. J. Inorg. Chem.* **2000**, 113-119.

(179) Baranoff, E.; Jung, I.; Scopelliti, R.; Solari, E.; Grätzel, M.; Nazeeruddin, M. K. Room-Temperature Combinatorial Screening of Cyclometallated Iridium(III) Complexes for a Step Towards Molecular Control of Colour Purity. *Dalton Trans.* **2011**, *40*, 6860-6867.

(180) Meier, S. B.; Sarfert, W.; Junquera-Hernández, J. M.; Delgado M.; Tordera, D.; Ortí, E.; Bolink, H. J.; Kessler, F.; Scopelliti, R., et al. A Deep-Blue Emitting Charged Bis-Cyclometallated Iridium(III) Complex for Light-Emitting Electrochemical Cells. *J. Mater. Chem. C* **2013**, *1*, 58-68.

(181) O'Regan, B.; Grätzel, M. A Low-Cost, High-Efficiency Solar-Cell Based on Dye-Sensitized Colloidal TiO_2 Films. *Nature* **1991**, *353*, 737-740.

(182) Nazeeruddin, M. K.; Baranoff, E.; Grätzel, M. Dye-Sensitized Solar Cells: A Brief Overview. *Solar Energy* **2011**, *85*, 1172-1178.

(183) Wadman, S. H.; Kroon, J. M.; Bakker, K.; Lutz, M.; Spek, A. L.; van Klink, G. P. M.; van Koten, G. Cyclometalated Ruthenium Complexes for Sensitizing Nanocrystalline TiO_2 Solar Cells. *Chem. Commun.* **2007**, 1907-1909.

(184) Koivisto, B. D.; Robson, K. C. D.; Berlinguette, C. P. Systematic Manipulation of the Light-Harvesting Properties for Tridentate Cyclometalated Ruthenium(II) Complexes. *Inorg. Chem.* **2009**, *48*, 9644-9652.

(185) Robson, K. C. D.; Bomben, P. G.; Berlinguette, C. P. Cycloruthenated Sensitizers: Improving the Dye-Sensitized Solar Cell with Classical Inorganic Chemistry Principles. *Dalton Trans.* **2012**, *41*, 7814-7829.

(186) Wu, S.-H.; Burkhardt, S. E.; Zhong, Y.-W.; Abruña, H. D. Cyclometalated Ruthenium Oligomers with 2,3-Di(2-pyridyl)-5,6- diphenylpyrazine: A Combined Experimental, Computational, and Comparison Study with Noncyclometalated Analogous. *Inorg. Chem.* **2012**, *51*, 13312-13320.

(187) Zhong, Y.-W.; Wu, S.-H.; Burkhardt, S. E.; Yao, C.-J.; Abruña, H. D. Mononuclear and Dinuclear Ruthenium Complexes of 2,3-Di-2-pyridyl-5,6-diphenylpyrazine: Synthesis and Spectroscopic and Electrochemical Studies. *Inorg. Chem.* **2011**, *50*, 517-524.

(188) Yao, C.-J.; Zhong, Y.-W.; Nie, H.-J.; Abruña, H. D.; Yao, J. Near-IR Electrochromism in Electropolymerized Films of a Biscyclometalated Ruthenium Complex Bridged by 1,2,4,5-Tetra(2-pyridyl)benzene. *J. Am. Chem. Soc.* **2011**, *133*, 20720-20723.

(189) Kreitner, C.; Mengel, A. K. C.; Lee, T. K.; Cho, W.; Char, K.; Kang, Y. S.; Heinze, K. Strongly Coupled Cyclometalated Ruthenium Triarylamine Chromophores as Sensitizers for DSSCs. *Chem. Eur. J.* **2016**, *22*, 8915-8928.

(190) Beley, M.; Chodorowski, S.; Collin, J.-P.; Sauvage, J.-P.; Flamigni, L.; Barigelletti, F. Luminescent Dinuclear Complexes Containing Ruthenium(II)- and Osmium(II)-Terpyridine-type Chromophores Bridged by a Rigid Biscyclometalating Ligand. *Inorg. Chem.* **1994**, *33*, 2543-2547.

(191) Collin, J.-P. Kayhanian, R.; Sauvage, J.-P.; Calogero, G.; Barigelletti, F.; De Cianc, A.; Fischer, J. A Cyclometallated Ruthenium(ii) Complex with a Sterically Hindered Ligand Displaying a Long-Lived MLCT Excited State. *Chem. Commun.* **1997**, 775-776.

(192) Wang, H.; Shao, J.-Y.; Duan, R.; Wang, K.-Z.; Zhong, Y.-W. Synthesis and Electronic Coupling Studies of Cyclometalated Diruthenium Complexes Bridged By 3,3',5,5'-Tetrakis(Benzimidazol-2-Yl)-Biphenyl. *Dalton Trans.* **2021**, *50*, 4219-4230.

(193) Kreitner, C.; Heinze, K. The Photochemistry of Mono- and Dinuclear Cyclometalated Bis(Tridentate)Ruthenium(II) Complexes: Dual Excited State Deactivation and Dual Emission. *Dalton Trans.* **2016**, *45*, 5640-5658.

(194) Maity, D.; Bhaumik, C.; Karmakar, S; Baitalik, S. Photoinduced Electron and Energy Transfer and pH-Induced Modulation of the Photophysical Properties in Homo- and Heterobimetallic Complexes of Ruthenium (II) and Rhodium (III)

Based on a Heteroditopic Phenanthroline-Terpyridine Bridge. *Inorg. Chem.* **2013**, *52*, 7933-7946.

(195) Bissell, R. A.; Córdova, E.; Kaifer, A. E.; Stoddart, J. F. A Chemically and Electrochemically Switchable Molecular Shuttle. *Nature* **1994**, *369*, 133-137.

(196) Crowley, J. D.; Leigh, D. A.; Lusby, P. J.; McBurney, R. T.; Perret-Aebi, L. E.; Petzold, C.; Slawin, A. M. Z.; Symes, M. D. A Switchable Palladium-Complexed Molecular Shuttle and its Metastable Positional Isomers. *J. Am. Chem. Soc.* **2007**, *129*, 15085-15090.

(197) MacDonald, T. S. C.; Schmidt, T. W.; Beves, J. E. An All-Photonic Molecular Amplifier and Binary Flip-Flop. J. *Phys. Chem. Lett*. **2021**, *12*, 1236-1243.

(198) Ishizuka, T.; Tobita, K.; Yano, Y.; Shiota, Y.; Yoshizawa, K.; Fukuzumi, S.; Kojima, T. Proton-Coupled Electron Shuttling in a Covalently Linked Ruthenium-Copper Heterodinuclear Complex. *J. Am. Chem. Soc.* **2011**, *133*, 18570-18573.

(199) Gan, Q.; Ferrand, Y.; Bao, C.; Kauffmann, B.; Grélard, A.; Jiang, H.; Huc, I. Helix-Rod Host-Guest Complexes with Shuttling Rates Much Faster than Disassembly. *Science* **2011**, *331*, 1172-1175.

(200) Yam, V. W. W.; Lau, V. C. Y.; Wu, L. X. Synthesis, Photophysical, Photochemical and Electrochemical Properties of Rhenium(I) Diimine Complexes with Photoisomerizable Pyridyl-Azo, -Ethenyl or -Ethyl Ligands. *J. Chem. Soc*. *Dalton Trans*. **1998**, 1461-1468.

(201) Yam, V. W. W.; Yang, Y.; Zhang, J.; Chu, B. W.-K.; Zhu, N. Synthesis, Characterization, and Photoisomerization Studies of Azo- and Stilbene-Containing Surfactant Rhenium(I) Complexes. *Organometallics* **2001**, *20,* 4911-4918.

(202) Wrighton, M. S.; Morse, D. L.; Pdungsap, L. Intraligand Lowest Excited States in Tricarbonylhalobis(Styrylpyridine)Rhenium(I) Complexes. *J. Am. Chem. Soc.* **1975**, 97, *125*, 2073-2079.

(203) Wenger, O. S.; Henling, L. M.; Day, M. W.; Winkler, J. R.; Gray, H. B. Photoswitchable Luminescence of Rhenium(I) Tricarbonyl Diimines. *Inorg. Chem.* **2004**, *43*, 2043-2048.

(204) Amaral, R. C.; Iha, N. Y. M. Molecular Engineered Rhenium(I) Carbonyl Complexes to Promote Photoisomerization of Coordinated Stilbene-Like Ligands in the Visible Region. *Dalton Trans.* **2018**, *47*, 13081-13087.

(205) Amaral, R. C.; Matos, L. S.; Zanoni, K. P. S.; Iha, N. Y. M. Photoreversible Molecular Motion of StpyCN Coordinated to Fac-$[Re(CO)_3(NN)]^+$ Complexes. *J. Phys. Chem. A* **2018**, 122, 6071-6080.

(206) Faustino, L. A.; Machado, A. E. H.; Patrocinio, A. O. T. Photochemistry of *fac*-$[Re(CO)_3(dcbH_2)(trans\text{-stpy})]^+$: New Insights on the Isomerization Mechanism of Coordinated Stilbene-Like Ligands. *Inorg. Chem.* **2018**, *57*, 2933-2941.

(207) Sakamoto, R.; Murata, M.; Kume, S.; Sampei, H.; Sugimoto, M. Nishihara, H. Photo-Controllable Tristability of a Dithiolato-Bipyridine-Pt(II) Complex Molecule Containing Two Azobenzene Moieties. *Chem. Commun.* **2005**, 1215-1217.

(208) Lin, J.-L.; Chen, C.-W.; Sun, S.-S.; Lees, A. J. Photoswitching Tetranuclear Rhenium(I) Tricarbonyl Diimine Complexes with a Stilbene-Like Bridging Ligand. *Chem. Commun.* **2011**, *47*, 6030-6032.

(209) Lewis, J. D.; Perutz, R. N.; Moore, J. N. Proton-Controlled Photoisomerization: Rhenium(I) Tricarbonyl Bipyridine Linked to Amine or Azacrown Ether Groups by a Styryl Pyridine Bridging Ligand. *Chem. Commun.* **2000**, 1865-1866.

(210) Pérez-Miqueo, J.; Telleria, A.; Muñoz-Olasagasti, M.; Altube, A.; García-Lecina, E.; de Cózarc, A.; Freixa, Z. Azobenzene-Functionalized Iridium(III) Triscyclometalated Complexes. *Dalton Trans.* **2015**, *44*, 2075-2091.

(211) Pal, P.; Ganguly, T.; Sahoo, A.; Baitalik, S. Emission Switching in the Near-Infrared by Reversible Trans-Cis Photoisomerization of Styrylbenzene-Conjugated Osmium Terpyridine Complexes. *Inorg. Chem.* **2021**, *60*, 4869-4882.

(212) Mukherjee, S., Pal, P.; Maity, D.; Baitalik, S. Photophysics and Luminescence Switching Properties of a Series of Photochromic Styrylbenzene-Terpyridine Conjugate: Experimental and DFT/TD-DFT Investigation. *J Photochem. Photobiol. A* **2019**, *378*, 94-104.

(213) Mukherjee, S.; Pal, P.; Sahoo, A.; Baitalik, S. Photo-Switchable Iron-Terpyridine Complexes Functionalized with Styrylbenzene Unit. *J Photochem. Photobiol. A* **2021**, *407*, 113059.

(214) Ganguly, T.; Abedin, T.; Maity, D.; Baitalik, S. Remarkable Increase in the Rate of Trans-Cis Photoisomerization of Os(II)-Terpyridine Complexes via Oxidation and Reduction. *Inorg. Chem.* **2025**, *64*, 4415-4430.

(215) Ganguly, T.; Das, S.; Maity, D.; Baitalik, S. Luminescent Ruthenium-Terpyridine Complexes Coupled with Stilbene-Appended Naphthalene, Anthracene, and Pyrene

Motifs Demonstrate Fluoride Ion Sensing and Reversible Trans-Cis Photoisomerization. *Inorg. Chem.* **2024**, *63*, 6883-6897.

(216) Liu, Y.; Li, M.; Zhao, Q.; Wu, H.; Huang, K.; Li, F. Phosphorescent Iridium(III) Complex with an N^O Ligand as a Hg^{2+}-Selective Chemodosimeter and Logic Gate. *Inorg. Chem.* **2011**, *50*, 5969-5977.

(217) Biancardo, M.; Bignozzi, C.; Doyle, H.; Gareth, R. A Potential and Ion Switched Molecular Photonic Logic Gate. *Chem. Commun.* **2005**, 3918-3920.

(218) Kumar, A.; Chhatwal, M.; Gupta, R. D.; Awasthi, S. K. Chemically-Driven "Molecular Logic Circuit" Based on Osmium Chromophore with a Resettable Multiple Readout. *RSC Adv.* **2015**, *5*, 5217-5220.

(219) Cui, B.-B.; Tang, J.-H.; Yao, J.; Zhong, Y.-W. A Molecular Platform for Multistate Near-Infrared Electrochromism and Flip-Flop, Flip-Flap-Flop, and Ternary Memory. *Angew. Chem.* **2015**, *127*, 9324-9329.

(220) Schmittel, M.; Mal, P.; de los Rios, A. Multiport Logic Operations Triggered by Protonation—A Trisphenanthroline as a 3-Input AND-NOR-OR Circuit. *Chem. Commun.* **2010**, *46*, 2031-2033.

(221) Mondal, D.; Bar, M.; Maity, D.; Baitalik, S. Anthraimidazoledione-Terpyridine-Based Optical Chemosensor for Anions and Cations That Works as Molecular Half-Subtractor, KeyPad Lock, and Memory Device. *J. Phys. Chem. C* **2015**, *119*, 25429-25441.

Chapter 2

Influences of Both N,N,N- and N,N,C-Coordination Modes of Tolyl-Terpyridine on the Photophysical Properties of Cyclometalated Ru(II) Complexes: Combined Experimental and Theoretical Investigations on Acid/Base Dependent Reversible Cyclometalation

2.1. Introduction

Ru(II) complexes derived from polypyridyl ligands are frequently used as model systems for their fruitful utilizations in diverse field of applications such as photosensitizers, functional constituents in molecular-level machines, optoelectronics, dye sensitized solar cells (DSSCs) and sensors.[1-8] Both the ground and excited state behavior of the complex arrays could be regulated upon judicious choice of the chelating ligands.[9-11] Consequently, wide varieties of ligands have been rationally designed to fine tune the structural features and electronic aspects of the resulting Ru(II) complexes.[10-14] $[Ru(bpy)_3]^{2+}$ (bpy =2,2′-bipyridine) and its derivatives have shown remarkable utility to this end because of their good redox stability in both the ground and excited states, a broad and tunable metal-to-ligand charge-transfer (MLCT) band in the visible domain and enhanced excited-state lifetime (τ = 860 ns) for $[Ru(bpy)_3](PF_6)_2$ in MeCN) and quantum yields (Φ = 0.062).[15,16] This sort of emission characteristics primarily originates from lowest-lying ^{3}MLCT states that are energetically well-separated from the deactivating triplet metal-centered (^{3}MC) excited states. The related bis(tridentate) complex, $[Ru(tpy)_2]^{2+}$ (tpy = 2,2':6',2''-terpyridine), possess many similar properties to that of $[Ru(bpy)_3]^{2+}$ but the acute bite angle of the terpyridines allow the ^{3}MC states to be thermally accessible which in turn drastically affect their emission characteristics together with the lifetimes (e.g., τ = 0.25 ns for $[Ru(tpy)_2](PF_6)_2$).[17,18] This observation is very frustrating as the inherent C_2 symmetry in $[Ru(tpy)_2]^{2+}$ can afford isomer-free functionalization of the complexes upon substitution at the 4-position of the tpy ligand so that vectorial transport of either electron or energy could be feasible.[18,19]

These observations motivate us to design Ru(II) complexes with bis-tridentate skeletons having long-lived excited-states and we already synthesized a wide variety of luminescent Ru(II)-bis tridentate complexes with long excited state lifetimes during last few years.[20-27] Several methodologies have been adopted to enhance the energy barrier between emissive ^{3}MLCT and quenching ^{3}MC states through proper derivatization of the tpy moiety by electron-withdrawing/donating species,[28-33] coplanar aromatic motifs[23,26,34-36] or organic chromophores having the energy of ^{3}LC level comparable to those of the ^{3}MLCT states.[11] Computational investigations based on density functional theory (DFT) suggest that for the prototypical polypyridyl-based complexes, the highest occupied molecular orbitals (HOMOs) lie mostly on the Ru d orbitals, while ligand part constitutes the lowest unoccupied molecular orbitals (LUMOs).[37,38] Additionally, due to their large

energy gap between HOMO and LUMO the subsequent absorption spectral profile leaves out an intrinsic part of the solar spectrum in the red region.

Another effective approach for the design of emissive Ru(II)-terpyridines is to destabilize the ^{3}MC level and enhance the donating capacity of the ligand through the use of carbanionic aromatic units (cyclometalating ligands).[31,39-43] The prototypical N-N-N coordination of the terpyridine ligands to the metal ion can be replaced with N-N-C/N-C-N type binding patterns to form cyclometalated complexes wherein carbon atoms replace one or more nitrogen donors for the betterment of the photo-redox characteristics of the resulting bis-tridentate arrays.[44-47] This protocol has permitted the accomplishment of Ru complexes in DSSCs towards achieving high conversion efficiency and enhanced chemical properties as demonstrated by the research groups of Gratzel,[48-51] van Koten,[52-55] Berlinguette,[56-59] and others.[60-67] The incorporation of Ru-C yields lower $Ru^{II/III}$ potentials and considerably red-shifted absorption and emission bands relative to the $[Ru(tpy)_2]^{2+}$ derivatives. Apart from their major interest in DSSCs, and near-infrared electrochromism, the cyclometalated Ru(II) complexes are believed to be potential candidates in photochemotherapy because of their increased lipophilicity and cellular uptake arising out of their lower charges.[68,69]

4'-(p-Methylphenyl)-2,2':6',2"-terpyridine ligand (tpy-$PhCH_3$) has been extensively employed by several research groups for the synthesis of linear achiral rod-like architectures with several transition metal ions.[18,70-73] During the synthesis of the aforementioned ligand, a positional isomer, viz. 6'-tolyl-2,2':4"-terpyridine, is also obtained as the minor product. Although the said isomeric form of tpy-$PhCH_3$ was previously reported,[74] there is no report till date, wherein the isomeric minor product was utilized for the synthesis of cyclometalated Ru(II) complexes via NNC coordination mode. To this end, with the goal of developing a new strategy to prepare luminescent Ru(II) complexes, we designed herein a new set of heteroleptic bis-tridentate complexes of the type, [(py-bpy-Ph-X)Ru(tpy-$PhCH_3$)]ClO_4 (X= CH_3, CH_2Br, and CHO) incorporating both non-cyclometalated tpy-$PhCH_3$ (NNN) and cyclometalated py-bpy-Ph-X (NNC) coordination motifs by using the two isomeric forms of tpy-$PhCH_3$ (Chart 2.1). To fine tune the photophysical and electrochemical properties, we substituted the -CH_3 group by -CH_2Br, and -CHO motifs. The electronic asymmetry around the central Ru(II) center together with higher field strength induced by cyclometalating ligand inhibits non-radiative decay channels by increasing the energy gap between the ^{3}MLCT and ^{3}MC states which in turn brings about a new class of luminescent complexes with relatively longer excited-state

lifetimes.[31,39,41,42] To the best of our knowledge, no documentation of luminescent cyclometalated complexes using 6'-tolyl-2,2':4''-terpyridine and Ru(II) is available in the literature. The absorption spectral window for the cyclometalated complexes increases substantially towards red-region with respect to their analogous $[Ru(tpy)_2]^{2+}$ type complexes and also emit in the NIR domain. The outer coordination sphere of the complexes also possesses non-coordinated nitrogen atom in the cyclometalated site and taking advantage of which fine modulation of the spectral properties could be feasible by acid-base equilibria. Thus, the present work reports the synthesis, structural characterization and thorough investigation of acid/base-induced modification of the photophysical characteristics of the complexes. In addition to experimental demonstration, computational investigations of the complexes have been performed by density functional theory (DFT) and time-dependent (TD-DFT) to elucidate both the electronic structure as well as appropriate band assignment of the complexes.

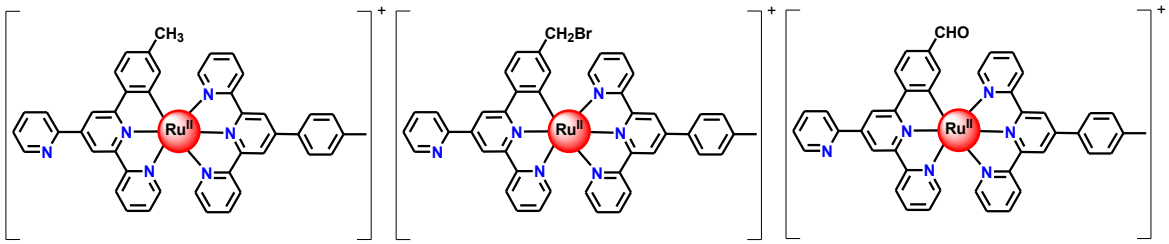

[(py-bpy-Ph-CH_3)Ru(tpy-PhCH_3)]ClO_4 (**1**) [(py-bpy-Ph-CH_2Br)Ru(tpy-PhCH_3)]ClO_4 (**2**) [(py-bpy-Ph-CHO)Ru(tpy-PhCH_3)]ClO_4 (**3**)

Chart 2.1. Molecular structures of the complexes (**1-3**) under present investigation.

2.2. Experimental Section

2.2.1. Materials. Reagent grade chemicals were purchased from Merck. Solvents and other chemicals were purchased from local vendors. 4'-(p-Methylphenyl)-2,2':6',2''-terpyridine (tpy-PhCH_3) was synthesized according to the literature procedures.[75] [Ru(tpy-PhCH_3)Cl_3] was prepared by the reaction of $RuCl_3.3H_2O$ with tpy-PhCH_3 in 1:1 molar ratio in refluxing ethanol.

2.2.2. Synthesis of the Ligands. The synthetic procedures of 6'-tolyl-2,2':4''-terpyridine {py-bpy-Ph-CH_3 (L1)}, 6'-bromomethylphenyl-2,2':4''-terpyridine {py-bpy-Ph-CH_2Br (L2)} and 6'-formyl-2,2':4''-terpyridine {py-bpy-Ph-CHO (L3)} ligands are provided below.

6'-Tolyl-2,2':4',2''-terpyridine (L1). A mixture of 2-acetyl-pyridine (12.5 g, 0.10 mol), p-tolualdehyde (6.2 g, 0.05 mol), acetamide (92.0 g, 1.6 mol), and ammonium acetate (59.0 g, 0.76 mol) was stirred under reflux for 2 h. The reaction mixture was cooled to 120˚C; then a solution of NaOH (10 g) in water (100 mL) was added, and refluxing was continued for a further 2 h. At room temperature, the black, rubber-like solid that formed was filtered off and washed with water and then with ethanol. The raw product was then recrystallized from ethanol. The needles thus obtained (6.0 g) were dissolved in an ethanol-dichloromethane mixture (1:1, 200 mL), and upon addition of an ethanolic solution of ferrous perchlorate (2.72 g in 50 mL) a violet crystalline compound was deposited. The filtrate was collected and dried in rotary evaporator. The solid compound was purified through column chromatography by eluting with a mixture of ethyl acetate and petroleum ether (1:9, v/v). The solution was again dried in rotary evaporator. Finally, the solid compound was recrystallized from methanol. Yield: 0.5 g (3%). Anal. Calcd for $C_{22}H_{17}N_3$: C, 81.70; H, 5.29; N, 12.99. Found: C, 81.75; H, 5.26; N, 12.97. ^{1}H NMR (400 MHz, DMSO-d_6): δ/ppm 9.04 (s, 1H, $1H_{3''}$), 8.80 (d, 1H, J=4 Hz, $1H_3$), 8.75 (d, 1H, J=4 Hz, $1H_{3'}$), 8.61 (d, 1H, J=8 Hz, $1H_{6'}$), 8.56 (s, 1H, $1H_{3'''}$), 8.31 (d, 1H, J=8 Hz, $1H_6$), 8.23 (d, 2H, J=8 Hz, $2H_7$), 8.02-7.98 (m, 2H, $1H_4$+$1H_{4'}$), 7.53-7.48 (m, 2H, $1H_5$+$1H_{5'}$), 7.35 (d, 2H, J=8 Hz, $2H_8$), 2.38 (s, 3H, -CH_3). Electrospray ionization mass spectrometry (ESI-MS) (positive, MeCN) *m/z*: 324.12 (100%) [**L1**+H]$^+$

6'-Bromomethylphenyl-2,2':4',2''-terpyridine (L2). A mixture of 6'-tolyl-2,2':4',2" terpyridine (**L1**) (1.00 g, 3.09 mmol), N-bromosuccinamide (0.56 g, 3.09 mmol), and benzoyl peroxide (0.025 g, 0.10 mmol) in CCl_4 (20 mL) was heated at reflux for 5 h under N_2 protection and then cooled down to room temperature. The solid that formed was filtered and washed with CCl_4 (20 mL). The filtrate along with the washings was rotary evaporated, and the solid residue obtained was recrystallized from ethanol-acetone (3:1, v/v) mixture. The resulting solid was collected and washed with cold ethanol. Yield: 0.52 g (42%). Anal. Calcd for $C_{22}H_{16}N_3Br$: C, 65.68; H, 4.01; N, 10.44; Br, 19.86. Found: C, 65.64; H, 4.03; N, 10.47. ^{1}H NMR (400 MHz, DMSO-d_6): δ/ppm 9.04 (s, 1H, $1H_{3''}$), 8.82 (d, 2H, J=4 Hz, $1H_3$+$1H_{3'}$), 8.73 (d, 1H, J=8 Hz, $1H_{6'}$), 8.66 (s, 1H, $1H_{3'''}$), 8.40-8.35 (m, 3H, $2H_7$+$1H_6$), 8.09-8.04 (m, 2H, $1H_4$+$1H_{4'}$),7.70-7.63 (m, 3H, $2H_8$+$1H_5$), 7.58-7.55 (t, 1H, J=12 Hz, $1H_{5'}$), 4.82 (s, 2H, -CH_2Br). Electrospray ionization mass spectrometry (ESI-MS) (positive, MeCN) *m/z*: 403.34 (30%) [**L2**+H]$^+$, 322.10 (100%) [**L2**-Br]$^+$.

6'-Formyl-2,2':4',2''-terpyridine (L3). A mixture of 6'-Tolyl-2,2':4',2''-terpyridine (**L1**) (1.00 g, 3.09 mmol), N-bromosuccinamide (1.23 g, 6.18 mmol), and benzoyl peroxide (0.049 g, 0.20 mmol) in CCl_4 (20 mL) was heated at reflux for 24 h under N_2 protection. After removal of CCl_4, the residue obtained was recrystallized by dissolving it in 50 mL of an ethanol-acetone (3:1) mixture. The solid was collected and washed with cold ethanol. This obtained product is 6'-Dibromomethylphenyl-2,2':4',2''-terpyridine. A suspension of 6'-dibromomethylphenyl-2,2':4',2''-terpyridine (0.45 g, 0.93 mmol) and $CaCO_3$ (1.00 g, 10 mmol) in a mixture of 1,4-dioxane-water (4:1, 50 mL) was heated at reflux for 30 h. The resulting mixture was then filtered. The filtrate was extracted with CH_2Cl_2 (2×50 mL). The extracts were combined and washed successively with a 0.1 M aqueous EDTA solution (50 mL), 0.1 M aqueous HCl (50 mL), and then with water (2×50 mL) and kept over anhydrous sodium sulfate. The resulting solution was dried on a rotary evaporator. The product was recrystallized from DCM-hexane mixture and finally washed with hexane. Yield: 0.25 g (80%). Anal. Calcd for $C_{22}H_{15}N_3O$: C, 78.32; H, 4.48; N, 12.45; O, 4.74. Found: C, 78.35; H, 4.52; N, 12.47. ^{1}H NMR (400 MHz, DMSO-d_6): δ/ppm 10.13 (s, 1H, -CHO), 9.16 (s, 1H, $1H_{3''}$), 8.82 (d, 1H, J=4 Hz, $1H_3$), 8.77 (d, 1H, J=4 Hz, $1H_{3'}$), 8.75 (s, 1H, $1H_{3'''}$), 8.65 (d, 1H, J=8 Hz, $1H_{6'}$), 8.60 (d, 2H, J=8 Hz, $2H_7$), 8.40 (d, 1H, J=8 Hz, $1H_6$), 8.11 (d, 2H, J=8 Hz, $2H_8$), 8.04 (t, 2H, J=12 Hz, $1H_4$+$1H_{4'}$), 7.57-7.52 (m, 2H, $1H_5$+$1H_{5'}$). Electrospray ionization mass spectrometry (ESI-MS) (positive, MeCN) *m/z*: 338.08 (100%) [**L3**+H]$^+$.

2.2.3. Synthesis of the Metal Complexes. The metal complexes were prepared by adopting a common synthetic protocol described below.

[(py-(bpy-Ph-CH_3))Ru(tpy-$PhCH_3$)](ClO_4)·H_2O (1). A mixture of Ru(tpy-$PhCH_3$)Cl_3 (75 mg, 0.14 mmol) and $AgBF_4$ (92 mg, 0.47 mmol) in 30 mL of Me_2CO was refluxed with continuous stirring for 2h. After cooling down to room temperature, the precipitated AgCl was removed by filtration. 30 mL of 1-butanol was then added to the filtrate and residual Me_2CO was removed by rotary evaporation. To the resulting solution was added finely powdered **L1** (49 mg, 0.15 mmol) and the mixture was refluxed under basic condition for 6h with continuous stirring. After cooling, the solution was poured into aqueous solution of $NaClO_4·H_2O$ (1.5 g in 5 mL of water) when a violet-colored precipitate appeared. The compound was filtered and purified by silica gel column chromatography using MeCN as the eluent. Upon rotary evaporation of the eluent to a small volume (~10 mL), a microcrystalline complex was formed, which was filtered and recrystallized from

MeCN-MeOH (1:5, v/v) mixture. Yield: 79 mg (62%). Anal. Calcd for $C_{44}H_{35}N_6RuClO_5$: C, 61.14; H, 4.08; N, 9.72. Found: C, 61.11; H, 4.05; N, 9.75. ^{1}H NMR (400 MHz, DMSO-d_6): δ/ppm 9.24 (s, 2H, 2H$_{3'}$), 9.22 (s, 1H, 1H$_{3''}$), 8.95 (s, 1H, 1H$_{3'''}$), 8.92-8.87 (m, 4H, 2H$_6$+1H$_{12}$+1H$_{12'}$), 8.61 (d, 1H, *J*=8 Hz, 1H$_{9'}$), 8.28 (d, 2H, *J*=8 Hz, 2H$_7$), 8.12 (t, 1H, *J*=7.5 Hz, 1H$_{11'}$), 7.95-7.90 (m, 2H, 1H$_{10'}$+1H$_{14}$), 7.83 (t, 2H, *J*=7.5 Hz, 2H$_4$), 7.56 (t, 1H, *J*=7 Hz, 1H$_{11}$), 7.48 (d, 3H, *J*=8 Hz, 2H$_3$+1H$_9$), 7.39 (d, 2H, *J*=5.5 Hz, 2H$_8$), 7.15-7.11 (m, 3H, 2H$_5$+H$_{10}$), 6.52 (d, 1H, *J*=8Hz, 1H$_{15}$), 5.49 (s, 1H, 1H$_{13}$), 2.43 (s, 3H, -bpy-PhCH$_3$), 1.73 (s, 3H, -tpy-PhCH$_3$). Electrospray ionization mass spectrometry (ESI-MS) (positive, MeCN) *m/z*=374.02 (100%) [(HPy-(bpy-Ph-CH$_3$))Ru(tpy-PhCH$_3$)]$^{2+}$ and *m/z*=746.84 (55%) [(Py-(bpy-Ph-CH$_3$))Ru(tpy-PhCH$_3$)]$^+$.

[(py-(bpy-Ph-CH$_2$Br))Ru(tpy-PhCH$_3$)](ClO$_4$)·2H$_2$O (2). Yield: 83 mg (60%). Anal. Calcd for $C_{44}H_{36}N_6RuBrClO_6$: C, 54.98; H, 3.77; N, 8.74. Found: C, 54.95; H, 3.79; N, 8.71. ^{1}H NMR (400 MHz, DMSO-d_6): δ/ppm 9.45 (s, 1H, 1H$_{3''}$), 9.30 (s, 2H, 2H$_{3'}$), 9.03 (s, 1H, 1H$_{3'''}$), 8.99-8.92 (m, 4H, 2H$_6$+1H$_{12}$+1H$_{12'}$), 8.68 (d, 1H, *J*=8 Hz, 1H$_{9'}$), 8.32 (d, 2H, *J*=8 Hz, 2H$_7$), 8.16 (t, 1H, *J*=8 Hz, 1H$_{11'}$), 8.02 (d, 1H, 1H$_{14}$), 7.99 (t, 1H, *J*=7.5 Hz, 1H$_{10'}$), 7.88 (t, 2H, *J*= 7.5 Hz, 2H$_4$), 7.61 (t, 1H, *J*=6 Hz, 1H$_{11}$), 7.57 (d, 1H, *J*=5.5 Hz, 1H$_9$), 7.52 (d, 2H, *J*= 8 Hz, 2H$_3$), 7.43 (d, 2H, *J*= 5.5 Hz, 2H$_8$), 7.20-7.15 (m, 3H, 2H$_5$+1H$_{10}$), 6.63 (d, 1H, *J*=8 Hz, 1H$_{15}$), 5.73 (s, 1H, 1H$_{13}$), 3.95 (s, 2H, -CH$_2$Br), 2.47 (s, 3H, -CH$_3$). ESI-MS (positive, MeCN) *m/z*=413.47 (100%) [(HPy-(bpy-PhCH$_2$Br))Ru(tpy-PhCH$_3$)]$^{2+}$ and *m/z*=825.74 (55%) [(Py-(bpy-Ph-CH$_2$Br))Ru(tpy-PhCH$_3$)]$^+$.

[(py-(bpy-Ph-CHO))Ru(tpy-PhCH$_3$)](ClO$_4$)·H$_2$O (3). Yield: 83 mg (66%). Anal. Calcd for $C_{44}H_{33}N_6RuClO_5$: C, 61.29; H, 3.86; N, 9.75. Found: C, 61.41; H, 3.78; N, 9.72. ^{1}H NMR (400 MHz, DMSO-d_6): δ/ppm 9.47 (s, 1H, -CHO), 9.41 (s, 1H, 2H$_{3''}$), 9.33 (s, 2H, 2H$_{3'}$), 9.22 (s, 1H, 1H$_{3'''}$), 8.98 (d, 3H, *J*= 8 Hz, 2H$_6$+1H$_{12}$), 8.94 (d,1H, *J*= 4.5 Hz, 1H$_{12'}$), 8.71 (d, 1H, *J*= 8 Hz, 1H$_{9'}$), 8.35-8.29 (m, 3H, 2H$_7$+1H$_{14}$), 8.18 (t, 1H, *J*=7.5 Hz, 1H$_{11'}$), 8.01 (t, 1H, J= 7.5 Hz, 1H$_{10'}$), 7.88 (t, 2H, *J*= 8 Hz, 2H$_4$), 7.63 (t, 1H, *J*=6.5 Hz, 1H$_{11}$), 7.58 (d, 1H, *J*=5 Hz, 1H$_9$), 7.53 (d, 2H, *J*= 8 Hz, 2H$_3$), 7.43 (d, 2H, *J*= 5.5 Hz, 2H$_8$), 7.27 (d, 1H, *J*= 7.5 Hz, 1H$_{15}$), 7.23 (t, 1H, *J*= 6.5 Hz, 1H$_{10}$), 7.15 (t, 2H, *J*= 6.5 Hz, 2H$_5$), 6.34 (s, 1H, 1H$_{13}$), 2.48 (s, 3H, -CH$_3$). ESI-MS (positive, MeCN) *m/z*=381.01 (100%) [(HPy-(bpy-Ph-CHO))Ru(tpy-PhCH$_3$)]$^{2+}$ and *m/z*=760.83 (19%) [(Py-(bpy-Ph-CHO))Ru(tpy-PhCH$_3$)]$^+$.

Caution! Perchlorate salts of the metal complexes are potentially explosive and therefore should be handled in small quantities with care.

2.2.4. Physical Measurements. Elemental analyses of the compounds were performed with a Vario-Micro V2.0.11 elemental (CHNSO) analyzer. NMR spectra were collected on a Bruker 400 MHz spectrometer in DMSO-d_6 and CD_3CN. High resolution mass spectrometry was performed on a Waters Xevo G2 QTOF mass spectrometer. The UV-vis absorption spectra were recorded with a Shimadzu UV 1800 spectrophotometer. Steady state luminescence spectra were obtained by a Horiba Fluoromax-4 spectrofluorometer. Luminescence quantum yields were determined by using literature method taking $[Ru(bpy)_3]^{2+}$ as the standard. Luminescence lifetime measurements were carried out by using time-correlated single photon counting set up from Horiba Jobin-Yvon. The luminescence decay data were collected on a Hamamatsu MCP photomultiplier (R3809) and were analyzed by using IBH DAS6 software.

Experimental uncertainties are as follows: absorption maxima, ±2 nm; molar absorption coefficients, 10%; emission maxima, ±5 nm; excited-state lifetimes, 10%; luminescence quantum yields, 20%.

Electrochemical measurements were carried out in deaerated acetonitrile with a BAS epsilon electrochemistry system and a three-electrode set up consisting of a Pt (for oxidation) or glassy carbon (for reduction) working electrode, Pt auxiliary electrode, and Ag/AgCl as reference electrode. The cyclic voltammetric (CV) and square wave voltammetric (SWV) measurements are carried out at 25 °C in MeCN solution of the complexes ($\sim 1\times10^{-3}$ M) and the concentration of the supporting electrolyte, tetraethylammonium perchlorate (TEAP), is maintained at 0.1 M. Freshly distilled acetonitrile is used as solvent and the electrodes are cleaned thoroughly after each individual scan. Additionally, nitrogen was thoroughly purged into the complex solutions after every scan to maintain an inert atmosphere. The scan rate is 100 mV/s for CV and 20 mV/s for SWV. The potentials measured are compensated for the *iR* drop in the cell. All of the potentials reported in this study are referenced against the Ag/AgCl electrode, which under the given experimental conditions give a value of 0.36 V for the ferrocene/ferrocenium couple.

2.2.5. Computational Methods. All calculations were performed with the Gaussian 09 program[76] employing the DFT method with Becke's three-parameter hybrid functional and LeeYang-Parr's gradient corrected correlation functional B3LYP level of theory.[77,78] 6-31G(d) basis set was employed for the C, H, N, Br and O while SDD basis set was used for Ru atom.[79] Geometries were fully optimized using the criteria of the

respective programs. TD-DFT[80-83] calculations of the singlet-singlet excitations were performed in acetonitrile simulated by the CPCM model[84] by using the so-called non-equilibrium approach, which has been designed for the study of the absorption process.[85,86] We also performed the UKS calculations directly on the triplet state of the complexes to calculate singlet-triplet energy gap. Orbital analysis was completed with Gauss View[87] and Gauss sum 2.2.[88]

2.2.6. X-ray Crystal Structure Determination. Crystals suitable for structure determination were obtained by diffusing toluene to a solution of **1** in MeCN-DCM (1:4, v/v). X-ray diffraction data for the crystal of **1** mounted on a glass fiber and coated with perfluoropolyether oil was collected on a Bruker-AXS SMART APEX II diffractometer at 296 K equipped with CCD detector using graphite-monochromated MoK_α radiation (λ =0.71073 Å). The crystallographic data were processed with SAINT and absorption corrections were made with SADABS.[89] The structure was solved by direct methods using SHELXT[90] program and refined by full matrix least-squares method based on F 2 by using SHELXL program through Olex-2.[91] The non hydrogen atoms were refined anisotropically, while the hydrogen atoms were placed with fixed thermal parameters at idealized positions. In the structure of **1**, one free methanol molecule remains in the crystal packing which was highly disordered and the structure was finally solved by removing the disordered methanol molecule by running the program SQUEEZE.[92] The electron density map also showed the presence of some unassignable peaks, which were removed by running the program SQUEEZE. The crystallographic figure has been generated using Mercury 2022.3.0 software.[93]

2.2.7. Photolysis of the Complexes. Photolysis of all the three complexes were carried out in photocatalytic reactor (Model No: 66901) designed by Newport corporation, USA. A 1-cm light path length quartz cell was used for the photolysis measurements. The concentration of the complexes was maintained in the range of 5×10^{-6} M - 1×10^{-5} M, and the solution was thoroughly degassed with N_2 before photoirradiation and stirred magnetically during photolysis. Light of specific wavelengths were isolated using band pass filters -- 280, 330 and 500 nm. The rate constant of the Ru-C bond cleavage was evaluated from the absorbance titration data using equation (1).[94]

$$\ln\{(A_0 - A_f)/(A_t - A_f)\} = k_c t \qquad (1)$$

where A_0, A_t, and A_f is the absorbance of the free receptor, after time t, and at the conclusion of the reaction. k_c is the rate constant of photolysis and t is the required time for the completion of the photolysis process. Both k_c and A_f were estimated by nonlinear least-

square method. The intensity of the light source was ~0.11 W. Quantum yields (φ) of the photolysis process were obtained by using the equation,[95]

$$\nu = (\varphi I_0/V)(1\text{-}10^{-Abs})$$

where ν is the rate of the photolysis, I_0 is the photon flux at the front of the cell, V is the volume of the solution, and Abs is the initial absorbance at the irradiation wavelength.

2.3. Results and Discussion

2.3.1. Synthesis and Characterization. The 6'-tolyl-2,2':4''-terpyridine ligand and its derivatives were synthesized according to the procedure already stated above in the experimental section. The solvated precursor, $([(tpy\text{-}PhCH_3)Ru(Me_2CO)_3]^{3+}$ obtained upon treating $(tpy\text{-}PhCH_3)RuCl_3$ with $AgBF_4$ in acetone, is refluxed with respective ligand in presence of base for the synthesis of the desired products. The products are purified by chromatographic and recrystallization techniques and characterized via NMR and mass spectrometry along with elemental (C, H, and N) analyses. Details of synthesis and characterization data are already provided in the previous experimental Section. Solid state structure of **1** is also obtained by single-crystal X-ray diffraction.

2.3.2. NMR Spectra. ^{1}H NMR spectra of **1-3** are delineated in Figure 2.1. For complex **1**, two different types of $-CH_3$ protons appear as two individual singlet (not shown in Figure 2.1). Due to the presence of a carbanionic center, the $-CH_3$ group associated with the cyclometalating ligand resonates towards the up-field region (1.73 ppm) than that of the non-cyclometalating ligand (2.43 ppm). Singlets corresponding to $H_{3'}$, $H_{3''}$ and $H_{3'''}$ protons appear at the down-field region of 8.95-9.45 ppm due to the complexation with Ru^{II} ion. For **3**, the aldehydic proton appears at ~9.5 ppm. The H_{13} proton adjacent to the carbanionic center moves to the remarkably up-field region of 5.50-6.34 ppm and thus confirms the formation of cyclometalated complexes. For **2**, the $-CH_2Br$ protons appear as a singlet at 3.95 ppm (not shown in Figure 2.1).

2.3.3. Mass Spectra. ESI mass spectra of **1-3** inclusive of their simulated isotopic distributions are portrayed in Figure 2.2. Two intense peaks are observed for all complexes. The most abundant peak with its *m/z* value ranging between 374.02 and 413.47, separated by 0.5 Da, corresponds to the di-positive cations, $[(Hpy\text{-}bpy\text{-}Ph\text{-}X)Ru(tpy\text{-}PhCH_3)]^{2+}$, while the less intense peak with its *m/z* spanning within the range of 746.84-826.04, separated by 1 Da, indicates the presence of mono-positive cations, $[(py\text{-}bpy\text{-}Ph\text{-}X)Ru(tpy\text{-}PhCH_3)(ClO_4)]^{+}$. Good correlation is observed between the experimental and calculated isotopic patterns for all the complexes.

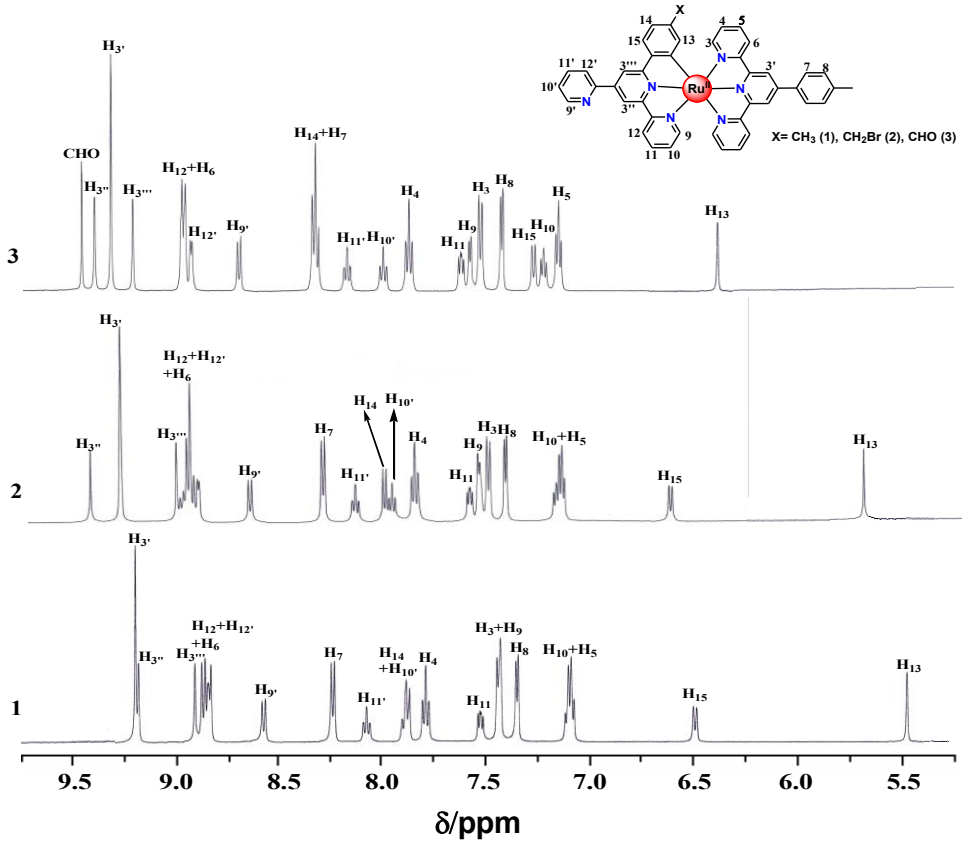

Figure 2.1. Proton NMR spectra of **1-3** in DMSO-d_6.

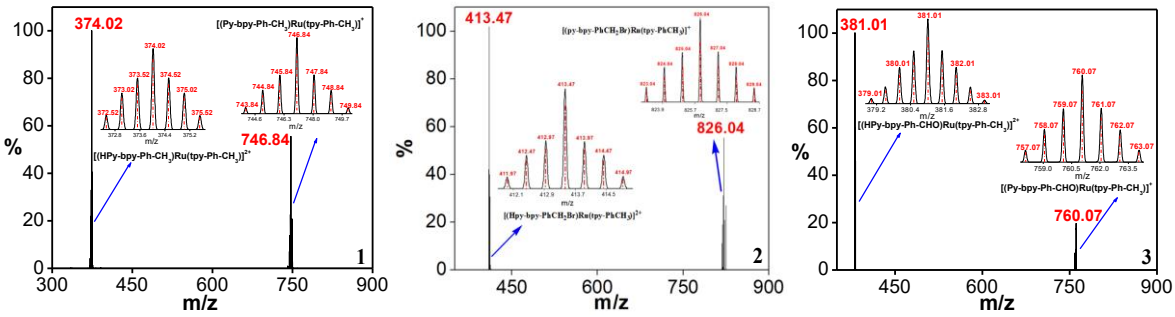

Figure 2.2. Experimental and simulated ESI (positive) mass spectra of **1-3** in MeCN.

2.3.4. Structural Description of 1. Single crystal X-ray structure of **1** is depicted in Figure 2.3 which displays distorted octahedral geometry around the Ru^{II} center. **1** crystallizes in triclinic mode with P-1 space group. Selected bond distances and bond angles are provided in Table 2.1. The central Ru-N bond length is considerably shorter compared to the terminal Ru-N bond lengths probably owing to efficient overlap between t_{2g} orbital

of Ru^{II} and π* orbitals of the central pyridyl moiety of tpy-$PhCH_3$. The comparatively larger terminal Ru-N distances in the non-cyclometalating ligand arise mostly because of the strained cisoid conformation in the metal complex. The peripheral Ru1-N5 bond {2.168(3) Å} gets elongated in the cyclometalated ligand. Additionally, because of the stronger σ donating ability of the carbanionic center, the Ru1-C23 bond is slightly shorter than that of the Ru1-N5 bond. The chelate bite angles lie within the range of 75.71°(10)-110.73°(10) whereas the trans angles span between 155.55°(11) and 173.42°(10). Ru-N distances vary within 1.950(2)-2.168(3) Å. (*CCDC reference number: 2254384 for* ***1***).

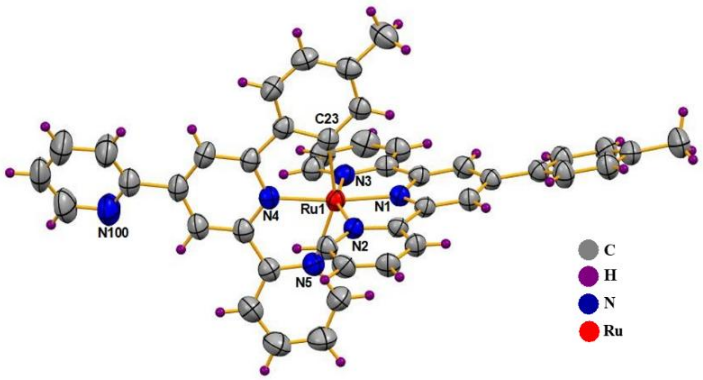

Figure 2.3. ORTEP view of $\mathbf{1}^{+}$ showing 50% probability ellipsoid plots.

Table 2.1. Crystallographic Data for **1**.

Compound	**1**
Formula	$C_{44}H_{33}ClN_6O_4Ru$
fw	846.28
T (K)	296 K
Cryst. Syst.	Triclinic
Space group	P-1
a (Å)	10.2661(4)
b (Å)	14.3192(5)
c (Å)	14.6891(5)
α (deg)	99.102(2)
β (deg)	97.063(2)
γ (deg)	100.061(2)
V (Å3)	2074.02(13)
Dc(g cm-3)	1.355
Z	2
μ (mm-1)	0.491
F(000)	864.0
θ range (deg)	2.27-25.74
Data/restraints/params	9461/0/507
GOF on F2	1.061
R1 [I > 2σ(I)]a,	0.0473
wR2 (all data)b	0.1413
Δρmax/Δρmin (e Å)	0.980/ -0.685
aR1(F) = [∑ || F0 | - |FC || / ∑ | F0], bwR2 (F2) = [∑ w(F02 - FC2)2 / ∑ w(F02)2]1/2	

2.3.5. Theoretical Investigations. Theoretical calculations on both the ground and excited state of the complexes are carried out in MeCN utilizing B3LYP functional along with 6-31G(d) and SDD basis set. Ground state optimized structures of **1-3** are presented in Figure 2.4 and the corresponding metrical parameters for **1** are tabulated in Table 2.2. The values obtained from single crystal X-ray structure are in good correlation with the theoretical parameters. The frontier MOs and their compositions are provided in Figures 2.5-2.7 and Tables 2.3 and 2.4. The HOMOs are mainly situated on Ru^{II}, while the LUMOs are situated on the terpyridine units of both cyclometalated and non-cyclometalated ligands. The HOMO-LUMO energy gap lies in the range of 2.98-3.02 eV. The electron density distribution across the complex backbone has been displayed in their electrostatic surface potential (ESP) plots (Figure 2.8). Green color implies the electron-rich portion, whereas the blue color indicates the electron-deficient region. ESP plots indicate that the non-coordinated pyridine nitrogen in the outer sphere of the complexes as well as the carbanionic center on the cyclometalating part is the electron-rich region.

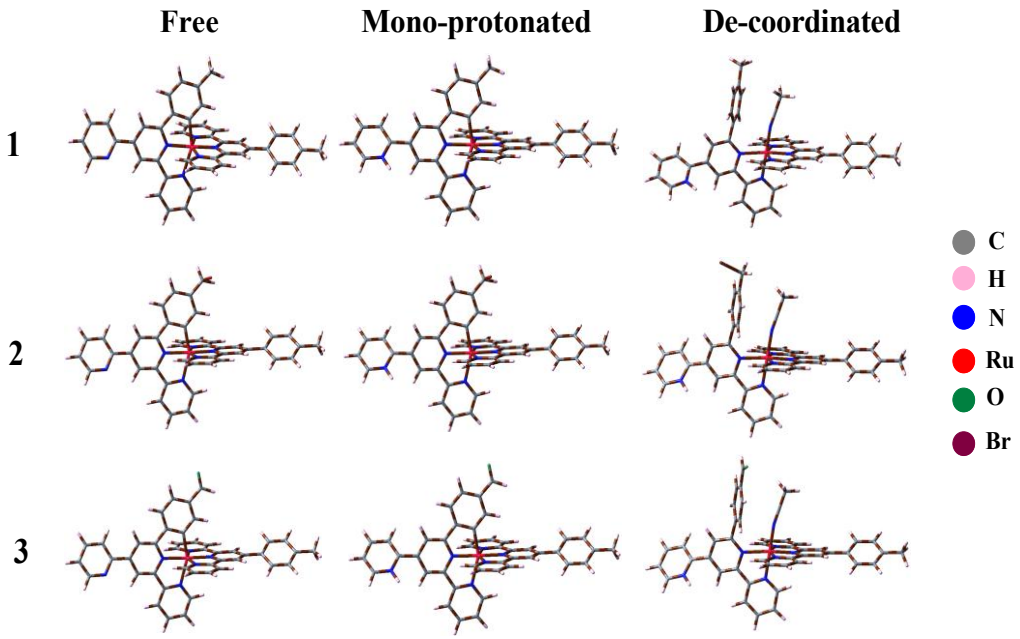

Figure 2.4. Ground state optimized geometries of the free (left panel), mono-protonated (middle panel), and de-coordinated forms (right panel) of **1-3** in acetonitrile.

Table 2.2. Selected Experimental and Calculated Bond Distances (Å) and Angles (deg) for **1**.

	1		
	Exptl.	Soln. (singlet)	Soln. (triplet)
Ru1-N1	1.950(2)	1.979	2.003
Ru1-N2	2.060(2)	2.097	2.106
Ru1-N3	2.064(2)	2.098	2.106
Ru1-N4	2.017(2)	2.044	2.046
Ru1-N5	2.168(3)	2.210	2.315
Ru1-C23	2.045(3)	2.050	2.018
N1-Ru1-C23	93.67(11)	98.5	102.1
N1-Ru1-N4	173.42(10)	178.3	177.1
C23-Ru1-N4	79.94(11)	79.8	80.7
N1-Ru1-N3	78.81(9)	78.6	78.3
C23-Ru1-N3	93.58(10)	91.8	91.1
N4-Ru1-N3	99.87(10)	101.4	101.8
N1-Ru1-N5	110.73(10)	105.8	101.8
C23-Ru1-N5	155.55(11)	155.7	156.1
N4-Ru1-N5	75.71(10)	75.8	75.4
N3-Ru1-N5	92.74(10)	92.9	93.8
N1-Ru1-N2	78.95(9)	78.6	78.4
C23-Ru1-N2	92.03(10)	91.7	91.1
N4-Ru1-N2	102.71(9)	101.3	101.6
N3-Ru1-N2	157.35(10)	157.2	156.6
N5-Ru1-N2	91.16(10)	93.0	93.6

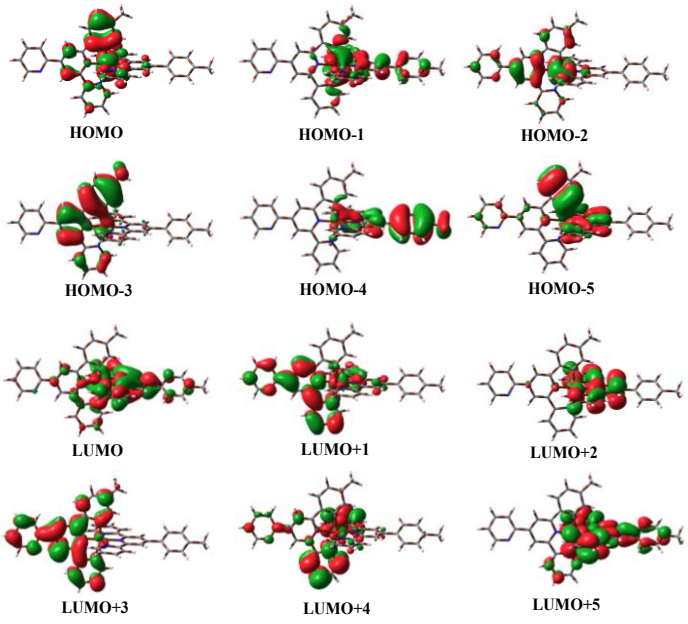

Figure 2.5. Schematic drawings of the selective frontier molecular orbitals of **1** in acetonitrile.

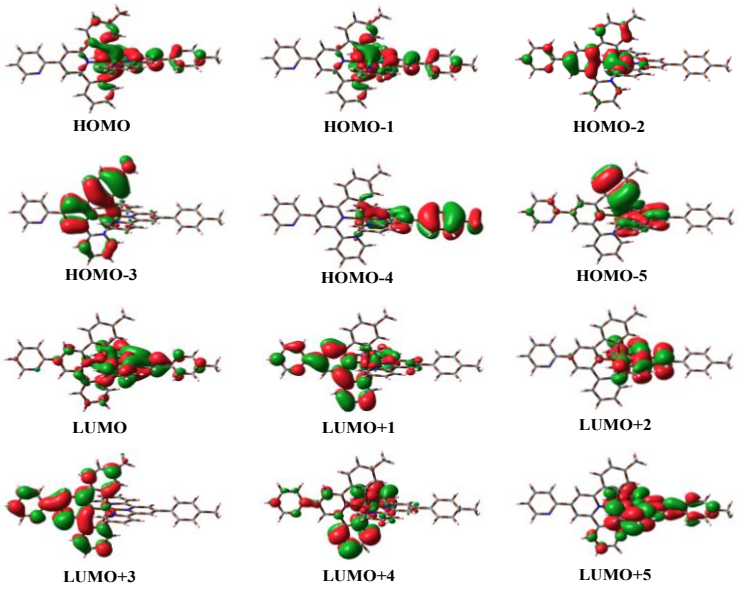

Figure 2.6. Schematic drawings of the selective frontier molecular orbitals of **2** in acetonitrile.

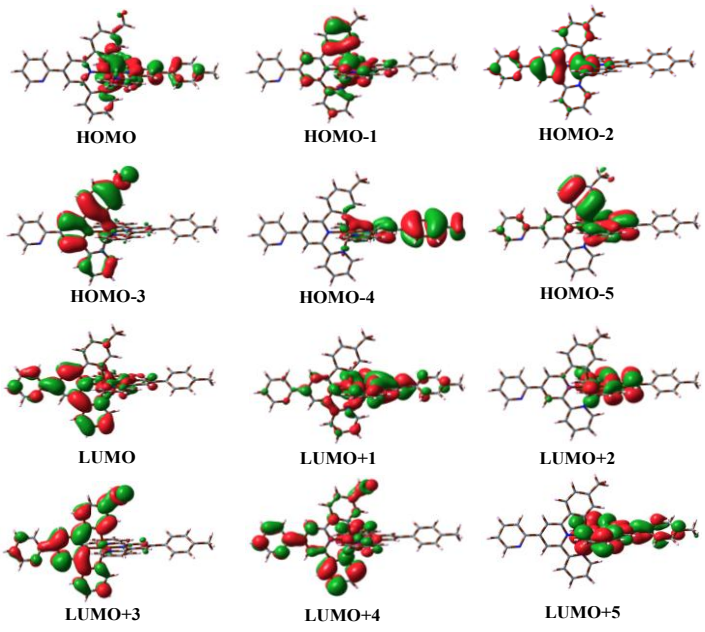

Figure 2.7. Schematic drawings of the selective frontier molecular orbitals of **3** in acetonitrile.

Table 2.3. Selected MOs along with their Energies and Compositions in the Ground State for **1** in MeCN.

MO	1															
	Energy/eV			% Compositions												
				Free				Mono-protonated				De-coordinated				
	Free	Mono- protonated	De-coordinated	Tolu	Tpy	Ru	Mpt	Tolu	Tpy	Ru	mpt	Tolu	Tpy	Ru	mpt	MeCN
LUMO+5	-1.27	-1.55	-1.78	0.00	6.36	1.64	91.93	14.83	78.45	1.83	4.89	2.43	78.51	1.35	17.16	0.54
LUMO+4	-1.27	-2.04	-2.28	1.23	64.20	0.78	33.79	7.32	88.73	1.32	2.63	2.09	96.41	0.71	0.71	0.07
LUMO+3	-1.70	-2.23	-2.56	13.07	84.19	1.75	0.98	0.58	4.47	1.97	92.97	0.02	2.21	1.61	96.01	0.15
LUMO+2	-2.13	-2.35	-2.72	0.61	2.80	2.33	94.26	0.85	3.07	12.23	83.84	0.25	89.61	1.99	7.92	0.22
LUMO+1	-2.21	-2.38	-2.84	1.26	79.85	7.20	11.69	0.50	92.28	3.39	3.82	0.06	6.96	5.32	87.52	0.14
LUMO	-2.23	-3.05	-3.38	1.04	10.73	12.97	75.25	1.07	93.18	5.00	0.75	0.83	95.11	3.33	0.66	0.07
HOMO	-5.21	-5.39	-6.27	25.28	8.75	55.28	10.67	25.47	8.38	55.48	10.66	0.42	5.78	74.79	14.80	4.21
HOMO-1	-5.24	-5.43	-6.36	5.80	5.16	59.82	29.22	6.14	5.32	60.40	28.14	0.36	1.80	57.99	35.96	3.88
HOMO-2	-5.53	-5.78	-6.44	4.40	18.53	69.70	7.37	6.42	17.40	68.76	7.41	1.92	12.58	74.99	9.40	1.10
HOMO-3	-6.22	-6.44	-7.00	58.25	29.12	9.09	3.53	62.04	25.41	8.93	3.62	0.54	0.65	18.95	77.79	2.07
HOMO-4	-6.69	-6.75	-7.24	1.36	0.81	3.32	94.50	1.26	0.79	4.03	93.91	3.77	1.45	0.13	94.55	0.09
HOMO-5	-6.75	-6.89	-7.25	61.19	5.95	7.25	25.60	54.04	2.08	6.69	37.19	66.04	23.82	1.47	7.23	1.44

Table 2.4. Selected MOs along with their Energies and Compositions in the Ground State of **2** in MeCN.

MO	2															
	Energy/eV			% Compositions												
				Free				Mono-protonated				Decoordinated				
	Free	Mono- protonated	De-coordinated	$PhCH_2Br$	Tpy	Ru	Mpt	$PhCH_2Br$	Tpy	Ru	mpt	$PhCH_2Br$	Tpy	Ru	Mpt	MeCN
LUMO+5	-1.29	-1.73	-1.86	0.00	0.40	1.71	97.93	26.28	71.07	1.43	1.23	28.38	63.69	1.14	6.21	0.58
LUMO+4	-1.32	-2.14	-2.32	8.65	73.36	0.33	17.65	18.77	68.52	2.12	10.59	6.65	91.45	0.86	0.96	0.07
LUMO+3	-1.88	-2.27	-2.57	29.98	64.95	1.95	3.11	3.12	10.11	1.63	85.13	0.05	2.21	1.57	96.02	0.15
LUMO+2	-2.16	-2.39	-2.72	1.70	2.15	1.77	94.38	0.82	1.83	11.85	85.49	0.25	87.80	2.16	9.56	0.22
LUMO+1	-2.26	-2.42	-2.85	1.42	14.06	12.42	72.10	0.90	93.34	3.06	2.69	0.12	8.95	5.11	85.68	0.13
LUMO	-2.27	-3.09	-3.39	2.99	75.77	7.92	13.32	1.50	92.27	5.41	0.81	1.06	94.79	3.37	0.71	0.07
HOMO	-5.29	-5.49	-6.28	7.91	5.56	59.98	26.54	22.61	7.68	58.48	11.22	0.57	5.69	74.61	14.98	4.13
HOMO-1	-5.30	-5.50	-6.38	19.88	7.64	58.73	13.74	5.74	5.30	60.76	28.20	0.25	1.90	57.41	36.62	3.82
HOMO-2	-5.58	-5.85	-6.46	3.37	19.12	70.10	7.41	4.70	18.21	69.59	7.50	2.16	12.44	74.72	9.48	1.20
HOMO-3	-6.40	-6.63	-7.01	55.96	33.93	6.60	3.51	61.42	28.58	6.17	3.83	0.61	0.68	19.66	76.94	2.11
HOMO-4	-6.71	-6.77	-7.20	1.14	0.75	3.62	94.48	1.11	0.77	4.41	93.70	76.66	19.91	1.70	0.61	1.12
HOMO-5	-6.86	-6.99	-7.24	43.26	5.27	2.91	48.56	30.66	1.21	1.91	66.22	0.03	0.01	0.06	99.88	0.00

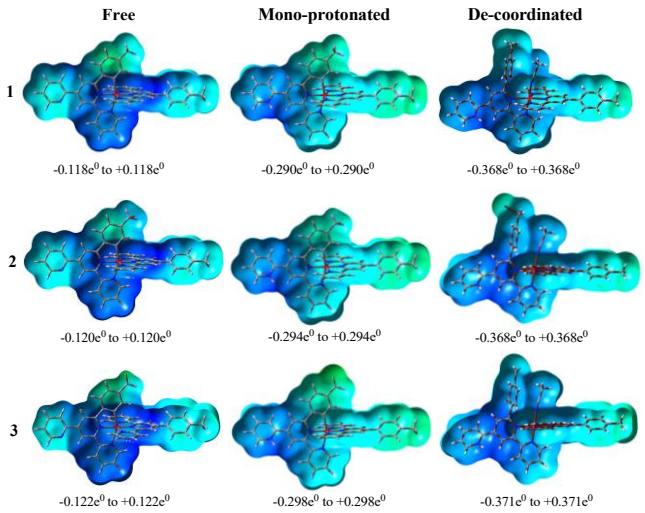

Figure 2.8. ESP plots of **1-3** in their free (left panel), mono-protonated (middle panel), and de-coordinated (right panel) forms in MeCN.

2.3.6. Absorption Spectra. The absorption spectra of the complexes are acquired in MeCN (Figure 2.9) and related spectral data are furnished in Table 2.5. The assignments of the bands are made possible upon comparing the spectra of the related complexes and by TD-DFT calculations. The spectral parameters and the assignment of bands for a representative complex **1** are shown in Table 2.6. A reasonably good correlation is noticed between the experimental observation and theoretical calculations. It appears that the lowest energy bands are mainly due to the transitions from Ru(II)→tpy-$PhCH_3$ and Ru(II)→tpy unit of cyclometalating ligand. The next higher energy broad bands are the admixture of MLCT, LLCT and π-π* transitions, while the intense bands in the UV occur due to mixed LLCT and π-π* transitions. Electron density difference map (EDDM) and natural transition orbital (NTO) analysis further confirm that the band at lowest energy is of MLCT character (Figures 2.10-2.12). Interestingly, the large bathochromic shift of MLCT band of the complexes is observed compared to parent $[Ru(tpy)_2]^{2+}$ (λ_{max}=474 nm)[17,18] and $[Ru(tpy\text{-}PhCH_3)_2]^{2+}$ (λ_{max}=490 nm)[70] complexes due to higher electron density at the metal center induced by the carbanionic cyclometalating ligands. The observed bathochromic shift is also reproduced by TD-DFT calculations.

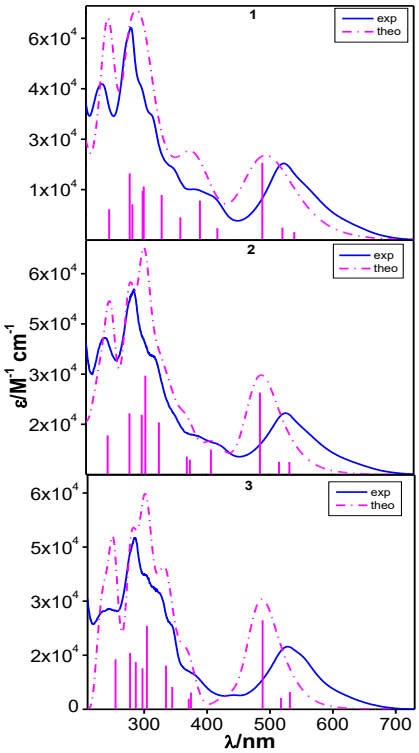

Figure 2.9. Overlay of the experimental (blue) and theoretical (magenta) absorption spectra of **1-3** in MeCN.

Table 2.5. Photophysical Data of **1-3**.

Compounds		Absorption λ_{max}/ nm (ε, $M^{-1}cm^{-1}$)	Luminescence		
			λ_{max} / nm	τ	Φ
1	MeCN (298 K)	524(21200), 402(br)(12900), 349(sh)(19800), 302(sh) (41700), 281(58800), 236(43200)	818	τ_1= 0.8 ns (38%) τ_2= 6.6 ns (62%)	1.5×10^{-4}
2		526(18400), 402(br)(9900), 319(sh)(35000), 286(55300), 240(41000)	714	τ_1= 0.9 ns (32%) τ_2= 8.6 ns (68%)	3.9×10^{-4}
3		528(17200), 440(br)(4000), 378(sh)(10000), 345(sh)(23000), 323(sh)(33000), 304(sh)(37000), 286(47200), 239(27400)	794	τ_1= 0.3 ns (18%) τ_2= 9.9 ns (82%)	2.4×10^{-4}
1	EtOH-MeOH (77 K)	-	798	τ_1= 0.8 μs (22%) τ_2= 3.8 μs (78%)	2.5×10^{-2}
2		-	700	τ_1= 2.6 μs (34%) τ_2= 8.6 μs (66%)	4.8×10^{-2}
3		-	773	τ_1= 1.1 μs (44%) τ_2= 3.1 μs (56%)	3.7×10^{-2}

Table 2.6. Selected UV-vis Energy Transitions at the TD-DFT/B3LYP Level of **1** in MeCN.

λ_{expt}/ nm	λ_{cal}/ nm	Oscillator strength(f)	Excited state	Key transitions	Character
Free					
570	541	0.04	S_4	H-1→L (37%), H→L+2 (49%)	MLCT
524	522	0.06	S_6	H-1→L+2 (93%)	MLCT
	490	0.41	S_7	H-2→L+1 (27%), H-1→L (28%), H→L+2 (35%)	
402	418	0.06	S_{11}	H-2→L+1 (12%), H-2→L+3 (15%), H→L+3 (57%)	MLCT, LLCT
	390	0.21	S_{12}	H-2→L+3 (72%)	MLCT, LLCT
349	359	0.12	S_{19}	H-3→L+1 (77%)	LLCT
315	329	0.24	S_{26}	H-1→L+7 (68%), H→L+8 (13%)	LLCT, π-π*, MLCT
302	300	0.30	S_{40}	H-3→L+3 (25%), H-2→L+8 (45%), H-2→L+9 (14%)	π-π*, LLCT
	298	0.26	S_{43}	H-6→L (61%), H-4→L+2 (16%)	
281	282	0.20	S_{52}	H-8→L+1 (44%)	π-π*, LLCT
	277	0.35	S_{55}	H-6→L+2 (60%), H-3→L+4 (14%)	
Mono-protonated					
568	548	0.30	S_4	H-2→L (67%), H-1→L+2 (13%), H→L+1 (13%)	MLCT
528	510	0.20	S_7	H-2→L (15%), H→L+1 (53%), H→L+3 (19%)	MLCT
363	368	0.08	S_{19}	H-1→L+6 (66%), H→L+6 (24%)	MLCT, LLCT
	356	0.08	S_{25}	H→L+7 (82%)	
315	310	0.15	S_{44}	H-9→L (37%), H-3→L+4 (46%)	π-π*, LLCT
	300	0.31	S_{49}	H-7→L+2 (20%), H-6→L+2 (57%)	
286	278	0.29	S_{60}	H-7→L+3 (11%), H-6→L+3 (14%), H-1→L+13 (11%), H-1→L+21 (20%)	π-π*, LLCT
	267	0.29	S_{72}	H-11→L (16%), H-7→L+4 (11%), H-6→L+4 (25%), H-3→L+7 (26%)	
240	243	0.20	S_{98}	H-10→L+3 (34%), H-5→L+6 (11%), H-4→L+7 (40%)	π-π*
De-coordinated					
481	486	0.33	S_4	H-2→L (87%)	MLCT
331	340	0.22	S_{22}	H-3→L+1 (89%)	MLCT, π-π*
305	302	0.33	S_{40}	H-7→L+1 (29%), H-2→L+6 (43%), HOMO→L+6 (15%)	LLCT, π-π*
282	272	0.49	S_{61}	H-10→LUMO (21%), H-8→L+2 (49%), H-5→L+4 (13%)	π-π*, LLCT

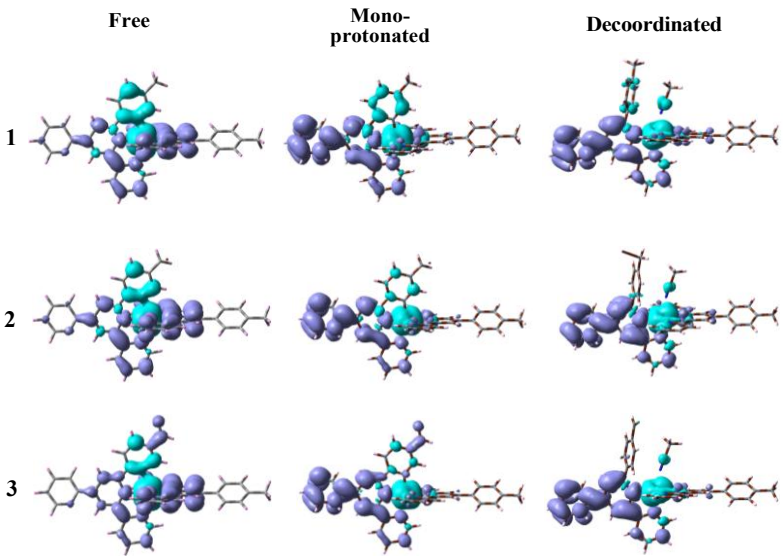

Figure 2.10. Difference in electron density upon excitation from the ground S_0 state to the lowest energy singlet excited state of complexes **1-3**. Cyan and violet color shows regions of decreasing and increasing electron density, respectively.

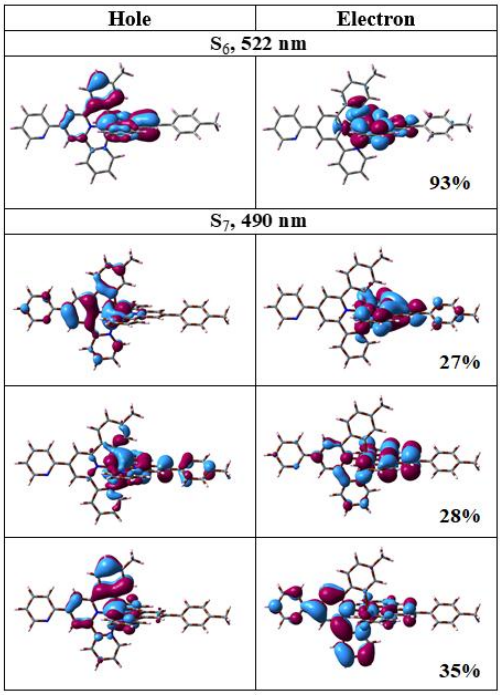

Figure 2.11. NTOs illustrating the nature of optically active singlet excited states in the absorption bands at 522 nm (S_6) and 490 nm (S_7) for a representative complex **1**. The occupied (holes) and unoccupied (electrons) NTO pairs that contribute more than 20% to each excited state are only represented. All transitions are of purely ^{1}MLCT character.

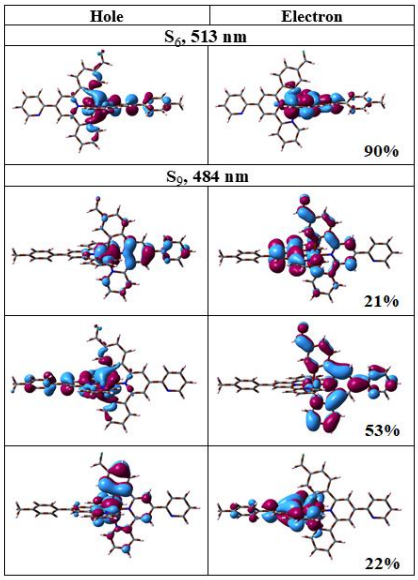

Figure 2.12. NTOs illustrating the nature of optically active singlet excited states in the absorption bands at 513 nm (S_6) and 484 nm (S_9) for **3**. The occupied (holes) and unoccupied (electrons) NTO pairs that contribute more than 20% to each excited state are only represented. All transitions are of purely ^{1}MLCT character.

2.3.7. Luminescence Spectra. Steady-state emission spectra and the lifetime of complexes are collected in MeCN at RT (Figure 2.13) as well as in EtOH-MeOH (4:1, v/v) glass at 77 K (Figure 2.14, Table 2.5). Upon excitation at the ^{1}MLCT maximum, a broad emission band is observed in the NIR domain (714-818 nm in MeCN) at RT. The close resemblance of the excitation and absorption spectra indicate that the observed emission is due to radiative deactivation of the complexes and not because of any impurity (Figure 2.15, for **1**). In order to understand the emission characteristics, UKS calculations are executed on the triplet state of **1-3** and the comparison data is provided in Table 2.7. Reasonably good correlation suggests that the observed emission in the complexes arise because of radiative deactivation of their triplet MLCT states. In case of ruthenium-terpyridine type complexes (such as $[Ru(tpy)_2]^{2+}$), the metal center experiences a weak ligand field because of the distorted octahedral geometry. Consequently, the excited-state deactivation occurs from the equilibrated state of radiating ^{3}MLCT and non-radiating ^{3}MC states yielding either non-emissive or very weakly emissive complexes. Due to stronger σ-donating ability of the cyclometalating ligand, the luminescent ^{3}MLCT levels move to low energy and the ^{3}MC levels shift to high energy, thereby making the complexes luminescent at RT by increasing the ^{3}MLCT-^{3}MC energy gap. Besides, as suggested by the "energy gap

law",[96] a decrease in energy-gap between the luminescent ^{3}MLCT level and the ground state occurs due to which the emission maximum is substantially red-shifted towards the NIR region.

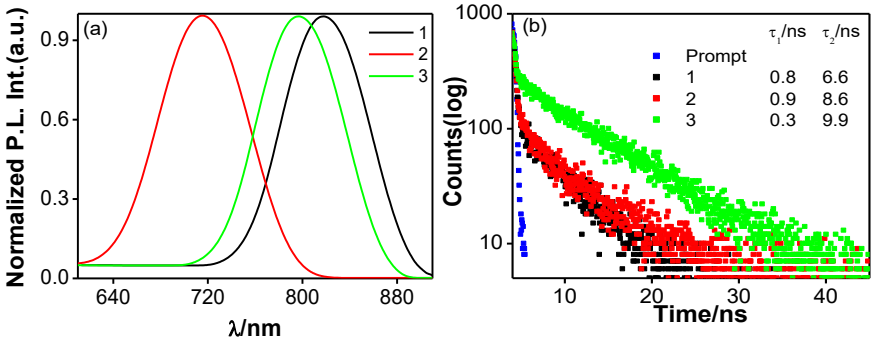

Figure 2.13. (a) Photoluminescence spectra (λ_{ex}=525 nm) and (b) excited-state decays (λ_{ex}=505 nm) of **1-3** in MeCN at RT. Inset to figure b shows the lifetime values.

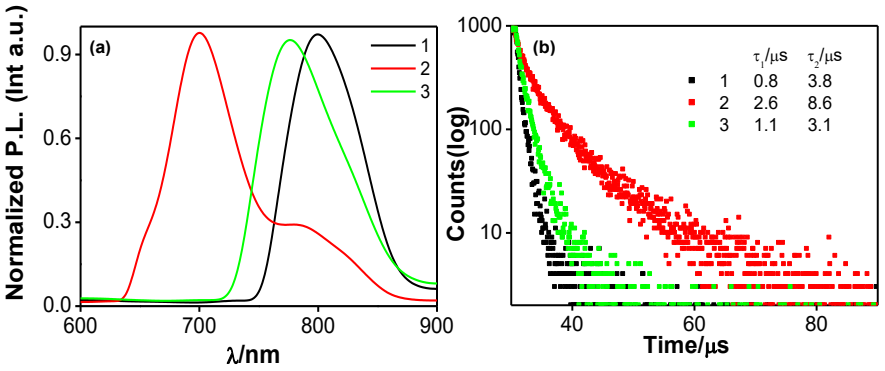

Figure 2.14. (a) Emission spectra and (b) emission decays of **1-3** in EtOH-MeOH (4:1, v/v) glass at 77 K. Inset to figure b shows the lifetime values.

All three complexes display biexponential decay in MeCN at RT. The first-component lifetimes vary within the domain of 0.3-0.9 ns, while the second long-lived component ranges between 6.6 and 9.9 ns. The initial short-lived component is probably due to ^{3}MLCT level, whereas the second relatively long-lived component probably appears from the equilibrated triplet state of substituted cyclometalated fragment (^{3}LLCT) and ^{3}MLCT, although no direct proof of the hypothesis could be provided. The observed values are about two orders of magnitudes greater than that of parent $[Ru(tpy)_2]^{2+}$ (0.25 ns) and $[Ru(tpy\text{-}PhCH_3)_2]^{2+}$ (0.95 ns) complexes. At 77 K, a hypsochromic shift (λ_{max}= 700-798 nm) of the emission maxima occurs with enormous increase in Φ and τ (Figure 2.14 and Table 2.5). Zero-zero spectroscopic energy (E_{00}) measured from their emission maxima at 77 K varies between 1.55 and 1.77 eV.

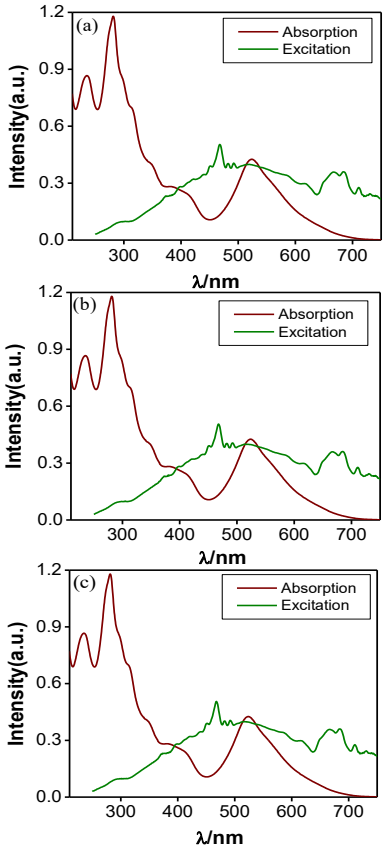

Figure 2.15. Overlay of the absorption and excitation {(a) λ_{em}= 780 nm, (b) λ_{em}= 818 nm, and (c) λ_{em}= 830 nm} spectrum of **1** in MeCN.

Table 2.7. Emission Maxima of **1-3** in MeCN according to UKS Calculations and Associated Experimental Values.

Compounds	Free		Mono-protonated		De-coordinated	
	λ_{exp}/nm	λ_{cal}/nm	λ_{exp}/nm	λ_{cal}/nm	λ_{exp}/nm	λ_{cal}/nm
1	818	750	780	1048	701	737
2	714	730	700	949	700	740
3	794	720	745	1033	705	744

2.3.8. Redox Properties. The redox properties of **1-3** are investigated in acetonitrile through cyclic voltammetry (CV). The voltammograms are portrayed in Figure 2.16 and corresponding electrochemical data are given in Table 2.8. The anodic region of the CV shows a reversible wave corresponding to one-electron oxidation of the Ru^{II} center, while the cathodic region consists of two successive reversible and/or quasi-reversible peaks resulting from reduction of the coordinated polypyridine ligands. An enormous cathodic-shift (~700 mV) of the Ru^{II}/Ru^{III} potential is observed due to strong σ-donating character

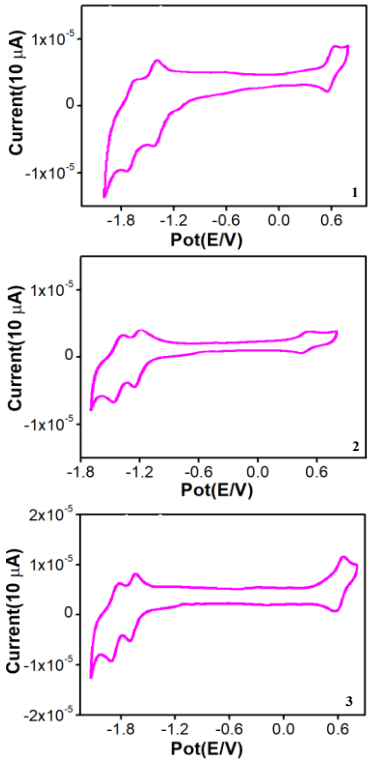

Figure 2.16. Cyclic voltammograms of **1-3** in acetonitrile at a scan rate of 100 mV/s showing both oxidation and reduction processes using Ag/AgCl as the reference electrode.

of the anionic ligands as compared to their tpy analogues ($[Ru(tpy)_2]^{2+}$, $E_{1/2}$(ox)=1.30 V). The presence of the cyclometalating ligand also shifts the ligand-centered reductions to more negative potential domain. We also performed DFT calculations to support our assignments of the redox couples of the complexes. Spin density computed on both the oxidized and reduced form (by one electron) indicates that in their oxidized form the density mostly resides on the Ru^{II} center, while upon reduction it is predominantly confined to the terpyridine unit (Figure 2.17).

Table 2.8. Electrochemical Data[a] for Complexes **1-3** in MeCN.

Compounds	Oxidation[b] $E_{1/2}$(ox)/V	Reduction[c] $E_{1/2}$(red)/V
1	0.59	-1.69, -1.36
2	0.55	-1.74, -1.49
3	0.62	-1.73, -1.50
$[Ru(tpy)_2]^{2+}$	1.30	-1.24
$[Ru(tpy\text{-}PhCH_3)_2]^{2+}$	1.25	-1.24

[a]All the potentials are referenced against Ag/AgCl electrode with $E_{1/2}$=0.36 V for Fc/Fc^+ couple. [b]Reversible electron transfer process with a Pt working electrode. [c]$E_{1/2}$ values for the reduction processes obtained with glassy carbon electrode

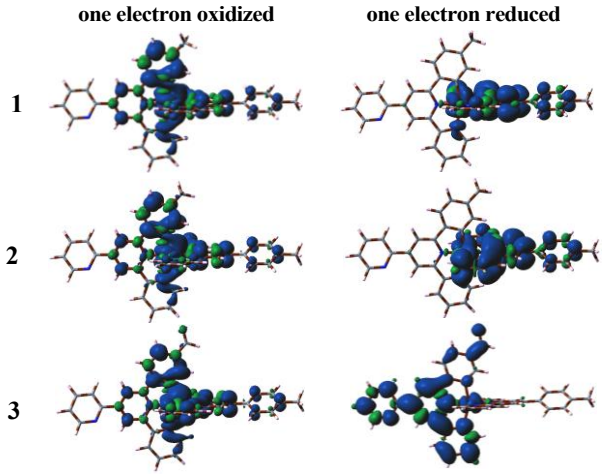

Figure 2.17. Spin density plots of **1-3** in MeCN. Left panel indicates one-electron oxidized forms while one-electron reduced forms are shown in right panel.

2.3.9. Acid-Induced Modulation of the Photophysical and Redox Properties of the Complexes. We have already pointed out that the outer coordination sphere of the complexes possesses non-coordinated nitrogen atom in the cyclometalated site and taking advantage of which modulation of the spectral properties could be feasible by acid-base equilibria. In this regard, we have performed the absorption and emission spectral titrations of the complexes in MeCN upon cumulative addition of $HClO_4$ and the spectral profiles are portrayed in Figures 2.18-2.20. Two-step changes are noticed in their spectral profiles. The presence of clear isosbestic points in each step indicates that two species are in equilibrium. In the first step, the MLCT band undergoes a substantial red-shift (within 33-44 nm) depending on the substituents. The spectral characteristics of all three complexes is similar in the first step although the amount of acid required for saturation is different, viz. 2, 4 and 8 equiv for complex **1**, **2** and **3**, respectively. For **1**, protonation of only the non-coordinated N is feasible, whereas in case of **2** and **3**, apart from N-H protonation, abstraction of Br^- from $-CH_2Br$ moiety and protonation of the oxygen atom of -CHO group in the cyclometalated part is also a distinct possibility. Upon continued addition of 1M of $HClO_4$, the absorbance of the bands at ~568 and ~360 nm is gradually reduced in the second-step with concomitant evolution and intensification of strong peak at ~480 nm. The saturation occurs upon addition of 8, 16 and 32 equiv of $HClO_4$ for complex **1**, **2** and **3**, respectively. This large hypsochromic shift of the MLCT band (~85 nm) is also reproduced in their visual color change from deep violet to reddish yellow (inset of Figure 2.18).

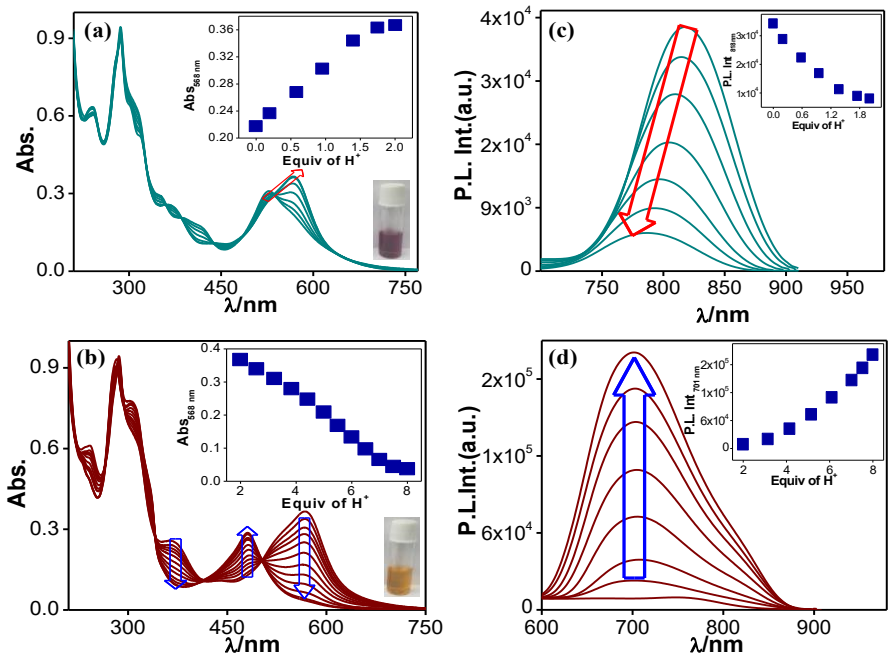

Figure 2.18. Two-step changes in absorption (a and b) and emission (c and d) spectral profiles of **1** on incremental addition of H^+ in MeCN. The insets to figure a and b show the alteration of absorbance with the equivalent of H^+ and visual color change while the insets to figure c and d display the variation of luminescence intensity as a function of H^+.

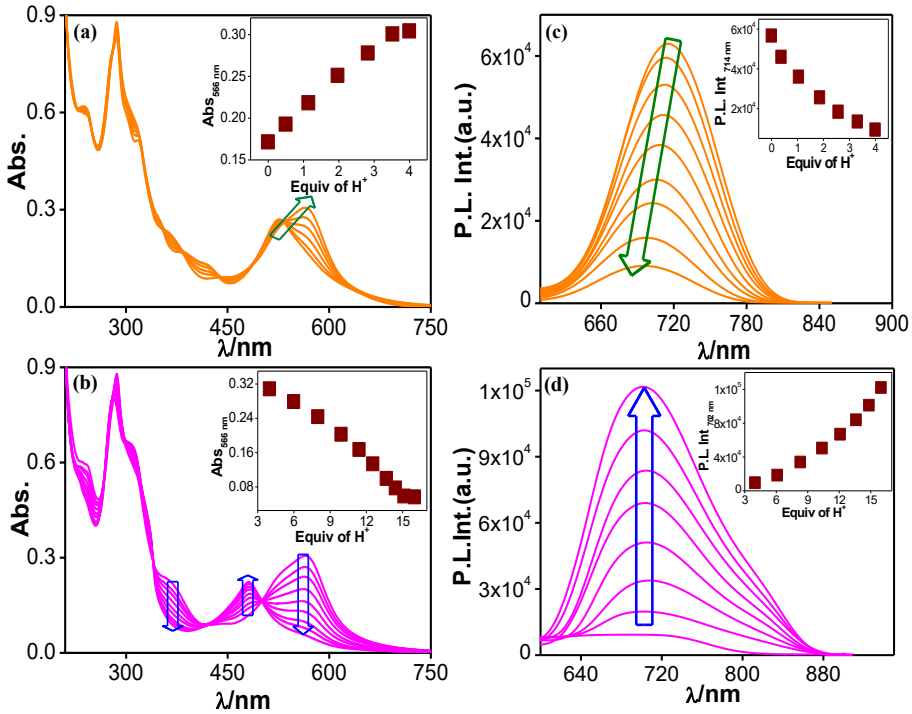

Figure 2.19. Two-step changes in absorption (a and b) and luminescence (c and d) spectral profiles of **2** upon incremental addition of H^+ in MeCN. The insets to figures show the change of absorbance and luminescence intensity as a function of the equivalent of H^+.

The emission titration profiles indicate gradual decrease in emission intensity for all three complexes in the first step with substantial blue-shift of emission maximum (up to the extent of ~50 nm). In the second step, a new emission peak is evolved at ~700 nm and intensified substantially upon step-by-step addition of acid (Figures 2.18-2.20). Lifetimes acquired upon increased addition of $HClO_4$ also reveals two reversed trends as shown in Figures 2.21 and 2.22. In line with steady state spectra, lifetime values gradually decrease in the first step, while the values systematically increase (up to 23.5-26.9 ns) in the second step.

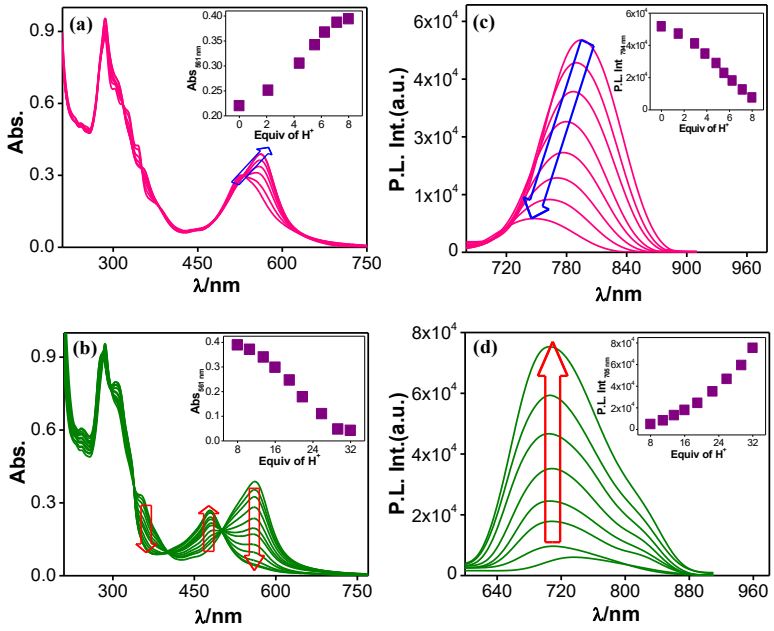

Figure 2.20. Two-step changes in absorption (a and b) and emission (c and d) spectral profiles of **3** on incremental addition of H^+ in MeCN. The insets to figures show the change of absorbance and luminescence intensity as a function of the equivalent of H^+.

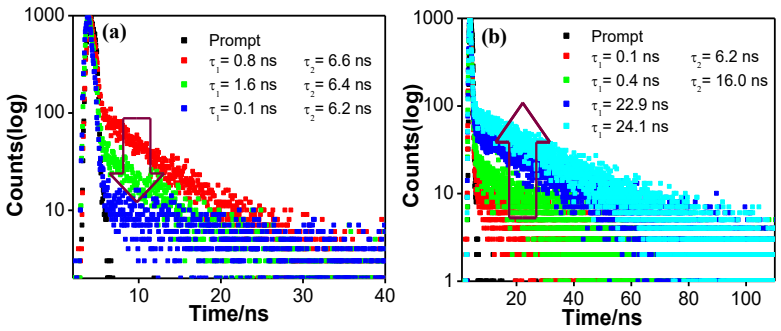

Figure 2.21. First (a) and second (b) step changes in luminescence decays of **1** upon incremental addition of H^+ ion in acetonitrile. The insets to figure a and b show the corresponding lifetime values.

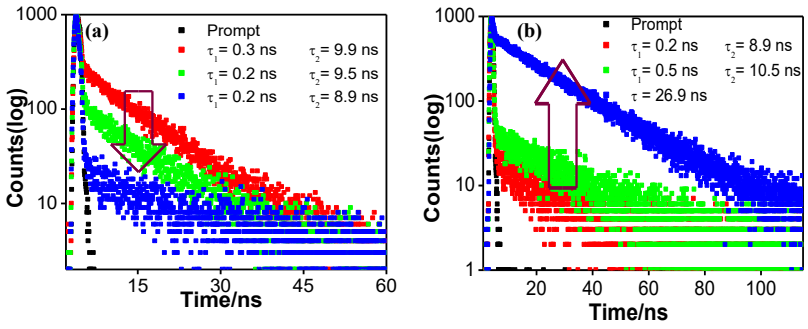

Figure 2.22. First (a) and second (b) step changes in luminescence decays of **3** upon incremental addition of H^+ ion in acetonitrile. The insets to figure a and b show the corresponding lifetime values.

We have also measured the Ru(II/III) oxidation potential of all three complexes via cyclic (CV) and square-wave (SWV) voltammetry before and after the addition of acid and the results are displayed in Figure 2.23 and Table 2.9. In presence of acid, the Ru(II/III) potential increases in all three complexes and the extent of increase varies within the range of ~30-60 mV. Increase of the Ru(II/III) oxidation potential is probably because of the increase in the overall charge of the complex from +1 (cyclometalated) to +2 (after Ru-C bond cleavage).

We are interested to understand the reason for the aforementioned changes in the spectral behaviors as well as to explore the possibility of any of their structural changes in presence of acid. To this end, we carried out ^{1}H NMR titration of a representative complex (**1**) upon gradual addition of H^+ in CD_3CN and the spectral profiles are displayed in Figure 2.24. Upon incremental addition of H^+, a new peak is generated at δ=12.50 ppm probably because of protonation of non-coordinated pyridine moiety in the cyclometalated site of the complex backbone. This sort of protonation decreases the electron density in the said pyridine ring and consequently $H_{9'}$-$H_{12'}$ proton resonances move towards the down-field region up to 2 equiv of acid. Additionally, the peak intensity of H_{13} and H_{15} protons decreases to a small extent with concomitant emergence of two doublets (not well-resolved) at ~δ=7.4 ppm and δ=8.05 ppm probably because of $H_{13'}$ and $H_{15'}$protons (right-side inset structure of Figure 2.24). Upon continued addition of acid (up to 8 equiv), the signals due to H_{13} and H_{15} get completely removed whereas the doublets due to $H_{13'}$ and $H_{15'}$ become intensified, well-resolved and get small up-field shifted. In addition, $H_{3''}$ exhibits a small up-field shift (9.05→9.00 ppm) while $H_{3'''}$ displays a large up-field shift from 8.85 to 8.30 ppm. The protons associated with terpyridine moiety of the non-cyclometalated site

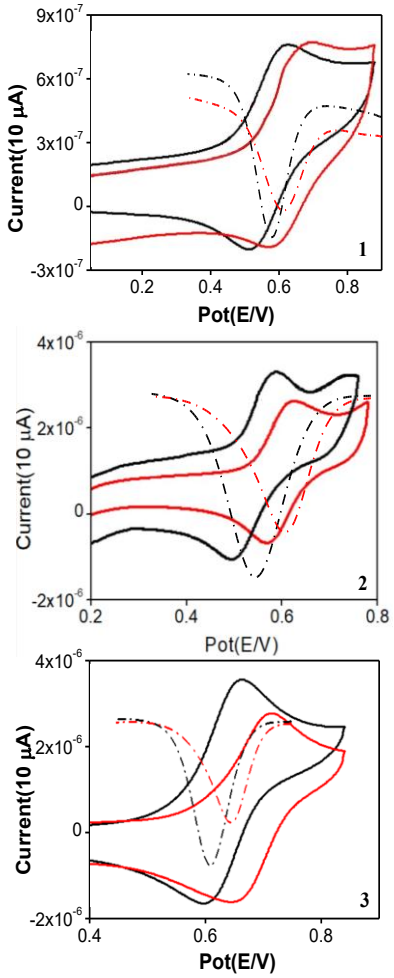

Figure 2.23. CVs and SWVs of **1-3** in MeCN. The black color represents the free form, while the red color corresponds to the de-coordinated forms of the complexes.

Table 2.9. Oxidation Potentials of Complexes **1-3** in their Free and De-coordinated Forms in MeCN.

Compounds	Oxidation $E_{1/2}$(ox)/V	
	Free	De-coordinated
1	0.59	0.62
2	0.55	0.61
3	0.62	0.68

undergo only small change in their chemical shift values upon acidification. Thus, the outcome of the NMR titration suggests that up to the addition of 2 equiv of acid, protonation of the non-coordinated pyridine ring in the cyclometalated site of the complex occurs which is evidenced by the down-field shifts of proton resonances of the said pyridine ring. We

surmise that continued addition of acid leads to the protonation of carbanionic site of Ru-C bond and eventually Ru-C bond gets cleaved. The final spectrum clearly suggests the existence of the structure wherein the central Ru^{II} center is coordinated via a tridentate (NNN)- as well as bidentate (NN)- fashion as shown on the right-hand side inset of Figure 2.24.

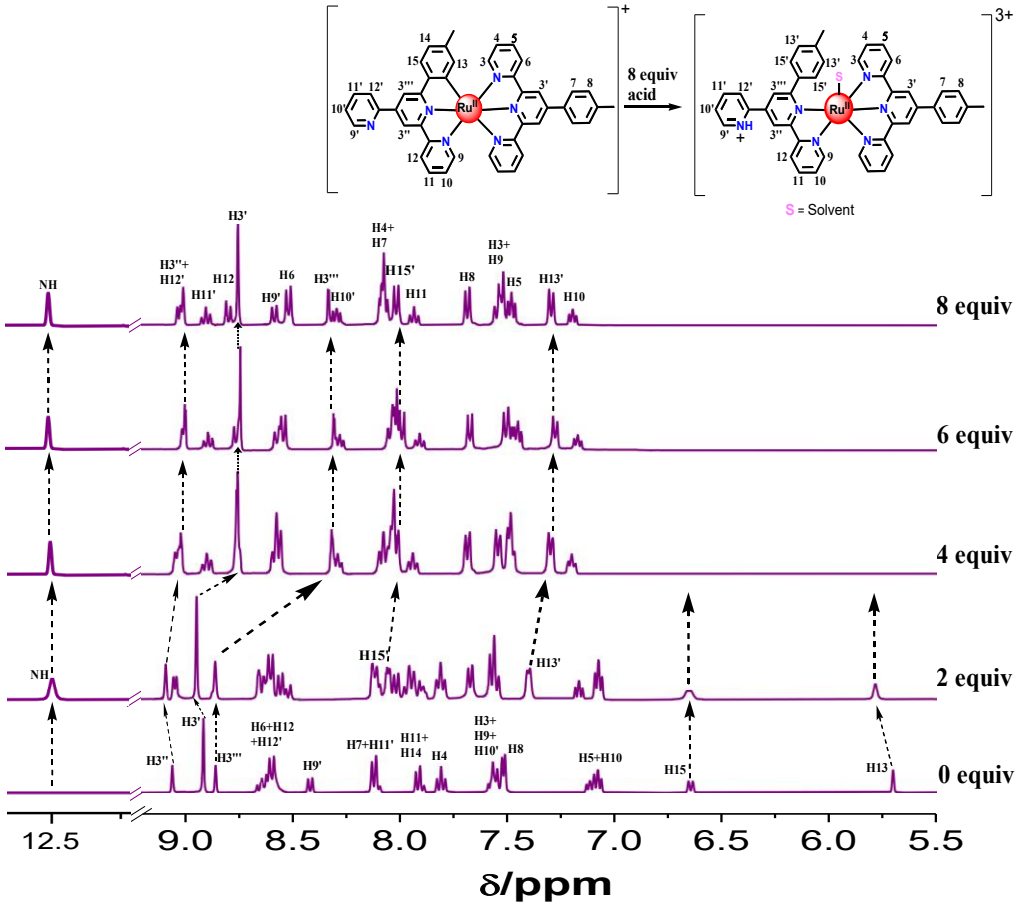

Figure 2.24. ^{1}H NMR spectral profile of **1** with incremental addition of H^+ (up to 8.0 equiv) in CD_3CN.

To get further confirmation, we also acquired the ESI mass spectra of acid-saturated acetonitrile solutions of the complexes (Figure 2.25) and observed only one peak (*m/z*= 373.97 for **1,** 413.15 for **2** and 380.85 for **3**) in each case. Taking into consideration good correlation between experimental and calculated isotopic patterns, the peak corresponds to the bi-positive species of the type, $[Ru(N^N^N)(N^N\text{-ph})(S)]^{2+}$ (S=solvent) in all three cases. The existence of the bi-positive species indicates the cleavage of Ru-C bond in the cyclometalated complexes.

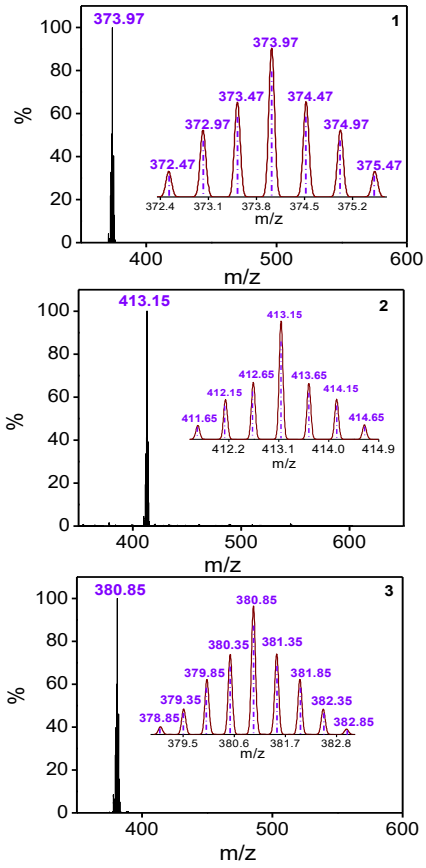

Figure 2.25. ESI (positive) mass spectrum for de-coordinated ([Ru(N^N^N)(N^N-ph)(S)]$^{2+}$) forms of **1-3** in acetonitrile showing both observed and simulated isotopic distribution patterns.

In order to prove our hypothesis, we again performed DFT and TD-DFT calculations on both the mono-protonated as well as the de-coordinated forms of the complexes. Interestingly, the calculated spectra correlate well with the experimental observations for the respective species (Figure 2.26). MOs associated with the lowest energy spin-allowed transition in the free-, mono-protonated and de-coordinated states of **1** are shown in Figure 2.27-2.29. In comparison to their free forms, upon N-H protonation, the LUMOs of the complexes are stabilized to a greater extent than the HOMOs due to which the lowest-energy band gets shifted towards the higher wavelength region. On the other hand, after de-coordination, the HOMOs get more stabilized than the LUMOs in comparison to their previously mono-protonated forms. The HOMO-LUMO energy gap lies in the range of 2.34-2.42 eV for the mono-protonated forms, while within the domain of 2.89-2.91 eV for the de-coordinated forms. Hence, a large hypsochromic shift is observed in their absorption spectral profiles upon de-coordination in all cases. We have

also performed ESP and EDDM calculations for both the mono-protonated and the de-coordinated forms and they correlate well with the experimental observations (Figures 2.8 and 2.10).

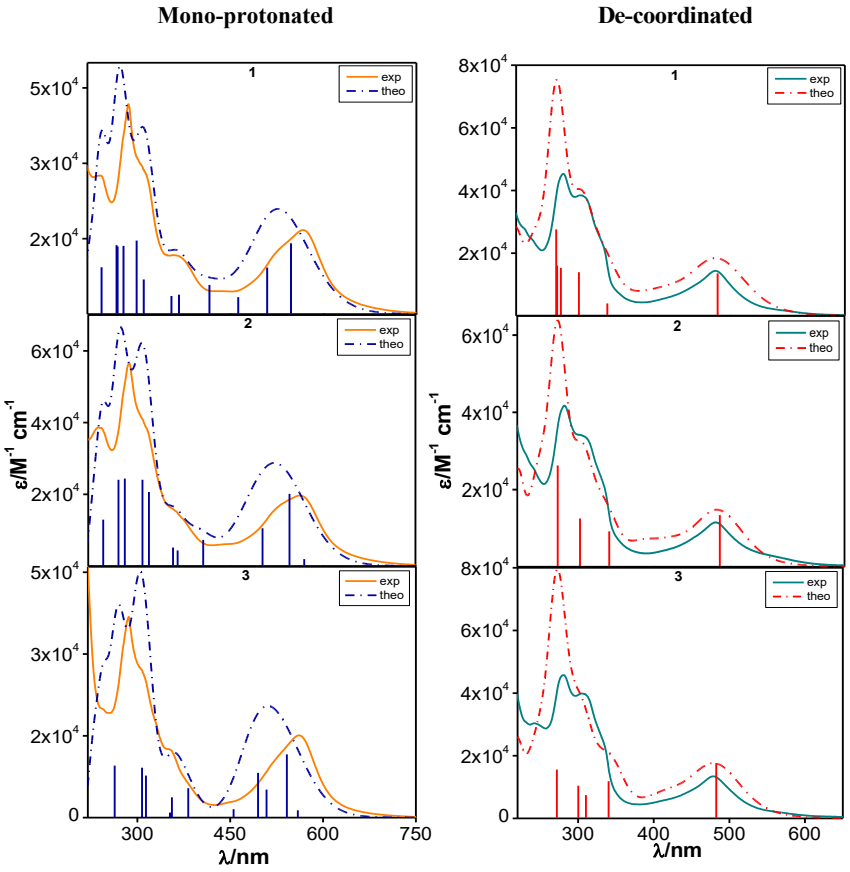

Figure 2.26. Overlay of the experimental and theoretical absorption spectra of the mono-protonated (left panel) and de-coordinated (right panel) forms of **1**-**3** in acetonitrile.

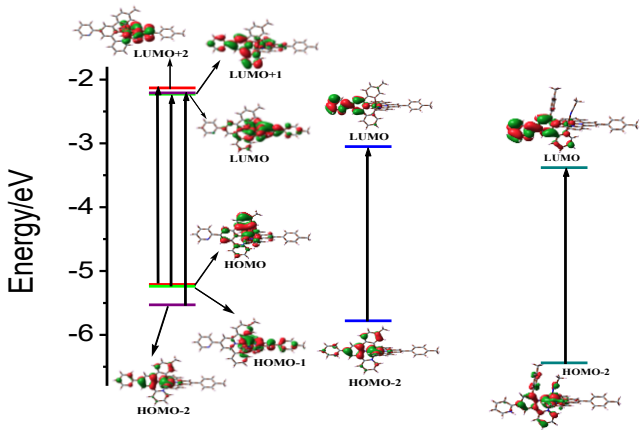

Figure 2.27. Dominant transitions involved in the lowest-energy absorption band in free (left panel), mono-protonated (middle panel) and de-coordinated (right panel) forms of a representative complex **1** in MeCN.

UKS calculations are also performed on the mono-protonated and the de-coordinated forms of the complexes to take into account the observed emission spectral behaviors of the complexes in presence of acid (Table 2.7). The correlation between the experimental and theoretical emission maxima for the free and the de-coordinated complexes is quite reasonable.

DFT calculations also support the shift of the Ru(II/III) oxidation potential to higher values upon cleavage of Ru-C bond. It is observed that the energy of HOMO decreases in the de- coordinated form compared to the coordinated analogue. As a result, the Ru(II/III) oxidation that involves transfer of electron from HOMO to LUMO becomes more difficult in the de-coordinated forms.

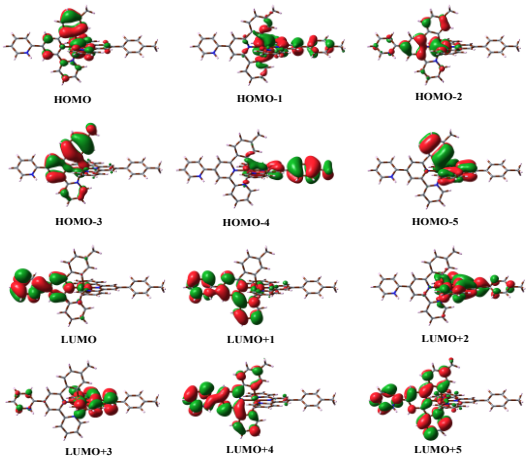

Figure 2.28. Schematic drawings of the selective frontier molecular orbitals of the mono-protonated form of **1** in acetonitrile.

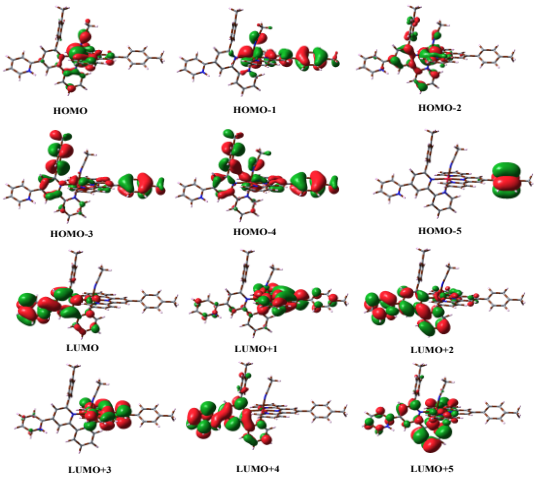

Figure 2.29. Schematic drawings of the selective frontier molecular orbitals of the de-coordinated form of **1** in acetonitrile.

We are curious to elucidate whether protonation to the pyridine group of the side chain is a necessary condition for Ru-C bond cleavage, or whether protonation to the phenyl group can directly cleave the Ru-C bond as observed in similar Ru(N^N^C) type cyclometalated complexes without a pyridine side chain.[43] We are also interested to explore the possibility of photo-induced cleavage of Ru-C bond in the complexes. In order to address the issues, two sets of experiment were performed. Initially, the acetonitrile solutions of the complexes are irradiated with light of 500 nm wavelength in absence of acid and the progress of reaction was monitored via absorption and emission spectroscopy. Even after irradiation up to ~8 h, almost no change in the spectral profiles of the complexes is noticed. In the second set of experiment, we take the acid-treated solutions of the complexes up to their first saturation point and then treated with the said light source. A systematic change in both the absorption and emission spectral profiles was observed which is in-line with the changes that were observed during the Ru-C bond cleavage in presence of acid (Figure 2.30).

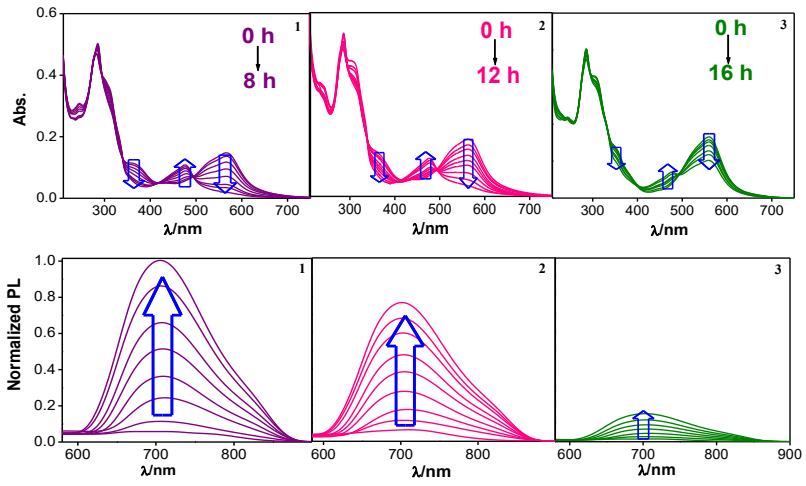

Figure 2.30. UV-vis absorption (upper panel) and emission (lower panel) spectral changes of **1-3** in acetonitrile upon irradiation with visible light. Excitation wavelength for recording the emission is 530 nm.

The time of saturation depends on the substituent on the cyclometalated complex (8 h for **1,** 12 h for **2).** We are unable to reach the saturation level for **3** even after photolysis of more than 16 h. Close inspection reveals that the spectrum obtained after photolysis is very similar to the final spectrum (particularly for **1** and **2**) of the second-step change in presence acid only (without light). The outcomes of the above experiments indicate that the photo-induced cleavage of Ru-C bond is feasible only in presence of acid.

We have also calculated the rate as well as the quantum yield for the photo-induced Ru-C cleavage process of the complexes and the corresponding data and figures are provided in Table 2.10 and Figure 2.31. Both the rate and quantum yield of bond cleavage follows the order **1**>**2**>**3**. The observed trend is probably due to dissimilar electronic environment in the complex backbone that is imparted by different substituents. The electron-withdrawing (-R) effect of the meta-directing CHO group probably increases the Ru-C bond strength, thereby making it difficult to cleave. On the other hand, for **1** and **2**, the inductive effect of $-CH_3$ and $-CH_2Br$ has a small impact on the Ru-C bond and hence assist in the Ru-C cleavage. Thus, the electronic nature of the substituents also plays a key role in the Ru-C bond cleavage process. This disparity is also noticed in the equivalents of acid required for the Ru-C cleavage in the complexes (in absence of light).

Table 2.10. Quantum Yield and Rate Constants for the Photo-induced Ru-C Bond Cleavage of **1-3**.

Compounds	Quantum yield ($\Phi\times10^3$)	Rate constant ($k_{iso}\times10^4/s^{-1}$)
1	7.5	1.2
2	5.4	0.6
3	1.8	0.2

We also tried to revert back to the original cyclometalated form of the complexes upon treating with UV light sources in the de-coordinated forms of the complexes in presence of base. But even after continuous exposure for a long period of time we are unable to restore the Ru-C bond. Thus, reversible transformation of de-coordinated to the cyclometalated forms are not feasible upon light irradiation.

We also kept the MeCN solutions of the complexes under fluorescent light but no significant changes are observed in their absorption and emission spectra. On the other hand, treatment of the acidulated solution of the complexes (up to the level of first saturation) with light or with additional amount of acid can only bring about the Ru-C bond cleavage in the complexes. Thus, it appears that protonation of appended pyridyl group assists the cleavage and probably is a prerequisite for Ru-C bond cleavage.

2.3.10. Molecular Switching. In the previous section, we have witnessed substantial modulation of the absorption and emission spectral properties of all three Ru(II) complexes in presence of acid. The changes are ascribed due to initial protonation of a pyridine motif in their outer coordination sphere followed by cleavage of Ru-C bond and

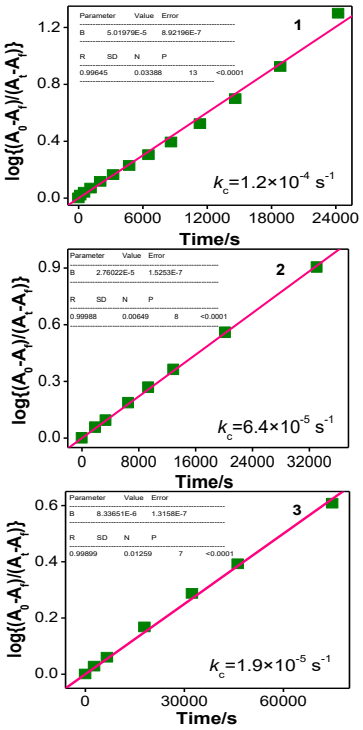

Figure 2.31. Linear plot of log $\{(A_0-A_f)/(A_t-A_f)\}$ *vs*. time for **1-3** gives the value of rate constant of photolysis process.

thereby altering the coordination mode of the resulting complexes. We are interested to check whether the overall process is reversible and the initial state of the complexes could be restored in presence of base. In order to check the reversibility, we take the acid-treated solutions of the complexes and to it was gradually added a standard solution of base and the process was monitored via absorption and emission spectroscopic techniques (Figures 2.32 and 2.33). Initially, we take the acidic solution of the complexes when they reached to their first saturation level. Upon cumulative addition of OH^-, the successive absorption spectrum approaches towards their initial sate and finally reverts back to their original state upon addition of 4.0 equiv of base. Thereafter, we take the acid-treated solution when they reached their second level of saturation that is when the de-coordination of the Ru-C bond has taken place. Upon gradual addition of OH^-, almost no-change in the spectral profiles is noticed. At this stage, we gradually increased the temperature and upon reaching to ~70˚C, the complex restored to its initial cyclometalated form. In the emission side, for the first-step process, the emission intensity gradually increases upon treatment with OH^- and eventually reverts back to its initial state. In the second step, treatment of the acid-saturated solution with both base and heat again, leads to the formation of original cyclometalated

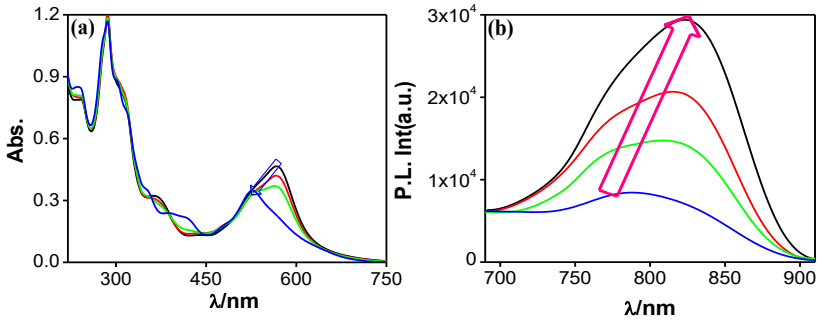

Figure 2.32. Absorption (a) and luminescence (b) spectral profiles obtained upon incremental addition of OH^- (4 equiv) to the first acid-saturated solution of **1** in MeCN.

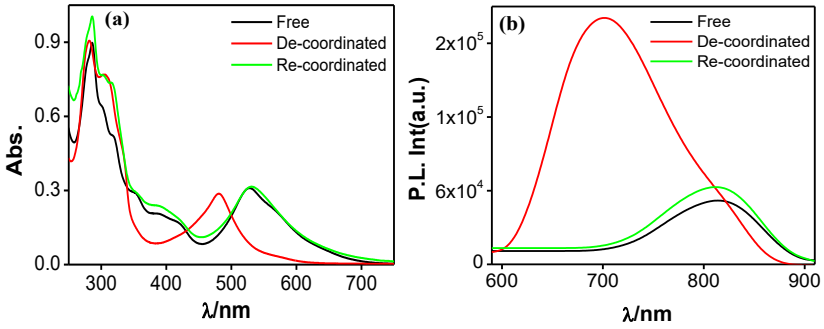

Figure 2.33. Absorption (a) and luminescence (b) spectral profiles of **1** in its free, de-coordinated and re-coordinated forms.

form accompanied with quenching of emission. The color of the solution also changes from reddish-yellow to its original deep violet form. So, the above observations conclude that after de-coordination in presence of acid, Ru(II) is re-coordinated in presence of excess base and temperature (Scheme 2.1). Thus, reversible breaking and making of cyclometalated Ru-C bond is possible upon sequential utilization of acid, base and temperature. In essence, "on-off" emission switching occurs in presence of acid/base, while "off-on" switching is feasible upon treatment with acid, base and heat in appropriate order.

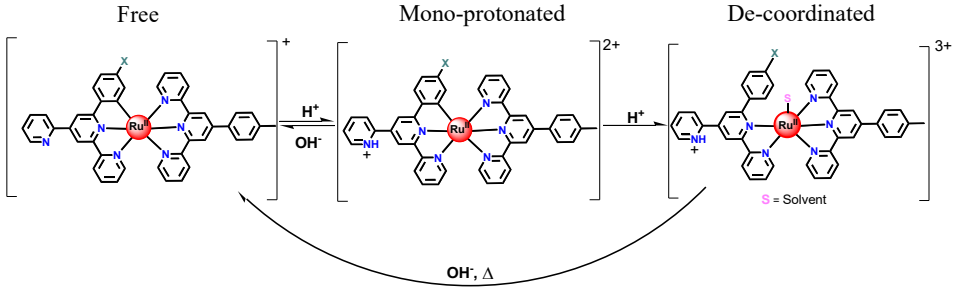

Scheme 2.1. Acid-base equilibria operating among the three forms of the complexes.

2.4. Conclusions

With regard to our sustained interest in developing luminescent Ru(II)-tpy type complexes, we fabricated herein a new array of bis-tridentate Ru(II) complexes by incorporating 4'-(p-methylphenyl)-2,2':6',2"-terpyridine (tpy-PhCH$_3$) and its positional isomer, 6'-tolyl-2,2':4"-terpyridine (py-bpy-Ph-X). The substituent X has been varied (CH$_3$, CH$_2$Br and CHO) to fine tune the photo-redox behaviour in the resulting complexes. 6'-tolyl-2,2':4"-terpyridine and its two derivatives act as cyclometalating ligands in presence of base. Interestingly, the carbanionic site in the cyclometalating ligands has an immense effect on the photophysical and electrochemical properties of the resulting complexes. Increased electron density on Ru(II) center leads to a substantial bathochromic shift of the MLCT absorption and emission maxima compared to their non-cyclometalated counterparts (such as $[Ru(tpy)_2]^{2+}$). All the complexes display emission in the NIR region with long-lived excited-states.

Taking advantage of non-coordinated nitrogen atom in their outer coordination sphere, reversible modulation of absorption and emission spectral properties of the complexes have been achieved upon successive treating with acid and base. Additionally, de-coordination of Ru-C bond by acid followed by its re-coordination upon heating the solution of the complexes under basic condition is feasible. In essence, “on-off” and “off-on” emission switching is achieved upon sequential addition of acid and base as well as by increasing temperature. Interestingly, Ru-C bond cleavage is made possible upon treating the acidified solution of the complexes with visible light source, although reverse cyclometallation is not feasible upon irradiating with UV light sources in presence of base. Finally, detailed computational investigations by DFT and TD-DFT have been performed to assign the experimental spectral bands as well as to understand structural changes associated with the switching behaviors of the complexes. Thus, present cyclometalated Ru(II) complexes could be useful building blocks for fabrication of potential molecular switches.

2.5. References

(1) Badjic, J. D.; Balzani, V.; Credi, A.; Silvi, S.; Stoddart, J. F. A Molecular Elevator. *Science* **2004**, *303*, 1845-1849.

(2) Grätzel, M. Photoelectrochemical Cells. *Nature* **2001**, *414*, 338-344.

(3) Li, Q. Intelligent Stimuli-Responsive Materials. John Wiley & Sons, Inc.: Hoboken, Nj, **2013**.

(4) Harriman, A.; Ziessel, R. Making Photoactive Molecular-Scale Wires. *Chem. Commun*. **1996**, 1707-1716.

(5) Ward, M. D. Metal-Metal Interactions in Binuclear Complexes Exhibiting Mixed Valency; Molecular Wires and Switches. *Chem. Soc. Rev.* **1995**, *24*, 121-134.

(6) Shum, J.; Leung, P. K.-K.; Lo, K. K.-W. Luminescent Ruthenium(II) Polypyridine Complexes for a Wide Variety of Biomolecular and Cellular Applications. *Inorg. Chem.* **2019**, *58*, 2231-2247.

(7) Kalyanasundaram, K.; Grätzel, M. Applications of Functionalized Transition Metal Complexes in Photonic and Optoelectronic Devices. *Coord. Chem. Rev.* **1998**, *177*, 347-414.

(8) Wadman, S. H.; Kroon, J. M.; Bakker, K.; Havenith, R. W. A.; van Klink, G. P. M.; van Koten, G. Cyclometalated Organoruthenium Complexes for Application in Dye-Sensitized Solar Cells. Organometallics **2010**, *29*, 1569-1579.

(9) Ashford, D. L.; Glasson, C. R. K.; Norris, M. R.; Concepcion, J. J.; Keinan, S.; Brennaman, M. K.; Templeton, J. L.; Meyer, T. J. Controlling Ground and Excited State Properties through Ligand Changes in Ruthenium Polypyridyl Complexes. *Inorg. Chem.* **2014**, *53*, 5637-5646.

(10) Hissler, M.; El-ghayoury, A.; Harriman, A.; Ziessel, R. Fine-Tuning the Electronic Properties of Binuclear Bis(Terpyridyl)-Ruthenium(II) Complexes. *Angew. Chem., Int. Ed.* **1998**, *37*, 1717-1720.

(11) Duati, M.; Tasca, S.; Lynch, F. C.; Bohlen, H.; Vos, J. G.; Stagni, S.; Ward, M. D. Enhancement of Luminescence Lifetimes of Mononuclear Ruthenium(II)-Terpyridine Complexes by Manipulation of the Sigma-Donor Strength of Ligands. *Inorg. Chem.* **2003**, *42*, 8377-8384.

(12) Wang, X.; Guerzo, A.; Baitalik, S.; Simon, G.; Shaw, G. B.; Chen, L. X.; Schmehl, R. H. The Influence of Bridging Ligand Electronic Structure on the Photophysical

Properties of Noble Metal Diimine and Triimine Light Harvesting Systems. *Photosynth. Res.* **2006**, *87*, 83-103.

(13) Medlycott, E. A.; Hanan, G. S. Designing Tridentate Ligands for Ruthenium(II) Complexes with Prolonged Room Temperature Luminescence Lifetimes. *Chem. Soc*. *Rev*. **2005**, *34*, 133-142.

(14) Rudd, J. A.; Brennaman, M. K.; Michaux, K. E.; Ashford, D. L.; Murray, R. W.; Meyer, T. J. Synthesis, Electrochemistry, and Excited-State Properties of Three Ru(II) Quaterpyridine Complexes. *Phys. Chem. A* **2016**, *120*, 1845-1852.

(15) Campagna, S.; Puntoriero, F.; Nastasi, F.; Bergamini, G.; Balzani, V. Photochemistry and Photophysics of Coordination Compounds: Ruthenium. *Top. Curr. Chem.* **2007**, *280*, 117-214.

(16) Juris, A.; Balzani, V.; Barigelletti, F.; Campagna, S.; Belser, P.; Von Zelewsky, A. Ru(II) Polypyridine Complexes: Photophysics, Photochemistry, Eletrochemistry, and Chemiluminescence. *Coord. Chem. Rev.* **1988**, *84*, 85-277.

(17) Brown, D. G.; Sanguantrakun, N.; Schulze, B.; Schubert, U. S.; Berlinguette, C. P. Bis(tridentate) Ruthenium−Terpyridine Complexes Featuring Microsecond Excited-State Lifetimes. *J. Am. Chem. Soc.* **2012**, *134*, 12354-12357.

(18) Hofmeier, H.; Schubert, U. S. Recent Developments in the Supramolecular Chemistry of Terpyridine-Metal Complexes. *Chem. Soc. Rev.* **2004**, *33*, 373-399.

(19) Baranoff, E.; Collin, J.-P.; Flamigni, L.; Sauvage, J.-P. From Ruthenium(II) to Iridium(III): 15 Years of Triads Based on Bis-Terpyridine Complexes. *Chem. Soc. Rev.* **2004**, *33*, 147-155.

(20) Paul, A.; Bar, M.; Deb, S.; Baitalik, S. Long-Lived Trimetallic Complexes of Fe(II), Ru(II), and Os(II) Based on a Heteroditopic Bipyridine-Terpyridine Bridge: Synthesis, Photophysics, and Electronic Energy Transfer. *Inorg. Chem.* **2019**, *58*, 10065-10077.

(21) Deb, S.; Sahoo, A.; Pal, P.; Baitalik, S. Exploitation of the Second Coordination Sphere to Promote Significant Increase of Room-Temperature Luminescence Lifetime and Anion Sensing in Ruthenium-Terpyridine Complexes. *Inorg. Chem.* **2021**, *60*, 6836-6851.

(22) Mondal, D.; Bar, M.; Mukherjee, S.; Baitalik, S. Design of Ru(II) Complexes Based on Anthraimidazoledione-Functionalized Terpyridine Ligand for Improvement of Room-Temperature Luminescence Characteristics and Recognition of Selective Anions: Experimental and DFT/TD-DFT Study. *Inorg. Chem.* **2016**, *55*, 9707-9724.

(23) Maity, D.; Bhaumik, C.; Mondal, D.; Baitalik, S. Ru(II) and Os(II) Complexes Based on Terpyridyl-Imidazole Ligand Rigidly Linked to Pyrene: Synthesis, Structure, Photophysics, Electrochemistry, and Anion-Sensing Studies. *Inorg. Chem.* **2013**, *52*, 13941-13955.

(24) Mondal, D.; Biswas, S.; Paul, A.; Baitalik, S. Luminescent Dinuclear Ruthenium Terpyridine Complexes with a Bis-Phenylbenzimidazole Spacer. *Inorg. Chem.* **2017**, *56*, 7624-7641.

(25) Bar, M.; Deb, S.; Paul, A.; and Baitalik, S. Stimuli-Responsive Luminescent Bis-Tridentate Ru(II) Complexes Toward the Design of Functional Materials. *Inorg. Chem.* **2018**, *57*, 12010-12024.

(26) Ganguly, T.; Pal, P.; Maity, D.; Baitalik, S. Synthesis, Characterization and Emission Switching Behaviors of Styrylphenyl-Conjugated Ru(II)-Terpyridine Complexes via Aggregation and Trans-Cis Photoisomerization. *J. Photochem. Photobiol. A* **2023**, *440*, 114662.

(27) Karmakar, S.; Maity, D.; Mardanya, S.; Baitalik, S. Multichromophoric Bimetallic Ru(II) Terpyridine Complexes Based on Pyrenyl-bis-phenylimidazole Spacer: Synthesis, Photophysics, Spectroelectrochemistry, and TD-DFT Calculations. *Inorg. Chem.* **2014**, *53*, 12036-12049.

(28) Pal, P.; Mukherjee, S.; Maity, D.; Sujoy Baitalik Synthesis, Structural Characterization, and Luminescence Switching of Diarylethene-Conjugated Ru(II)-Terpyridine Complexes by Trans-Cis Photoisomerization: Experimental and DFT/TD-DFT Investigation. *Inorg. Chem.* **2018**, *57*, 5743-5753.

(29) Pal, P.; Ganguly, T.; Maity, D.; Baitalik, S. Experimental and Theoretical Exploration of Photophysics and Trans-Cis Photoisomerization of Styrylbenzene Conjugated Terpyridine Complexes of Ru(II): Strong Effect of Deprotonation from Second Coordination Sphere. *J. Photochem. Photobiol. A* **2020**, *392*, 112409.

(30) Wang, J.; Fang, Y. Q.; Hanan, G. S.; Loiseau, F.; Campagna, S. Synthesis and Properties of the Elusive Ruthenium(II) Complexes of 4′- cyano-2,2′:6′,2″-terpyridine. *Inorg. Chem.* **2005**, *44*, 5-7.

(31) Indelli, M. T.; Bignozzi, C. A.; Scandola, F.; Collin, J.-P. Design of Long-Lived Ru(II) Terpyridine MLCT States. Tricyano Terpyridine Complexes. *Inorg. Chem.* **1998**, *37*, 6084-6089.

(32) Kübel, J.; Schroot, R.; Wachtler, M.; Schubert, U. S.; Dietzek, B.; Jager, M. Photoredox-Active Dyads Based on a Ru(II) Photosensitizer Equipped with

Electron Donor or Acceptor Polymer Chains: A Spectroscopic Study of Light-Induced Processes Toward Efficient Charge Separation. *J. Phys. Chem. C* **2015**, *119*, 4742-4751.

(33) Maestri, M.; Armaroli, N.; Balzani, V.; Constable, E. C.; Thompson, A. M. W. C. Complexes of the Ruthenium(II)-2,2′:6′,2″- Terpyridine Family. Effect of Electron-Accepting and -Donating Substituents on the Photophysical and Electrochemical Properties. *Inorg. Chem.* **1995**, *34*, 2759-2767.

(34) Maity, D.; Das, S.; Mardanya, S.; Baitalik, S. Synthesis, Structural Characterization, and Photophysical, Spectroelectrochemical, and Anion-Sensing Studies of Heteroleptic Ruthenium(II) Complexes Derived from 4′-Polyaromatic-Substituted Terpyridine Derivatives and 2,6-Bis(benzimidazol-2-yl)pyridine. *Inorg. Chem.* **2013**, *52*, 6820-6838.

(35) Encinas, S.; Flamigni, L.; Barigelletti, F.; Constable, E. C.; Housecroft, C. E.; Schofield, E. R.; Figgemeier, E.; Fenske, D.; Neuburger, M., et al. Electronic Energy Transfer and Collection in Luminescent Molecular Rods Containing Ruthenium(II) and Osmium(II) 2,2′:6′,2″-Terpyridine Complexes Linked by Thiophene-2,5- diyl Spacers. *Chem. - Eur. J.* **2002**, *8*, 137-150.

(36) Dietrich, J.; Thorenz, U.; Förster, C.; Heinze, K. Effects of Sequence, Connectivity, and Counter Ions in New Amide-Linked $Ru(tpy)_2$-Re(bpy) Chromophores on Redox Chemistry and Photophysics. *Inorg. Chem.* **2013**, *52*, 1248-1264.

(37) Borg, O. A.; Godinho, S. S. M. C.; Lundqvist, M. J.; Lunell, S.; Persson, P. Computational Study of the Lowest Triplet State of Ruthenium Polypyridyl Complexes Used in Artificial Photosynthesis. *Phys. Chem. A* **2008**, *112*, 4470-4476.

(38) Sun, Q.; Dereka, B.; Vauthey, E.; Daku, L. M. L.; Hauser, A. Ultrafast Transient IR Spectroscopy and DFT Calculations of Ruthenium(II) Polypyridyl Complexes. *Chem. Sci.* **2017**, *8*, 223-230.

(39) Wadman, S. H.; Lutz, M.; Tooke, D. M.; Spek, A. L.; Hartl, F.; Havenith, R. W. A.; van Klink, G. P. M.; van Koten, G. Consequences of N,C,N- and C,N,N-Coordination Modes on Electronic and Photophysical Properties of Cyclometalated Aryl Ruthenium(II) Complexes. *Inorg. Chem.* **2009**, *48*, 1887-1900.

(40) Kreitner, C.; Erdmann, E.; Seidel, W. W.; Heinze, K. Understanding the Excited State Behavior of Cyclometalated Bis(tridentate)ruthenium(II) Complexes: A Combined Experimental and Theoretical Study. *Inorg. Chem.* **2015**, *54*, 11088-11104.

(41) Beley, M.; Collin, J.-P.; Louis, R.; Metz, B.; Sauvage, J.-P. 3,3',5,5'-Tetrapyridylbiphenyl: A Biscyclometalating Bridging Ligand with a High Coupling Ability in Ru^{III}, Ru^{II} Mixed Valence Systems. *J. Am. Chem. Soc.* **1991**, *113*, 8522-8524.

(42) Duati, M.; Fanni, S.; Vos, J. G. A New Luminescent Ru(terpy) Complex Incorporating a 1,2,4-Triazole Based σ-Donor Ligand. *Inorg. Chem. Commun.* **2000**, *3*, 68-70.

(43) Constable, E. C.; Dunne, S. J.; Rees, D. G. F.; Schmitt, C. X. Reversible Cyclometallation at a Ruthenium(II) Centre. *Chem. Commun.* **1996**, 1169.

(44) Barigelletti, F.; Ventura, B.; Collin, J.-P.; Kayhanian, R.; Gavin˜a, P.; Sauvage, J.-P. Electrochemical and Spectroscopic Properties of Cyclometallated and Non-Cyclometallated Ruthenium(II) Complexes Containing Sterically Hindering Ligands of the Phenanthroline and Terpyridine Families. *Eur. J. Inorg. Chem.* **2000**,113-119.

(45) Dikova, Y. M.; Yufit, D. S.; Williams, J. A. G. Platinum(IV) Complexes with Tridentate, NNC-Coordinating Ligands: Synthesis, Structures, and Luminescence. *Inorg. Chem.* **2023**, *62*, 1306-1322.

(46) Develay, S.; Blackburn, O.; Thompson, A. L.; Williams, J. A. G. Cyclometalated Platinum(II) Complexes of Pyrazole-Based, N^C^N-Coordinating, Terdentate Ligands: The Contrasting Influence of Pyrazolyl and Pyridyl Rings on Luminescence. *Inorg. Chem.* **2008**, *47*, 11129-11142.

(47) Wilkinson, A. J.; Goeta, A. E.; Foster, C. E.; Williams, J. A. G. Synthesis and Luminescence of a Charge-Neutral, Cyclometalated Iridium(III) Complex Containing N^C^N- and C^N^C-Coordinating Terdentate Ligands. *Inorg. Chem.* **2004**, *43*, 6513-6515.

(48) O'Regan, B.; Grätzel, M. A Low-Cost, High-Efficiency Solar-Cell Based on Dye-Sensitized Colloidal TiO_2 Films. *Nature* **1991**, *353*, 737-740.

(49) Nazeeruddin, M. K.; Baranoff, E.; Grätzel, M. Dye-Sensitized Solar Cells: A Brief Overview. *Solar Energy* **2011**, *85*, 1172-1178.

(50) Baranoff, E.; Jung, I.; Scopelliti, R.; Solari, E.; Grätzel, M.; Nazeeruddin, M. K. Room-Temperature Combinatorial Screening of Cyclometallated Iridium(III) Complexes for a Step Towards Molecular Control of Colour Purity. *Dalton Trans.* **2011**, *40*, 6860-6867.

(51) Meier, S. B.; Sarfert, W.; Junquera-Hernández, J. M.; Delgado M.; Tordera, D.; Ortí, E.; Bolink, H. J.; Kessler, F.; Scopelliti, R., et al. A Deep-Blue Emitting Charged Bis-Cyclometallated Iridium(III) Complex for Light-Emitting Electrochemical Cells. *J. Mater. Chem. C* **2013**, *1*, 58-68.

(52) Wadman, S. H.; Kroon, J. M.; Bakker, K.; Lutz, M.; Spek, A. L.; van Klink, G. P. M.; van Koten, G. Cyclometalated Ruthenium Complexes for Sensitizing Nanocrystalline TiO_2 Solar Cells. *Chem. Commun.* **2007**, 1907-1909.

(53) Wadman, S. H.; van Leeuwen, Y. M.; Havenith, R. W. A.; van Klink, G. P. M.; van Koten, G. A Redox Asymmetric, Cyclometalated Ruthenium Dimer: Toward Upconversion Dyes in Dye-Sensitized TiO_2 Solar Cells. *Organometallics* **2010**, *29*, 5635-5645.

(54) Wadman, S. H.; Havenith, R. W. A.; Hartl, F.; Lutz, M.; Spek, A. L.; van Klink, G. P. M.; van Koten, G. Redox Chemistry and Electronic Properties of 2,3,5,6-Tetrakis(2-pyridyl)pyrazine-Bridged Diruthenium Complexes Controlled by *N*,*C*,*N*′-BisCyclometalated Ligands. *Inorg. Chem.* **2009**, *48*, 5685-5696.

(55) Albrecht, M.; van Koten, G. Platinum Group Organometallics Based on "Pincer" Complexes: Sensors, Switches, and Catalysts. *Angew. Chem. Int. Ed.* **2001**, *40*, 3750-3781.

(56) Bomben, P. G.; Robson, K. C. D.; Sedach, P. A.; Berlinguette, C. P. On the Viability of Cyclometalated Ru(II) Complexes for Light-Harvesting Applications. *Inorg. Chem.* **2009**, *48*, 9631-9643.

(57) Koivisto, B. D.; Robson, K. C. D.; Berlinguette, C. P. Systematic Manipulation of the Light-Harvesting Properties for Tridentate Cyclometalated Ruthenium(II) Complexes. *Inorg. Chem.* **2009**, *48*, 9644-9652.

(58) Robson, K. C. D.; Bomben, P. G.; Berlinguette, C. P. Cycloruthenated Sensitizers: Improving the Dye-Sensitized Solar Cell with Classical Inorganic Chemistry Principles. *Dalton Trans.* **2012**, *41*, 7814-7829.

(59) Robson, K. C. D.; Koivisto, B. D.; Yella, A.; Sporinova, B.; Nazeeruddin, M. K.; Baumgartner, T.; Grätzel, M.; Berlinguette, C. P. Design and Development of Functionalized Cyclometalated Ruthenium Chromophores for Light-Harvesting Applications. *Inorg. Chem.* **2011**, *50*, 5494-5508.

(60) Wu, S.-H.; Burkhardt, S. E.; Zhong, Y.-W.; Abruña, H. D. Cyclometalated Ruthenium Oligomers with 2,3-Di(2-pyridyl)-5,6- diphenylpyrazine: A Combined

Experimental, Computational, and Comparison Study with Noncyclometalated Analogous. *Inorg. Chem.* **2012**, *51*, 13312-13320.

(61) Zhong, Y.-W.; Wu, S.-H.; Burkhardt, S. E.; Yao, C.-J.; Abruña, H. D. Mononuclear and Dinuclear Ruthenium Complexes of 2,3-Di-2-pyridyl-5,6-diphenylpyrazine: Synthesis and Spectroscopic and Electrochemical Studies. *Inorg. Chem.* **2011**, *50*, 517-524.

(62) Yao, C.-J.; Zhong, Y.-W.; Nie, H.-J.; Abruña, H. D.; Yao, J. Near-IR Electrochromism in Electropolymerized Films of a Biscyclometalated Ruthenium Complex Bridged by 1,2,4,5-Tetra(2-pyridyl)benzene. *J. Am. Chem. Soc.* **2011**, *133*, 20720-20723.

(63) Wang, H.; Shao, J.-Y.; Duan, R.; Wang, K.-Z. Zhong, Y.-W. Synthesis and Electronic Coupling Studies of Cyclometalated Diruthenium Complexes Bridged by 3,3',5,5'-Tetrakis(benzimidazol-2-yl)-Biphenyl. *Dalton Trans.* **2021**, *50*, 4219-4230.

(64) Shao, J.-Y.; Yang, W.-W.; Yao, J.; Zhong, Y.-W. Biscyclometalated Ruthenium Complexes Bridged by 3,3′,5,5′-Tetrakis(N-methylbenzimidazol-2-yl)biphenyl: Synthesis and Spectroscopic and Electronic Coupling Studies. *Inorg. Chem.* **2012**, *51*, 4343-4351.

(65) Kreitner, C.; Heinze, K. Excited State Decay of Cyclometalated Polypyridine Ruthenium Complexes: Insight from Theory and Experiment. *Dalton Trans.* **2016**, *45*, 13631-13647.

(66) Kreitner, C.; Heinze, K. The Photochemistry of Mono- and Dinuclear Cyclometalated Bis(Tridentate)Ruthenium(II) Complexes: Dual Excited State Deactivation and Dual Emission. *Dalton Trans.* **2016,** *45*, 5640-5658.

(67) Kreitner, C.; Mengel, A. K. C.; Lee, T. K.; Cho, W.; Char, K.; Kang, Y. S.; Heinze, K. Strongly Coupled Cyclometalated Ruthenium Triarylamine Chromophores as Sensitizers for DSSCs. *Chem. Eur. J.* **2016**, *22*, 8915-8928.

(68) Zeng, L.; Gupta, P.; Chen, Y.; Wang, E.; Ji, L.; Chao, H.; Chen, Z.-S. The Development of Anticancer Ruthenium(II) Complexes: From Single Molecule Compounds to Nanomaterials. *Chem. Soc. Rev.* **2017**, *46*, 5771-5804.

(69) Cutillas, N.; Yellol, G. S.; de Haro, C.; Vicente, C.; Rodríguez, V.; Ruiz, J. Anticancer Cyclometalated Complexes of Platinum Group Metals and Gold. *Coord. Chem. Rev*. **2013**, *257*, 2784-2797.

(70) Sauvage, J.-P.; Collin, J.-P.; Chambron, J.-C.; Guillerez, S.; Coudret, C.; Balzani,V.; Barigelletti, F.; De Cola, L.; Flamigni, L. Ruthenium(II) and Osmium(II) Bis(terpyridine) Complexes in Covalently-Linked Multicomponent Systems: Synthesis, Electrochemical Behavior, Absorption Spectra, and Photochemical and Photophysical Properties. *Chem. Rev.* **1994**, *94*, 993-1019.

(71) Flamigni, L.; Barigelletti, F.; Armaroli, N.; Ventura, B.; Collin, J.-P.; Sauvage, J.-P.; Williams, J. A. G. Triplet-Triplet Energy Transfer between Porphyrins Linked via a Ruthenium(II) Bisterpyridine Complex. *Inorg. Chem.* **1999**, *38*, 661-667.

(72) Pal, A. K.; Hanan, G. S. Design, Synthesis and Excited-State Properties of Mononuclear Ru(II) Complexes of Tridentate Heterocyclic Ligands. *Chem. Soc. Rev.* **2014**, *43*, 6184- 6197.

(73) Medlycott, E. A.; Hanan, G. S. Synthesis and Properties of Mono- and Oligo-Nuclear Ru(II) Complexes of Tridentate Ligands: The Quest for Long-Lived Excited States at Room Temperature. *Coord. Chem. Rev.* **2006**, *250*, 1763-1782.

(74) Rajalakshmanan, E.; Alexander, V. Synthesis, Luminescence, and Electrochemical Studies of Tris(homoleptic) Ruthenium(II) and Osmium(II) Complexes of 6′-Tolyl-2,2′:4′,2″-terpyridine. *Inorg. Chem*. **2007**, *46*, 6252-6260.

(75) Bhaumik, C.; Das, S.; Saha, D.; Dutta, S.; Baitalik, S. Synthesis, Characterization, Photophysical, and Anion-Binding Studies of Luminescent Heteroleptic Bis-Tridentate Ruthenium(II) Complexes Based on 2,6-Bis(Benzimidazole-2-yl)Pyridine and 4'-Substituted 2,2':6',2'' Terpyridine Derivatives. *Inorg. Chem.* **2010**, *49*, 5049-5062.

(76) Frisch, M. J.; Trucks, G. W.; Schlegel, H. B.; Scuseria, G. E.; Robb, M. A.; Cheeseman, J. R.; Scalmani, G.; Barone, V.; Mennucci, B.; Petersson, G. A., et al. Gaussian 09, revision A.02; Gaussian Inc.: Wallingford, CT, **2009**.

(77) Becke, A. D. Density Functional Thermochemistry. III. The Role of Exact Exchange. *J. Chem. Phys.* **1993**, *98*, 5648-5652.

(78) Lee, C. T.; Yang, W. T.; Parr, R. G. Development of the Colle-Salvetti Correlation-Energy Formula into a Functional of the Electron Density. *Phys. Rev. B* **1988**, *37*, 785-789.

(79) (a) Andrae, D.; Haeussermann, U.; Dolg, M.; Stoll, H.; Preuss, H. Energy-Adjusted ab initio Pseudopotentials for the Second and Third Row Transition Elements. *Theor. Chim. Acta.* **1990**, *77*, 123-141. (b) Fuentealba, P.; Preuss, H.; Stoll, H.;

Szentpaly, L. V. A Proper Account of Core-Polarization with Pseudopotentials: Single Valence-Electron Alkali Compounds. *Chem. Phys. Lett.* **1989**, *89*, 418-422.

(80) Hay, P. J.; Wadt, W. R. Ab initio Effective Core Potentials for Molecular Calculations. Potentials for K to Au Including the Outermost Core Orbitals. *J. Chem. Phys.* **1985**, *82*, 299-310.

(81) Casida, M. E.; Jamorski, C.; Casida, K. C.; Salahub, D. R. Molecular Excitation Energy to High-Lying Bound State from Time-Dependent Density Functional Response Theory: Characterization and Correction of the Time Dependent Local Density Approximation Ionization Threshold. *J. Chem. Phys.* **1998**, *108*, 4439-4449.

(82) Stratmann, R. E.; Scuseria, G. E.; Frisch, M. J. An Efficient Implementation of Time Dependent Density-Functional Theory for the Calculation of Excitation Energies of Large Molecules. *J. Chem. Phys.* **1998**, *109*, 8218-8224.

(83) Walters, V. A.; Hadad, C. M.; Thiel, Y.; Colson, S. D.; Wiberg, K. B.; Johnson, P. M.; Foresman, J. B. Assignment of the A State in Bicyclobutane. The Multiphoton Ionization Spectrum and Calculations of Transition Energies. *J. Am. Chem. Soc.* **1991**, *113*, 4782-4791.

(84) (a) Tomasi, J.; Mennucci, B.; Cammi, R. Quantum Mechanical Continuum Solvation Models. *Chem. Rev.* **2005**, *105*, 2999-3094. (b) Cossi, M.; Scalmani, G.; Rega, N.; Barone, V. New Developments in the Polarizable Continuum Model for Quantum Mechanical and Classical Calculations on Molecules in Solution. *J. Chem. Phys.* **2002**, *117*, 43-54.

(85) Caricato, M.; Mennucci, B.; Tomasi, J.; Ingrosso, F.; Cammi, R.; Corni, S.; Scalmani, G. Formation and Relaxation of Excited States in Solution: A New Time Dependent Polarizable Continuum Model Based on Time Dependent Density Functional Theory. *J. Chem. Phys.* **2006**, *124*, 124520-124530.

(86) Mennucci, B.; Cappelli, C.; Guido, C. A.; Cammi, R.; Tomasi, J. Structures and Properties of Electronically Excited Chromophores in Solution from the Polarizable Continuum Model Coupled to the Time-Dependent Density Functional Theory. *J. Phys. Chem. A* **2009**, *113*, 3009.

(87) Dennington, R. II.; Keith T.; Millam, J. Gauss View 3; Semichem, Inc.: Shawnee Mission, KS, **2007**.

(88) O Boyle, N. M.; Tenderholt, A. L.; Langner, K. M. cclib: A Library for Package Independent Computational Chemistry Algorithms. *J. Comput. Chem.* **2008**, *29*, 839.

(89) SAINT (version 6.02), SADABS (version 2.03); Bruker AXS Inc.: Madison, WI, (**2002**).

(90) Sheldrick, G. M. SHELXT - Integrated Space-Group and Crystal-Structure Determination. *Acta Cryst. A* **2015**, *71*, 3-8.

(91) Dolomanov, O. V.; Bourhis, L. J.; Gildea, R. J.; J. Howard, A. K.; Puschmann, H. J. A Complete Structure Solution, Refinement and Analysis Program. *Appl. Crystallogr.* **2009**, *42*, 339-341.

(92) Spek, A. L. Single-Crystal Structure Validation with the Program PLATON. *J. Appl. Cryst.* **2003**, *36*, 7-13.

(93) Macrae, C. F.; Sovago, I.; Cottrell, S. J.; Galek, P. T. A.; McCabe, P.; Pidcock, E.; Platings, M.; Shields, G. P.; Stevens, J. S., et al. Mercury 4.0: From Visualization to Analysis, Design and Prediction. *J. Appl. Crystallogr.* **2020**, *53*, 226-235.

(94) Gille, K.; Knoll, H.; Quitzsch, K. Rate constants of the thermal cis-trans isomerization of azobenzene dyes in solvents, acetone/water mixtures, and in microheterogeneous surfactant solutions. *Int. J. Chem. Kinet.* **1999**, *31*, 337-350.

(95) Otsuki, J.; Suwa, K.; Narutaki, K.; Sinha, C.; Yoshikawa, I.; Araki, K. Photochromism of 2-(phenylazo)imidazoles. *J. Phys. Chem A* **2005**, *109*, 8064-8069.

(96) Meyer, T. J. Photochemistry of Metal Coordination Complexes: Metal to Ligand Charge Transfer Excited States. *Pure Appl. Chem.* **1986**, *58*, 1193-1206.

Chapter 3

Design of Near Infrared Emissive Molecular Switches Based on Stilbene-Appended Cyclometalated Bimetallic Ru(II)-Terpyridine Complexes

3.1. Introduction

Design of molecular species capable of displaying near-infrared (NIR) phosphorescence has emerged as promising as well as challenging area of research because of their potential applications in diverse fields, viz. solar energy conversion, NIR light-emitting diodes, telecommunications, lasers, optical sensors and switches, night-vision-readable displays, and biological imaging.[1-12] It is noteworthy to mention that ~50% of the solar energy reaching the Earth is composed of NIR radiation. As this is invisible to the human eye and insignificantly interferes with biological tissues, NIR light is particularly advantageous for biological recognition and sensing.[8-12] Organic molecules have been extensively utilized for designing NIR emissive materials.[13-16] Despite offering the advantage of tunable structures, these organic chromophores often face several challenges such as susceptibility to photo-bleaching and a limited Stokes shifts.[6] To overcome this lacuna, transition metal complexes have emerged as a promising alternative for the design of NIR emissive materials.[17-22] Coordination of appropriate transition metal ions with suitable organic ligands offers rigid molecular architectures with well-defined geometries and desirable properties.[23-25] The physicochemical properties of the resulting metal-ligand assembly could further be modulated under the influence of suitable external stimuli.[26-28] Among diverse stimuli, light is particularly useful and advantageous as it offers exceptional control over spatial and temporal parameters, enabling precise system manipulation. Additionally, light is a clean and environmentally benign energy source, supporting sustainable technology development and stimulating green applications.[29-30] Molecular species that are capable to reversibly alter characteristic signal(s) (such as emission) among two or more distinct states upon exposure to specific wavelength(s) of light are of particular interest for the fabrication of potential photochemical molecular switches.[31-34] Hence, judicious incorporation of light-responsive motifs onto the molecular architecture allows precise modulation of their functionalities.[35-36]

Ru(II) complexes derived from polyheterocyclic ligands are found to be promising building blocks for the fabrication of effective molecular photoswitches because of their fascinating as well as tuneable photophysical properties.[37-40] In order to develop effective photo-molecular switches, the photoisomerization behavior of several Ru(II)-polypyridine complexes comprising of azo- and stilbene-motifs have already been extensively investigated.[41-54] Among them, systems based on terpyridine-type coordination motifs in combination with stilbene unit are relatively sparse compared to those of the bipyridine-

type coordinating units in combination with either stilbene or azo-units.[42-45,49] Our group has recently developed different types of emissive Ru(II)-terpyridine complexes appended with one or more stilbene units and thoroughly investigated their photo-isomerization behaviors.[55-58] However, most of the reported systems emit in the visible region (~610-700 nm).[43-48,55-58] Our target in this work is to design Ru(II)-terpyridine complexes capable of displaying emission in the NIR domain. A promising strategy for designing NIR-emissive Ru(II)-terpyridine complexes involves incorporation of carbanionic heteroaromatic units, particularly cyclometalating ligands, into the molecular framework, wherein the prototype N-N-N chelating unit of terpyridine is replaced by N-N-C or N-C-N coordinating motifs.[59-71] In Ru-tpy type complexes, the Ru center experiences weak ligand field, because of the distortion arising out of unfavorable bite angle imposed by terpyridine units. Consequently, most of the $Ru(tpy)_2$-type complexes are either non-emissive or weakly emissive at RT because of excited-state equilibrium between the radiative ^{3}MLCT state and the non-radiative ^{3}MC state.[72-73] Judicious incorporation of cyclometalating ligands with strong σ-donating properties often shifts the luminescent ^{3}MLCT state to lower energies and the ^{3}MC state to higher energies, thereby expanding the energy gap between these states.[74-76] This expanded ^{3}MLCT-^{3}MC energy gap stabilizes the luminescent ^{3}MLCT state and the resulting complexes become emissive at RT. Besides, according to the "energy gap law", reducing the energy gap between the emissive ^{3}MLCT state and the ground state brings about a significant red-shift of the emission maximum, pushing it into the NIR region.[77]

Aligned with our objective of designing NIR emissive molecular photoswitches, we herein synthesized and thoroughly characterized two bimetallic Ru(II) complexes of compositions $[(ttpy)Ru(tpvpt')Ru(ttpy)](ClO_4)_3$ and $[(ttpy)Ru(t'pvpvpt')Ru(ttpy)](ClO_4)_2$ (Chart 3.1). These complexes have been specifically designed by integrating cyclometalated coordinating motif(s) as well as phenylene-vinylene bridge onto their molecular architectures. The 4'-(p-Methylphenyl)-2,2':6',2"-terpyridine ligand (ttpy) has been widely utilized by different researchers for synthesizing achiral and rod-like architectures with various d-block metals. Notably, during the course of synthesis of ttpy, a positional isomer, namely 6'-tolyl-2,2':4"-terpyridine, is also produced as a minor product. We previously reported a series of Ru(II) monomers using this isomer as the cyclometalating ligand.[78] The present investigation aims to design two distinct bridging ligands, one asymmetric and the other one symmetric, to modulate the photo-redox properties in general and room temperature emission characteristics in particular, for the resulting complexes. The asymmetric ligand contains a single phenylene-vinylene unit

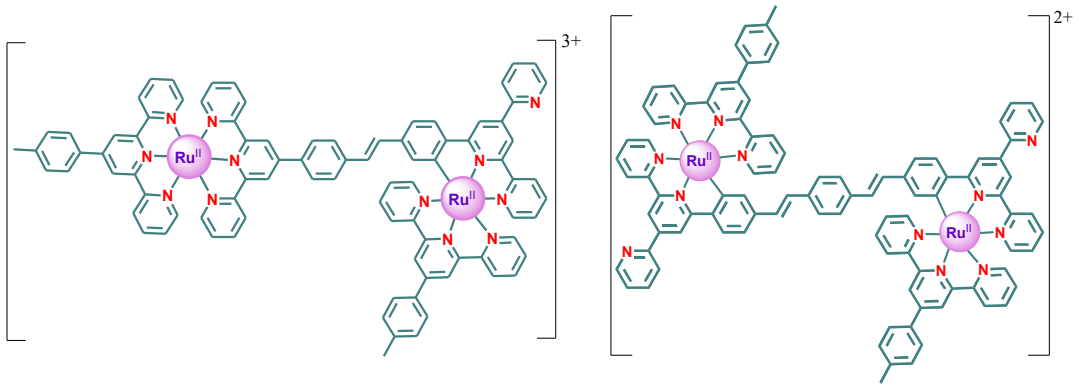

[(ttpy)Ru(tpvpt')Ru(ttpy)](ClO$_4$)$_3$ (**1**) [(ttpy)Ru(t'pvpvpt')Ru(ttpy)](ClO$_4$)$_2$ (**2**)

Chart 3.1. Molecular architectures of the complexes investigated in this study.

between two different terminal terpyridine-type motifs, featuring non-cyclometalated N-N-N- and cyclometalated N-N-C-chelating units (tpvpt'). On the other hand, the symmetric bridging ligand comprises of two consecutive phenylene-vinylene units attached to two terminal cyclometalated N-N-C-coordination units (t'pvpvpt'). The integration of strong σ-donating cyclometalating unit(s) along with phenylene-vinylene motifs in the bridging ligands widens the absorption spectral window across the entire visible domain and emission spectral window into NIR region. Moreover, the phenylene-vinylene units demonstrate reversible *trans*⇌*cis* photoisomerization with remarkable alteration in the absorption and emission spectral behaviors of the complexes. To the best of our knowledge, such NIR emissive cyclometalated Ru(II) complexes conjugated with photoisomerizable phenylene-vinylene units were not previously documented in the literature.

This work reports combined experimental and theoretical investigation of the photo-redox properties of the two Ru(II) dimers. These complexes feature non-coordinated nitrogen atom(s) at the cyclometalated sites in their outer coordination sphere, enabling scope for further modulation of their spectral characteristics through acid-base equilibria. Moreover, we have thoroughly investigated the photoisomerization behavior of these complexes in both of their free-form as well as in presence of acid to systematically regulate their rate of isomerization. One of the most intriguing aspects of this study is the substantial enhancement in the rate and quantum yield of photoisomerization in the presence of acid. Moreover, efficient "on-off" and "off-on" emission switching could be feasible via appropriate choice of external stimuli like acid, base, temperature or light of particular wavelengths. The "on-off" photo-switching properties of complexes involving heavier transition metals such as Re, Rh, Ir, Pt and Ru particularly those appended with azobenzene,

diarylethene, and stilbene moieties, have been extensively investigated by several research groups, including Yam, Phillips, Nishihara, Iha, Bozec, to name a few.[43,45,48,79-83] Table 3.1 provides representative examples of metal complexes that exhibit "on-off" photo-switching induced by either reversible *trans-cis* isomerization or electrocyclization. Most of the reported systems comprise either bpy- or tpy-type chelating units connected with isomerizable motif(s). Our group recently reported photoisomerization behaviors of a new array of Ru(II) complexes utilizing stilbene-appended terpyridine ligands, which display efficient "on-off" emission switching.[49,56-58,84] However, reports based on cyclometalated complexes of transition metals derived from stilbene-appended terpyridine ligands have not so far been reported in the literature. Recently, the group of Yam and Freixa demonstrated the photo-switching behavior of cyclometalated Pt(II) and Ir(III) complexes bearing dithienylethene and azobenzene units, respectively.[60,85] In contrary to the most of the reported systems, we demonstrated herein efficient and multi-stage "on-off" and "off-on" emission switching of two stilbene-appended Ru(II) dimers incorporating both cyclometalated and non-cyclometalated units.

Table 3.1. Representative Metal Complexes Exhibiting 'On-Off' Photo-Switching.

Compounds	Solvent	Irradiating wavelength	Ref.
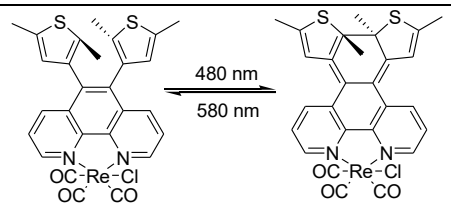	Benzene	480 nm (open→closed) 580 nm (closed→open)	79
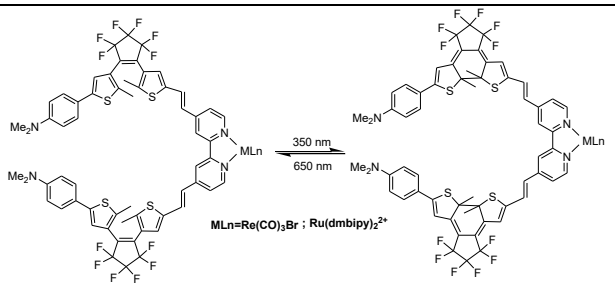	DCM	350 nm (open→closed) 650 nm (closed→open)	80

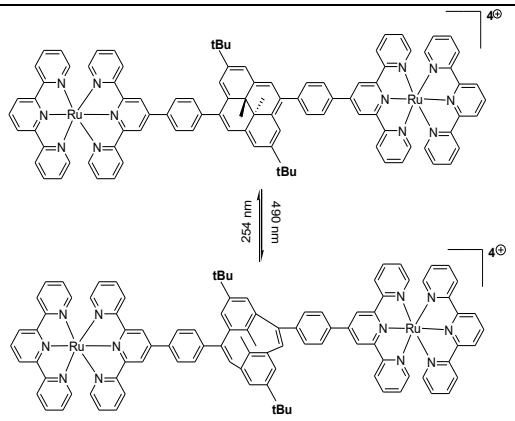	MeCN	490 nm (closed→open) 254 nm (open→closed)	81
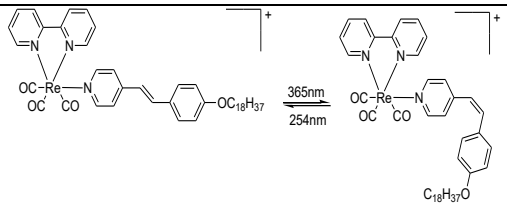	DCM	365 nm (*trans*→*cis*) 254 nm (*cis*→*trans*)	82
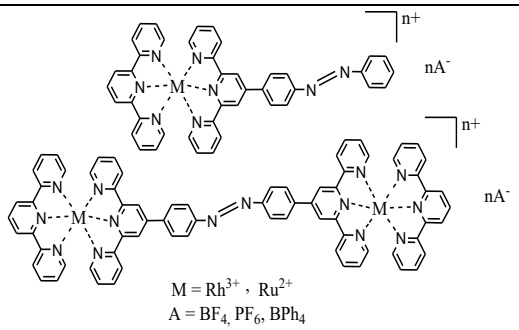	DMSO	366 nm (*trans*→*cis*) 430 nm (*cis*→*trans*)	45
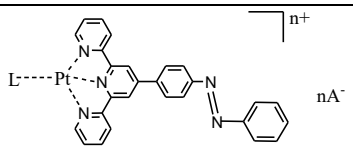	DMSO	366 nm (*trans*→*cis*) 430 nm/Δ (*cis*→*trans*)	43
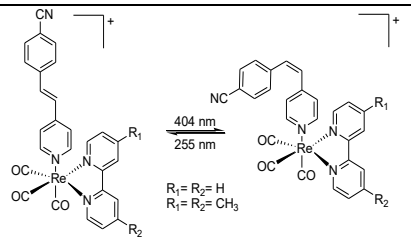	MeCN	404 nm (*trans*→*cis*) 255 nm (*cis*→*trans*)	48
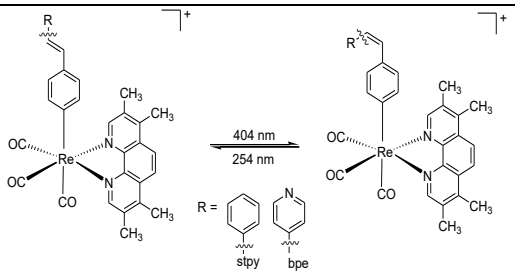	MeCN	404 nm (*trans*→*cis*) 254 nm (*cis*→*trans*)	83

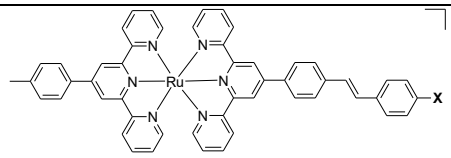	MeCN-DCM	280 nm (*trans*→*cis*) 500 nm/Δ (*cis*→*trans*) 500 nm (*trans*→*cis*) 280 nm (*cis*→*trans*)	56, 57
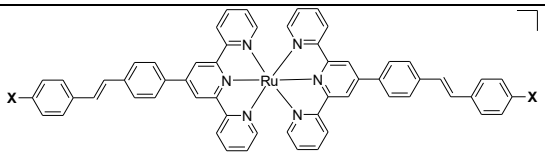	MeCN-DCM	280 nm (*trans*→*cis*) 500 nm (*cis*→*trans*)	49, 84
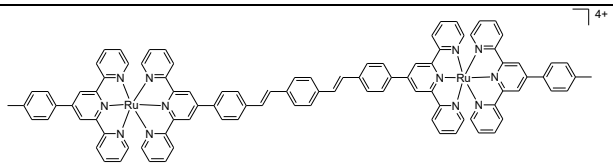	MeCN	500 nm (*trans*→*cis*) 270 nm (*cis*→*trans*)	58
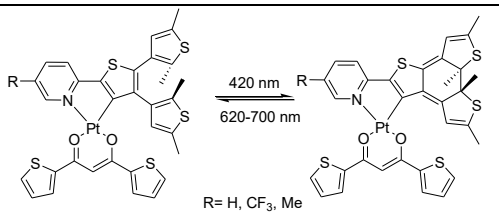	Benzene	420 nm (open→closed) 620-700 nm (closed→open)	60
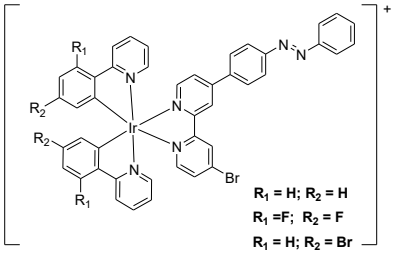	MeCN	336-351 nm (*cis*→*trans*)	85

3.2. Experimental Section

3.2.1. Materials. Both the phenylene-vinylene-substituted terpyridyl bridging ligands (tpvpt' and t'pvpvpt') as well as [Ru(ttpy)Cl_3] precursor is synthesized by following our reported literature procedures.[86-90]

3.2.2. Synthesis of the Ligands. The adopted synthetic procedures for the ligands are described below.

2-(4-(4-(4-(4,6-di(pyridine-2-yl)pyridine-2-yl)styryl)phenyl)-6-(pyridine-2-yl) pyridine-2-yl)pyridine (tpvpt'). A mixture of [6'-(Triphenylphosphoniummethylphenyl)-2,2':4',2"-terpyridine]Bromide (332 mg, 0.5 mmol) and 4'-(*p*-Formylphenyl)-2,2':6',2"-terpyridine (tpy-PhCHO) (169 mg, 0.5 mmol) was thoroughly dissolved in dry dichloromethane and was cooled to 0-5 °C under nitrogen protection. To the mixture, *t*-BuOK (0.12 g, 1.0 mmol) was added slowly and the resulting mixture was stirred

magnetically for ~12 h. The volume of the resulting solution was reduced and upon addition of methanol to it, a solid compound deposited. The crude compound was washed with water, dried in air and purified by silica gel column chromatography using 10:1 (v/v) $CHCl_3$-MeOH mixture. The compound was finally purified by recrystallization from $CHCl_3$-MeOH (1:2, v/v) mixture. Yield: 167 mg (52%). Anal. Calcd for $C_{44}H_{30}N_6$: C, 82.22; H, 4.70; N, 13.07. Found: C, 82.24; H, 4.66; N, 13.05. ^{1}H NMR (400 MHz, $CDCl_3$): δ/ppm 8.93 (s, 1H, $1H_{3a}$), 8.80 (s, 1H, $1H_{3b}$), 8.76 (s, 2H, $2H_{3''}$), 8.74-8.67 (m, 5H, $2H_3$+$2H_{3'}$+$1H_9$), 8.57 (d, 1H, *J*=16 Hz, $1H_{10}$), 8.33 (d, 1H, *J*=8 Hz, $1H_{6'}$), 8.23 (d, 2H, *J*=8 Hz, $2H_7$), 8.07 (t, 2H, *J*=8 Hz, $2H_6$), 7.98 (d, 1H, *J*=8 Hz, $1H_{6'}$), 7.89 (t, 4H, *J*=8 Hz, $2H_4$+$2H_{4'}$), 7.85 (d, 2H, *J*=8 Hz, $2H_8$), 7.74-7.71 (m, 2H, $2H_{11}$), 7.50-7.47 (m, 2H, $2H_{12}$), 7.42-7.34 (m, 4H, $2H_5$+$2H_{5'}$). Electrospray ionization mass spectrometry (ESI-MS) (positive, MeOH) *m/z*: 643.43 (52%) [**tpvpt'**+H]$^+$, 322.23 (100%) [**tpvpt'**+2H]$^{2+}$.

2-(6-(4-(4-(4-(4,6-di(pyridine-2-yl)pyridine-2-yl)styryl)styryl)phenyl)-4-(pyridine-2-yl)pyridine-2-yl)pyridine (t'pvpvpt'). A mixture of [6'-(Triphenylphosphonium methylphenyl)-2,2':4',2"-terpyridine]Bromide (664 mg, 1.0 mmol) and terephthaldehyde (67 mg, 0.5 mmol) was dissolved in dry dichloromethane and was cooled to 0-5 °C under nitrogen protection. To the mixture, *t*-BuOK (0.24 g, 2.0 mmol) was added slowly and the resulting mixture was stirred magnetically for ~12 h. The volume of the resulting solution was reduced by rotary evaporation and methanol was added to it for precipitation. The crude compound was washed with water, dried in air and purified by silica gel column chromatography using 10:1 (v/v) $CHCl_3$-MeOH mixture. The compound was finally purified by recrystallization from $CHCl_3$-MeOH (1:2, v/v) mixture. Yield: 179 mg (48%). Anal. Calcd for $C_{52}H_{36}N_6$: C, 83.85; H, 4.87; N, 11.28. Found: C, 83.82; H, 4.90; N, 11.24. ^{1}H NMR (400 MHz, $CDCl_3$): δ/ppm 8.93 (s, 2H, $2H_{3'}$), 8.83 (d, 2H, *J*=8 Hz, $2H_3$), 8.77-8.72 (m, 6H, $2H_3$+$4H_6$), 8.52 (s, 2H, $2H_{3''}$), 8.32 (d, 4H, *J*=8 Hz, $4H_7$), 8.08 (d, 2H, *J*=8 Hz, $2H_4$),7.96 (d, 2H, *J*=20 Hz, $2H_9$), 7.90 (t, 2H, *J*=8 Hz, $2H_4$), 7.84 (d, 2H, *J*=20 Hz, $2H_{10}$), 7.71 (d, 4H, *J*=8 Hz, $4H_8$), 7.60 (s, 4H, $4H_{11}$), 7.42-7.37 (m, 4H, $4H_5$). Electrospray ionization mass spectrometry (ESI-MS) (positive, MeOH) *m/z*: 745.39 (9%) [**t'pvpvpt'**+H]$^+$, 373.20 (100%) [**t'pvpvpt'**+2H]$^{2+}$, 249.14 (6%) [**t'pvpvpt'**+3H]$^{3+}$.

3.2.3. Synthesis of the Metal Complexes. The Ru(II)complexes are prepared by adopting a common synthetic protocol as described below.

[(ttpy)Ru(tpvpt')Ru(ttpy)](ClO$_4$)$_3$·2H$_2$O (1). A mixture of Ru(ttpy)Cl_3 (0.17 g, 0.32 mmol) and $AgBF_4$ (196 mg, 0.47 mmol) in 30 mL of Me_2CO was refluxed with

continuous stirring for 2h. After cooling down to room temperature, the precipitated AgCl was removed by filtration. 30 mL of 1-butanol was then added to the filtrate and residual Me_2CO was removed by rotary evaporation. To the resulting solution was added finely powdered tpvpt' ligand (96 mg, 0.15 mmol) and the mixture was refluxed under basic condition (NaOH) for 12 h with continuous stirring. After cooling, the solution was poured into aqueous solution of $NaClO_4 \cdot H_2O$ (1.5 g in 5 mL of water) when a reddish-purple colored precipitate appeared. The compound was filtered and purified by silica gel column chromatography using MeCN as the eluent. Upon rotary evaporation of the eluent to a small volume (~10 mL), a microcrystalline complex was formed, which was filtered and recrystallized from MeCN-MeOH (1:5, v/v) mixture. Yield: 161 mg (60%). Anal. Calcd for $C_{88}H_{67}N_{12}Ru_2O_2Cl_3O_{14}$: C, 58.04; H, 3.71; N, 9.23. Found: C, 58.08; H, 3.69; N, 9.25. ^{1}H NMR (400 MHz, CD_3CN) δ/ppm 9.13 (s, 1H, $1H_{3b}$), 9.02 (d, J = 8.1 Hz, 6H, $2H_{3a}$+$2H_{3d}$+$2H_{3e}$), 8.96 (s, 1H, $1H_{3c}$), 8.73-8.61 (m, 8H, $2H_6$+$2H_{6'}$+$2H_{6''}$+$1H_{12}$+$1H_{12'}$), 8.47 (d, J = 7.9 Hz, 1H, $1H_{9'}$), 8.21 (d, J = 8.1 Hz, 2H, $2H_{7'}$), 8.16-8.13 (m, 5H, $2H_7$+$2H_8$+$1H_{10}$), 8.09 (d, J = 8.1 Hz, 1H, $1H_{11'}$), 7.96 (t, J = 8.0 Hz, 5H, $2H_{4'}$+$2H_{4''}$+$1H_{14}$), 7.85 (t, J = 8.0 Hz, 2H, $2H_4$), 7.71 (d, J = 8.4 Hz, 2H, $2H_{8'}$), 7.62-7.56 (m, 8H, $2H_3$+$1H_9$+$1H_{10'}$+$1H_{18}$+$1H_{19}$+$1H_{20}$+$1H_{21}$), 7.45 (t, J = 6.1 Hz, 4H, $2H_{3'}$+$2H_{3''}$), 7.22-7.10 (m, 8H, $2H_5$+$2H_{5'}$+$2H_{5''}$+$1H_{11}$+$1H_{15}$), 6.95 (d, 1H, J=15.0 Hz, $1H_{16}$), 6.87 (d, 1H, J=15.0 Hz, $1H_{17}$), 6.13 (s, 1H, $1H_{13}$), 2.39 (s, 3H, -CH_3), 2.21 (s, 3H, -CH_3). ^{13}C NMR (400 MHz, CD_3CN): δ/ppm 184.34, 163.51, 158.27, 158.24, 157.30, 156.58, 155.45, 155.38, 154.36, 153.97, 153.44, 152.44, 150.83, 150.75, 150.27, 148.36, 147.52, 147.12, 145.04, 141.23, 141.07, 139.66, 139.61, 138.03, 137.75, 137.44, 136.89, 135.43, 135.22, 134.81, 133.91, 133.60, 130.73, 130.31, 130.22, 128.02, 127.68, 127.46, 127.42, 127.38, 127.26, 126.05, 124.82, 124.51, 123.38, 123.12, 121.50, 121.38, 121.15, 119.96, 119.87, 116.58, 115.47, 20.43. Electrospray ionization mass spectrometry (ESI-MS) (positive, MeCN) m/z=497.13 (100%) $[(ttpy)Ru(tpvpt')Ru(ttpy)]^{3+}$, m/z=373.10 (35%) $[(ttpy)Ru(tpvpt'H)Ru(ttpy)]^{4+}$.

$[(ttpy)Ru(t'pvpvpt')Ru(ttpy)](ClO_4)_2.3H_2O$ (2). Yield: 169 mg (63%). Anal. Calcd for $C_{96}H_{74}N_{12}Ru_2Cl_2O_{11}$: C, 62.50; H, 4.04; N, 9.11. Found: C, 62.45; H, 4.08; N, 9.13. ^{1}H NMR (400 MHz, CD_3CN) δ/ppm 9.09 (s, 2H, $2H_{3b}$), 8.94 (s, 4H, $4H_{3a}$), 8.89 (s, 2H, $2H_{3c}$), 8.67-8.58 (m, 8H, $4H_6$+$2H_{12}$+$2H_{12'}$), 8.43 (d, J = 8.0 Hz, 2H, $2H_{9'}$), 8.15-8.09 (m, 6H, $4H_7$+$2H_{11'}$), 8.01-7.89 (m, 4H, $2H_{14}$+$2H_{10}$), 7.79 (t, J = 7.8 Hz, 4H, $4H_4$), 7.59-7.51 (m, 12H, $4H_3$+$4H_8$+$2H_9$+$2H_{10'}$), 7.17 (s, 4H, $4H_{18}$), 7.15-6.99 (m, 8H, $4H_5$+$2H_{11}$+$2H_{15}$), 6.68 (d, 2H, J=16.0 Hz, $2H_{16}$), 6.63 (d, 2H, J=16.0 Hz, $2H_{17}$), 5.97 (s,

2H, $2H_{13}$), 2.55 (s, 6H, $-CH_3$). ^{13}C NMR (400 MHz, CD_3CN): δ/ppm 184.08, 163.52, 157.24, 156.56, 154.25, 153.95, 153.38, 150.82, 150.67, 150.24, 146.45, 144.98, 141.09, 139.57, 137.68, 137.39, 137.20, 136.61, 135.18, 134.71, 132.99, 130.17, 128.37, 128.11, 127.21, 126.53, 126.02, 125.97, 124.72, 124.46, 123.34, 123.05, 121.43, 119.82, 116.41, 115.30, 20.45. Electrospray ionization mass spectrometry (ESI-MS) (positive, MeCN) *m/z*=796.25 (100%) [(ttpy)Ru(t'pvpvpt')Ru (ttpy)]$^{2+}$, *m/z*=531.17 (65%) [(ttpy)Ru(Ht'pvpvpt')Ru(ttpy)]$^{3+}$ and *m/z*=398.62 (41%) [(ttpy)Ru(Ht'pvpvpt'H)Ru (ttpy)]$^{4+}$.

Caution! Perchlorate salts of the metal complexes are potentially explosive and therefore should be handled in small quantities with care.

3.2.4. Instruments and Physical Methods. The details of different equipment used and experimental process to measure absorption and luminescence spectral behavior as well as computational studies using DFT and TD-DFT methods have already been discussed in chapter 2.

3.2.5. Determination of *Trans-Cis* Photoisomerization Quantum Yields. A 1 cm light path length quartz cell was used for the photoisomerization measurements. The concentration of the complexes was maintained in the range of 2×10^{-6} M- 4×10^{-6} M, and the solution was thoroughly degassed with N_2 before photoirradiation and stirred magnetically during *trans*-to-*cis* isomerization. Isomerization studies were carried out in photocatalytic reactor (Model No: 66901) designed by Newport corporation, USA. Light of specific wavelengths were isolated using band pass filters of 280 and 500 nm. The rate constant of the isomerization process was evaluated from the absorbance titration data using equation (1).[91]

$$\ln\{(A_0 - A_f)/(A_t - A_f)\} = k_{iso}t \quad (1)$$

where A_0, A_t, and A_f is the absorbance of the free receptor, after time t, and at the conclusion of the reaction. K_{iso} is the rate constant of isomerization and t is the required time for the completion of the isomerization process. Both k_{iso} and A_f were estimated by nonlinear least-square method. The intensity of the light source was ~0.11 W. Quantum yields (φ) of the isomerization process were obtained by using the following equation,[92]

$$\nu = (\varphi I_0/V)(1-10^{-Abs})$$

where *v* is the rate of the *trans-to-cis* isomerization, I_0 is the photon flux at the front of the cell, V is the volume of the solution, and Abs is the initial absorbance at the irradiation wavelength.

3.3. Results and Discussion

3.3.1. Synthesis and Characterization. The metal complexes were prepared according to a method previously described by our group.[86] Subsequent purification of the final products was achieved through column chromatography followed by recrystallization technique. The compounds were appropriately characterized using elemental analysis (C, H, and N), ^{1}H, {^{1}H-^{1}H} COSY, ^{13}C NMR and ESI mass spectrometry.

3.3.2. NMR Spectra. The ^{1}H and {^{1}H-^{1}H} COSY NMR spectra of complex **1** and **2** are presented in Figures 3.1 and 3.2. Tentative assignment of all the proton resonances in the complexes was made with the help of their {^{1}H-^{1}H} COSY NMR spectra, relative areas of peaks, usual chemical shifts and coupling constants of the protons. Due to asymmetric nature of complex **1**, the H_{3a}, H_{3b}, H_{3c}, H_{3d} and H_{3e} protons mostly appear as singlet in the downfield region of 9.12-8.97 ppm. The olefinic protons (H_{16} and H_{17}) appearing as two closely situated doublets having the coupling constant (*J*) of 16 Hz, lie in the range of 7.02-6.87 ppm. The coupling constant clearly suggests that the complex adopts *trans* configuration. The H_{13} proton adjacent to the cyclometalating carbon is observed as a singlet in the most up-field region at 6.13 ppm. In contrast, complex **2**, being symmetrical, exhibits fewer proton signals compared to **1**. The sharp singlets for H_{3a}, H_{3b} and H_{3c} protons again lie in the most downfield region of 9.08-8.88 ppm. The olefinic protons (H_{16} and H_{17}) get more up-field shifted compared to **1**, probably due to the two adjacent cyclometalating

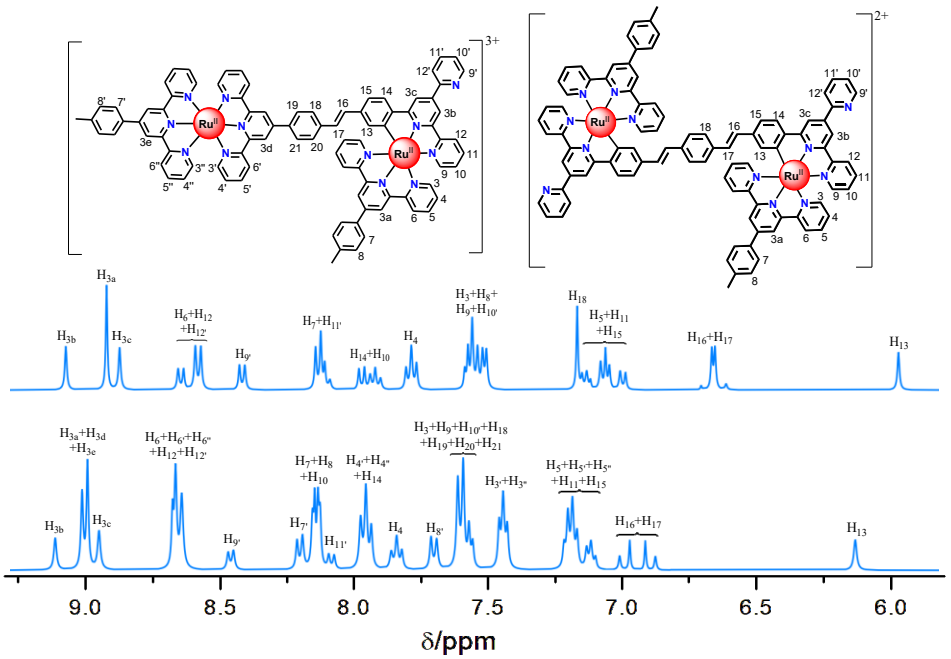

Figure 3.1. ^{1}H NMR spectra of **1** and **2** in CD_3CN.

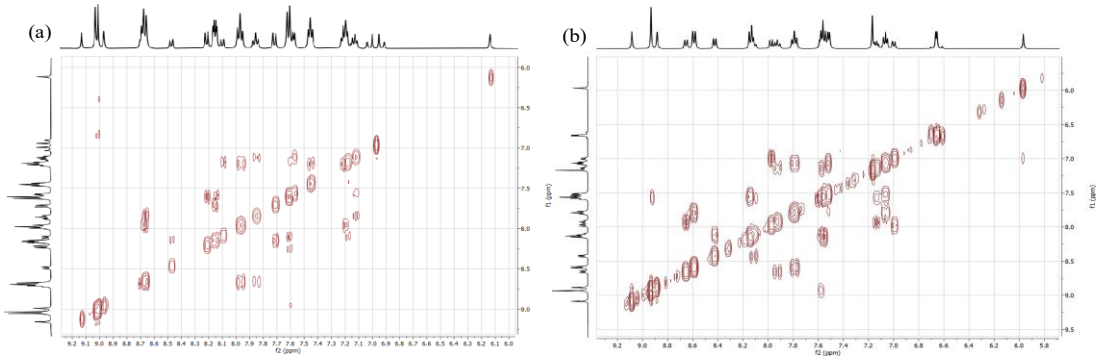

Figure 3.2. {^{1}H-^{1}H} COSY NMR spectrum of **1** (a) and **2** (b) in CD_3CN.

units. Their *J* value of 16 Hz again indicates that complex **2** exists in the *trans-trans* (*t-t*) orientation. The H_{13} protons next to the carbanionic centers appear as a singlet at 5.97 ppm. In order to locate the carbanionic center in the complexes, we also acquired their ^{13}C NMR spectra in CD_3CN (Figure 3.3). Both complexes display a characteristic signal in the most down-field region {at δ=184.34 ppm (**1**) and δ=184.03 ppm (**2**)}, which clearly indicates the presence of Ru-C bond within the complex framework.

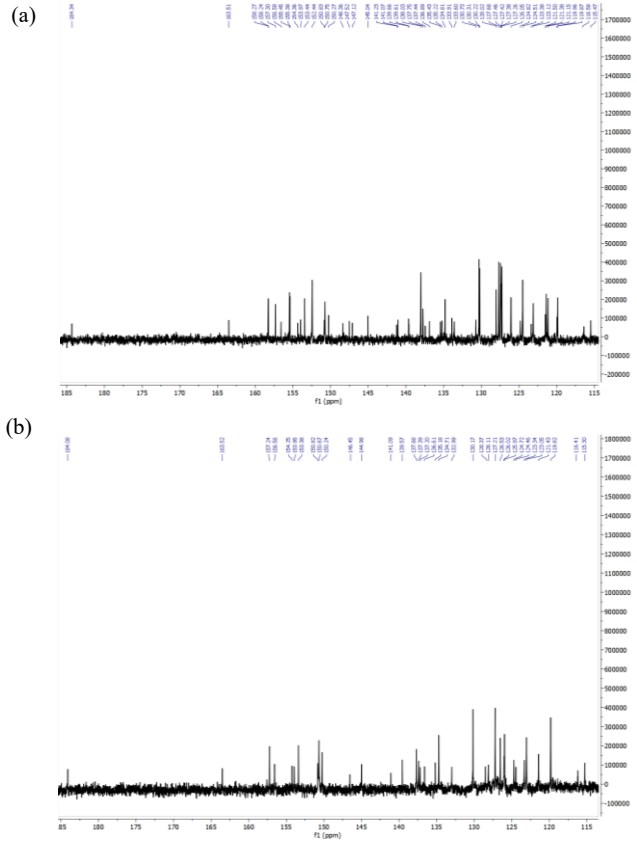

Figure 3.3. ^{13}C NMR spectrum of **1** (a) and **2** (b) in CD_3CN.

3.3.3. Mass Spectra. The ESI mass spectra of **1** and **2** in MeCN along with the simulation of the peaks are portrayed in Figure 3.4. The correlation among the experimental and simulated spectra is found to be good in all cases. Complex **1** displays two peaks, while three peaks are observed for **2** in the positive *m/z* region. For **1**, the most abundant peak at *m/z*=497.13, separated by 0.33 Da, corresponds to the tri-positive cation, [(ttpy)Ru (tpvpt')Ru(ttpy)]$^{3+}$. Another peak at *m/z*=373.10 corresponds to tetra-positive cation, [(ttpy)Ru(tpvpt'H)Ru (ttpy)]$^{4+}$, as the separation among consecutive isotopic lines is found to be 0.25 Da. The most abundant peak for **2** that appears at *m/z*=796.25 indicates the presence of a di-positive cation, [(ttpy)Ru(t'pvpvpt')Ru(ttpy)]$^{2+}$. Another intense peak at *m/z*=531.17 with a separation of 0.33 Da among the consecutive isotopic lines, corresponds to a tri-positive cation, [(ttpy)Ru(Ht'pvpvpt')Ru(ttpy)]$^{3+}$. The weak peak at *m/z*=398.62 corresponds to tetra-positive cation, [(ttpy)Ru(Ht'pvpvpt'H)Ru(ttpy)]$^{4+}$.

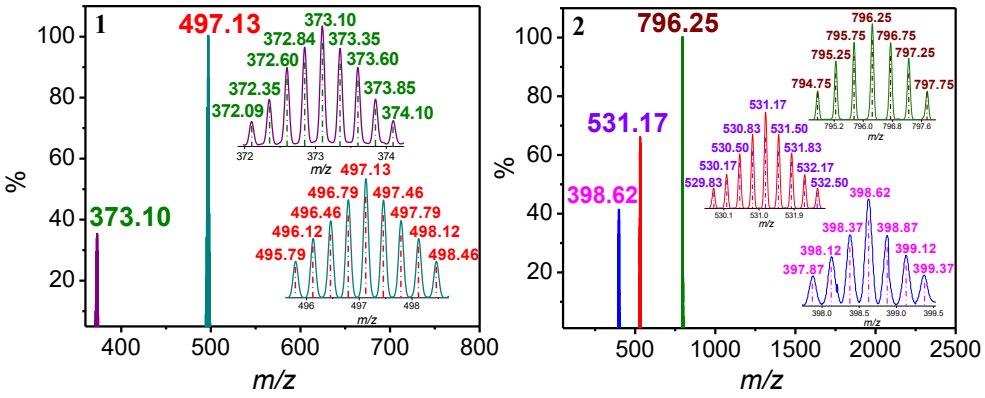

Figure 3.4. ESI-MS (positive) spectra of **1** and **2** in MeCN, with insets displaying the observed and simulated isotopic distribution patterns of the complex cations.

3.3.4. Theoretical Calculations. Computational studies for both complexes were performed using density functional theory (DFT) and time-dependent (TD)-DFT. The ground state optimized geometries are displayed in Figure 3.5. The frontier molecular orbitals and their compositions are illustrated in Figures 3.6 and 3.7 and detailed in Table 3.2. The HOMOs are primarily localized on the ruthenium centers and, to a lesser extent, on the cyclometalated (N-N-C) site. The LUMOs are predominantly localized across the terpyridine- and phenylene-vinylene units. TD-DFT calculations are employed for accurate assignment of the experimental absorption spectral bands, while Unrestricted Kohn-Sham (UKS) calculations are executed directly on the triplet state of the complexes to get insight about their luminescence spectral behavior.

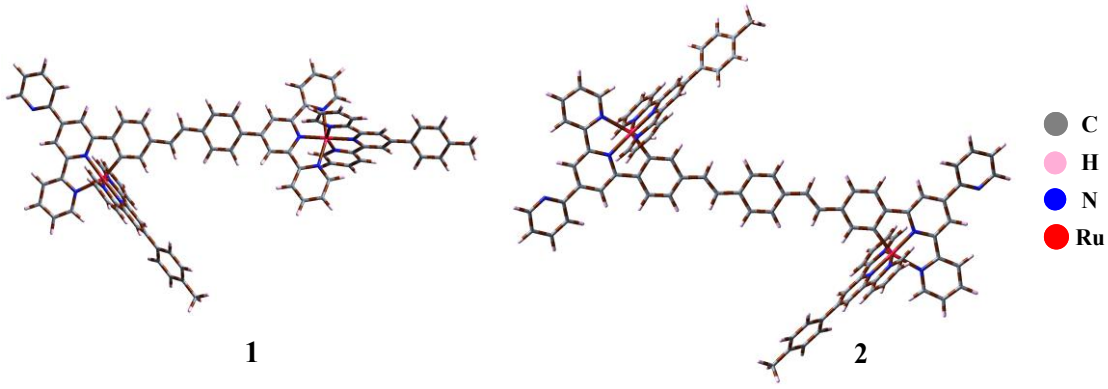

Figure 3.5. Ground state optimized geometries of **1** and **2** in acetonitrile.

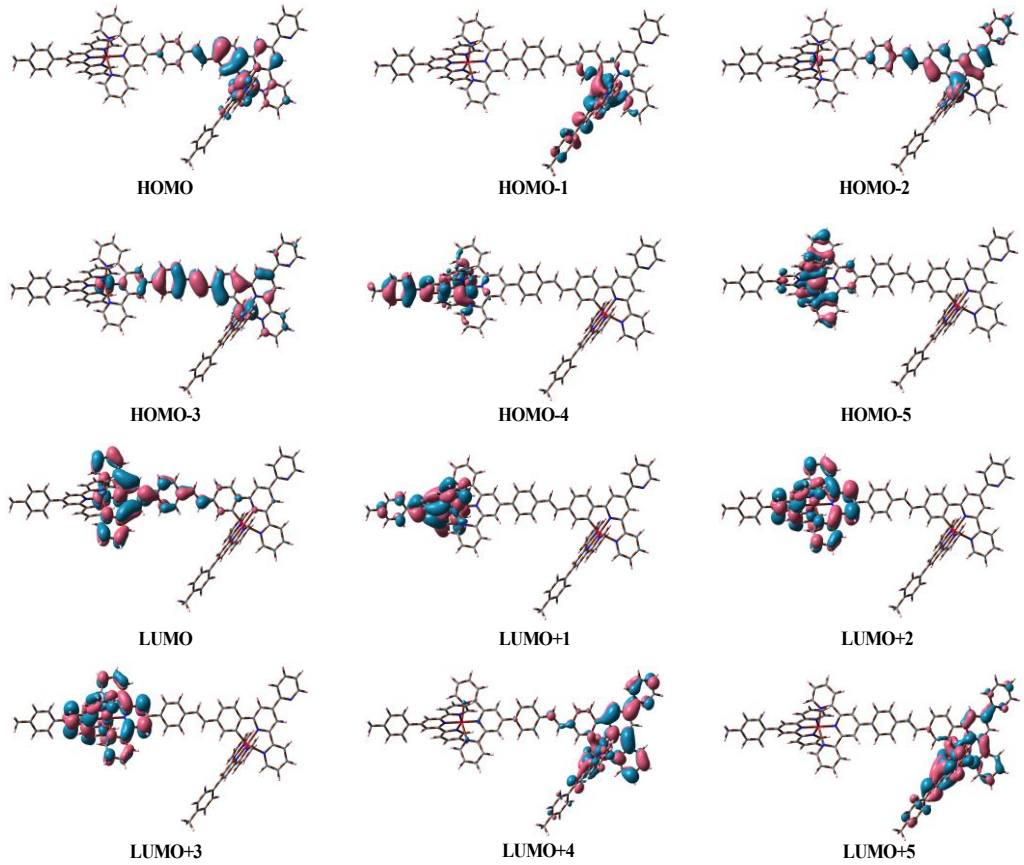

Figure 3.6. Schematic drawings of the selective frontier molecular orbitals of **1** in acetonitrile.

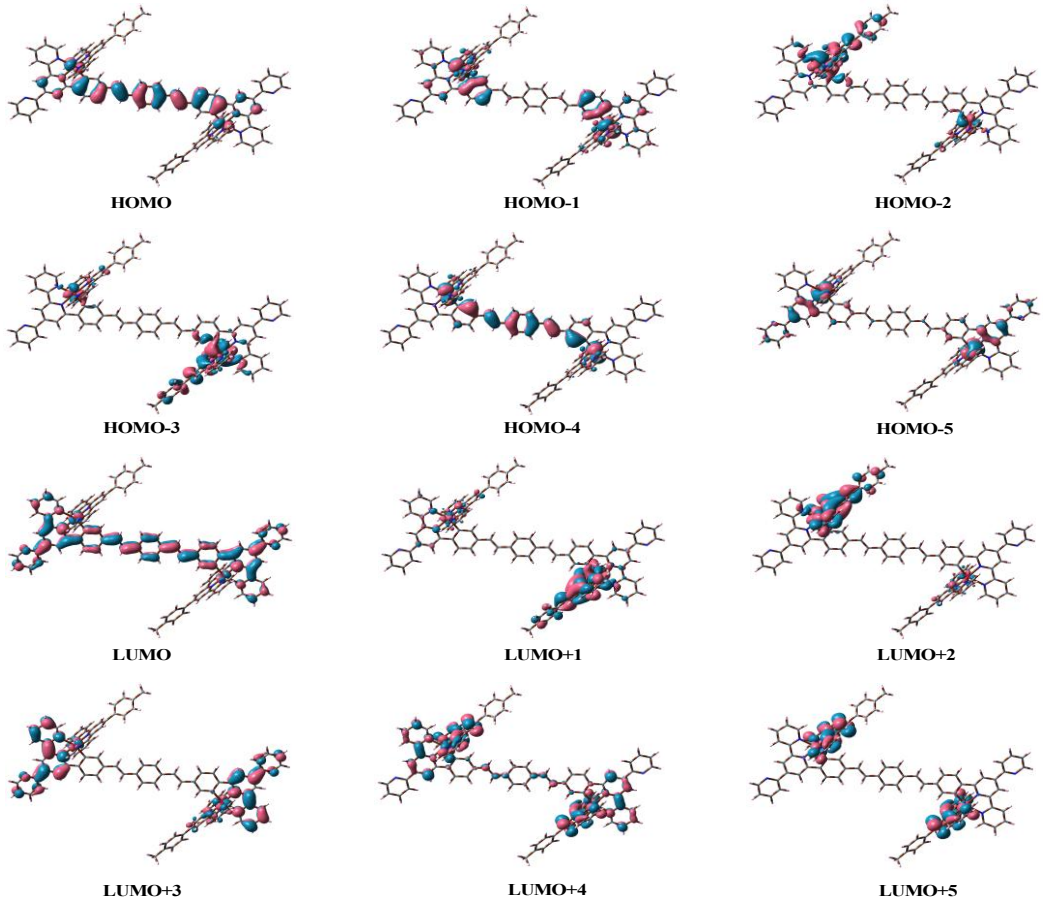

Figure 3.7. Schematic drawings of the selective frontier molecular orbitals of **2** in acetonitrile.

Table 3.2. Selected MOs along with their Energies and Compositions in the Ground State for **1** in MeCN.

	1											
	Energy/eV		% Compositions									
	trans	*cis*	*trans*					*cis*				
			Ru	mpt	N,N,N-tpy	N,N,C-tpy	pvp	Ru	mpt	N,N,N-tpy	N,N,C-tpy	pvp
LUMO+5	-2.30	-2.30	11.91	63.05	0.92	21.44	2.68	13.36	81.91	0.08	3.55	1.09
LUMO+4	-2.31	-2.30	8.58	21.78	2.74	60.94	5.96	7.14	1.92	1.39	84.72	4.83
LUMO+3	-2.43	-2.44	3.11	53.76	42.82	0.00	0.30	3.11	54.69	41.91	0.00	0.29
LUMO+2	-2.51	-2.52	0.01	44.68	54.94	0.00	0.36	0.02	43.78	55.84	0.00	0.36
LUMO+1	-2.67	-2.68	7.86	90.60	1.51	0.00	0.02	7.84	90.02	2.04	0.00	0.09
LUMO	-2.74	-2.73	7.70	1.52	74.57	1.64	14.57	7.82	2.13	78.01	0.80	2.13
HOMO	-5.29	-5.29	50.22	9.65	0.35	9.93	29.84	53.26	12.67	0.02	8.84	12.67
HOMO-1	-5.32	-5.33	60.20	29.00	0.00	5.15	5.65	59.73	25.94	0.00	6.17	25.94
HOMO-2	-5.58	-5.60	59.63	6.80	0.83	14.13	18.61	65.71	7.13	0.27	16.91	7.13
HOMO-3	-5.78	-5.87	31.64	4.51	4.45	10.00	49.39	26.23	4.05	5.82	7.61	4.05
HOMO-4	-6.10	-6.10	60.46	32.81	6.73	0.00	0.00	60.51	32.70	6.78	0.00	32.70
HOMO-5	-6.15	-6.16	69.92	15.13	14.93	0.00	0.02	69.84	15.11	14.91	0.02	15.11

3.3.5. Absorption Spectra. The absorption spectra of **1** and **2** are acquired in MeCN at RT and the spectral details are presented in Table 3.3. The bands are assigned with the help of TD-DFT computations. Relevant spectral data along with the band assignments of **2** are tabulated in Table 3.4. Overlay of calculated and experimental spectra are displayed in Figure 3.8, bearing good correlation among themselves. The lowest energy broad band in the wavelength range of 450-700 nm for both the complexes is predominantly due to Ru→(N-N-N) charge transfer (MLCT) together with a small contribution of Ru→(N-N-C) charge transfer (MLCT) transitions.[75] The MLCT band that appeared at 527 nm for **2** is relatively broader and also more red-shifted compared to **1**, probably due to the presence of two carbanionic centers which induces more electron density around Ru(II). The next higher energy band ranging between 350 and 450 nm is also due to Ru→(N-N-C) charge transfer, along with a finite contribution of ILCT state, primarily localized on the π-conjugated bridging cyclometalating ligands, which is believed to be situated in close proximity of the Ru→(N-N-C) MLCT state.[93] As the π-conjugation in the bridging ligand in complex **2** is much greater than that of **1**, the ILCT contribution is expected to be higher in case of **2**, which is also reflected in enhanced absorptivity (ε) value for the said band (within 350-450 nm domain) in the latter one.[94] The UV region bands at ~285 nm emerge as a result of mixed ILCT and π-π* transitions.

Table 3.3. Photophysical Data of **1** and **2**.

Compounds		Absorption λ_{max}/ nm (ε, M^{-1} cm^{-1})[a]	Luminescence		
			λ_{max}/ nm	τ[b]	Φ[c]
1	MeCN (298 K)	497(39130), 396(sh)(38900), 373(sh) (44300), 311 (69250), 286(73970)	818	τ_1=1.4 ns (35%), τ_2=9.1 ns (65%)	6.5×10^{-4}
2		527(br)(34570), 386(br)(128900), 322(94000), 285(143160)	852	τ_1=2.0 ns (36%), τ_2=10.3 ns (64%)	7.0×10^{-4}
1	EtOH-MeOH (4:1) (77 K)	-	655	τ_1=3.6 μs (32%), τ_2=39.0 μs (68%)	7.2×10^{-2}
2		-	695	τ_1=5.7 μs (43%), τ_2=41.2 μs (57%)	8.3×10^{-2}

[a]Molar extinction coefficient (ε). [b]Lifetime (τ). [c]Emission quantum yield (Φ).

Table 3.4. Selected UV-vis Energy Transitions at the TD-DFT/B3LYP Level of **2** in MeCN.

λ_{expt}/nm	λ_{cal}/nm	Excited state	Oscillator strength(f)	Key transitions	Character
2 (*t-t*)					
527	539	S_7	0.09	H-3→L+1 (11%), H-2→L+2 (14%), H-1→L+5 (19%), H→L+4 (17%)	MLCT, ILCT
	505	S_{13}	0.78	H-4→L (18%), H-1→L+5 (11%), H→L (26%), H→L+6 (19%)	
	458	S_{25}	0.83	H-5→L+3 (10%), H-4→L+4 (12%), H-4→L+6 (17%), H→L+4 (11%), H→L+6 (22%)	
386	369	S_{63}	0.31	H→L+8 (48%), H→L+12 (12%)	MLCT, ILCT
322	328	S_{94}	0.53	H-6→L+8 (12%), H-3→L+17 (23%), H-2→L+16 (33%)	MLCT, ILCT
285	297	S_{153}	0.38	H-14→L+2 (20%), H-13→L+1 (12%), H-10→L+2 (17%)	π-π*, ILCT
2 (*t-c*)					
515	538	S8	0.07	H-3→L+1 (30%), H-1→L+4 (21%), H→L+5 (17%)	MLCT, ILCT
	520	S_{12}	0.07	H-3→L+4 (53%), H-3→L+5 (32%)	
	492	S_{14}	0.63	H-5→L (13%), H-2→L+2 (15%), H-1→L+4 (11%), H→L+5 (17%)	
413	449	S_{25}	0.61	H-5→L+3 (11%), H-4→L+6 (20%), H→L+6 (20%)	MLCT, ILCT
	433	S_{29}	0.21	H-4→L (26%), H-1→L+3 (14%), H-1→L+5 (17%)	
	394	S_{46}	0.13	H-4→L+6 (20%), H-1→L+7 (39%)	
351	343	S_{81}	0.15	H-7→L+4 (11%), H-4→L+8 (32%), H-1→L+13 (12%)	ILCT, π-π*
310	311	S_{121}	0.19	H-9→L+1 (11%), H-8→L+2 (55%)	π-π*, ILCT
	307	S_{126}	0.09	H-4→L+13 (29%), H-4→L+15 (17%)	
	297	S_{151}	0.25	H-14→L+1 (60%)	
2 (*c-c*)					
514	519	S_{12}	0.10	H-3→L+4 (19%), H-3→L+5 (51%), H-2→L+4 (16%)	MLCT
	492	S_{13}	0.69	H-5→L+3 (13%), H-4→L (13%), H-1→L+5 (15%), H→L+4 (13%)	
	475	S_{15}	0.28	H-1→L+7 (11%), H→L+4 (16%), H→L+6 (26%)	
412	440	S_{25}	0.40	H-5→L+3 (11%), H-4→L+6 (17%), H→L+6 (23%)	MLCT, ILCT
	425	S_{33}	0.45	H-6→L (15%), H-4→L (40%)	
	385	S_{51}	0.30	H-6→L+6 (32%), H-4→L+6 (21%), H-1→L+7 (17%)	
358	327	S_{94}	0.48	H-3→L+16 (25%), H-2→L+17 (36%)	ILCT, π-π*
305	297	S_{151}	0.32	H-14→L+1 (14%), H-13→L+2 (10%)	π-π*, ILCT

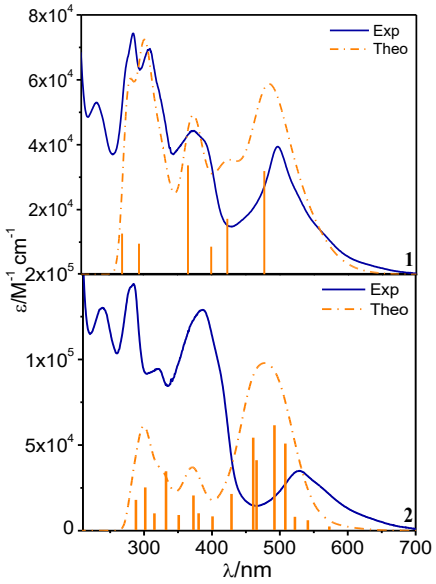

Figure 3.8. Experimental (royal blue) and calculated (orange) absorption spectra of **1** and **2** in MeCN.

3.3.6. Emission Spectra. The emission spectra and excited-state decays of the complexes are recorded in MeCN at RT as well as in EtOH-MeOH (4:1, v/v) glass at 77 K (Figure 3.9). The corresponding parameters are tabulated in Table 3.3. The complexes exhibit a broad emission in the NIR region ranging from 700 to 980 nm at RT. We have also performed UKS calculations on the triplet state of both complexes and reasonably good correlation between the experimental and calculated values of emission maxima indicates that the observed emission arises due to the radiative deactivation of ^{3}MLCT state (Table 3.5). The close proximity of radiative ^{3}MLCT and non-radiative ^{3}MC states is mostly responsible of either non-emissive or very weak emission characteristics in majority of ruthenium terpyridine type complexes.[72-73,95] Owing to the presence of stronger σ-donating cyclometalating units, the radiating ^{3}MLCT state shifts to the lower energy region, while the non-radiating ^{3}MC state moves to the higher energy level, thereby augmenting the energy gap between them, which in turn enhances the luminescence characteristics of the present complexes.[68] Thus, the broad band with its maximum at ~820 nm for **1** and at ~850 nm for **2** is predominantly due to $^{3}MLCT_{(Ru\rightarrow N\text{-}N\text{-}N)}$ unit, although equilibration with $^{3}MLCT_{(Ru\rightarrow N\text{-}N\text{-}C)}$ state could not be ruled out. Both the complexes demonstrate bi-

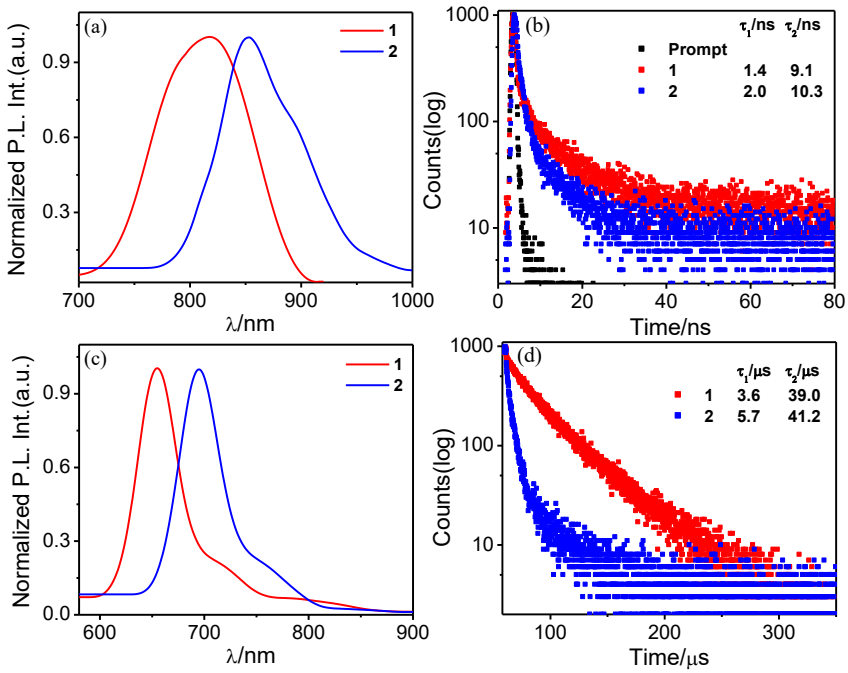

Figure 3.9. Steady-state emission spectra and excited-state decay profiles of **1** and **2** in MeCN (a and b, respectively) and in EtOH-MeOH (4:1, v/v) glass at 77 K (c and d, respectively). Insets to figure b and d show the corresponding lifetime values.

exponential decay at RT as displayed in Figure 3.9. The RT lifetime of the complexes is found to be 9.1 ns for **1** and 10.3 ns for **2**. At 77 K, the emission maxima of the complexes get considerably blue-shifted along with substantial increase in the lifetimes (39.0 μs for **1** and 41.2 μs for **2**), which is typical of ^{3}MLCT emitters. To our surprise, we observed bi-exponential decay for both complexes at 77 K. We do not know the actual reason for this type of behavior at 77 K. We surmise that the observed bi-exponential decay for both the complexes is probably due to the involvement of two types of ^{3}MLCT states, arising out of Ru→(N-N-N) and Ru→(N-N-C) charge transfer transitions, although no direct proof of the hypothesis could be provided. The zero-zero spectroscopic energy values (E_{00}) of the complexes, determined from their 77 K emission maxima, are found to be 1.89 eV and 1.76 eV for **1** and **2**, respectively.

Table 3.5. Emission Maxima of **1** and **2** in MeCN according to UKS Calculations and Associated Experimental Values.

1				**2**			
trans		*cis*		*trans-trans*		*trans-cis*	
λ_{expt}/nm	λ_{cal}/nm	λ_{expt}/nm	λ_{cal}/nm	λ_{expt}/nm	λ_{cal}/nm	λ_{expt}/nm	λ_{cal}/nm
818	838	657	836	852	841	698	741

3.3.7. Redox Properties. We explored the redox properties of the complexes in MeCN via cyclic voltammetry and associated voltammograms and data are presented in Figure 3.10 and Table 3.6. Complex **1** displays two successive reversible peaks at 0.62 and 1.31 V in the positive potential window probably due to Ru^{II}/Ru^{III} oxidation at the cyclometalated and non-cyclometalated site, respectively. Similarly, in the negative

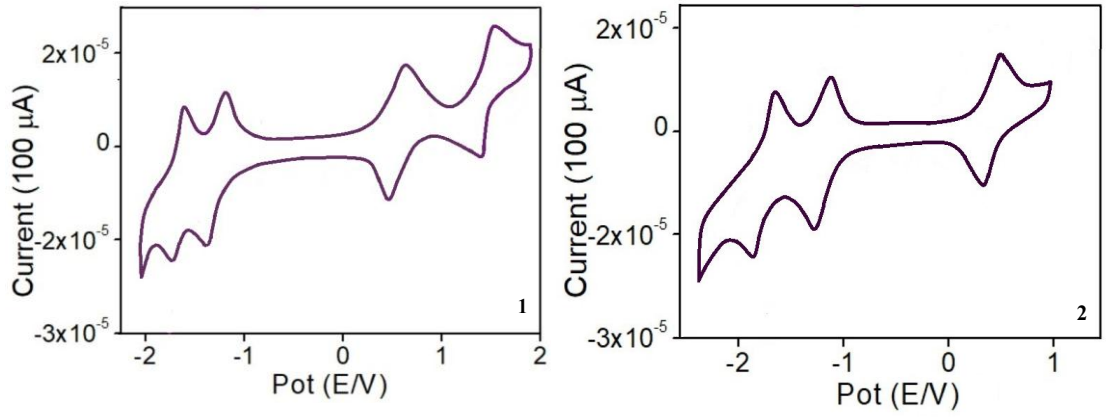

Figure 3.10. CVs of **1** and **2** in MeCN at a scan rate of 100 mV/s using Ag/AgCl as the reference electrode.

potential region, two peaks are observed at -1.17 and -1.62 V due to reduction of two different types of terpyridine units in the complex backbone. Complex **2**, on the other hand, exhibits a single reversible peak at 0.46 V due to simultaneous oxidation of two distant Ru^{II} moieties (Ru-Ru distance: 18.8 Å, estimated from the DFT optimized geometry). The dramatic reduction in Ru^{II}/Ru^{III} potential in **2** is due to accumulation of negative charge on the metal center induced by two cyclometalated units. Complex **2** also displays two reversible and/or quasi-reversible peaks at -1.22 and -1.74 V due to the reduction of the terpyridine units in the complex. DFT calculations are also conducted to substantiate the assignments of the redox couples. It is evident that spin density is predominantly localized on the Ru^{II} center in the oxidized state, while on the terpyridine units of non-cyclometalated parts, and to a lesser extent on the cyclometalated region, in their reduced forms (Figure 3.11).

Table 3.6. Electrochemical Data[a] for **1** and **2** in MeCN.

Compounds	Oxidation[b] $E_{1/2}$(ox)/V	Reduction[c] E(red)/V
1	0.62, 1.31	-1.17, -1.62
2	0.46	-1.22, -1.74

[a]All the potentials are referenced against Ag/AgCl electrode with $E_{1/2}$=0.36 V for Fc/Fc^+ couple. [b]Reversible electron transfer process with a Pt working electrode. [c]E(red) values for the reduction processes obtained with glassy carbon electrode

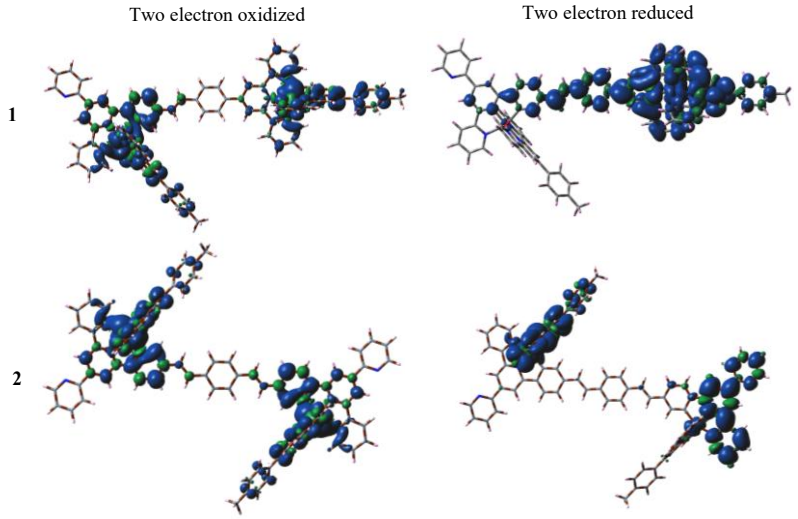

Figure 3.11. Spin density plots of **1** and **2** in MeCN. Left panel indicates two-electron oxidized forms while two-electron reduced forms are shown in right panel.

3.3.8. Acid-Induced Changes in the Photo-Redox Behavior of the Complexes.

We are now interested to explore the acid-base behavior of the complexes by exploiting the non-coordinated nitrogen atoms in their secondary coordination sphere. For this purpose, we have first treated the acetonitrile solution of the complexes with $HClO_4$ and monitored the changes via absorption and emission spectroscopy (Figures 3.12 and 3.13). Both the complexes display two-step changes accompanied with isosbestic points in each step. For complex **1**, upon addition of 2 equiv of acid, a small hump arises at ~567 nm region, keeping the MLCT band intensity at 497 nm almost unchanged. In case of **2**, the MLCT band moves about 40 nm to the red region and it appears as a broad band ranging between 495 and 600 nm with its peak maximum at ~566 nm. The spectral characteristics as well as the amount of acid required to reach the first saturation are different, viz. 2 and 4 equiv for complex **1** and **2**, respectively. For **1**, only one non-coordinated N is free to accept a proton, while the number is two for **2**. In the first step, the solution color remains almost unchanged for both the cases. Upon continued addition of acid, the said absorption band (at ~567 nm) was observed to be substantially reduced in intensity and at the same time, a small but finite

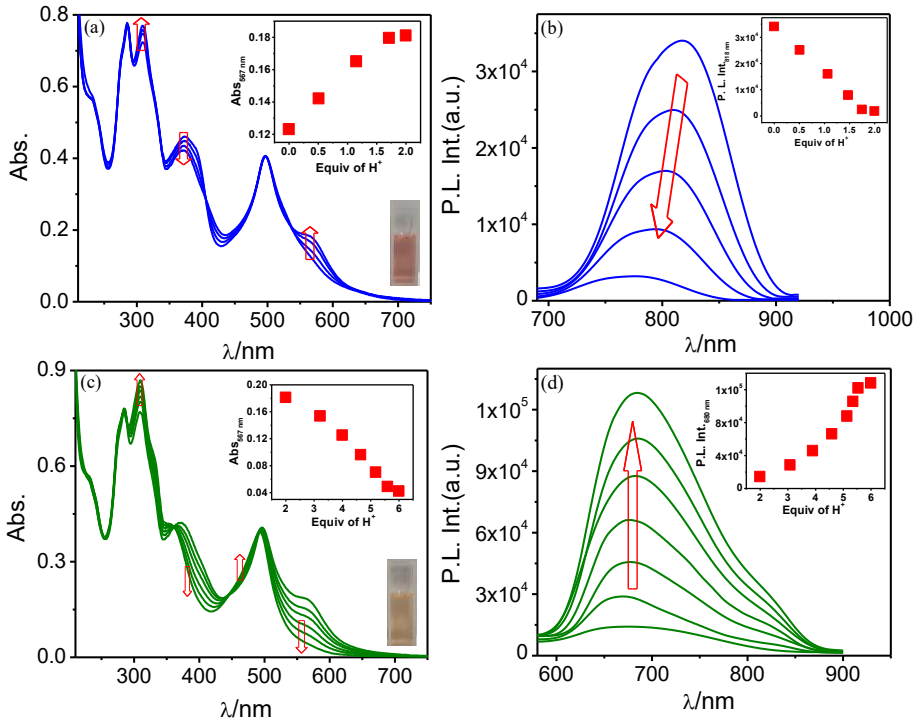

Figure 3.12. Stepwise changes in absorption (a and c) and emission (b and d) spectral profiles of **1** upon successive addition of H^+ in MeCN. The insets to figure a and c show the alteration of absorbance with the equivalent of H^+ and visual color change while the insets to figure b and d display the variation of luminescence intensity as a function of H^+.

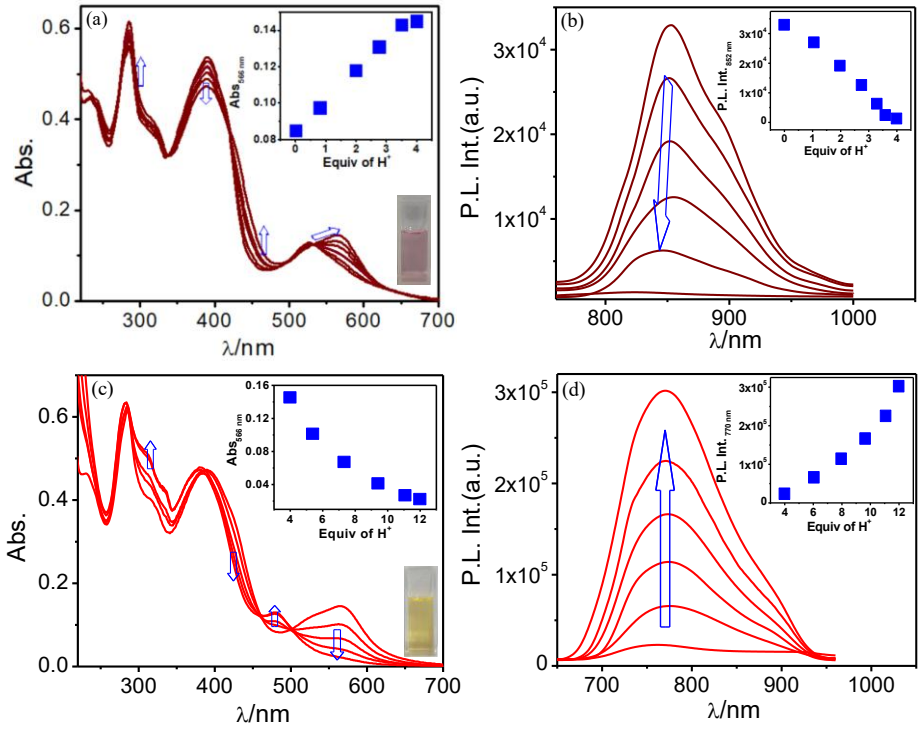

Figure 3.13. Stepwise changes in absorption (a and c) and emission (b and d) spectral profiles of **2** upon successive addition of H^+ in MeCN. The insets to figure a and c show the alteration of absorbance with the equivalent of H^+ and visual color change while the insets to figure b and d display the variation of luminescence intensity as a function of H^+.

increase in absorbance in the wavelength domain of 450-480 nm takes place for **1**. In case of **2**, upon continued addition of acid, the broad band at ~566 nm gets reduced gradually and an upsurge of a new band is observed at 480 nm. It is to be noted that the extent of change is more marked in **2** than that in **1** as the former one possesses two Ru-C bonds. The required amount of acid to reach the second saturation also differs, viz. 6 equiv for **1** and 12 equiv for **2**. The color of the solution also changes from reddish-purple to reddish-orange for **1**, while the purple color of **2** is changed to yellowish-orange upon acid saturation.

In the emission side, the intensity of the band for both complexes gets almost fully-quenched together with a blue-shift of ~50 nm in the first step. On the other hand, evolution of a new band at ~680 nm for **1** and at ~770 nm for **2**, followed by their substantial intensification takes place upon continued addition of acid. In line with the steady state spectra, the lifetime of the complexes decreases in the first step (9.1→4.6 ns for **1** and 10.3→6.1 ns for **2**), while significantly increases in the second step (4.6→23.5 ns for **1** and 6.1→ 25.7 ns for **2**) (Figure 3.14).

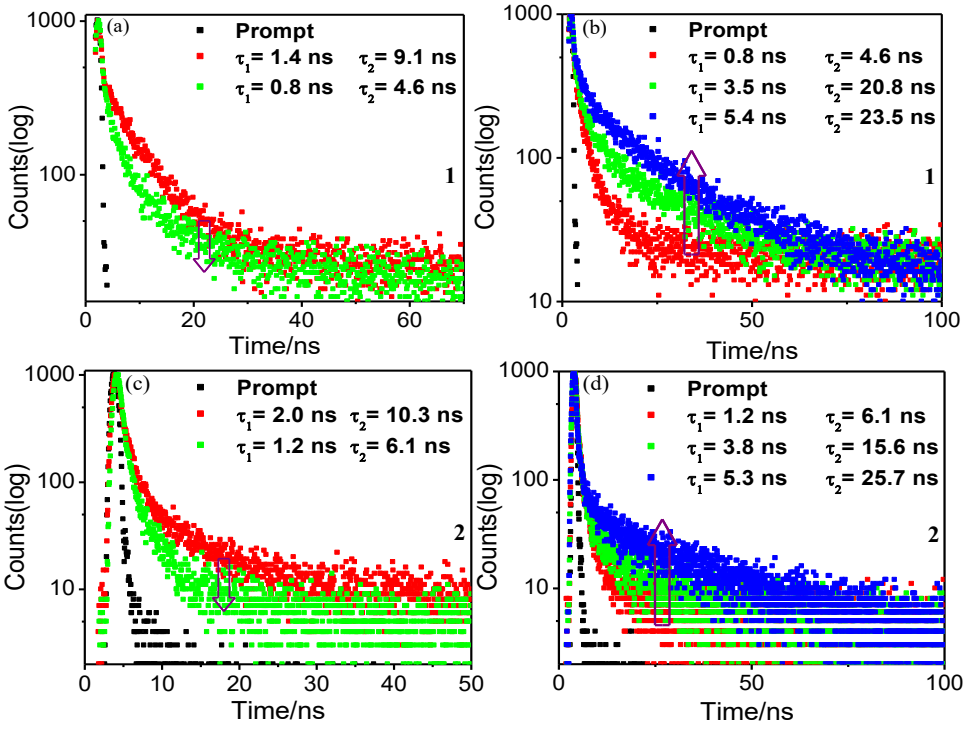

Figure 3.14. First (a and c) and second (b and d) step changes in luminescence decays of **2** upon incremental addition of H^+ ion in acetonitrile. The insets to the figures show the corresponding lifetime values.

We also acquired the CVs of both complexes in acid-saturated condition and overlaid the same with those in absence of acid (Table 3.7 and Figure 3.15). We have already observed that **1** shows two reversible couples with the $E_{1/2}$ values of 0.62 V and 1.31 V, while complex **2** displays a single oxidation peak at $E_{1/2}$=0.46 V. The acid-saturated solution of **1** is found to exhibit two closely associated reversible couples having their $E_{1/2}$ of 1.26 V and 1.35 V. Complex **2**, on the other hand, displays a single reversible couple with $E_{1/2}$ of 1.34 V.

Table 3.7. Oxidation Potentials of **1** and **2** in their Free and De-coordinated Forms in MeCN.

Compounds	Oxidation $E_{1/2}$(ox)/V	
	Free	De-coordinated
1	0.62, 1.31	1.26, 1.35
2	0.46	1.34

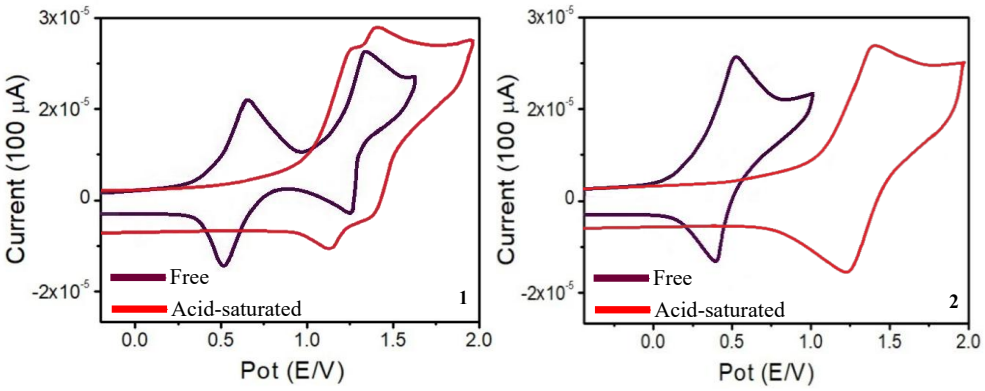

Figure 3.15. CVs of free- and acid-saturated forms of **1** and **2** in MeCN at a scan rate of 100 mV/s using Ag/AgCl as the reference electrode.

To investigate the reasons behind the observed changes in the absorption, emission and electrochemical behavior in presence of acid, we conducted ^{1}H NMR titrations of the complexes upon gradual addition of deuterated trifluoroacetic acid (TFA-*d*) in CD_3CN (Figures 3.16 and 3.17). With incremental addition of acid up to 2-6 equiv, the signal intensity of H_{13}-H_{15} protons gradually decreases with concomitant appearance of two new and unresolved doublets in the region of ~7.15-7.80 ppm, probably corresponding to $H_{13'}$ and $H_{15'}$ protons (insets of Figures 3.16 and 3.17). Additionally, a new peak emerges at δ=12.65 ppm (for **1**) and 13.00 ppm (for **2**), likely due to protonation of the non-coordinated pyridine units within the cyclometalated site of the complexes. This sort of protonation leads to decrease in electron density of the aforementioned pyridine moieties, which in turn results in a significant down-field shift of $H_{9'}$-$H_{12'}$ proton resonances. The olefinic protons (H_{16} and H_{17}) also undergo a down-field shift in presence of acid. Further addition of acid (up to 6-12 equiv) leads to disappearance of H_{13}-H_{15} proton signals, while the signal intensities of $H_{13'}$ and $H_{15'}$ protons get gradually enhanced, better resolved and slightly up-field shifted. Furthermore, H_{3a}, H_{3b}, H_{3d}, H_{3e} protons (for **1**) and H_{3a}, H_{3b} protons (for **2**) get slightly up-field shifted, whereas H_{3c} protons for both complexes experience substantial up-field shift from ~8.88 to ~8.64 ppm. It is to be noted that the protons closer to the non-cyclometalating units experience only a small chemical shift upon acid-treatment. We also acquired the ^{13}C NMR spectrum of a representative complex (**1**) in presence of acid, particularly to locate the signal of the carbon atom coordinated to Ru(II) center (Figure 3.18). The original complex displays a signal in the most down-field region of δ=184.34 ppm, which clearly indicates the presence of Ru-C bond within the complex framework.

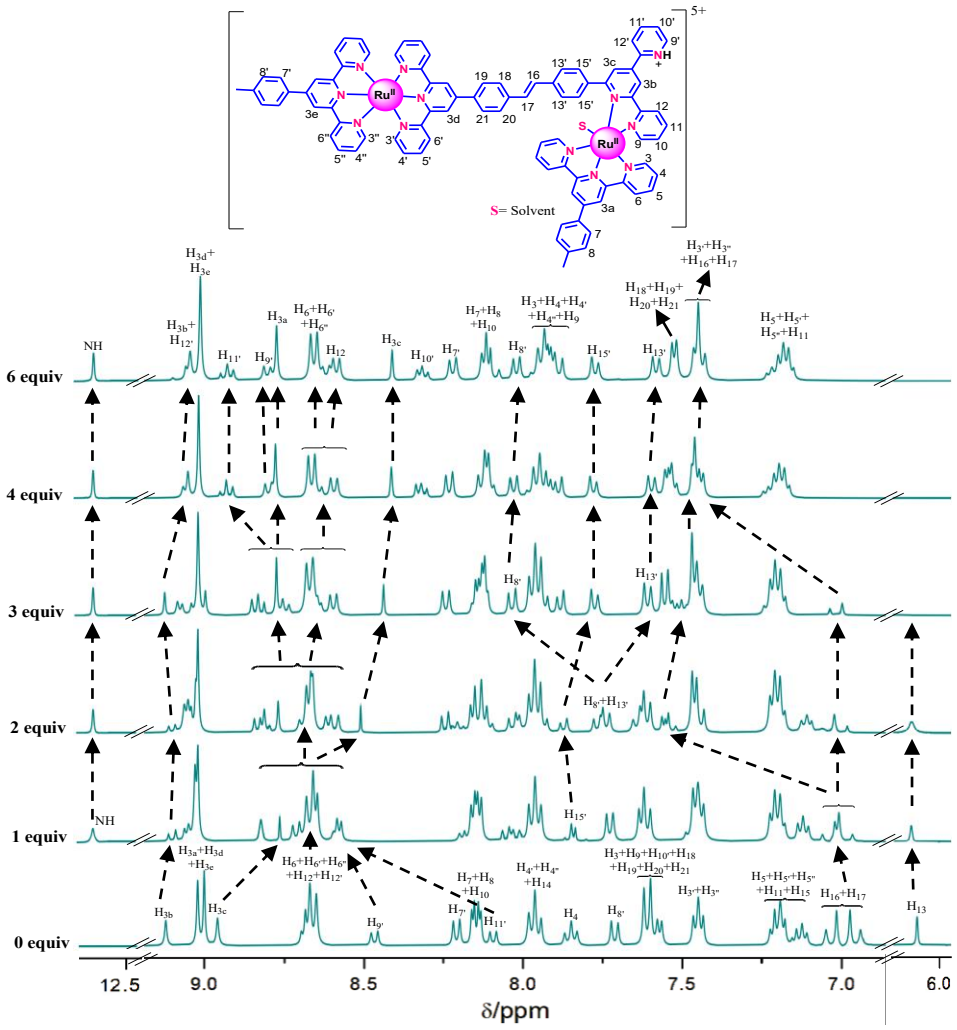

Figure 3.16. ^{1}H NMR spectral changes of **1** upon gradual addition of H^{+} (up to 6.0 equiv) in CD_3CN.

But in the acid saturated form, the said signal is not visible, indicating the cleavage of Ru-C bond. Small but finite change in the chemical shift of the remaining carbon atoms is also noticed upon cleavage. Thus, the outcomes of both ^{1}H and ^{13}C NMR experiments indicate that initial addition of acid up to 2-6 equiv induces protonation of the pyridine rings within the cyclometalated unit which is evidenced by observed downfield-shift of the protons associated with the said pyridine rings. It is further hypothesized that subsequent acid addition results in protonation at the carbanionic center of the Ru-C bond and ultimately cleavage of the same. Upon careful consideration of the final NMR spectrum, it appears that significant structural transformation takes place in each complex. The N-N-C-Ru coordination motif(s) in each complex has been converted into N-N-Ru type motif as depicted in Figures 3.16 and 3.17.

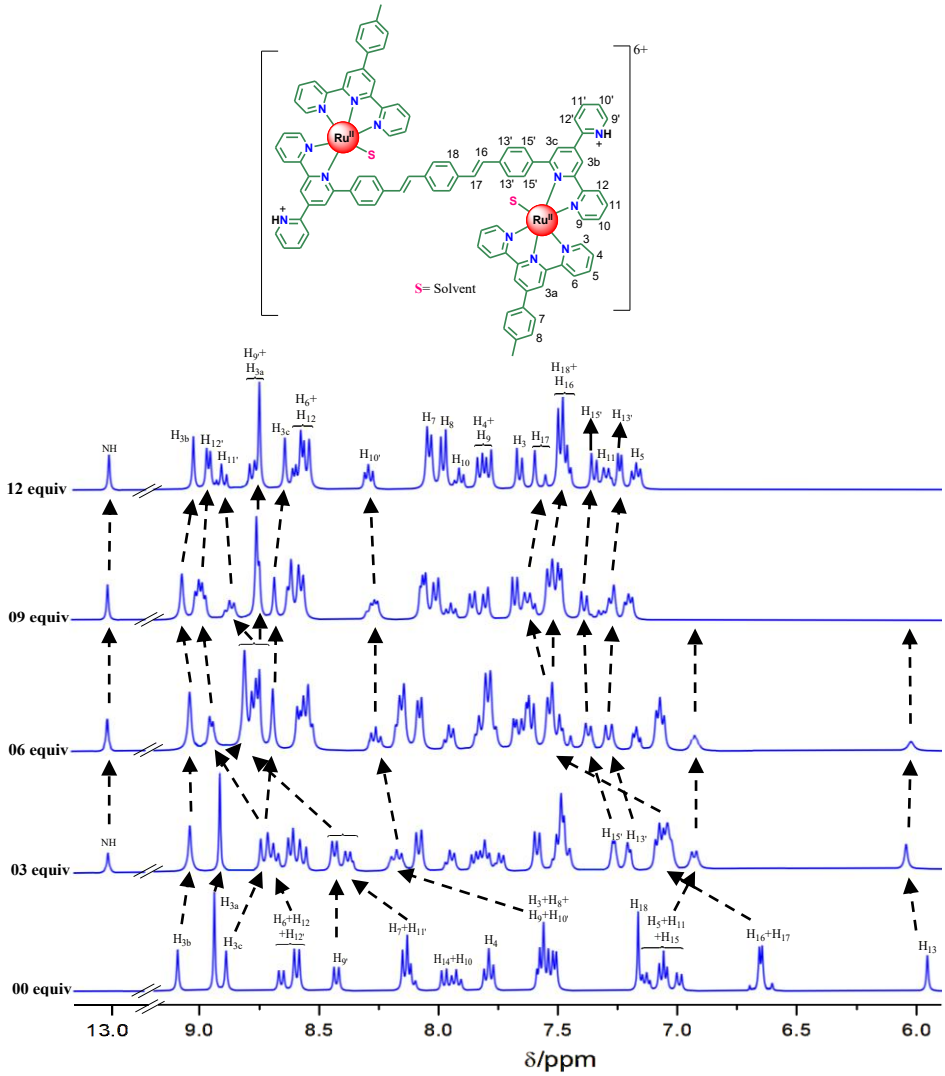

Figure 3.17. ^{1}H NMR spectral profile of **2** with incremental addition of H^{+} (up to 12.0 equiv) in CD_3CN.

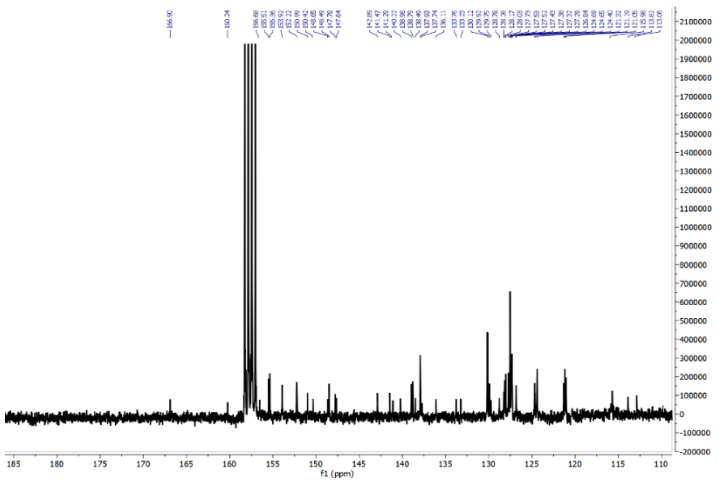

Figure 3.18. ^{13}C NMR spectrum of acid-saturated form of **1** in CD_3CN.

To substantiate our hypothesis of initial protonation followed by de-coordination in presence excess acid, DFT and TD-DFT calculations are also executed on the protonated and de-coordinated forms of the complexes. The optimized geometries of both the forms are presented in Figure 3.19. The frontier molecular orbitals along with their compositions for a representative complex **2** are presented in Figures 3.20 and 3.21 and Table 3.8. Additionally, the absorption spectral parameters and band assignments for **2** are summarized in Table 3.9. Notably, the computed spectra show reasonably good correlation with the respective experimental spectra, as illustrated in Figure 3.22. The molecular orbitals that are involved in the lowest-energy transition for free-, protonated-, and de-coordinated forms are depicted in Figure 3.23. On protonation, the LUMOs experience greater stabilization relative to the HOMOs, resulting in red-shift of the said ^{1}MLCT band. Conversely, upon de-coordination, the HOMOs undergo greater stabilization than LUMOs relative to their protonated counterparts. The HOMO-LUMO energy barrier in the protonated forms is observed within the range of 2.21-2.37 eV, while for the de-coordinated forms, it shifts to a higher energy domain of 2.43-2.64 eV. Consequently, upon de-coordination, a hypsochromic shift is observed in the absorption spectra for both complexes. The extent of shift is found to be more prominent for **2**, due to the presence of two cyclometalating units, in contrast to **1** possessing only one cyclometalating unit.

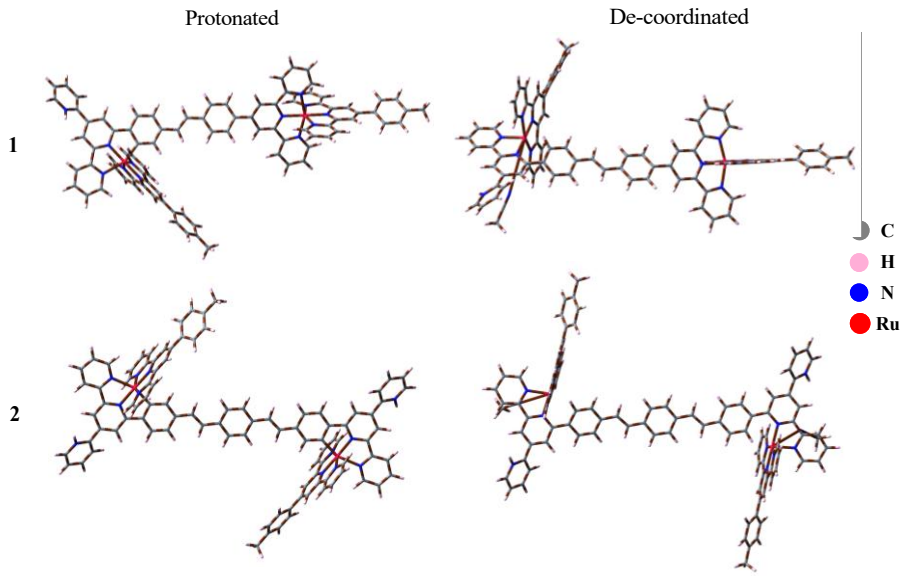

Figure 3.19. Ground state optimized geometries of protonated (left panel) and de-coordinated (right panel) forms of **1** and **2** in acetonitrile.

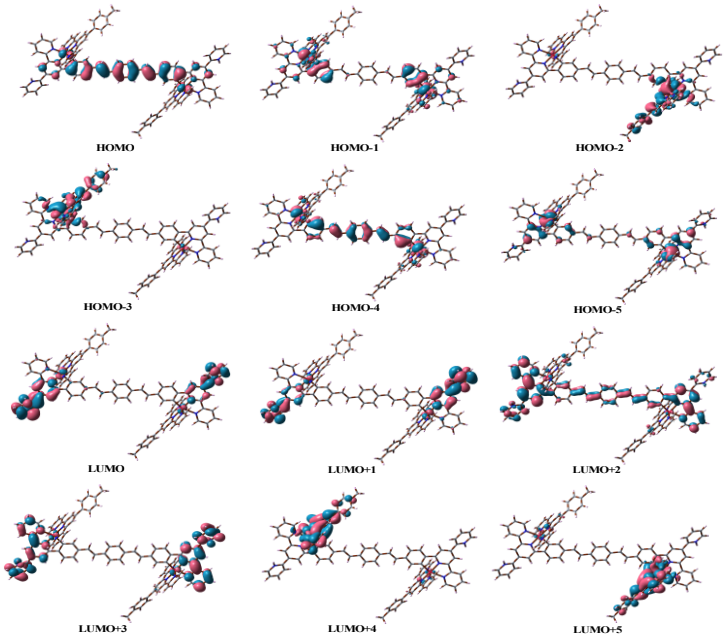

Figure 3.20. Schematic drawings of the selective frontier molecular orbitals of the protonated form of **2** in acetonitrile.

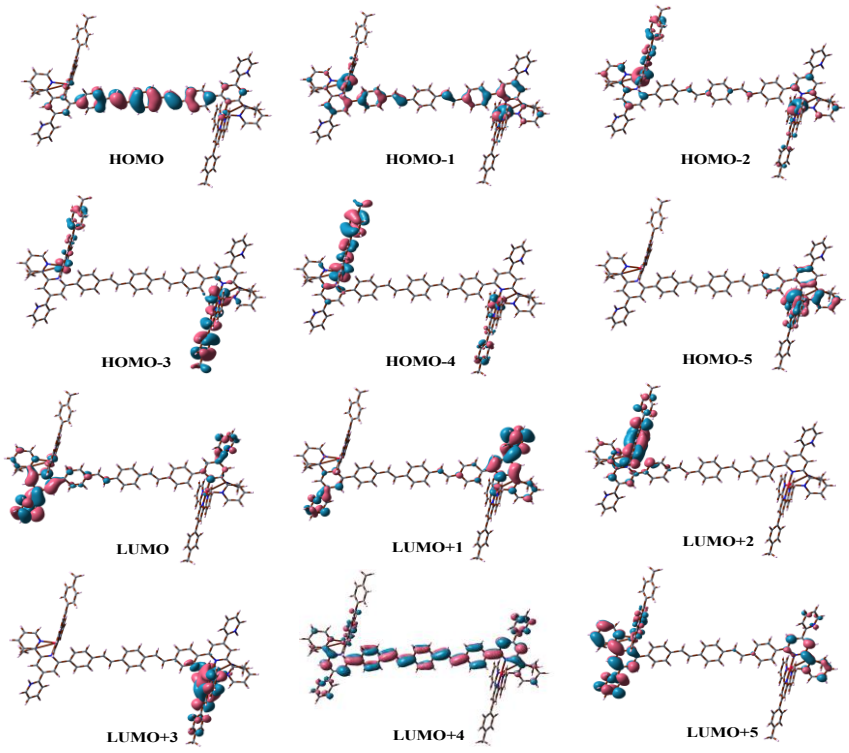

Figure 3.21. Schematic drawings of the selective frontier molecular orbitals of the de-coordinated form of **2** in acetonitrile.

Table 3.8. Selected MOs along with their Energies and Compositions in the Ground State for Protonated and De-coordinated Forms of **2** in MeCN.

	2										
	Energy/eV		% Compositions								
	Protonated	De-coordinated	Protonated				De-coordinated				
			Ru	mpt	N,N,C-tpy	pvp	Ru	mpt	N,N,C-tpy	pvp	MeCN
LUMO+5	-2.41	-2.82	11.87	83.03	3.50	1.60	1.85	8.30	87.57	2.12	0.01
LUMO+4	-2.41	-2.96	11.96	83.70	2.91	1.42	0.92	7.80	49.21	42.04	0.02
LUMO+3	-2.43	-3.06	3.13	3.05	92.87	0.95	13.12	80.31	5.85	0.67	0.02
LUMO+2	-2. 44	-3.08	1.52	7.05	72.01	19.42	11.92	74.52	8.63	4.88	0.01
LUMO+1	-3.10	-3.37	5.12	0.77	92.49	1.60	4.22	0.88	92.27	2.57	0.03
LUMO	-3.11	-3.41	5.47	0.82	90.82	2.88	4.53	0.90	87.62	6.90	0.04
HOMO	-5.32	-5.84	16.02	2.72	10.45	70.79	3.14	0.38	7.78	88.68	0.00
HOMO-1	-5.48	-6.48	56.12	10.98	8.43	24.46	56.32	10.42	17.25	15.99	0.02
HOMO-2	-5.50	-6.57	60.63	28.29	5.26	5.81	61.76	18.75	14.50	4.96	0.02
HOMO-3	-5.50	-6.61	60.60	28.16	5.29	5.95	40.71	50.37	8.32	0.58	0.00
HOMO-4	-5.58	-6.61	49.95	9.66	2.83	3.76	48.31	45.05	5.31	1.31	0.00
HOMO-5	-5.84	-6.63	67.32	7.29	17.01	8.38	72.98	14.18	10.47	2.25	0.10

Table 3.9. Selected UV-vis Energy Transitions at the TD-DFT/B3LYP Level of Protonated and De-coordinated Forms of **2** in MeCN.

λ_{expt} /nm	λ_{cal}/ nm	Excited state	Oscillator strength(f)	Key transitions	Character
2 (Protonated)					
567	619	S_5	0.20	H-4→L (27%), H-1→L+1 (13%), H→L (51%)	MLCT, ILCT
	538	S_{13}	0.27	H-6→L (23%), H-5→L+1 (18%), H-4→L (17%)	
	506	S_{22}	0.50	H-5→L+1 (10%), H-1→L+3 (20%), H-1→L+7 (10%), H→L+2 (19%)	
	490	S_{25}	1.85	H→L+2 (24%), H→L+6 (51%)	
388	472	S_{29}	0.26	H-6→L (11%), H-5→L+1 (12%), H-4→L+2 (24%), H→L+2 (18%)	MLCT, ILCT
	445	S_{39}	0.27	H-6→L+2 (17%), H-5→L+3 (13%), H-1→L+3 (13%)	
	394	S_{65}	0.22	H-1→L+9 (30%), H→L+10 (41%)	
	365	S_{79}	0.09	H-3→L+13 (20%), H-2→L+14 (40%)	
317	318	S_{142}	0.11	H-11→L+5 (13%), H-10→L+5 (21%), H-8→L+7 (11%), H-8→L+8 (11%)	ILCT, π-π*
285	298	S_{182}	0.50	H-17→L+5 (20%), H-16→L+4 (18%), H-16→L+5 (11%)	π-π*
2 (De-coordinated)					
482	568	S_2	0.04	H→L+1 (92%)	MLCT, ILCT
	499	S_7	0.53	H-6→L (14%), H-5→L+1 (12%), H→L+4 (22%)	
	464	S_{16}	0.35	H-3→L+1 (29%), H-2→L (10%)	
380	400	S_{34}	0.13	H-6→L+4 (10%), H-4→L+2 (14%)	MLCT, ILCT
	367	S_{59}	0.09	H-6→L+7 (30%)	
312	334	S_{92}	0.09	H-13→L+3 (36%), H-10→L+3 (15%)	ILCT, π-π*
	327	S_{107}	0.09	H-13→L+3 (19%), H→L+17 (59%)	
283	293	S_{178}	0.14	H-6→L+16 (22%)	π-π*, ILCT

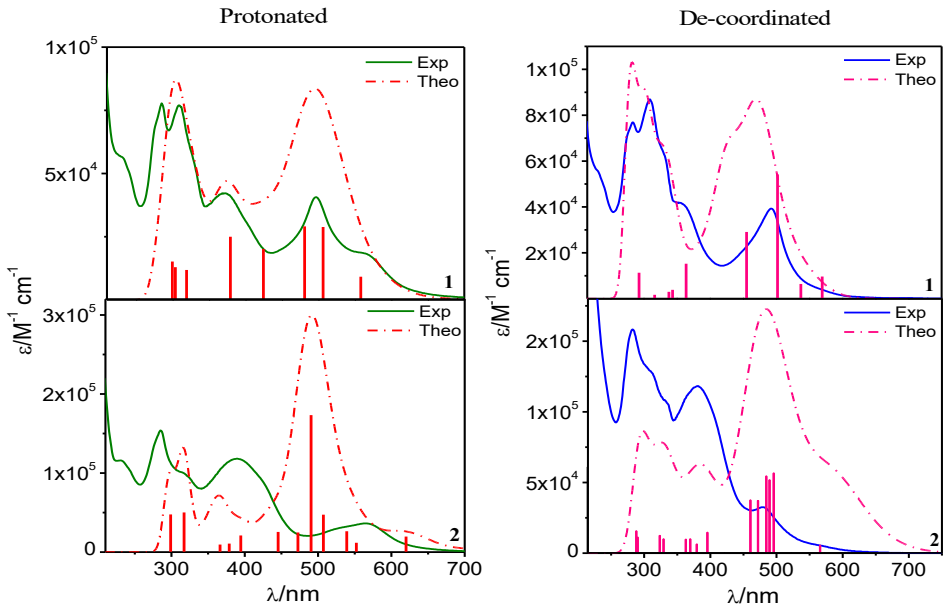

Figure 3.22. Overlay of the experimental and theoretical absorption spectra of the protonated (left panel) and de-coordinated (right panel) forms of **1** and **2** in acetonitrile.

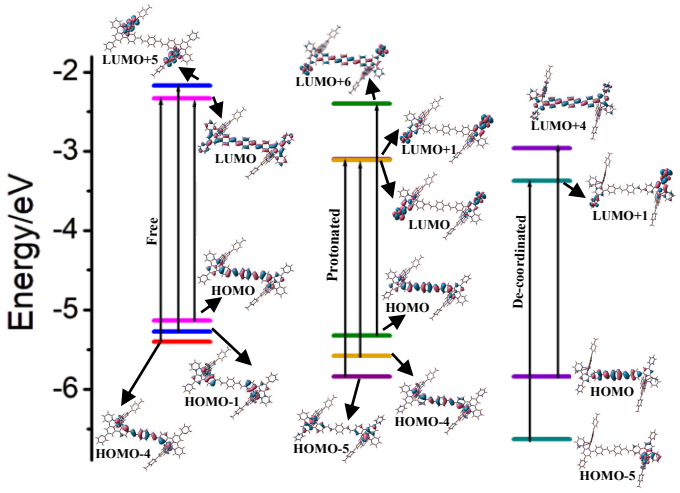

Figure 3.23. Dominant transitions involved in the lowest-energy absorption band in free (left panel), protonated (middle panel) and de-coordinated (right panel) forms of **2** in MeCN.

In earlier sections, we have witnessed substantial modulation in the absorption, emission and electrochemical properties of the complexes in presence of acid. Furthermore, the acid-dependent ^{1}H NMR titration experiments clearly indicate initial protonation of the pyridine rings associated with the cyclometalated site followed by Ru-C bond cleavage in presence of excess acid in the second step. Hence, the observed first-step change in the absorption and emission spectral behavior of the complexes is also ascribed to protonation

of their non-coordinated nitrogen atom(s). In practice, a small but finite increase in absorption intensity together with a red-shift of the lowest energy MLCT band takes place in the first step. By contrast, diminution of the said MLCT bands takes place in the second step due to Ru-C bond cleavage under the influence of excess acid.

We have already discussed that the emission maximum at ~820 and ~850 nm for complex **1** and **2**, respectively, arises due to radiative deactivation of $^3MLCT_{Ru\rightarrow(N\text{-}N\text{-}N)}$ state as the N-N-N tpy unit is thought to be better π-accepting in nature under proton-free condition. Upon addition of acid up to their first saturation, the N-N-C unit becomes more π-accepting relative to N-N-N tpy motif and the electron density will now flow from Ru(II) towards the protonated cyclometalated unit which in turn is probably responsible for emission quenching at ~820 nm for **1** and ~850 nm for **2**. Further addition of acid finally leads to Ru-C bond cleavage, leading to the formation of Ru(bidentate N-N)(tpy)(CH_3CN) type motifs. As the protonated pyridine unit is attached to the bipyridine-type moiety, the charge transfer probably takes place from Ru center to the said bpy-type unit, leading to the generation of a new band in the higher energy region. As the Ru(bpy) type moiety is usually more emissive relative to its Ru(tpy) counterpart, the enhanced emission at ~680 and ~770 nm for complex **1** and **2**, respectively, is probably due to radiative deactivation of $^3MLCT_{Ru\rightarrow(N\text{-}N)}$ state for both the complexes under high proton concentration.

In cyclic voltammetry, we obtained the $E_{1/2}$ of 0.62 V (for the cyclometalated unit) and 1.31 V (for non-cyclometalated) for **1**, while for complex **2**, we found a single peak with $E_{1/2}$ of 0.46 V. The acid-saturated solution of **1** is found to exhibit two closely associated reversible couples having their $E_{1/2}$ of 1.26 V and 1.35 V. Complex **2**, on the other hand, displays only one reversible couple with its $E_{1/2}$ of 1.34 V. Thus, $E_{1/2}$ value associated with cyclometalated units gets substantially enhanced upon acid saturation and the final potential becomes closer to that of $[Ru(tpy)(bpy)(CH_3CN)]^{2+}$ ($E_{1/2}$=1.29 V) as observed by Petersen's group.[96] Therefore, acid-induced Ru-C bond cleavage leads to change in coordination environment from Ru(tridentate N-N-C)(tpy) to Ru(bidentate N-N)(tpy)(CH_3CN) motifs in both complexes. Thus, the observed shift in $E_{1/2}$ values (particularly for the cyclometalated parts) towards more positive potential domain unambiguously indicates the Ru-C bond cleavage upon acid treatment. It is quite logical that carbanionic center that is connected to Ru(II)-center is expected to be electron rich compared to the coordinated nitrogen atoms. Thus, the carbanionic center is prone to accept proton and eventually gets de-coordinated in presence of excess acid.[71,97,98]

We are now interested to check whether the overall process is reversible and re-coordination of Ru-C bond is possible or not in presence of base (NaOH). Absorption and emission spectroscopy were employed for this purpose (Figures 3.24 and 3.25). Initially, the complexes were treated with acid up to their first saturation point. Gradual addition of OH^- to the acidulated solutions results in a gradual shift of the absorption spectra back toward their original states and complete restoration is achieved upon addition of 2-4 equiv of base. Next, we took the acidulated solutions of the complexes after reaching a second saturation level, where the cleavage of Ru-C bond occurs. At this stage, the addition of OH^- caused minimal spectral changes. However, upon heating the solutions up to ~70 °C, the complexes reverted back to their original cyclometalated form. The solution colors also found to revert back to their initial state. The first-step process showed a gradual increase in emission intensity upon OH^- treatment, eventually returning to the initial state. In the subsequent step, the acid-saturated solution restored to their original cyclometalated form together with emission quenching upon treatment with base and heat. These observations indicate that after acid-induced de-coordination, Ru(II) can be re-coordinated under the influence of base and temperature (Scheme 3.1). This demonstrates that the cyclometalated Ru-C bond can undergo reversible breaking and forming through sequential application of acid, base, and heat. Thus, "on-off" emission switching occurs with acid/base treatment, while "off-on" switching is achievable with the correct sequence of acid, base, and thermal treatment.

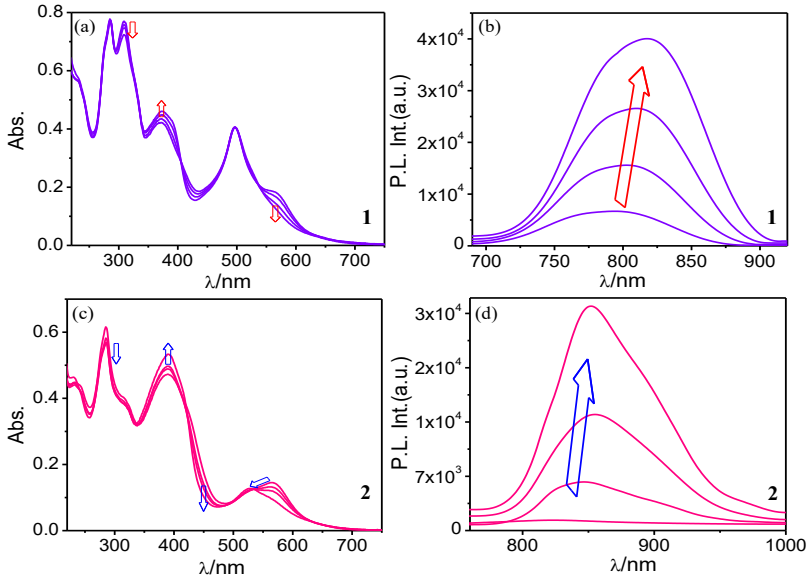

Figure 3.24. Absorption (a and c) and luminescence (b and d) spectral profiles obtained upon incremental addition of OH^- (2-4 equiv) to the first acid-saturated solution of **1** and **2** in MeCN.

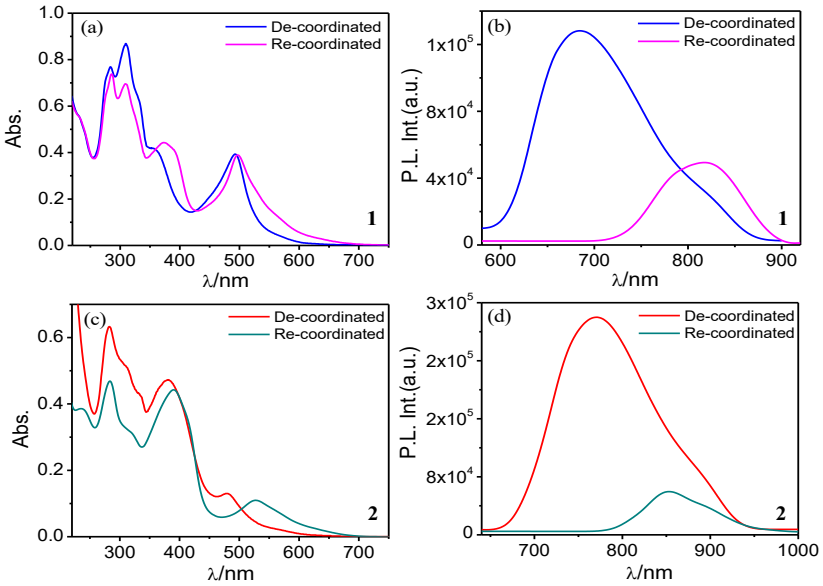

Figure 3.25. Absorption (a and c) and luminescence (b and d) spectral profiles of **1** and **2** in their de-coordinated and re-coordinated forms.

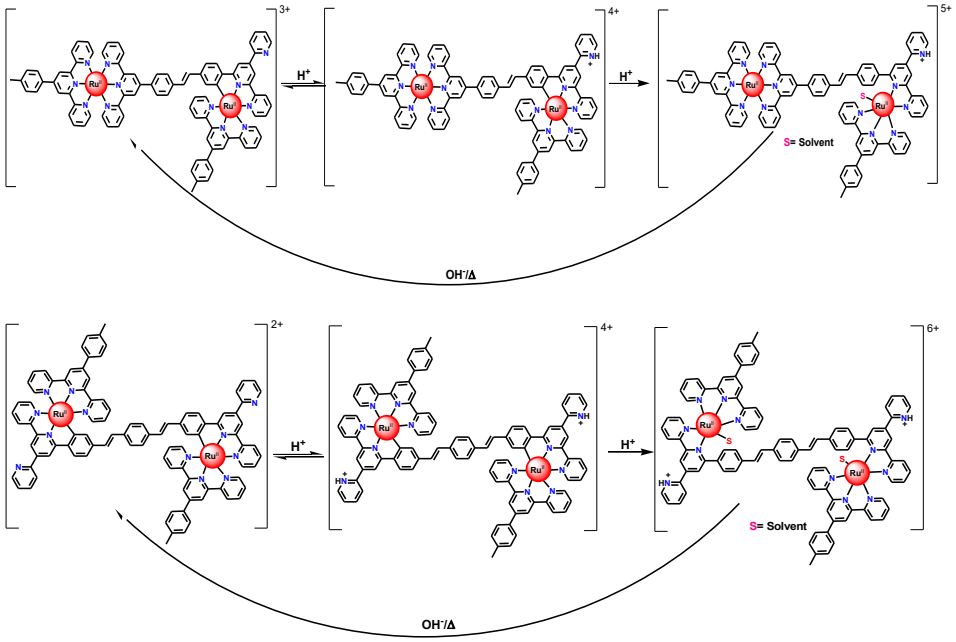

Scheme 3.1. The structural changes among the three forms of the complexes under the influence of acid, base and temperature.

3.3.9. Photoisomerization Studies. Owing to the presence of stilbene motif(s), both complexes showcase *trans-cis* photoisomerization upon light irradiation. Herein, we irradiated acetonitrile solution of the complexes with visible light (500 nm) and monitored the changes by means of absorption and emission spectroscopy (Figure 3.26). Isomerization

proceeds through a single step change for both complexes. Upon light irradiation, the lowest energy MLCT absorption bands (within 450-700 nm range) get reduced in intensity together with slight blue-shift. The next higher energy band within the spectral domain of 350-450 nm, which are believed to be admixture of both MLCT and ILCT transitions, are also reduced enormously. Thus, both MLCT and ILCT bands get reduced during the course of light irradiation, while the UV region bands get intensified. The successive absorption spectrum is found to pass through several well-resolved isosbestic points. It is of interest to note that reduction in intensity of the band within the spectral domain of 350-450 nm is almost four times greater compared to that of the lowest energy band within the range of 450-700 nm in both cases. The presence of distinct isosbestic points suggest the existence of two species in equilibrium, with the initial *trans* (*t*) form converting to *cis* (*c*) form for **1**, while for **2**, the *trans-trans* (*t-t*) form is transformed to either *trans-cis* (*t-c*) or *cis-cis* (*c-c*) form under photo-irradiation. The time required to reach the photo-stationary state is almost 3-5 h for the complexes.

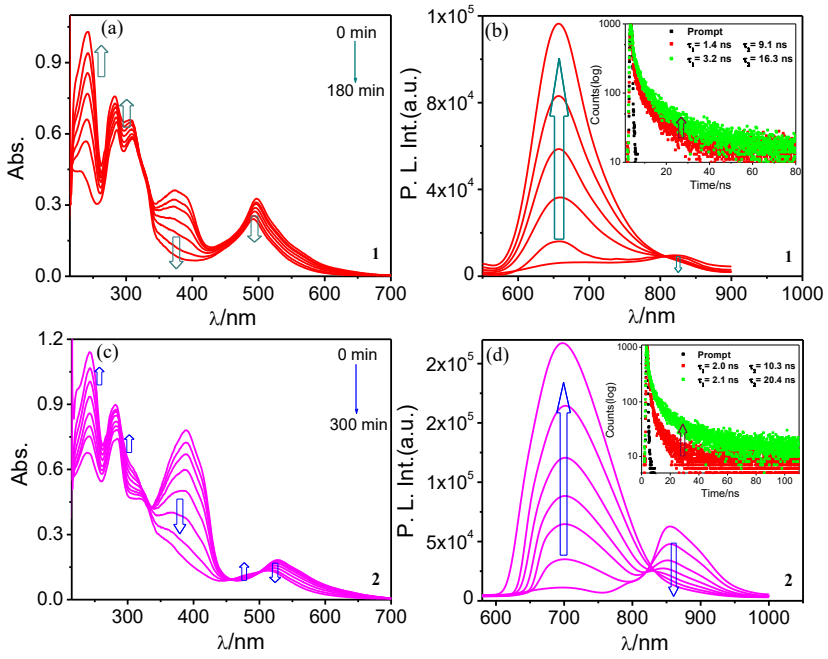

Figure 3.26. Absorption (a and c) and emission (b and d) spectral change of **1** and **2** in MeCN upon treatment with light of λ=500 nm. Inset to figure b and d shows the decay profiles of the complexes before and after photolysis along with their lifetime values.

In the emission side, the original $^{3}MLCT_{(Ru\rightarrow N\text{-}N\text{-}N)}$ band intensity at ~820 nm (for **1**) and ~850 nm (for **2**) is gradually quenched with concomitant intensification of the broad

band within the spectral range of 600-800 nm. Actually, the emission enhancement is quite remarkable for both complexes and the emission maximum is found to be at ~655 nm for **1** and at ~700 nm for **2** at saturation. During *trans-cis* isomerization, the linear structure of the complexes gets distorted and consequently the π-delocalization across the complex backbone gets hampered. With the help of literature reports, we believed that the isomerization process most probably occurs through the intermediacy of ^{3}ILCT state which is again in close proximity of the $^3MLCT_{(Ru\rightarrow N\text{-}N\text{-}C)}$ state.[46-48] As the energy of $^3MLCT_{(Ru\rightarrow N\text{-}N\text{-}C)}$ state is higher than that of $^3MLCT_{(Ru\rightarrow N\text{-}N\text{-}N)}$ state, the emission maximum gets blue-shifted in both complexes. Additionally, as the excited state localization shifts from $^3MLCT_{(Ru\rightarrow N\text{-}N\text{-}N)}$ to the $^3MLCT_{(Ru\rightarrow N\text{-}N\text{-}C)}$ state, the emission intensity at ~820 nm (for **1**) and at ~850 nm (for **2**) gradually decreases with concomitant increase of the band at ~655 nm for **1** and at ~700 nm for **2**. Therefore, the highly intense emission band at ~655 nm for **1** and at ~700 nm for **2** is probably due to the radiative deactivation of either $^3MLCT_{(Ru\rightarrow N\text{-}N\text{-}C)}$ state or from the equilibrated excited states of $^3MLCT_{(Ru\rightarrow N\text{-}N\text{-}C)}$ and ^{3}ILCT.

For understanding the mode of isomerization, we acquired the ^{1}H NMR spectra of the photolyzed solutions of both complexes in CD_3CN and compared with their respective un-photolyzed forms (Figures 3.27 and 3.28). After photolysis, the spectra reveal an overall up-field shift of most of the proton resonances in both cases, although to a small extent. Significant reduction in intensity of the olefinic proton signals (H_{16} and H_{17} with J=16 Hz) together with evolution of two new doublets corresponding to H_{16}^i and H_{17}^i protons in the range of 6.00-6.50 ppm possessing J value of ~12 Hz is noticed. The signals due to the protons (H_{13}-H_{15} and H_{18}-H_{20}), adjacent to the olefinic double bonds, also show a substantial decrease in intensity upon photo-irradiation. Additionally, new unresolved proton signals appear in the range of ~5.90-8.00 ppm, likely corresponding to the H_{13}^i-H_{15}^i and H_{18}^i-H_{20}^i protons. In complex **1**, a slight reduction in peak intensity of $H_{9'}$-$H_{12'}$ protons is also observed, along with the appearance of new peaks corresponding to $H_{9'}^i$-$H_{12'}^i$ protons. The comparison of the ^{1}H NMR spectra of the initial and photolyzed forms of the complexes, together with significant reduction in J value of the olefinic H_{16}^i and H_{17}^i protons, suggests that isomerization is taking place in both cases. However, complete conversion from *trans* to *cis* (for **1**) or from *t-t* to *c-c* (for **2**) does not occur, even after prolonged light irradiation. It is therefore plausible that both *trans* and *cis* forms in **1**, and *t-t*, *t-c*, as well as *c-c* forms in **2** coexist, irrespective of their relative abundance, in the photostationary state.

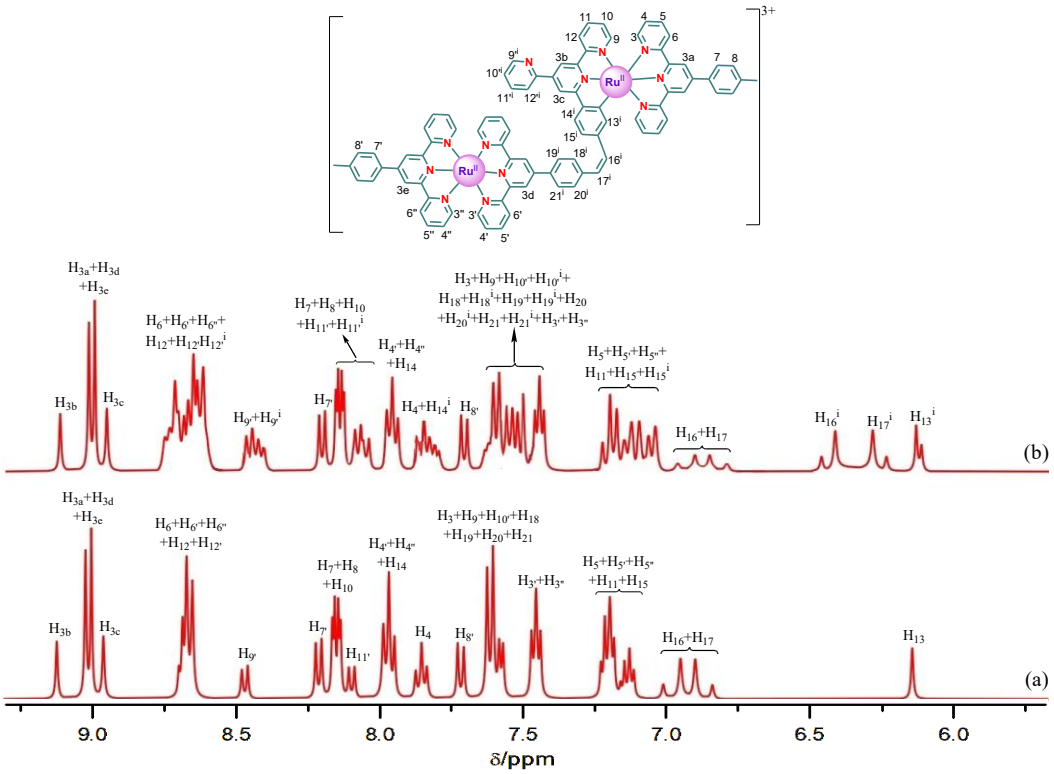

Figure 3.27. ^{1}H NMR spectrum of **1** in CD_3CN before (a) and after (b) photolysis with light of λ=500 nm for 8 h.

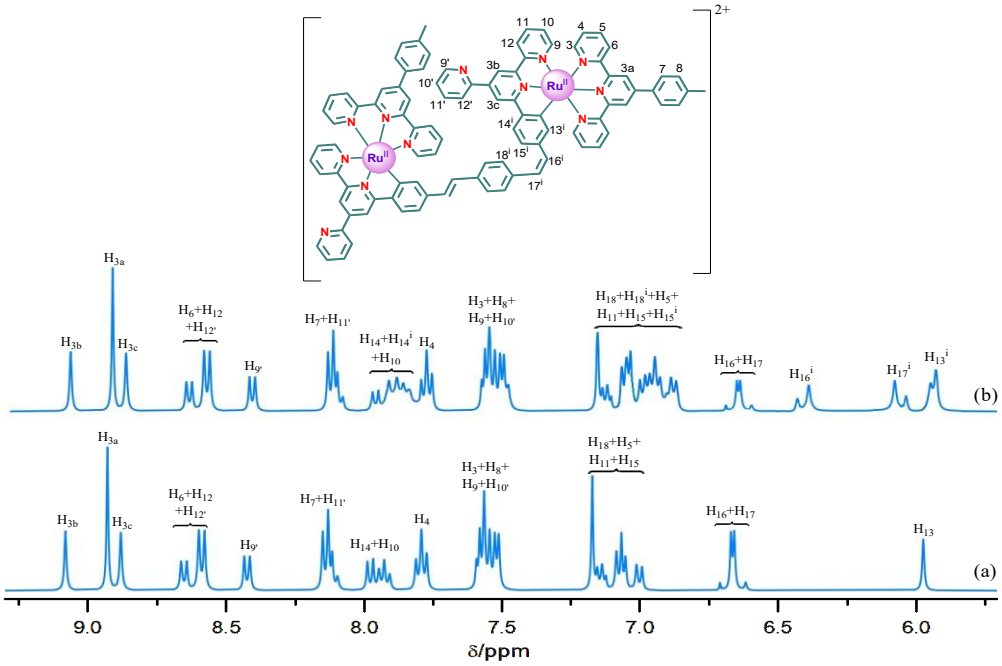

Figure 3.28. ^{1}H NMR spectrum of **2** in CD_3CN before (a) and after (b) photolysis with light of λ=500 nm for 10 h.

To validate our experimental findings, we conducted theoretical calculations on the *cis* form of **1**, as well as the *t-c* and *c-c* isomers of **2**. The optimized geometries of all the forms are presented in Figures 3.29 and 3.30. The frontier molecular orbitals of **2** are presented in Figures 3.31 and 3.32. Additionally, the absorption spectral parameters and band assignments are summarized in Table 3.4. Interestingly, the experimental absorption spectra of **1** after photoisomerization exhibit a remarkable resemblance with the calculated spectra of *cis* form as shown in Figure 3.33a. On the other hand, Figure 3.33b depicts the overlay of the experimental absorption spectra after photoisomerization and the calculated spectra of both *t-c* and *c-c* forms of **2**. This overlay demonstrates a strong correlation between the experimental and theoretical spectra of the *t-c* form. We have also performed UKS calculation on the T1 state of the *cis* form of **1** as well as the *t-c* form of **2** in their triplet optimized geometries. The comparison of the theoretical and experimental emission maxima is tabulated in Table 3.5 which indicates that the correlation is reasonably good for **2**, but differs quite substantially for **1**.

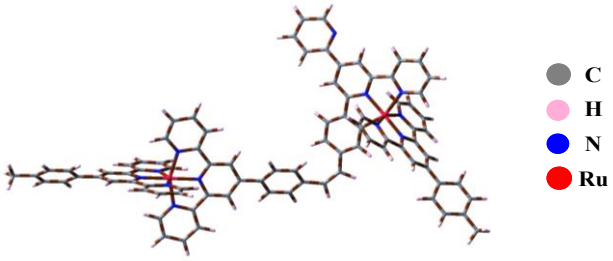

Figure 3.29. Ground state optimized geometry of *cis* form of **1** acetonitrile.

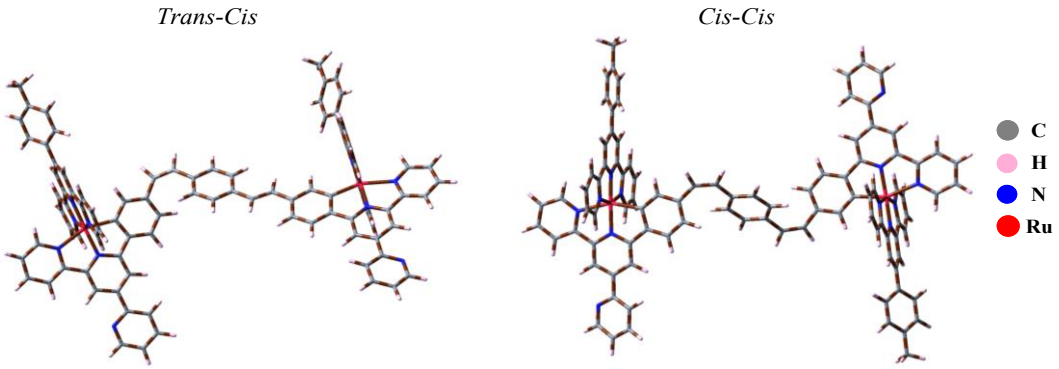

Figure 3.30. Ground state optimized geometries of *trans-cis* and *cis-cis* forms of **2** in acetonitrile.

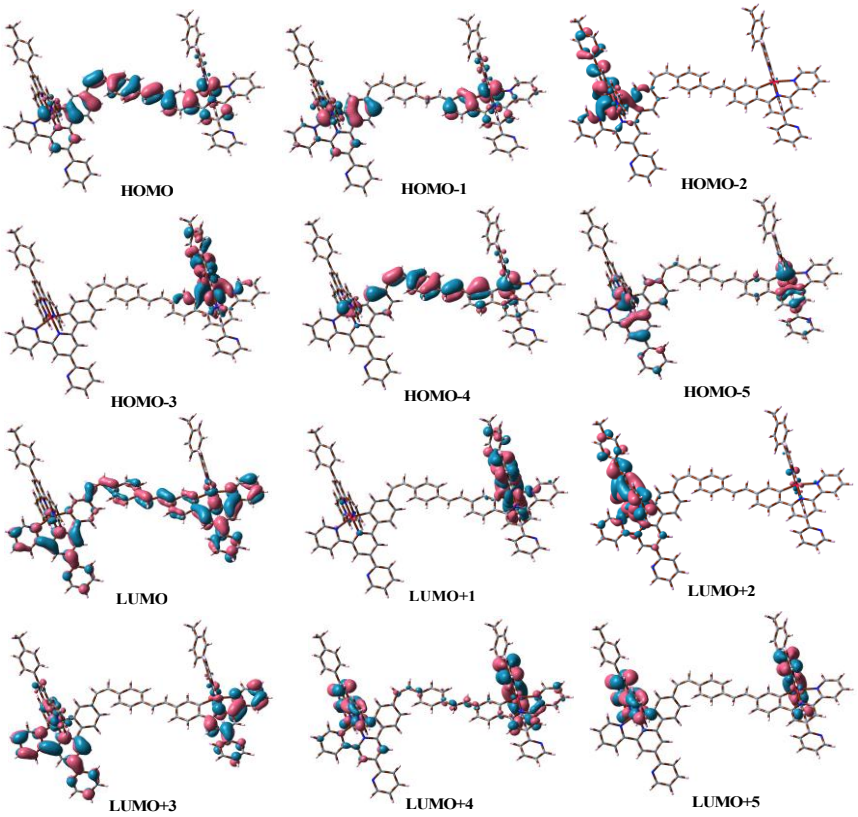

Figure 3.31. Schematic drawings of the selective frontier molecular orbitals of the *trans-cis* form of **2** in acetonitrile.

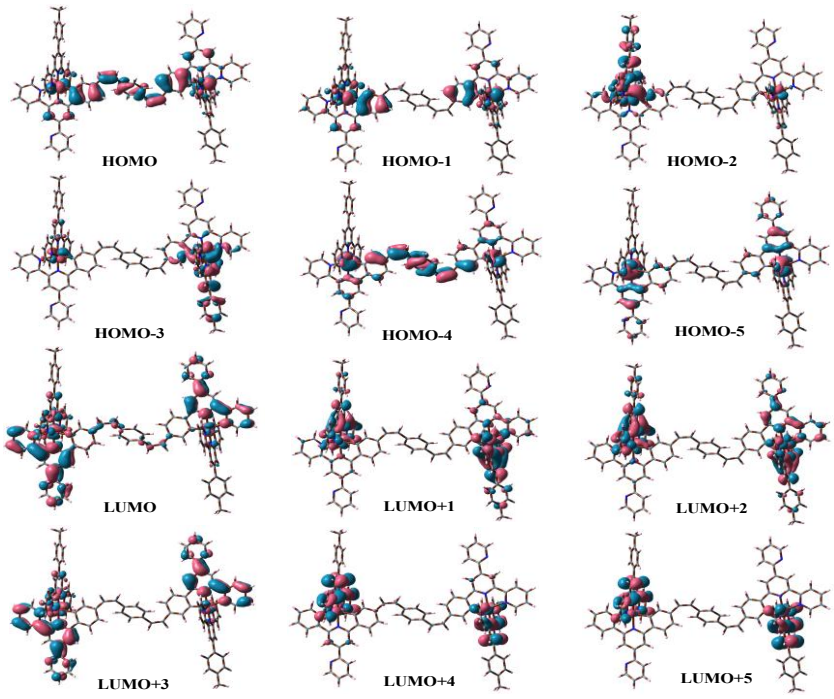

Figure 3.32. Schematic drawings of the selective frontier molecular orbitals of the *cis-cis* form of **2** in acetonitrile.

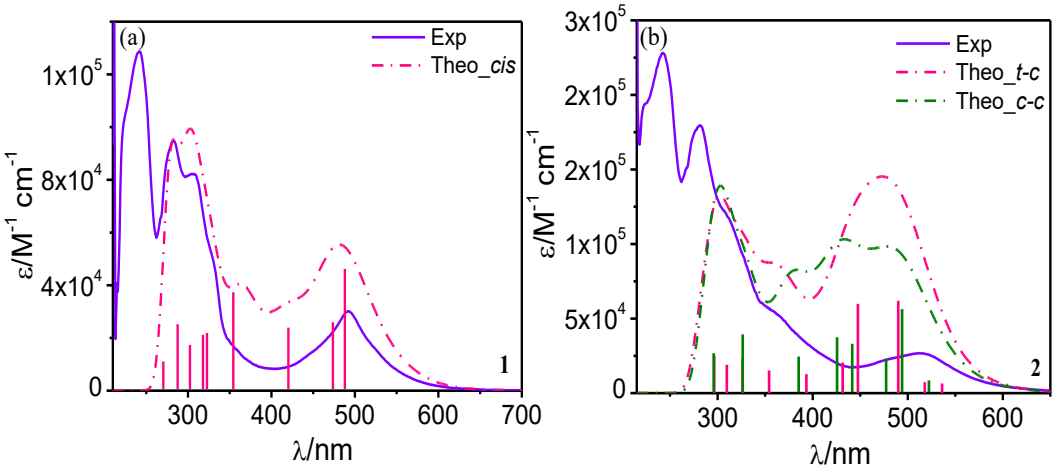

Figure 3.33. Overlay of the experimental and theoretical absorption spectra of **1** (a) and **2** (b) in MeCN.

The conversion yield (*trans*→*cis* or *t-t*→*t-c*) of the complexes was quantified by calculating the percentage based on the ratio of the ^{1}H NMR signal integrals corresponding to the H_{16} and H_{17} protons of the respective pair of isomers at their photostationary states. It is observed that the conversion efficiency is ~73-77% for both the complexes. The rate constants (k_{iso}) and quantum yields ($\Phi_t \rightarrow \Phi_c / \Phi_{tt} \rightarrow \Phi_{tc}$) associated with the photoisomerization process were also determined using absorption titration profiles. Relevant data are summarized in Table 3.10 and graphically presented in Figure 3.34. The rate constant values range from 1.5×10^{-4} to 2.3×10^{-4} s^{-1}, while $\Phi_t \rightarrow \Phi_c$ and $\Phi_{tt} \rightarrow \Phi_{tc}$ are 1.2×10^{-2} and 5.4×10^{-3}, respectively. Notably, the rate constant for **1** is higher than that for **2**, likely due to the bulkier size of **2** compared to **1**.

To inspect the reversibility of the isomerization process, the photolyzed complexes were again subjected to UV light (270 nm), and the progress of the transformation was monitored using absorption and emission spectroscopy (Figure 3.35). A critical analysis of the spectral bands reveals that the predominant *cis* (for **1**) or *t-c* (for **2**) forms of the complexes almost revert back to their initial *trans* or *t-t* form. However, the reverse process is much slower (6-7 h) compared to the forward one. Thus, "on-off" and "off-on" emission switching is feasible upon alternate exposure to UV and visible light. The rate constant (k_{iso}) and quantum yield ($\Phi_c \rightarrow \Phi_t / \Phi_{tc} \rightarrow \Phi_{tt}$) values for the reverse processes are also estimated and presented in Table 3.10 and Figure 3.36. The k_{iso} values vary from 7.2-9.4×10^{-5} s^{-1} and $\Phi_c \rightarrow \Phi_t / \Phi_{tc} \rightarrow \Phi_{tt}$ ranges from 2.6-6.3×10^{-3}.

Table 3.10. Quantum Yield (Φ) and Rate Constants (k_{iso}) of Photoisomerization of **1** and **2** in MeCN.

	Forward process		Reverse process		Acidulated Form	
Compounds	Quantum yield ($\Phi \times 10^3$)	Rate constant ($k_{iso} \times 10^4/s^{-1}$)	Quantum yield ($\Phi \times 10^3$)	Rate constant ($k_{iso} \times 10^4/s^{-1}$)	Quantum yield ($\Phi \times 10^2$)	Rate constant ($k_{iso} \times 10^3/s^{-1}$)
1	12.2	2.3	6.3	0.9	5.4	1.4
2	5.4	1.5	2.6	0.7	3.6	0.8

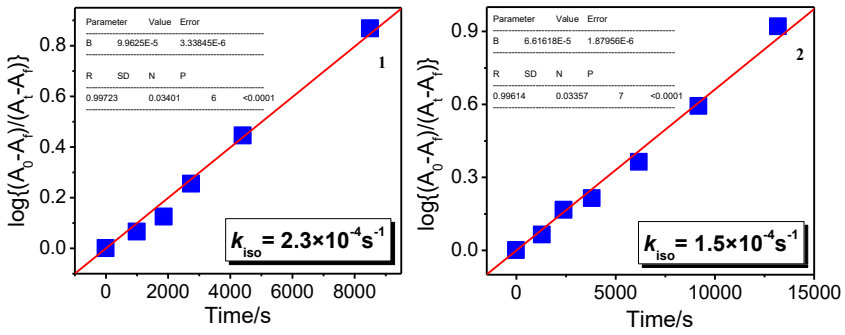

Figure 3.34. Linear plot of log $(A_0-A_f)/(A_t-A_f)$ *vs.* time (t) for absorption spectral changes upon irradiation of the MeCN solution of **1** and **2** with 500 nm light**.** These plots give the values of rate constant of forward photo-isomerization for the complexes.

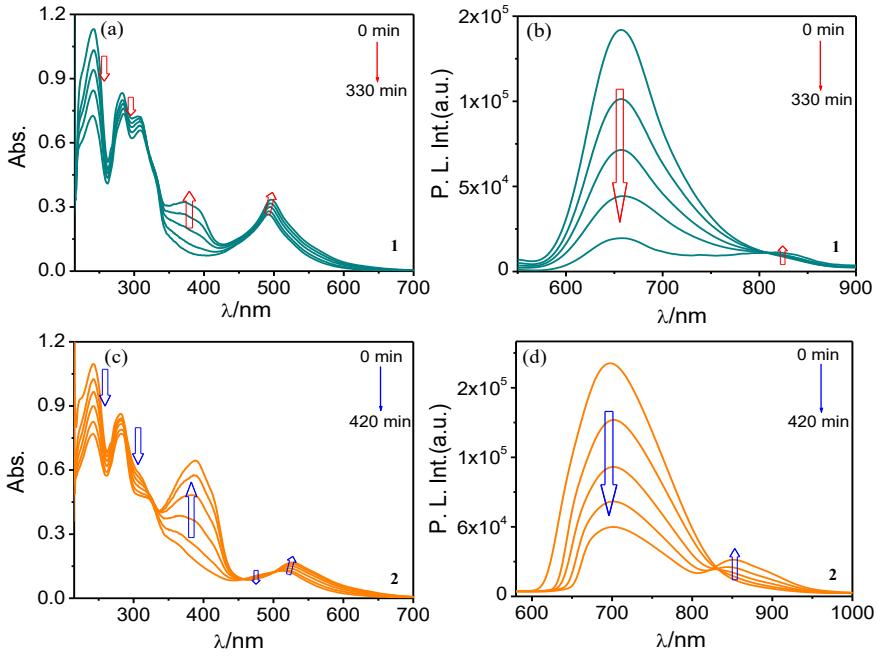

Figure 3.35. UV-vis absorption (a and c) and emission (b and d) spectral changes upon irradiating the photolyzed MeCN solution of **1** and **2** with 270 nm light. Insets show the irradiation time.

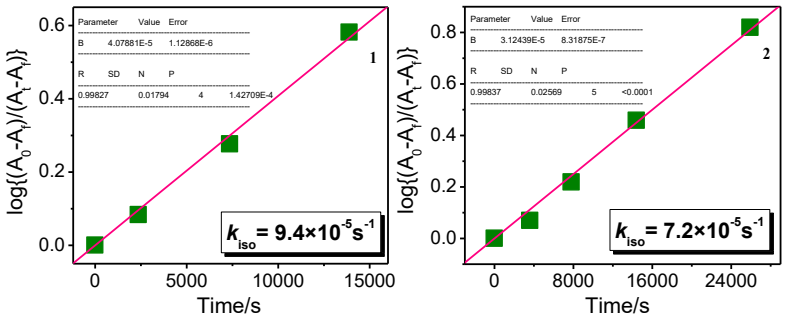

Figure 3.36. Linear plot of log $(A_0-A_f)/(A_t-A_f)$ *vs.* time (t) for absorption spectral changes upon irradiation of the photolyzed solution in MeCN with 270 nm light for **1** and **2.** These plots give the values of rate constant of reverse photo-isomerization for the complexes.

We are now interested to explore the effect of acid on the photoisomerization behavior of the complexes. To achieve this, we conducted two sets of experiments. Initially, the MeCN solution of the complexes is treated with acid up to their first saturation, wherein the non-coordinated N atoms in the outer coordination sphere of the complexes get protonated as already shown in Figures 3.12 and 3.13. The acidulated solution is then subjected to light irradiation (λ_{ex}=500 nm) and the progress of the reaction is monitored spectroscopically (Figures 3.37 and 3.38). Upon light irradiation, substantial reduction in band intensity at ~567 nm as well as at ~370 nm together with slight increase in the absorbance in the UV region (220-330 nm) is noticed for complex **1** in a single step. The observed change indicates that Ru-C bond cleavage and *trans*→*cis* isomerization processes take place simultaneously. In case of emission spectra, a new band at ~665 nm is evolved and gets intensified quite substantially together with a slight blue-shift of the emission

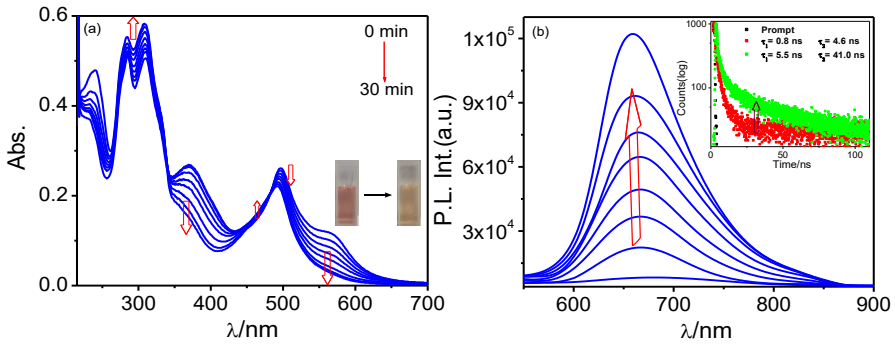

Figure 3.37. Absorption (a) and emission (b) spectral changes of acidulated MeCN solutions of **1** upon irradiating with visible light (500 nm). Insets to figure a show the irradiation time and the color change observed in naked eye upon irradiating with visible light. Inset to figure b shows the decay profile before and after photolysis along with the lifetime values.

maximum. This substantial increase in emission intensity is probably due to cumulative effect induced by bidentate (NN)-type motif brought about by Ru-C bond cleavage, and *trans-cis* isomerization. Interestingly, the time required to reach the photo-stationary state is only 30 min for **1** in contrast to 180 min for its non-acidulated counterpart. The process is also accompanied with a visual color change from reddish-purple to reddish-orange.

Complex **2**, on the other hand, exhibits two-step changes upon light irradiation on its acid-treated solution up to first saturation (Figure 3.38). In the absorption spectra, the band at ~570 nm gets totally quenched together with a small rise in intensity at ~480 nm in the first step. Additionally, the highly intense band at ~390 nm gets reduced to some extent, while a moderate increase in intensity of the band at ~315 nm is observed. The color change for the solution is also observed from purple to yellowish-orange during light irradiation. These observations clearly indicate that upon light irradiation on the acidulated solution of **2**, both Ru-C bond cleavage and photoisomerization take place simultaneously. However, we surmise that the contribution of photocleavage is predominant over the isomerization process in the first step. In the second step, the absorption band at 480 nm gets slightly reduced and a remarkable decrease in the band intensity at ~390 nm is noticed, while the band at 243 nm is gradually increased. Therefore, light irradiation on the acidulated solution

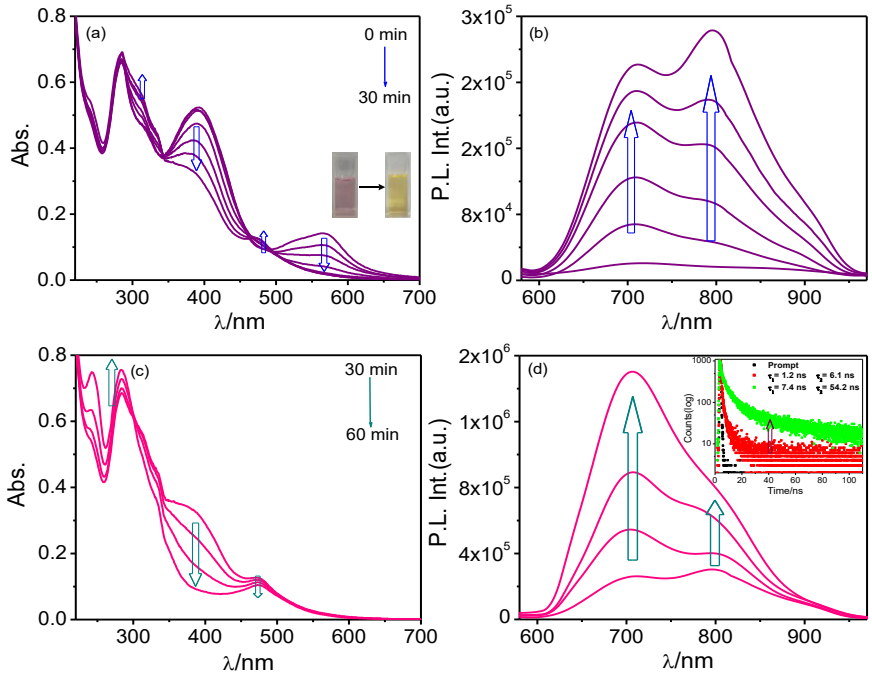

Figure 3.38. Two-step changes in absorption (a and c) and emission (b and d) spectral changes of acidulated MeCN solutions of **2** upon irradiating with visible light (500 nm). Insets to figure a show the irradiation time and visual change. Inset to figure d shows the decay profile and lifetime before and after photolysis.

of **2** leads to the photoisomerization of its de-coordinated form in the second step. Interestingly, the spectral saturation for this acid-treated photoisomerization process occurs within 60 min for **2**, which is significantly shorter than the time required (300 min) to reach the photo-stationary state in the absence of acid. In the emission side, a broad band spanning in the domain of 650-850 nm, is generated in the first step. Eventually, this broad band splits into two closely situated bands with their maxima at ~710 and 795 nm. The intensity of these two emission bands continues to increase considerably upon light irradiation, although the increase at 795 nm (probably due to Ru-C bond cleavage) is slightly greater than that at 710 nm (probably due to photoisomerization). Continued photo-irradiation leads to further enhancement in the intensity of the said two bands in the second step, although the extent of increase in intensity of the band at ~710 nm is more relative to that at ~795 nm. Eventually, the band at 795 nm gets overlapped with the highly intense peak at 710 nm and it looks like a hump. Essentially, a highly intense and broad band is observed at saturation in the second step of light irradiation. The outcomes of the TCSPC measurements indicate that the lifetime of acid-treated solutions of the complexes also increases substantially upon light irradiation (4.6 ns→41.0 ns for **1** and 6.1 ns→54.2 ns for **2**) compared with their non-acidulated counterpart (insets of Figure 3.37b and Figure 3.38d).

The rate constants (k_{iso}) and quantum yield of photoisomerization for the acid-treated solutions of the complexes were also evaluated (Table 3.10 and Figure 3.39). The rate constant values vary from 8.5×10^{-4} to 1.4×10^{-3} s^{-1}, while the quantum yields are 3.6×10^{-2} and 5.4×10^{-2}. The observed values clearly indicate that the photoisomerization process of the acid-treated complexes is much faster than that in absence of acid. Upon acid treatment, the N atoms in the outer coordination sphere get protonated, thereby increasing the overall

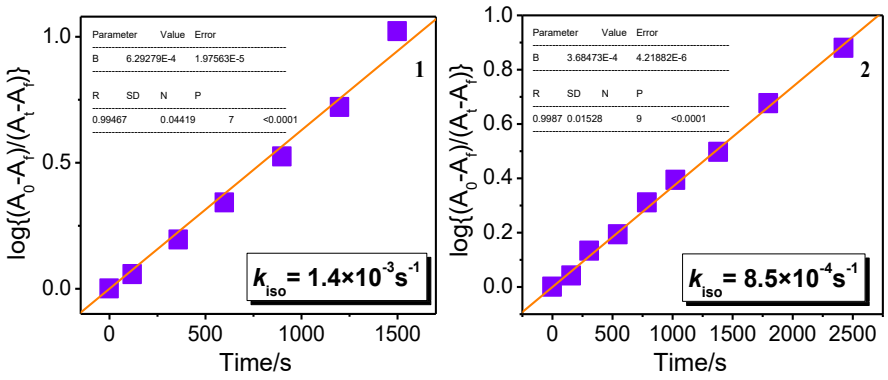

Figure 3.39. Linear plot of log $(A_0-A_f)/(A_t-A_f)$ *vs.* time (t) for absorption spectral changes upon irradiation of the acid-treated solution in MeCN with 500 nm light for **1** and **2**.

charge of the complexes. The increased charge, in turn, reduces the electron density across the C=C bond, thereby imparting more single-bond character. Consequently, light irradiation makes rotation across the phenylene-vinylene motifs more feasible in the protonated forms of the complexes, which is also evident from the rate constant values of the isomerization processes (Table 3.10).

3.4. Conclusions

With regard to our objective of designing NIR-emissive molecular photoswitches, we report herein the synthesis and thorough characterization of two Ru(II)-terpyridine dimers having cyclometalated as well as phenylene-vinylene units integrated in the bridging ligands and investigated their photophysical and electrochemical properties in presence of various external stimuli such as acid, base, heat and light. For fine tuning of the photophysical and electrochemical properties, we have synthesized one symmetric and one asymmetric bridging ligand. The presence of strong σ-donating cyclometalating units increases the electron density around Ru(II) centers, which in turn causes a significant red-shift in absorption and emission maxima compared to the parent complex $[Ru(tpy)_2]^{2+}$. Interestingly, both the complexes emit in the NIR domain (820-850 nm) at RT. Due to the presence of non-coordinated nitrogen atom(s) at the cyclometalated sites in the outer coordination sphere, substantial alteration of the spectral and redox properties of the complexes is feasible through acid-base equilibria. Besides, de-coordination of Ru-C bonds in presence of excess acid and re-coordination of the same in presence of base and heat are also made possible. On the other hand, the phenylene-vinylene units in the bridging ligands promote *trans*→*cis*/*trans-trans*→*trans-cis* isomerization upon irradiation with visible light. The reverse *cis*→*trans* or *trans-cis*→*trans-trans* isomerization is also achieved by irradiating the photolyzed complexes with UV light, although the process is slower than the forward one. Thus, "on-off" and "off-on" emission switching in NIR region is attained via appropriate and sequential choice of external stimuli, viz. acid, base, temperature and light of particular wavelengths. Another important aspect of the present study is the significant enhancement of the rate and quantum yield of photoisomerization in presence of acid. In essence, these smart NIR-emissive molecular photoswitches could act as potential building blocks in the field of bioimaging, drug delivery and photoswitchable molecular devices in the NIR region.

3.5. References

(1) Valeur, B. Molecular Fluorescence: Principles and Applications; Wiley, **2002**.

(2) Prodi, L.; Bolletta, F.; Montalti, M. Luminescent Chemosensors for Transition Metal Ions. *Coord. Chem. Rev.* **2000**, *205*, 59-83.

(3) Michalet, X.; Pinaud, F. F.; Bentolila, L. A.; Tsay, J. M.; Doose, S.; Li, J. J.; Sundaresan, G.; Wu, A. M.; Gambhir, S. S.; Weiss, S. Quantum Dots for Live Cells, in Vivo Imaging, and Diagnostics. *Science* **2005**, *307*, 538-544.

(4) Müllen, K.; Scherf, U. Organic Light Emitting Devices–Synthesis, Properties and Applications; Wiley, **2006**.

(5) Nguyen, T. N.; Ebrahim, F. M.; Stylianou, K. C. Photoluminescent, Upconversion Luminescent and Nonlinear Optical Metal-Organic Frameworks: From Fundamental Photophysics to Potential Applications. *Coord. Chem. Rev.* **2018**, *377*, 259-306.

(6) Martinic, I.; Eliseeva, S. V.; Nguyen, T. N.; Pecoraro, V. L.; Petoud, S. Near-Infrared Optical Imaging of Necrotic Cells by Photostable Lanthanide-Based Metallacrowns. *J. Am. Chem. Soc.* **2017**, *139*, 8388-8391.

(7) Creutz, S. E.; Fainblat, R.; Kim, Y.; De Siena, M. C.; Gamelin, D. R. A Selective Cation Exchange Strategy for the Synthesis of Colloidal Yb^{3+}-Doped Chalcogenide Nanocrystals with Strong Broadband Visible Absorption and Long-Lived Near-Infrared
Emission. *J. Am. Chem. Soc.* **2017**, *139*, 11814-11824.

(8) Müller, B. J.; Borisov, S. M.; Klimant, I. Red- to NIR-Emitting, BODIPY-Based, K^{+}-Selective Fluoroionophores and Sensing Materials. *Adv. Funct. Mater.* **2016**, *26*, 7697-7707.

(9) Luo, S. L.; Zhang, E. L.; Su, Y. Q.; Cheng, T. M.; Shi, C. M. A Review of NIR Dyes in Cancer Targeting and Imaging. *Biomaterials* **2011**, *32*, 7127-7138.

(10) Kiyose, K.; Kojima, H.; Nagano, T. Functional Near-Infrared Fluorescent Probes. *Chem. - Asian J.* **2008**, *3*, 506-515.

(11) Hilderbrand, S. A.; Weissleder, R. Near-Infrared Fluorescence: Application to In Vivo Molecular Imaging. *Curr. Opin. Chem. Biol.* **2010**, *14*, 71-79.

(12) Gao, J.; Chen, X.; Cheng, Z. Near-Infrared Quantum Dots as Optical Probes for Tumor Imaging. *Curr. Top. Med. Chem.* **2010**, *10*, 1147-1157.

(13) Qian, G.; Wang, Z. Y. Near-Infrared Organic Compounds and Emerging Applications. *Chem. Asian J.* **2010**, *5*, 1006-1029.

(14) Zhuo, M.-P.; Wang, X.-D.; Liao, L.-S. Recent Progress of Novel Organic Near-Infrared-Emitting Materials. *Small Sci.* **2022**, *2*, 2200029.

(15) Zampetti, A. Minotto, A.; Cacialli, F. Near-Infrared (NIR) Organic Light-Emitting Diodes (OLEDs): Challenges and Opportunities. *Adv. Funct. Mater.* **2019**, *29*, 1807623.

(16) Li, H.; Kim, Y.; Jung, H.; Hyun, J. Y.; Shin, I. Near-Infrared (NIR) Fluorescence-Emitting Small Organic Molecules for Cancer Imaging and Therapy. *Chem. Soc. Rev.* **2022**, *51*, 8957-9008.

(17) Otto, S.; Grabolle, M.; Forster, C.; Kreitner, C.; Resch-Genger, U.; Heinze, K. $[Cr(ddpd)_2]^{3+}$: A Molecular, Water-Soluble, Highly NIR-Emissive Ruby Analogue. *Angew. Chem. Int. Ed.* **2015**, *54*, 11572-11576.

(18) Sinha, N.; JimØnez, J.-R.; Pfund, B.; Prescimone, A.; Piguet, C.; Wenger, O. S. A Near-Infrared-II Emissive Chromium(III) Complex. *Angew. Chem.* **2021**, *133*, 23915-23921.

(19) Hua, L.; Zhang, K. Y.; Liu, H.-W.; Chan, K.-S.; Lo, K. K.-W. Luminescent Iridium(III) Porphyrin Complexes as Near-Infrared-Emissive Biological Probes. *Dalton Trans.* **2023**, *52*, 12444-12453.

(20) Chung, C. Y.-S.; Li, S. P.-Y.; Louie, M.-W.; Lo, K. K.-W.; Yam, V. W.-W. Induced Self-Assembly and Disassembly of Water-Soluble Alkynylplatinum(II) Terpyridyl Complexes with "Switchable" Near-Infrared (NIR) Emission Modulated by Metal-Metal Interactions Over Physiological pH: Demonstration of pH-Responsive NIR Luminescent Probes in Cell-Imaging Studies. *Chem. Sci.* **2013**, *4*, 2453-2462.

(21) Bar, M.; Maity, D.; Deb, S.; Das, S.; Baitalik, S. Ru-Os Dyads Based on a Mixed Bipyridine-Terpyridine Bridging Ligand: Modulation of the Rate of Energy Transfer and pH-Induced Luminescence Switching in the Infrared Domain. *Dalton Trans.* **2017**, *46*, 12950-12963.

(22) Mardanya, S.; Karmakar, S.; Mondal, D.; Baitalik, S. Homo- and Heterobimetallic Ruthenium(II) and Osmium(II) Complexes Based on a Pyrene-Biimidazolate Spacer as Efficient DNA-Binding Probes in the Near-Infrared Domain. *Inorg. Chem.* **2016**, *55*, 3475-3489.

(23) Kayanuma, M.; Gindensperger, E.; Daniel, C. Inorganic Photoisomerization: The Case Study of Rhenium(I) Complexes. *Dalton Trans.* **2012**, *41*, 13191-13203.

(24) Costa, P. J.; Calhorda, M. J.; Bossert, J.; Daniel, C.; Romão, C. C. Photochemistry of Methyltrioxorhenium Revisited: A DFT/TD-DFT and CASSCF/MS-CASPT2 Theoretical Study. *Organometallics* **2006**, *25*, 5235-5241.

(25) Kayanuma, M.; Daniel, C.; Koppel, H.; Gindensperger, E. Photophysics of Isomerizable Re(I) Complexes: A Theoretical Analysis. *Coord. Chem. Rev.* **2011**, *255*, 2693-2703.

(26) Deb, S.; Sahoo, A.; Pal, P.; Baitalik, S. Exploitation of the Second Coordination Sphere to Promote Significant Increase of Room-Temperature Luminescence Lifetime and Anion Sensing in Ruthenium-Terpyridine Complexes. *Inorg. Chem.* **2021**, *60*, 6836-6851.

(27) Mondal, D.; Biswas, S.; Paul, A.; Baitalik, S. Luminescent Dinuclear Ruthenium Terpyridine Complexes with a Bis-Phenylbenzimidazole Spacer. *Inorg. Chem.* **2017**, *56*, 7624-7641.

(28) McConnell, A. J.; Wood, C. S.; Neelakandan, P. P.; N`itschke, J. R. Stimuli-Responsive Metal-Ligand Assemblies. *Chem. Rev.* **2015**, *115*, 7729-7793.

(29) Brieke, C.; Rohrbach, F.; Gottschalk, A.; Mayer, G.; Heckel, A. Light-Controlled Tools. *Angew. Chem., Int. Ed.* **2012**, *51*, 8446-8476.

(30) Ankenbruck, N.; Courtney, T.; Naro, Y.; Deiters, A. Optochemical Control of Biological Processes in Cells and Animals. *Angew. Chem., Int. Ed.* **2018**, *57*, 2768-2798.

(31) Badjic, J. D.; Balzani, V.; Credi, A.; Silvi, S.; Stoddart, J. F. A Molecular Elevator. *Science* **2004**, *303*, 1845-1849.

(32) Saha, S.; Stoddart, J. F. Photo-Driven Molecular Devices. *Chem. Soc. Rev.* **2007**, *36*, 77-92.

(33) Lubbe, S.; Szymanski, W.; Feringa, B. L. Recent Developments in Reversible Photoregulation of Oligonucleotide Structure and Function. *Chem. Soc. Rev.* **2017**, *46*, 1052-1079.

(34) Russew, M.-M.; Hecht, S. Photoswitches: From Molecules to Materials. *Adv. Mater.* **2010**, *22*, 3348-3360.

(35) Yagai, S.; Kitamura, A. Recent Advances in Photoresponsive Supramolecular Self-Assemblies. *Chem. Soc. Rev.* **2008**, *37*, 1520-1529.

(36) Dattler, D.; Fuks, G.; Heiser, J.; Moulin, E.; Perrot, A.; Yao, X.; Giuseppone, N. Design of Collective Motions from Synthetic Molecular Switches, Rotors, and Motors. *Chem. Rev.* **2020**, *120*, 310-433.

(37) Juris, A.; Balzani, V.; Barigelletti, F.; Campagna, S.; Beleser, P.; Zelewsky, A. V. Ru(II) Polypyridine Complexes: Photophysics, Photochemistry, Eletrochemistry, and Chemiluminescence. *Coord. Chem. Rev*. **1988**, *84*, 85-277.

(38) Sauvage, J.-P.; Collin, J. P. J.; Chambron, C.; Guillerez, S.; Coudret, C.; Balzani, V.; Barigelletti, F.; de Cola, L.; Flamigni, L. Ruthenium(II) and Osmium(II) Bis(Terpyridine) Complexes in Covalently-Linked Multicomponent Systems: Synthesis, Electrochemical Behavior, Absorption Spectra, and Photochemical and Photophysical Properties. *Chem. Rev*. **1994**, *94*, 993-1019.

(39) Maity, D.; Bhaumik, C.; Mardanya, S.; Karmakar, S.; Baitalik, S. Light Harvesting and Directional Energy Transfer in Long-Lived Homo- and Heterotrimetallic Complexes of Fe^{II}, Ru^{II}, and Os^{II}. *Chem. Eur. J.* **2014**, *20*, 13242-13252.

(40) Balzani, V.; Juris, A.; Venturi, M.; Campagna, S.; Serroni, S. Luminescent and Redox-Active Polynuclear Transition Metal Complexes. *Chem. Rev*. **1996**, *96*, 759-834.

(41) Bandara, H. M. D.; Burdette, S. C. Photoisomerization in Different Classes of Azobenzene. *Chem. Soc. Rev.* **2012**, *41*, 1809-1825.

(42) Kurihara, M.; Nishihara, H. Azo- and Quinone-Conjugated Redox Complexes-Photo- and Proton-Coupled Intramolecular Reactions Based on d-π Interaction. *Coord. Chem. Rev.* **2002**, *226*, 125-135.

(43) Yutaka, T.; Mori, I.; Kurihara, M.; Mizutani, J.; Tamai, N.; Kawai, T.; Irie, M.; Nishihara, H. Photoluminescence Switching of Azobenzene-Conjugated Pt(II) Terpyridine Complexes by Trans-Cis Photoisomerization. *Inorg. Chem.* **2002**, *41*, 7143-7150.

(44) Yutaka, T.; Kurihara, M.; Kubo, K.; Nishihara, H. Novel Photoisomerization Behavior of Rh Binuclear Complexes Involving an Azobenzene-Bridged Bis(Terpyridine) Ligand. Strong Effects of Counter-Ion and Solvent and the Induction of Redox Potential Shift. *Inorg. Chem.* **2000**, *39*, 3438-3439.

(45) Yutaka, T.; Mori, I.; Kurihara, M.; Mizutani, J.; Kubo, K.; Furusho, S.; Matsumura, K.; Tamai, N.; Nishihara, H. Synthesis, Characterization, and Photochemical Properties of Azobenzene-Conjugated Ru(II) and Rh(III) Bis(Terpyridine) Complexes. *Inorg. Chem.* **2001**, *40*, 4986-4995.

(46) Amaral, R. C.; Iha, N. Y. M. Molecular Engineered Rhenium(I) Carbonyl Complexes to Promote Photoisomerization of Coordinated Stilbene-Like Ligands in the Visible Region. *Dalton Trans.* **2018**, *47*, 13081-13087.

(47) Zanoni, K. P. S.; Iha, N. Y. M. Reversible Trans ⇌ Cis Photoisomerizations of $[Re(CO)_3(Ph_2phen)(StpyCN)]^+$ Towards Molecular Machines. *Dalton Trans.* **2017**, *46*, 9951-9958.

(48) Amaral, R. C.; Matos, L. S.; Zanoni, K. P. S.; Iha, N. Y. M. Photoreversible Molecular Motion of stpyCN Coordinated to fac-$[Re(CO)_3(NN)]^+$ Complexes. *J. Phys. Chem. A* **2018**, *122*, 6071-6080.

(49) Ganguly, T.; Pal, P.; Maity, D.; Baitalik, S. Synthesis, Characterization and Emission Switching Behaviors of Styrylphenyl-Conjugated Ru(II)-Terpyridine Complexes via Aggregation and Trans-Cis Photoisomerization. *J. Photochem. Photobiol. A* **2023**, *440*, 114662.

(50) Gindensperger, E.; Koppel, H.; Daniel, C. Mechanism of Visible-Light Photoisomerization of a Rhenium(I) Carbonyl-Diimine Complex. *Chem. Commun.* **2009**, *46*, 8225.

(51) Irie, M.; Yokoyama, Y. Diarylethenes for Memories and Switches. *Chem. Rev.* **2000**, *100* (5), 1685-1716.

(52) Irie, M.; Fukaminato, T.; Matsuda, K.; Kobatake, S. Photochromism of Diarylethene Molecules and Crystals: Memories, Switches, and Actuators. *Chem. Rev.* **2014**, *114*, 12174-12277.

(53) Matsuda, K.; Irie, M. Diarylethene as a Photoswitching Unit. *J. Photochem. Photobiol. C* **2004**, *5* (2), 169-182.

(54) Irie, M.; Sakemura, K.; Okinaka, M.; Uchida, K. Photochromism of Dithienylethenes with Electron-Donating Substituents. *J. Org. Chem.* **1995**, *60*, 8305-8309.

(55) Pal, P.; Ganguly, T.; Sahoo, A.; Baitalik, S. Emission Switching in the Near-Infrared by Reversible Trans-Cis Photoisomerization of Styrylbenzene-Conjugated Osmium Terpyridine Complexes. *Inorg. Chem.* **2021**, *60*, 4869-4882.

(56) Ganguly, T.; Das, S.; Maity, D.; Baitalik, S. Luminescent Ruthenium-Terpyridine Complexes Coupled with Stilbene-Appended Naphthalene, Anthracene, and Pyrene Motifs Demonstrate Fluoride Ion Sensing and Reversible Trans-Cis Photoisomerization. *Inorg. Chem.* **2024**, *63*, 6883-6897.

(57) Pal, P.; Mukherjee, S.; Maity, D.; Baitalik, S. Synthesis, Structural Characterization, and Luminescence Switching of Diarylethene-Conjugated Ru(II)-Terpyridine Complexes by Trans-Cis Photoisomerization: Experimental and DFT/TD-DFT Investigation. *Inorg. Chem.* **2018**, *57*, 5743-5753.

(58) Das, S.; Bar, M.; Ganguly, T.; Baitalik, S. Control of Photoisomerization Kinetics via Multistage Switching in Bimetallic Ru(II)-Terpyridine Complexes. *Inorg. Chem.* **2024**, *63*, 6600-6615.

(59) Wei, F.; Lai, S.-L.; Zhao, S.; Ng, M.; Chan, M.-Y.; Yam, V. W.-W.; Wong, K. M.-C. Ligand Mediated Luminescence Enhancement in Cyclometalated Rhodium(III) Complexes and their Applications in Efficient Organic Light-Emitting Devices. *J. Am. Chem. Soc.* **2019**, *141*, 12863-12871.

(60) Fung, T. H.-C.; Ng, M.; Wu, N. M.-W.; Yam, V. W.-W. Dithienylethene-Containing Cyclometalated Platinum(II) Complexes with Tunable Photochromic and Photophysical Properties. *Eur. J. Inorg. Chem.* **2022**, *2022*, e202200534.

(61) Liu, J.; Chan, A. K.-W.; Ng, M.; Hong, E. Y.-H.; Wu, N. M.-W.; Wu, L.; Yam, V. W.-W. Synthesis, Characterization, and Photochromic Studies of Cyclometalated Iridium (III) Complexes Containing a Spironaphthoxazine Moiety. *Organometallics* **2019**, *38*, 3542-3552.

(62) Chan, A. K.-W.; Lam, E. S.-H.; Tam, A. Y.-Y.; Tsang, D. P.-K.; Lam, W. H.; Chan, M.-Y.; Wong, W.-T.; Yam, V. W.-W. Synthesis and Characterization of Luminescent Cyclometalated Platinum(II) Complexes of 1,3-Bis-Hetero-Azolylbenzenes with Tunable Color for Applications in Organic Light-Emitting Devices through Extension of π Conjugation by Variation of the Heteroatom. *Chem. Eur. J.* **2013**, *19*, 13910-13924.

(63) Wu, S.-H.; Burkhardt, S. E.; Zhong, Y.-W.; Abruña, H. D. Cyclometalated Ruthenium Oligomers with 2,3-Di(2-Pyridyl)-5,6-Diphenylpyrazine: A Combined Experimental, Computational, and Comparison Study with Non-cyclometalated Analogous. *Inorg. Chem.* **2012**, *51*, 13312-13320.

(64) Yang, W.-W.; Zhong, Y.-W.; Yoshikawa, S.; Shao, J.-Y.; Masaoka, S.; Sakai, K.; Yao, J.; Haga, Masa-aki. Tuning of Redox Potentials by Introducing a Cyclometalated Bond to Bis-tridentate Ruthenium(II) Complexes Bearing Bis(N-methylbenzimidazolyl)benzene or -pyridine Ligand. *Inorg. Chem.* **2012**, *51*, 890-899.

(65) Yao, C.-J.; Zhong, Y.-W.; Nie, H.-J.; Abruña, H. D.; Yao, J. Near-IR Electrochromism in Electropolymerized Films of a Biscyclometalated Ruthenium Complex Bridged by 1,2,4,5-Tetra(2-pyridyl)benzene. *J. Am. Chem. Soc.* **2011**, *133*, 20720-20723.

(66) Wang, H.; Shao, J.-Y.; Duan, R.; Wang, K.-Z. Zhong, Y.-W. Synthesis and Electronic Coupling Studies of Cyclometalated Diruthenium Complexes Bridged by 3,3',5,5'-Tetrakis(benzimidazol-2-yl)-Biphenyl. *Dalton Trans.* **2021**, *50*, 4219-4230.

(67) Shao, J.-Y.; Yang, W.-W.; Yao, J.; Zhong, Y.-W. Biscyclometalated Ruthenium Complexes Bridged by 3,3′,5,5′-Tetrakis(N-methylbenzimidazol-2-yl)biphenyl: Synthesis and Spectroscopic and Electronic Coupling Studies. *Inorg. Chem.* **2012**, *51*, 4343-4351.

(68) Wadman, S. H.; Lutz, M.; Tooke, D. M.; Spek, A. L.; Hartl, F.; Havenith, R. W. A.; van Klink, G. P. M.; van Koten, G. Consequences of N,C,N- and C,N,N-Coordination Modes on Electronic and Photophysical Properties of Cyclometalated Aryl Ruthenium(II) Complexes. *Inorg. Chem.* **2009**, *48*, 1887-1900.

(69) Wadman, S. H.; Havenith, R. W. A.; Hartl, F.; Lutz, M.; Spek, A. L.; van Klink, G. P. M.; van Koten, G. Redox Chemistry and Electronic Properties of 2,3,5,6-Tetrakis(2-pyridyl)pyrazine-Bridged Diruthenium Complexes Controlled by *N*,*C*,*N*′-Bis-Cyclometalated Ligands. *Inorg. Chem.* **2009**, *48*, 5685-5696.

(70) Robson, K. C. D.; Koivisto, B. D.; Yella, A.; Sporinova, B.; Nazeeruddin, M. K.; Baumgartner, T.; Grätzel, M.; Berlinguette, C. P. Design and Development of Functionalized Cyclometalated Ruthenium Chromophores for Light-Harvesting Applications. *Inorg. Chem.* **2011**, *50*, 5494-5508.

(71) Constable, E. C.; Dunne, S. J.; Rees, D. G. F.; Schmitt, C. X. Reversible Cyclometallation at a Ruthenium(II) Centre. *Chem. Commun.* **1996**, 1169.

(72) Brown, D. G.; Sanguantrakun, N.; Schulze, B.; Schubert, U. S.; Berlinguette, C. P. Bis(tridentate) Ruthenium-Terpyridine Complexes Featuring Microsecond Excited-State Lifetimes. *J. Am. Chem. Soc.* **2012**, *134*, 12354-12357.

(73) Hofmeier, H.; Schubert, U. S. Recent Developments in the Supramolecular Chemistry of Terpyridine-Metal Complexes. *Chem. Soc. Rev.* **2004**, *33*, 373-399.

(74) Kreitner, C.; Erdmann, E.; Seidel, W. W.; Heinze, K. Understanding the Excited State Behavior of Cyclometalated Bis(tridentate)ruthenium(II) Complexes: A Combined Experimental and Theoretical Study. *Inorg. Chem.* **2015**, *54*, 11088-11104.

(75) Kreitner, C.; Heinze, K. Excited State Decay of Cyclometalated Polypyridine Ruthenium Complexes: Insight from Theory and Experiment. *Dalton Trans.* **2016**, *45*, 13631-13647.

(76) Indelli, M. T.; Bignozzi, C. A.; Scandola, F.; Collin, J.-P. Design of Long-Lived Ru(II) Terpyridine MLCT States. Tricyano Terpyridine Complexes. *Inorg. Chem.* **1998**, *37*, 6084-6089.

(77) Meyer, T. J. Photochemistry of Metal Coordination Complexes: Metal to Ligand Charge Transfer Excited States. *Pure Appl. Chem.* **1986**, *58*, 1193-1206.

(78) Das, S.; Pal, P.; Ganguly, T.; Baitalik, S. Influences of Both N,N,N- and N,N,C-Coordination Modes of Tolyl-terpyridine on the Photophysical Properties of Cyclometalated Ru(II) Complexes: Combined Experimental and Theoretical Investigations on Acid/Base-Dependent Reversible Cyclometalation. *Inorg. Chem.* **2023**, *62*, 12872-12885.

(79) Ko, C.-C.; Kwok, W.-M.; Yam, V. W.-W.; Phillips, D. L. Triplet MLCT Photosensitization of the Ring-Closing Reaction of Diarylethenes by Design and Synthesis of a Photochromic Rhenium(I) Complex of a Diarylethene-Containing 1,10-Phenanthroline Ligand. *Chem. Eur. J.* **2006**, *12*, 5840-5848.

(80) Ordronneau, L.; Nitadori, H.; Ledoux, I.; Singh, A.; Williams, J. A. G.; Akita, M.; Guerchais, V.; Bozec, H. L. Photochromic Metal Complexes: Photoregulation of both the Nonlinear Optical and Luminescent Properties. *Inorg. Chem.* **2012**, *51*, 5627-5636.

(81) Vila, N.; Royal, G.; Loiseau, F.; Deronzier, A. Photochromic and Redox Properties of Bisterpyridine Ruthenium Complexes Based on Dimethyldihydropyrene Units as Bridging Ligands. *Inorg. Chem.* **2011**, *50*, 10581-10591.

(82) Yam, V. W.-W.; Yang, Y.; Zhang, J.; Chu, B. W.-K.; Zhu, N. Synthesis, Characterization, and Photoisomerization Studies of Azo- and Stilbene-Containing Surfactant Rhenium(I) Complexes. Organometallics **2001**, *20*, 4911-4918.

(83) Patrocı´nio, A. O. T.; Iha, N. Y. M. Photoswitches and Luminescent Rigidity Sensors Based on fac-$[Re(CO)_3(Me_4phen)(L)]^+$. *Inorg. Chem.* **2008**, *47*, 10851-10857.

(84) Pal, P.; Mukherjee, S.; Maity, D.; Baitalik, S. Synthesis, Photophysics, and Switchable Luminescence Properties of a New Class of Ruthenium(II)-Terpyridine Complexes Containing Photoisomerizable Styrylbenzene Units. *ACS Omega* **2018**, *3*, 14526-14537.

(85) Telleria, A.; Perez-Miqueo, J.; Altube, A.; García-Lecina, E.; de Cozar, A.; Freixa, Z. Azobenzene-Appended Bis-Cyclometalated Iridium(III) Bipyridyl Complexes. *Organometallics* **2015**, *34*, 5513-5529.

(86) Bhaumik, C.; Saha, D.; Das, S.; Baitalik, S. Synthesis, Structural Characterization, Photophysical, Electrochemical, and Anion-Sensing Studies of Luminescent Homo and Heteroleptic Ruthenium(II) and Osmium(II) Complexes Based on Terpyridyl-imidazole Ligand. *Inorg. Chem.* **2011**, *50*, 12586-12600.

(87) Wang, X. Y.; Guerzo, A.; Schmehl, R. H. Preferential Solvation of an ILCT Excited State in Bis(Terpyridine-Phenylene-Vinylene) Zn(II) Complexes. *Chem. Commum.* **2002**, 2344-2345.

(88) Baitalik, S.; Wang, X.-Y.; Schmehl, R. H. A Trimetallic Mixed Ru(II)/Fe(II) Terpyridyl Complex with a Long-Lived Excited State in Solution at Room Temperature. *J. Am. Chem. Soc.* **2004**, *126*, 16304-16305.

(89) Wang, X.-Y.; Del Guerzo, A.; Tunuguntla, H.; Schmehl, R. H. Photophysical Behavior of Ru(II) and Os(II) Terpyridyl Phenylene Vinylene Complexes: Perturbation of MLCT State by Intra-Ligand Charge-Transfer State. *Res. Chem. Intermed.* **2007**, *33*, 63-77.

(90) Wang, X.-Y.; Del Guerzo, A.; Baitalik, S.; Simon, G.; Shaw, G. B.; Chen, L. X.; Schmehl, R. The Influence of Bridging Ligand Electronic Structure on the Photophysical Properties of Noble Metal Diimine and Triimine Light Harvesting Systems. *Photosynth. Res.* **2006**, *87*, 83-103.

(91) Gille, K.; Knoll, H.; Quitzsch, K. Rate Constants of the Thermal Cis-Trans Isomerization of Azobenzene Dyes in Solvents, Acetone/Water Mixtures, and in Microheterogeneous Surfactant Solutions. Int. J. Chem. Kinet. 1999, 31, 337-350.

(92) Otsuki, J.; Suwa, K.; Narutaki, K.; Sinha, C.; Yoshikawa, I.; Araki, K. Photochromism of 2-(phenylazo)imidazoles. J. Phys. Chem A 2005, 109, 8064-8069.

(93) Sainuddin, T.; McCain, J.; Pinto, M.; Yin, H.; Gibson, J.; Hetu, M.; McFarland, S. A. Organometallic Ru(II) Photosensitizers Derived from π-Expansive Cyclometalating Ligands: Surprising Theranostic PDT Effects. *Inorg. Chem.* **2016**, *55*, 83-95.

(94) Huff, G. S.; Lo, W. K. C.; Horvath, R.; Turner, J. O.; Sun, X.-Z.; Weal, G. R.; Davidson, H. J.; Kennedy, A. D. W.; McAdam, C. J. et al. Excited States of Triphenylamine-Substituted 2-Pyridyl-1,2,3-triazole Complexes. *Inorg. Chem.* **2016**, *55*, 12238-12253.

(95) Spettel, K. E.; Damrauer, N. H. Synthesis, Electrochemical Characterization, and Photophysical Studies of Structurally Tuned Aryl-Substituted Terpyridyl Ruthenium(II) Complexes. *J. Phys. Chem. A* **2014**, *118*, 10649-10662.

(96) Rasmussen, S. C.; Ronco, S. E.; Mlsna, D. A.; Billadeau, M. A.; Pennington, W. T.; Kolis, J. W.; Petersen, J. D. Ground- and Excited-State Properties of Ruthenium(II) Complexes Containing Tridentate Azine Ligands, Ru(tpy)(bpy)L^{2+}, Where L is a Polymerizable Acetylene. *Inorg. Chem.* **1995**, *34*, 821-829.

(97) Su, X.; Zeng, R.; Li, X.; Dang, W.; Yao K.; Tang, D. Cycloruthenated Complexes: pH-Dependent Reversible Cyclometallation and Reactions with Nitrite at Octahedral Ruthenium Centers. *Dalton Trans.* **2016**, *45*, 7450-7459.

(98) Wu, Y.; Wang, Y.; Sun, Y.; Li, Z.; Li, X.; Zhou, Z.; Tang, D. Dissociation of Bipyridine and Coordination with Nitrosyl: Cyclometalated Ruthenium Nitrosyl Complex. *Inorg. Chem.* **2022**, *61*, 8997-9011.

Chapter 4

Control of Photoisomerization Kinetics via Multistage Switching in Bimetallic Ru(II)-Terpyridine Complexes

4.1. Introduction

Molecular photoswitches have recently garnered significant attention owing to their potential applications in diverse fields of research.[1-5] These switches have remarkable ability to reversibly change their characteristic signal(s) among two or more distinct states, when exposed to light of specific wavelength(s). Incorporation of this sort of light-responsive units also promotes fine tuning in the properties and functions of the resulting devices.[6-9] Light is especially well-suited for this purpose as it offers exceptional spatiotemporal precision and represents a clean and environment-friendly energy source that aligns with the principles of sustainable technologies and applications.[10,11] Over the past few decades, the most extensively explored photoswitches include azobenzene,[12-16] diarylethene,[17-20] stilbene,[21,22] and spiropyran[23] motifs. Majority of these photoswitches typically involve just a single reaction coordinate, such as *trans-cis* isomerization or electrocyclization.[24-27] These two-stage photoswitch systems have claimed considerable interest due to their remarkable 'on/off' control capabilities as well as their capability to symbolize binary digits (0/1) for encoding circuit information.[28] Expansion beyond binary systems necessitates the use of photoswitches capable of undergoing controlled changes across multiple potential reaction pathways.[29-33] These versatile switches could empower the creation of advanced materials upon implementing multi-addressable units, enhanced information storage, and intricate logic circuits.[30,34,35] The efficacy of these photoswitches critically depends on their rate of isomerization. Slow photoisomerization is unsuitable for meeting the need for a quick response. Additionally, extended exposure to high-intensity radiation could bleach the photo-responsive molecules. Therefore, inducing fast photoswitching is one of the major prerequisites for majority of applications such as optical switches,[36-38] drug delivery,[39] information storage,[40,41] to ensure a rapid response to the light signal. Thus, rational design of fast and single-component photoswitch with the ability to selectively manipulate numerous metastable intermediates across a multi-step process often offers numerous benefits over the multi-component complicated systems. Photoisomerization of the conventional photoswitches often requires UV light for activation which in turn could lead to degradation of the materials and also limit their applications in biological systems. In order to overcome the shortcomings associated with UV light, several strategies have been adopted to shift the excitation wavelengths bathochromically to the visible region.[42-45]

To this end, suitable heteroaromatic moieties incorporating multiple chromophoric units might be designed which could also act as potential ligands for metal ion complexation.[46-51] The spectral window could be further augmented upon incorporation of appropriate transition metals into the photoisomerizable ligands.[52-54] Transition metal complexes have received great attention of the researchers in recent decades for fabrication of photo-switching molecular devices, sensors, and memory storage systems because of their versatile structures and very rich as well as tuneable photophysical and redox properties.[55-59] Among various transition metals, Ru(II) complexes based on polypyridine-type ligands stand out as highly advantageous.[60-66] This is primarily because they feature broad and adjustable absorption and long-lived emission band (MLCT) encompassing a wider domain of the visible region and also exhibit very rich redox properties.[60,67,68] In this context, both bipyridine- and terpyridine-type chelating units offer the means to create a wide array of Ru(II) complexes. Terpyridines, in particular, exhibit greater effectiveness than bipyridines due to their ability to generate isomer-free rod-like structures when substituted at the 4' position.[69-71] Additionally, these structures are capable of transferring energy and/or electron quite efficiently in a predetermined direction. However, it is worth-noting that Ru(II) terpyridines are often poorly emissive at room temperature because of the close proximity of ^{3}MLCT and ^{3}MC states.[72,73] To address the limitation, various synthetic strategies could be employed. These strategies include incorporation of electron-donating or withdrawing groups,[74-80] planar polyaromatic moieties,[81-85] or organic chromophores.[86] These groups can finely adjust the electronic coupling between the ligand-centered ($^3\pi$-π^*/^{3}LC) and ^{3}MLCT states. Another approach involves destabilizing the non-emissive ^{3}MC state by utilizing cyclometalated ligands.[87-90] In essence, the luminescence of Ru(II) terpyridine complexes can be significantly enhanced either by extending conjugation in the complex structure or by reducing non-radiative pathways.

With regard to our aim of designing highly luminescent, fast and multi-state photoswitchable functional materials, we designed a new series of Ru(II) dimers of composition, $[XRu(tpvpvpt)RuX]^{4+}$ where X= ttpy, H_2bip and Me_2bip. Although one of the complexes (X= ttpy) is previously reported by Schmehl's group,[91] there is no report till date on photoisomerization studies of this type of Ru(II) complexes. The bridging bis-terpyridine ligand is synthesized by incorporating two consecutive phenylene-vinylene units in between two terminal terpyridine motifs. The bimetallic Ru(II) complexes are prepared by capping with three different type of tridentate terpyridine-type chelatig units coordinated to Ru(II) as presented in Chart 4.1. The phenylene-vinylene units boost the RT

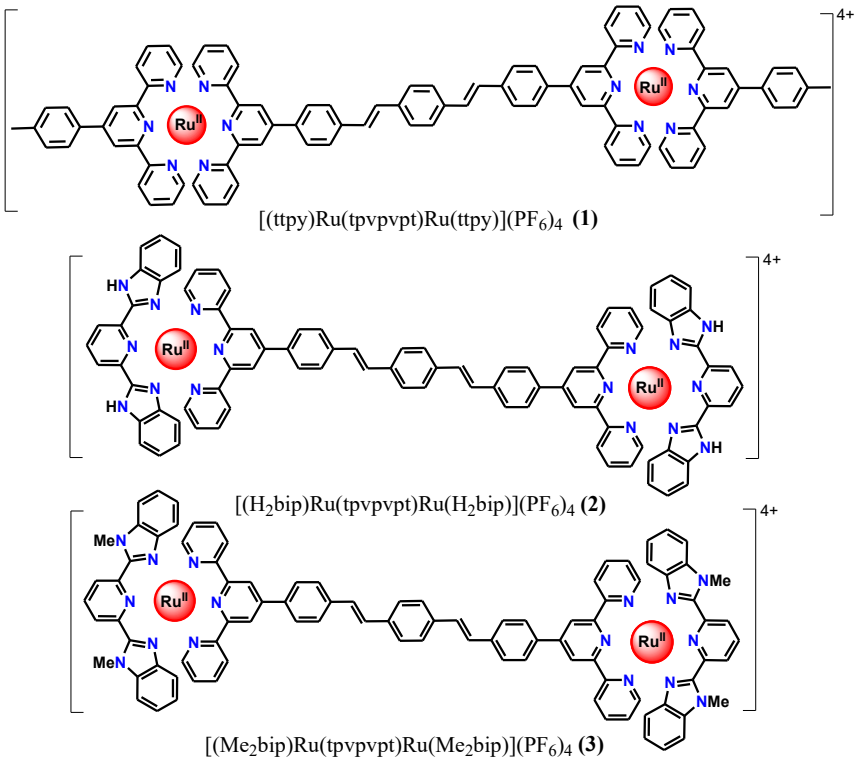

Chart 4.1. Chemical Structures of the complexes.

emission characteristics of the complexes via π-electron delocalization throughout the complex backbone, as well as undergo reversible photoisomerization. We previously reported the photoisomerization behavior of various monometallic (both homo- as well as heteroleptic) transition metal complexes containing coupled terpyridine-phenylene-vinylene conjugate.[74,75,82,92,93] However, the photoisomerization studies of bimetallic Ru(II)-terpyridine complexes having two phenylene-vinylene units in the ligand side are not precedented in the literature. The present work presents synthesis, characterization and thorough investigation on the photo-redox as well as photoisomerization behaviors of a new array of Ru(II)-dimers. Three different type of capping units are used here for systematic tuning of the photophysical characteristics and the rate of the photoisomerization process. One of the most interesting aspects of the present study is remarkable improvement of rate and quantum yield of photo-isomerization via chemical oxidation as well as reduction of the complexes. To the best of our knowledge, no report is available in the literature exhibiting this type of multi-state photo-switching accompanied with remarkable augmentation of rate and quantum yield of photoisomerization. Finally, we have also performed theoretical investigations of the complexes in both of their *trans*

and *cis* isomers by executing DFT and TD-DFT studies to get a clear picture of their electronic environment and also for appropriate assignment of absorption and emission spectral bands.

4.2. Experimental Section

4.2.1. Materials. The bridging phenylene-vinylene-substituted terpyridyl ligand (tpvpvpt) as well as the Ru(II)-precursors that are employed here as capping units are synthesized and characterized by following our reported literatures.[94-97]

4.2.2. Synthesis of the Metal Complexes. The Ru(II) complexes are prepared by adopting a common synthetic protocol as described below.

[(ttpy)Ru(tpvpvpt)Ru(ttpy)](PF$_6$)$_4$.2H$_2$O(1). A mixture of tpvpvpt (0.10 g, 0.13 mmol) and (ttpy)RuCl$_3$ (0.15 g, 0.3 mmol) in 25 mL of ethylene glycol was heated at 180ºC with stirring for 12 h under N_2 atmosphere when a red solution was formed. After cooling, the solution was poured to NH_4PF_6 (1.5 g in 5 mL of water) and stirred for few minutes, when a red colored precipitate appeared. The compound was filtered and purified by silica gel column chromatography using MeCN as the eluent. Upon rotary evaporation of the eluent to a small volume (~10 mL), a micro crystalline complex was formed which was filtered and recrystallized from MeCN-MeOH (1:5, v/v) mixture. Yield: 0.18g (64%). Anal. Calcd for $C_{96}H_{74}N_{12}Ru_2O_2P_4F_{24}$: C, 52.14; H, 3.17; N, 7.64. Found: C, 52.18; H, 3.19; N, 7.61. ^{1}H NMR (400 MHz, DMSO-d_6): δ/ppm 9.50 (s, 4H, 4H$_{3'''}$), 9.44 (s, 4H, 4H$_{3''}$), 9.10 (t, 8H, *J*=7.6 Hz, 4H$_6$+4H$_{6'}$), 8.52 (d, 4H, *J*=6.4 Hz, 4H$_8$), 8.45 (d, 4H, *J*=6.4 Hz, 4H$_7$), 8.10-8.04 (m, 12H, 4H$_{8'}$+4H$_4$+4H$_{4'}$), 7.82 (s, 4H, 4H$_{11}$), 7.61-7.56 (m, 16H, 4H$_{7'}$+4H$_3$+4H$_{3'}$+2H$_9$+2H$_{10}$), 7.32-7.29 (m, 8H, 4H$_5$+4H$_{5'}$), 2.52 (s, 6H, -CH$_3$). ^{13}C NMR (400 MHz, DMSO-d_6): δ/ppm 158.57, 155.60, 155.43, 155.39, 152.71, 147.40, 146.71, 140.86, 139.72, 138.50, 137.21, 135.36, 133.61, 130.49, 128.51, 128.23, 128.01, 127.92, 127.79, 127.75, 125.30, 121.21, 118.56, 21.46. HRMS (positive, MeCN) *m/z*=398.5346 (100%) [(ttpy)Ru(tpvpvpt)Ru(ttpy)]$^{4+}$.

[(H$_2$bip)Ru(tpvpvpt)Ru(H$_2$bip)](PF$_6$)$_4$.3H$_2$O(2). Yield: 0.17 g (62%). Anal. Calcd for $C_{90}H_{68}N_{16}Ru_2O_3P_4F_{24}$:C, 49.08; H, 3.15; N, 10.12. Found: C, 49.05; H, 3.11; N,10.17. ^{1}H NMR (400 MHz, DMSO-d_6): δ/ppm 15.07 (s, 4H, -NH), 9.62 (s, 4H, 4H$_{3'}$), 9.04 (d, 4H, *J*=8.5 Hz, 4H$_6$), 8.81-8.78 (m, 4H, 2H$_{12}$+2H$_7$), 8.67-8.62 (m, 6H, 4H$_{13}$+2H$_7$), 8.08 (d, 4H, *J*=8.5 Hz, 4H$_8$), 7.97 (t, 4H, *J*=7.0 Hz, 4H$_4$), 7.84 (s, 4H, 4H$_{11}$), 7.68-7.64 (m, 6H, 4H$_3$+2H$_9$), 7.60 (d, 2H, *J*=16.0 Hz, 2H$_{10}$), 7.50 (d, 4H, *J*=6.0 Hz, 4H$_{14}$), 7.29-7.24 (m, 8H, 4H$_{15}$+4H$_5$), 7.04 (t, 4H, *J*=7.8 Hz, 4H$_{16}$), 6.10 (d, 4H, *J*=8.0 Hz, 4H$_{17}$). ^{13}C NMR (400

MHz, DMSO-d_6): δ/ppm 167.39, 158.62, 157.19, 153.37, 152.84, 152.61, 149.06, 141.40, 139.87, 137.79, 136.99, 135.20, 134.65, 132.16, 131.96, 130.51, 128.71, 127.79, 124.45, 122.86, 120.39, 114.76. HRMS (positive, MeCN) *m/z*=392.5233 (100%) $[(H_2bip)Ru(tpvpvpt)Ru(H_2bip)]^{4+}$ and *m/z*=522.6983 (12%) $[(H_2bip)Ru(tpvpvpt)Ru(Hbip)]^{3+}$.

$[(Me_2bip)Ru(tpvpvpt)Ru(Me_2bip)](PF_6)_4.3H_2O$(3). Yield: 0.19 g (68%). Anal. Calcd for $C_{94}H_{76}N_{16}Ru_2O_3P_4F_{24}$: C, 49.93; H, 3.37; N, 9.95. Found: C, 49.96; H, 3.39; N, 9.92. ^{1}H NMR (400 MHz, DMSO-d_6): δ/ppm 9.60 (s, 4H, $4H_{3'}$), 8.99 (d, 4H, *J*=8.0Hz, $4H_6$), 8.63 (t, 2H, *J*=10.5 Hz, $2H_{12}$), 8.65-8.50 (m, 6H, $4H_{13}$+$2H_7$), 8.08 (d, 2H, *J*=8.0 Hz, $2H_7$), 7.95 (d, 4H, *J*=8.0 Hz, $4H_8$), 7.84 (s, 4H, $4H_{11}$), 7.72 (t, 4H, *J*=7.5 Hz, $4H_4$), 7.64 (d, 2H, *J*=16.0 Hz, $2H_9$), 7.59 (d, 2H, *J*=15.5 Hz, $2H_{10}$), 7.50-7.45 (m, 8H, $4H_{14}$+$4H_3$), 7.32 (t, 4H, *J*=7.5 Hz, $4H_5$), 7.27 (t, 4H, *J*=6.5 Hz, $4H_{15}$), 7.05 (t, 4H, *J*=7.8 Hz, $4H_{16}$), 6.03 (d, 4H, *J*=8.0 Hz, $4H_{17}$), 4.50 (s, 12H, -NMe). ^{13}C NMR (400 MHz, DMSO-d_6): δ/ppm 158.40, 156.94, 153.72, 152.05, 149.49, 146.72, 139.93, 137.90, 135.80, 128.76, 128.26, 128.21, 127.81, 127.75, 127.30, 125.89, 125.57, 124.81, 124.48, 120.60, 114.75, 113.34, 33.34. HRMS (positive, MeCN) *m/z*=406.5436 (100%) $[(Me_2bip)Ru(tpvpvpt)Ru(Me_2bip)]^{4+}$.

4.2.3. Instruments and Physical Methods. The details of different equipment used and experimental process to measure absorption and luminescence spectral behavior, computational studies using DFT and TD-DFT methods as well as *trans-cis* photoisomerization quantum yields have been discussed in chapters 2 and 3.

Complex **2** and **3** (3.0×10^{-6} M in MeCN) were oxidized by ceric ammonium nitrate (CAN). The stock solution of CAN (0.1 M) was prepared in aqueous medium in slightly acidic (HNO_3) condition and stored in dark. The stock solution of CAN was diluted to 1.0×10^{-2} M and the spectroscopic titrations were carried out by incremental addition of CAN solution in a 2.5 mL MeCN solution of **2** and **3**. Similarly, complex **3** was reduced by metallic sodium. The stock solution of metallic Na (0.1 M) was prepared in MeCN and stored in dark. The stock solution of metallic Na was also diluted to 1.0×10^{-2} M and the spectroscopic titrations were carried out by incremental addition of the said Na solution in a 2.5 mL MeCN solution of **3**.

4.3. Results and Discussion

4.3.1. Synthesis and Characterization. The binuclear complexes are synthesized by refluxing the mixture of tpvpvpt and respective Ru(II) precursors in 1:2 molar ratio in

ethylene glycol under N_2 protection. The metal complexes are purified using column chromatography and recrystallization techniques and characterized by elemental analysis as well as by ^{1}H NMR, ^{13}C NMR and high-resolution mass spectrometry (HRMS), the details of which are already presented in the section 4.2.

4.3.2. NMR Spectra. ^{1}H-NMR and ^{13}C-NMR spectroscopy are employed to confirm the structure of the complexes in their solution state (Figures 4.1 and 4.2). The symmetrical environment around the Ru(II) centers in all complexes is evident in their relatively straightforward spectral patterns in ^{1}H NMR. In case of **1**, $H_{3''}$ and $H_{3'''}$ protons resonate in the most downfield region. For compound **2**, the -NH protons exhibit a singlet peak at ~15.00 ppm. The protons associated with the olefinic double bond (H_9 and H_{10}) that appeared within the spectral domain of 7.60-7.80 ppm, are in a *trans-trans* (*t-t*) orientation, as indicated by the value of the coupling constant of ~16 Hz. H_{11} protons for all three complexes are found in the range of 7.82-7.84 ppm as singlet. Additionally, the -CH_3 protons in compound **1** are observed as a singlet at around 2.52 ppm, while in case of **3**, the -NMe protons display a sharp singlet at 4.50 ppm (not shown in Figure 4.1).

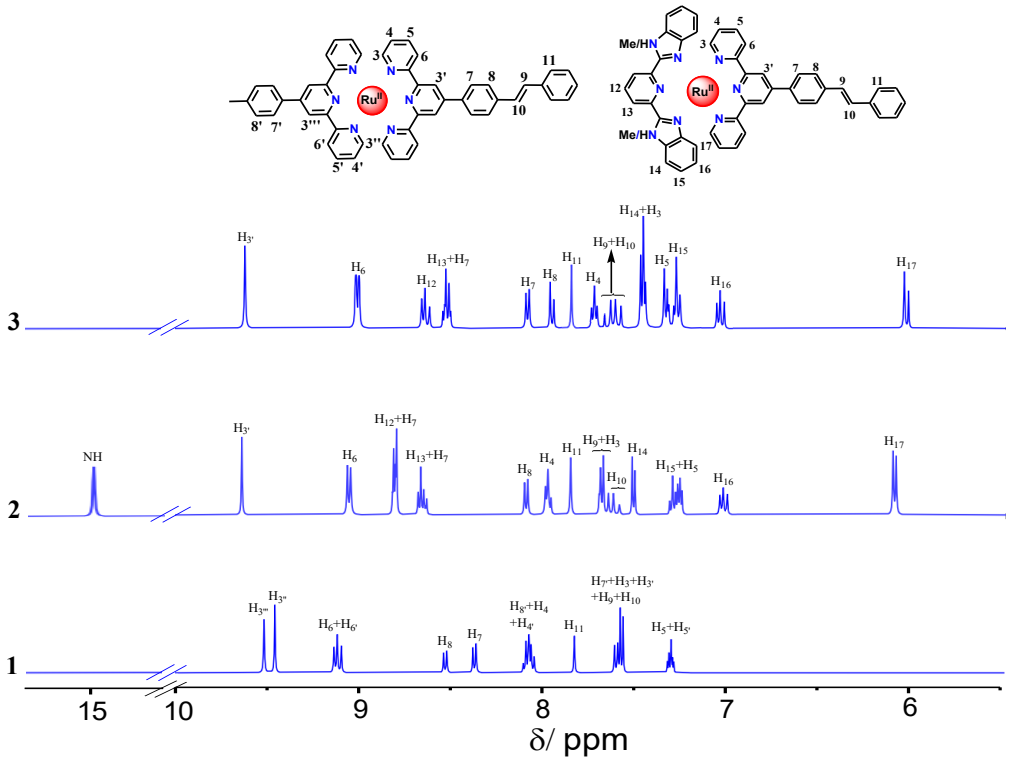

Figure 4.1. ^{1}H NMR spectra of **1-3** in DMSO-d_6.

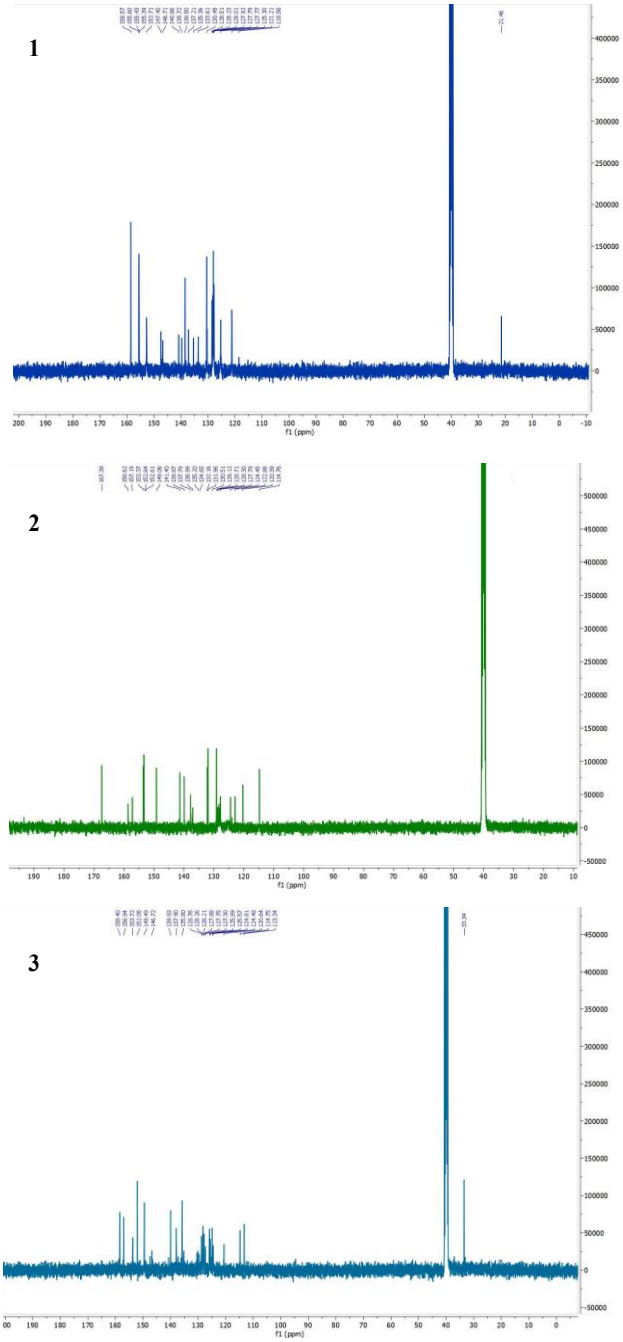

Figure 4.2. ^{13}C NMR spectra of **1-3** in DMSO-d_6.

4.3.3. Mass Spectra. The high-resolution mass spectra (HRMS) of **1-3** in MeCN is presented in Figure 4.3. Correspondence among the experimental and simulated isotopic pattern is pretty good. An abundant peak is observed within the *m/z* values of 392.5233-406.5436. The separation of 0.25 mass unit among the successive isotopic lines corresponds to the tetra-positive cations in all cases. For **2**, an additional peak is observed, which is less abundant and attributes to the tri-positive cation.

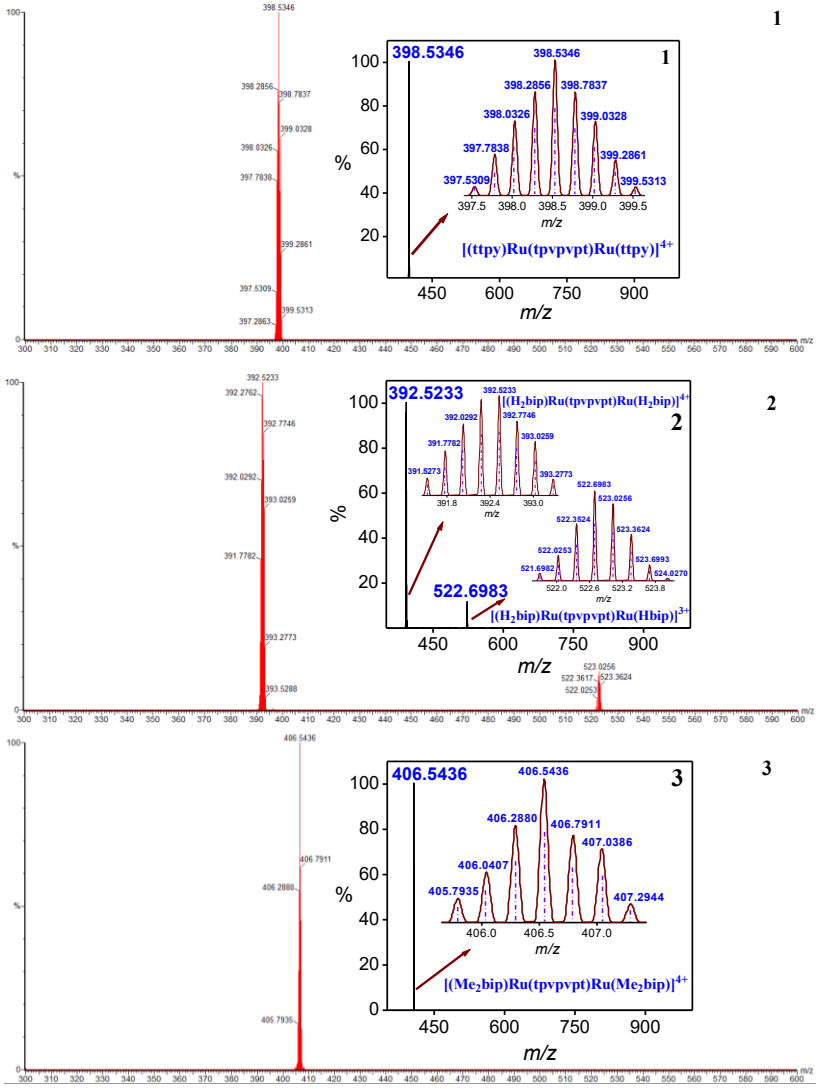

Figure 4.3. HRMS (positive) spectra of the complexes **1-3** in MeCN. Insets show observed and simulated isotopic distribution patterns of the complex cation of **1** [(ttpy)Ru(tpvpvpt) Ru(ttpy)]$^{4+}$ (*m/z*=398.5346) (*z*=4), **2** [(H$_2$bip)Ru(tpvpvpt)Ru(H$_2$bip)]$^{4+}$ (*m/z*=392.5233) (*z*=4) and [(H$_2$bip)Ru(tpvpvpt)Ru(Hbip)]$^{3+}$ (*m/z*=522.6983) (*z*=3) and **3** [(Me$_2$bip)Ru(tpvpvpt)Ru (Me$_2$bip)]$^{4+}$ (*m/z*=406.5436) (*z*=4).

4.3.4. Theoretical Studies. The computational investigations are performed on the *t-t* conformations of **1-3** by using B3LYP functional in MeCN. The optimized geometries are shown in Figure 4.4. The frontier molecular orbitals along with their compositions of **1** are shown in Figure 4.5 and Table 4.1. The HOMOs primarily reside on the Ru centers and to some extent on tpy and styrylbenzene units, while the LUMOs are predominantly on both the tpy and styrylbenzene units. For all the complexes, the energy difference between HOMO and LUMO is almost similar (from 2.72 to 2.80 eV).

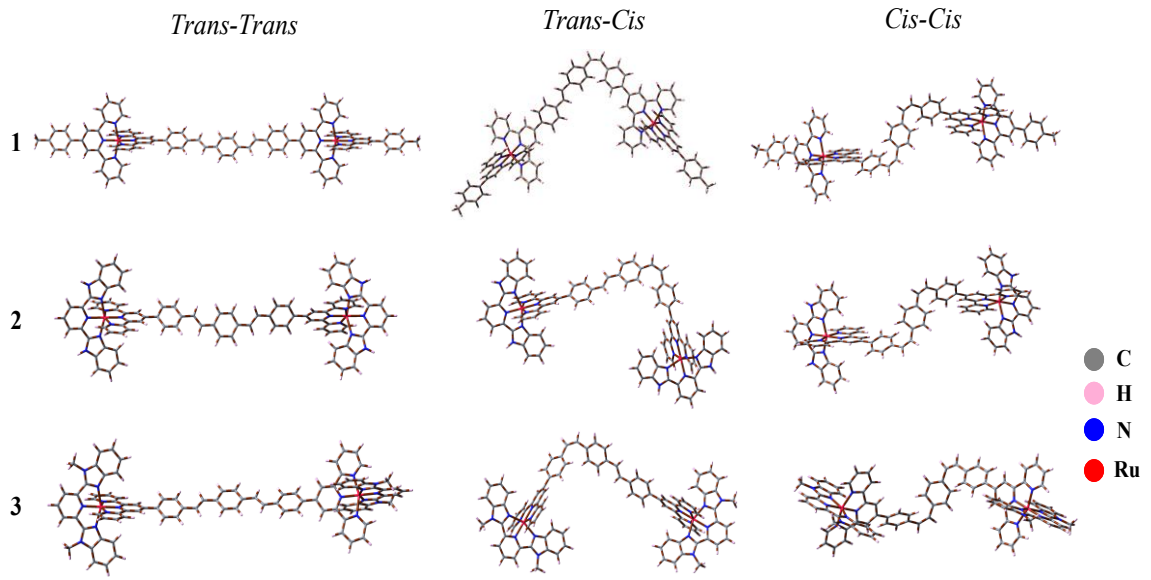

Figure 4.4. Ground state optimized structures of **1-3** in their *t-t* (left panel), *t-c* (middle panel) and *c-c* (right panel) forms.

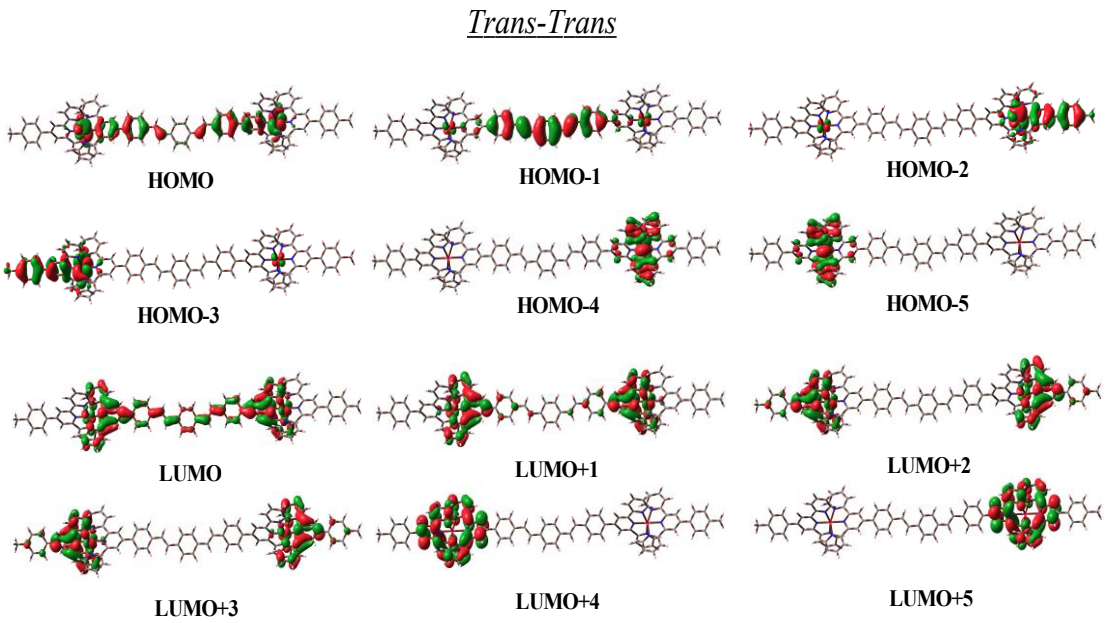

Figure 4.5. Schematic drawings of the selective frontier molecular orbitals of **1** (*t-t*) in acetonitrile.

Table 4.1. Selected MOs along with their Energies and Compositions in the Ground State for **1** in MeCN.

	1															
	Energy/eV			% Compositions												
	t-t	*t-c*	*c-c*	*t-t*				*t-c*				*c-c*				
				Ru	tpy	Styryl-benz	Tolu	Ru	tpy	Styryl-benz	Tolu	Ru	tpy	Styryl-benz	Tolu
LUMO+5	-2.52	-2.53	-2.54	0.02	99.37	0.35	0.26	0.03	99.35	0.36	0.26	0.03	99.32	0.40	0.25
LUMO+4	-2.52	-2.53	-2.54	0.02	99.37	0.35	0.26	0.02	99.36	0.36	0.25	0.03	99.34	0.37	0.25
LUMO+3	-2.68	-2.69	-2.70	7.90	86.35	0.44	5.30	7.87	86.41	0.14	5.57	7.84	86.47	0.05	5.63
LUMO+2	-2.68	-2.69	-2.70	7.86	86.47	0.06	5.61	7.85	86.48	0.08	5.59	7.83	86.51	0.08	5.58
LUMO+1	-2.70	-2.72	-2.73	7.78	84.05	7.83	0.33	7.85	83.93	8.08	0.14	7.89	83.37	8.67	0.07
LUMO	-2.80	-2.78	-2.78	7.17	69.35	23.46	0.01	7.42	73.42	19.14	0.01	7.66	77.05	15.27	0.01
HOMO	-5.52	-5.61	-5.74	53.68	22.92	23.33	0.07	54.37	23.12	22.46	0.05	52.92	22.73	24.34	0.00
HOMO-1	-6.09	-6.10	-6.10	5.43	5.59	88.98	0.00	6.28	5.67	88.04	0.00	8.75	6.51	84.73	0.00
HOMO-2	-6.11	-6.12	-6.13	60.43	25.22	0.03	14.30	60.33	25.24	0.07	14.36	60.24	25.22	0.00	14.52
HOMO-3	-6.11	-6.12	-6.13	60.45	25.20	0.08	14.26	60.38	25.23	0.01	14.38	60.44	25.34	0.01	14.20
HOMO-4	-6.16	-6.17	-6.18	70.02	29.95	0.01	0.01	69.93	30.01	0.01	0.05	69.95	29.99	0.04	0.02
HOMO-5	-6.16	-6.17	-6.18	70.02	29.95	0.01	0.02	69.96	30.00	0.01	0.02	69.79	29.85	0.01	0.34

4.3.5. Absorption Spectral Characteristics. The absorption spectra of **1-3** are recorded in both MeCN and DMSO (Figures 4.6 and 4.7) and the corresponding data are presented in Table 4.2. The spectral nature is almost similar for all three complexes. For the correct assignment of the bands, we also executed DFT and TD-DFT calculations on the *t-t* conformations of **1-3** in MeCN using CPCM model. The spectral parameters and

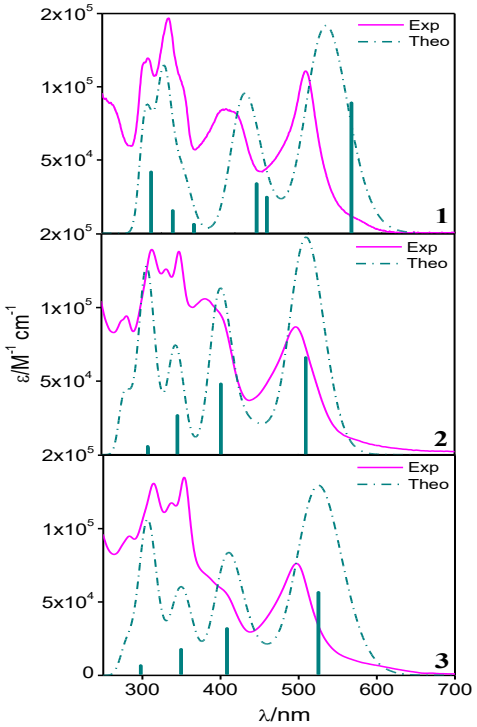

Figure 4.6. Experimental (magenta) and calculated (deep cyan) absorption spectra of **1-3** in MeCN.

band assignments for **1** are depicted in Table 4.3. The theoretical and experimental overlaid spectra show that there is a fairly good correlation between them (Figure 4.6). The lowest energy absorption band emerges due to combined Ru(II)→tpy and styrylbenzene→tpy transitions, thus possesses both MLCT and ILCT characters. The band in the region of 382-395 nm is quite broad in nature and originates mainly because of ILCT and π-π* transitions together with a small contribution of MLCT. The highest energy absorption band in the UV region is predominantly due to the π-π* transition.

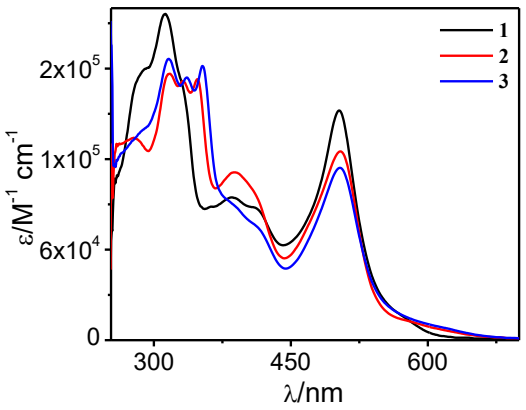

Figure 4.7. Absorption spectral profiles of **1-3** in DMSO at RT.

Table 4.2. Absorption and Emission Spectral Data of **1-3**.

Compounds		Absorption λ_{max}/ nm (ε,$M^{-1}cm^{-1}$)	Luminescence		
			λ_{max}/nm	τ/ns	Φ
1	MeCN(298K)	497(110200), 392(br)(84100), 330(sh)(100500), 310 (146600), 282(119200)	690	τ_1=13.8 (10%), τ_2=282.4 (90%)	0.9×10^{-3}
2		498(87000), 382(br)(106100), 348(139700), 332(sh)(126000), 314(139700), 282(94800)	676	τ_1=15.2 (33%), τ_2=64.4 (67%)	2.8×10^{-3}
3		498(76600), 395(br)(61700), 354(140000), 338(sh)(119500), 313(133500), 282(96900)	677	τ_1=24.5 (38%), τ_2=60.3 (62%)	7.2×10^{-3}
1	DMSO (298K)	502(151700), 400(br)(90200), 312 (215900)	706	τ_1=52.5 (8%), τ_2=410.5 (92%)	1.4×10^{-3}
2		504(125100), 388(br)(111100), 347(172700), 330(sh)(171700), 316(176100)	694	τ_1=67.5 (27%), τ_2=207.0 (73%)	7.3×10^{-3}
3		504(114100), 402(br)(80500), 354(181400), 336(sh)(173500), 316(186600)	689	τ_1=80.6 (33%), τ_2=225.7 (67%)	10.0×10^{-3}
1	EtOH-MeOH (4:1) (77K)	-	677	23.8 μs	0.14
2		-	668	12.6 μs	0.28
3		-	666	11.4 μs	0.42

Table 4.3. Selected UV-vis Energy Transitions at the TD-DFT/B3LYP Level of **1** in MeCN.

λ_{expt}/nm	λ_{cal}/nm	Excited state	Oscillator strength(f)	Key transitions	Character
1 (*t*-*t*)					
497	525	S_1	2.65	H→L (89%)	MLCT, ILCT
392	421	S_{25}	0.73	H-5→L+4 (40%), H-4→L+5 (40%)	MLCT, ILCT, π-π*
	408	S_{29}	1.01	H→L+8 (88%)	
310	305	S_{123}	0.46	H-17→L (15%), H-16→L+1 (13%), H-15→L (19%)	ILCT, π-π*
282	278	S_{198}	1.24	H-14→L+7 (21%), H-13→L+6 (21%)	π-π*
1 (*t*-*c*)					
492	508	S_1	1.32	H→L (85%)	MLCT, ILCT
	483	S_8	0.40	H→L+1 (71%)	
354	420	S_{25}	0.23	H-5→L+4 (88%)	MLCT, ILCT
	397	S_{31}	0.82	H→L+8 (90%)	
330	345	S_{61}	0.40	H-1→L+8 (26%), H→L+9 (49%)	ILCT, π-π*
309	305	S_{121}	0.29	H-16→L (26%), H-16→L+1 (23%), H-5→L+9 (14%)	π-π*, ILCT
	304	S_{123}	0.35	H-17→L (18%), H-15→L (17%), H-15→L+1 (10%), H-4→L+9 (11%), H-4→L+14 (18%)	
1 (*c*-*c*)					
492	490	S_3	0.63	H-4→L (12%), H→L (58%)	MLCT
354	378	S_{41}	0.41	H-6→L (13%), H→L+8 (78%)	MLCT, ILCT
330	341	S_{62}	0.37	H-1→L+8 (32%), H→L+9 (54%)	ILCT, π-π*
309	302	S_{127}	0.46	H-16→L+2 (15%), H-9→L+7 (11%), H-8→L+6 (14%)	π-π*, ILCT

4.3.6. Emission Spectral Characteristics. The emission spectra and excited state lifetime of all three complexes are acquired in MeCN and DMSO at RT (Figure 4.8). The spectra at 77 K are recorded in EtOH-MeOH (4:1, v/v) glass (Figure 4.9). Related data are provided in Table 4.2. The emission maximum lies between 676 and 690 nm in MeCN. Bathochromic shift of the emission maximum together with enhancement of the emission quantum yield (Φ) are observed on passing from MeCN to DMSO. It is known that $Ru(tpy)_2$ type complexes are weakly emissive in nature due to small energy gap between the radiative ^{3}MLCT and the non-radiative ^{3}MC states. To enhance the emission characteristics of such complexes, the non-radiative deactivation channel through the ^{3}MC state has to be reduced by increasing the energy gap between ^{3}MLCT and ^{3}MC state. Alternatively, the energy of the triplet ligand-centered states, viz. ^{3}ILCT and/or ^{3}π-π* in the resulting complexes could be lowered down below the ^{3}MLCT. By incorporating extended conjugation in bridging ligand, the energy of the triplet ligand-centered states (^{3}ILCT and/or ^{3}π-π*) of the complexes could be lowered down below the ^{3}MLCT state so that the observed emission

could be either due to radiative deactivation of the equilibrated triplet states of ^{3}MLCT and ^{3}ILCT and/or $^3\pi$-π^* state or from pure ^{3}ILCT and/or $^3\pi$-π^* state. The broad and overlapping emission band, especially for complex **1**, suggests the observed emission is probably due to the deactivation of the said equilibrated excited states (^{3}MLCT and ^{3}ILCT and/or $^3\pi$-π^*).

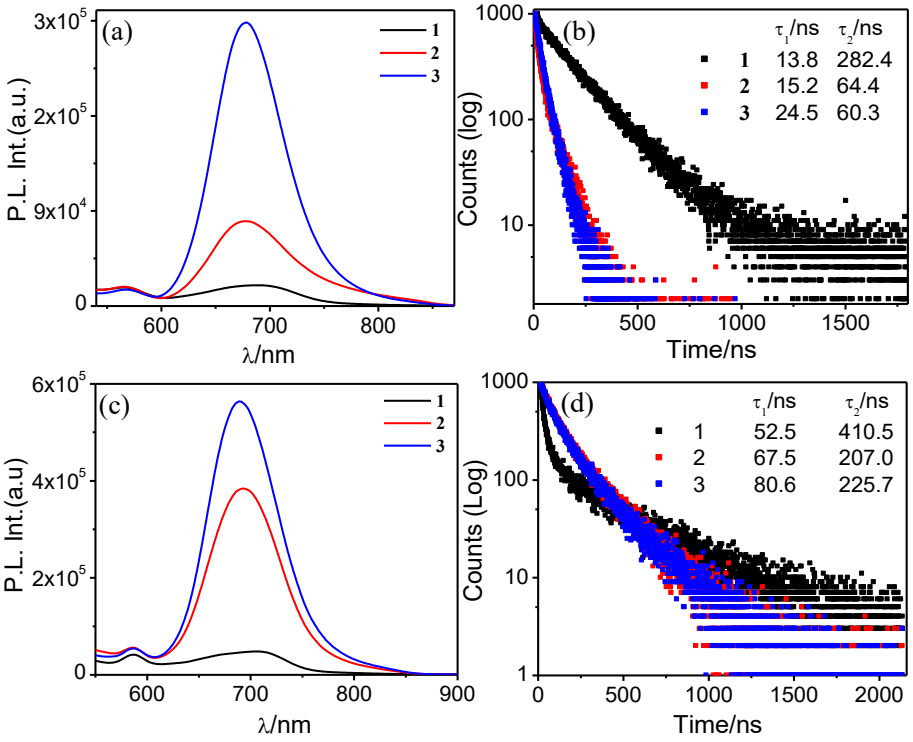

Figure 4.8. Steady-state emission spectra (λ_{ex}=490 nm) and excited-state decay profiles (λ_{ex}=490 nm) of **1**-**3** in MeCN (a and b, respectively) and in DMSO (c and d, respectively) at RT. Inset to figure b and d shows the corresponding lifetime values.

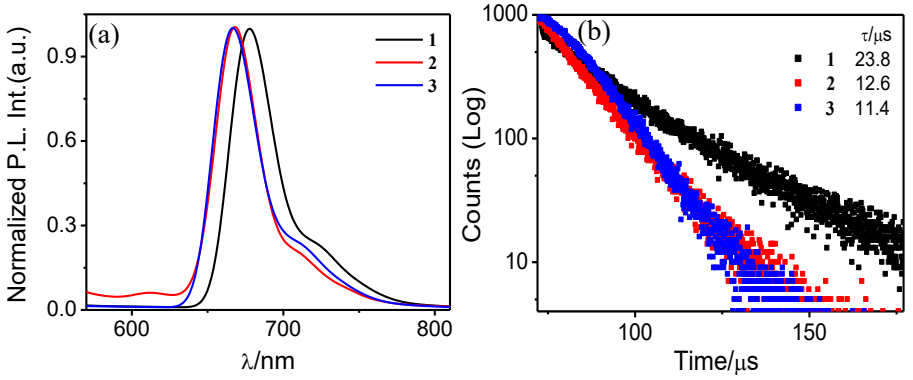

Figure 4.9. (a) Emission spectra (λ_{ex}=490 nm) and (b) emission decays (λ_{ex}=490 nm) of **1**-**3** in EtOH-MeOH (4:1, v/v) glass at 77 K. Inset to figure b shows the lifetime values.

For understanding the deactivation dynamics, UKS calculations are carried out on the triplet states of the *t-t* orientation of the complexes. Comparison of the experimental and calculated data is tabulated in Table 4.4. A fairly strong correspondence indicates the probable occurrence of radiative deactivation of respective triplet MLCT states. All the complexes exhibit bi-exponential decay at RT (Figure 4.8). The RT emission lifetime of the complexes lies within 60.3-282.4 ns in MeCN, while substantially elevated in DMSO (207.0-410.5 ns). It is probable that the initial short component accounts for deactivation of the ^{3}MLCT state, whereas the long-lived component arises from the equilibrated triplet state of ^{3}MLCT and ^{3}ILCT and/or $^3\pi$-π^* state of styrylbenzene units. A hypsochromic shift of emission maximum (~10 nm) and a huge increase in lifetime values (11.4-23.8 μs) are noticed at 77 K (Figure 4.9). Zero-zero spectroscopic energy (E_{00}) of the complexes, acquired from their 77 K emission maxima, are found to vary between 1.83 and 1.86 eV.

Table 4.4. Emission Maxima of **1-3** in MeCN according to UKS Calculations and Associated Experimental Values.

	Before Photolysis		After Photolysis		After Photolysis	
	λ_{expt}/nm	λ_{cal}(*t-t*)/nm	λ_{expt}/nm	λ_{cal}(*t-c*)/nm	λ_{expt}/nm	λ_{cal}(*c-c*)/nm
1	690	720	662	768	662	612
2	677	731	676	641	676	758
3	677	660	677	653	677	659

We also have a keen interest in exploring the dynamics of excited state deactivation in complexes **1-3**. To investigate this, we conducted both steady-state and time-resolved emission spectral studies upon varying the temperature (Figures 4.10 and 4.11, for **3**). Notably, we observed a gradual decrease in quantum yield as well as lifetime values with systematic increase in temperature. This phenomenon can be attributed to narrowing the energy gap between the radiative ^{3}MLCT and non-radiative ^{3}MC states, ultimately leading to a higher population of the ^{3}MC state at elevated temperatures. Consequently, the non-radiative deactivation pathway becomes increasingly favourable. We employed a non-linear regression analysis (equation 1) for the temperature-dependent lifetime plot.

$$[\tau(T)]^{-1} = [k_1 + k_2 \exp(-\Delta E_2/RT])]/[1 + \exp[(-\Delta E_2/RT)] \quad (1)$$

where k_1 is the temperature-independent rate constant which is obtained by the sum of both radiative (k_r) and non-radiative (k_{nr}) rate constants at 77 K. The value of k_1 ranges from 7.9×10^4 to 3.6×10^6 s^{-1}. The rate constant for approaching ^{3}MC state from ^{3}MLCT state is represented by k_2, which is temperature-dependent and ΔE_2 is the activation energy

associated with this process. k_2 and ΔE_2 values are in the range of 2.6×10^{11}-1.0×10^{12} s^{-1} and 3015±77-4354±12 cm^{-1}, respectively. ΔE_2 value increases enormously for all the three complexes compared to that of $[Ru(tpy)_2]^{2+}$ (ΔE_2=1500 cm^{-1}) and $[Ru(ttpy)_2]^{2+}$ (ΔE_2=1800 cm^{-1}). This huge escalation in ΔE_2 is probably due to the extended π-delocalization in the excited state of the complex backbone.

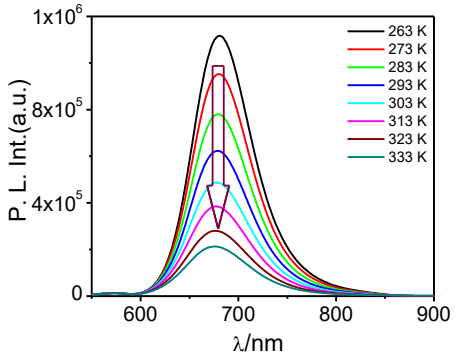

Figure 4.10. Change in steady-state emission (λ_{ex} = 490 nm) spectra for **3** upon variation of temperature in MeCN.

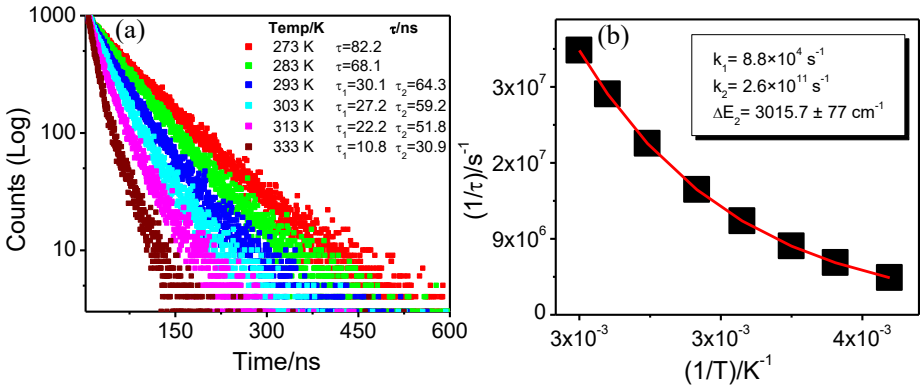

Figure 4.11. Temperature-dependent decay profiles together with the values of lifetime of **3** (a) in MeCN. Nonlinear fitting of temperature-dependent lifetime data via equation 1 for **3** (b) to acquire the values of the different parameters as presented in the inset of figure b.

4.3.7. Electrochemical Properties. We investigated the electrochemical characteristics of the complexes in MeCN (2.0×10^{-4} M) using cyclic voltammetry (CV) and relevant plots are illustrated in Figure 4.12, while the data are summarized in Table 4.5. In the positive potential domain, a single reversible oxidation peak (ranging between 1.11 V and 1.34 V) corresponding to simultaneous oxidation of two Ru(II) centers ($Ru^{II}Ru^{II}/Ru^{III}Ru^{III}$) is observed.[98] In contrast, two successive reversible and/or quasi-reversible peaks are noticed between -1.15 and -1.47 V in negative potential which could

be attributed to the reduction of the terpyridine units. Theoretical calculations were also conducted to support these findings. The spin density plots presented in Figure 4.13 reveal that the electron density is predominantly localized on the Ru centers in the oxidized (Ru^{III}-Ru^{III}) forms. Conversely, in the reduced forms, the electron density is primarily confined to the terpyridine units.

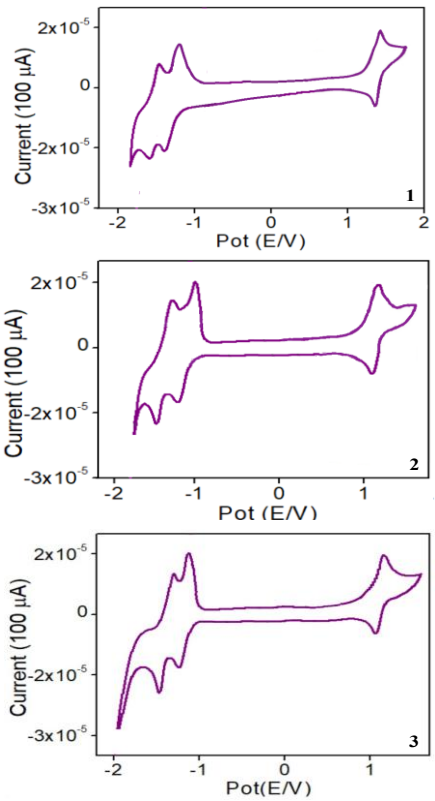

Figure 4.12. CVs of **1-3** in MeCN at a scan rate of 100 mV/s showing both oxidation and reduction processes using Ag/AgCl as the reference electrode.

Table 4.5. Electrochemical Data[a] for Complexes **1-3** in MeCN before and after Photolysis.

Compounds	Oxidation[b] $E_{1/2}$(ox)/V	Reduction[c] E(red)/V
1(*t*-*t*)	1.34	-1.47, -1.22
2(*t*-*t*)	1.11	-1.40, -1.18
3(*t*-*t*)	1.12	-1.38, -1.15
1(*c*-*c*)	1.36, 1.16	-1.67, -1.34, -1.22
2(*c*-*c*)	1.13, 1.02	-1.60, -1.28, -1.18
3(*c*-*c*)	1.17, 0.94	-1.56, -1.23, -1.14

[a]All the potentials are referenced against Ag/AgCl electrode with $E_{1/2}$=0.36 V for Fc/Fc^+ couple. [b]Reversible electron transfer process with a Pt working electrode. [c]E(red) values for the reduction processes obtained with glassy carbon electrode.

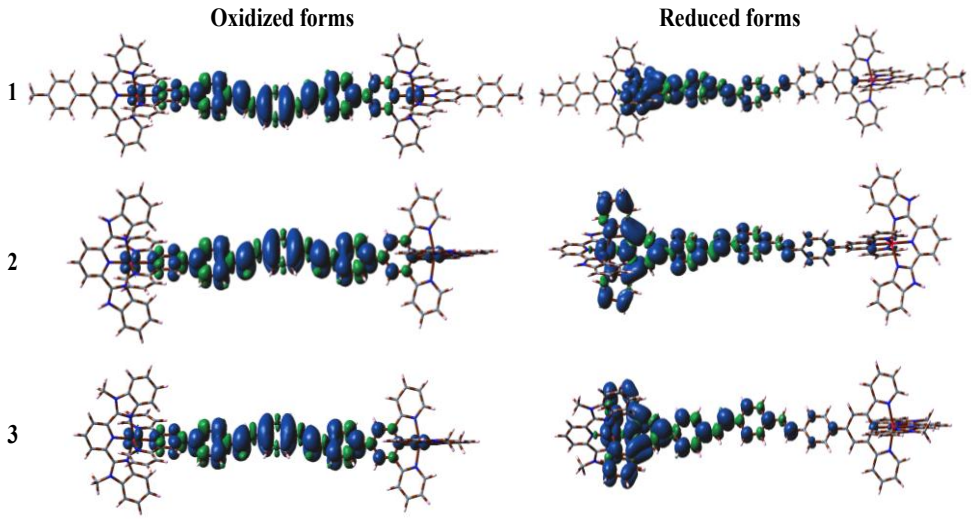

Figure 4.13. Spin density plots of **1-3** in MeCN. Left panel indicates the oxidized forms (Ru^{III}-Ru^{III}) while the reduced forms are shown in right panel.

4.3.8. Photoisomerization Studies. Phenylene-vinylene-like compounds usually take part in *trans-cis* isomerization upon exposure to light. In our study, we conducted the photoisomerization of all three complexes in MeCN under visible light irradiation. The isomerization process is continuously monitored by recording absorption and emission spectra, with corresponding profiles presented in Figure 4.14. This process involves a single-step transformation in all cases, requiring a time span of 290-530 min, depending on the nature of terminal tridentate ligand, to reach the photo-stationary state. Upon exposure to light, we observed a gradual reduction in both the MLCT and ILCT bands, along with an increase in intensity of the band in the UV region (at ~290 nm). Notably, the decrease in the ILCT band was more pronounced than that of the MLCT band. The presence of a clear isosbestic point in the UV region indicates the presence of two species in equilibrium, with the initial *trans-trans* (*t-t*) form converting to either *trans-cis* (*t-c*) or *cis-cis* (*c-c*) forms during photo-irradiation. In the emission spectra, we observed a gradual rise in emission intensity with a slight blue-shift for complex **1**, while for **2** and **3**, the intensity of the emission band substantially increased with no shift in their emission maxima. We also recorded the emission decays of the photolyzed solutions of the complexes (insets of Figure 4.14). In contrast to the steady-state spectra, the lifetime of complexes decreases to small extent and the magnitude of decrease is found to be almost similar for all three complexes.

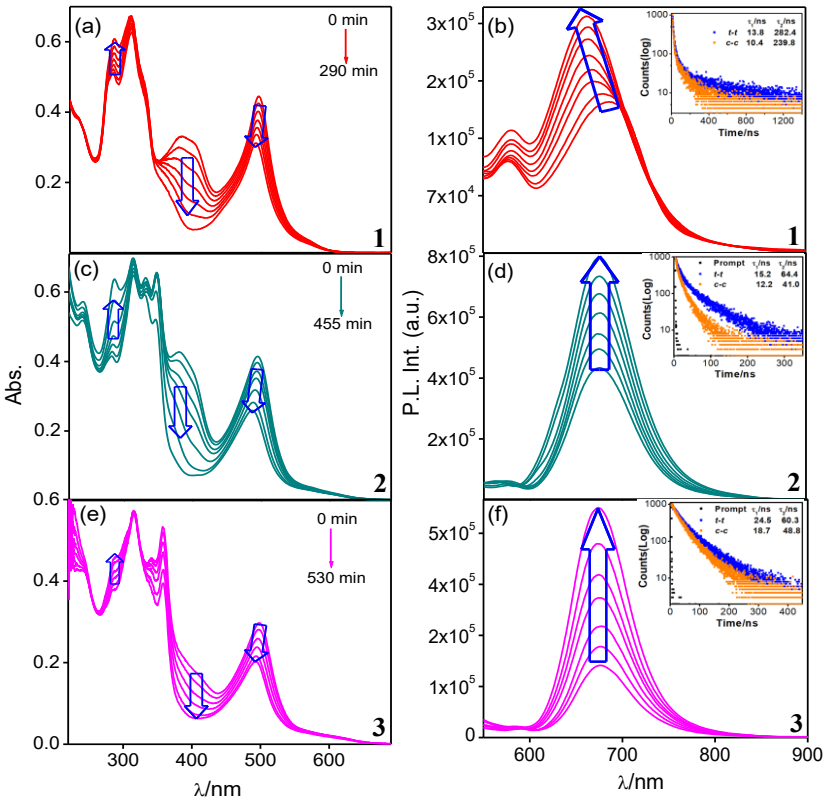

Figure 4.14. Absorption (a, c, e) and emission (λ_{ex} =490 nm) (b, d, f) spectral change of **1** (a, b), **2** (c, d), and **3** (e, f) in MeCN (4.0×10^{-6} M) upon treatment with light of λ=500 nm. Inset to figure b, d and f shows the decay profiles of the complexes before and after photolysis along with their lifetime values.

We also acquired the CVs of the photolyzed solutions of the complexes (2.0×10^{-4} M) and associated voltammograms and data are presented in Figure 4.15 and Table 4.5. It is of interest to note that the single reversible peak due to simultaneous oxidation of two remote Ru(II) centers in the *t-t* form splits into two closely situated reversible peaks after photolysis. In the negative potential window, we also obtained three successive reversible reduction waves compared with two in their respective *t-t* forms. One probable reason of splitting of the redox waves could be due to the closeness of two Ru(II) centres in their isomerized forms (*t-c* or *c-c*). To this end, we checked the distance between the two Ru(II) centres from the optimized structures. The inter-metallic distance varies between 28.58 and 28.63 Å in the *t-t*, within 21.10-21.35 Å in *t-c*, while between 20.68 and 21.19 Å in the *c-c* forms, depending upon the terminal tridentate ligand. Thus, through space intermetallic distance is drastically reduced upon isomerization which in turn is probably responsible for splitting of the Ru(II/III) oxidation as well as the ligand-centered reduction waves.

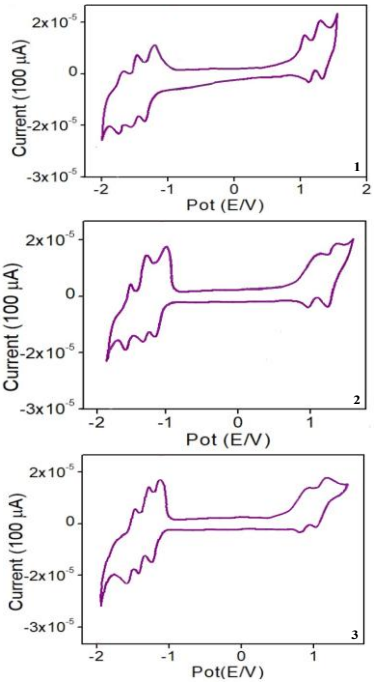

Figure 4.15. CVs of the photolyzed solutions of **1-3** in MeCN at a scan rate of 100 mV/s showing both oxidation and reduction processes using Ag/AgCl as the reference electrode.

To elucidate the mode of isomerization process, we conducted ^{1}H NMR spectroscopy on the initial and photolyzed solutions of all three complexes in CD_3CN. The spectra of **2** and **3** are presented in Figures 4.16 and 4.17. The spectra after photolysis exhibit an overall up-field shift of most of the proton resonances in all three cases, albeit to a small extent. The intensity of the olefinic proton signals (H_9 and H_{10}) with a coupling constant (*J*) of ~16 Hz gets significantly decreased with concomitant emergence of two new doublets ($H_{9'}$ and $H_{10'}$) in the range of ~6.20-7.20 ppm possessing the *J* value of ~12 Hz. The H_7, H_8, and H_{11} protons adjacent to the olefinic double bond also experienced a substantial reduction in signal intensity upon photo-irradiation. Additionally, we observed some new unresolved proton signals in the region of ~7.25-8.25 ppm, which are attributed to the presence of $H_{7'}$, $H_{8'}$, and $H_{11'}$ protons. Upon analyzing the ^{1}H NMR spectra of the initial and photolyzed form of complexes as well as by taking into consideration of substantial decrease in the *J* value of the olefinic $H_{9'}$ and $H_{10'}$ protons, it is inferred that the isomerization is definitely taking place in all cases but complete conversion from the *t-t* to *c-c* forms does not take place even after prolonged light irradiation. In principle, co-existence of all the three forms (*t-t*, *t-c* and *c-c*), irrespective of their percentage contribution, is a finite possibility in the photostationary state.

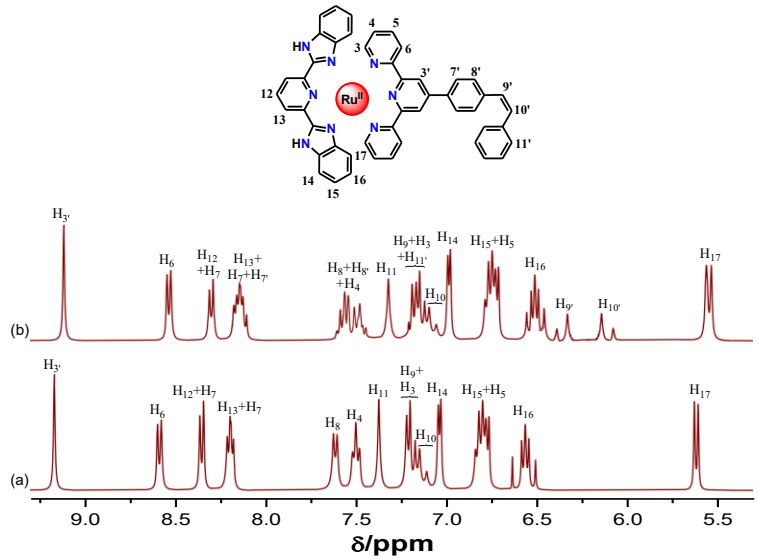

Figure 4.16. ^{1}H NMR spectrum of **2** in CD_3CN before (a) and after (b) photolysis with light of λ=500 nm for 16 h.

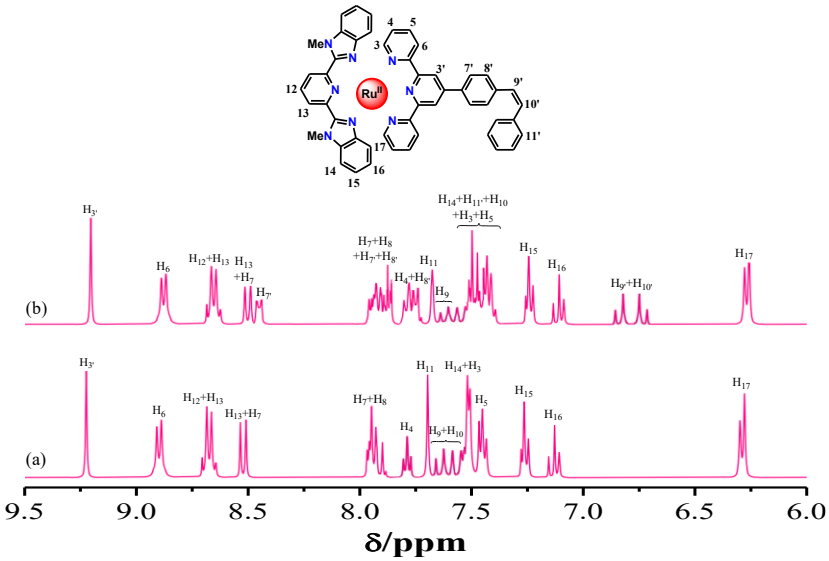

Figure 4.17. ^{1}H NMR spectrum of **3** in CD_3CN before (a) and after (b) photolysis with light of λ=500 nm for 24 h.

In order to check the dominancy of the isomer among *t-c* and *c-c* in the photostationary state, we conducted DFT and TD-DFT computations on both forms of the complexes. The optimized geometries of *t-c* and *c-c* forms are shown in Figure 4.4. The optimized energies of all the three forms of the complexes are provided in Table 4.6. The frontier molecular orbitals along with their compositions are shown in Figures 4.18 and 4.19 (for **1**) and Table 4.1. The absorption spectral parameters and band assignment for **1**

are depicted in Table 4.3. Interestingly, the experimental absorption spectra after photoisomerization exhibit a remarkable resemblance with the *c-c* form of the calculated spectra as shown in Figure 4.20. The molecular orbitals (MOs) involved in the lowest energy transitions in *t-t*, *t-c* and *c-c* forms of the complexes are illustrated in Figure 4.21. In the *c-c* forms, the energy of the LUMOs remains almost similar, while the HOMOs become more stabilized, leading to a wider HOMO-LUMO energy gap compared to their *t-t* counterparts. Specifically, the HOMO-LUMO gap ranges from 2.96 eV to 2.97 eV in the *c-c* forms, whereas in the *t-t* forms, it varies from 2.72 eV to 2.80 eV. Additionally, the TD-DFT calculations also indicate a slight hypsochromic shift in the MLCT band upon conversion from *t-t* to *c-c*.

Table 4.6. Calculated Energies of Ground State Singlets and Excited State Triplets of **1-3** and $[(ttpy)Zn(tpvpvpt)Zn(ttpy)]^{4+}$.

Compounds	Energy ($E\times10^{17}$ kJ)					
	t-t		*t-c*		*c-c*	
	Singlet	Triplet	Singlet	Triplet	Singlet	Triplet
1	-1.982390	-1.982362	-1.982386	-1.982360	-1.982382	-1.982345
2	-1.976104	-1.976077	-1.976100	-1.976069	-1.976096	-1.976069
3	-2.044653	-2.044623	-2.044648	-2.044618	-2.044644	-2.044614
$[(ttpy)Zn(tpvpvpt)Zn(ttpy)]^{4+}$	-2.097650	-2.097644				

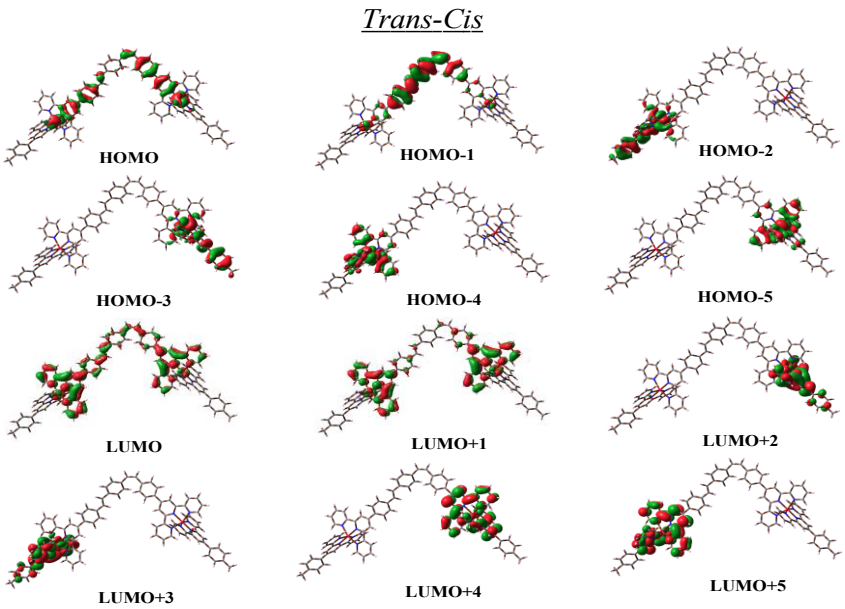

Figure 4.18. Schematic drawings of the selective frontier molecular orbitals of the *t-c* form of **1** in acetonitrile.

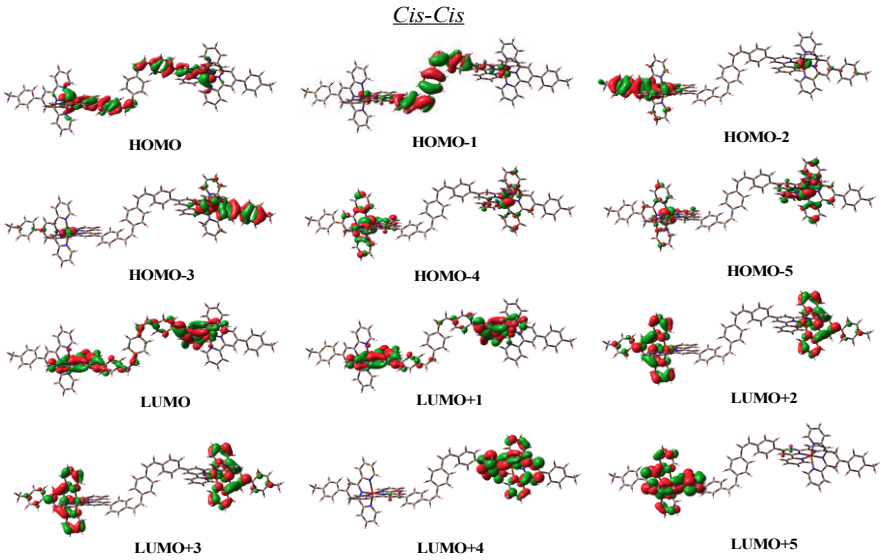

Figure 4.19. Schematic drawings of the selective frontier molecular orbitals of the *c-c* form of **1** in acetonitrile.

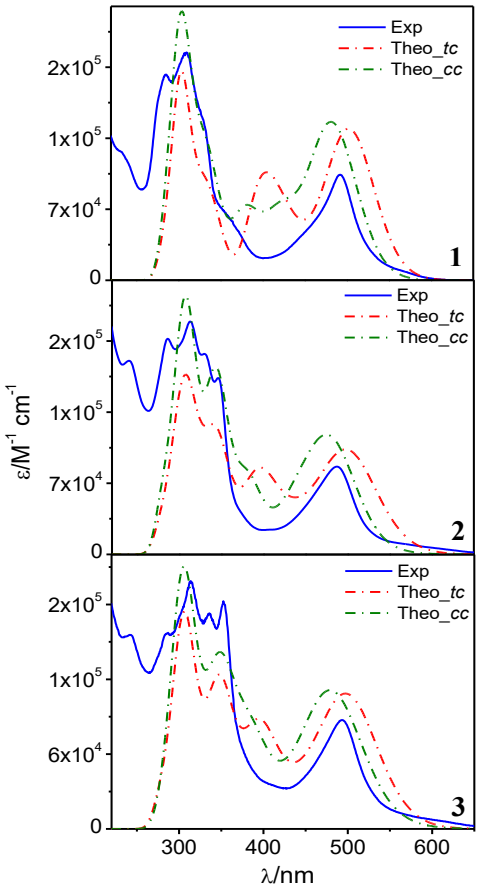

Figure 4.20. Overlay of the experimental (blue) and calculated absorption spectra of both *t-c* (red) and *c-c* (olive) forms of **1-3** in MeCN.

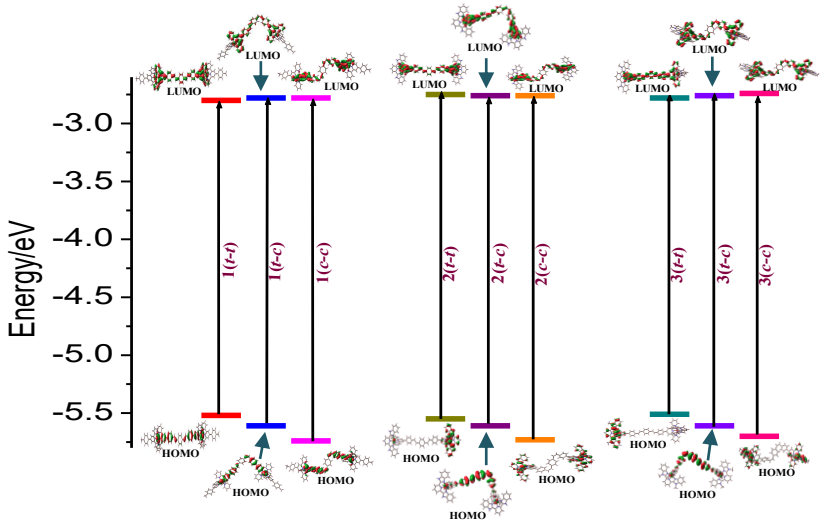

Figure 4.21. Energy level diagram showing dominant transitions involved in the lowest-energy absorption band of **1** (left panel), **2** (middle panel) and **3** (right panel) in MeCN.

We also conducted UKS calculations on all the three forms of the complexes to have an estimate of the energy of their ^{3}MLCT state as well as to acquire insights about the emission behaviors of the complexes after light irradiation. Additionally, we conducted DFT calculation on the ground state singlet and excited state triplet of the Zn(II) complex of the type $[(ttpy)Zn(tpvpvpt)Zn(ttpy)]^{4+}$ to have an estimate of the energy of the ^{3}ILCT state in the complexes (Figure 4.22 and Table 4.6). The emission maxima of the irradiated solutions of the complexes exhibit a fairly strong correlation with those of the theoretical *c-c* forms than that of the *t-c* forms (Table 4.4). Therefore, we can infer that the complexes underwent from their *t-t* state to predominantly *c-c* forms upon photo-irradiation. Based on the outcomes of the experimental observations as well as those of computational investigations, we propose the following Jablonski diagram showing the approximate relative energies of the triplet MLCT and ILCT states of *t-t* and *c-c* isomers as well as their involvement in the isomerization processes (Figure 4.23).

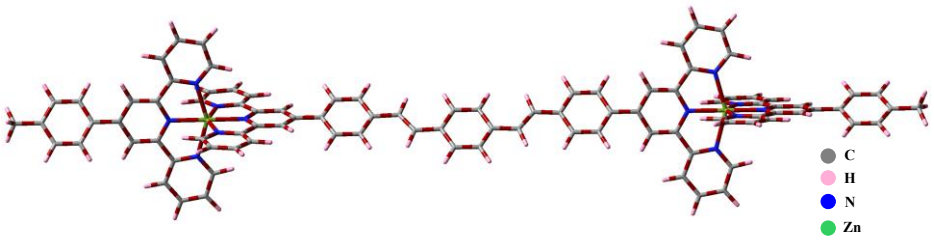

Figure 4.22. Ground state optimized structure of $[(ttpy)Zn(tpvpvpt)Zn(ttpy)]^{4+}$ in its *t-t* form.

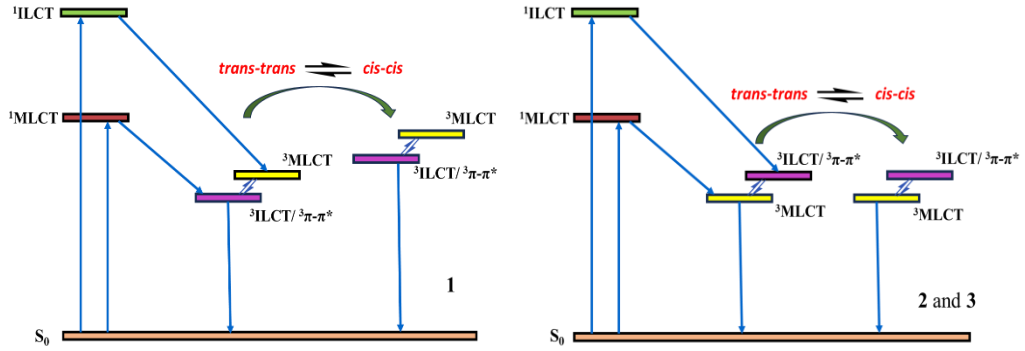

Figure 4.23. Simplified Jablonski diagram of **1-3** indicating photophysical and photoisomerization processes in the complexes.

We also calculated the percentage of the conversion yield (*t-t* to *c-c*) of the complexes by estimating the ratio of ^{1}H NMR signal integrals (for H_9 and H_{10} protons) for *c-c* and *t-t* isomers in their photosatonary states. It is found that the conversion efficiency is highest for complex **1** (80%), while least for **3** (70%) with an intermediate value of 77% for **2**.

We determined the rate constants (k_{iso}) and quantum yields ($\Phi_{tt}\rightarrow\Phi_{cc}$) associated with the photoisomerization process using absorption titration profiles. The corresponding data have been summarized in Table 4.7. The rate constant values fall from 0.68×10^{-4} to 1.12×10^{-4} s^{-1}, while $\Phi_{tt}\rightarrow\Phi_{cc}$ ranges from 1.5×10^{-3} to 2.1×10^{-3}. It is noteworthy that the rate constants exhibit the order **1**>**2**>**3**, probably because of difference in electronic environments of the capping ligands within the complex structures.

Table 4.7. Quantum Yield and Rate Constants for the Forward and Reverse Photoisomerization of **1-3** in MeCN.

	Forward process		Reverse process	
Compounds	Quantum yield ($\Phi\times10^3$)	Rate constant ($k_{iso}\times10^4/s^{-1}$)	Quantum yield ($\Phi\times10^3$)	Rate constant ($k_{iso}\times10^4/s^{-1}$)
1	2.12	1.12	0.61	0.66
2	1.59	0.85	0.56	0.52
3	1.53	0.68	0.46	0.35

Thermal stability of the *c-c* isomer plays very crucial role for proper utilization of the complexes as photoswitches. In order to check the thermal stability, we recorded the absorption spectra of the acetonitrile solutions of the *c-c* forms of the complexes as a

function of temperature up to 80 ºC. No change in spectral characteristics is observed and all the spectra retain the characteristic feature of *c-c* isomer, indicating thermal stability of the complexes.

In order to check the reversibility of the isomerization process, we again irradiated the photolyzed solutions of the complexes with UV light source and the progress of the transformation is monitored through absorption and emission spectroscopy (Figure 4.24). Upon critical scrutiny of the spectral bands, it appears that the predominant *c-c* form of the complexes gradually approaches towards their initial *t-t* form but complete restoration of their *t-t* form could not be achieved even after prolonged time of UV irradiation (9-14 h). Thus, in-line with forward process, co-existence of all the three forms (*t-t*, *t-c* and *c-c*) of the complexes is also a distinct possibility in the photostationary state of the reverse process. We also calculated the rate constant (k_{iso}) and quantum yield ($\Phi_{cc}\rightarrow\Phi_{tt}$) values of the reverse process and the corresponding data has been compiled in Table 4.7. The reverse *c-c* to *t-t* process is much slower as evident by their k_{iso} and $\Phi_{cc}\rightarrow\Phi_{tt}$ values (k_{iso} varies in the domain of $0.35\text{-}0.66\times10^{-4}$ s^{-1} and $\Phi_{cc}\rightarrow\Phi_{tt}$ ranges from $0.46\text{-}0.61\times10^{-3}$).

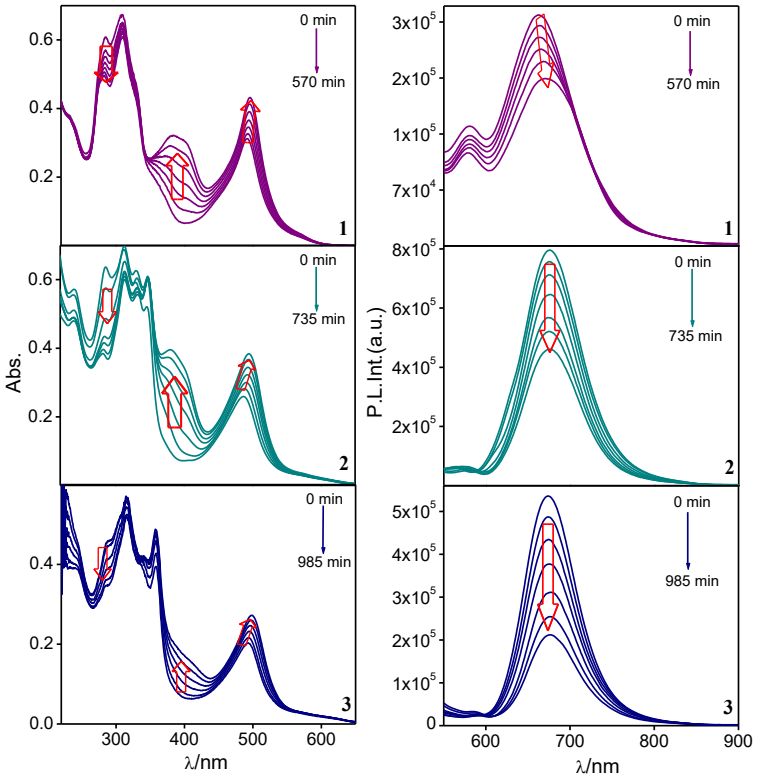

Figure 4.24. UV-vis absorption (a) and emission (λ_{ex} = 490 nm) (b) spectral changes upon irradiating the photolyzed MeCN solution of **1-3** with 270 nm light. Insets show the irradiation time.

4.3.9. Enhancement of Photoisomerization Rate via Chemical Oxidation and Reduction. We are now interested to tune the rate and quantum yield of the photoisomerization process of the complexes. To this end, we first oxidized the Ru(II) centers in their MeCN solutions under the influence of ceric ammonium nitrate (CAN, 1.0×10^{-2} M solution) and the process is again monitored via absorption and emission spectroscopy (Figure 4.25). Among the three complexes, **2** and **3** exhibit substantial changes in their spectral profiles. By contrast, practically no change is noticed for **1**, probably because of its higher oxidation potential ($E_{1/2}$ = 1.34 V) compared with both **2** ($E_{1/2}$ = 1.11 V) and **3** ($E_{1/2}$ = 1.12 V). Upon gradual addition of CAN, the ^{1}MLCT absorption band at ~500 nm is systematically diminished with concomitant evolution of broad band in the longer wavelength region (680-950 nm for **2** and 640-830 nm for **3**). We assigned these new bands as terpyridine to Ru^{3+} charge transfer (LMCT) transition as Ru-centers become electron-deficient upon oxidation.[99] Visual color change from reddish-brown to greenish yellow is also noticed during the oxidation process (inset of Figure 4.25). In the emission side, systematic quenching of emission intensity is noticed for both complexes upon gradual addition of CAN and almost complete quenching of emission takes place at

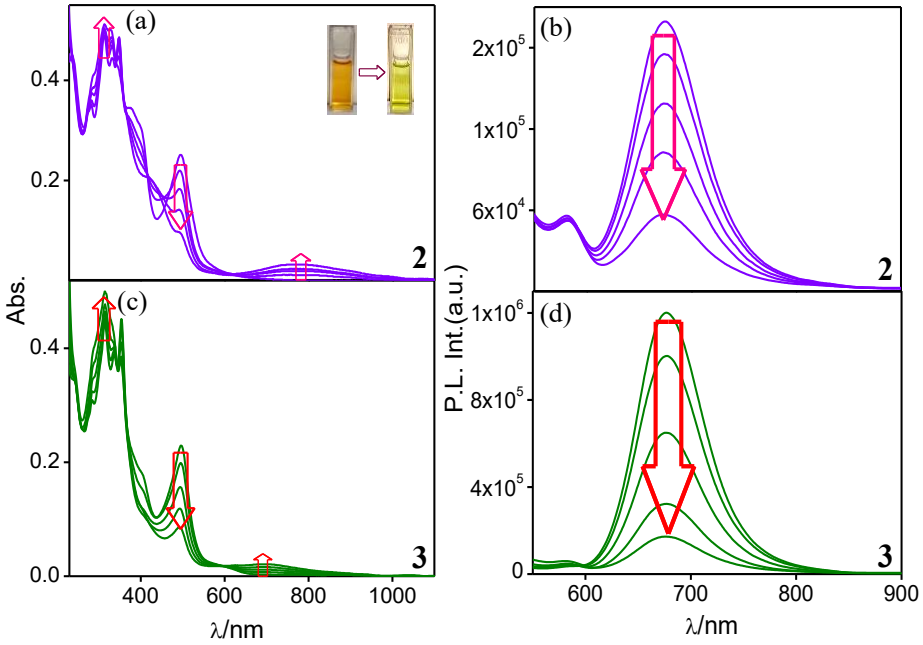

Figure 4.25. Absorption and emission (λ_{ex} =490 nm) (b, d) spectral changes of **2** (a and b, respectively) and **3** (c and d, respectively) in MeCN (3.0×10^{-6} M) upon treating with 4 equiv of CAN. Inset to figure a show the color change observed in naked eye upon addition of CAN.

saturation. The quenching of emission in both complexes is probably due to electron transfer from the terpyridine-type motif(s) to the excited luminophore. Thus, by the use of CAN, it is expected that the *t-t* forms of the complexes in their Ru^{II}-Ru^{II} states get converted to their respective *t-t* forms in Ru^{III}-Ru^{III} states.

We are now interested to investigate the isomerization behavior of the oxidized form of the complexes (*t-t* forms in their Ru^{III}-Ru^{III} states). The CAN-treated solutions of the complexes are subjected to two different conditions, viz. kept in the dark and treated with visible light of 500 nm, and monitored their isomerization behavior through absorption and emission spectroscopy. Associated spectral changes are displayed in Figure 4.26. Upon light irradiation, the LMCT band gets totally diminished and at its expense the MLCT band regains its intensity. The ILCT band, on the other hand, gets further diminished after light irradiation. The extent of rise in the MLCT band at ~490 nm is about two times while the decrease in the ILCT band is much less. The successive absorption spectrum was found to pass through multiple isosbestic points. The spectral saturation takes place after ~15 min of light irradiation and the resulting solution regains its initial reddish-brown color (inset of Figure 4.26). Upon close look, it appears that the resulting spectrum at saturation is almost identical to the spectrum obtained upon photolysis of the respective complex in absence of CAN and also correlates well with the calculated spectrum of the *c-c* forms

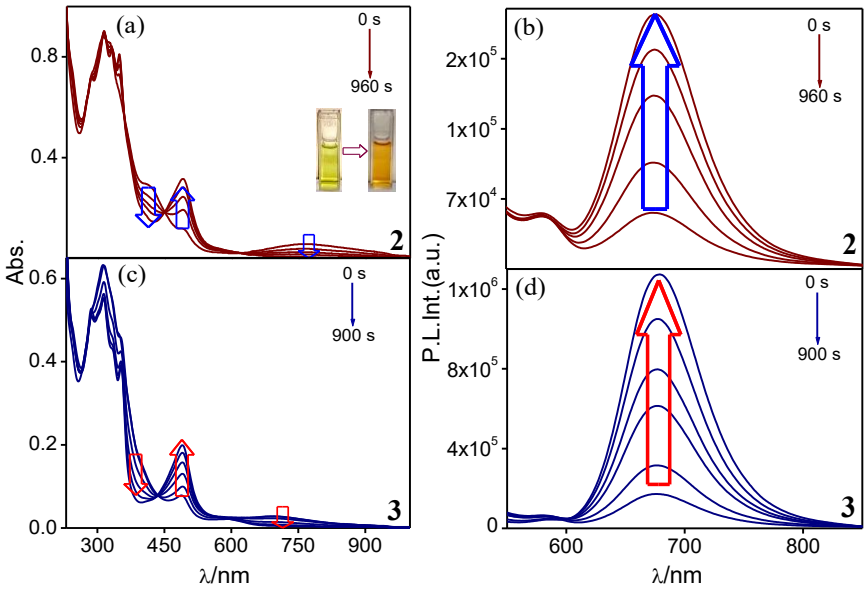

Figure 4.26. Absorption and emission spectral changes of CAN-treated MeCN solutions of **2** (a and b, respectively) and **3** (c and d, respectively) upon irradiating with visible light (500 nm). Inset to figure a shows the color change observed in naked eye upon irradiating with visible light.

of Ru(II)-Ru(II) dimers. The quenched emission band of the complexes induced by CAN gradually regains its intensity without any change in its peak position upon light irradiation and finally the emission intensity gets almost restored to its initial state upon saturation. Thus, photolysis of the CAN-treated solutions of **2** and **3** leads to simultaneous reduction of two Ru(III) centers along with isomerization predominantly to their *c*-*c* forms. Most surprisingly, the said photoisomerization completed within only 15 min which is in sharp contrast with the required time of about 6-7 h for the conversion of *t*-*t*→*c*-*c* form in case of Ru(II)-Ru(II) state. Furthermore, no signature for re-oxidation of the Ru(II)-*c*-*c*-Ru(II) form of the complexes is noticed even on keeping for several hours. On the other hand, practically no change in color and/or their spectral profiles is noticed when the CAN-treated solutions of the complexes are kept in the dark for more than 12 h. The rate constant (k_{iso}) and the quantum yields ($\Phi_{tt}\rightarrow\Phi_{cc}$) of the isomerization process executed under visible light (500 nm) are estimated and presented in Table 4.8 and Figure 4.27. k_{iso} varies in the domain of 0.52-1.03×10^{-2} s^{-1}, while $\Phi_{tt}\rightarrow\Phi_{cc}$ ranges from 0.20-0.54, depending on the terminal tridentate ligands. Thus, it is evident that the isomerization process becomes extremely fast when Ru^{2+} gets oxidized to Ru^{3+} state. The oxidation of the Ru(II)-Ru(II) species leads to decrease in electron density on the Ru centers which in turn decreases the overall electron density across C=C bond, thereby inducing more single bond character. Hence, upon light irradiation, rotation across the phenylene-vinylene motifs becomes more feasible in the oxidized forms of the complexes which is also reflected in the rate of *t*-*t* to *c*-*c* isomerization process (Table 4.8).

Table 4.8. Quantum Yield and Rate Constants for the Photoisomerization of **2** and **3** in MeCN in their Oxidized Forms.

		CAN		$KMnO_4$	
Compounds	Light source	Quantum yield (Φ)	Rate constant (k_{iso}×10^3/s^{-1})	Quantum yield (Φ)	Rate constant (k_{iso}×10^3/s^{-1})
2	270	0.33	10.4	0.14	4.83
	500	0.20	5.20	0.12	2.56
	700	0.04	0.65	0.05	0.76
3	270	0.38	13.2	0.44	9.76
	500	0.54	10.4	0.92	6.63
	700	0.06	0.58	0.17	0.88

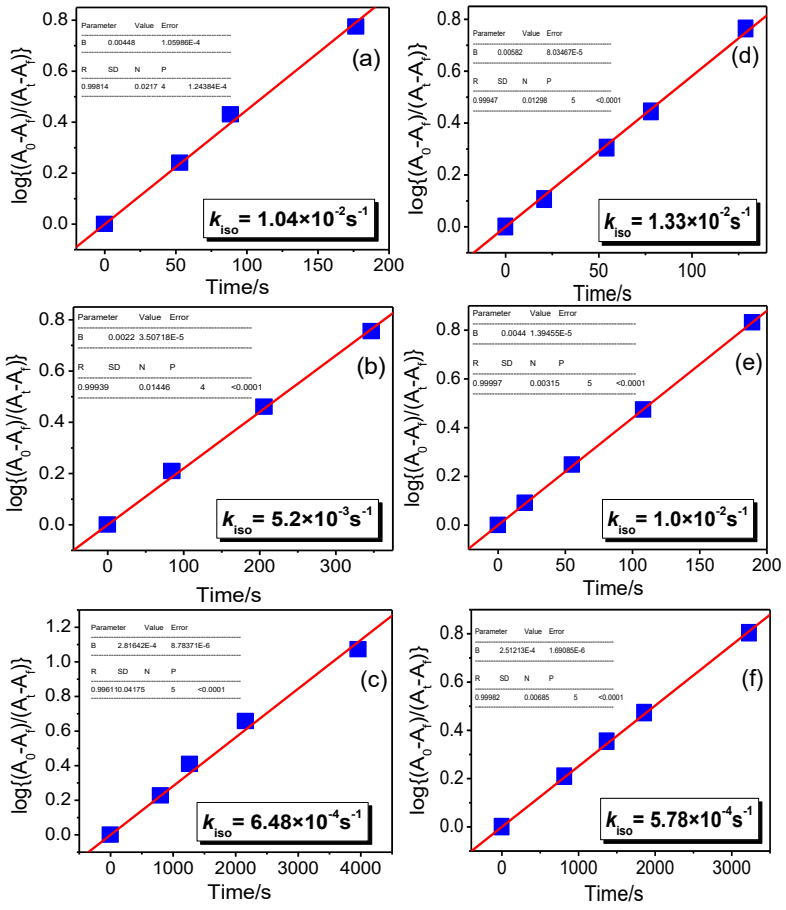

Figure 4.27. Linear plot of log $(A_0-A_f)/(A_t-A_f)$ *vs*. time (t) for absorption spectral changes upon irradiation of the CAN-treated solution in MeCN with (a,d) 270 nm, (b,e) 500 nm and (c,f) 700 nm light for **2** (left panel) and **3** (right panel).

Unfortunately, in the said oxidation-induced photoisomerization process, we are unable to locate the Ru(III)-*c*-*c*-Ru(III) form. With regard to our desire to obtain the *c*-*c* isomer of Ru(III)-Ru(III) state in the complexes, we used $KMnO_4$ as an additional oxidant. The $KMnO_4$-induced oxidation process of the complexes (**2** and **3**) again monitored via absorption and emission spectroscopy and the spectral profiles are found to be almost identical to those caused by CAN (Figure 4.28 for **3**). Thereafter, we irradiated the $KMnO_4$-treated solutions of the complexes with visible light of 500 nm and again monitored via absorption and emission spectroscopy. Similar phenomena are also noticed in this case as we previously observed with CAN (Figure 4.29). The time taken to reach the saturation point is ~20 min. The extent of change in the spectral profiles is found to be almost same with both the oxidants, although the rate and quantum yield of isomerization differ slightly (Table 4.8).

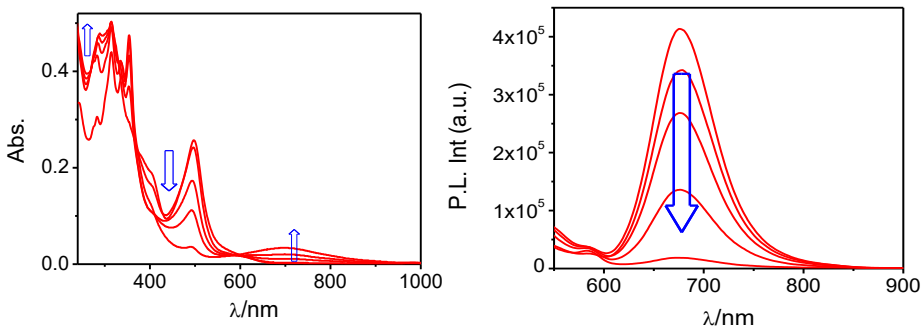

Figure 4.28. Absorption (left) and emission (right) spectral profile of a representative complex **3** (3.0×10^{-6} M) in MeCN upon incremental addition of 6 equiv of $KMnO_4$.

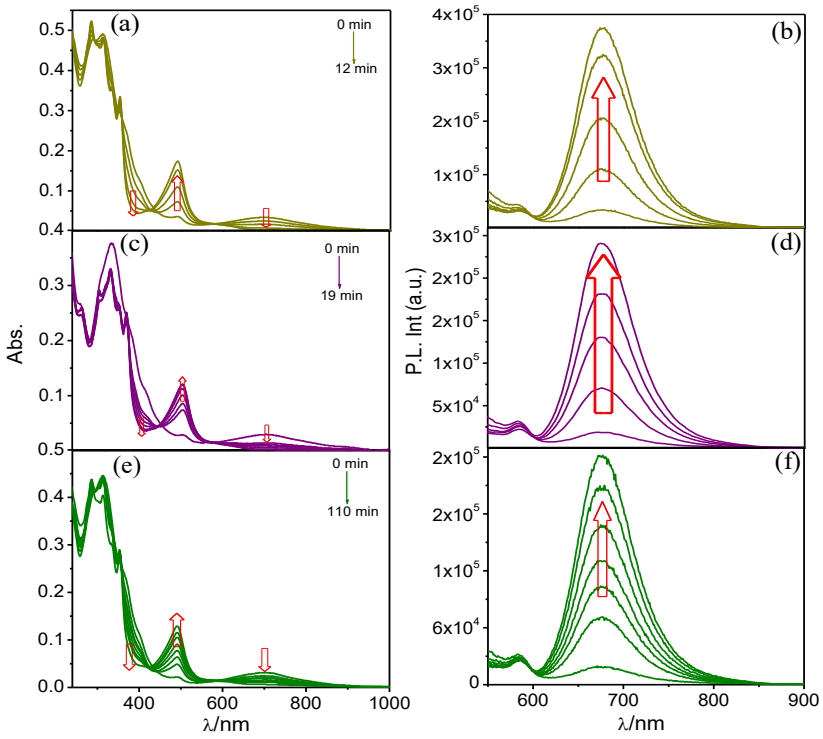

Figure 4.29. Absorption (left) and emission (right) spectral profiles of a representative complex **3** upon irradiation with (a, b) 270 nm, (c, d) 500 nm and (e, f) 700 nm light to the $KMnO_4$-oxidized forms.

In order to elucidate the role of active species in the reduction-coupled isomerization process, we also performed wavelength-dependent photoisomerization of the Ru(III)-Ru(III) forms of the complexes, induced by both CAN and $KMnO_4$. To this end, two other light sources, viz. 270 and 700 nm have been employed in addition to the previously used 500 nm source (Figures 4.29-4.31). Interestingly, all the three light sources

are capable of inducing reduction as well as isomerization. But the time taken to reach the *c-c* form in Ru^{II}-Ru^{II} state differs quite substantially. It is observed that the time taken is least (~6-12 min) with 270 nm light, while highest for 700 nm source (~97-112 min) with an intermediate value of ~15-20 min with 500 nm light source with both the oxidants (CAN and $KMnO_4$). The observed rate (k_{iso}) of photoisomerization also follows the above trend (Figure 4.27).

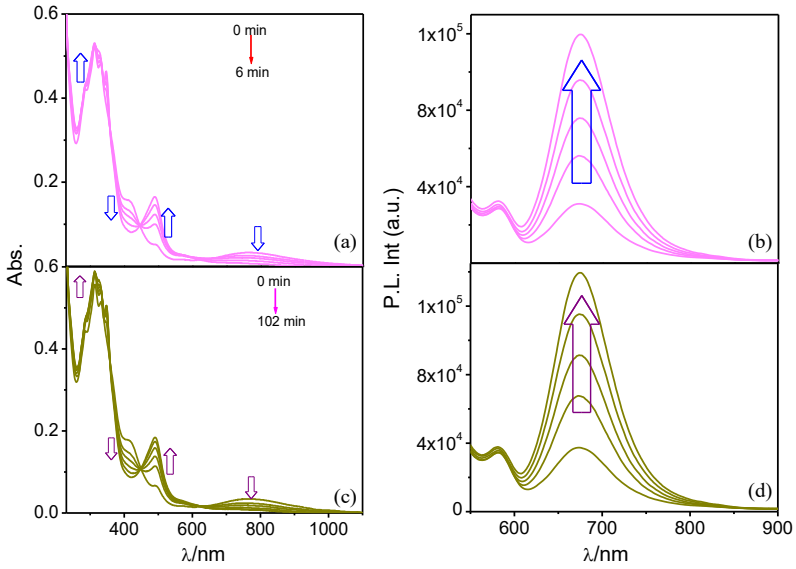

Figure 4.30. Absorption (left) and emission (right) spectral profile of **2** upon irradiation with 270 (a and b) and 700 nm (c and d) light to the CAN-oxidized forms.

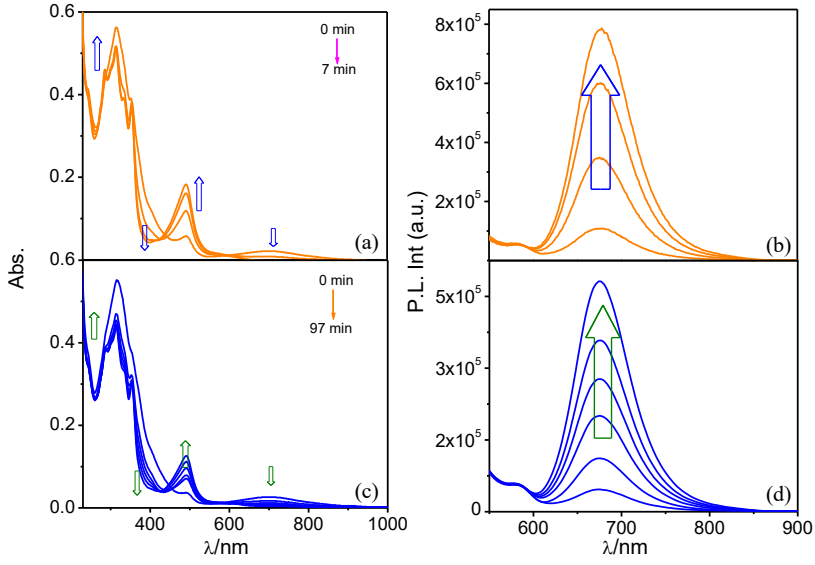

Figure 4.31. Absorption (left) and emission (right) spectral profile of **3** upon irradiation with 270 (a and b) and 700 nm (c and d) light to the CAN-oxidized forms.

The aforementioned observations shed some light on the mechanistic aspects on the photo-switching process involving oxidation-reduction and *trans-cis* isomerization processes. Since the absorption spectrum of both Ce(III) and Mn(II) species span the spectral domain of 200-400 nm, the UV irradiation most probably leads to direct photo-excitation to Ce(III)*/Mn(II)* which in-turn leads to facile reduction {Ru(III)-Ru(III) to Ru(II)-Ru(II)} as well as isomerization (from *t-t* to *c-c* forms) with concomitant formation of oxidized forms of Ce(III) and Mn(II).[100,101] It is quite surprising that simultaneous reduction as well as isomerization is also taking place upon treatment with 700 nm light source, wherein the capability of light absorption by Ce(III)/Mn(II) species is quite negligible. Only the Ru(III)-Ru(III) species possess absorption at ~700 nm. In that case, Ru(III)-Ru(III) species could absorb light of 700 nm and gets photo-excited to [Ru(III)-Ru(III)]* species which may oxidize Ce(III) or Mn(II) to its higher oxidation states and itself gets reduced to Ru(II)-Ru(II).

The remarkable enhancement in the rate of photoisomerization via chemical oxidant, inspires us to explore the isomerization behavior of the complexes in their reduced states. Herein, we employed metallic sodium as the reducing agent. For this purpose, we have chosen complex **3** as the representative case. Metallic Na is first dissolved in MeCN (2.0×10^{-2} M) and added incrementally to the MeCN solution of **3** and the progress of reduction is monitored via absorption and emission spectroscopy (Figure 4.32). It is seen that the absorbance of π-π* band within the spectral domain of 220-280 nm increases drastically, while practically no change is noticed in their MLCT or ILCT bands, spanning within 300-650 nm.[102] This suggests that the electron donated by Na is housed mainly in the ligand-based π* orbitals located in the higher energy region. In the emission side,

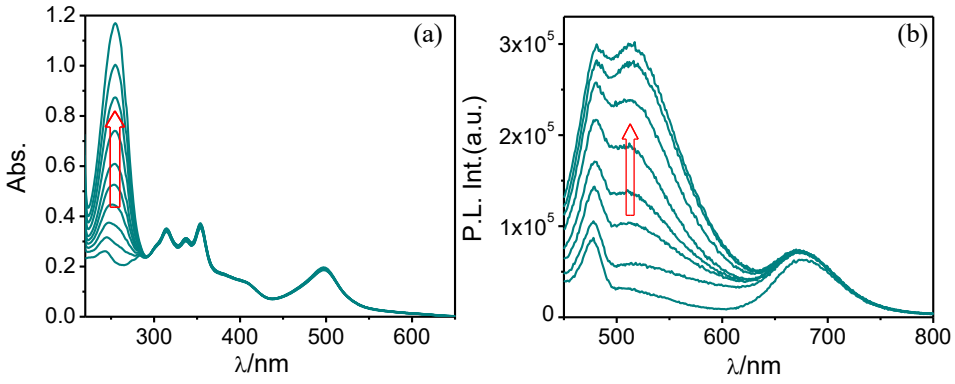

Figure 4.32. Absorption (a) and emission (λ_{ex} =430 nm) (b) spectral changes of **3** (2.5×10^{-6} M) in MeCN upon treating with 10 equiv of Na metal.

complex **3** exhibits large increase in emission intensity within the spectral domain of 450-600 nm (probably due to radiative deactivation of ^{3}ILCT and/or $^3\pi$-π^* state), keeping the band intensity at ~677 nm (due to ^{3}MLCT) almost unaltered.

Now the reduced form of the complex is subjected to light irradiation and the changes are monitored spectroscopically (Figure 4.33). Two-step changes are observed in the spectral profile during the course of photolysis. In the first step, the absorbance of the high intensity π-π^* band that was generated under the influence of Na metal, decreases dramatically. By contrast, only a small decrease in intensity takes place for MLCT and ILCT bands. In the second stage of photolysis, MLCT and ILCT bands continue to decrease in intensity, while a small but finite increase in intensity is noticed for the band at ~244 nm at saturation. Time required to reach the photostationary state is ~3 h.

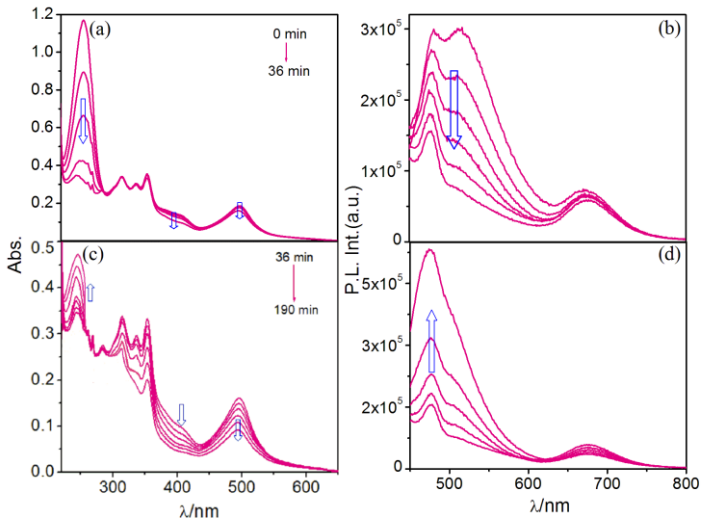

Figure 4.33. Two-step change in the absorption (a, c) and emission (b, d) spectral profiles of the reduced forms of **3** upon irradiation with 500 nm light.

Two-step changes are also noticed in the emission spectral profiles. Upon light irradiation, the intense emission band in the spectral domain of 450-600 nm gradually decreases, keeping the ^{3}MLCT emission at 677 nm almost constant, in the first step. Continued irradiation with light, on the other hand, leads to gradual increase in emission intensity in the same spectral domain. Upon close inspection, it appears that the spectrum obtained after photolysis of the sodium-treated solution of the complex is almost similar to that of Ru(II)-*c*-*c*-Ru(II) (particularly the absorption spectral profile). Thus, upon shining light, the reduced form of **3** most probably reverts back to its initial state [{Ru(II)-Ru(II)}$^{4+}$] along with isomerization from *t*-*t* to *c*-*c*. We also calculated the rate constant (k_{iso}=2.96×10$^-$

^{4} s^{-1}) and quantum yield (Φ=7.64×10^{-3}) of isomerization, indicating the process being much faster in the reduced state than that of its non-reduced form (Figure 4.34). Upon reduction, the overall charge of the complex reduces which in turn decreases the solvation of the complex in polar solvent like MeCN. Lesser solvation, on the other hand, leads to decrease in effective rotor volume of the complex which in turn facilitates the movement of the groups across the double bond. Thus, remarkable modulation of the kinetics of the photoisomerization process becomes feasible via oxidation as well as reduction of the complexes. Scheme 4.1 illustrates reversible multi-state switching processes in the complexes involving light of appropriate wavelength and suitable chemical oxidant and reductant.

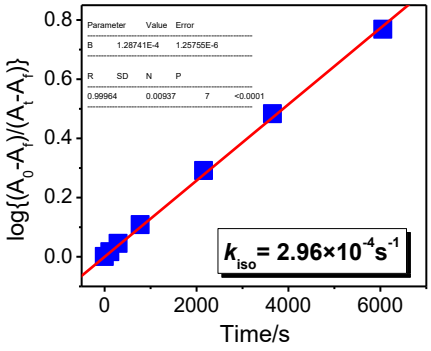

Figure 4.34. Linear plot of log $(A_0-A_f)/(A_t-A_f)$ *vs*. time (t) for absorption spectral changes upon irradiation of the Na-treated solution in MeCN with 500 nm light for **3**.

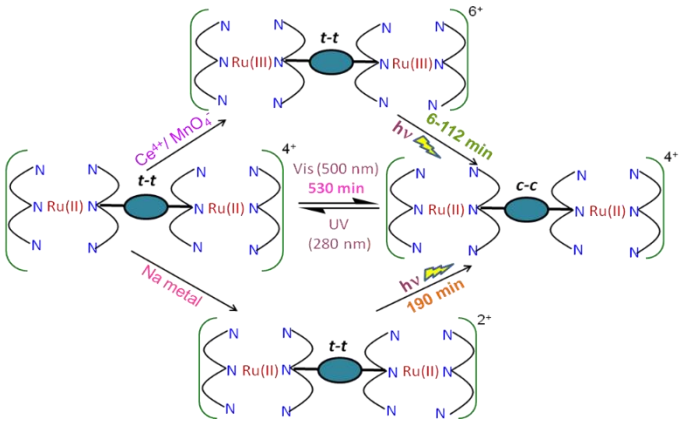

Scheme 4.1. Multi-step switching via oxidation-reduction and reversible *t-t*⇌*c-c* isomerization.

4.4. Conclusions

In summary, a new family of luminescent bimetallic Ru(II) complexes containing two consecutive phenylene-vinylene motifs in between the two terpyridine units in the ligand site, have been designed in this work. Three different capping tridentate units are incorporated for fine tuning of properties. Two consecutive phenylene-vinylene motifs in the bridge induce extended π-electron conjugation throughout the entire complex skeleton and as result of which all three complexes are emissive at RT with reasonably long lifetimes. Besides, these phenylene-vinylene units promote isomerization upon irradiation with visible light that is clearly evident from absorption, emission, cyclic voltammetry and ^{1}H NMR spectroscopic investigations as well as by theoretical calculations. The reverse *c*-*c* to *t*-*t* isomerization is also feasible upon subjecting UV light irradiation, albeit at a slower rate, compared with the forward process. The quantum yield (Φ) and the rate (*k*) of these two-stage photoisomerization processes are estimated which are found to depend upon the capping unit in the complexes.

The most interesting aspect of the present work is significant enhancement of rate of photoisomerization through the use of chemical oxidants (CAN and $KMnO_4$) as well as reductant (metallic sodium). Essentially, an efficient multi-state switching has been achieved in the present complexes via judicious choice of chemical oxidant and/or reductants as well as light of appropriate wavelength. Hence, these smart and multi-state molecular photo-switches revealed from this study can be effectively employed in promoting rapid and complex switching phenomena for diverse applications such as information storage, intricate logic gates, optical switches and drug delivery.

4.5. References

(1) Badjic, J. D.; Balzani, V.; Credi, A.; Silvi, S.; Stoddart, J. F. A Molecular Elevator. *Science* **2004**, *303*, 1845-1849.

(2) Ko, C.-C.; Yam, V.-W.-W. Coordination Compounds with Photochromic Ligands: Ready Tunability and Visible Light-Sensitized Photochromism. *Acc. Chem. Res.* **2018**, *51*, 149-159.

(3) Saha, S.; Stoddart, J. F. Photo-Driven Molecular Devices. *Chem. Soc. Rev.* **2007**, *36*, 77-92.

(4) Hofmeier, H.; Schubert, U. S. Recent Developments in the Supramolecular Chemistry of Terpyridine-Metal Complexes. *Chem. Soc. Rev.* **2004**, *33*, 373-399.

(5) Kawata, S.; Kawata, Y. Three-Dimensional Optical Data Storage Using Photochromic Materials. *Chem. Rev.* **2000**, *100*, 1777-1788.

(6) Lubbe, S.; Szymanski, W.; Feringa, B. L. Recent Developments in Reversible Photoregulation of Oligonucleotide Structure and Function. *Chem. Soc. Rev.* **2017**, *46*, 1052-1079.

(7) Yagai, S.; Kitamura, A. Recent Advances in Photoresponsive Supramolecular Self-Assemblies. *Chem. Soc. Rev.* **2008**, *37*, 1520-1529.

(8) Russew, M.-M.; Hecht, S. Photoswitches: From Molecules to Materials. *Adv. Mater.* **2010**, *22*, 3348-3360.

(9) Dattler, D.; Fuks, G.; Heiser, J.; Moulin, E.; Perrot, A.; Yao, X.; Giuseppone, N. Design of Collective Motions from Synthetic Molecular Switches, Rotors, and Motors. *Chem. Rev.* **2020**, *120*, 310-433.

(10) Brieke, C.; Rohrbach, F.; Gottschalk, A.; Mayer, G.; Heckel, A. Light-Controlled Tools. *Angew. Chem., Int. Ed.* **2012**, *51* (34), 8446-8476.

(11) Ankenbruck, N.; Courtney, T.; Naro, Y.; Deiters, A. Optochemical Control of Biological Processes in Cells and Animals. *Angew. Chem., Int. Ed.* **2018**, *57* (11), 2768-2798.

(12) Bandara, H. M. D.; Burdette, S. C. Photoisomerization in Different Classes of Azobenzene. *Chem. Soc. Rev.* **2012**, *41* (5), 1809-1825.

(13) Kurihara, M.; Nishihara, H. Azo- and Quinone-Conjugated Redox Complexes-Photo- and Proton-Coupled Intramolecular Reactions Based On d-π Interaction. *Coord. Chem. Rev.* **2002**, *226*, 125-135.

(14) Yutaka, T.; Mori, I.; Kurihara, M.; Mizutani, J.; Tamai, N.; Kawai, T.; Irie, M.; Nishihara, H. Photoluminescence Switching of Azobenzene-Conjugated Pt(II) Terpyridine Complexes by Trans-Cis Photoisomerization. *Inorg. Chem.* **2002**, *41*, 7143-7150.

(15) Yutaka, T.; Kurihara, M.; Kubo, K.; Nishihara, H. Novel Photoisomerization Behavior of Rh Binuclear Complexes Involving an Azobenzene-Bridged Bis(Terpyridine) Ligand. Strong Effects of Counter-Ion and Solvent and the Induction of Redox Potential Shift. *Inorg. Chem.* **2000**, *39*, 3438-3439.

(16) Yutaka, T.; Mori, I.; Kurihara, M.; Mizutani, J.; Kubo, K.; Furusho, S.; Matsumura, K.; Tamai, N.; Nishihara, H. Synthesis, Characterization, and Photochemical Properties of Azobenzene-Conjugated Ru(II) and Rh(III) Bis(Terpyridine) Complexes. *Inorg. Chem.* **2001**, *40*, 4986-4995.

(17) Irie, M.; Yokoyama, Y. Diarylethenes for Memories and Switches. *Chem. Rev.* **2000**, *100* (5), 1685-1716.

(18) Irie, M.; Fukaminato, T.; Matsuda, K.; Kobatake, S. Photochromism of Diarylethene Molecules and Crystals: Memories, Switches, and Actuators. *Chem. Rev.* **2014**, *114*, 12174-12277.

(19) Matsuda, K.; Irie, M. Diarylethene as a Photoswitching Unit. *J. Photochem. Photobiol. C* **2004**, *5* (2), 169-182.

(20) Irie, M.; Sakemura, K.; Okinaka, M.; Uchida, K. Photochromism of Dithienylethenes with Electron-Donating Substituents. *J. Org. Chem.* **1995**, *60*, 8305-8309.

(21) Waldeck, G. H. Photoisomerization Dynamics of Stilbenes. *Chem. Rev.* **1991**, *91*, 415-436.

(22) Villarón, D.; Wezenberg, S. J. Stiff-Stilbene Photoswitches: From Fundamental Studies to Emergent Applications. *Angew. Chem.* **2020**, *132*, 13292-13302.

(23) Klajn, R. Spiropyran-Based Dynamic Materials. *Chem. Soc. Rev.* **2014**, *43*, 148-184.

(24) Polo, A. S.; Itokazu, M. K.; Frin, K. M.; de Toledo Patrocínio, A. O.; Iha, N. Y. M. Light Driven Trans-to-Cis Isomerization of Stilbene-Like Ligands in fac-[Re(CO)3(NN) (Trans-L)]$^{+}$ and Luminescence of their Photoproducts. *Coord. Chem. Rev.* **2006**, *250* (13- 14), 1669-1680.

(25) Zanoni, K. P. S.; Iha, N. Y. M. Reversible Trans ⇌ Cis Photoisomerizations of $[Re(CO)_3(Ph_2phen)(StpyCN)]^+$ Towards Molecular Machines. *Dalton Trans.* **2017,** *46* (30), 9951-9958.

(26) Matos, S.; Amaral, R. C.; Iha, N. Y. M. Visible Photosensitization of Trans-Styrylpyridine Coordinated to fac-$[Re(CO)_3(Dcbh_2)]^+$: New Insights. *Inorg. Chem.* **2018**, *57* (15), 9316-9326.

(27) Ko, C.-C.; Kwok, W.-M.; Yam, V. W.-W.; Phillips, D. L. Triplet MLCT Photosensitization of the Ring-Closing Reaction of Diarylethenes by Design and Synthesis of a Photochromic Rhenium(I) Complex of a Diarylethene-Containing 1,10-Phenanthroline Ligand. *Chem.-Eur. J.* **2006**, *12*, 5840-5848.

(28) Stricker, F.; Sanchez, D. M.; Raucci, U.; Dolinski, N. D.; Zayas, M. S.; Meisner, J.; Hawker, C. J.; Martínez, T. J.; Read de Alaniz, J. A Multi-Stage Single Photochrome System for Controlled Photoswitching Responses. *Nat. Chem.* **2022**, *14*, 942-948.

(29) Mrozek, T.; Görner, H.; Daub, J. Towards Multifold Cycloswitching of Biphotochromes: Investigation on a Bond-Fused Dihydroazulene/ Vinylheptafulvene and Dithienylethene/ Dihydrothienobenzothiophene. *Chem. Commun.* **1999**, 1487-1488.

(30) Fihey, A.; Perrier, A.; Browne, W. R.; Jacquemin, D. Multiphotochromic Molecular Systems. *Chem. Soc. Rev.* **2015**, *44*, 3719-3759**.**

(31) Nie, H.; Self, J. L.; Kuenstler, A. S.; Hayward, R. C.; Read de Alaniz, J. Multiaddressable Photochromic Architectures: From Molecules to Materials. *Adv. Opt. Mater.* **2019**, *7*, 1900224**.**

(32) Fu, H.; Pramanik, S.; Aprahamian, I. Metal and Proton Relay-Controlled Hierarchical Multistep Switching Cascade. *J. Am. Chem. Soc.* **2023**, *145*, 36, 19554-19560.

(33) Jago, D.; Walkey, M. C.; Gaschk, E. E.; Spackman, P. R.; Piggott, M. J.; Moggach, S. A. Koutsantonis, G. A. Multistate Switching of Some Ruthenium Alkynyl and Vinyl Spiropyran Complexes. *Inorg. Chem.* **2023**, *62*, 31, 12283-12297.

(34) Perrier, A.; Maurel, F.; Jacquemin, D. Single Molecule Multiphotochromism with Diarylethenes. *Acc. Chem. Res.* **2012**, *45*, 1173-1182.

(35) Andréasson, J.; Pischel, U. Light-Stimulated Molecular and Supramolecular Systems for Information Processing and Beyond. *Coord. Chem. Rev.* **2021**, *429*, 213695.

(36) Feringa, B. L. The Art of Building Small: From Molecular Switches to Molecular Motors. *J. Org. Chem.* **2007**, *72*, 6635-6652.

(37) Lerch, M. M.; Szymański, W.; Feringa, B. L. The (Photo)Chemistry of Stenhouse Photoswitches: Guiding Principles and System Design. *Chem. Soc. Rev.* **2018**, *47*, 1910-1937.

(38) Aprahamian, I. Hydrazone Switches and Things in between. *Chem. Commun.* **2017**, *53*, 6674-6684.

(39) Jia, S.; Fong, W.-K.; Graham, B.; Boyd, B. J. Photoswitchable Molecules in Long-Wavelength Light-Responsive Drug Delivery: From Molecular Design to Applications. *Chem. Mater.* **2018**, *30*, 2873-2887.

(40) Credi, A.; Balzani, V.; Langford, S. J.; Stoddart, J. F. Logic Operations at the Molecular Level. An XOR Gate Based on a Molecular Machine. *J. Am. Chem. Soc.* **1997**, *119*, 2679-2681.

(41) de Silva, A. P.; Dixon, I. M.; Gunaratne, H. Q. N.; Gunnlaugsson, T.; Maxwell, P. R. S.; Rice, T. E. Integration of Logic Functions and Sequential Operation of Gates at the Molecular-Scale. *J. Am. Chem. Soc.* **1999**, *121*, 1393-1394.

(42) Bléger, D.; Hecht, S. Visible-Light-Activated Molecular Switches. *Angew. Chem. Int. Ed.* **2015**, *54*, 11338-11349.

(43) Dong, M.; Babalhavaeji, A.; Samanta, S.; Beharry, A. A.; Woolley, G. A. Red-Shifting Azobenzene Photoswitches for in Vivo Use. *Acc. Chem. Res.* **2015**, *48*, 2662-2670.

(44) Gindensperger, E.; Koppel, H.; Daniel, C. Mechanism of Visible-Light Photoisomerization of a Rhenium(I) Carbonyl-Diimine Complex. *Chem. Commun.* **2009**, *46* (43), 8225.

(45) Yao, L.-Y.; Yam, V. W.-W. Photoinduced Isomerization-Driven Structural Transformation between Decanuclear and Octadecanuclear Gold(I) Sulfido Clusters. *J. Am. Chem. Soc.* **2015**, *137*, 3506-3509.

(46) Kayanuma, M.; Gindensperger, E.; Daniel, C. Inorganic Photoisomerization: The Case Study of Rhenium(I) Complexes. *Dalton Trans.* **2012**, *41*, 13191-13203.

(47) Costa, P. J.; Calhorda, M. J.; Bossert, J.; Daniel, C.; Romão, C. C. Photochemistry of Methyltrioxorhenium Revisited: A DFT/TD-DFT and CASSCF/MS-CASPT2 Theoretical Study. *Organometallics* **2006**, *25*, 5235-5241.

(48) Kayanuma, M.; Daniel, C.; Koppel, H.; Gindensperger, E. Photophysics of Isomerizable Re(I) Complexes: A Theoretical Analysis. *Coord. Chem. Rev.* **2011**, *255* (21-22), 2693-2703.

(49) Ko, C.-C.; Yam, V. W.-W. Transition Metal Complexes with Photochromic Ligands-Photosensitization and Photoswitchable Properties. *J. Mater. Chem.* **2010**, *20*, 2063-2070.

(50) Ko, C.-C.; Wu, L.-X.; Wong, K. M.-C.; Zhu, N.; Yam, V. W.-W. Synthesis, Characterization and Photochromic Studies of Spirooxazine-Containing 2,2′-Bipyridine Ligands and their Rhenium(i) Tricarbonyl Complexes. *Chem.-Eur. J.* **2004**, *10*, 766-776.

(51) Kume, S.; Nishihara, H. Metal-Based Photoswitches Derived from Photoisomerization. *Struct. Bonding* **2007**, *123*, 79-112.

(52) Passalacqua, R.; Loiseau, F.; Campagna, S.; Fang, Y.-Q.; Hanan, G. S. In Search of Ruthenium(II) Complexes Based on Tridentate Polypyridine Ligands that Feature Long-Lived Room-Temperature Luminescence: The Multichromophore Approach. *Angew. Chem. Int. Ed.* **2003**, *42*, 1608-1611.

(53) Medlycott, E. A.; Hanan, G. S. Synthesis and Properties of Mono- and Oligo-Nuclear Ru(II) Complexes of Tridentate Ligands: The Quest for Long-Lived Excited States at Room Temperature. *Coord. Chem. Rev.* **2006**, *250*, 1763-1782.

(54) Rupp, M. T.; Shevchenko, N.; Hanan, G. S.; Kurth, D. G. Enhancing the Photophysical Properties of Ru(II) Complexes by Specific Design of Tridentate Ligands. *Coord. Chem. Rev.* **2021**, *446*, 214127.

(55) Alstrum-Acevedo, J. H.; Brennaman, M. K.; Meyer, T. J. Chemical Approaches to Artificial Photosynthesis 2. *Inorg. Chem.* **2005**, *44*, 6802-6827.

(56) Evans, R. C.; Douglas, P.; Winscom, C. J. Coordination Complexes Exhibiting Room-Temperature Phosphorescence: Evaluation of their Suitability as Triplet Emitters in Organic Light Emitting Diodes. *Coord. Chem. Rev.* **2006**, *250*, 2093-2126.

(57) Campagna, S.; Puntoriero, F.; Nastasi, F.; Bergamini, G.; Balzani, V. In Photoche mistry and Photophysics of Coordination Compounds I; Balzani, V.; Campagna, S., Eds.; *Top. Curr. Chem.* **2007**, *280*, 117-214.

(58) Yersin, H.; Rausch, A. F.; Czerwieniec, R.; Hofbeck, T.; Fischer, T. The Triplet State of Organo-Transition Metal Compounds. Triplet Harvesting and Singlet Harvesting for Efficient OLEDs. *Coord. Chem. Rev.* **2011**, *255*, 2622-2652.

(59) Hardy, J. G. Metallosupramolecular Grid Complexes: Towards Nanostructured Materials with High-Tech Applications. *Chem. Soc. Rev.* **2013**, *42*, 7881-7899.

(60) Juris, A.; Balzani, V.; Barigelletti, F.; Campagna, S.; Beleser, P.; Zelewsky, A. V. Ru(II) Polypyridine Complexes: Photophysics, Photochemistry, Eletrochemistry, and Chemiluminescence. *Coord. Chem. Rev*. **1988***, 84,* 85-277.

(61) Balzani, V.; Juris, A.; Venturi, M.; Campagna, S.; Serroni, S. Luminescent and Redox-Active Polynuclear Transition Metal Complexes. *Chem. Rev*. **1996**, *96*, 759-834.

(62) Sauvage, J.-P.; Collin, J. P. J.; Chambron, C.; Guillerez, S.; Coudret, C.; Balzani, V.; Barigelletti, F.; de Cola, L.; Flamigni, L. Ruthenium(II) and Osmium(II) Bis(Terpyridine) Complexes in Covalently-Linked Multicomponent Systems: Synthesis, Electrochemical Behavior, Absorption Spectra, and Photochemical and Photophysical Properties. *Chem. Rev*. **1994**, *94*, 993-1019.

(63) Browne, W. R.; O'Boyle, N. M.; McGarvey, J. J.; Vos, J. G. Elucidating Excited State Electronic Structure and Intercomponent Interactions in Multicomponent and Supramolecular Systems. *Chem. Soc. Rev.* **2005**, *34*, 641-663.

(64) Steinke, S. J.; Gupta, S.; Piechota, E. J.; Moore, C. E.; Kodanko, J. J.; Turro, C. Photocytotoxicity and Photoinduced Phosphine Ligand Exchange in a Ru(II) Polypyridyl Complex. *Chem. Sci.* **2022**, *13*, 7, 1933-1945.

(65) Li, A.; Turro, C.; Kodanko, J. J. Ru (II) Polypyridyl Complexes Derived from Tetradentate Ancillary Ligands for Effective Photocaging. *Acc. Chem. Res.* **2018**, *51*, 6, 1415-1421.

(66) Knoll, J. D.; Turro, C. Control and Utilization of Ruthenium and Rhodium Metal Complex Excited States for Photoactivated Cancer Therapy. *Coord. Chem. Rev.* **2015**, *282–283*, 110-126.

(67) Williams, J. A. G. The Coordination Chemistry of Dipyridylbenzene: N-Deficient Terpyridine or Panacea for Brightly Luminescent Metal Complexes. *Chem. Soc. Rev.* **2009**, *38*, 1783-1801.

(68) Maity, D.; Bhaumik, C.; Mardanya, S.; Karmakar, S.; Baitalik, S. Light Harvesting and Directional Energy Transfer in Long-Lived Homo- and Heterotrimetallic Complexes of Fe^{II}, Ru^{II}, and Os^{II}. *Chem. Eur. J.* **2014**, *20*, 13242-13252.

(69) Constable, E. C. 2,2′:6′,2″-Terpyridines: From Chemical Obscurity to Common Supramolecular Motifs. *Chem. Soc. Rev.* **2007**, *36*, 246.

(70) Hofmeier, H.; Schubert, U. S. Recent Developments in the Supramolecular Chemistry of Terpyridine-Metal Complexes. *Chem. Soc. Rev.* **2004**, *33*, 373.

(71) Medlycott, E. A.; Hanan, G. S. Designing Tridentate Ligands for Ruthenium(II) Complexes with Prolonged Room Temperature Luminescence Lifetimes. *Chem. Soc*. *Rev*. **2005**, *34*, 133-142.

(72) Brown, D. G.; Sanguantrakun, N.; Schulze, B.; Schubert, U. S.; Berlinguette, C. P. Bis(Tridentate) Ruthenium-Terpyridine Complexes Featuring Microsecond Excited-State Lifetimes. *J. Am. Chem. Soc.* **2012**, *134*, 12354-12357.

(73) Hofmeier, H.; Schubert, U. S. Recent Developments in the Supramolecular Chemistry of Terpyridine-Metal Complexes. *Chem. Soc. Rev.* **2004**, *33*, 373-399.

(74) Pal, P.; Mukherjee, S.; Maity, D.; Baitalik, S. Synthesis, Structural Characterization, and Luminescence Switching of Diarylethene-Conjugated Ru(II)-Terpyridine Complexes by Trans-Cis Photoisomerization: Experimental and DFT/TD-DFT Investigation. *Inorg. Chem.* **2018**, *57*, 5743-5753.

(75) Pal, P.; Ganguly, T.; Maity, D.; Baitalik, S. Experimental and Theoretical Exploration of Photophysics and Trans-Cis Photoisomerization of Styrylbenzene Conjugated Terpyridine Complexes of Ru(II): Strong Effect of Deprotonation from Second Coordination Sphere. *J. Photochem. Photobiol. A* **2020**, *392*, 112409.

(76) Mondal, D.; Bar, M.; Mukherjee, S.; Baitalik, S. Design of Ru(II) Complexes Based on Anthraimidazoledione-Functionalized Terpyridine Ligand for Improvement of Room-Temperature Luminescence Characteristics and Recognition of Selective Anions: Experimental and DFT/TD-DFT Study. *Inorg. Chem.* **2016**, *55*, 9707-9724.

(77) Karmakar, S.; Maity, D.; Mardanya; S.; Baitalik, S. Multichromophoric Bimetallic Ru(II) Terpyridine Complexes Based on Pyrenyl-Bis-Phenylimidazole Spacer: Synthesis, Photophysics, Spectroelectrochemistry, and TD-DFT Calculations. *Inorg. Chem.* **2014**, *53*, 12036-12049.

(78) Wang, J.; Fang, Y. Q.; Hanan, G. S.; Loiseau, F.; Campagna, S. Synthesis and Properties of the Elusive Ruthenium(II) Complexes of 4′- cyano-2,2′:6′,2″-terpyridine. *Inorg. Chem.* **2005**, *44*, 5-7.

(79) Indelli, M. T.; Bignozzi, C. A.; Scandola, F.; Collin, J.-P. Design of Long-Lived Ru(II) Terpyridine MLCT States. Tricyano Terpyridine Complexes. *Inorg. Chem.* **1998**, *37*, 6084-6089.

(80) Maestri, M.; Armaroli, N.; Balzani, V.; Constable, E. C.; Thompson, A. M. W. C. Complexes of the Ruthenium(II)-2,2′:6′,2″- Terpyridine Family. Effect of Electron-

Accepting and -Donating Substituents on the Photophysical and Electrochemical Properties. *Inorg. Chem.* **1995**, *34*, 2759-2767.

(81) Maity, D.; Bhaumik, C.; Mondal, D.; Baitalik, S. Ru(II) and Os(II) Complexes Based on Terpyridyl-Imidazole Ligand Rigidly Linked to Pyrene: Synthesis, Structure, Photophysics, Electrochemistry, and Anion-Sensing Studies. *Inorg. Chem.* **2013**, *52*, 13941-13955.

(82) Ganguly, T.; Pal, P.; Maity, D.; Baitalik, S. Synthesis, Characterization and Emission Switching Behaviors of Styrylphenyl-Conjugated Ru(II)-Terpyridine Complexes via Aggregation and Trans-Cis Photoisomerization. *J. Photochem. Photobiol. A* **2023**, *440*, 114662.

(83) Maity, D.; Das, S.; Mardanya, S.; Baitalik, S. Synthesis, Structural Characterization, and Photophysical, Spectroelectrochemical, and Anion-Sensing Studies of Heteroleptic Ruthenium(II) Complexes Derived from 4′-Polyaromatic-Substituted Terpyridine Derivatives and 2,6-Bis(benzimidazol-2-yl)pyridine. *Inorg. Chem.* **2013**, *52*, 6820-6838.

(84) Encinas, S.; Flamigni, L.; Barigelletti, F.; Constable, E. C.; Housecroft, C. E.; Schofield, E. R.; Figgemeier, E.; Fenske, D.; Neuburger, M., et al. Electronic Energy Transfer and Collection in Luminescent Molecular Rods Containing Ruthenium(II) and Osmium(II) 2,2′:6′,2″-Terpyridine Complexes Linked by Thiophene-2,5- diyl Spacers. *Chem. - Eur. J.* **2002**, *8*, 137-150.

(85) Dietrich, J.; Thorenz, U.; Förster, C.; Heinze, K. Effects of Sequence, Connectivity, and Counter Ions in New Amide-Linked Ru(tpy)$_2$-Re(bpy) Chromophores on Redox Chemistry and Photophysics. *Inorg. Chem.* **2013**, *52*, 1248-1264.

(86) Duati, M.; Tasca, S.; Lynch, F. C.; Bohlen, H.; Vos, J. G.; Stagni, S.; Ward, M. D. Enhancement of Luminescence Lifetimes of Mononuclear Ruthenium(II)-Terpyridine Complexes by Manipulation of the Sigma-Donor Strength of Ligands. *Inorg. Chem.* **2003**, *42*, 8377-8384.

(87) Wadman, S. H.; Lutz, M.; Tooke, D. M.; Spek, A. L.; Hartl, F.; Havenith, R. W. A.; van Klink, G. P. M.; van Koten, G. Consequences of N,C,N- and C,N,N-Coordination Modes on Electronic and Photophysical Properties of Cyclometalated Aryl Ruthenium(II) Complexes. *Inorg. Chem.* **2009**, *48*, 1887-1900.

(88) Kreitner, C.; Erdmann, E.; Seidel, W. W.; Heinze, K. Understanding the Excited State Behavior of Cyclometalated Bis(tridentate)ruthenium(II) Complexes: A

Combined Experimental and Theoretical Study. *Inorg. Chem.* **2015**, *54*, 11088-11104.

(89) Duati, M.; Fanni, S.; Vos, J. G. A New Luminescent Ru(terpy) Complex Incorporating a 1,2,4-Triazole Based σ-Donor Ligand. *Inorg. Chem. Commun.* **2000**, *3*, 68-70.

(90) Das, S.; Pal, P.; Ganguly, T.; Baitalik, S. Influences of Both N,N,N- and N,N,C-Coordination Modes of Tolylterpyridine on the Photophysical Properties of Cyclometalated Ru(II) Complexes: Combined Experimental and Theoretical Investigations on Acid/Base-Dependent Reversible Cyclometalation. *Inorg. Chem.* **2023**, *62*, 12872-12885.

(91) Wang, X.-Y.; Del Guerzo, A.; Tunuguntla, H.; Schmehl, R. H. Photophysical Behavior of Ru(II) and Os(II) Terpyridyl Phenylene Vinylene Complexes: Perturbation of MLCT State by Intra-Ligand Charge-Transfer State. *Res. Chem. Intermed.* **2007**, *33*, 63-77.

(92) Pal, P.; Ganguly, T.; Sahoo, A.; Baitalik, S. Emission Switching in the Near-Infrared by Reversible Trans-Cis Photoisomerization of Styrylbenzene-Conjugated Osmium Terpyridine Complexes. *Inorg. Chem.* **2021**, *60*, 4869-4882.

(93) Mukherjee, S.; Pal, P.; Sahoo, A.; Baitalik, S. Photo-Switchable Iron-Terpyridine Complexes Functionalized with Styrylbenzene Unit. *J. Photochem. Photobiol. A* **2021**, *407*, 113059.

(94) Bhaumik, C.; Das, S.; Saha, D.; Dutta, S.; Baitalik, S. Synthesis, Characterization, Photophysical, and Anion-Binding Studies of Luminescent Heteroleptic Bis-Tridentate Ruthenium(II) Complexes Based on 2,6-Bis(Benzimidazole-2-yl)Pyridine and 4'-Substituted 2,2':6',2'' Terpyridine Derivatives. *Inorg. Chem.* 2010, *49*, 5049-5062.

(95) Bhaumik, C.; Saha, D.; Das, S.; Baitalik, S. Synthesis, Structural Characterization, Photophysical, Electrochemical, and Anion-Sensing Studies of Luminescent Homo and Heteroleptic Ruthenium(II) and Osmium(II) Complexes Based on Terpyridyl-imidazole Ligand. *Inorg. Chem.* 2011, *50*, 12586-12600.

(96) Wang, X. Y.; Guerzo, A.; Schmehl, R. H. Preferential Solvation of an ILCT Excited State in Bis(Terpyridine-Phenylene-Vinylene) Zn(II) Complexes. *Chem. Commum.* 2002, 2344-2345.

(97) Baitalik, S.; Wang, X.-Y.; Schmehl, R. H. A Trimetallic Mixed Ru(II)/Fe(II) Terpyridyl Complex with a Long-Lived Excited State in Solution at Room Temperature. *J. Am. Chem. Soc.* **2004**, *126*, 16304-16305.

(98) Yang, W.-W.; Zhong, Y.-W.; Yoshikawa, S.; Shao, J.-Y.; Masaoka, S.; Sakai, K.; Yao, J.; Haga, Masa-aki. Tuning of Redox Potentials by Introducing a Cyclometalated Bond to Bis-tridentate Ruthenium(II) Complexes Bearing Bis(N-methylbenzimidazolyl)benzene or -pyridine Ligand. *Inorg. Chem.* **2012**, *51*, 890-899.

(99) Nagashima, T.; Nakabayashi, T.; Suzuki, T.; Kanaizuka, K.; Ozawa, H.; Zhong, Y.-W.; Masaoka, S.; Sakai, K.; Haga, Masa-aki. Tuning of Metal-Metal Interactions in Mixed-Valence States of Cyclometalated Dinuclear Ruthenium and Osmium Complexes Bearing Tetrapyridylpyrazine or -benzene. *Organometallics* **2014**, *33*, 4893-4904.

(100) Bamwenda, G. R.; Arakawa, H. The Photoinduced Evolution of O_2 and H_2 from a WO_3 Aqueous Suspension in the Presence of Ce^{4+}/Ce^{3+}. *Sol. Energy Mater. Sol. Cells.* **2001**, 70, 14.

(101) Berglund-Baudin, H.; Sun, L.; Davidov, R.; Sundahl, M.; Styring, S.; Akermark, B.; Almgren, M.; Hammarstrom, L. Intramolecular Electron Transfer from Manganese(II) Coordinatively Linked to a Photogenerated Ru(III)-Polypyridine Complex: A Kinetic Analysis. *J. Phys. Chem. A* **1998**, *102*, 2512-2518.

(102) Berger, R. M.; McMillin, D. R. Localized States in Reduced and Excited-State Ruthenium(II) Terpyridyls. *Inorg. Chem.* **1988**, *27*, 23.

Chapter 5

Advancing Molecular-Scale Logic Devices through Multistage Switching in a Luminescent Bimetallic Ru(II)-Terpyridine Complex

5.1. Introduction

Research on molecular-level information processing and computation has experienced rapid advancement since the pioneering work of de Silva[1-4], who demonstrated the feasibility of storing logical states at the molecular level. Over the past two decades, the field of chemistry has witnessed the development of a diverse array of molecular and supramolecular systems, bolstering this emerging domain.[5-14] Central to information processing in computers is the application of Boolean algebra, where logic gates execute binary arithmetic and logical functions. Consequently, molecular-level computation relies on systems capable of efficiently integrating simple logic gates into various connective circuits.[15-24] Moreover, molecular-based logic holds promise for smaller, faster, and more efficient devices compared to conventional silicon-based circuitries. Although significant research has been dedicated to developing molecular systems that replicate fundamental and intricate logic gates and functions like AND, OR, XOR, NOR, NAND, or INHIBIT, as well as advanced circuitry such as combinational, encoders, decoders, voters, keypad locks, to name a few,[25-36] there remains a scarcity of literature on intelligent functional systems that can mimic the complex logic operations necessary for diverse circuits. Thus, there exists an opportunity to tailor the design of smart molecules which upon interaction with diverse external stimuli, can generate multiple optical signals which in turn could facilitate sequential and intricate logic functions. In this context, Ru(II) complexes derived from polyheterocyclic ligands have shown immense potential by virtue of their very rich photophysical and electrochemical properties which in turn could be modulated under the influence of a wide variety of external stimuli.[37-46]

In this study, we employed our recently reported bimetallic Ru(II) complex, $[\{(Me_2bip)Ru(tpvpvpt)Ru(Me_2bip)\}^{4+}]$ $\{\mathbf{1}^{4+}(t\text{-}t)\}$, featuring consecutive phenylene-vinylene motifs in-between the two terpyridine units within the ligand architecture (Chart 5.1).[47] The phenylene-vinylene units facilitate *trans-trans* (*t-t*) to *cis-cis* (*c-c*) isomerization upon visible light irradiation, while reverse *c-c* to *t-t* isomerization upon exposure to UV light with remarkable change in its absorption and emission spectral profiles in both ways.[48-58] Furthermore, the rate of photoisomerization of the complex has been significantly enhanced in presence of chemical oxidant (Ce^{4+}) as well as reductant (metallic sodium). Inclusion of Ce^{4+} leads to the oxidation of the *t-t* form of the complex from its 4^+ to 6^+ state $\{\mathbf{1}^{4+}(t\text{-}t)\rightarrow\mathbf{1}^{6+}(t\text{-}t)\}$, which upon light irradiation leads to simultaneous reduction as well as isomerization from the *t-t* to the *c-c* form $\{\mathbf{1}^{6+}(t\text{-}t)\rightarrow\mathbf{1}^{4+}(c\text{-}c)\}$. On the other hand,

reduction of the *t-t* form of the complex from its 4^+ to 2^+ state $\{\mathbf{1}^{4+}(t\text{-}t) \rightarrow \mathbf{1}^{2+}(t\text{-}t)\}$ takes place upon addition of metallic sodium which upon light irradiation induces simultaneous oxidation as well as *t-t*→*c-c* isomerization, yielding $\mathbf{1}^{4+}(c\text{-}c)$. This type of fast and efficient multi-state switching phenomena involving oxidation-reduction coupled reversible *trans-cis* photoisomerization is extremely rare in the literature and expected to hold promise for the development of intricate logic systems for molecular-level computation as the spectral responses of the complex can be substantially altered by appropriate combinations of different ionic inputs as well as light inputs of varying wavelength.

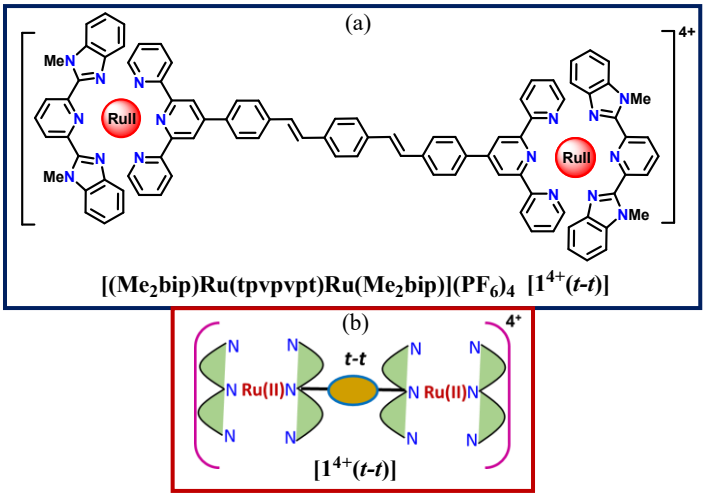

Chart 5.1. Chemical structure of the complex $\mathbf{1}^{4+}(t\text{-}t)$ (a) and its schematic representation (b).

Most of the previously reported binary logic gate articles primarily focused on the execution of basic operations, viz. NAND, NOR, AND, OR, and XOR etc.[1,8,9,14,18,22,26] In our earlier papers, we have used anion, cation as well as light of different wavelengths as the inputs and absorption or emission intensity as the outputs to mimic function of fundamental as well as complex logic functions.[19,20,28,33,34] Compared to most of the reported systems, we herein employed four inputs as well as their different combinations for the fabrication of sequential and complicated logic functions, which in turn could offer valuable insights for designing complex digital systems.

In the present study, we will initially showcase the Boolean logic function of IMPLICATION (defining logical consequences) logic gate. But as the exploration progresses, the focus shifts to the realm of combinational logic systems, where the intricacies of AND, OR, and NOT gates come to the fore.[59-66] Leveraging the unique multi-

step switching feature, the investigation delves into the intricacies of molecular decision-making processes. Through meticulous analysis and interpretation of emission spectral behavior under the influence of multiple external stimuli, the study navigates the maze of input combinations and output states, shedding light on the intricacies of molecular computation. Herein, we have successfully designed circuit diagram of 2-input 2-output and 3-input 2-output combinational logic. However, the journey does not halt at elucidating molecular logic dynamics; it extends into computational modelling, where Python's versatility shines as a potent tool for logical decision-making through conditional statements (***if-elif-else***).[67-76] By merging logic circuits with chemical processes, computational models mark a new era of exploration, offering a structured approach to deciphering chemical states based on input conditions. Our Python model, "logic_circuit," emulates a logic circuit but with a twist: instead of binary outputs, it produces chemical state outputs based on input conditions. This pioneering integration blends logic circuits with chemical processes, unlocking intricate interactions, transcending Boolean logic, and showcasing the symbiosis of chemistry and computation for unprecedented innovation. Thus, with complex $\mathbf{1}^{4+}$(*t-t*) as its cornerstone, the journey into molecular logic ventures into uncharted territories, promising to redefine the boundaries of molecular computation.

5.2. Experimental Section

5.2.1. Synthesis and Characterization of the Complex $\mathbf{1}^{4+}$(*t-t*). The synthesis and characterization of the bimetallic Ru(II) complex of composition, [(Me_2bip)Ru(tpvpvpt)Ru(Me_2bip)]$^{4+}$ has already been discussed in chapter 4.

5.2.2. Instruments and Physical Methods. The details of different equipment used and experimental process to measure absorption and luminescence spectral behavior have been discussed in chapters 2 and 3.

5.3. Results and Discussion

5.3.1. Overview of Multistage Switching Induced by Light as well as Chemical Oxidant and Reductant. The synthesis, characterization and photoisomerization behavior of $\mathbf{1}^{4+}$(*t-t*) have been thoroughly described in the previous chapter. A concise summary of the spectral changes under the influence of chemical oxidant (Ce^{4+}), reductant (Na metal) as well as light of different wavelengths is again provided here for the benefit of the readers. The complex shows a strong absorption band at 498 nm in MeCN mainly due to

Ru(II)→tpy charge transfer (MLCT) and multiple moderate to strong bands in the UV region due to intraligand charge transfer (ILCT) and/or π-π* transition. Upon excitation at the MLCT absorption maximum, the complex displays an emission band at 675 nm arising out of the radiative deactivation of its ^{3}MLCT state possessing a lifetime (τ) of 60 ns and quantum yield (Φ) of 7.2×10^{-3} at RT. Additionally, a weak emission peak at ~570 nm is observed which is probably due to the radiative deactivation of ^{3}ILCT and/or $^3\pi$-π^* state of phenylene-vinylene-substituted terpyridine bridge. The complex exhibits one reversible oxidation at 1.12 V and two successive reversible and/or quasi-reversible reduction waves within the potential domain between -1.0 and -2.2 V.

By virtue of its olefinic double bonds, the complex demonstrates *t-t* to *c-c* isomerization upon irradiating with 500 nm light source, inducing decrease in its MLCT and ILCT absorption band intensities along with increase in emission intensity without any change in emission maximum, as presented in the previous chapter (Figure 4.14). Upon treatment with 270 nm light source, the complex almost reverts back to its initial (*t-t*) form as evidenced by its absorption and emission spectral profiles (Figure 4.24 in chapter 4). Taking advantage of its reversible oxidation and reduction behavior, the photoisomerization experiment is also performed in its oxidized as well as reduced forms.

Upon addition of Ce^{4+} to the MeCN solution of the complex, the ^{1}MLCT absorption band at ~500 nm is systematically diminished with concomitant evolution of broad band in the spectral domain of 640-830 nm, due to terpyridine to Ru^{3+} charge transfer (LMCT) transition (Figure 4.25 in chapter 4).[77] The emission intensity is also quenched substantially due to the formation of $\mathbf{1}^{6+}$(*t-t*). Upon light-irradiation (500 nm) on the Ce(IV)-treated solution of the complex, the LMCT band gets totally diminished and at its expense the MLCT band regains its intensity, which has been portrayed in chapter 4 (Figure 4.26). The quenched emission band also regains its intensity without any change in its band position. Thus, photolysis of the oxidized form of the complex causes simultaneous reduction of the two Ru(III) centers along with isomerization to its *c-c* form {$\mathbf{1}^{4+}$(*c-c*)}. $\mathbf{1}^{6+}$(*c-c*) form of the complex is also obtained upon addition of Ce^{4+} to $\mathbf{1}^{4+}$(*c-c*), which upon treatment with UV light of 270 nm reverts back to $\mathbf{1}^{4+}$(*t-t*), as evidenced by absorption and emission spectroscopy (Figures 5.1 and 5.2).

Subsequently, the complex [$\mathbf{1}^{4+}$(*t-t*)] was reduced via incremental addition of metallic Na and during the course, the absorption band within the spectral domain of 220-280 nm increases drastically, keeping the intensities of both MLCT and ILCT almost unaltered (Figure 4.32 in chapter 4). A remarkable increase in the emission intensity takes place in

between 450 and 600 nm region, keeping the MLCT band intensity at 675 nm almost unaltered and saturation in its spectral profiles indicates the completion of the reduction process with transformation to the $\mathbf{1}^{2+}$(*t*-*t*).[78] When the complex is treated with Na, the Ru(II) centers do not experience any reduction. Instead, the π-accepting terpyridine units in the bridging ligand probably accept the electrons from metallic sodium, resulting in net reduction of the complex which in turn could be responsible for huge escalation in absorption and emission band intensities in shorter wavelength region (220-280 nm for absorption and 450-600 nm for emission). In order to investigate the electronic structure of complex in presence of Na, we also conducted DFT calculations on the 2-electron reduced

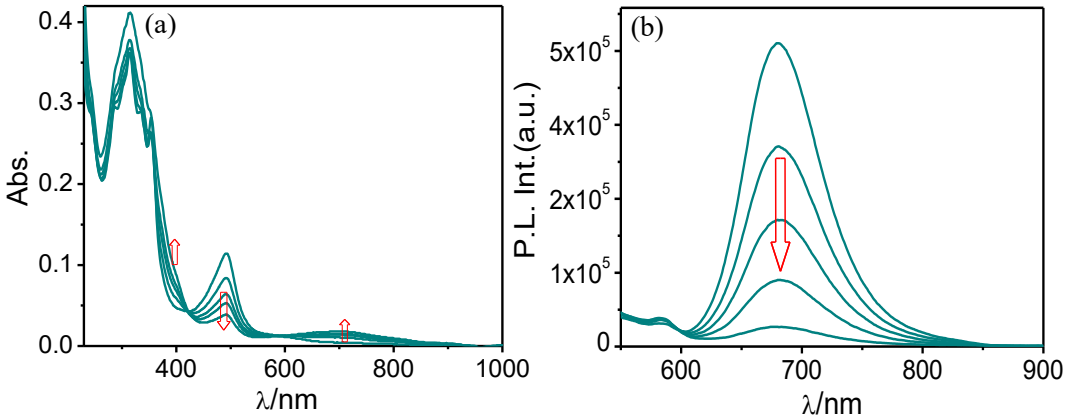

Figure 5.1. Absorption (a) and emission (λ_{ex} =490 nm) (b) spectral changes of the light-irradiated MeCN solution of $\mathbf{1}^{4+}$(*t*-*t*) (3.0×10^{-6} M) upon treating with 4 equiv of 1.0×10^{-2} M Ce^{4+}.

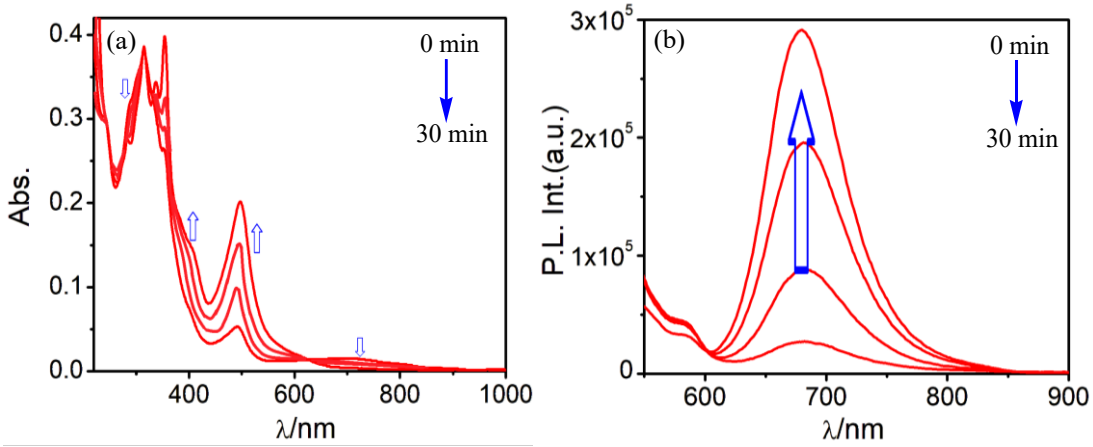

Figure 5.2. Absorption (a) and emission (λ_{ex} =490 nm) (b) spectral changes of MeCN solution of $\mathbf{1}^{6+}$(*c*-*c*) upon irradiating with UV light (270 nm).

form of the complex and the relevant spin density plot is provided in Figure 5.3. The plot reveals that upon reduction, the electron density is predominantly localized on the terpyridine units. The terpyridine units, due to their low-lying π-acceptor orbitals, mainly accept the electrons, leading to the reduction of the complex.

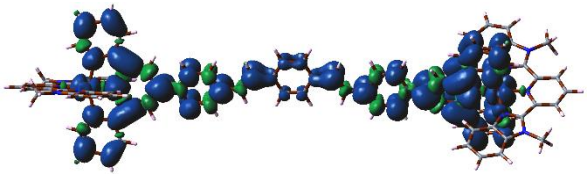

Figure 5.3. Spin density plot of two-electron reduced form of $\mathbf{1}^{4+}$(*t*-*t*) in MeCN.

Upon irradiation on the Na-treated solution with 500 nm light, two-step changes in the spectral profiles are noticed (Figure 4.33 in chapter 4). In the first step, the absorbance of the π-π* band decreases dramatically, while only a small decrease in intensity takes place for MLCT and ILCT bands. In the subsequent step, the MLCT and ILCT bands continue to decrease in intensity, while a small but finite increase in intensity is noticed for the band at ~244 nm at saturation. The intense emission band within 450-600 nm domain gradually decreases, keeping the ^{3}MLCT emission at 675 nm almost constant, in the first step. Continued irradiation with light, on the other hand, leads to gradual increase in emission intensity in the same spectral domain. The final spectrum obtained after photolysis of the sodium-treated solution of the complex is almost similar to that of $\mathbf{1}^{4+}$(*c*-*c*), which on treatment with UV light of 270 nm reverts back to $\mathbf{1}^{4+}$(*t*-*t*). Reversible multi-stage switching processes that occur under the influence of light (of wavelengths 500 and 270 nm), Ce^{4+} and metallic Na are portrayed in Scheme 5.1.

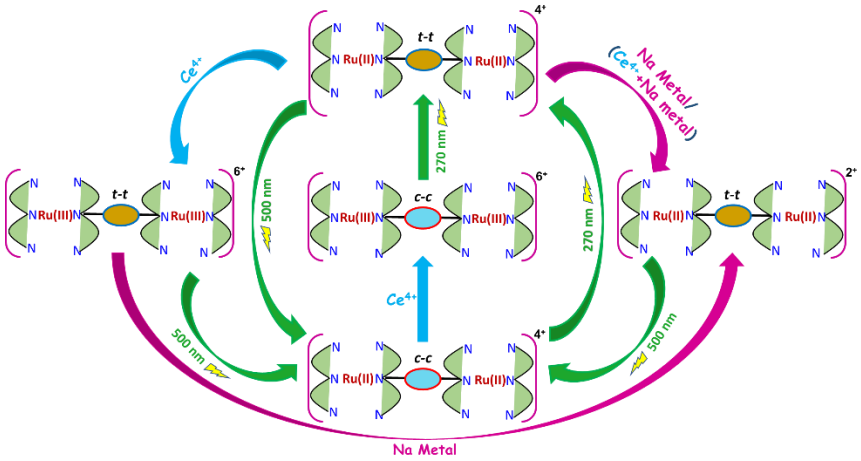

Scheme 5.1. Multi-step switching via oxidation-reduction and reversible *t*-*t*⇌*c*-*c* isomerization.

5.3.2. Unveiling the Power of the Complex in Executing Boolean Logic Functions. Boolean logic gates are the foundational elements of digital circuits, operating on binary signals to execute logical operations. AND gate outputs are true only when both inputs are true, while OR gate outputs are true if at least one input is true. Conversely, NOT gates invert their input signal. Governed by Boolean algebra, these gates form the basis of complex functions in digital systems. Through combinations of these gates, intricate logic operations enable tasks such as arithmetic calculations and data processing. In this endeavour, our focus rests on complex $\mathbf{1}^{4+}$(*t*-*t*), a molecular marvel poised to redefine the landscape of logic operations. With meticulous experimentation and analysis, we embark on a journey to emulate fundamental IMPLICATION logic gate as well as exploring the intricacies of combinational logic systems utilizing the emission spectral intensities of $\mathbf{1}^{4+}$(*t*-*t*) at distinct wavelengths.

5.3.3. Mimicking IMPLICATION Logic Function. The utilization of an IMPLICATION logic gate, particularly in the context of "material implication," is pivotal due to its potency in logical operations. Molecular logic gates exhibiting robust implication activity (IMP) are relatively scarce in literature. In our study, we employ complex $\mathbf{1}^{4+}$(*t*-*t*) as a representative model for constructing an IMPLICATION logic gate. In our experimental setup, we designate Ce^{4+} as input 1 and the photon of 500 nm wavelength as input 2. The resulting emission maximum at 675 nm serves as the output signal. The truth table (Figure 5.4c) illustrates that intense emission at 675 nm is observed when neither of

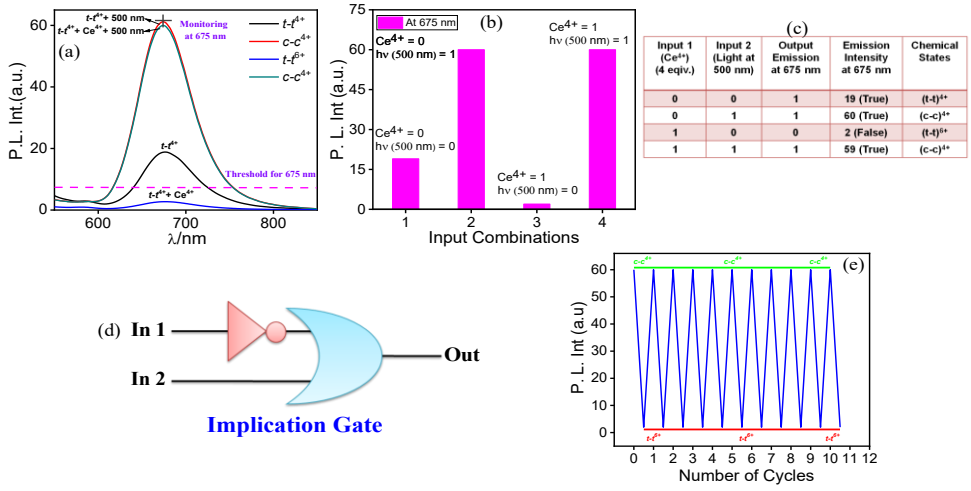

Figure 5.4. (a) The emission spectral change of $\mathbf{1}^{4+}$(*t*-*t*) when exposed to two given inputs. (b) Histogram of emission intensities. (c) The corresponding truth table. (d) Circuit diagram of IMPLICATION gate. (e) Change in the luminescence intensity at 675 nm in presence of the inputs (up to ten cycles).

the inputs is present, indicating the system's on state (1). Conversely, the sole presence of input 1 results in significant decrease in emission intensity, corresponding to the off state (0). Furthermore, two other combinations of the inputs also yield an output signal above the threshold value, indicating the on state (1) of the system. By analyzing the emission spectral changes at 675 nm induced by two inputs, we effectively mimic the functionality of an IMPLICATION gate (Figure 5.4d). In addition, the on-off-on loop could be repeated ten times without appreciable loss of the emission intensity at 675 nm (Figure 5.4e). This demonstrates the ability to manipulate logical operations through molecular interactions, thereby opening avenues for advanced Boolean logic implementations at the molecular level.

5.3.4. 2-Input 2-Output Combinational Systems. In this section, we delve into a specific type of combinational digital logic implemented through Boolean circuits, namely, AND, OR, and NOT gates. Our investigation focuses on utilizing the emission spectral intensities of complex $\mathbf{1}^{4+}$(*t*-*t*) at two distinct wavelengths (675 nm as output 1 and 515 nm as output 2) upon inclusion of Ce^{4+} as input 1 and Na as input 2 (Figure 5.5a). In absence of both inputs, we observe a robust emission intensity surpassing the threshold barrier at 675 nm, while no signal is detected at 515 nm, indicating the "ON" and "OFF" states of the

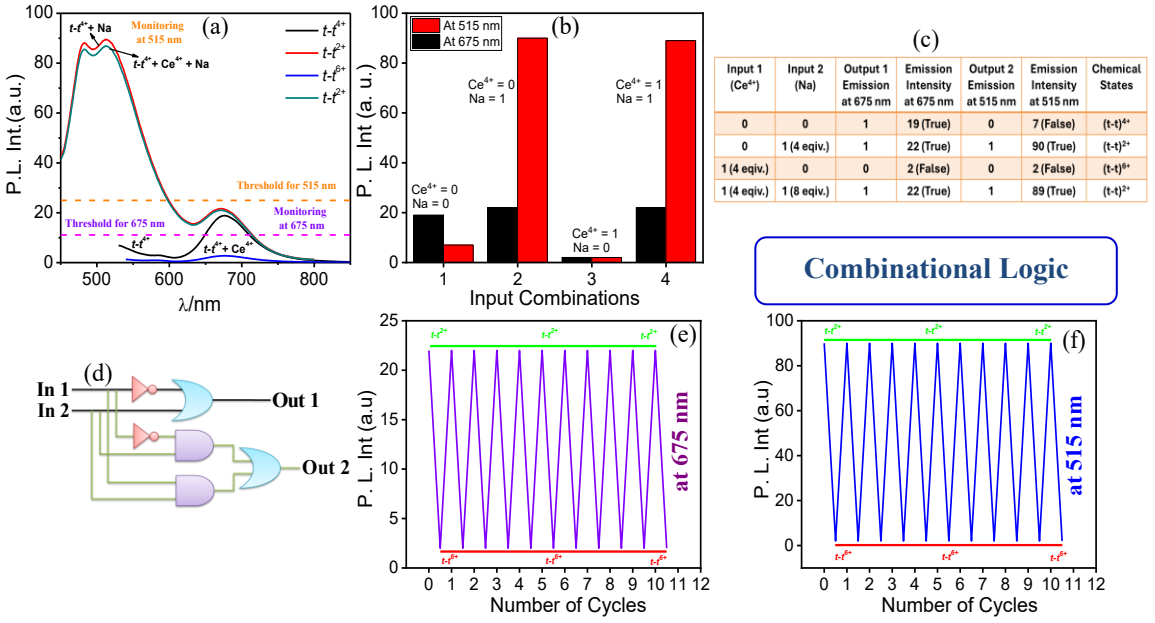

Figure 5.5. (a) The emission spectral change of complex $\mathbf{1}^{4+}$(*t*-*t*) in the presence of Ce^{4+} and Na. (b) Histogram of emission intensities. (c) Corresponding truth table for the combinational logic. (d) Circuit diagram of the 2-input 2-output logic function. (e and f) Change in the emission intensity of $\mathbf{1}^{4+}$(*t*-*t*) at 675 and 515 nm in presence of inputs (up to ten cycles).

system, respectively. The truth table depicted in Figure 5.5c elucidates that only in the presence of input 2 or both inputs; we observe strong emission intensity surpassing the threshold barrier at both outputs, representing the "ON" state. Conversely, the sole presence of input 1 fails to generate emission intensities at both outputs that can overcome the threshold barrier, indicating the "OFF" state of the system. By scrutinizing the emission spectral behavior of complex $\mathbf{1}^{4+}$(*t*-*t*) under the influence of various inputs, we can effectively mimic the function of a 2-Input 2-Output combinational logic system (Figure 5.5d). In addition, the on-off-on loop could be repeated ten times without appreciable loss of the emission intensity at both 675 and 515 nm (Figures 5.5e and 5.5f).

We have also introduced another variant of a 2-input 2-output combinational logic by altering the input combinations. Our investigation centers on leveraging the emission spectral intensities of complex 1^{4+}(*t*-*t*) at two specific wavelengths (675 nm as output 1 and 515 nm as output 2) when exposed to Na as input 1 and a photon of 500 nm as input 2 (Figure 5.6a). In the absence of both inputs, we observe a strong emission intensity exceeding the threshold barrier at 675 nm, while no signal is detected at 515 nm, indicating the "ON" and "OFF" states of the system, respectively. The truth table presented in Figure

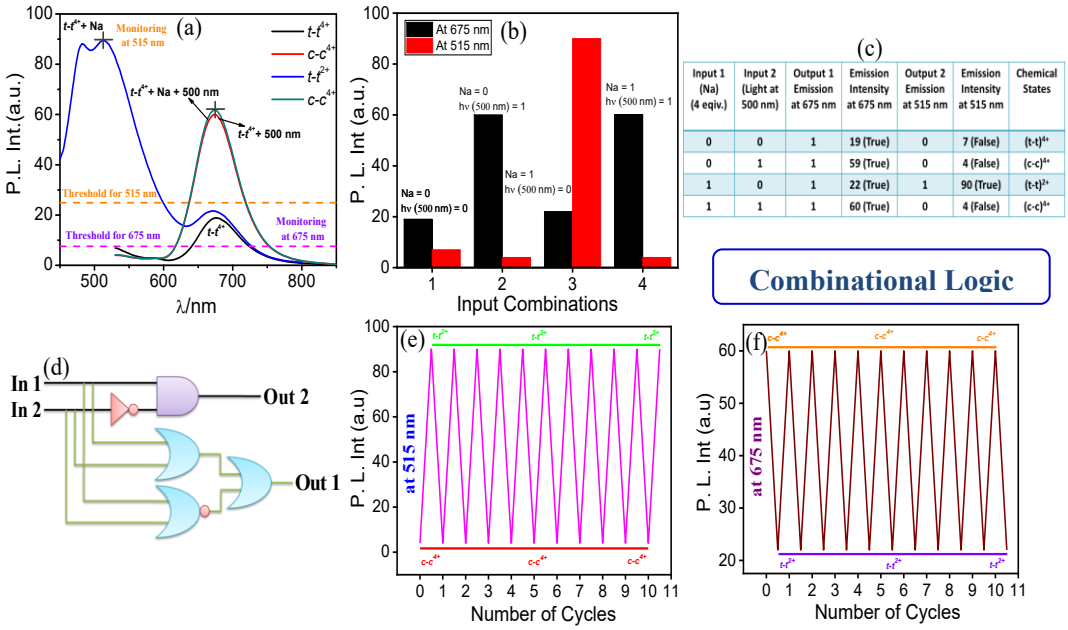

Input 1 (Na) (4 eqiv.)	Input 2 (Light at 500 nm)	Output 1 Emission at 675 nm	Emission Intensity at 675 nm	Output 2 Emission at 515 nm	Emission Intensity at 515 nm	Chemical States
0	0	1	19 (True)	0	7 (False)	$(t\text{-}t)^{4+}$
0	1	1	59 (True)	0	4 (False)	$(c\text{-}c)^{4+}$
1	0	1	22 (True)	1	90 (True)	$(t\text{-}t)^{2+}$
1	1	1	60 (True)	0	4 (False)	$(c\text{-}c)^{4+}$

Figure 5.6. (a) The emission spectral change of $\mathbf{1}^{4+}$(*t*-*t*) in the presence of Na and photon of 500 nm. (b) Histogram of emission intensities. (c) Corresponding truth table for the combinational logic. (d) Circuit diagram of the 2-input 2-output logic function. (e and f) Change in the emission intensity of $\mathbf{1}^{4+}$(*t*-*t*) at 675 and 515 nm in presence of the inputs (up to ten cycles).

5.6c clarifies that only in the presence of input 1, a strong emission intensity is detected, surpassing the threshold barrier at both outputs, representing the "ON" state. Conversely, the other two potential input combinations result in "ON" states at output 1 but fail to produce sufficient emission intensities at output 2 to overcome the threshold barrier, indicating the "OFF" state of the system. By analyzing the emission spectral behavior of complex 1^{4+}(*t-t*) under various input influences, we can effectively emulate the function of a 2-input 2-output combinatorial logic system (Figure 5.6d). Additionally, this process could be repeated up to ten times without appreciable loss of the emission intensity at both 675 and 515 nm (Figures 5.6e and 5.6f).

5.3.5. 3-Input 2-Output Combinational Logic System. The intricacy of complex 3-input 2-output combinational logic system refers to the multifaceted challenges encountered in their design, analysis, and implementation. With three input and two output variables, this system presents a maze of possibilities in input combinations and output states. Our investigation revolves around harnessing the emission spectral intensities of complex $\mathbf{1}^{4+}$(*t-t*) at specific wavelengths: 675 nm as output 1 and 515 nm as output 2, when subjected to inputs of Ce^{4+}, Na, and photon of 500 nm (Figure 5.7a). In presence or

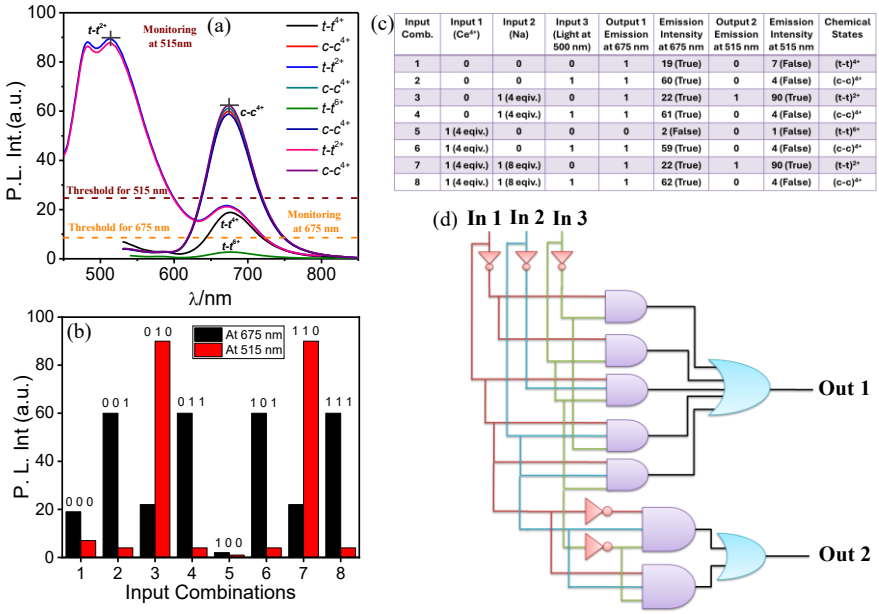

Input Comb.	Input 1 (Ce^{4+})	Input 2 (Na)	Input 3 (Light at 500 nm)	Output 1 Emission at 675 nm	Emission Intensity at 675 nm	Output 2 Emission at 515 nm	Emission Intensity at 515 nm	Chemical States
1	0	0	0	1	19 (True)	0	7 (False)	(t-t)$^{4+}$
2	0	0	1	1	60 (True)	0	4 (False)	(c-c)$^{4+}$
3	0	1 (4 eqiv.)	0	1	22 (True)	1	90 (True)	(t-t)$^{2+}$
4	0	1 (4 eqiv.)	1	1	61 (True)	0	4 (False)	(c-c)$^{4+}$
5	1 (4 eqiv.)	0	0	0	2 (False)	0	1 (False)	(t-t)$^{4+}$
6	1 (4 eqiv.)	0	1	1	59 (True)	0	4 (False)	(c-c)$^{4+}$
7	1 (4 eqiv.)	1 (8 eqiv.)	0	1	22 (True)	1	90 (True)	(t-t)$^{2+}$
8	1 (4 eqiv.)	1 (8 eqiv.)	1	1	62 (True)	0	4 (False)	(c-c)$^{4+}$

Figure 5.7. (a) The emission spectral change of $\mathbf{1}^{4+}$(*t-t*) in the presence of Ce^{4+}, Na and photon of 500 nm. (b) Histogram of emission intensities. (c) Corresponding truth table for the combinational logic. (d) Circuit diagram of the two 3-input 2-output combinational logic functions.

in absence of all the three inputs, an intense emission signal at 675 nm is observed above the threshold barrier, while no emission signal is detected at 515 nm, delineating the "ON" and "OFF" states of the system, respectively (Figure 5.7a). The elucidating truth table in Figure 5.7c reveals that only in the presence of input 1, we detect emission intensity failing to surpass the threshold barrier at both outputs, signifying the "OFF" state. Conversely, input combinations 3 and 7 yield emission intensities at both outputs sufficient to surpass the threshold barrier, indicating the "ON" states of the system (Figure 5.7c). Through meticulous analysis of the emission spectral behavior of complex $\mathbf{1}^{4+}$(*t-t*) under varied input influences, we adeptly replicate the function of a 3-input 2-output combinational logic system (Figure 5.7d).

5.3.6. Advancing Logical Decision-Making (*if-elif-else*) via Python Interpreter. The significance of Python over traditional Boolean logic lies in its ability to offer a more intuitive, versatile, and scalable approach to logical decision-making. Unlike Boolean logic gates, which are constrained by their fixed structure and limited functionality, Python provides a high-level programming language that allows for the creation of custom logical functions tailored to specific requirements. Python's expressive syntax and extensive standard library enable developers to implement complex logical operations with ease, accommodating multiple inputs and conditions seamlessly. Moreover, Python's dynamic typing and support for various data types enhance its flexibility, allowing for the manipulation of diverse data structures within logical expressions. Additionally, Python's popularity and widespread use in various fields, including scientific computing, data analysis, and artificial intelligence, make it a preferred choice for implementing logical decision-making algorithms. Overall, Python's versatility, readability, and extensive ecosystem make it a powerful tool for tackling complex logical problems with precision and efficiency, surpassing the limitations of traditional Boolean logic.

Herein, we have designed a Python model (with PyCharm IDE) called “logic_circuit” that emulates the behavior of a logic circuit, albeit with a twist: instead of traditional binary outputs, it produces chemical state outputs based on input conditions. In this model, four parameters, "Ce^{4+}", "Na", "500 nm light", and "270 nm light", are used to represent different conditions or signals within the system (Figure 5.8a). Each parameter can take binary values of either 0 or 1, reflecting the absence or presence of a particular signal or condition. This model is constructed using a series of ***if-elif-else*** statements to evaluate the input conditions against predefined criteria (Figures 5.8b and 5.8c). Depending on the combination of input values, the model generates specific chemical states as the

outputs, viz. "*t*-*t*$^{4+}$", "*c*-*c*$^{4+}$", "*t*-*t*$^{6+}$" or "*t*-*t*$^{2+}$". This model offers a novel approach to decision-making in chemical systems, providing a structured method to determine chemical states based on input conditions (Figure 5.8d). By integrating principles of logic circuits with chemical processes, this model opens up possibilities for exploring complex interactions and reactions in chemical systems.

(a)

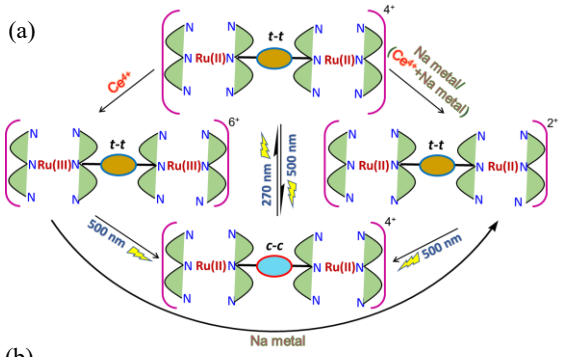

(b)

Input Comb.	Input 1 (Ce^{4+})	Input 2 (Na)	Input 3 (Light at 500 nm)	Input 4 (Light at 270 nm)	Output 1 (Emission at 675 nm)	Emission Intensity at 675 nm	Output 2 (Emission at 515 nm)	Emission Intensity at 515 nm	Chemical States
1	0	0	0	0	1	19 (True)	0	7 (False)	(t-t)$^{4+}$
2	0	0	0	1	1	19 (True)	0	7 (False)	(t-t)$^{4+}$
3	0	0	1	0	1	60 (True)	0	4 (False)	(c-c)$^{4+}$
4	0	0	1	1	1	19 (True)	0	7 (False)	(t-t)$^{4+}$
5	0	1 (4 eqiv.)	0	0	1	22 (True)	1	90 (True)	(t-t)$^{2+}$
6	0	1 (4 eqiv.)	0	1	1	60 (True)	0	4 (False)	(c-c)$^{4+}$
7	0	1 (4 eqiv.)	1	0	1	60 (True)	0	4 (False)	(c-c)$^{4+}$
8	0	1 (4 eqiv.)	1	1	1	19 (True)	0	7 (False)	(t-t)$^{4+}$
9	1 (4 eqiv.)	0	0	0	0	2 (False)	0	1 (False)	(t-t)$^{6+}$
10	1 (4 eqiv.)	0	0	1	1	60 (True)	0	4 (False)	(c-c)$^{4+}$
11	1 (4 eqiv.)	0	1	0	1	60 (True)	0	4 (False)	(c-c)$^{4+}$
12	1 (4 eqiv.)	0	1	1	1	19 (True)	0	7 (False)	(t-t)$^{4+}$
13	1 (4 eqiv.)	1 (8 eqiv.)	0	0	1	22 (True)	1	90 (True)	(t-t)$^{2+}$
14	1 (4 eqiv.)	1 (8 eqiv.)	0	1	1	60 (True)	0	4 (False)	(c-c)$^{4+}$
15	1 (4 eqiv.)	1 (8 eqiv.)	1	0	1	60 (True)	0	4 (False)	(c-c)$^{4+}$
16	1 (4 eqiv.)	1 (8 eqiv.)	1	1	1	19 (True)	0	7 (False)	(t-t)$^{4+}$

(c) **Python codes**

```
def logic_circuit(Ce4, Na, Light_500nm, Light_270nm):
    if Ce4 == 0 and Na == 0 and Light_500nm == 0 and Light_270nm == 0:
        return "tt4+"
    elif Ce4 == 0 and Na == 0 and Light_500nm == 0 and Light_270nm == 1:
        return "tt4+"
    elif Ce4 == 0 and Na == 0 and Light_500nm == 1 and Light_270nm == 0:
        return "cc4+"
    elif Ce4 == 0 and Na == 0 and Light_500nm == 1 and Light_270nm == 1:
        return "tt4+"
    elif Ce4 == 0 and Na == 1 and Light_500nm == 0 and Light_270nm == 0:
        return "tt2+"
    elif Ce4 == 0 and Na == 1 and Light_500nm == 0 and Light_270nm == 1:
        return "cc4+"
    elif Ce4 == 0 and Na == 1 and Light_500nm == 1 and Light_270nm == 0:
        return "cc4+"
    elif Ce4 == 0 and Na == 1 and Light_500nm == 1 and Light_270nm == 1:
        return "tt4+"
    elif Ce4 == 1 and Na == 0 and Light_500nm == 0 and Light_270nm == 0:
        return "tt6+"
    elif Ce4 == 1 and Na == 0 and Light_500nm == 0 and Light_270nm == 1:
        return "cc4+"
    elif Ce4 == 1 and Na == 0 and Light_500nm == 1 and Light_270nm == 0:
        return "cc4+"
    elif Ce4 == 1 and Na == 0 and Light_500nm == 1 and Light_270nm == 1:
        return "tt4+"
    elif Ce4 == 1 and Na == 1 and Light_500nm == 0 and Light_270nm == 0:
        return "tt2+"
    elif Ce4 == 1 and Na == 1 and Light_500nm == 0 and Light_270nm == 1:
        return "cc4+"
    elif Ce4 == 1 and Na == 1 and Light_500nm == 1 and Light_270nm == 0:
        return "cc4+"
    elif Ce4 == 1 and Na == 1 and Light_500nm == 1 and Light_270nm == 1:
        return "tt4+"
    else:
        return "Invalid input combination"

# Input values
Ce4 = int(input("Enter Ce4 value (0 or 1): "))
Na = int(input("Enter Na value (0 or 1): "))
Light_500nm = int(input("Enter Light_500nm value (0 or 1): "))
Light_270nm = int(input("Enter Light_270nm value (0 or 1): "))

# Get the chemical state outputs based on the input values
output = logic_circuit(Ce4, Na, Light_500nm, Light_270nm)

# Print the output
print("Output:", output)
```

(d) **Examples**

```
Enter Ce4 value (0 or 1): 0
Enter Na value (0 or 1): 0
Enter Light_500nm value (0 or 1): 0
Enter Light_270nm value (0 or 1): 0
Output: tt4+

Enter Ce4 value (0 or 1): 0
Enter Na value (0 or 1): 1
Enter Light_500nm value (0 or 1): 0
Enter Light_270nm value (0 or 1): 0
Output: tt2+

Enter Ce4 value (0 or 1): 1
Enter Na value (0 or 1): 0
Enter Light_500nm value (0 or 1): 0
Enter Light_270nm value (0 or 1): 0
Output: tt6+

Enter Ce4 value (0 or 1): 1
Enter Na value (0 or 1): 1
Enter Light_500nm value (0 or 1): 1
Enter Light_270nm value (0 or 1): 0
Output: cc4+
```

Figure 5.8. (a) Multi-step switching via oxidation-reduction and reversible *t*-*t*⇌*c*-*c* isomerization. (b) Truth table for this multi-step switching. (c) Python codes to define the multi-step switching. (d) Examples to show the model accuracy to detect the accurate chemical state.

5.4. Conclusions

In our ongoing pursuit of advancing smart molecular systems for information processing and computation at the molecular level, the research outlined in this article showcases the extraordinary versatility of a luminescent binuclear Ru(II) complex derived from a phenylene-vinylene-substituted terpyridyl ligand. Through reversible oxidation-reduction and *trans-cis* isomerization phenomena, the complex exhibits dynamic optical

properties that can be manipulated with precision. The ability to undergo emission switching with visible and UV light, along with multi-state switching facilitated by chemical oxidants and reductants, underscores its potential for molecular-level information processing and computation. By replicating fundamental IMPLICATION logic gate, as well as exploring intricate combinational logic systems (2-input 2-output and 3-input 2-output), this research opens new avenues in the field of molecular logic. Furthermore, the integration of Python's versatility in logical decision-making provides a scalable and intuitive approach to analyzing complex systems. The "logic_circuit" Python model, in particular, offers a structured method for determining chemical states based on input conditions, bridging the gap between logic circuits and chemical processes. In essence, this work highlights the potential of the luminescent binuclear Ru(II) complex as a versatile tool for molecular-level computation and logic operations. By unravelling the intricacies of its optical properties and logical functionalities, this research contributes to advancing the field of molecular logic, paving the way for future innovations in information processing at the molecular scale.

5.5. References

(1) de Silva, P. A.; Gunaratne, N. H. Q.; McCoy, C. P. A Molecular Photoionic AND Gate Based on Fluorescent Signalling. *Nature* **1993**, *364*, 42-44.

(2) de Silva, A. P.; McClenaghan, N. D. Molecular-Scale Logic Gates. *Chem. - Eur. J.* **2004**, *10*, 574-586.

(3) Ling, J.; Daly, B.; Silverson, V. A. D.; de Silva, A. P. Taking Baby Steps in Molecular Logic-Based Computation. *Chem. Commun.* **2015**, *51*, 8403-8409.

(4) Prasanna de Silva, A. Molecular Logic Gate Arrays. *Chem. - Asian J.* **2011**, *6*, 750-766.

(5) Conrad, M. Molecular Computing. *Adv. Comput.* **1990**, *31*, 235-324.

(6) Gentili, P. L. A Strategy to Face Complexity: The Development of Chemical Artificial Intelligence. In Advances in Artificial Life, Evolutionary Computation, and Systems Chemistry; Rossi, F., Piotto, S., Concilio, S., Eds.; Springer: Cham, Switzerland; New York, NY, USA.,2017; Vol. *708*, pp 151-160.

(7) Szaciłowski, K. Digital Information Processing in Molecular Systems. *Chem. Rev.* **2008**, *108*, 3481-3548.

(8) Szaciłowski, K. Molecular Logic Gates Based on Pentacyanoferrate Complexes: From Simple Gates to Three-Dimensional Logic Systems. *Chem.- Eur. J.* **2004**, *10*, 2520-2528.

(9) Szaciłowski, K.; Macyk, W.; Stochel, G. Light-Driven OR and XOR Programmable Chemical Logic Gates. *J. Am. Chem. Soc.* **2006**,*128*, 4550-4551.

(10) Adamatzky, A.; De Lacy Costello, B. P. Experimental Logical Gates in a Reaction-Diffusion Medium: The XOR Gate and Beyond. *Phys. Rev. E* **2002**, *66*, 046112.

(11) Adamatzky, A.; Tegelaar, M.; Wosten, H. A. B.; Powell, A. L.; Beasley, A. E.; Mayne, R. On Boolean Gates in Fungal Colony. *Biosystems* **2020**, *193-194*, 104138.

(12) Adamatzky, A.; Jones, J.; Mayne, R.; Tsuda, S.; Whiting, J. Logical Gates and Circuits Implemented in Slime Mould. *Adv. Physarum Mach.* **2016**, *21*, 37-74.

(13) Shu, Q.; Birlenbach, L.; Schmittel, M. A. Bis (Ferrocenyl)Phenanthroline Iridium(III) Complex as a Lab-on-a-Molecule for Cyanide and Fluoride in Aqueous Solution. *Inorg. Chem.* **2012**, *51*,13123-13127.

(14) Schmittel, M.; Qinghai, S. A Lab-on-a-Molecule for Anions in Aqueous Solution: Using Kolbe Electrolysis and Radical Methylation at Iridium for Sensing. *Chem. Commun.* **2012**, *48*, 2707-2709.

(15) Gentili, P. L. Boolean and Fuzzy Logic Gates Based on the Interaction of Flindersine with Bovine Serum Albumin and Tryptophan. *J. Phys. Chem. A* **2008**, *112*, 11992-11997.

(16) Gentili, P. L. The Fundamental Fuzzy Logic Operators and Some Complex Boolean Logic Circuits Implemented by the Chromogenism of a Spirooxazine. *Phys. Chem. Chem. Phys.* **2011**,*13*, 20335-20344.

(17) Gentili, P. L.; Giubila, M. S.; Heron, B. M. Processing Binary and Fuzzy Logic by Chaotic Time Series Generated by a Hydrodynamic Photochemical Oscillator. *ChemPhysChem* **2017**, *18*, 1831-1841.

(18) Cui, B. B.; Tang, J. H.; Yao, J.; Zhong, Y. W. A Molecular Platform for Multistate Near-Infrared Electrochromism and Flip-Flop, Flip-Flap-Flop, and Ternary Memory. *Angew. Chem., Int. Ed.* **2015**, *54*, 9192-9197.

(19) Mukherjee, S.; Sahoo, A.; Deb, S.; Baitalik, S. Light and Cation-Driven Optical Switch Based on a Stilbene-Appended Terpyridine System for the Design of Molecular-Scale Logic Devices. *J. Phys.Chem. A* **2021**, *125*, 8261-8273.

(20) Mardanya, S.; Mondal, D.; Karmakar, S.; Baitalik, S. Smart Ruthenium and Osmium Complexes Mimic the Complicated Functions of Traffic Signal and Memory Device. *Sens. Actuators, B* **2017**, *239*, 635-641.

(21) Pyne, A.; Layek, S.; Patra, A.; Sarkar, N. An Easy and Smart Way to Explore the Light-Emitting Responses of Carbon Dot and Doxorubicin Hydrochloride Assembly: White Light Generation and pH-Dependent Reversible Photoswitching. *J. Mater. Chem. C* **2019**, *7*, 6414-6425.

(22) Strack, G.; Ornatska, M.; Pita, M.; Katz, E. Biocomputing Security System: Concatenated Enzyme-Based Logic Gates Operating as a Biomolecular Keypad Lock. *J. Am. Chem. Soc.* **2008**, *130*, 4234-4235.

(23) Ali, M.; Mafe, S.; Ramirez, P.; Neumann, R.; Ensinger, W. Logic Gates Using Nanofluidic Diodes Based on Conical Nanopores Functionalized with Polyprotic Acid Chains. *Langmuir* **2009**, *25*,11993-11997.

(24) Macdonald, J.; Li, Y.; Sutovic, M.; Lederman, H.; Pendri, K.; Lu, W.; Andrews, B. L.; Stefanovic, D.; Stojanovic, M. N. Medium Scale Integration of Molecular Logic Gates in an Automaton. *NanoLett.* **2006**, *6*, 2598-2603.

(25) Schmittel, M.; Mal, P.; de los Rios, A. Multiport Logic Operations Triggered by Protonation-A Tris-Phenanthroline as a 3-Input AND-NOR-OR Circuit. *Chem. Commun.* **2010**, *46*, 2031-2033.

(26) Chen, K.; Schmittel, M. An Iridium(III) Complex as a Versatile Platform for Molecular Logic Gates: An Integrated Full Subtractor and 1:2 Demultiplexer. *Anal. Bioanal. Chem.* **2016**, *408*, 7077-7083.

(27) Biswas, P. K.; Saha, S.; Gaikwad, S.; Schmittel, M. Reversible Multicomponent AND Gate Triggered by Stoichiometric Chemical Pulses Commands the Self-Assembly and Actuation of Catalytic Machinery. *J. Am. Chem. Soc.* **2020**, *142*, 7889-7897.

(28) Mondal, D.; Bar, M.; Maity, D.; Baitalik, S. Anthraimidazole-dione-Terpyridine-Based Optical Chemosensor for Anions and Cations that Works as Molecular Half Subtractor, Key-Pad Lock, and Memory Device. *J. Phys. Chem. C* **2015**, *119*, 25429-25441.

(29) Pan, Y.; Shi, Y.; Chen, Z.; Chen, J.; Hou, M.; Chen, Z.; Li, C.-W.; Yi, C. Design of Multiple Logic Gates Based on Chemically Triggered Fluorescence Switching of Functionalized Polyethylenimine. *ACS Appl. Mater. Interfaces* **2016**, *8*, 9472-9482.

(30) Resta, G. V.; Balaji, Y.; Lin, D.; Radu, I. P.; Catthoor, F.; Gaillardon, P. E.; De Micheli, G. Doping-Free Complementary Logic Gates Enabled by Two-Dimensional Polarity-Controllable Transistors. *ACS Nano* **2018**, *12*, 7039-7047.

(31) Paul, P.; Karar, M.; Mallick, A.; Majumdar, T. A Photonic Multifunctional Moleculator Powered by Two-Step Energy Transfer. *J. Mater. Chem. C* **2021**, *9*, 11229-11241.

(32) Zhou, X.-S.; Fan, R.-Q.; Ye, H.-X.; Xing, K.; Wang, A.-N.; Wang, P.; Hao, S.-E.; Yang, Y.-L. A Dual Associated-Functional Fluorescent Switch: From Alternate Detection Cycle for Fe(III) and pH to Molecular Logic Operations. *Inorg. Chem.* **2019**, *58*, 2122-2132.

(33) Mardanya, S.; Karmakar, S.; Das, S.; Baitalik, S. Anion and Cation Triggered Modulation of Optical Properties of a Pyridyl-Imidazole Receptor Rigidly Linked to Pyrene and Construction of INHIBIT, OR and XOR Molecular Logic Gates: A Combined Experimental and DFT/TD-DFT Investigation. *Sens. Actuators, B* **2015**, *206*, 701-713.

(34) Karmakar, S.; Mardanya, S.; Maity, D.; Baitalik, S. Polypyridyl-Imidazole Based Os(II) Complex as Optical Chemosensor for Anions and Cations and Multi-Readout Molecular Logic Gates and Memory Device: Experimental and DFT/TDDFT Study. *Sens. Actuators, B* **2016**, *226*, 388-402.

(35) Sahoo, A.; Ahmed, T.; Deb, S.; Baitalik, S. Neuro-Fuzzification Architecture for Modeling of Electrochemical Ion-Sensing Data of Imidazole-Dicarboxylate-Based Ru(II)-Bipyridine Complex. *Inorg. Chem.* **2022**, *61*, 10242-10254.

(36) Sahoo, A.; Bhattacharya, S.; Jana, S.; Baitalik, S. Neural Network and Decision Tree-Based Machine Learning Tools to Analyse the Anion-Responsive Behaviours of Emissive Ru(II)-Terpyridine Complexes. *Dalton Trans.* **2023**, *52*, 97-108.

(37) Juris, A.; Balzani, V.; Barigelletti, F.; Campagna, S.; Belser, P.; von Zelewsky, A. Ru(II) Polypyridine Complexes: Photophysics, Photochemistry, Eletrochemistry, and Chemiluminescence. *Coord. Chem. Rev.* **1988**, *84*, 85-277.

(38) Balzani, V.; Juris, A.; Venturi, M.; Campagna, S.; Serroni, S. Luminescent and Redox-Active Polynuclear Transition Metal Complexes. *Chem. Rev.* **1996**, *96*, 759-834.

(39) Sauvage, J.-P.; Collin, J. P. J.; Chambron, C.; Guillerez, S.; Coudret, C.; Balzani, V.; Barigelletti, F.; de Cola, L.; Flamigni, L. Ruthenium(II) and Osmium(II) Bis(Terpyridine) Complexes in Covalently-Linked Multicomponent Systems: Synthesis, Electrochemical Behavior, Absorption Spectra, and Photochemical and Photophysical Properties. *Chem. Rev.* **1994**, *94*, 993-1019.

(40) Browne, W. R.; O'Boyle, N. M.; McGarvey, J. J.; Vos, J. G. Elucidating Excited State Electronic Structure and Intercomponent Interactions in Multicomponent and Supramolecular Systems. *Chem. Soc. Rev.* **2005**, *34*, 641-663.

(41) Steinke, S. J.; Gupta, S.; Piechota, E. J.; Moore, C. E.; Kodanko, J. J.; Turro, C. Photocytotoxicity and Photoinduced Phosphine Ligand Exchange in a Ru(II) Polypyridyl Complex. *Chem. Sci.* **2022**, *13* (7), 1933-1945.

(42) Li, A.; Turro, C.; Kodanko, J. J. Ru (II) Polypyridyl Complexes Derived from Tetradentate Ancillary Ligands for Effective Photocaging. *Acc. Chem. Res.* **2018**, *51* (6), 1415-1421.

(43) Knoll, J. D.; Turro, C. Control and Utilization of Ruthenium and Rhodium Metal Complex Excited States for Photoactivated Cancer Therapy. *Coord. Chem. Rev.* **2015**, *282-283*, 110-126.

(44) Maity, D.; Bhaumik, C.; Mardanya, S.; Karmakar, S.; Baitalik, S. Light Harvesting and Directional Energy Transfer in Long-Lived Homo- and Heterotrimetallic Complexes of Fe^{II}, Ru^{II}, and Os^{II}. *Chem.- Eur. J.* **2014**, *20*, 13242-13252.

(45) Das, S.; Saha, D.; Karmakar, S.; Baitalik, S. Effect of pH on the Photophysical and Redox Properties of a Ruthenium(II) Mixed Chelate Derived from Imidazole-4,5-

dicarboxylic Acid and 2,2′-Bipyridine: An Experimental and Theoretical Investigation. *J. Phys. Chem. A* **2012**, *116*, 5216-5226.

(46) Mondal, D.; Biswas, S.; Paul, A.; Baitalik, S. Luminescent Dinuclear Ruthenium Terpyridine Complexes with a Bis-Phenyl-benzimidazole Spacer. *Inorg. Chem.* **2017**, *56*, 7624-7641.

(47) Das, S.; Bar, M.; Ganguly, T.; Baitalik, S. Control of Photoisomerization Kinetics via Multistage Switching in Bimetallic Ru(II)-Terpyridine Complexes. *Inorg. Chem.* **2024**, *63*, 6600-6615.

(48) Bandara, H. M. D.; Burdette, S. C. Photoisomerization in Different Classes of Azobenzene. *Chem. Soc. Rev.* **2012**, *41* (5), 1809-1825.

(49) Kurihara, M.; Nishihara, H. Azo- and Quinone-Conjugated Redox Complexes-Photo- and Proton-Coupled Intramolecular Reactions Based On d-π Interaction. *Coord. Chem. Rev.* **2002**, *226*,125-135.

(50) Yutaka, T.; Mori, I.; Kurihara, M.; Mizutani, J.; Tamai, N.; Kawai, T.; Irie, M.; Nishihara, H. Photoluminescence Switching of Azobenzene-Conjugated Pt(II) Terpyridine Complexes by Trans-Cis Photoisomerization. *Inorg. Chem.* **2002**, *41*, 7143-7150.

(51) Yutaka, T.; Kurihara, M.; Kubo, K.; Nishihara, H. Novel Photoisomerization Behavior of Rh Binuclear Complexes Involving an Azobenzene-Bridged Bis(Terpyridine) Ligand. Strong Effects of Counter-Ion and Solvent and the Induction of Redox Potential Shift. *Inorg. Chem.* **2000**, *39*, 3438-3439.

(52) Yutaka, T.; Mori, I.; Kurihara, M.; Mizutani, J.; Kubo, K.; Furusho, S.; Matsumura, K.; Tamai, N.; Nishihara, H. Synthesis, Characterization, and Photochemical Properties of Azobenzene-Conjugated Ru(II) and Rh(III) Bis(Terpyridine) Complexes. *Inorg. Chem.* **2001**, *40*, 4986-4995.

(53) Waldeck, D. H. Photoisomerization Dynamics of Stilbenes. *Chem. Rev.* **1991**, *91*, 415-436.

(54) Pal, P.; Ganguly, T.; Sahoo, A.; Baitalik, S. Emission Switching in the Near-Infrared by Reversible Trans-Cis Photoisomerization of Styrylbenzene-Conjugated Osmium Terpyridine Complexes. *Inorg. Chem.* **2021**, *60*, 4869-4882.

(55) Pal, P.; Mukherjee, S.; Maity, D.; Baitalik, S. Synthesis, Structural Characterization, and Luminescence Switching of Diarylethene-Conjugated Ru(II)-Terpyridine Complexes by Trans-Cis Photoisomerization: Experimental and DFT/TD-DFT Investigation. *Inorg. Chem.* **2018**, *57*, 5743-5753.

(56) Zanoni, K. P. S.; Murakami Iha, N. Y. Reversible Trans ⇌ Cis Photoisomerizations of $[Re(CO)_3(Ph_2phen)(StpyCN)]^+$ Towards Molecular Machines. *Dalton Trans.* **2017**, *46* (30), 9951-9958.

(57) Matos, L. S.; Amaral, R. C.; Murakami Iha, N. Y. Visible Photosensitization of Trans-Styrylpyridine Coordinated to fac-$[Re\text{-}(CO)_3(Dcbh_2)]^+$: New Insights. *Inorg. Chem.* **2018**, *57* (15), 9316-9326.

(58) Ko, C.-C.; Kwok, W.-M.; Yam, V. W.-W.; Phillips, D. L. Triplet MLCT Photosensitization of the Ring-Closing Reaction of Diarylethenes by Design and Synthesis of a Photochromic Rhenium(I) Complex of a Diarylethene-Containing 1,10-Phenanthroline Ligand. *Chem. - Eur. J.* **2006**, *12*, 5840-5848.

(59) Omana, M.; Papasso, G.; Rossi, D.; Metra, C. A Model for Transient Fault Propagation in Combinatorial Logic. In *9th IEEE On-Line Testing Symposium*; IEEE, 2003; pp 111-115.

(60) Zhang, Y.; Liu, W.; Zhang, W.; Yu, S.; Yue, X.; Zhu, W.; Zhang, D.; Wang, Y.; Wang, J. DNA-Mediated Gold Nanoparticle Signal Transducers for Combinatorial Logic Operations and Heavy Metal Ions Sensing. *Biosens. Bioelectron.* **2015**, *72*, 218-224.

(61) Goldsworthy, V.; LaForce, G.; Abels, S.; Khisamutdinov, E. F. Fluorogenic RNA Aptamers: A Nano-Platform for Fabrication of Simple and Combinatorial Logic Gates. *Nanomaterials* **2018**, *8*, 984.

(62) Magri, D. C.; Spiteri, J. C. Proof of Principle of a Three-Input AND-INHIBIT-OR Combinatorial Logic Gate Array. *Org. Biomol. Chem.* **2017**, *15*, 6706-6709.

(63) Privman, M.; Tam, T. K.; Pita, M.; Katz, E. Switchable Electrode Controlled by Enzyme Logic Network System: Approaching Physiologically Regulated Bioelectronics. *J. Am. Chem. Soc.* **2009**,*131* (3), 1314-1321.

(64) Pu, F.; Ren, J.; Qu, X. Plug and Play" Logic Gates Based on Fluorescence Switching Regulated by Self-Assembly of Nucleotide and Lanthanide Ions. *ACS Appl. Mater. Interfaces* **2014**, *6* (12), 9557-9562.

(65) Barnoy, E. A.; Motiei, M.; Tzror, C.; Rahimipour, S.; Popovtzer, R.; Fixler, D. Biological Logic Gate Using Gold Nanoparticles and Fluorescence Lifetime Imaging Microscopy. *ACS Appl. Nano Mater.* **2019**, *2* (10), 6527-6536.

(66) Lian, W.; Yu, X.; Wang, L.; Liu, H. Biomacromolecular Logic Devices Based on Simultaneous Electrocatalytic and Electrochemiluminescence Responses of

Ru(bpy)$_3^{2+}$ at Molecularly Imprinted Polymer Film Electrodes. *J. Phys. Chem. C* **2015**, *119* (34), 20003-20010.

(67) Barente, A. S.; Villén, J. A Python Package for the Localization of Protein Modifications in Mass Spectrometry Data. *J. Proteome Res.* **2023**, *22* (2), 501-507.

(68) Abdul Kadhar, K. M.; Anand, G. Basics of Python Programming. In Data Science with Raspberry Pi: Real-Time Applications Using a Localized Cloud; AIMS Press, 2021; pp 13-47.

(69) van Staveren, M. Integrating Python into a Physical Chemistry Lab. *J. Chem. Educ.* **2022**, *99* (7), 2604-2609.

(70) Janet, J. P.; Liu, F.; Nandy, A.; Duan, C.; Yang, T.; Lin, S.; Kulik, H. J. Designing in the Face of Uncertainty: Exploiting Electronic Structure and Machine Learning Models for Discovery in Inorganic Chemistry. *Inorg. Chem.* **2019**, *58* (16), 10592-10606.

(71) Gugler, S.; Janet, J. P.; Kulik, H. J. Enumeration of de Novo Inorganic Complexes for Chemical Discovery and Machine Learning. *Mol. Syst. Des. Eng.* **2020**, *5* (1), 139-152.

(72) Qiu, J.; Moeller, A.; Zhen, J.; Yang, H.; Din, L.; Adelstein, N. Teaching Heterogeneous Electrocatalytic Water Oxidation with Nickel-and Cobalt-Based Catalysts Using Cyclic Voltammetry and Python Simulation. *J. Chem. Educ.* **2023**, *100* (8), 3036-3043.

(73) Ong, S. P.; Richards, W. D.; Jain, A.; Hautier, G.; Kocher, M.; Cholia, S.; Gunter, D.; Chevrier, V. L.; Persson, K. A.; Ceder, G. Python Materials Genomics (Pymatgen): A Robust, Open-Source Python Library for Materials Analysis. *Comput. Mater. Sci.* **2013**, *68*, 314-319.

(74) Turcani, L.; Tarzia, A.; Szczypiński, F. T.; Jelfs, K. E. stk: An Extendable Python Framework for Automated Molecular and Supramolecular Structure Assembly and Discovery. *J. Chem. Phys.* **2021**, *154* (21), 214102.

(75) Bhattacharya, S.; Sahoo, A.; Baitalik, S. Human Brain-Inspired Chemical Artificial Intelligence Tools for the Analysis and Prediction of the Anion-Sensing Characteristics of an Imidazole-Based Luminescent Os(II)-Bipyridine Complex. *Dalton Trans.* **2023**, *52* (20), 6749-6762.

(76) Sahoo, A.; Deb, S.; Das, S.; Baitalik, S. Multi-Channel Anion and Cation Sensing Conduct of a Terpyridyl-Imidazole Receptor: Experimental Demonstration and

Implication of Artificial Intelligence Tools for Analysis and Data Prediction. *Dyes Pigm.* **2023**, *218*, 111425.

(77) Yang, W.-W.; Zhong, Y.-W.; Yoshikawa, S.; Shao, J.-Y.; Masaoka, S.; Sakai, K.; Yao, J.; Haga, M.-A. Tuning of Redox Potentials by Introducing a Cyclometalated Bond to Bis-tridentate Ruthenium(II) Complexes Bearing Bis(N-methylbenzimidazolyl)-benzene or -pyridine Ligands. *Inorg. Chem.* **2012**, *51*, 890-899.

(78) Berger, R. M.; McMillin, D. R. Localized States in Reduced and Excited-State Ruthenium(II) Terpyridyls. *Inorg. Chem.* **1988**, *27*, 4245-4249.

Chapter 6

Multistimuli-Responsive Molecular Photoswitches Based on Bimetallic Ru(II) and Os(II) Terpyridine Complexes

6.1. Introduction

Stimuli-responsive luminescent materials that exhibit emission switching in response to external stimuli are crucial for their potential practical applications in optoelectronics, including sensors, memory devices, and molecular photoswitches.[1-12] Multistimuli-responsive materials could be activated by various external triggers, enabling them for more precise and adaptable functionality, over their single-stimuli responsive counterparts. Hence, these substances often offer greater control and tunability relative to single-stimuli responsive materials in molecular photoswitches. Such beneficial aspects of multi-stimuli responsive materials escalate stability, reversibility, and their applicability in complex environments, making them superior building blocks for the fabrication of advanced smart materials and molecular devices.[13-17] Light is the most essential and important stimulus for constructing molecular photoswitches, which provides high spatiotemporal precision and serves as a clean, environmentally benign energy source, making it well-suited for sustainable technologies and applications.[18,19] Organic molecules have been widely employed in designing and developing multi-stimuli responsive photoswitches.[20-22] Despite offering advantages of tunable structures, organic chromophores often encounter challenges such as susceptibility to photobleaching and limited Stokes shifts.[23] To address these limitations, transition metal complexes have emerged as a promising alternative for designing efficient molecular photoswitches.[24-28] The coordination of suitable transition metal ions with appropriate organic ligands facilitates the formation of rigid molecular frameworks with distinct geometries and desirable properties.[29-39] Furthermore, the physicochemical characteristics of these metal-ligand assemblies can be precisely modulated in response to various external stimuli for enhancing their functional versatility.[1,40-47] Among various transition metals, Ru(II)- and Os(II)-based coordination complexes have emerged as promising building blocks for the development of efficient molecular photoswitches.[48-56] Their exceptional photophysical and optoelectronic properties, primarily arising from metal-to-ligand charge transfer (MLCT) excited states, make them highly suitable for advanced applications in this field. To design efficient molecular photoswitches, the isomerization behavior of various Ru(II)-polypyridine complexes incorporating azo and stilbene moieties have been extensively studied.[5,28,57-68] However, systems utilizing terpyridine-based coordination frameworks in conjunction with stilbene units remain relatively less explored compared to their bipyridine-based analogs, featuring either stilbene or azo functionalities.[59-61,65] Most of

these complexes exhibit absorption and emission at relatively short wavelengths, with the MLCT absorption typically arising below 500 nm. This spectral limitation significantly restricts the applicability of these photoswitches in biological systems. Moreover, the small energy gap among the ^{3}MLCT and ^{3}MC states in the terpyridine complexes of Ru(II) often results in short excited-state lifetimes, thereby restricting their utility in molecular photoswitches.[69,70] To overcome these shortcomings, ligands with extended π-conjugation could be judiciously incorporated into the molecular framework. Additionally, upon replacing Ru(II) by Os(II), the absorption and emission spectral window of the resulting complexes could be extended to NIR region, by taking advantage of stronger spin-orbit coupling efficacy of heavier osmium metal.[71-78] In pursuit of making efficient molecular switches with extended spectral range, the photoisomerization behavior of various Ru(II)- and Os(II)-terpyridine complexes functionalized with one or more stilbene units have been widely researched by our group.[54,55,64,68,79-81] Nevertheless, most of these systems exhibit emission switching exclusively in response to light stimuli. In practice, the response of such systems to multiple stimuli has largely been unexplored hitherto. To address this knowledge gap, the present study aims to develop multi-stimuli-responsive molecular photoswitches with an expanded spectral coverage upon strategic selection of appropriate ligands and metals.

Herein, we have synthesized and thoroughly characterized two dimeric Ru(II)- and Os(II)-terpyridine complexes incorporating active methylene group, phosphonium motifs, and stilbene units (Chart 6.1). Prior to this work, our group[82,83] as well as the group of Amitava Das[84] reported mononuclear Ru(II) and Os(II)-terpyridine complexes incorporating one or two -$CH_2PPh_3^+$ motif(s). In all these earlier investigations, the primary focus was to elucidate the anion-responsive behavior of the complexes via multiple optical tools. In contrast, the present work deals with two symmetrical dinuclear Ru(II) and Os(II) terpyridine complexes based on two phenylene-vinylene linkers and tpy-$PhCH_2PPh_3Br$ unit as the capping ligand. A central objective of this study is to explore the multi-stimuli-responsive photo-redox behavior of these complexes. The capping ligands continue to provide anion-responsive functionality, while the phenylene-vinylene units in the bridge introduce photo-responsive behavior in the resulting complexes. Further modulation of the physicochemical characteristics could be achieved via oxidation and reduction of the complexes followed by photoisomerization of the respective species. Thus, it is quite expected that the present complexes would offer a versatile platform for modulating as well

as switching of their photo-redox behavior under the influence of multiple stimuli, viz. anion, oxidant, reductant as well as light of appropriate wavelengths in a sequential manner.

[(tpy-PhCH$_2$PPh$_3^{+}$Br^{-})$_2$Ru$_2$(tpvpvpt)](PF$_6$)$_4$ (1)

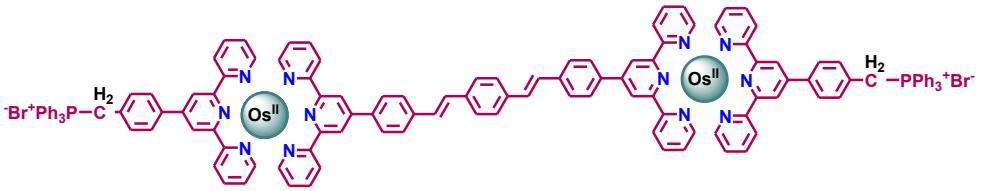

[(tpy-PhCH$_2$PPh$_3^{+}$Br^{-})$_2$Os$_2$(tpvpvpt)](PF$_6$)$_4$ (2)

Chart 6.1. Molecular Frameworks of the Complexes in this Study.

6.2. Experimental Section

6.2.1. Materials. The bridging terpyridyl ligand (tpvpvpt) as well as the capping ligand (tpy-PhCH$_2$PPh$_3$Br) and its Ru(II) and Os(II) precursors are synthesized by following the literature procedures.[85-88]

6.2.2. Synthesis of the Metal Complexes. Both the complexes are prepared by undertaking a general synthetic procedure which is discussed below.

[(tpy-PhCH$_2$PPh$_3$Br)Ru(tpvpvpt)Ru(tpy-PhCH$_2$PPh$_3$Br)](PF$_6$)$_4$ (1). A mixture of tpvpvpt (0.10 g, 0.13 mmol) and (tpy-PhCH$_2$PPh$_3$Br)RuCl$_3$ (0.25 g, 0.3 mmol) in 5 mL of ethylene glycol was heated at 180 ºC with stirring for 12 h under N$_2$ atmosphere when a reddish-brown solution was formed. After cooling, the solution was poured to NH$_4$PF$_6$ (1.5 g in 5 mL of water) and stirred for few minutes, when a reddish-brown colored precipitate appeared. The compound was filtered and purified by silica gel column chromatography using MeCN as the eluent. Upon rotary evaporation of the eluent to a small volume (~10 mL), a micro crystalline complex was formed which was filtered and recrystallized from MeCN-MeOH (1:5, v/v) mixture. Yield: 0.23 g (62 %). Anal. Calcd for C$_{132}$H$_{98}$N$_{12}$Br$_2$Ru$_2$P$_6$F$_{24}$: C, 55.51; H, 3.46; N, 5.88. Found: C, 55.53; H, 3.45; N, 5.84. ^{1}H NMR (400 MHz, CD$_3$CN) δ/ppm 9.09 (s, 4H, 4H$_{3'''}$), 8.96 (s, 4H, 4H$_{3''}$), 8.71 (d, J = 8.3 Hz, 4H, 4H$_{6'}$), 8.65 (d, J = 8.5 Hz, 4H, 4H$_6$), 8.30 (d, J = 8.3 Hz, 4H, 4H$_{7'}$), 8.07 (d, J = 7.5 Hz, 4H, 4H$_7$), 8.04-7.94 (m, 18H, 4H$_4$+4H$_{4'}$+4H$_{13}$+4H$_{15}$+2H$_{20}$), 7.82-7.77 (m, 16H, 4H$_{14}$+4H$_{16}$+4H$_{17}$+4H$_{18}$), 7.74-7.69 (m, 12H, 4H$_{11}$+4H$_{19}$+2H$_9$+2H$_{10}$), 7.53 (d, J = 6.8 Hz,

4H, $4H_{3'}$), 7.49 (d, J = 5.4 Hz, 4H, $4H_{8'}$), 7.43 (d, J = 5.6 Hz, 4H, $4H_3$), 7.34 (d, J = 6.5 Hz, 4H, $4H_8$), 7.22 (q, J = 7.0 Hz, 8H, $4H_5$+$4H_{5'}$), 4.88 (d, J = 16.0 Hz, 4H, $4H_{12}$). High resolution mass spectrometry (HRMS) (positive, MeCN) *m/z*=352.7672 (100%) [(tpy-$PhCH_2PPh_3$)$_2Ru_2$(tpvpvpt)]$^{6+}$, *m/z*=423.5817 (60%) [(tpy-$PhCHPPh_3$)Ru(tpvpvpt)Ru(tpy-$PhCH_2PPh_3$)]$^{5+}$, *m/z*=529.1445 (22%) [(tpy-$PhCHPPh_3$)$_2Ru_2$(tpvpvpt)]$^{4+}$.

[(tpy-$PhCH_2PPh_3Br$)Os(tpvpvpt)Os(tpy-$PhCH_2PPh_3Br$)]$(PF_6)_4$ (2). A mixture of tpvpvpt (0.10 g, 0.13 mmol) and (tpy-$PhCH_2PPh_3Br$)$OsCl_3$ (0.28 g, 0.3 mmol) was refluxed in 5 mL ethylene glycol at 180 ºC for 12 h. Then similar procedure was followed for purification and recrystallization of the complex. Yield: 0.27 g (68 %). Anal. Calcd for $C_{132}H_{98}N_{12}Br_2Os_2P_6F_{24}$: C, 52.25; H, 3.25; N, 5.54. Found: C, 52.23; H, 3.28; N, 5.52. ^{1}H NMR (400 MHz, CD_3CN) δ/ppm 9.11 (s, 4H, $4H_{3''}$), 8.97 (s, 4H, $4H_{3'}$), 8.68 (d, J = 8.0 Hz, 4H, $4H_{6'}$), 8.63 (d, J = 8.3 Hz, 4H, $4H_6$), 8.26 (d, J = 7.9 Hz, 4H, $4H_{7'}$), 8.05-7.96 (m, 12H, $4H_7$+$4H_4$+$4H_{4'}$), 7.89-7.76 (m, 26H, $4H_{13}$+$4H_{14}$+$4H_{15}$+$4H_{16}$+$4H_{17}$+$4H_{18}$+$2H_{20}$), 7.74-7.69 (m, 12H, $4H_{8'}$+$2H_9$+$2H_{10}$+$4H_{19}$), 7.52 (s, 4H, $4H_{11}$), 7.35 (t, J = 6.3 Hz, 8H, $4H_3$+$4H_{3'}$), 7.30 (d, J = 5.8 Hz, 4H, $4H_8$), 7.15 (q, J = 6.9 Hz, 8H, $4H_5$+$4H_{5'}$), 4.88 (d, J = 16.0 Hz, 4H, $4H_{12}$). High resolution mass spectrometry (HRMS) (positive, MeCN) *m/z*=382.4407 (98%) [(tpy-$PhCH_2PPh_3$)$_2Os_2$(tpvpvpt)]$^{6+}$, *m/z*=406.7200 (100%) [(tpy-$PhCH_3$)Os_2(tpvpvpt)(tpy-$PhCH_2PPh_3$)]$^{5+}$.

6.2.3. Instruments and Physical Methods. The details of different equipment used and experimental process to measure absorption and luminescence spectral behavior as well as *trans-cis* photoisomerization quantum yields have been discussed in chapters 2 and 3.

For absorption spectral studies, stock solutions of **1** and **2** (5.0×10^{-4} M) were prepared in dry and distilled acetonitrile and stored in dark. The stock solutions were then diluted to effective final concentration of 3.0×10^{-6} M for most of the spectroscopic studies. Stock solutions of the tetrabutylammonium (TBA) salts of F^-, Cl^-, Br^-, I^-, AcO^-, $H_2PO_4^-$, and HO^- (0.1 M in CH_3CN) were prepared and stored in cold and dark condition. For titrations, the stock solutions of the anions (particularly for F^-) were first diluted to 1.0×10^{-2} M and this solution was then added incrementally to a 2.5 mL solution of **1** and **2** (3.0×10^{-6} M in CH_3CN) by a micropipette and the corresponding spectra were recorded at room temperature. After completion of the titration experiments, the binding/equilibrium constants were evaluated from absorption/emission titration data using equation (1) at a specific wavelength.[89,90]

$$\Delta A = \frac{\Delta\varepsilon b([H]+[G]+(1/K)) \pm \sqrt{\Delta\varepsilon^2 b^2([H]+[G]+(1/K))^2 - 4\Delta\varepsilon^2 b^2[H][G]}}{2} \quad (1)$$

where ΔA is the change in absorbance, [H] and [G] is the concentration of metal complex and added anion, respectively. Δε is the change in molar extinction coefficient, b is the absorption path length, and *K* is the binding constant. Non-linear regression analysis of absorption/emission titration data as a function of anion concentration leads to the value of binding constants. Binding constants were performed in duplicate, and the average value is reported.

Luminescence quantum yields of the complexes are determined by a relative method via the equation (2)

$$\Phi_r = \Phi_{std} (A_{std}/A_r) (I_r/I_{std}) (\eta_r^2/\eta_{std}^2) \quad (2)$$

using $[Ru(bpy)_3]^{2+}$ and $[Os(bpy)_3]^{2+}$ as the standards for binuclear Ru(II) and Os(II) complex, respectively. The subscripts r and std refer to the unknown sample and the standard, respectively. Φ, I, A and η are the quantum yields, the integrated emission intensity, the absorbance at the excitation wavelength and the refractive index of the solvent, respectively. For $[Ru(bpy)_3]^{2+}$, Φ_{std}= 0.032 and for $[Os(bpy)_3]^{2+}$, Φ_{std}= 0.005, at RT in MeCN at λ_{ex}= 500 nm.

6.3. Results and Discussion

6.3.1. Synthesis and Characterization. The metal complexes are synthesized by refluxing tpvpvpt ligand with (tpy-$PhCH_2PPh_3Br$)$RuCl_3$ and (tpy-$PhCH_2PPh_3Br$)$OsCl_3$ in 1:2 molar ratio in ethylene glycol. The products obtained are purified by column chromatography and recrystallized in MeCN-MeOH mixture. The characterization of the complexes is carried out via ^{1}H NMR, mass spectrometry and elemental (C, H, and N) analyses and the corresponding data are already provided in section 6.2.

6.3.2. NMR Spectra. Both the complexes are characterized via ^{1}H NMR spectroscopy in CD_3CN solvent and the corresponding spectra are presented in Figure 6.1. The relatively simple spectral pattern for **1** and **2** reveals the symmetrical nature of the complexes. $H_{3''}$ and $H_{3'''}$ protons for both complexes appear as two sharp singlets in the most downfield region of ~9.11-8.96 ppm due to coordination of Ru(II) and Os(II) metals with terpyridine units. Upon comparing with the ^{1}H NMR spectra of our previously reported dinuclear Ru(II) complexes based on the same bridging ligand,[79] we surmise that the olefinic protons (H_9 and H_{10}) in the present complexes appear within the multiplets,

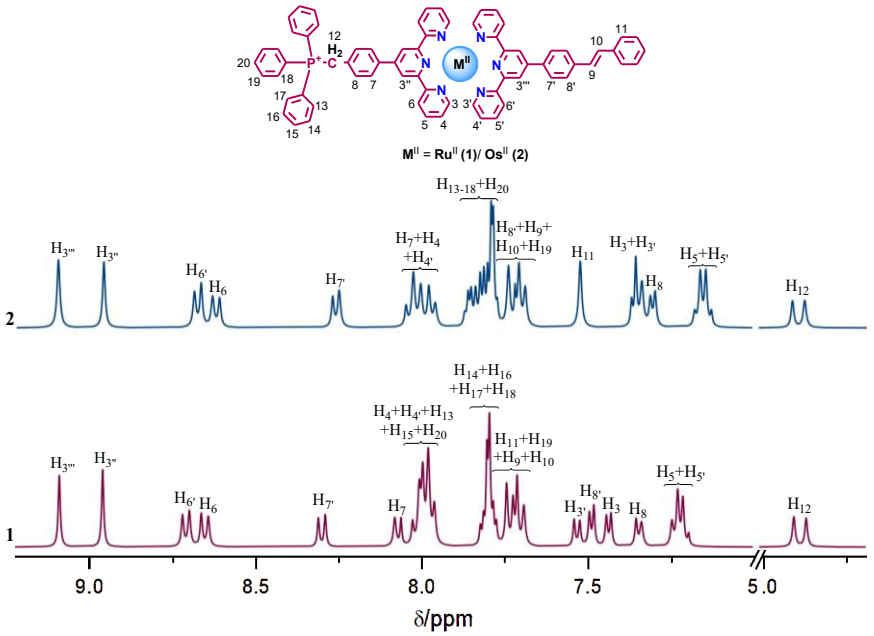

Figure 6.1. ^{1}H NMR spectra of **1** and **2** in CD_3CN.

spanning in the range between 7.82 and 7.70 ppm and the value of the coupling constant (*J*) for the said protons is approximated to be ~16 Hz. The observed findings correspond to *trans-trans* conformations of the complexes. The doublets at ~4.88 ppm, on the other hand, correspond to the methylene (-CH_2) protons present in both complexes.[82-84] Additionally, the protons associated with the phenyl rings in the -PPh_3 units appear as multiplets in the region of 8.05-7.65 ppm.

6.3.3. Mass Spectra. The high-resolution mass spectra (HRMS) of the complexes along with the isotopic distribution of the peaks and their corresponding simulations are portrayed in Figures 6.2 and 6.3. A strong correlation is observed between the experimental and simulated spectra. Complex **1** shows the most-abundant peak at *m/z*= 352.7672, separated by 0.16 Da, corresponds to the hexapositive cation [(tpy-$PhCH_2PPh_3$)$_2$$Ru_2$(tpvpvpt)]$^{6+}$. Two other less abundant peaks at *m/z*= 423.5187 and *m/z*= 529.1445, separated by 0.20 and 0.25 Da, are indicative of the presence of pentapositive and tetrapositive cations of the type [(tpy-$PhCHPPh_3$)Ru(tpvpvpt)Ru(tpy-$PhCH_2PPh_3$)]$^{5+}$ and [(tpy-$PhCHPPh_3$)$_2$$Ru_2$(tpvpvpt)]$^{4+}$, respectively. In contrast, two highly abundant peaks are observed at *m/z*= 382.4407 and *m/z*= 406.7200 for **2**. The first peak, having isotopic separation of 0.16 Da suggests the presence of hexapositive cation [(tpy-$PhCH_2PPh_3$)$_2$$Os_2$(tpvpvpt)]$^{6+}$, while a difference of 0.20 Da among the isotopic patterns for the second peak corresponds to a pentapositive cation of the type, [(tpy-$PhCH_3$)Os_2(tpvpvpt)(tpy-$PhCH_2PPh_3$)]$^{5+}$.

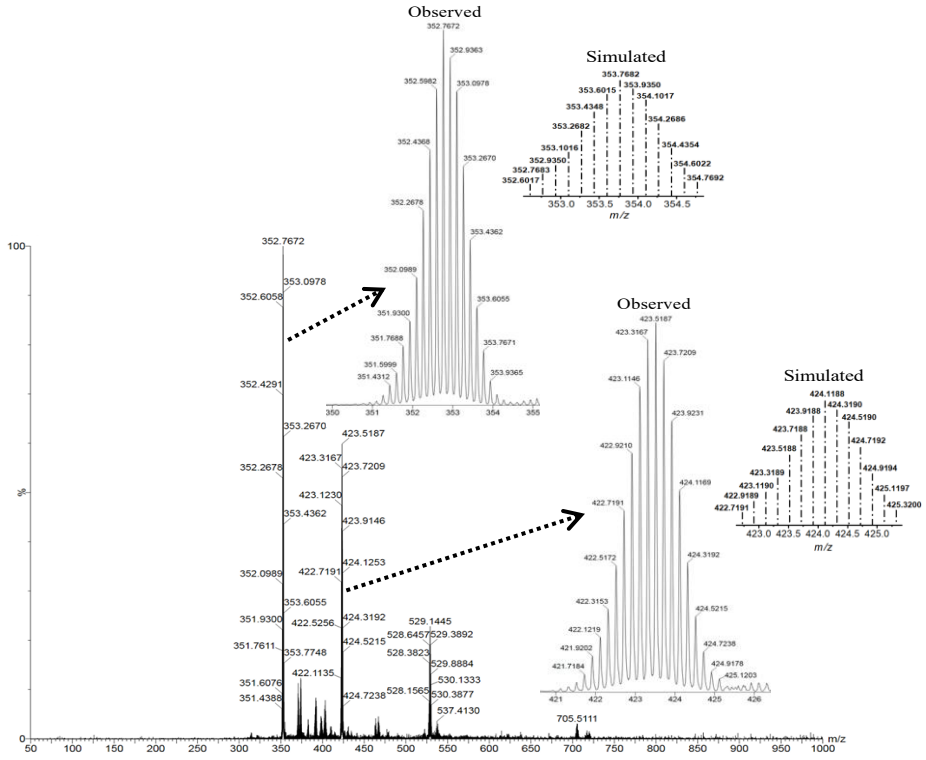

Figure 6.2. HRMS (positive) spectrum of **1** in MeCN, with insets displaying the observed and simulated isotopic distribution patterns of the complex cations $[(tpy\text{-}PhCH_2PPh_3)_2Ru_2(tpvpvpt)]^{6+}$ (*m/z*=352.7672), $[(tpy\text{-}PhCHPPh_3)Ru(tpvpvpt)Ru(tpy\text{-}PhCH_2PPh_3)]^{5+}$ (*m/z*=423.5187), and $[(tpy\text{-}PhCHPPh_3)_2Ru_2(tpvpvpt)]^{4+}$ (*m/z*=529.1445).

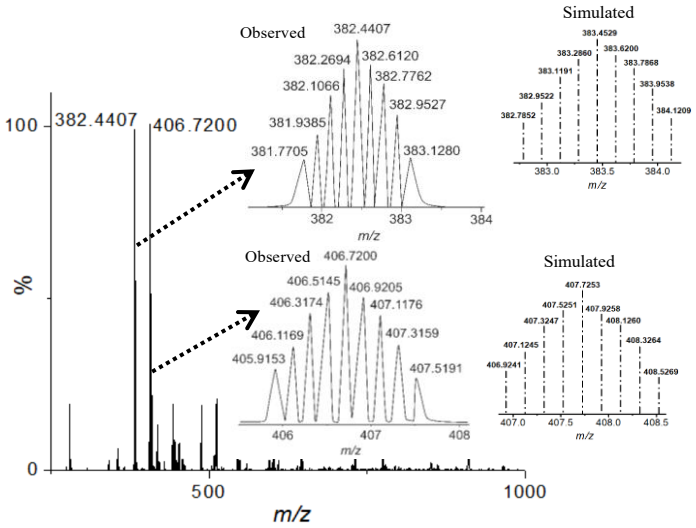

Figure 6.3. HRMS (positive) spectrum of **2** in MeCN, with insets displaying the observed and simulated isotopic distribution patterns of the complex cations $[(tpy\text{-}PhCH_2PPh_3)_2Os_2(tpvpvpt)]^{6+}$ (*m/z*=382.4407) and $[(tpy\text{-}PhCH_3)Os_2(tpvpvpt)(tpy\text{-}PhCH_2PPh_3)]^{5+}$ (*m/z*=406.7200).

6.3.4. Absorption Spectral Properties. The absorption spectra of the complexes are recorded in MeCN at RT and the corresponding figure and spectral data are presented in Figure 6.4a and Table 6.1, respectively. The spectral feature of both complexes is almost similar with the exception in the region of 600-800 nm. The lowest energy broad band at ~670 nm for **2** is assigned as spin-forbidden $^{1}[Os^{II}(d\pi)^{6}]\rightarrow{}^{3}[Os^{II}(d\pi)^{5}tpy(\pi^{*})^{1}]$ MLCT transition, arising out of spin-orbit coupling-mediated intensity stealing from the singlet states.[50,74,91] The absorption band at ~495 nm for both complexes arises due to Ru/Os→tpy-$PhCH_2PPh_3Br$ and/or Ru/Os→tpy (tpvpvpt) MLCT transitions.[82,83] The next higher energy band, observed at ~395 nm, is primarily attributed to ILCT transitions, together with some contribution from π-π* transitions. The highly intense bands in the UV region of 280-320 nm, on the other hand, is predominantly associated with the π-π* transitions.

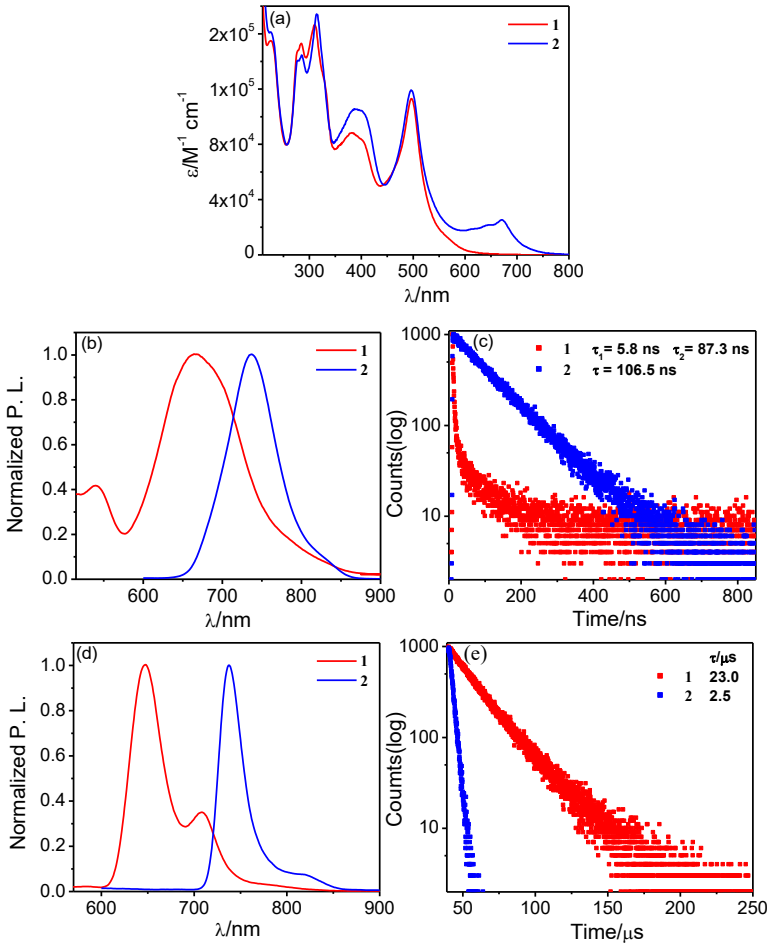

Figure 6.4. Absorption spectra (a) as well as steady-state (b and d) and excited-state decay profiles (c and e) of **1** and **2** (3×10^{-6} M) in MeCN at RT and in EtOH-MeOH (4:1, v/v) glass at 77 K. Insets to figure c and e show the corresponding lifetime values.

Table 6.1. Photophysical Data for **1** and **2**.

Compounds		Absorption λ_{max}/ nm (ε, M^{-1} cm^{-1})[a]	Luminescence		
			λ_{max}/nm	τ[b]	Φ[c]
1	MeCN (298 K)	497(112400), 385(87690), 312 (165160), 286(152180)	665	τ_1=5.8 ns (40%), τ_2=87.3 ns (60%)	2.7×10^{-3}
2		671(25120), 497(118460), 395(104750), 314(173960), 286(152670)	737	τ_1=106.5 ns	8.4×10^{-3}
1	EtOH-MeOH (4:1) (77 K)	-	647	τ=23.0 µs	-
2		-	736	τ=2.5 µs	-

[a]Molar extinction coefficient (ε). [b]Lifetime (τ). [c]Emission quantum yield (Φ)

6.3.5. Emission Spectral Properties. The emission spectra of the complexes are recorded both in MeCN at RT and in EtOH-MeOH (4:1, v/v) glass at 77 K (Figures 6.4b and 6.4d), and the associated spectral parameters are presented in Table 6.1. The excited-state decay profiles of **1** and **2** are portrayed in Figures 6.4c and 6.4e. The emission spectrum of **1** is quite broad; having its maximum at ~665 nm in MeCN at RT. Complex **2**, on the other hand, displays a strong emission band with its maximum at ~740 nm. The emission quantum yield (Φ) of **2** is found to be almost two times higher than that of **1**. Lifetime decay plot shows that the Ru(II) complex (**1**) exhibits a bi-exponential decay, while the Os(II) complex (**2**) displays a mono-exponential decay (Figure 2c). The lifetime values (τ) are found to be 87.3 ns for **1**, while 106.5 ns for **2** at RT. At 77 K, a blue-shift of emission maxima (in case of **1** only) and a huge increase in τ values are observed for both complexes. The zero-zero spectroscopic energy values (E_{00}) of **1** and **2**, obtained from their 77 K emission maxima are found to be 1.91 and 1.68 eV, respectively.

In order to elucidate the origin of emission in the complexes, particularly for the Ru(II) complex, we also acquired the emission spectrum of the bridging ligand in DCM at RT as well as in THF at 77 K (Figure 6.5). At RT, a broad and structured emission is observed having its maxima at 430, 455 nm and a broad shoulder stretching up to ~600 nm. The spectrum of the ligand at 77 K is found to be more intense and structured accompanied with a small blue-shift of the maxima. Upon comparing the spectrum of complex **1** and the bridging ligand both at RT and 77 K, we surmise that the observed emission in **1** is

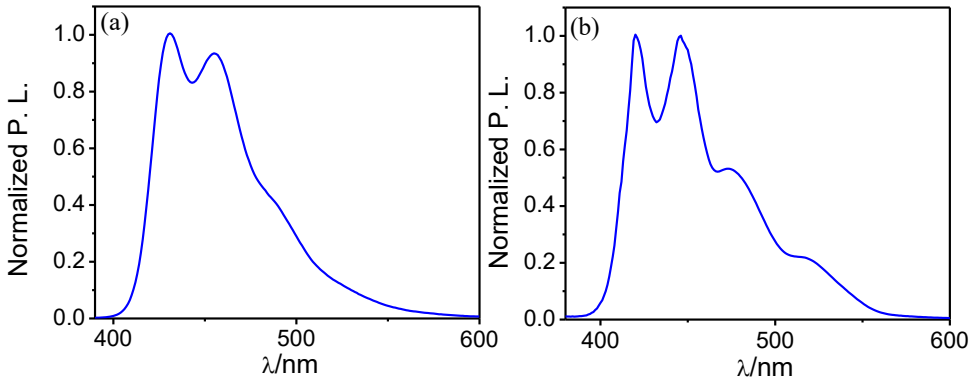

Figure 6.5. Normalized emission (λ_{ex}=380 nm) spectra of the bridging ligand (tpvpvpt) in DCM at RT (a) and in THF glass at 77 K (b).

originated from the equilibrated states of ^{3}MLCT and ^{3}ILCT/$^3\pi$-π* transitions.[87] By contrast, for Os(II) complex, the observed emission is predominantly due to deactivation of its ^{3}MLCT state only. The enhanced emission characteristics of the Os(II) complex relative to its Ru(II) counterpart is probably due to its larger energy barrier among the emitting ^{3}MLCT and non-emitting ^{3}MC states relative to that of the analogous Ru(II) counterpart.

6.3.6. Electrochemical Behavior. To investigate the electrochemical behavior of the complexes, we acquired both cyclic and square wave voltammograms (CV and SWV) of the complexes in MeCN. The overlay of CVs and SWVs are presented in Figure 6.6, while the relevant redox data are presented in Table 6.2. The data obtained from CVs and SWVs are found to correlate well with each other. Both the CVs clearly reveal a single reversible oxidation wave in the positive potential domain, while featuring three successive reduction waves in the negative potential region.[92] The oxidation wave involves a two-electron process and is attributable to the simultaneous oxidation of both the metal centers ($Ru^{II}Ru^{II}/Ru^{III}Ru^{III}$ and $Os^{II}Os^{II}/Os^{III}Os^{III}$).[79] Regarding the reduction processes, we surmise that each of the three observed peaks corresponds to a one-electron transfer process. Among these, the two peaks in the range of -1.24 to -1.75 V are tentatively assigned to the successive reductions of two terpyridine moieties. The third peak, appearing at around -2.00 V, is hypothesized to arise from the reduction of the phosphonium unit,[82,83] although no direct evidence for this assignment could be provided.

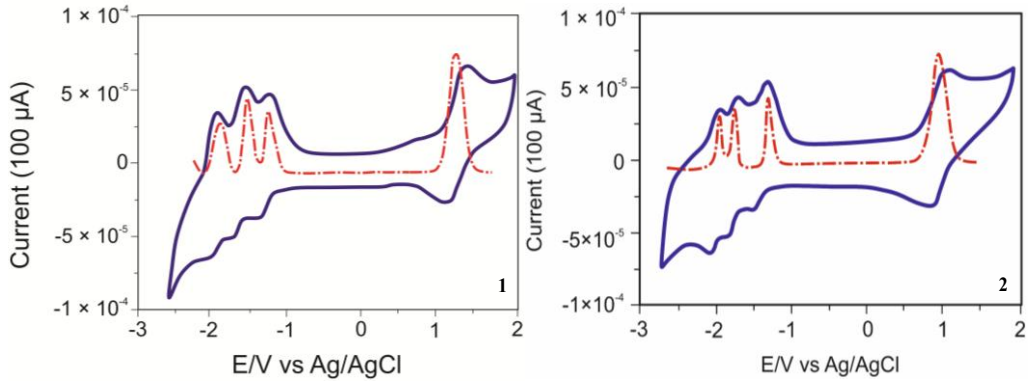

Figure 6.6. CVs (blue solid lines) and SWVs (red dotted lines) of **1** and **2** in MeCN (1×10^{-3} M) displaying both oxidation and reduction processes using glassy carbon as the working electrode and Ag/AgCl as the reference electrode.

Table 6.2. Electrochemical Data[a] for **1** and **2** in MeCN.

Compounds	Oxidation[b] $E_{1/2}$(ox)/V	Reduction[c] E(red)/V
1	1.32	-1.24, -1.67, -1.96
2	0.94	-1.34, -1.75, -1.98

[a]All the potentials are referenced against Ag/AgCl electrode with $E_{1/2}$=0.36 V for Fc/Fc^+ couple. [b]Reversible electron transfer process with a Pt working electrode. [c]E(red) values for the reduction processes obtained with glassy carbon electrode.

6.3.7. Anion-Responsive Behavior. The coordinating influence of Ru(II)/Os(II) centers as well as the impact of positively charged phosphonium motifs (-PPh_3^+ ion) are expected to make the methylene protons acidic in nature. Therefore, these protons could be removed via deprotonation in presence of basic anions. Hence, to explore the anion-responsive behavior of the complexes, we monitored their absorption and emission spectral changes upon addition of the tetrabutylammonium salts of F^-, OH^-, Cl^-, Br^-, I^-, AcO^- and $H_2PO_4^-$ in MeCN (Figure 6.7). The change in spectral profiles is found to be quite substantial for both **1** and **2** in presence of F^- and OH^-, relatively small with OAc^-, while almost negligible with the remaining anions. Thus, the observed spectral change correlates well with the basicity of the said anions. In case of absorption, the band intensities decrease, along with a small red-shift in the ^{1}MLCT band for both complexes in presence of F^- and OH^-. The emission intensity is almost quenched in case of **2** without alteration of the emission maximum, while for **1**, the emission quenching takes place, albeit to a smaller extent, accompanied with evolution of a new broad band in the longer wavelength region.

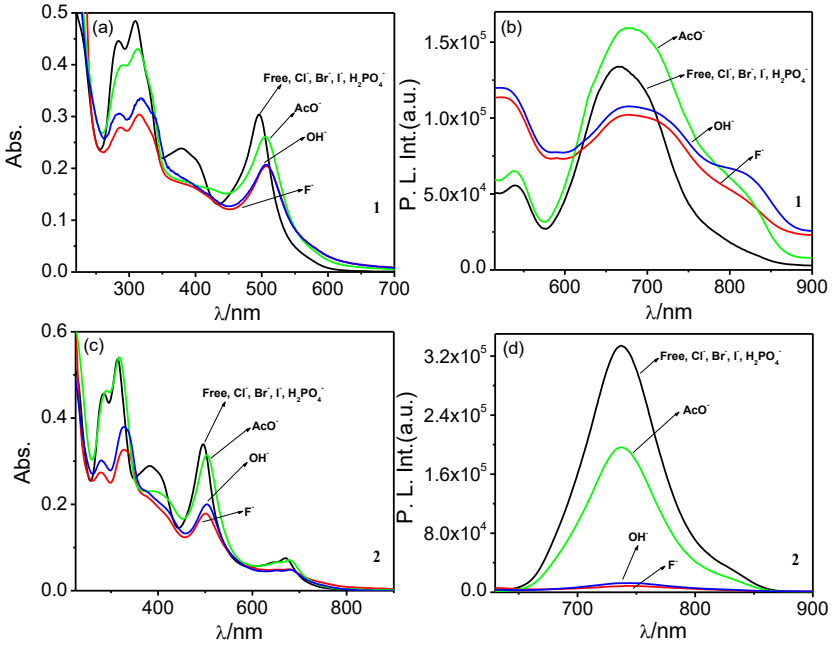

Figure 6.7. Absorption (a and c) and emission (b and d) spectral profile of **1** and **2** in MeCN (3×10^{-6} M) in presence of different anions.

To acquire quantitative insight about the interplay among the complexes and anions, the absorption and emission titration experiments are executed upon incremental addition of F^- in MeCN. Complex **1** displays two-step change in its absorption and emission spectral profiles (Figure 6.8). A gradual decrease in MLCT band intensity accompanied with a small red-shift (10 nm) occurs up to the addition of 10 equiv of F^-. A small but finite increase in the absorbance in the longer wavelength (550-700 nm) region also takes place. The ILCT and π-π* band intensities in the spectral domain of 280-450 nm, on the other hand, decreases gradually. In the second step, again a small but finite change in absorbance of the said bands takes place in their respective direction up to the addition of 40 equiv of F^-. In case of emission, the intensity of the band at ~665 nm gradually increases along with a red-shift (~50 nm) of the emission maximum in the first step. During the process, evolution of a new broad band centered at ~815 nm along with its gradual intensification is also noticed. Continued addition of F^-, on the other hand, leads to systematic quenching of emission within the spectral domain of 650-900 nm. The successive emission spectral lines also pass through an isoemissive point at ~610 nm in the second step. In contrast to the steady state spectra, only a single-step change is observed in the excited state decay profile and the lifetime value is found to decrease gradually from 87.3 ns to 15.7 ns (Figure 6.9).

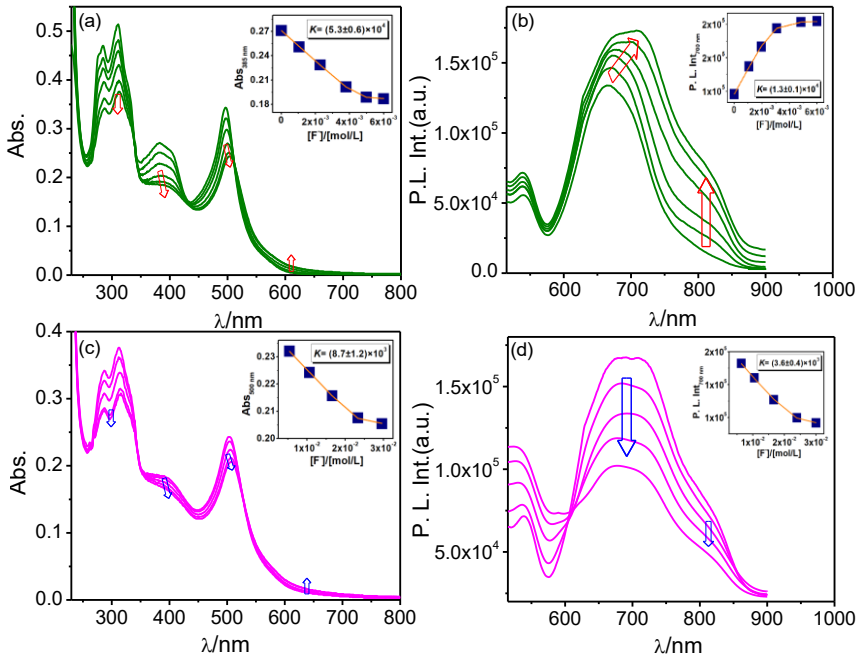

Figure 6.8. Two step changes in absorption (a and c) and emission (b and d) (λ_{ex} = 500 nm) spectra of **1** (3×10^{-6} M) in MeCN upon gradual addition of F^- (up to 40 equiv). Insets show the fit of the experimental absorbance and luminescence data to a 1:1 binding profile.

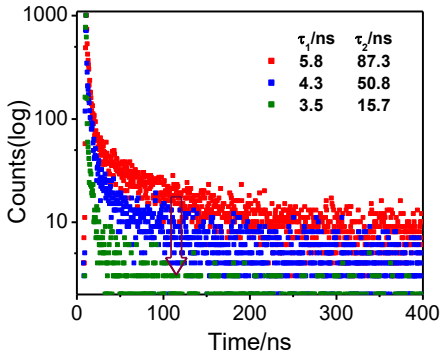

Figure 6.9. Change in excited-state decays of **1** (3×10^{-6} M) upon incremental addition of F^- (up to 40 equiv) in acetonitrile. The inset shows the corresponding lifetime values.

In contrast to **1**, complex **2** undergoes four step changes upon incremental addition of F^- (Figure 6.10). In the first step, the ^{3}MLCT band intensity within 600-800 nm domain increases considerably, while the ^{1}MLCT band at ~495 nm decreases in intensity. Additionally, a slight increase in the absorbance at ~395 nm and a small but finite decrease in intensity in the UV region bands (within 285-315 nm) is noticed. In the second step, the changes in the aforementioned bands take place in the reverse direction relative to the first step. In the third step, a diminution of both the MLCT bands and ILCT band is observed,

although the extent of reduction in the intensity of the ^{1}MLCT band is more pronounced compared to other two bands. Finally, a slight attenuation in the MLCT and ILCT band intensity with concomitant increase in the UV region bands takes place in the fourth step. In each step, successive absorption spectra are found to pass through one or more isosbestic point(s). The amount of F^- required to reach the saturation in these four steps is 4, 8, 15

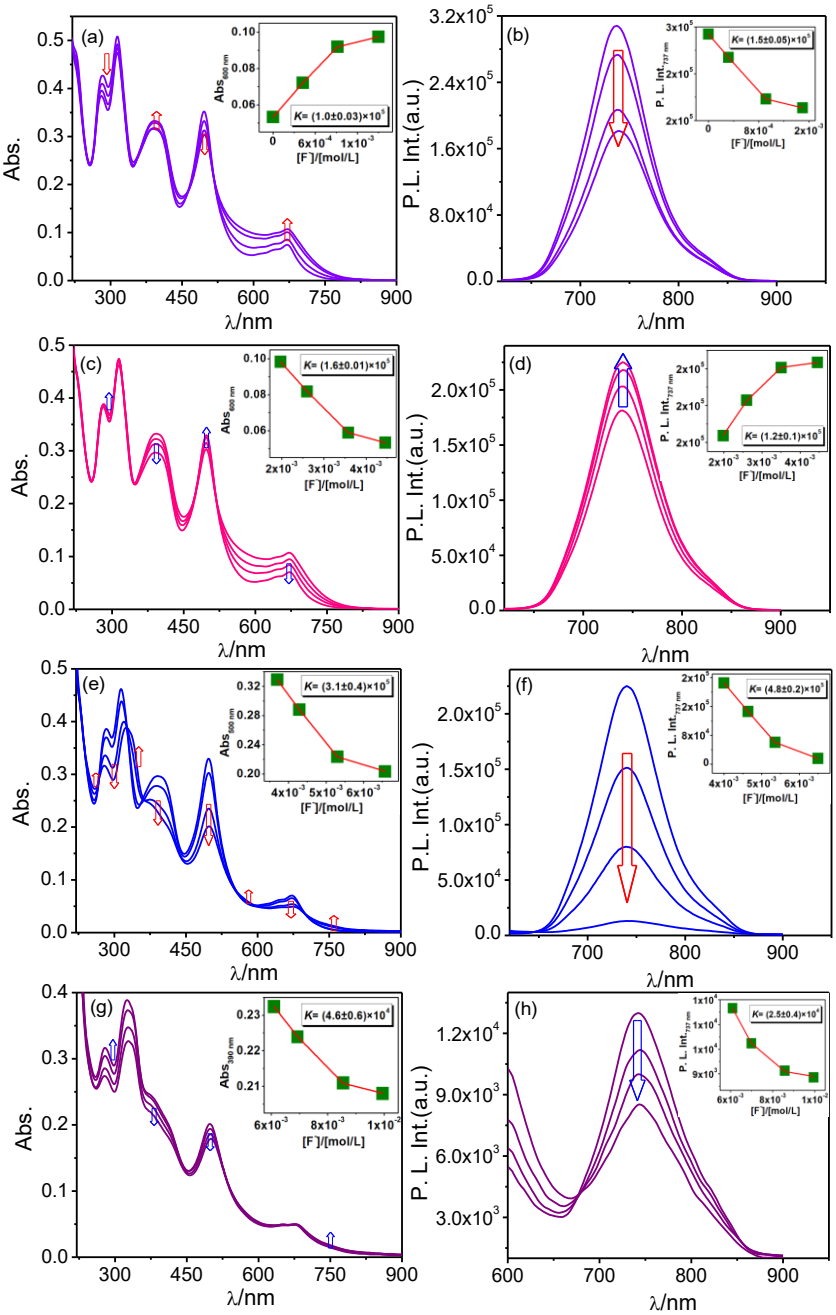

Figure 6.10. Four step changes in absorption (a, c, e and g) and emission (b, d, f and h) (λ_{ex} = 500 nm) spectra of **2** (3×10^{-6} M) in MeCN upon gradual addition of F^- (up to 30 equiv). Insets show the fit of the experimental absorbance and luminescence data to a 1:1 binding profile.

and 30 equiv, respectively. In the emission side, band intensity decreases substantially in the first step, while a small increase in the intensity is noticed in the second step. In the third step, the emission intensity again decreases remarkably and finally gets fully quenched in the fourth step. In contrast to absorption and emission spectral trends, the lifetime of the complex decreases (106.5 ns→82.7 ns) only in a single step (Figure 6.11). The change in the absorption and emission spectral profiles of the complexes in presence of OH^- are found to be almost similar to that of F^-.

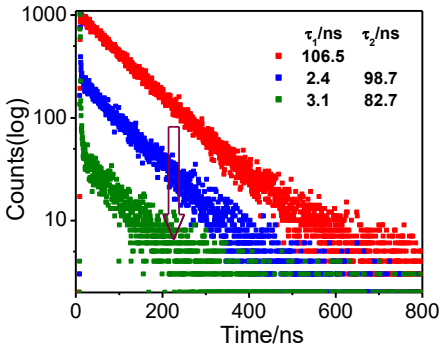

Figure 6.11. Change in excited-state decays of **2** (3×10^{-6} M) upon incremental addition of F^- (up to 30 equiv) in acetonitrile. The inset shows the corresponding lifetime values.

To get a quantitative insight about the receptor-anion interaction, we have also calculated the binding constant values (K) by using both the absorption and emission titration profiles of **1** and **2** via equation 1 (insets of Figures 6.8 and 6.10 and Table 6.3). The values are mostly within the order of ~10^3-10^5 M^{-1}. The values of K, obtained from absorption and emission spectral data are found to be almost comparable.

Table 6.3. Equilibrium Constants (K) for **1** and **2** Towards F^- in MeCN.

Compounds	Binding Constant (K)							
	Absorption				Emission			
	K_1	K_2	K_3	K_4	K_1	K_2	K_3	K_4
1	5.3×10^4	8.7×10^3	-	-	1.3×10^4	3.6×10^3	-	-
2	1.0×10^5	1.6×10^5	3.1×10^5	4.6×10^4	1.5×10^5	1.2×10^5	4.8×10^5	2.5×10^4

To investigate the effects of F^- on the oxidation potential of the complexes, we have acquired both CVs and SWVs of the F^- saturated solution of both **1** and **2** in MeCN. Voltammograms of the complexes in presence and in absence of F^- are presented in Figure 6.12 and the associated voltammetric data are presented in Table 6.4. In both complexes,

the $E_{1/2}$ values of M^{II}/M^{III} couple shift towards lower potential domain, albeit in different extent (1.32 V→1.16 V for **1**, while 0.94 V→0.72 V for **2**). Thus, the extent of shift is found to be more marked in case of the Os(II) complex (**2**) in presence of F^-. Upon addition of excess F^-, the methylene proton(s) probably get deprotonated, which in turn leads to the increase in the electron density around metal centers and as a result, the negative shift of the $E_{1/2}$ value is observed.

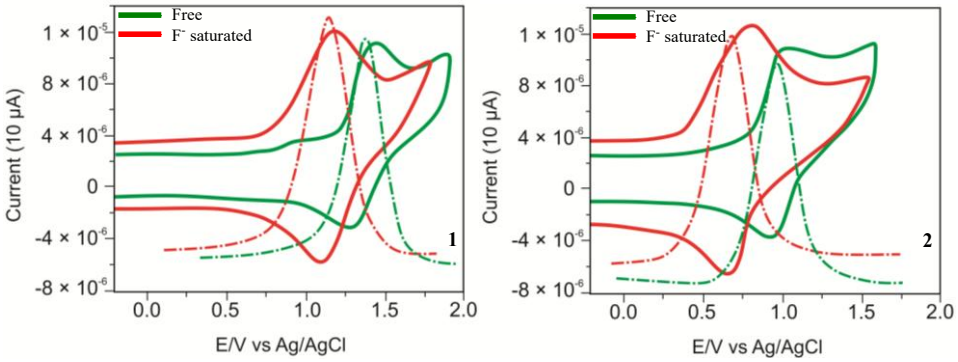

Figure 6.12. CVs (solid lines) and SWVs (dotted lines) of free- and F^- saturated forms of **1** and **2** in MeCN showing the oxidation process using Pt as the working electrode and Ag/AgCl as the reference electrode.

Table 6.4. Oxidation Potentials of **1** and **2** in their Free and Deprotonated Forms in MeCN.

Compounds	Oxidation $E_{1/2}$(ox)/V	
	Free	Deprotonated
1	1.32	1.16
2	0.94	0.72

To elucidate the mode of interaction between the complex and anion, we performed ^{1}H NMR titration of both complexes with incremental additions of F^- in DMSO-d_6 (Figures 6.13 and 6.14). In the ^{1}H NMR spectra, the doublet at 5.38 ppm with its integration count of 4 protons due to the methylene ($-CH_2$) units, exhibits a decrease in intensity accompanied with signal broadening and finally disappears upon addition of 20 equiv (for **1**) and 15 equiv (for **2**) of F^-. At its expense, a new singlet emerges in the downfield region (~6.72 ppm) and gets intensified. The signal broadening is probably due to H-C-H···F^- type of hydrogen bonding interaction. Thereafter, complete disappearance of the initial $-CH_2$ signal at 5.38 ppm takes place in presence of excess F^- (40 equiv for **1** and 30 equiv for **2**). The observed change is attributed to abstraction of one of the two methylene protons from each side of the complex. The generated negative charge onto the $-CH^-$ unit is presumably

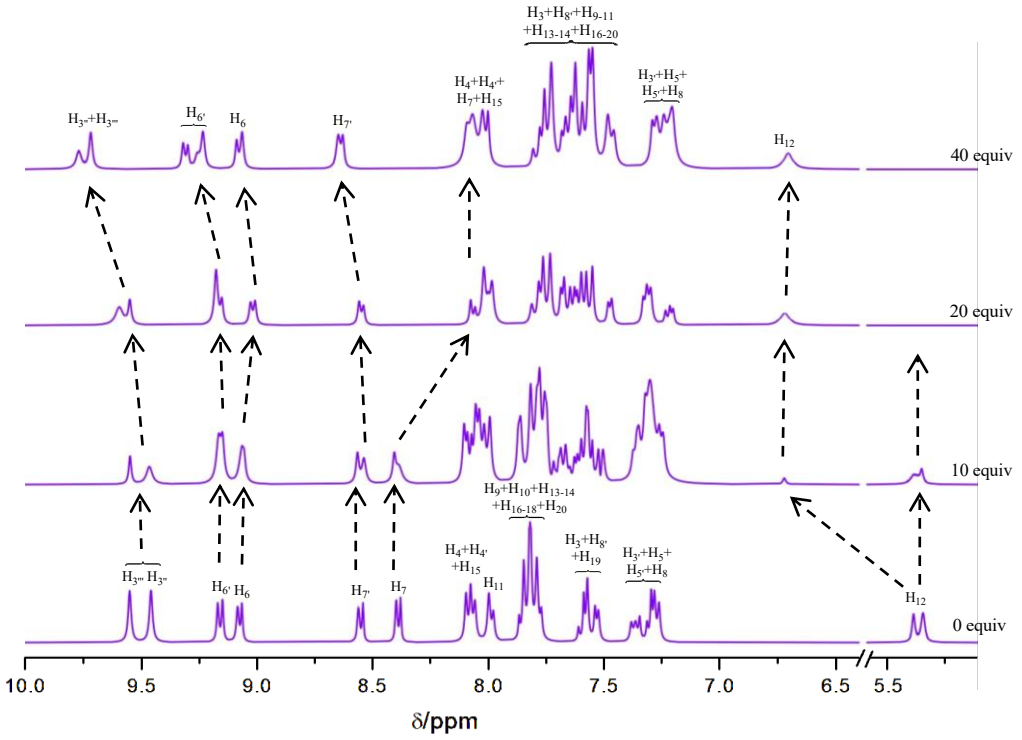

Figure 6.13. ^{1}H NMR spectral changes of **1** upon gradual addition of F^- (up to 40 equiv) in DMSO-d_6.

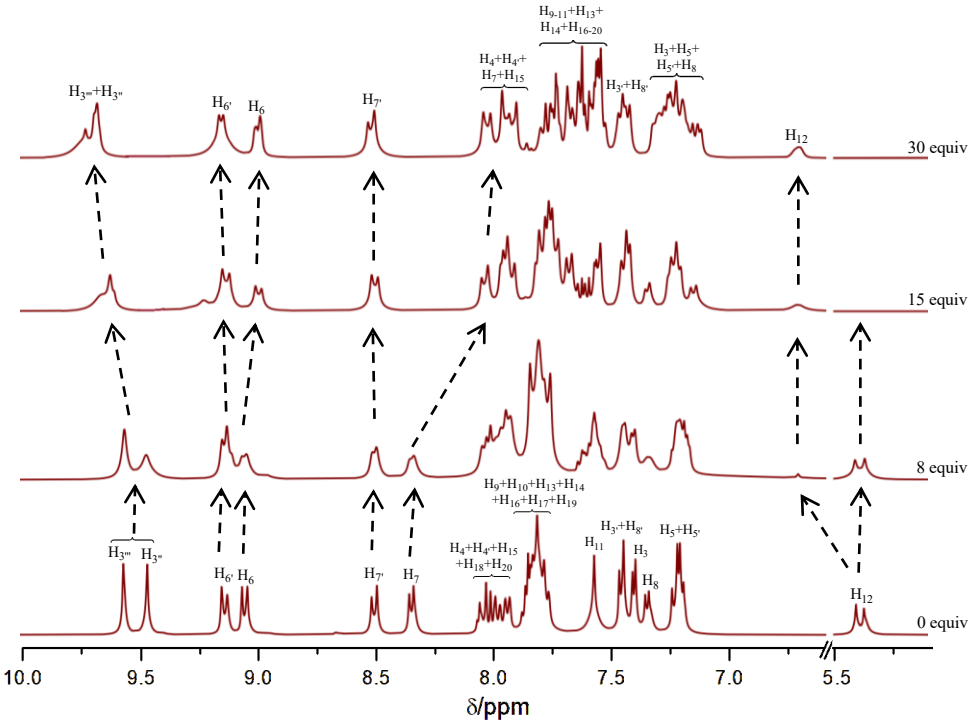

Figure 6.14. ^{1}H NMR spectral changes of **2** upon gradual addition of F^- (up to 30 equiv) in DMSO-d_6.

delocalized into the adjacent phosphonium (PPh_3^+) moiety, facilitating the formation of a C=P double bond. This structural reorganization induces a significant downfield shift of the -CH^- signal which reappears as a broad singlet at 6.72 ppm with its integration count of 2 protons. Additionally, the phenyl proton signals associated with the PPh_3 units become well-resolved, accompanied by a slight up-field shift. The H_6 and H_7 proton resonances also experience an up-field shift, likely as a consequence of fluoride-induced deprotonation. By contrast, the signal broadening together with downfield shift observed for the $H_{3''}$ and $H_{3'''}$ protons can be attributed to their interaction with F^- ions, which is facilitated by the increased acidity of these protons arising from the coordinating effect of the Ru(II) centers, as well as the influence of the adjacent phosphonium ions.

The $^{31}P\{^1H\}$ NMR spectra of both the initial and F^- saturated forms of complexes **1** and **2** are also acquired in DMSO-d_6 (Figures 6.15 and 6.16). In their initial forms, the ^{31}P signal is observed at 23.10 ppm (for **1**) and at 23.43 ppm (for **2**), while upon fluoride saturation, the said signals undergo a downfield shift to 25.55 ppm (for **1**) and 25.66 ppm (for **2**). This shift is likely attributed to the formation of hydrogen bonds of the type H-C-H···F^-, which facilitate partial double-bond character between the methylene and phosphonium units. If the interaction could be solely governed by ion-pair formation, an up-field shift of the ^{31}P signal would be expected. Consequently, the combined evidence from ^1H and $^{31}P\{^1H\}$ NMR spectroscopy indicates that F^- initially engages in hydrogen bonding with the methylene protons, eventually leading to deprotonation.

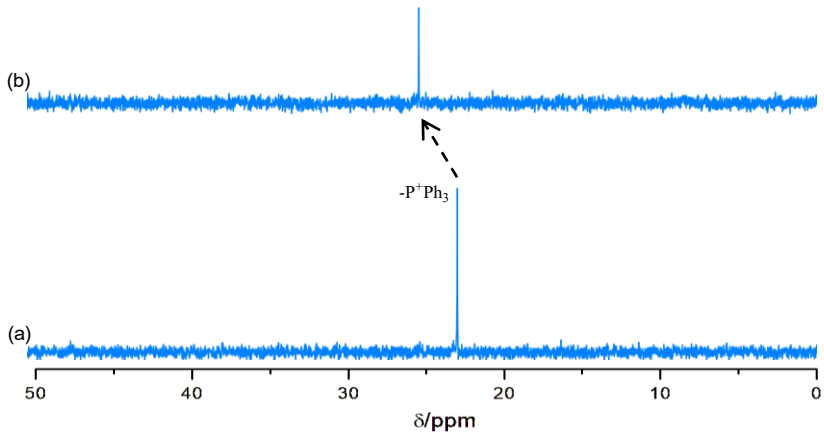

Figure 6.15. $^{31}P\{^1H\}$ NMR spectrum of **1** in DMSO-d_6 in its free (a) and F^- saturated (b) forms.

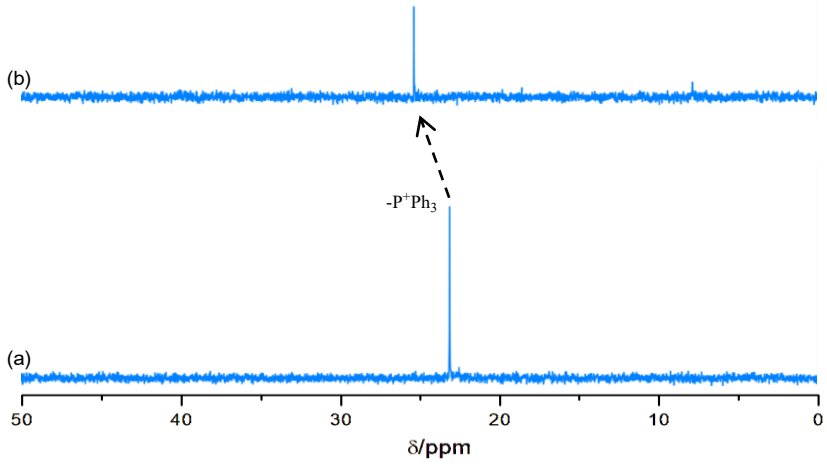

Figure 6.16. $^{31}P\{^{1}H\}$ NMR spectrum of **2** in DMSO-d_6 in its free (a) and F^- saturated (b) forms.

6.3.8. Photoisomerization Behavior. Due to the presence of two stilbene motifs in the bridge, we are also interested to investigate the photoisomerization behavior of the complexes in MeCN upon irradiating with 500 nm light. The overall process was carefully monitored via absorption and emission spectroscopic techniques, with the corresponding spectral changes portrayed in Figure 6.17. For both cases, a single step change is observed. Upon light irradiation, the intensity of MLCT band at ~495 nm and ILCT band at ~395 nm

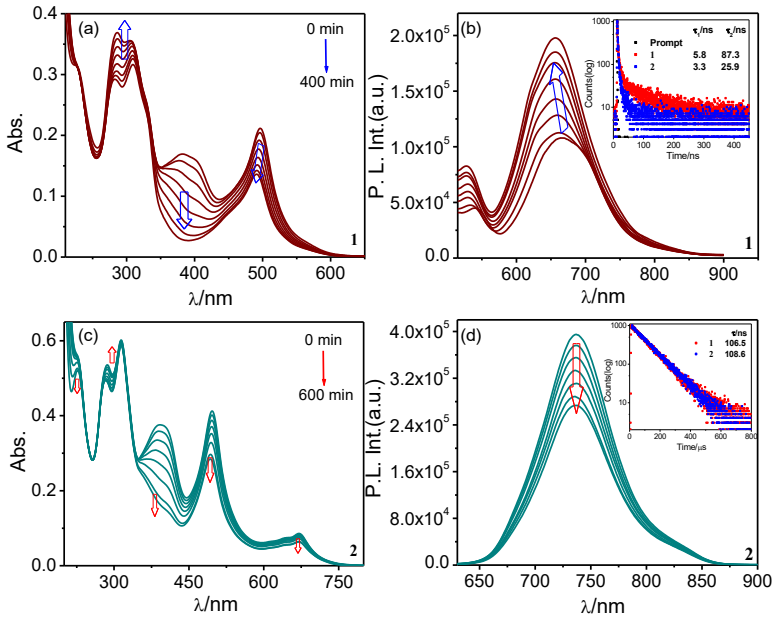

Figure 6.17. Absorption (a and c) and emission (b and d) spectral changes of **1** (2×10^{-6} M) and **2** (3.5×10^{-6} M) in MeCN upon treatment with light of λ=500 nm. Inset to figure b and d shows the decay profiles of the complexes before and after photolysis along with their lifetime values.

gradually decreases, while the UV region bands in the domain of 280-320 nm increase in intensity for both **1** and **2**. The ILCT band exhibited a reduction in intensity nearly 2 to 5 times greater than that of the MLCT band. A single isosbestic point at ~330 nm for each complex suggests an equilibrium between at least two species, where the original *trans-trans* (*t-t*) form converts to either *trans-cis* (*t-c*) or *cis-cis* (*c-c*) forms. Complex **1** reaches the photostationary state after 400 min, while complex **2** takes 600 min, likely due to the larger size of the Os(II) center compared to the Ru(II) center.

In the emission spectra, a gradual increase in the emission intensity along with a blue shift (~10 nm) of the emission maximum is observed for **1**. For **2**, on the other hand, the emission intensity decreases gradually without altering its emission maximum. We also recorded the emission decay of the photolyzed solutions of the complexes (insets of Figures 6.17b and 6.17d). Complex **1** exhibits a decrease in lifetime values (τ_1= 5.8→3.3 ns and τ_2= 87.3→25.9 ns), while the change is almost negligible for **2**.

We have also recorded both the CVs and SWVs of the photolyzed solutions (MeCN) of the complexes in the positive potential region. The overlay of CVs and SWVs are presented in Figure 6.18 and the corresponding data are presented in Table 6.5. The data obtained from CVs and SWVs are found to correlate well with each other. It is of interest to note that the single reversible oxidation peak observed for the *t-t* isomers splits, albeit to a small extent, into two closely spaced overlapping peaks after photo-irradiation (Figure 6.18). The observed splitting is probably due to a decreased metal-metal separation in the isomerized forms of the complexes.[92]

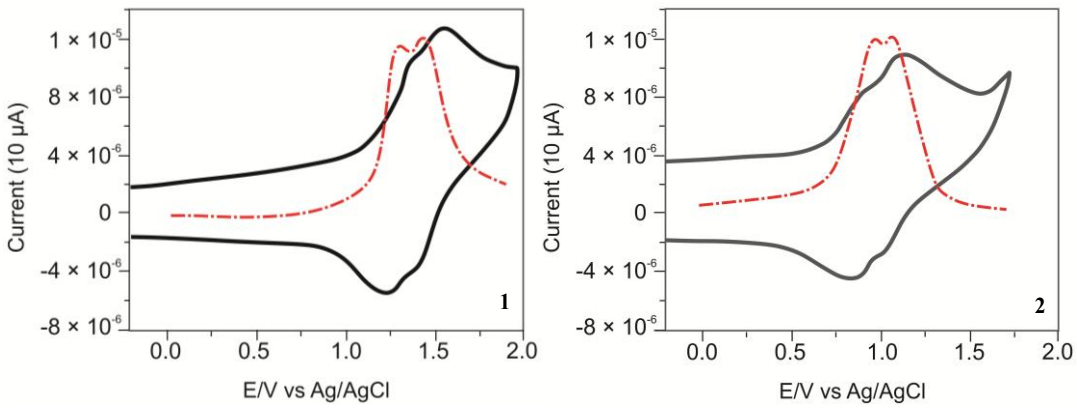

Figure 6.18. CVs (black solid lines) and SWVs (red dotted lines) of the photolyzed solutions of **1** and **2** in MeCN (~1×10^{-3} M) showing oxidation process using Pt as the working electrode and Ag/AgCl as the reference electrode.

Table 6.5. Oxidation Potentials of **1** and **2** in their Photolyzed Forms in MeCN.

Compounds	Oxidation $E_{1/2}$(ox)/V
1(*t-c*)	1.31, 1.43
2(*t-c*)	0.92, 1.03

We have performed ^{1}H NMR spectroscopy on the original and photolyzed solutions of both **1** and **2** in CD_3CN in order to clarify the actual mode of isomerization process (Figures 6.19 and 6.20). Small but finite up-field shift of majority of the proton resonances are observed in the final spectrum. Upon light irradiation, two new doublets (H_9^i and H_{10}^i) with J=12 Hz appear in the region of 7.00-6.50 ppm. The singlet corresponding to the $H_{3'''}$ protons undergoes splitting due to the presence of $H_{3'''}^i$ protons. Additionally, the two doublets associated with H_6 and $H_{6'}$ protons merge, forming a multiplet, likely due to the H_6^i and $H_{6'}^i$ protons. For **1**, the singlet corresponding to the H_{11} protons exhibit a slight increase in intensity, accompanied by the emergence of a distinct singlet (H_{11}^i) at ~7.63

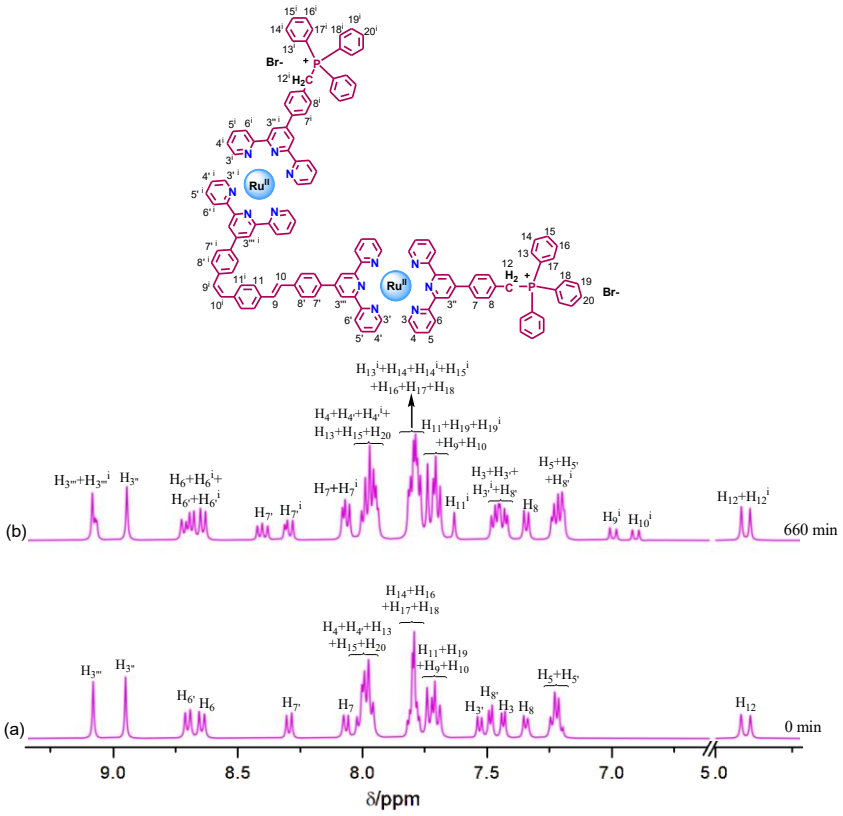

Figure 6.19. ^{1}H NMR spectrum of **1** in CD_3CN before (a) and after (b) photolysis with light of λ=500 nm for 660 min.

ppm. In case of **2**, the original signal intensity of H_{11} decreases along with a small splitting. Additionally, the H_{11}^{i} proton signal appears within a multiplet resulting from overlap with other proton signals in the region of 7.42-7.25 ppm. Furthermore, the H_7, $H_{7'}$, H_8, and $H_{8'}$ protons display alterations in their signal multiplicity, likely due to the presence of their isomerized counterparts. The overall spectral changes observed upon photolysis indicate significant modifications in the chemical environment in most of the proton signals. A comparative analysis of the ^{1}H NMR spectra of the initial and photolyzed forms of the complexes, along with the substantial decrease in the coupling constant of the olefinic H_9^{i} and H_{10}^{i} protons, confirms the isomerization of the complexes predominantly from their *t-t* to *t-c* forms.

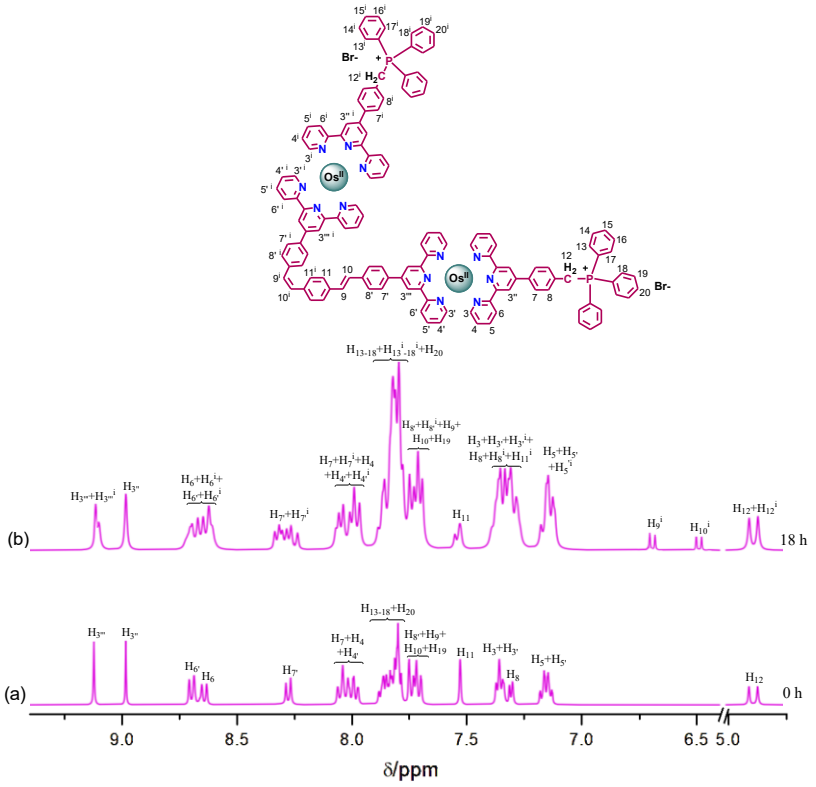

Figure 6.20. ^{1}H NMR spectrum of **2** in CD_3CN before (a) and after (b) photolysis with light of λ=500 nm for 18 h.

The rate constants (k_{iso}) and quantum yields ($\Phi_{tt\rightarrow tc}$) for the photoisomerization process are evaluated by analyzing the absorption titration profiles of both complexes. The associated data and figures are presented in Table 6.6. k_{iso} values are found to be 1.6×10^{-4} and 9.7×10^{-5} s^{-1} for **1** and **2**, respectively, while $\Phi_{tt\rightarrow tc}$ values lie in the range of $1.5\text{-}4.5\times10^{-3}$. It is to be noted that the k_{iso} value for **1** is higher than that of **2** possibly because of the bulkier size of Os(II) centers than Ru(II) centers.

To assess the reversibility of the isomerization process, the absorption and emission spectral changes of the photolyzed solutions of the complexes are monitored upon irradiation with 270 nm light (Figure 6.21). Spectral analysis confirms that the *t-c* isomers of the complexes gradually revert back to their original *t-t* forms; however, complete conversion is not achieved even after prolonged irradiation. Furthermore, k_{iso} and $\Phi_{tc\rightarrow tt}$ for the reverse isomerization process were determined, with k_{iso} values ranging from 3.6-4.1×10^{-5} s^{-1} and $\Phi_{tc\rightarrow tt}$ values falling within the range of 1.8×10^{-3}-3.5×10^{-4} (Table 6.6). These findings demonstrate that the complexes exhibit reversible emission switching upon exposure to visible and UV light, alternately.

Table 6.6. Quantum Yield and Rate Constants for the Forward and Reverse Photoisomerization of **1** and **2** in MeCN.

	Forward process (500 nm light)		Reverse process (270 nm light)	
Compounds	Quantum yield (Φ)	Rate constant (k_{iso}/s^{-1})	Quantum yield (Φ)	Rate constant (k_{iso}/s^{-1})
1	4.5×10^{-3}	1.6×10^{-4}	1.8×10^{-3}	4.1×10^{-5}
2	1.5×10^{-3}	9.7×10^{-5}	3.5×10^{-4}	3.6×10^{-5}

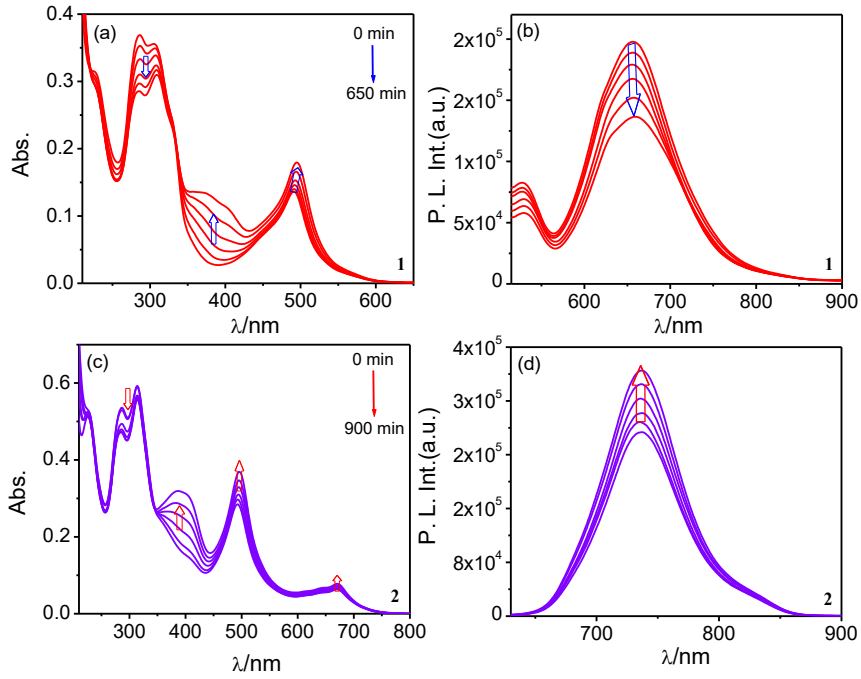

Figure 6.21. UV-vis absorption (a and c) and emission (b and d) spectral changes upon irradiating the photolyzed MeCN solution of **1** (2×10^{-6} M) and **2** (3.5×10^{-6} M) with 270 nm light. Insets show the irradiation time.

6.3.9. Multistimuli-Responsive Photoswitching. We are now interested to investigate the multi-stimuli-responsive photoswitching behavior of the complexes. To this end, the complexes were first subjected to oxidation in MeCN medium using ceric ammonium nitrate (CAN), and the progress of the reaction were monitored via absorption and emission spectroscopy (Figure 6.22). Notably, complex **1** exhibited no response to CAN oxidation, whereas complex **2** underwent significant spectral modifications. This difference is likely attributed to the higher oxidation potential of **1** relative to **2**, which

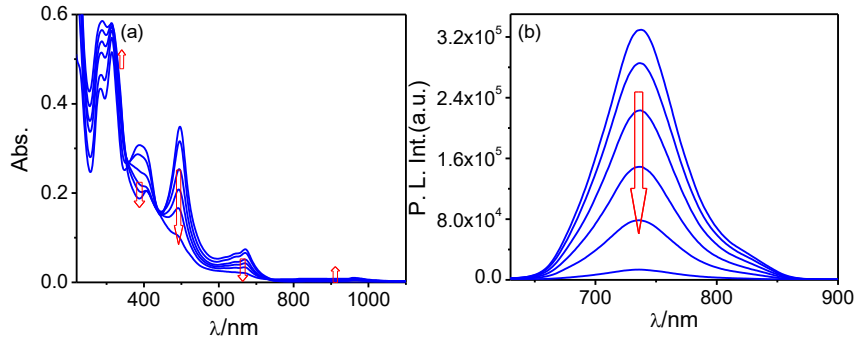

Figure 6.22. Absorption and emission (λ_{ex} =495 nm) spectral changes of **2** (3×10^{-6} M) (a and b, respectively) in MeCN upon gradual addition of CAN (up to 4 equiv).

renders the former more resistant towards oxidation. Upon incremental addition of CAN, the intensities of both the ^{1}MLCT and ^{3}MLCT bands are nearly quenched. Simultaneously, a new broad absorption band with a low ε value (~2670 M^{-1} cm^{-1}) emerges in the longer wavelength region (~750-1050 nm). The quenching of the MLCT bands is likely attributed to the oxidation of Os(II) to Os(III), which facilitates electron transfer from the terpyridine units to the Os(III) centers, resulting in the appearance of a ligand-to-metal charge transfer (LMCT) band in the NIR region. The spectral saturation is obtained after addition of 4 equiv of CAN. This oxidation process is also accompanied by a noticeable color change from dark brown to greenish-yellow upon reaching saturation. Additionally, almost complete quenching of the emission band is observed, further supporting the Os(II)→Os(III) oxidation. Thus, the addition of CAN is expected to facilitate the oxidation of the *t-t* form of **2** from Os(II)-Os(II) state to the *t-t* form in the Os(III)-Os(III) state.

We now intend to explore the isomerization behavior of the oxidized form of complex **2**. To achieve this, the CAN-treated solution of the complex is exposed to 500 nm light irradiation, and the resulting changes are visualized via absorption and emission spectroscopy (Figure 6.23). Upon irradiation, the MLCT bands regain their intensities, accompanied by complete disappearance of the LMCT band. Further diminution in the

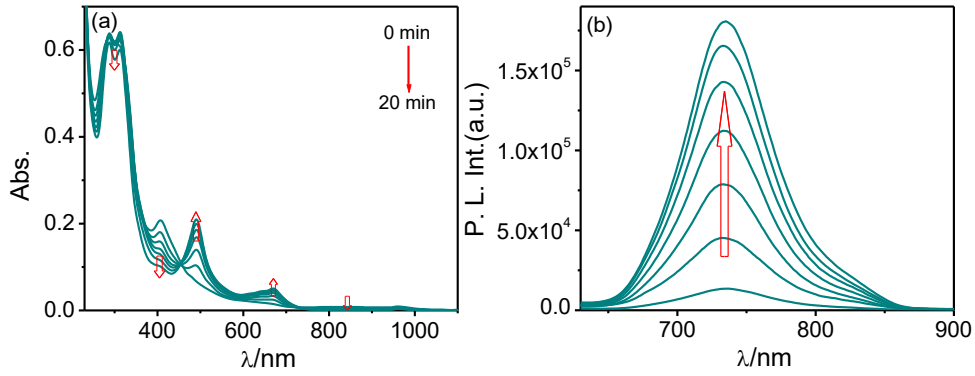

Figure 6.23. Absorption and emission spectral changes of CAN-treated MeCN solutions of **2** (a and b, respectively) upon irradiating with visible light (500 nm).

ILCT band intensity also takes place during the process. Concurrently, the greenish-yellow solution gradually reverts back to its initial brown color. Detailed spectral analysis reveals that the final absorption spectrum closely resembles that of the *t*-*c* isomer in the Os(II)-Os(II) state of the complex. Gradual increase in emission intensity is also noted upon light irradiation, with no shift in the peak maximum. These spectral observations suggest that light exposure induces simultaneous reduction of the Os(III) centers and isomerization from the *t*-*t* to *t*-*c* configuration, leading to the formation of Os(II)-*t*-*c*-Os(II) species. Notably, saturation is achieved within just 20 min, indicating a significant reduction in time compared to the isomerization of the complex in the absence of CAN. Moreover, no evidence of re-oxidation of the Os(II)-*t*-*c*-Os(II) species is observed, even after keeping for prolonged time. We have also estimated the k_{iso} and $\Phi_{tt\rightarrow tc}$ values for the isomerization of oxidized form of **2** from the absorption titration profile and the related data and figure are presented in Table 6.7 and Figure 6.24. k_{iso} value is found to be 6.7×10^{-3} s^{-1}, while the quantum yield for the isomerization process ($\Phi_{tt\rightarrow tc}$) is 0.35.

Table 6.7. Quantum Yield and Rate Constants for the Photoisomerization of **1** and **2** in MeCN in their Oxidized, Reduced and Deprotonated Forms.

	CAN		Na		F^-	
Compounds	Quantum yield (Φ)	Rate constant (k_{iso}/s^{-1})	Quantum yield (Φ)	Rate constant (k_{iso}/s^{-1})	Quantum yield (Φ)	Rate constant (k_{iso}/s^{-1})
1	-	-	1.2×10^{-2}	6.4×10^{-4}	7.2×10^{-3}	2.9×10^{-4}
2	0.35	6.7×10^{-3}	3.8×10^{-3}	1.9×10^{-4}	2.7×10^{-3}	1.4×10^{-4}

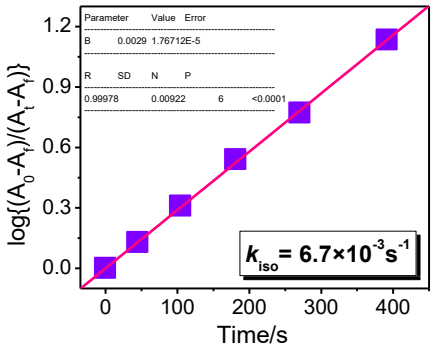

Figure 6.24. Linear plot of log $(A_0-A_f)/(A_t-A_f)$ *vs*. time (t) for absorption spectral changes upon irradiation of the CAN-treated solution in MeCN with 500 nm light for **2**.

The observed changes in the absorption and emission spectral profiles suggest that light irradiation of the oxidized complex initiates the photoexcitation of Ce(III) to its excited state, Ce(III)*. This process subsequently facilitates the reduction of Os(III) to Os(II), coupled with isomerization from the *t-t* to *t-c* configuration, while Ce(III) is simultaneously re-oxidized to its initial Ce(IV) state. The significantly enhanced rate constant further confirms that the oxidized complex undergoes a very fast photoisomerization process compared to its free form.

To elucidate the role of light in this isomerization process, the CAN-saturated solution of **2** was kept in the dark and we acquired its absorption and emission spectra in the time interval of 1 h to see whether any spectral change is occurring or not. Almost after 3 h, we observed that the diminished absorbance of the MLCT band again starts to increase gradually, which indicates the occurrence of the reduction of the complex even in absence of light. In case of emission also, the quenched ^{3}MLCT band starts to regain its intensity after ~3 h. However, the rate of reduction of the complex is very much slow and it takes almost 24 h to revert back to its initial Os(II) state. On the other hand, when the oxidized complex was irradiated with light, this reduction process gets completed within only 20 min which is much faster compared to that in absence of light. Therefore, light plays a crucial role for driving this reduction process much faster.

The oxidation of Os(II) centers induces electron deficiency, thereby pulling apart the electron density from the C=C bond is favored, which in turn induces greater single-bond character in the stilbene unit. Consequently, light irradiation enables more facile and rapid rotation around the stilbene units in the oxidized complexes, directly contributing to the significantly enhanced *t-t* to *t-c* isomerization rate (Table 6.7).

The significant acceleration in the isomerization rate of the oxidized complexes prompts us to investigate the isomerization behavior of the complexes in their reduced states. To this end, complexes **1** and **2** were subjected to reduction using metallic sodium in MeCN as the reducing agent and the whole process is again monitored via absorption and emission spectroscopy (Figure 6.25). In both cases, a single-step change is observed. The intensities of the MLCT and ILCT absorption bands within 300-800 nm range remain almost unaffected, whereas a remarkable enhancement in the π-π* band intensity at ~255 nm is noticed upon incremental addition of metallic Na. This finding strongly suggests

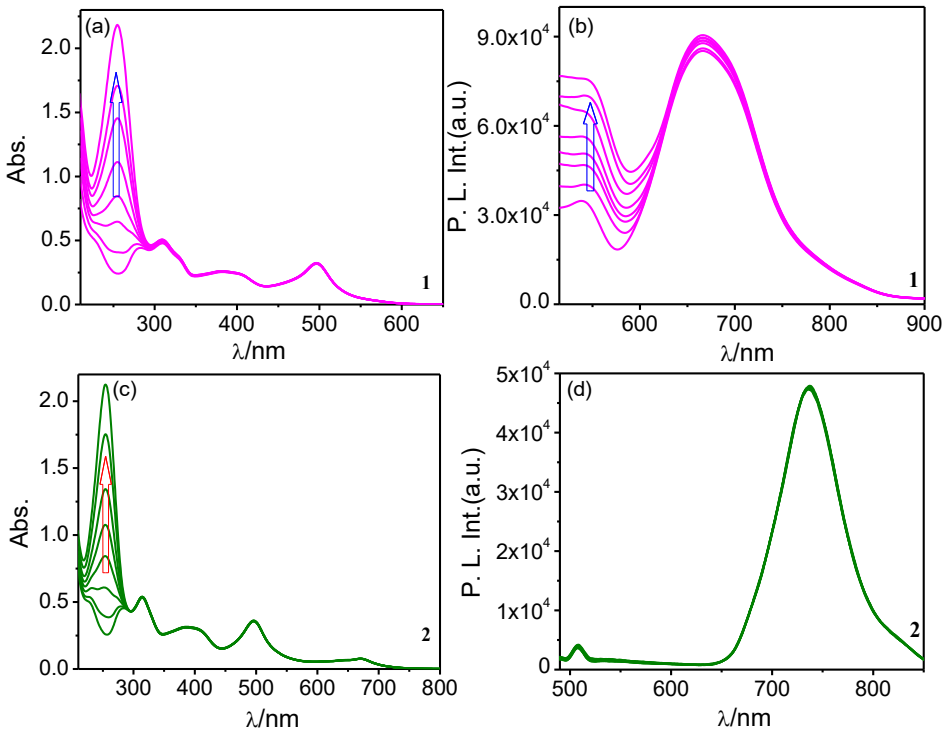

Figure 6.25. Absorption and emission (λ_{ex}= 495 nm) spectral changes of **1** (3×10^{-6} M) (a and b, respectively) and **2** (3×10^{-6} M) (c and d, respectively) in MeCN upon addition of MeCN solution of metallic Na (up to 4 equiv).

that the electrons donated by sodium primarily populate in the low-lying π* orbital of the terpyridine moieties within the molecular framework.[92] The spectral saturation takes place upon addition of 4 equiv. of metallic Na. In contrast, the impact of reduction on the emission spectra is less pronounced. For complex **1**, a slight increase in emission intensity at ~570 nm is observed, while the ^{3}MLCT band intensity remains nearly unchanged. However, for **2**, the emission spectra within 480-850 nm range exhibit no discernible changes, indicating a minimal influence of reduction on its emissive properties.

Now, to investigate the isomerization behavior of the reduced form of the complexes, their Na-treated solutions are again subjected to two different experimental conditions, viz. kept in the dark and exposed to visible light of 500 nm. The associated changes are monitored through absorption and emission spectroscopy. For both **1** and **2**, two-step changes are noticed under light irradiation (Figures 6.26 and 6.27). The π-π* band intensity at ~255 nm is reduced drastically, while the change in intensity of the MLCT

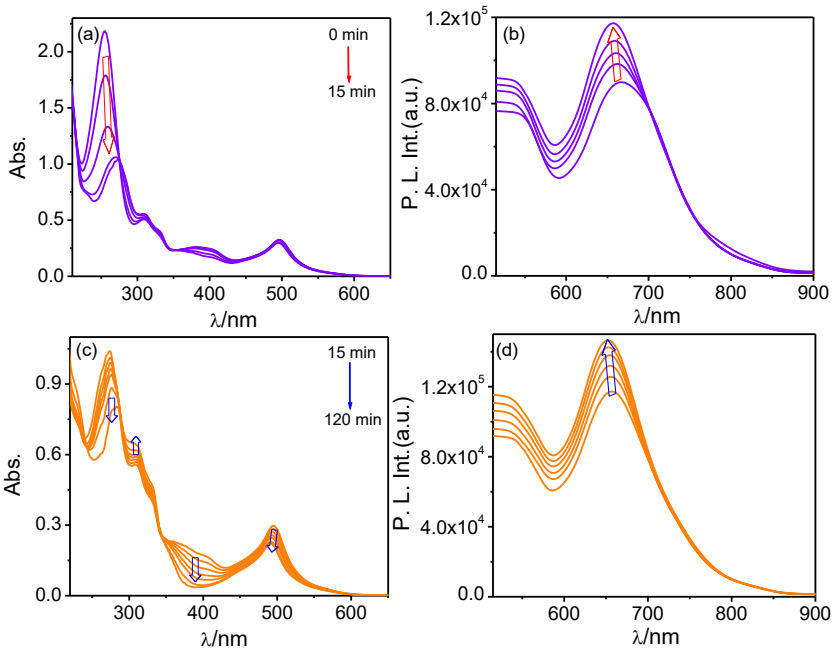

Figure 6.26. Two-step changes in the absorption (a and c) and emission (b and d) spectral profiles of the reduced forms of **1** upon irradiation with 500 nm light.

and ILCT bands within the range of 300-800 nm is almost negligible in the first step. The MLCT band intensity decreases with a slight blue-shift, while a sharp decrease in intensity of the ILCT band is noticed during second stage of photolysis. Detailed spectral analysis reveals that the final absorption spectra closely resemble that observed in the isomerization process in the absence of the reducing agent. This observation suggests that light irradiation on the reduced form of the complexes results in the formation of the [M(II)-*t*-*c*-M(II)]$^{4+}$ species [M(II)= Ru(II) and Os(II)]. The photostationary state is reached within ~120-240 min, which is nearly three times faster than that of their free forms. Upon light irradiation, the emission intensity gradually increases for **1**, accompanied with a minor blue-shift (~5 nm) during the first step, wherein an isoemissive point is also evident in the spectral profile. In the second step, the emission intensity undergoes a further increase, along with an

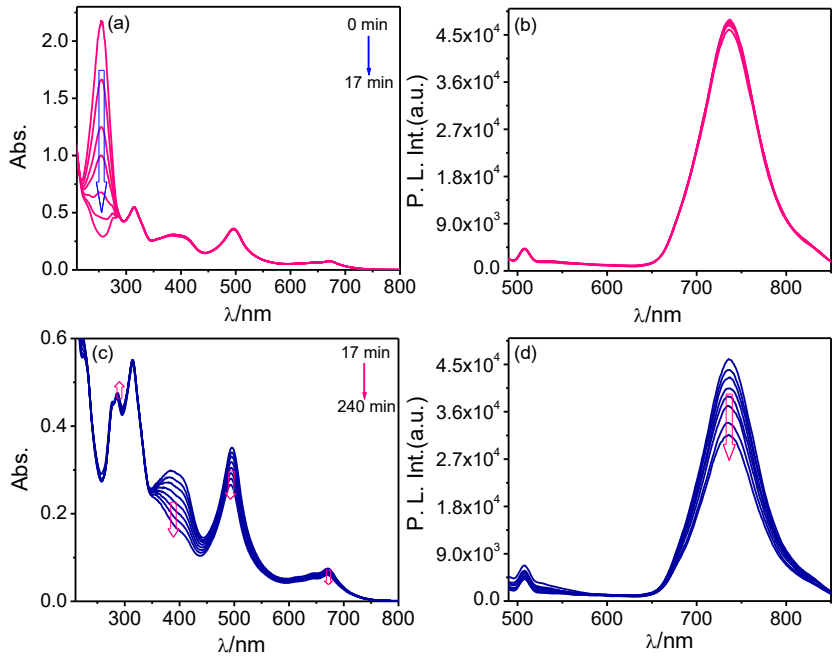

Figure 6.27. Two-step changes in the absorption (a and c) and emission (b and d) spectral profiles of the reduced forms of **2** upon irradiation with 500 nm light.

additional blue shift of ~5 nm. In case of **2**, the emission intensity remains unchanged in the first step, while the intensity of the ^{3}MLCT emission band gradually decreases in the second step without alteration of its emission maximum. In contrast, no significant spectral changes were observed when the Na-treated solutions of the complexes were kept in the dark for more than 24 h.

Thus, the observed changes in the absorption and emission spectra clearly indicates that the reduced terpyridine units rapidly revert back to their initial form along with transformation from *t-t* to *t-c* isomers upon light irradiation on the reduced form of the complexes. We have also calculated the rate constant (k_{iso}) and quantum yield ($\Phi_{tt\rightarrow tc}$) of the isomerization process by employing their absorption titration profiles (Figure 6.28 and Table 6.7). The estimated k_{iso} value is 6.4×10^{-4} for **1** and 1.9×10^{-4} for **2**, while the $\Phi_{tt\rightarrow tc}$ value is 1.2×10^{-2} and 3.8×10^{-3} for **1** and **2**, respectively. The observed values also indicate a much faster isomerization rate of the reduced form of the complexes compared to their non-reduced counterparts. Reduction of the complexes decreases their overall charge, leading to reduced solvation in polar solvents like MeCN. Consequently, the effective rotor volume of the complexes decreases, thereby enhancing the rotational flexibility of molecular fragments across the double bond and accelerating the isomerization process.

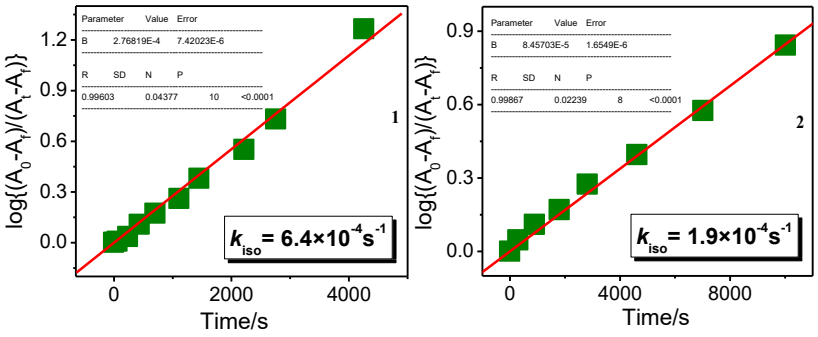

Figure 6.28. Linear plot of log $(A_0-A_f)/(A_t-A_f)$ *vs*. time (t) for absorption spectral changes upon irradiation of the Na-treated solution in MeCN with 500 nm light for **1** and **2**.

Previously, we have observed anion-induced deprotonation of the methylene protons from the molecular backbone of the complexes. Now, we are interested to explore the isomerization behavior of both complexes in presence of F^-. For this purpose, the F^- saturated solution of both **1** and **2** in MeCN are irradiated with 500 nm light and the changes are monitored through absorption and emission spectroscopy (Figure 6.29). Both complexes display a single step change in their spectral profiles. In case of absorption, all the spectral lines pass through one isosbestic point at ~330 nm. The MLCT band

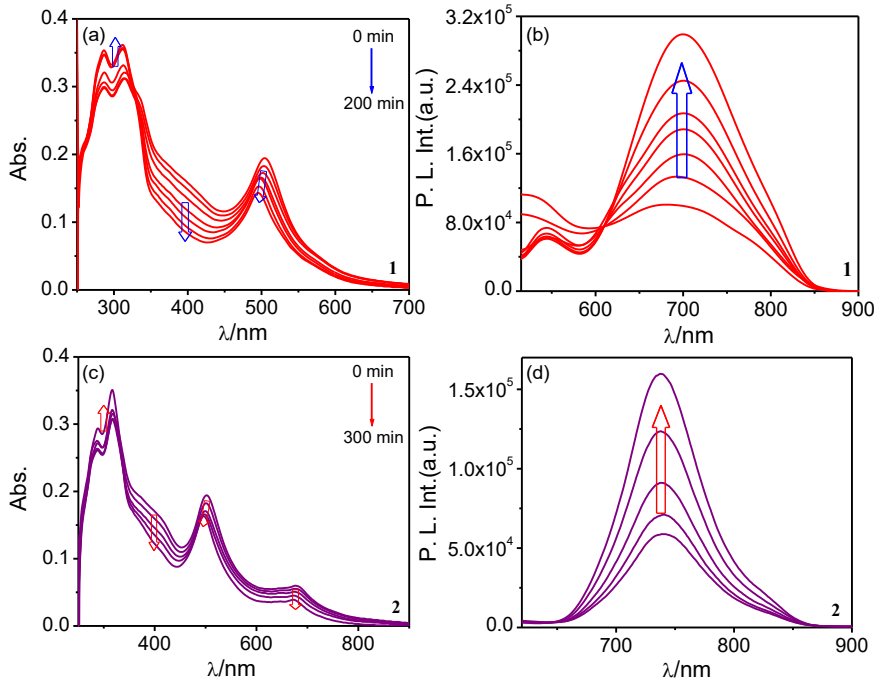

Figure 6.29. Absorption and emission (λ_{ex} =495 nm) spectral changes of the deprotonated forms of **1** (a and b, respectively) and **2** (c and d, respectively) in MeCN upon irradiation with 500 nm light.

intensities decrease with a small hypsochromic shift. The ILCT bands also decrease in intensity with the extent of shift being more marked relative to the MLCT bands. By contrast, a rise in intensity of the π-π* bands in the UV region is also noticed upon irradiation with light. The time to reach the photostationary state is ~200 min for **1** and ~300 min for **2** in their deprotonated states, which are again much faster compared to that of their initial forms. The final spectra probably correspond to the *t-c* forms in their deprotonated states. The broad emission band, on the other hand, gets intensified and ends up with a band having its maximum at ~680 nm for **1**. For **2**, the quenched emission band at ~735 nm also shows an increase in its intensity upon light irradiation. Despite, the actual reason behind this increase in emission intensity is not very clear to us, we surmise that deprotonation of the methylene proton(s) leads to a decrease in the overall charge of the complex. During the course of *trans-cis* isomerization, one of the two $Os(tpy)_2$ units in the complex backbone rotates across the double bond(s), bringing the two units into a closer proximity. This sort of spatial closeness among the two units appears to be more favorable in the deprotonated form of the complex relative to its protonated counterpart, likely due to reduced electrostatic repulsion as a result of the decreased overall charge. We surmise that this sort of close proximity in the deprotonated form stabilizes the ^{3}MLCT state, which in turn leads to increase in emission intensity, although no direct experimental proof could be provided. Moreover, since the emission maximum and overall spectral features remain largely unchanged during the isomerization process, the involvement or mixing of other excited states with the ^{3}MLCT state is quite unlikely.

We have also evaluated the rate constant and quantum yield of isomerization of the deprotonated complexes (Figure 6.30 and Table 6.7). k_{iso} values vary within the range of 2.9-1.4×10^{-4} s^{-1} and Φ values are found to be 7.2×10^{-3} and 2.7×10^{-3} for **1** and **2**, respectively. As the removal of the methylene proton(s) reduces the overall charge, the extent of solvation is reduced in the polar solvents such as MeCN. The lesser solvation, in turn, leads to a decrease in the effective rotor volume of the complexes, thereby enhancing the rotational flexibility of the groups across the double bond and facilitating the isomerization process.

Thus, both complexes exhibit emission switching behavior in response to multiple external stimuli, including light, oxidizing agents, reducing agents, and anions. Notably, the rate of photoisomerization is significantly accelerated in presence of these stimuli. This enhanced responsiveness suggests that these complexes serve as highly efficient building

blocks for the development of multi-stimuli-responsive molecular photoswitches, operating across a broad spectral range from the visible to the near-infrared (NIR) region.

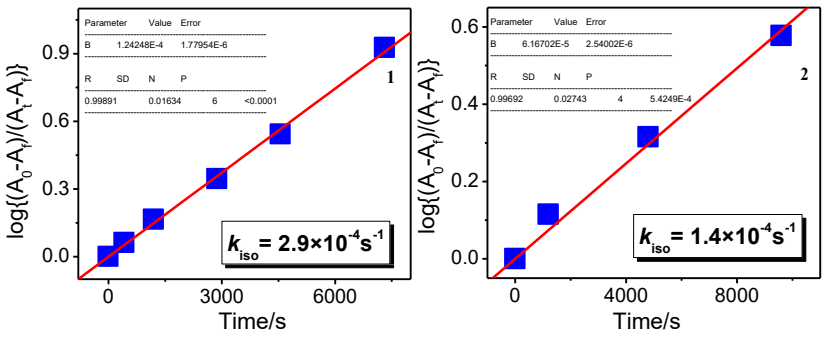

Figure 6.30. Linear plot of log $(A_0-A_f)/(A_t-A_f)$ *vs*. time (t) for absorption spectral changes upon irradiation of the F^- saturated solution in MeCN with 500 nm light for **1** and **2**.

6.4. Conclusions

In pursuit of developing multi-stimuli-responsive molecular photoswitches operating across a broad spectral domain, we have designed herein two symmetrical bimetallic complexes of the type $[(tpy\text{-}PhCH_2PPh_3Br)_2M_2(tpvpvpt)](PF_6)_4$, [where M=Ru(II) or Os(II)], featuring a bis-terpyridine bridging ligand (tpvpvpt) possessing two consecutive stilbene units. Detailed investigations on their photophysical and electrochemical properties were conducted in the presence of various external stimuli, including light, anions, oxidizing agents, and reducing agents. The presence of acidic methylene protons renders the complexes responsive to anions such as F^-, OH^- and OAc^-. Furthermore, the incorporation of two consecutive stilbene units enables reversible *trans-trans* to *trans-cis* photoisomerization upon alternate irradiation with visible and UV light. Additionally, the influence of oxidizing agents, reducing agents, and anionic guests on the isomerization behavior was systematically examined, revealing a substantial enhancement in the photoisomerization rate under all three conditions. Thus, these complexes facilitate rapid and efficient multi-stimuli-responsive emission switching within the visible to NIR spectral region. By judicious selection of appropriate chemical oxidants, reductants, anionic species and light of specific wavelength, precise control over the emission spectral behavior can be achieved. Consequently, these complexes hold significant potential as molecular building blocks for the fabrication of advanced molecular devices and functional photonic materials.

6.5. References

(1) McConnell, A. J.; Wood, C. S.; Neelakandan, P. P.; Nitschke, J. R. Stimuli-Responsive Metal-Ligand Assemblies. *Chem. Rev.* **2015**, *115*, 7729-7793.

(2) Li, Q. Intelligent Stimuli-Responsive Materials: From Well-Defined Nanostructures to Applications. Ed. Wiley: Hoboken, NJ, 2013.

(3) Martinez-Manez, R.; Sancenon, F. Fluorogenic and Chromogenic Chemosensors and Reagents for Anions. *Chem. Rev.* **2003**, *103*, 4419-4476.

(4) de Silva, A. P.; Gunaratne, H. Q. N.; Gunnlaugsson, T.; Huxley, A. J. M.; McCoy, C. P.; Rademacher, J. T.; Rice, T. E. Signaling Recognition Events with Fluorescent Sensors and Switches. *Chem. Rev.* **1997**, *97*, 1515-1566.

(5) Kurihara, M.; Nishihara, H. Azo- and Quinone-Conjugated Redox Complexes-Photo- and Proton-Coupled Intramolecular Reactions Based on d-π Interaction. *Coord. Chem. Rev.* **2002**, *226*, 125-135.

(6) Ko, C. C.; Yam, V. W. W. Coordination Compounds with Photochromic Ligands: Ready Tunability and Visible Light-Sensitized Photochromism. *Acc. Chem. Res.* **2018**, *51*, 149-159.

(7) Cui, B.-B.; Zhong, Y.-W.; Yao, J. Three-State Near-Infrared Electrochromism at the Molecular Scale. *J. Am. Chem. Soc.* **2015**, *137*, 4058-4061.

(8) Jia, C.; Wang, J.; Yao, C.; Cao, Y.; Zhong, Y.; Liu, Z.; Liu, Z.; Guo, X. Conductance Switching and Mechanisms in Single-Molecule Junctions. *Angew. Chem., Int. Ed.* **2013**, *52*, 8666-8670.

(9) Haga, M.; Ali, M. M.; Maegawa, H.; Nozaki, K.; Yoshimura, A.; Ohno, T. Photoexcited States of Dinuclear Ru Complexes Bridged by Proton-Dissociable Benzimidazole Derivatives. *Coord. Chem. Rev.* **1994**, *132*, 99-104.

(10) Motoyama, D.; Yoshikawa, K.; Ozawa, H.; Tadokoro, M.; Haga, M. Energy-Storage Applications for a pH Gradient between Two Benzimidazole-Ligated Ruthenium Complexes That Engage in Proton-Coupled Electron-Transfer Reactions in Solution. *Inorg. Chem.* **2017**, *56*, 6419-6428.

(11) Huynh, M. H. V.; Meyer, T. J. Proton-Coupled Electron Transfer. *Chem. Rev.* **2007**, *107*, 5004-5064.

(12) Coskun, A.; Banaszak, M.; Astumian, R. D.; Stoddart, J. F.; Grzybowski, B. A. Great Expectations: Can Artificial Molecular Machines Deliver on Their Promise? *Chem. Soc. Rev.* **2012**, *41*, 19-30.

(13) Benito, Q.; Goff, X. F. L.; Maron, S.; Fargues, A.; Garcia, A.; Martineau, C.; Taulelle, F.; Kahlal, S.; Gacoin, T.; Boilot, J.-P.; Perruchas, S. Polymorphic Copper Iodide Clusters: Insights into the Mechanochromic Luminescence Properties. *J. Am. Chem. Soc.* **2014**,*136*, 11311-11320.

(14) Lin, Z. H.; Mei, X. F.; Yang, E.; Li, X. J.; Yao, H. M.; Wen, G. X.; Chen, C. T.; Chow, T. J.; Ling, Q. D. Polymorphism-Dependent Fluorescence of Bisthienylmaleimide with Different Responses to Mechanical Crushing and Grinding Pressure. *CrystEngComm.* **2014**, *16*, 11018-11026.

(15) Wang, L.; Wang, K.; Zhang, H. Y.; Jiao, C. J.; Zou, B.; Ye, K. Q.; Zhang, H. Y.; Wang, Y. The Facile Realization of RGB Luminescence Based on One Yellow Emissive Four-Coordinate Organoboron Material. *Chem. Commun.* **2015**, *51*, 7701-7704.

(16) Dong, Y. J.; Zhang, J. B.; Tan, X.; Wang, L. J.; Chen, J. L.; Li, B.; Ye, L.; Xu, B.; Zou, B.; Tian, W. J. Multi-Stimuli Responsive Fluorescence Switching: The Reversible Piezochromism and Protonation Effect of a Divinylanthracene Derivative. *J. Mater. Chem. C* **2013**, *1*, 7554-7559.

(17) Yoon, S. J.; Chung, J. W.; Gierschner, J.; Kim, K. S.; Choi, M. G.; Kim, D.; Park, S. Y. Multi-Stimuli Two-Color Luminescence Switching via Different Slip-Stacking of Highly Fluorescent Molecular Sheets. *J.Am. Chem. Soc.* **2010**, *132*, 13675-13683.

(18) Brieke, C.; Rohrbach, F.; Gottschalk, A.; Mayer, G.; Heckel, A. Light-Controlled Tools. *Angew. Chem., Int. Ed.* **2012**, *51* (34), 8446-8476.

(19) Ankenbruck, N.; Courtney, T.; Naro, Y.; Deiters, A. Optochemical Control of Biological Processes in Cells and Animals. *Angew. Chem., Int. Ed.* **2018**, *57* (11), 2768-2798.

(20) Dou, C.; Han, L.; Zhao, S.; Zhang, H.; Wang, Y. Multi-Stimuli-Responsive Fluorescence Switching of a Donor-Acceptor π-Conjugated Compound. *J. Phys. Chem. Lett.* **2011**, *2*, 666-670.

(21) Xiong, J.; Wang, K.; Yao, Z.; Zou, B.; Xu, J.; Bu, X.-H. Multi-Stimuli-Responsive Fluorescence Switching from a Pyridine-Functionalized Tetraphenylethene AIEgen. *ACS Appl. Mater. Interfaces* **2018**, *10*, 5819-5827.

(22) Guragain, S.; Bastakoti, B. P.; Malgras, V.; Nakashima, K.; Yamauchi, Y. Multi-Stimuli-Responsive Polymeric Materials. *Chem. Eur. J.* **2015**, *21*, 13164-13174.

(23) Martinic, I.; Eliseeva, S. V.; Nguyen, T. N.; Pecoraro, V. L.; Petoud, S. Near-Infrared Optical Imaging of Necrotic Cells by Photostable Lanthanide-Based Metallacrowns. *J. Am. Chem. Soc.* **2017**, *139*, 8388-8391.

(24) Kayanuma, M.; Gindensperger, E.; Daniel, C. Inorganic Photoisomerization: The Case Study of Rhenium(I) Complexes. *Dalton Trans.* **2012**, *41*, 13191-13203.

(25) Kayanuma, M.; Daniel, C.; Koppel, H.; Gindensperger, E. Photophysics of Isomerizable Re(I) Complexes: A Theoretical Analysis. *Coord. Chem. Rev.* **2011**, *255* (21-22), 2693-2703.

(26) Ko, C.-C.; Yam, V. W.-W. Transition Metal Complexes with Photochromic Ligands-Photosensitization and Photoswitchable Properties. *J. Mater. Chem.* **2010**, *20*, 2063-2070.

(27) Ko, C.-C.; Wu, L.-X.; Wong, K. M.-C.; Zhu, N.; Yam, V. W.-W. Synthesis, Characterization and Photochromic Studies of Spirooxazine-Containing 2,2′-Bipyridine Ligands and their Rhenium(i) Tricarbonyl Complexes. *Chem.-Eur. J.* **2004**, *10*, 766-776.

(28) Kume, S.; Nishihara, H. Metal-Based Photoswitches Derived from Photoisomerization. *Struct. Bonding* **2007**, *123*, 79-112.

(29) Dietrich, J.; Thorenz, U.; Förster, C.; Heinze, K. Effects of Sequence, Connectivity, and Counter Ions in New Amide-Linked Ru(tpy)$_2$-Re(bpy) Chromophores on Redox Chemistry and Photophysics. *Inorg. Chem.* **2013**, *52*, 1248-1264.

(30) Kreitner, C.; Erdmann, E.; Seidel, W. W.; Heinze, K. Understanding the Excited State Behavior of Cyclometalated Bis(tridentate)ruthenium(II) Complexes: A Combined Experimental and Theoretical Study. *Inorg. Chem.* **2015**, *54*, 11088-11104.

(31) Kreitner, C.; Heinze, K. Excited State Decay of Cyclometalated Polypyridine Ruthenium Complexes: Insight from Theory and Experiment. *Dalton Trans.* **2016**, *45*, 13631-13647.

(32) Passalacqua, R.; Loiseau, F.; Campagna, S.; Fang, Y.-Q.; Hanan, G. S. In Search of Ruthenium(II) Complexes Based on Tridentate Polypyridine Ligands that Feature Long-Lived Room-Temperature Luminescence: The Multichromophore Approach. *Angew. Chem. Int. Ed.* **2003**, *42*, 1608-1611.

(33) Medlycott, E. A.; Hanan, G. S. Synthesis and Properties of Mono- and Oligo-Nuclear Ru(II) Complexes of Tridentate Ligands: The Quest for Long-Lived Excited States at Room Temperature. *Coord. Chem. Rev.* **2006**, *250*, 1763-1782.

(34) Rupp, M. T.; Shevchenko, N.; Hanan, G. S.; Kurth, D. G. Enhancing the Photophysical Properties of Ru(II) Complexes by Specific Design of Tridentate Ligands. *Coord. Chem. Rev.* **2021**, *446*, 214127.

(35) Alstrum-Acevedo, J. H.; Brennaman, M. K.; Meyer, T. J. Chemical Approaches to Artificial Photosynthesis 2. *Inorg. Chem.* **2005**, *44*, 6802-6827.

(36) Evans, R. C.; Douglas, P.; Winscom, C. J. Coordination Complexes Exhibiting Room-Temperature Phosphorescence: Evaluation of their Suitability as Triplet Emitters in Organic Light Emitting Diodes. *Coord. Chem. Rev.* **2006**, *250*, 2093-2126.

(37) Campagna, S.; Puntoriero, F.; Nastasi, F.; Bergamini, G.; Balzani, V. In Photoche mistry and Photophysics of Coordination Compounds I; Balzani, V.; Campagna, S., Eds.; *Top. Curr. Chem.* **2007**, *280*, 117-214.

(38) Yersin, H.; Rausch, A. F.; Czerwieniec, R.; Hofbeck, T.; Fischer, T. The Triplet State of Organo-Transition Metal Compounds. Triplet Harvesting and Singlet Harvesting for Efficient OLEDs. *Coord. Chem. Rev.* **2011**, *255*, 2622-2652.

(39) Hardy, J. G. Metallosupramolecular Grid Complexes: Towards Nanostructured Materials with High-Tech Applications. *Chem. Soc. Rev.* **2013**, *42*, 7881-7899.

(40) Zhang, K. Y.; Liu, S.; Zhao, Q.; Huang, W. Stimuli-Responsive Metallopolymers. *Coord. Chem. Rev.* **2016**, *319*, 180-195.

(41) Bar, M.; Deb, S.; Paul, A.; Baitalik, S. Stimuli-Responsive Luminescent Bis-Tridentate Ru(II) Complexes toward the Design of Functional Materials. *Inorg. Chem.* **2018**, *57*, 12010-12024.

(42) Bar, M.; Pal, P.; Maity, D.; Baitalik, S. Heterobimetallic Ru-Os Complexes Function as Multichannel Sensors for Selected Anions by Taking Profit of Metal-Ligand Interaction. *Sens. Actuators B: Chem.* **2018**, *266*, 493-505.

(43) Wu, S.-H.; Burkhardt, S. E.; Zhong, Y.-W.; Abruña, H. D. Cyclometalated Ruthenium Oligomers with 2,3-Di(2-Pyridyl)-5,6-Diphenylpyrazine: A Combined Experimental, Computational, and Comparison Study with Non-cyclometalated Analogous. *Inorg. Chem.* **2012**, *51*, 13312-13320.

(44) Yang, W.-W.; Zhong, Y.-W.; Yoshikawa, S.; Shao, J.-Y.; Masaoka, S.; Sakai, K.; Yao, J.; Haga, Masa-aki. Tuning of Redox Potentials by Introducing a Cyclometalated Bond to Bis-tridentate Ruthenium(II) Complexes Bearing Bis(N-methylbenzimidazolyl)benzene or -pyridine Ligand. *Inorg. Chem.* **2012**, *51*, 890-899.

(45) Yao, C.-J.; Zhong, Y.-W.; Nie, H.-J.; Abruña, H. D.; Yao, J. Near-IR Electrochromism in Electropolymerized Films of a Biscyclometalated Ruthenium Complex Bridged by 1,2,4,5-Tetra(2-pyridyl)benzene. *J. Am. Chem. Soc.* **2011**, *133*, 20720-20723.

(46) Wang, H.; Shao, J.-Y.; Duan, R.; Wang, K.-Z. Zhong, Y.-W. Synthesis and Electronic Coupling Studies of Cyclometalated Diruthenium Complexes Bridged by 3,3',5,5'-Tetrakis(benzimidazol-2-yl)-Biphenyl. *Dalton Trans.* **2021**, *50*, 4219-4230.

(47) Shao, J.-Y.; Yang, W.-W.; Yao, J.; Zhong, Y.-W. Biscyclometalated Ruthenium Complexes Bridged by 3,3′,5,5′-Tetrakis(N-methylbenzimidazol-2-yl)biphenyl: Synthesis and Spectroscopic and Electronic Coupling Studies. *Inorg. Chem.* **2012**, *51*, 4343-4351.

(48) Juris, A.; Balzani, V.; Barigelletti, F.; Campagna, S.; Beleser, P.; Zelewsky, A. V. Ru(II) Polypyridine Complexes: Photophysics, Photochemistry, Eletrochemistry, and Chemiluminescence. *Coord. Chem. Rev*. **1988***, 84,* 85-277.

(49) Balzani, V.; Juris, A.; Venturi, M.; Campagna, S.; Serroni, S. Luminescent and Redox-Active Polynuclear Transition Metal Complexes. *Chem. Rev*. **1996**, *96*, 759-834.

(50) Sauvage, J.-P.; Collin, J. P. J.; Chambron, C.; Guillerez, S.; Coudret, C.; Balzani, V.; Barigelletti, F.; de Cola, L.; Flamigni, L. Ruthenium(II) and Osmium(II) Bis(Terpyridine) Complexes in Covalently-Linked Multicomponent Systems: Synthesis, Electrochemical Behavior, Absorption Spectra, and Photochemical and Photophysical Properties. *Chem. Rev*. **1994**, *94*, 993-1019.

(51) Browne, W. R.; O'Boyle, N. M.; McGarvey, J. J.; Vos, J. G. Elucidating Excited State Electronic Structure and Intercomponent Interactions in Multicomponent and Supramolecular Systems. *Chem. Soc. Rev.* **2005**, *34*, 641-663.

(52) Steinke, S. J.; Gupta, S.; Piechota, E. J.; Moore, C. E.; Kodanko, J. J.; Turro, C. Photocytotoxicity and Photoinduced Phosphine Ligand Exchange in a Ru(II) Polypyridyl Complex. *Chem. Sci.* **2022**, *13*, 7, 1933-1945.

(53) Paul, A.; Sahoo, A.; Bhattacharya, S.; Baitalik, S. Anion and Temperature Responsive Molecular Switches Based on Trimetallic Complexes of Ru(II) and Os(II) That Demonstrate Advanced Boolean and Fuzzy Logic Functions. *Inorg. Chem.* **2022**, *61*, 3186-3201.

(54) Das, S.; Pal, P.; Biswas, R.; Baitalik, S. Design of Near-Infrared Emissive Molecular Switches Based on Stilbene-Appended Cyclometalated Bimetallic Ru(II)-Terpyridine Complexes. *Inorg. Chem.* **2024**, *63*, 23725-23741.

(55) Pal, P.; Ganguly, T.; Sahoo, A.; Baitalik, S. Emission Switching in the Near-Infrared by Reversible Trans-Cis Photoisomerization of Styrylbenzene-Conjugated Osmium Terpyridine Complexes. *Inorg. Chem.* **2021**, *60*, 4869-4882.

(56) Das, S.; Karmakar, S.; Saha, D.; Baitalik, S. A Combined Experimental and DFT/TD-DFT Investigation of Structural, Electronic, and Cation-Induced Switching of Photophysical Properties of Bimetallic Ru(II) and Os(II) Complexes Derived from Imidazole-4,5-Dicarboxylic Acid and 2,2′-Bipyridine. *Inorg. Chem.* **2013**, *52*, 6860-6879.

(57) Bandara, H. M. D.; Burdette, S. C. Photoisomerization in Different Classes of Azobenzene. *Chem. Soc. Rev.* **2012**, *41*, 1809-1825.

(58) Yutaka, T.; Mori, I.; Kurihara, M.; Mizutani, J.; Tamai, N.; Kawai, T.; Irie, M.; Nishihara, H. Photoluminescence Switching of Azobenzene-Conjugated Pt(II) Terpyridine Complexes by Trans-Cis Photoisomerization. *Inorg. Chem.* **2002**, *41*, 7143-7150.

(59) Yutaka, T.; Kurihara, M.; Kubo, K.; Nishihara, H. Novel Photoisomerization Behavior of Rh Binuclear Complexes Involving an Azobenzene-Bridged Bis(Terpyridine) Ligand. Strong Effects of Counter-Ion and Solvent and the Induction of Redox Potential Shift. *Inorg. Chem.* **2000**, *39*, 3438-3439.

(60) Yutaka, T.; Mori, I.; Kurihara, M.; Mizutani, J.; Kubo, K.; Furusho, S.; Matsumura, K.; Tamai, N.; Nishihara, H. Synthesis, Characterization, and Photochemical Properties of Azobenzene-Conjugated Ru(II) and Rh(III) Bis(Terpyridine) Complexes. *Inorg. Chem.* **2001**, *40*, 4986-4995.

(61) Amaral, R. C.; Iha, N. Y. M. Molecular Engineered Rhenium(I) Carbonyl Complexes to Promote Photoisomerization of Coordinated Stilbene-Like Ligands in the Visible Region. *Dalton Trans.* **2018**, *47*, 13081-13087.

(62) Zanoni, K. P. S.; Iha, N. Y. M. Reversible Trans ⇌ Cis Photoisomerizations of $[Re(CO)_3(Ph_2phen)(StpyCN)]^+$ Towards Molecular Machines. *Dalton Trans.* **2017**, *46*, 9951-9958.

(63) Amaral, R. C.; Matos, L. S.; Zanoni, K. P. S.; Iha, N. Y. M. Photoreversible Molecular Motion of stpyCN Coordinated to fac-$[Re(CO)_3(NN)]^+$ Complexes. *J. Phys. Chem. A* **2018**, *122*, 6071-6080.

(64) Ganguly, T.; Pal, P.; Maity, D.; Baitalik, S. Synthesis, Characterization and Emission Switching Behaviors of Styrylphenyl-Conjugated Ru(II)-Terpyridine Complexes via Aggregation and Trans-Cis Photoisomerization. *J. Photochem. Photobiol. A* **2023**, *440*, 114662.

(65) Gindensperger, E.; Koppel, H.; Daniel, C. Mechanism of Visible-Light Photoisomerization of a Rhenium(I) Carbonyl-Diimine Complex. *Chem. Commun.* **2009**, *46*, 8225.

(66) Irie, M.; Yokoyama, Y. Diarylethenes for Memories and Switches. *Chem. Rev.* **2000**, *100* (5), 1685-1716.

(67) Irie, M.; Fukaminato, T.; Matsuda, K.; Kobatake, S. Photochromism of Diarylethene Molecules and Crystals: Memories, Switches, and Actuators. *Chem. Rev.* **2014**, *114*, 12174-12277.

(68) Ganguly, T.; Abedin, T.; Maity, D.; Baitalik, S. Remarkable Increase in the Rate of Trans-Cis Photoisomerization of Os(II)-Terpyridine Complexes via Oxidation and Reduction. *Inorg. Chem.* **2025**, *64*, 4415-4430.

(69) Brown, D. G.; Sanguantrakun, N.; Schulze, B.; Schubert, U. S.; Berlinguette, C. P. Bis(Tridentate) Ruthenium-Terpyridine Complexes Featuring Microsecond Excited-State Lifetimes. *J. Am. Chem. Soc.* **2012**, *134*, 12354-12357.

(70) Hofmeier, H.; Schubert, U. S. Recent Developments in the Supramolecular Chemistry of Terpyridine-Metal Complexes. *Chem. Soc. Rev.* **2004**, *33*, 373-399.

(71) Argazzi, R.; Larramona, G.; Contado, C.; Bignozzi, C. A. Preparation and Photoelectrochemical Characterization of a Red Sensitive Osmium Complex Containing 4,4’,4’’-Tricarboxy2,2’:6’,2’’-Terpyridine and Cyanide Ligands. *J. Photochem. Photobiol. A* **2004**, *164*, 15-21.

(72) Altobello, S.; Argazzi, R.; Caramori, S.; Contado, C.; Fre, S.; Rubino, P.; Chone, C.; Larramona, G.; Bignozzi, C. A. Sensitization of Nanocrystalline TiO_2 with Black Absorbers Based on Os and Ru Polypyridine Complexes. *J. Am. Chem. Soc.* **2005**, *127*, 15342-15343.

(73) Wu, K. L.; Ho, S. T.; Chou, C. C.; Chang, Y. C.; Pan, H. A.; Chi, Y.; Chou, P. T. Engineering of Osmium(II)-Based Light Absorbers for Dye-Sensitized Solar Cells. *Angew. Chem. Int. Ed.* **2012**, *51*, 5642-5646.

(74) Ronca, E.; Angelis, F.; Fantacci, S. Time-Dependent Density Functional Theory Modeling of Spin-Orbit Coupling in Ruthenium and Osmium Solar Cell Sensitizers. *J. Phys. Chem. C* **2014**, *118*, 17067-7078.

(75) Fantacci, S.; Ronca, E.; Angelis, F. Impact of Spin-Orbit Coupling on Photocurrent Generation in Ruthenium Dye-Sensitized Solar Cells. *J. Phys. Chem. Lett.* **2014**, *5*, 375-380.

(76) Juwita, R.; Liao, J. M.; Chen, C. Y.; Tsai, H. H. G. Enhancing Near-Infrared Absorption in Terpyridyl Ru/Os Complexes with Ancillary Ligands to Activate Spin-Forbidden Transitions in Dye-Sensitized Solar Cells: A TDDFT Investigation. *J. Phys. Chem. A* **2024**, *128*, 880-894.

(77) Kinoshita, T.; Fujisawa, J.; Nakazaki, J.; Uchida, S.; Kubo, T.; Segawa, H. Enhancement of Near-IR Photoelectric Conversion in Dye-Sensitized Solar Cells Using an Osmium Sensitizer with Strong Spin-Forbidden Transition. *J. Phys. Chem. Lett.* **2012**, *3*, 394-398.

(78) Zhang, X.; Canton, S. E.; Smolentsev, G.; Wallentin, C. J.; Liu, Y.; Kong, Q.; Attenkofer, K.; Stickrath, A. B.; Mara, M. W.; Chen, L. X. Highly Accurate Excited-State Structure of $[Os(bpy)_2dcbpy]^{2+}$ Determined by X-ray Transient Absorption Spectroscopy. *J. Am. Chem. Soc.* **2014**, *136*, 8804-8809.

(79) Das, S.; Bar, M.; Ganguly, T.; Baitalik, S. Control of Photoisomerization Kinetics via Multistage Switching in Bimetallic Ru(II)-Terpyridine Complexes. *Inorg. Chem.* **2024**, *63*, 6600-6615.

(80) Pal, P.; Mukherjee, S.; Maity, D.; Baitalik, S. Synthesis, Structural Characterization, and Luminescence Switching of Diarylethene-Conjugated Ru(II)-Terpyridine Complexes by Trans-Cis Photoisomerization: Experimental and DFT/TD-DFT Investigation. *Inorg. Chem.* **2018**, *57*, 5743-5753.

(81) Pal, P.; Ganguly, T.; Maity, D.; Baitalik, S. Experimental and Theoretical Exploration of Photophysics and Trans-Cis Photoisomerization of Styrylbenzene Conjugated Terpyridine Complexes of Ru(II): Strong Effect of Deprotonation from Second Coordination Sphere. *J. Photochem. Photobiol. A* **2020**, *392*, 112409.

(82) Bhattacharya, S.; Pal, P.; Baitalik, S. Design of Molecular Sensors and Switches Based on Luminescent Ruthenium-Terpyridine Complexes Bearing Active Methylene and Triphenylphosphonium Motifs as Anion Recognition Sites: Experimental and DFT/TD-DFT Investigation. *Dalton Trans.* **2024**, *53*, 1307-1321.

(83) Bhattacharya, S.; Pal, P.; Gorain, S.; Baitalik, S. Enhancing Near-Infrared Absorption in Osmium(II) Complexes Under the Cumulative Influence of Terpyridine Ligand and Anions: Combined Experimental and DFT/TD DFT Investigation. *Eur. J. Inorg. Chem.* **2024**, e202400758.

(84) Agarwalla, H.; Jana, K.; Maity, A.; Kesharwani, M. K.; Ganguly, B.; Das, A. Hydrogen Bonding Interaction between Active Methylene Hydrogen Atoms and an Anion as a Binding Motif for Anion Recognition: Experimental Studies and Theoretical Rationalization. *J. Phys. Chem. A* **2014**, *118*, 2656-2666.

(85) Bhaumik, C.; Das, S.; Saha, D.; Dutta, S.; Baitalik, S. Synthesis, Characterization, Photophysical, and Anion-Binding Studies of Luminescent Heteroleptic Bis-Tridentate Ruthenium(II) Complexes Based on 2,6-Bis(Benzimidazole-2-yl)Pyridine and 4′-Substituted 2,2′:6′,2″ Terpyridine Derivatives. *Inorg. Chem.* **2010**, *49*, 5049-5062.

(86) Wang, X.-Y.; Del Guerzo, A.; Tunuguntla, H.; Schmehl, R. H. Photophysical Behavior of Ru(II) and Os(II) Terpyridyl Phenylene Vinylene Complexes: Perturbation of MLCT State by Intra-Ligand Charge-Transfer State. *Res. Chem. Intermed.* **2007**, *33*, 63-77.

(87) Wang, X. Y.; Guerzo, A.; Schmehl, R. H. Preferential Solvation of an ILCT Excited State in Bis(Terpyridine-Phenylene-Vinylene) Zn(II) Complexes. *Chem. Commum.* 2002, 2344-2345.

(88) Baitalik, S.; Wang, X.-Y.; Schmehl, R. H. A Trimetallic Mixed Ru(II)/Fe(II) Terpyridyl Complex with a Long-Lived Excited State in Solution at Room Temperature. *J. Am. Chem. Soc.* **2004**, *126*, 16304-16305.

(89) Schneider, H.-J.; Yatsimirsky, A. Principles and Methods in Supramolecular Chemistry. John Wiley & Sons, England, 2000, pp. p.142.

(90) Mo, H-J.; Wu, J-J.; Qiao, Z-P.; Ye, B-H. Interaction Between Biimidazole Complexes of Ruthenium and Acetate Hydrogen Bonding and Proton Transfer. Dalton Trans. 2012, 41, 7026-7036.Powell, B. J. Theories of Phosphorescence in Organo-Transition Metal Complexes from Relativistic Effects to Simple Models and Design Principles for Organic Light-Emitting Diodes. *Coord. Chem. Rev.* **2015**, *295*, 46-79.

(91) Berger, R. M.; McMillin, D. R. Localized States in Reduced and Excited-State Ruthenium(II) Terpyridyls. *Inorg. Chem.* **1988**, *27*, 23.

(92) Patoux, C.; Launay, J.-P.; Beley, M.; Chodorowski-Kimmes, S.; Collin, J.-P.; James, S.; Sauvage, J.-P. Long-Range Electronic Coupling in Bis(cyclometalated) Ruthenium Complexes. *J. Am. Chem. Soc.* **1998**, *120*, 3717-3725.

List of Publications

1. **Das, S.**; Biswas, R.; Baitalik, S. Multistimuli-Responsive Molecular Photoswitches Based on Bimetallic Ru(II) and Os(II) Terpyridine Complexes. *Inorg. Chem.* **2025**, *64*, 16361-16377.

2. **Das, S.**; Pal, P.; Biswas, R.; Baitalik, S. Design of Near-Infrared Emissive Molecular Switches Based on Stilbene-Appended Cyclometalated Bimetallic Ru(II)-Terpyridine Complexes. *Inorg. Chem.* **2024**, *63*, 23725-23741.

3. **Das, S.**; Sahoo, A.; Baitalik, S. Advancing Molecular-Scale Logic Devices through Multistage Switching in a Luminescent Bimetallic Ru(II)-Terpyridine Complex. *Inorg. Chem.* **2024**, *63*, 14933-14942.

4. **Das, S.**; Bar, M.; Ganguly, T.; Baitalik, S. Control of Photoisomerization Kinetics via Multistage Switching in Bimetallic Ru(II)-Terpyridine Complexes. *Inorg. Chem.* **2024**, *63*, 6600-6615.

5. **Das, S.**; Pal, P.; Ganguly, T.; Baitalik, S. Influences of Both N,N,N- and N,N,C-Coordination Modes of Tolyl-Terpyridine on the Photophysical Properties of Cyclometalated Ru(II) Complexes: Combined Experimental and Theoretical Investigations on Acid/Base Dependent Reversible Cyclometalation. *Inorg. Chem.* **2023**, *62*, 12872-12885.

6. Ganguly, T.; **Das, S.**; Maity, D.; Baitalik, S. Luminescent Ruthenium-Terpyridine Complexes Coupled with Stilbene-Appended Naphthalene, Anthracene and Pyrene Motifs Demonstrate Fluoride Ion Sensing and Reversible Trans-Cis Photoisomerization. *Inorg. Chem.* **2024**, *63*, 6883-6897.

7. Sahoo, A.; Deb, S.; **Das, S.**; Baitalik, S. Multi-Channel Anion and Cation Sensing Conduct of a Terpyridyl-Imidazole Receptor: Experimental Demonstration and Implication of Artificial Intelligence Tools for Analysis and Data Prediction. *Dyes and Pigments* **2023**, *218*, 111425.

8. Paul, A.; **Das, S.**; Bar, M.; Baitalik, S. Tuning of Photo-Redox Behaviours and Thermodynamic and Kinetic Aspects of Intercomponent Energy Transfer in Trimetallic Complexes of Ru (II) and Os(II) by Exploiting Their Second Coordination Sphere. *Dalton Trans*. **2021**, *50*, 14872-14883.

9. Pal, P.; Ganguly, T.; **Das, S.**; Baitalik, S. pH-Responsive Colorimetric, Emission and Redox Switches Based on Ru (II)-Terpyridine Complexes. *Dalton Trans*. **2021**, *50*, 186-196.

Publications 1-5 are included in the thesis